eman ta zabal zazu

Universidad del País Vasco
Euskal Herriko Unibertsitatea

A study of the charge storage mechanism in iron rich transition metal layered oxides for sodium-ion batteries: structural evolution, reaction kinetics and high voltage stability

Author
Begoña Silván

Supervised by
Dr. Damien Saurel
Dr. Elena C. Gonzalo

May 2021

eman ta zabal zazu

Universidad del País Vasco
Euskal Herriko Unibertsitatea

CIC energiGUNE
energy cooperative research centre

A study of the charge storage mechanism in iron rich transition metal layered oxides for sodium-ion batteries: structural evolution, reaction kinetics and high voltage stability

A Thesis Submitted in Fullfillment of the Requirements for the degree of Doctor in Philosophy in Physics

University of the Basque Country
CIC Energigune

Author
Begoña Silván

Supervised by
Dr. Damien Saurel
Dr. Elena C. Gonzalo

Tutor
Dr. Francisco Javier Zúñiga

May 2021

UPPSALA UNIVERSITET

ÅABC
Ångström Advanced Battery Centre

Resumen

Las baterías de sodio ión están consideradas como una de las tecnologías más prometedoras como alternativa a las baterías de litio ión en aplicaciones donde el peso o el volumen no sean limitantes. Una de las aplicaciones más interesantes es el almacenamiento de la energía de red de fuentes renovables. Y es que el sodio, a pesar de ser más pesado y grande que el litio, es más económico debido a su mayor abundancia, distribución homogénea en la superficie terrestre, y su fácil procesamiento.

Uno de los puntos claves en la investigación de baterías es el estudio de los cátodos o electrodos positivos. Existen diferentes familias, entre las que se encuentran los óxidos laminares, $NaTMO_2$ (TM = metal de transición). Estos materiales son muy versátiles, ya que pueden ser sintetizados a partir de un gran abanico de compuestos, lo que deriva en una variedad de comportamientos.

Este trabajo se centra en el estudio de óxidos laminares ricos en hierro, ya que este elemento reúne varias características interesantes. Es un elemento abundante, no tóxico y de fácil procesado, lo que hace que sea un material fácil de conseguir y de bajo coste. Además, las propiedades electroquímicas se basan en la reacción de reducción-oxidación entre Fe^{3+} y Fe^{4+}, con uno de los voltajes más altos entre los metales de transición.

Sin embargo, estos materiales laminares, y especialmente lo basados en hierro, sufren de un deterioro estructural, ya que al cargarlos y extraer el sodio de sus estructuras, se está vaciando una de cada dos capas del material. Este deterioro se traduce a su vez en un deterioro de las propiedades electroquímicas, problema que ha de ser solventado antes de que se puedan comercializar.

Esta tésis tratará de entender el mecanismo de carga y descarga los óxidos $NaFeO_2$ y $Na_{2/3}Fe_{2/3}Mn_{1/3}O_2$, incluyendo los mecanismos de degradación, con el fin de extrapolar los resultados a otros óxidos. Se utilizarán técnicas de caracterización estructural para poder entender los cambios que se producen durante su funcionamiento, como son la difracción de rayos-X *operando* o espectroscopía de Mössabuer *in-situ*. Se determinarán además la evolución de la resistencia interna y el coeficiente de difusión iónico mediante las técnicas de espectroscopía de impedancia electroquímica y titulación potenciostática intermitente acopladas.

La tésis se divide en 11 capítulos, que si bien tratan temas independientes, se hace referencia a resultados presentados anteriormente, por lo que se recomienda su lectura en el orden establecido.

Capítulo 1. Introducción

Este capítulo pone en contexto la tesis. Tras una descripción general del porqué de la investigación en baterías de sodio-ión, se describe el funcionamiento de las baterías recargables. También se describe de un modo general el estado del arte en lo que a investigación de baterías se refiere, enfocándose de manera más detallada en los óxidos laminares como cátodos para baterías de sodio. Ya que este capítulo trata de justificar la motivación detrás de la realización de este trabajo, sólo se recoge información publicada hasta que se inició la tésis a mediados de 2016. Cabe destacar que los avances relacionados y publicados desde entonces están recogidos en los capítulos posteriores.

Capítulo 2. Técnicas experimentales

En este capítulo se recogen las técnicas que se han utilizado durante la realización de este proyecto, explicando brevemente los fundamentos de cada técnica. Además, se especifican tanto las carácterísticas de los equipos utilizados como los detalles experimentales relevantes para entender la elección de las configuraciones elegidas.

A partir del capítulo 3 y hasta el capítulo 10 se muestran los resultados experimentales obtenidos durante la realización de este trabajo. Los capítulos están separados en tres bloques:

- Breve introducción al capítulo. En un párrafo se explica el motivo del capítulo, así como lo que se va a encontrar en el mismo.
- Resultados experimentales, análisis de datos y discusión. Dependiendo de los resultados, la organización del capítulo será diferente. Aún así, en todos los casos se mostrarán los resultados así como el análisis realizado posteriormente. Generalmente los resultados serán comparados con otros resultados publicados para los mismos compuestos u otros similares.
- Conclusión del capítulo. Al final de cada capítulo se ha incluido una breve conclusión de los resultados y discusión presentados.

Capítulo 3. Síntesis y caracterización

En este capítulo se detalla el proceso de síntesis de los materiales a estudiar. Se estudian tres materiales isoestructurales de composición $Na_xFe_{1-y}Mn_yO_2$ ($y = 0, 0.1, 1/3$). También se realiza una caracterización de los materiales obtenidos para determinar

sus estructuras cristalinas mediante difracción de rayos X, y morfológicas mediante microscopía electrónica. Se realizan además caracterizaciones de espectroscopía de Mössabuer y magnetismo, con el fin de conocer las propiedades más importantes de los materiales que nos pueden ayudar a entender más adelante los mecanismos de carga.

La síntesis es satisfactoria para todos los compuestos, ya que se obtienen polvos con la estructura objetivo: óxidos laminares puros con estructura O3.

Capítulo 4. Caracterización electroquímica

Los materiales sintetizados y caracterizados en el Capítulo 3 son caracterizados electroquímicamente en este capítulo. Se utiliza la técnica galvanostática, es decir, la aplicación de una corriente continua, limitando la carga y descarga mediante el voltaje. Se realizan diferentes experimentos, limitando la carga o descarga a diferentes voltajes o aplicando mayores o menores corrientes. Este capítulo tiene como objetivo entender las diferentes propiedades electroquímicas de los materiales, para tratar de estudiarlas más adelante mediante técnicas más avanzadas.

Se puede ver como el comportamiento de los tres compuestos es el esperado, con dos voltajes de reacción correspondientes a las reacciones de oxidación-reducción del hierro y el manganeso. Así, si bien el compuesto con mayor cantidad de Mn es el que mayor capacidad presenta, la mejoría en términos de densidad de energía no es tan notable debido a un voltaje de reacción medio menor.

Capítulos 5 y 6. Caracterización estructural de $NaFeO_2$ y $Na_{2/3}Fe_{2/3}Mn_{1/3}O_2$

Después de observar las limitaciones electroquímicas de los compuestos, estos capítulos tienen como objetivo tratar de relacionar la degradación electroquímica con los cambios estructurales por los que pasan los compuestos al cargar (extracción de Na) y descargar (reinserción de Na) las celdas. Se estudian los compuestos límites, $NaFeO_2$ (Capítulo 5) y $Na_{2/3}Fe_{2/3}Mn_{1/3}O_2$ (Capítulo 6).

Para ello la principal técnica es la difracción de rayos-X *operando*, es decir, durante el funcionamiento de la celda. El análisis de los datos se llevará a cabo de diferentes maneras, para asegurarnos de que las aproximaciones realizadas con cada método están bien fundamentadas. Las medidas *operando* se realizan con diferentes límites de voltaje, para tratar de entender tanto la reversibilidad como el deterioro completo del material.

Basándonos en la hipótesis mencionada en la literatura de la migración de los iones de hierro fuera de sus posiciones, y con la ayuda de simulaciones de patrones de difracción, se desarrolla un método que permite la estimación de la migración de estos iones.

Además estos resultados son confirmados con la ayuda de la espectroscopía Mössbauer *in-situ*, es decir, sin necesidad de desensamblar la celda para ser medida.

Finalmente, se comparan los resultados obtenidos con los publicados reciéntemente, y se hace un análisis de las similutudes y diferencias de las distintas publicaciones.

En estos capítulos se observa que la migración de los iones de Fe ocurre muy pronto durante la carga, antes de que sea apreciable la degradación electroquímica de los compuestos. Sorprendentemente, la migración es parcialmente reversible, lo que deja intuir que quizá no sea un problema insolventable tal y como se creía. Es decir, el hecho de que la migración ocurra en cierto compuesto no ha de ser obligatoriamente un impedimento para su uso como electrodo en una batería.

Capítulos 7 y 8. Caracterización electroquímica avanzada de $NaFeO_2$ y $Na_{2/3}Fe_{2/3}Mn_{1/3}O_2$

Después de analizar en los capítulos anteriors los cambios estructurales de $NaFeO_2$ y $Na_{2/3}Fe_{2/3}Mn_{1/3}O_2$ durante el ciclado, los capítulos 7 y 8 tratan de responder a la pregunta de cómo afectan estos a las propiedades electroquímicas de los compuestos $NaFeO_2$ y $Na_{2/3}Fe_{2/3}Mn_{1/3}O_2$ respectivamente.

Para ello, se acomplan dos técnicas generalmente utilizadas de manera independiente: espectroscopía de impedancia electroquímica y titulación potenciostática intermitente. Ambas técnicas nos dan información sobre la evolución de las resistencias internas de la celda así como de la difusión de los iones de Na durante los procesos de carga y descarga. Al utilizar ambas técnicas simultaneamente podemos comparar los resultados y comprobar que las aproximaciones utilizadas para uno y otro método son aceptables.

Los resultados obtenidos son comparados con aquellos publicados previamente para este material.

En estos capítulos podemos observar que la difusión iónica de estos compuestos no se ve afectada por su ciclado. Tal y como se ha visto en capítulos anteriores, a estados de desodiación altos, iones de hierro de encuentran en las capas de sodio, lo que podría dificultar su difusión, pero no es así. Sin embargo, sí que existe un aumento de la resistencia de transferencia de carga, que se traduce en un aumento de la histéresis de voltaje y una reducción de la reversibilidad electroquímica.

Capítulo 9. Estudio del efecto de la estructura inicial

Lo materiales estudiados hasta este momento comparten la característica de la estructura inicial, una estructura O3. Sin embargo, se ha demostrado que las estructuras tipo P son más reversibles electroquímicamente hablando.

En este capítulo se compara la evolución estructural del compuesto P2-$Na_{2/3}Fe_{2/3}Mn_{1/3}O_2$, ya que el hecho de tener la misma composición química que la muestra O3-$Na_{2/3}Fe_{2/3}Mn_{1/3}O_2$ combierte este compuesto un buen punto de partida para su comparación. Para ello, se analizan resultados de difracción de rayos-X *operando* y se hace una comparación directa de las características con aquellas de O3-$Na_{2/3}Fe_{2/3}Mn_{1/3}O_2$ presentadas anteriormente en el Capítulo 6.

Podemos ver que efectivamente la reversibilidad del compuesto de estructura P2 es mayor que la del compuesto con estructura O3. Generalmente se ha asociado a que en las estructurasl tipo P no se da la migración de metales de transición a las capas de sodio. Sin embargo, en este capítulo vemos que no es así, que la migración ocurre igualmente. La mayor reversibilidad está asociada con la estructura en la que la migración ocurre. La estructura "Z", que se da en compuestos P desodiados, es más resistente a cambios irreversibles debido al apilamiento aleatorio entre capas O (inestables) y capas P (estables).

Capítulo 10. Discusión

Este capítulo recoge los resultados y conclusiones de los capítulos anteriores y, junto a las conclusiones más recientemente publicadas, trata de dar un sentido global a todas las observaciones realizadas para los materiales analizados. Así, también trata de extrapolar las conclusiones para dar sentido al comportamiento general de los óxidos laminares, y no sólo a los analizados en este trabajo.

Basándonos en la literatura recogida para óxidos laminares ricos en litio, llegamos a la conclusión de que la migración de Fe está relacionada con la oxidación del oxígeno. Así mismo, cuando los compuestos se cargan a alto voltaje, la oxidación del oxígeno da paso a la creación y evolución de oxígeno gas. Este efecto, irreversible en todo caso, está acoplado con la imposibilidad de los iones de metal de transición para volver a sus posiciones originales. Así, aumenta la transferencia de carga de manera irreversible aumentando la histéresis de potencial y reduciendo la capacidad reversible de estos compuestos.

Capítulo 11. Conclusiones

Finalmente, las conclusiones obtenidas a lo largo de todo el trabajo se recogen en este breve capítulo, a modo de resumen, ya mencionadas en este resumen para cada capítulo.

Abstract

Sodium-ion batteries are considered to be one of the most promising alternatives to lithium-ion batteries when the applications are not limited by battery volume or weight. One of the most interesting applications is the energy storage from renewable energy sources. Indeed, sodium is bigger and heavier than lithium, but it is also cheaper due to its higher abundance, homogeneous distribution on the Earth's crust, and its easy processing.

One of the key steps in battery research is the study of the cathodes or positive electrodes. There are various families, among which layered oxides can be found, $NaTMO_2$ (TM = transition metal). These materials are very versatile, because they can be synthesized from a wide variety of compounds, which results in a wide range of working responses.

This work is focused on the study of iron-rich layered oxides, as this element comprises various interesting characteristics. It is an abundant and non-toxic element, which is easy to process, and is therefore a cheap material. Moreover, the electrochemical properties are based on the reversible reduction-oxidation reactions between Fe^{3+} and Fe^{4+}, which presents one of the highest potentials between the transition metals.

However, these layered materials, and especially those based on iron, suffer from a structural degradation. Indeed, during charge, when sodium ions are extracted from the structure, one every two layers is being emptied. This degradation is further translated in a degradation of the electrochemical properties, a problem that needs to be addressed before these materials can be commercialized.

This thesis will try to understand the charge and discharge mechanism of the $NaFeO_2$ and $Na_{2/3}Fe_{2/3}Mn_{1/3}O_2$ oxides, including the degradation mechanisms, and will try to extrapolate these results to other layered oxides. Different techniques will be used to try to asses the changes occurring upon cycling, such as *operando* X-ray diffraction o *in-situ* Mössbauer spectroscopy. Moreover, the evolution of the internal resistance and ionic diffusion coefficient will be determined by means of coupled electrochemical impedance spectrosocpy and potentiostatic intermittent titration techniques.

Laburpena

Sodio-ioi bateriak litio-ioi baterien etorkizun handiko alternatibatzat hartzen dira, beti ere, tamaina eta pisua kontuan hartu ez beharreko erabileretan. Erabilera interesgarrienetako bat, energia iturri berritzaileen energiaren metaketan datza. Izan ere, nahiz eta sodioa litioa baino handiagoa eta pisutsuagua den, bere ugaritasuna, lurrazalean duen banaketa homogeneoa eta bere prozesamendu erraza dela eta, litioa baino merkeagoa da.

Baterien ikerketako gako bat, katodo edo elektrodo positiboen ikerketan datza. Familia ugari daude, haien artean oxido laminarrak, $NaTMO_2$ (TM = trantsizio metala). Oso material moldakorrak dira. Izan ere, elementu ugariz sintetizatu daitezke, eta honek, portaera ugari dakartza.

Lan hau burdinean aberatsak diren oxido laminarretan oinarritzen da, elementu honek hainbat ezaugarri interesgarri batzen baititu. Elementu ugaria, ez-toxikoa eta prosezamendu errezekoa da, eta beraz, lortzeko material merkea da. Gainera, ezaugarri elektrokimikoak Fe^{3+} eta Fe^{4+} oxidazio egoeren arteko oxidazio eta erredukzio erreakzio itzulgarrietan oinarritzen da, trantsizio metalen artean dauden potentzial altuenetako bat.

Hala ere, material laminar hauek, eta batez ere burdinean oinarritutakoak, egituren hondatzea pairatzen dute. Izan ere, hauek kargatzean eta sodioa haien egituretatik ateratzean, bi geruzetatik bat husten ari da. Egitura hondatze honek, propietate elektrokimikoen hondatzea dakar, materiala komertzializatu ahal izateko konpondu beharreko arazoa.

Tesis honetan $NaFeO_2$ eta $Na_{2/3}Fe_{2/3}Mn_{1/3}O_2$ oxido laminarren karga eta descarga mekanismoa ulertzen saiatuko gara, hondatze mekanismoak barne, gero beste oxido laminarren portaera estrapolatzeko. Egitura karakterizazio teknika desberdinak erabiliko dira, lanean dagoen bitartean burutzen diren aldaketak ulertu ahal izateko. Horrela, *operando* X-izpien difrakzioa edo *in-situ* Mössbauer espektroskopia teknikak erabiliko dira. Gainera, barne erresistentzia eta difuzio ionikoaren koefizientea kalkulatuko dira, akoplaturiko inpedantzia elektrokimiko espektroskopia eta aldikazko titrazio potentioztatiko teknikak erabiliz.

Acknowledgements

Este trabajo ha sido posible gracias a la ayuda y colaboración de muchas personas.

Me gustaría empezar agradeciendo a mis directores de tesis por todo su apoyo y por todo lo que me han enseñado durante estos años. Gracias a Elena y Damien (merci!) por guiarme en cada paso, por pequeño que fuera. A Elena por enseñarme practicamente todo lo que sé de electroquímica y química en general, incluso moverme por el laboratorio. A Damien por mirar con ojo crítico cada resultado (e intertar enseñarme a hacerlo), y por ayudarme con la parte más relacionada con la física del proyecto. Y gracias a los dos por confiar en mi y por vuestra paciencia. Por lo que me habéis enseñado relacionado con la ciencia y fuera de ella.

Por supuesto al centro CIC Energigune por darme la oportunidad de trabajar en el centro y por la ayuda económica, así como al Ministerio de Economía y Competitividad (proyecto ENE2016-75242), y al Gobierno Vasco (proyecto ELKARTEL CICE17), and to the Australian Research Council (DE160100237/DP1701002). To all the ALBA staff in the beamlines BL04-MSPD (proposals 2016021566, 2017021977, 2018082922), BL22-CLÆSS (proposal 20180228002) and BL29-BOREAS (proposal 2019093921), and Australian Synchrotron staff at the Powder Diffraction beamline: Neeraj Sharma and his students in University of New South Wales (Australia), Marcel Risch and students in Gottingen University (Germany), Francois Fauth and Wojciech Olszewski, and the short nights at Alba Synchrotron.

A Maria Jauregi, por todas esas horas que ha pasado trabajando conmigo (o para mi) incluso en sus días libres. A Francisco Bonilla por las medidas de TEM y su análisis. Aunque hayan quedado fuera de este manuscrito, a Rosalía y Afshin por las medidas de XPS y su análisis; a Lian y Javi por los cálculos DFT. A Gene, Carlos y Montse G. por las medidas de XAS, y a Rosalía por ayudarme con la configuración experimental y análisis. Al resto de compañeros que me han ayudado con todo tipo de problemas o han colaborado haciendo medidas, analizando datos o con discusiones a la hora del café (Maider, Nuria, Montse Casas-Cabanas, Montse Galceran, Marine, Maria E., Guillermo, Begoña A.... y podría meter a prácticamente todo el CIC).

A todos los compañeros de penurias (a.k.a. doctorandos y recientes doctores de CIC, no os voy a nombrar a todos, pero ya sabéis quienes sois), y especialmente a Xabi y

María junto a quienes empecé hace ya unos cuantos añitos y con quienes he compartido tanto tiempo. A Ane y Nebil ya tal. Anna , Cristina... y los que han estado tanto dentro como fuera del CIC.

Of course, to all those people who helped me during the stay at Ångström laboratory (Ronnie and his stay-saving electrolyte). Special thanks to Mario Valvo, who despite being very busy he always made time to answer my silly questions. Of course, to the Mössbauer spectroscopy experts, Lennart Häggström and Tore Ericsson, who taught me everything about this technique that appears in this work and even more (Tack så mycket!). And to everyone else who showed me around the lab, with whom I shared interesting scientific (or not) conversations and great times. I cannot name you all, but I have to name Guiomar, muchas gracias por toda tu ayuda! A mi gemela, que primero me hizo un huequito en su mesa de laboratorio y luego en su casa de Suecia. Y no menos importante, a la familia Widehammar por su acogida como una más de la familia, y Kiara por la compañía.

To people at Lancaster University, that have received with open arms (respecting social distance, that is) before I could finish this work. Especially to Nuria Tapia-Ruiz for giving me the chance to work with her and all her patience, gràcies.

A las amigas que me llevan aguantado años, y los que les quedan. Gracias por escucharme y asentir aunque no supierais de qué estaba hablando. A los compañeros del agua, que me han ayudado a despejar la mente al menos durante 4 horitas semanales. Iván, te debo unas cuantas. And to Rob.

A Anton, aita, ama y toda la familia. Especialmente a quien vio el comienzo y no ha pedido ver el final de este proyecto.

Era batean edo bestean tesi hau burutzen lagundu duzuen guztioi.

If in doubt, paddle out.
Nat Young

Contents

List of Figures

List of Tables

Acronyms

ACMS	AC/DC magnetometry system
AM	active material
CFT	crystal field theory
CPE	constant phase element
CS	center shift
DF	dynamic factor
DFT	density functional theory
EC	ethylene carbonate
EDX	energy dispersive X-ray spectroscopy
EIS	electrochemical impedance spectroscopy
FC	field cool
FWHM	full width at half maximum
GEIS	galvanostatic electrochemical impedance spectroscopy
GITT	galvanostatic intermittent titration technique
HOMO	highest occupied orbital
HRXRD	high resolution X-ray diffraction
HS	high spin
ICP-OES	inductively coupled plasma optical emission spectrometry
JT	Jahn-Teller
KB	Ketjenblack
LIB	lithium-ion battery
LS	low spin
LUMO	lowest unoccupied orbital
MF	morphological factor
MSPD	Material Science and Powder Diffraction
NMP	N-Methyl-2-pyrrolidone
OCV	open circuit voltage
PC	propylene carbonate
PEIS	potentiostatic electrochemical impedance spectroscopy
PITT	potentiostatic intermittent titration technique
PPMS	physical property measurement system
PVdF	polyvinylidene fluoride
QS	quadrupole splitting

SAXS small angle X-ray scattering
SEI solid electrolyte interphase
SEM scanning electron microscopy
SG space group
SIB sodium-ion battery
SILD semi-infinite linear diffusion
SOM spin only moment
SPI solid permeable interface
STEM scanning transmission electron microscopy
TEM transmission electron microscopy
TF thermodynamic factor
TM transition metal
TMLO transition metal layered oxide
XAS X-ray absorption spectroscopy
XPS X-ray photoelectron spectroscopy
XRD X-ray diffraction
ZFC zero field cool

1 Introduction

Contents

1.1 Energy storage

The continuous industrial and economic growth of our society is directly translated into a steady increase in the world energy consumption as can be observed in Fig. 1.1. Indeed, since 1965 until 2018 the energy consumption has increased by about 275% [1], and a 28% growth until 2040 is forecast [2]. Most of the consumed energy comes from non-renewable energy sources, but in the recent years the renewable energy sources are the fastest growing energy source, as it can be appreciated with blue tones in Fig. 1.1. However, more than 80% of the energy consumed in 2018 still came from fossil fuels. As can be seen from Fig. 1.1 (discontinuous red line) the energy consumption is correlated with the carbon dioxide gas emission, which is the major human influence in global warming [3].

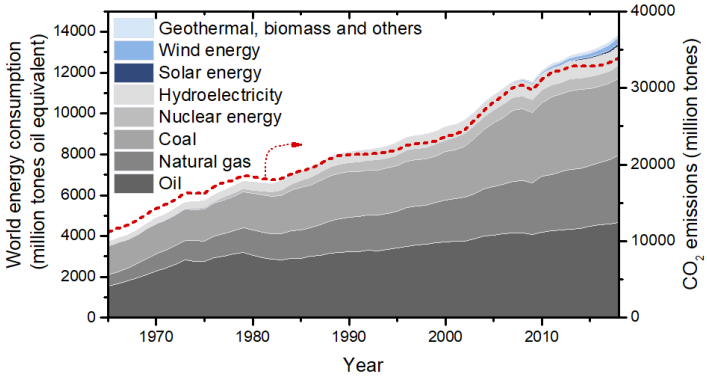

Figure 1.1: World energy consumption by energy source (solid colors, in gray tones for non-renewable energy sources and blue tones for renewable energy sources) and CO_2 gas emission due to energy generation (dashed red line) (1965-2018) [4].

The fast increment in the use of renewable energy sources is linked to the efforts that are being made worldwide to reduce the contaminant emissions, a research that started in the late 90s [5]. Within this scope, in 2016 the first legally binding universal agreement was reached in order to limit the global warming, in which 55 countries were included representing at least 55% of the global emissions [6]. During the year 2019, while the global emissions reached record levels, a call for the Climate Action Summit was done, with the final aim of reducing the CO_2 emissions to zero by 2050 [7]. This action requires concrete initiatives. Among others and in the context of this agreement, the European Union promotes the use of energy from renewable sources, including solar energy, wind power or geothermal for example. The main drawback of these sources is their time fluctuation and the associated uncertainty. To overcome this uncertainty and to have available energy whenever is required, energy storage technology for stationary applications is demanded. There are many types of electrical energy storage systems such as pumped hydroelectric, compressed air, fuel cells, flywheels, capacitors and several kinds of rechargeable batteries. The challenge is to develop energy storage systems that are competitive with the well-established

energy producing fossil-fuel technologies [8]. Nowadays, pumped hydroelectric is the most used energy storage system, which stores the 96% of the total stored energy [9]. However, as reflected in Table 1.1, there are many systems with higher energy density and conversion efficiency values, such as batteries. Indeed, and in comparison with other commonly used technologies, it can be seen that lithium-ion batteries (LIBs) have both high energy density and high efficiency values [10, 11]. Since the first commercialization of a Li-ion battery in 1991, they have been widely used to power portable electronic devices, and are already among the most used energy storage systems in mobile devices and electric transport applications [12].

Table 1.1: Comparison of major energy storage systems. The average energy density, efficiency and lifetime are presented [13–17].

Storage system	Energy density (W h kg^{-1})	Efficiency (%)	Lifetime (cycles)
PHE	0.3-1.3	65-80	20-80*
CA	3.2-60	60-80	20-40*
Flywheel	5-200	45-90	15-20*
TES	10-200	40-70	4000
Fuel-cell	300-600	30-85	1000
Capacitor	0.05-5	85-95	10^6
Pb-acid	30-40	60-90	200-500
Ni-Cd	40-60	50-75	500
NiMH	75-100	60-80	300-500
LIB	100-250	70-95	500-1000

* Lifetime in years

PHE: pumped hydroelectric; **CA**: compressed air; **TES**: thermal energy storage; **Pb-acid**: lead-acid battery; **Ni-Cd**: nickel-cadmium battery; **NiMH**:nickel metal-hydrade battery; **LIB**: lithium-ion battery

1.2 Historical context

A battery is a device that is able to convert chemical energy into electrical energy. Two different kind of batteries can be defined, the primary and the secondary ones. The primary batteries are able to convert chemical energy into electrical energy. The secondary batteries are able to do this conversion in a reversible manner. This is an interesting characteristic for their use in mobile and stationary energy storage applications.

In the brief timeline of the battery history presented in Fig. 1.2 one can see that although the primary battery was first described by Alessandro Volta in 1800 [18], it was not until 1859 that the first secondary battery was described, a lead-acid battery [19]. Nowadays lead-acid (Pb-acid) and nickel based batteries, such as nickel-metal hydride (NiMH) and nickel-cadmium (Ni-Cd), are common in everyday applications. Efforts are being made to replace these batteries for those containing non-toxic elements or with better electrochemical properties. In this context,

the first electrode materials for Li-ion batteries were proposed in the early 80s, such as $LiCoO_2$ for the cathode side and graphite for the anode side. The research is now focused in post-lithium technologies, among which sodium-ion batteries (SIBs) are the most studied ones.

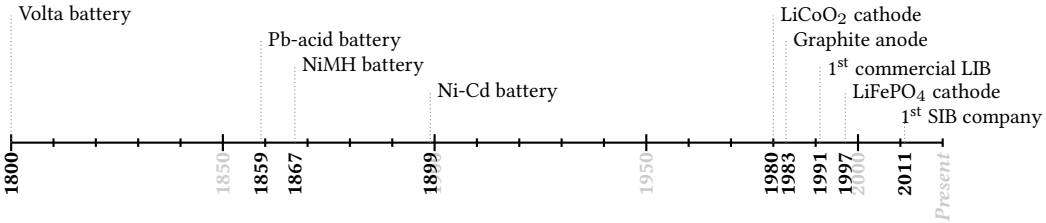

Figure 1.2: Brief timeline of the battery history. Data taken from Refs. [18–24].

The first commercial lithium-ion battery (LIB) was developed by Sony in 1991 with a layered oxide cathode, $LiCoO_2$, and a carbon anode [25], and nowadays lithium cobalt based layered oxide are still among the most common cathode materials in commercial LIBs, such as $Li(Ni,Mn,Co)O_2$ or $Li(Ni,Co,Al)O_2$. Lithium-ion batteries are widely used owing to their good electrochemical performance and lower toxicity comparing to other rechargeable battery systems [26]. They are good candidates to replace Pb and Ni containing batteries used in transport applications nowadays, due to their higher gravimetric energy densities and improved lifespan (see Table 1.1). Indeed, LIBs are successfully used in hybrid electronic vehicles and in mobile electronic devices [12, 27, 28]. Due to the increment of battery demand for their use in electric vehicles and mobile applications, cheap and non-toxic based materials have been investigated to substitute the cobalt based cathode materials in the batteries. In this context, the iron based phosphate cathode ($LiFePO_4$) was discovered in 1997 [22] and it has gained a market share for its properties. Indeed, this material is made from earth abundant elements, hence its low cost, and is stable at any state of charge. However, the electric vehicle battery market is forecast to increase over 50% in the next five years [29], and the grid-energy storage over 300% in the next five years, and over 1000% by 2040 [30]. This increment in the demand will require high amounts of raw materials. Geographically lithium is inhomogeneously distributed and 89% of its supply is controlled by four companies [31]. This, along with the increasing demand and the consequent reduction of its reserves, can result in a critical increase of Co and especially Li price [32]. Subsequently, new systems are being considered as an alternative to LIBs, such as sodium-ion batteries (SIBs), magnesium-based, calcium-based or metal air batteries. In addition, the replacement of toxic elements commonly used in LIBs by non-toxic and sustainable elements is also investigated [32–35].

1.3 Rechargeable batteries

A schematic representation of a secondary battery is presented in Fig. 1.3. It consists of a positive electrode (commonly called cathode in the battery research field), a negative electrode (commonly

called anode) and the electrolyte, which is an ionic conductor and electronic insulator medium. The single electrode-electrolyte-electrode stack is called a cell, and a battery is a collection of cells. A cell or a full-cell is composed of two half-cells. Each of them is composed of an electrode and the electrolyte. A common way to study the electrode materials is to study a half-cell vs. a counter electrode with a constant potential. In the case of Li-ion or Na-ion half-cells, the counter electrode consists respectively of metallic Li or Na. This counter electrode is overdimensioned, that is, it can store more charge than the working electrode.

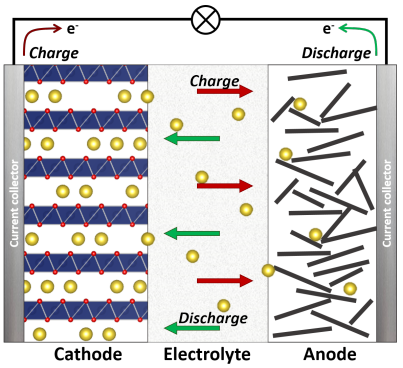

Figure 1.3: Schematic representation of a battery, with a layered transition metal oxide cathode and a carbon based anode. The positively charged ions are represented as yellow spheres.

The energy transformation between electronic and chemical energies occurs through the oxidation and the reduction of the electrodes. When the cell is being discharged (i.e. producing energy), a reduction reaction occurs in the cathode (potential μ_c), so the oxidation state of the material decreases and gains electrons. The oxidation reaction takes place simultaneously in the anode (potential μ_a), with a loss of electrons and an increase of the oxidation state of the material. To maintain the electro-neutrality, positive ions move from the anode to the cathode through the electrolyte, while the electrons move through an external circuit. The voltage of the battery, V_0, will correspond to the difference of the electrochemical potential of the two redox pairs, as shown in Fig. 1.4a [36–39]:

$$V_0 = \frac{\mu_a - \mu_c}{e} \tag{1.1}$$

In principle, the voltage does not depend on if the battery is being charged or discharged. However, and due to the internal battery resistances, the voltage during charge and discharge will be above and below the equilibrium voltage (V_0) respectively [39], as presented in Fig. 1.4b. The difference between the equilibrium voltage and the experimental result is called overpotential (OP).

Several concepts and terminology that will be used in the next chapters will be defined below.

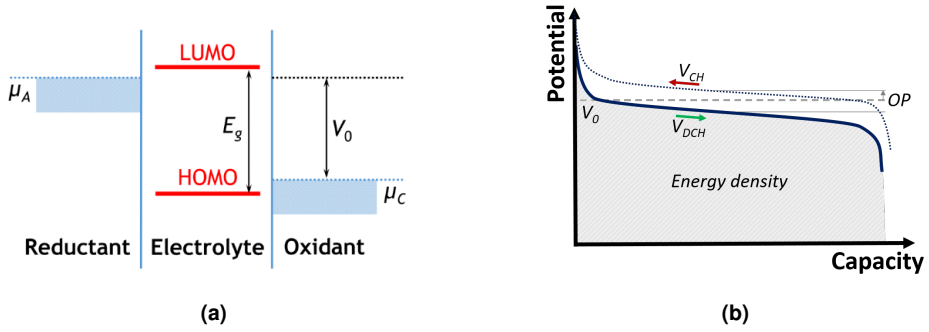

Figure 1.4: **(a)** Relative energies of the electrolyte window E_g and anode and cathode electrochemical potentials μ_a and μ_b respectively [39]. **(b)** Schematic representation of the voltage profile of a battery, where the equilibrium voltage (V_0), the overpotential (OP) and energy density as the integrated area are shown.

The capacity of a cell or a battery is a measurement of the amount of charge that can be stored in it. The value is generally normalized by weight or volume, which is then referred as the gravimetric or volumetric capacity respectively. The theoretical capacity is the maximum possible charge that an electrode can deliver in the ideal case that all the active material is reversibly used without any degradation. It can be calculated with the following expression:

$$Q_0 = \frac{nF}{M_m} \tag{1.2}$$

where n is the amount of electrons transferred per formula unit, F is Faraday's constant and M_m is the molar mass of the active material.

A common way to characterize the batteries is the galvanostatic cycling, where a constant current is applied between the electrodes forcing the charge transfer between them at a specific rate. The cycling rate, expressed as C/t is calculated as the time t that a certain material would need to reach the theoretical capacity.

The energy density of a battery is a measurement of the electrical energy that can be stored in the battery. As with the capacity, is generally normalized per weight or volume, and is then referred as gravimetric or volumetric energy density respectively. The theoretical energy density is given as:

$$E_0 = V_0 \times Q_0 \tag{1.3}$$

Thus, a maximization of both V_0 and Q_0 are required to increase the energy density of the battery.

Loss of energy in batteries has to be also considered as in any other real device. The energy provided to the system is always higher than the energy retrieved afterwards. The efficiency of a battery is commonly measured as Coulombic efficiency (CE) that describes the efficiency of the electron transfer. It can be calculated with the following expression in % units:

$$CE = \frac{Q_{DCH}}{Q_{CH}} \times 100 \tag{1.4}$$

where Q_{CH} and Q_{DCH} refer to the charge and discharge capacities respectively. A CE below 100% is related to an irreversible degradation of the material, and the lost capacity is never recovered in a full cell. However, the capacity loss can be compensated in half-cells obtaining the charge from the overdimensioned counter electrode.

The efficiency can also be measured in terms of stored energy, the round trip efficiency (RTE):

$$RTE = \frac{E_{DCH}}{E_{CH}} \times 100 \tag{1.5}$$

where E_{CH} and E_{DCH} refer to the charge and discharge energy respectively. In RTE, as opposed to Coulombic efficiency, the voltage hysteresis is accounted in the efficiency.

In Fig. 1.4b, the discharge energy density is shown as the integrated voltage curve, as the equilibrium voltage and the theoretical capacities are never reached in a real system.

All the battery components, active or not, should ideally be stable within the potential window at which the cell will be exposed to avoid its premature degradation. The potential of the redox pairs has to be ideally within the electrolyte window E_g, between the highest occupied orbital (HOMO) and the lowest unoccupied orbital (LUMO), to avoid electrolyte degradation upon cycling (see Fig. 1.4a). Otherwise, the electrolyte will spontaneously decompose. However, when this is associated with the formation of a passivation layer (solid electrolyte interphase (SEI) in the anode side and solid permeable interphase (SPI) in the cathode side) it can also protect the electrodes and electrolyte from further degradation [40, 41]. To passivate efficiently the electrodes, these layers need to be formed in a controlled manner with as little consumption of charges as possible, and be ionic conductors to not increase the internal resistance of the battery [38, 42].

There are different working mechanisms in secondary batteries: insertion, alloying, conversion, precipitation or shuttling. An schematic representation of these mechanisms is presented in Fig. 1.5. Note that although figures used above are based in insertion materials, the terminology used up to this point is common for all the secondary types.

Nowadays the most used electrodes are based on the insertion mechanism, where the alkali ion is reversibly intercalated from a host structure without major structural changes. The intercalation can occur either homogeneously (solid solution mechanism) or inhomogeneously (biphasic mechanism) as depicted in the top part of Fig. 1.5a. This mechanism has been thoroughly studied and many well performing materials are known. However, this kind of materials generally have limited theoretical capacity values [43].

The alloying and conversion type electrodes generally present a large improvement in the capacity with a cost in the efficiency. Alloying materials are based on the alloying of a metallic or semi-metallic compounds and alkali ions (see middle part of Fig. 1.5a). The mechanism leads to large volume changes that compromise the structural stability of the material. This results in low Coulombic efficiency values. Conversion mechanism is usually referred to the reaction between alkali metal and a binary transition metal compound, where the full reduction of the metallic compound is obtained (see bottom part of Fig. 1.5a). However, this kind of materials

usually present low round trip efficiency values due to large voltage hysteresis between oxidation and reduction reactions [43].

In metal-air batteries the metallic lithium or sodium reacts with the oxygen, and A_2O_2 superoxide (where A = Li, Na) precipitates to the surface of the electrodes (see Fig. 1.5b) [44]. However, the instability of the precipitated species within the electrolyte needs to be addressed [45].

In metal-S batteries (Fig. 1.5c) polysulfide chains are created. These chains are supposed to stay at the cathode side, but the partially oxidized sulfur chains are easily dissolved in the electrolyte. This way, they can travel from one electrode to another resulting in a short-circuit of the cell [46].

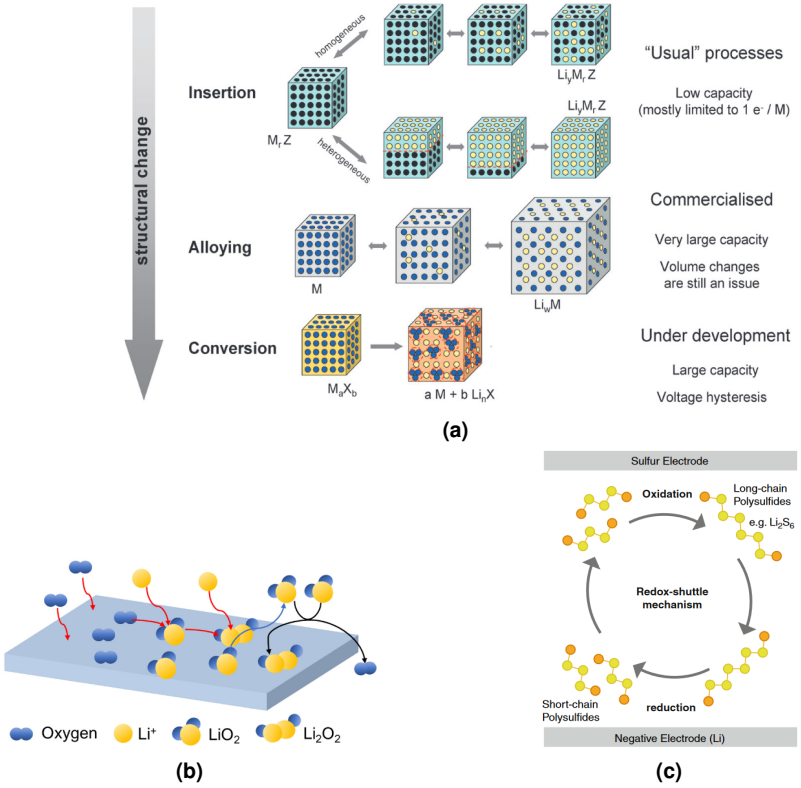

Figure 1.5: A schematic representation of the reaction mechanisms observed in electrode materials for secondary lithium batteries. **(a)** Insertion, alloying and conversion mechanisms, where lithium is presented with yellow circles, metals in blue, and voids in the crystal in black [43]. **(b)** Precipitation type, specific for metal-air batteries (Li-air in this figure), where Li is presented in yellow and oxygen in blue [44]. **(c)** Shuttle mechanism, specific of metal-sulfur batteries (Li-S in this figure), where Li is presented in orange and S in yellow [46].

Since this work will be based in the study of insertion compounds, the following definitions are characteristic of this type of materials.

In intercalation or insertion type compounds, the voltage profile of a battery will be defined by

the band structure. A discontinuous density of states function in cathode materials leads to a step-like discharge curve (Fig. 1.6a), while a continuous density of states function leads to a monotonic curve according to Gibbs' rule (Fig. 1.6b) [47].

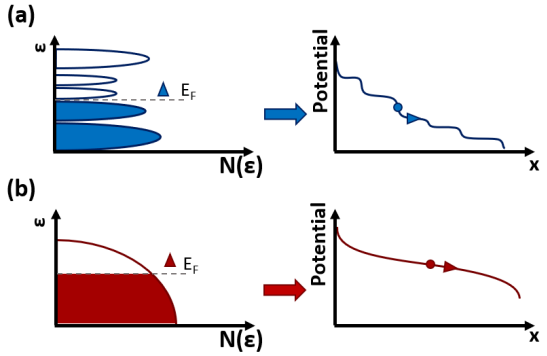

Figure 1.6: Band structure examples of an A_xTMO_2 cathode, where A can be Li or Na, and the resulting **(a)** step-like or **(b)** monotonic voltage profile. The Fermi level and its corresponding point in the voltage curve are shown with E_F and a circle respectively. Their movement upon discharge are marked with arrows.

The band structure of the material is defined by its thermodynamic properties. Biphasic structural transformations are usually reflected as a plateau in the voltage curve while solid solutions are reflected with a slopping profile due to changes in the band structure upon alkali ion density change [48, 49]. The changes in the transition metal oxidation state, the intercalation of alkali-ions and the structural changes can also result in a change of the band structure, and therefore, in the voltage profile. That is, the energy bands are not static, and they can be separated or united upon cycling. An example of the band structure change with alkali ion removal can be seen in Fig. 1.7 for the layered $LiCoO_2$ compound, which is one of the reference materials in commercial lithium-ion batteries [42]. In this example the cathode is cycled against metallic Li. The operating voltage will continuously increase, as the energy difference between the Fermi level (E_F) and the lithium metal (Li) is also increasing.

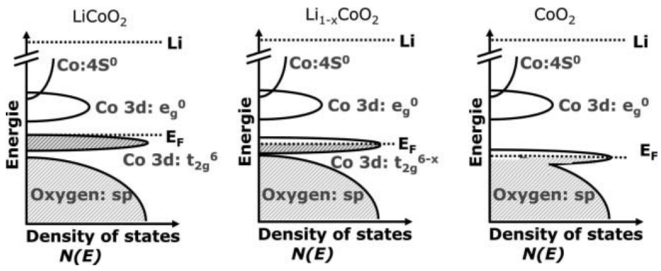

Figure 1.7: Schematic band structure evolution of a cathode ($LiCoO_2$) upon charging [42].

Many parameters unrelated to the active material can also affect the voltage and the capacity values, such as temperature, cycling rate, particle morphology or cycling voltage range [39]. For example, a fast charge-discharge cycling (high C rate) generally increases the polarization, lowers the capacity and inclines the plateau due to a limited mass-transport and to the electronic resistance [37].

1.4 Sodium-ion batteries

Research on the electrochemical properties of Na and Li intercalation compounds started together in the 70s, but research on sodium based batteries decreased in the following decades, probably due to the lower available energy density for Na based systems compared to the commercially successful Li-ion technology that appeared in 1991 [50]. The Fig. 1.8 shows the number publications on Na-ion in the electrochemistry research field, where it can be seen the drastic increment of the publication number after 2010.

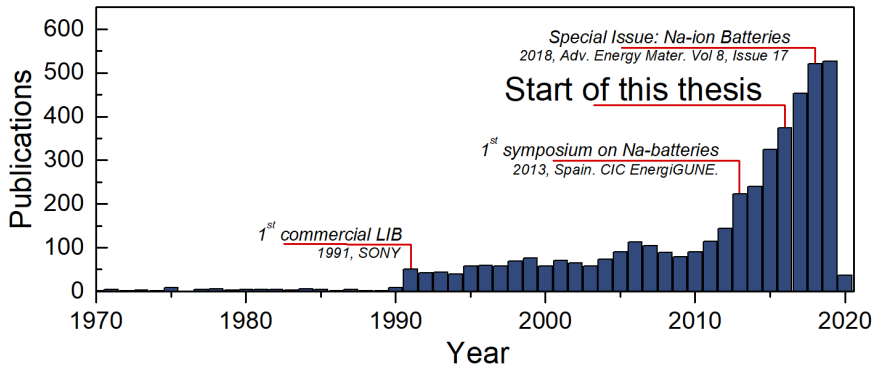

Figure 1.8: Number of publications related to the sodium-ion energy storage from 1970 until January 2020. Data obtained from the Web of Science, searching *Na-ion* or *sodium-ion* keywords under *electrochemistry* research field.

Li and Na, being both alkali metals, share physicochemical properties, hence SIB research can follow the already established LIB research work and fabrication system. Nevertheless the technology cannot be simply transferred from Li- to Na-based, because sodium ion is heavier ($m_{Na} = 22.99$ g mol^{-1}; $m_{Li} = 6.94$ g mol^{-1}) and has a larger radius ($r_{Na^+} = 102$ pm; $r_{Li^+} = 76$ pm). Due to the bigger size and heavier weight of sodium, mass diffusion and specific capacity values are affected [32, 51–53].

Moreover, sodium has a 340 mV higher standard electrode compared to Li [54, 55], which leads to lower operating cell potential in SIBs, and therefore, a lower energy density. This means that the active electrochemical window is 340 mV shorter for Na-ion. The materials that show Li intercalation below 340 mV, will result in Na plating instead. Thus, Na-ion technology still needs to be improved to become competitive in the battery market. However, in the last years the

research on SIBs is growing and many materials have been reported to work within the market standard requirements. Indeed, there are already a few number of companies that commercialize sodium-ion batteries, such as Faradion in the United Kingdom [24], Tiamat in France [56], Natron in the United States of America [57] or HiNa in China [58].

SIBs are best suited for applications where gravimetric and volumetric energy densities are not a limiting factor but cost-effective technologies are required, such as grid-storage applications.

Indeed, sodium-ion technology presents various advantages compared to LIBs [32, 59, 60]:

- Sodium is more abundant in the Earth's crust, and is homogeneously distributed. Therefore, its acquisition is easier and its price lower.
- Cobalt free sodium cathodes based on cheap, non-toxic and abundant Fe and Mn have been reported, which makes Na-ion technology potentially cheaper and safer than the Li-ion one.
- Sodium, as opposed to lithium, does not alloy with aluminum at low potentials. Therefore, the commonly used copper current collector in LIBs, can be substituted by the lighter and cheaper aluminum one.

1.4.1 Electrolytes

By similarity with the LIB technology, the most common electrolytes used in SIBs are based on organic carbonate solvents, such as ethylene carbonate, propylene carbonate or dymethyl carbonate. In order to achieve the best properties, a mixture of solvents is generally used. The stability of the solid electrolyte interphase (SEI) layer is a general issue, which is markedly different between lithium- and sodium-based technology, and that will depend on the solvent and the salt of the electrolyte, as well as the nature of the anode [61, 62]. The most common salts for sodium-ion batteries are sodium hexafluorophosphate ($NaPF_6$) and sodium perclorate ($NaClO_4$), followed by NaTFSI ($NaC_2F_6NO_4S_2$) and NaFSI ($NaF_2NO_4S_2$) [63]. In 2012 a thorough study of various solvent and salt combinations showed that, for hard carbon electrodes, the best choice was $NaClO_4$ or $NaPF_6$ salt in a mixture of ethylene carbonate (EC):propylene carbonate (PC) solvents [61].

Due to the high volatility and flammability of carbonate based electrolytes, research is shifting towards ionic liquids, aqueous or solid electrolytes. However, these electrolytes still need to improve their characteristics to outperform the carbonate based electrolytes, as it can be the high price of ionic liquids, the reduced voltage window of the aqueous electrolytes or the poor conductivity at room temperature of the solid electrolytes [64–66].

1.4.2 Anode materials

In the case of anode materials, low reaction potentials are desirable in order to increase the potential difference with the cathode and therefore, increase the energy density. Moreover, the materials with flat plateaus are generally sought in order to obtain batteries with a constant energy supply. However, voltages close to 0 V vs. Na^+/Na should be avoided to prevent the possible sodium plating. Sodium plating is the formation of a metallic Na layer, that can easily react with the electrolyte

or form dentrites which may end short-circuiting the cell inducing safety issues. Moreover, the deposited Na can lose electric contact with the anode, leading to a dead Na weight and thus, to a rapid capacity fading [67]. Beyond Na plating, most of the issues of anode materials in SIBs come from the fact that, like graphite in LIBs, they need to operate above the LUMO of the electrolyte to ensure large potential difference, inducing electrolyte decomposition. Like in LIBs a SEI is formed, but it tends to be less stable in the case of SIBs [31].

The most studied anode material's operating potential and specific capacity are shown in Fig. 1.9. It can be seen that they span within a broad range of capacity and voltage values, with most materials having a potential above 0.5 V, above which the cost in terms of energy density is high compared to graphite in LIBs.

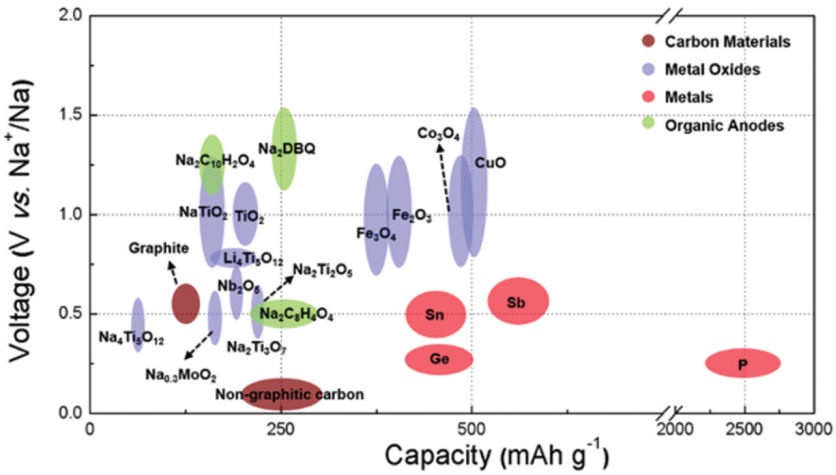

Figure 1.9: Statistical specific capacity and operating potentials of representative anode materials for sodium-ion batteries [68].

The most common anode material for LIBs is graphitic carbon, owing to its high specific capacity of 350 mA h g^{-1}, low operating voltage (below 0.2 V) and good electrochemical stability. Besides, it is a relatively low-cost material with a low environmental impact. Unluckily, while Li can be intercalated in graphite up to the composition LiC_6, Na ion intercalation is negligible. Reports of successful co-intercalation of diglyme solvated sodium in graphite, despite the larger radius of the intercalated species, has confirmed that the ionic radius of Na is not the issue [69, 70], but it is rather a matter of the negative reaction potential vs. Na [71]. However, the capacity remains less than half than that of graphite in LIBs and the voltage close to 1 V.

The research on anodes for SIBs has thus naturally evolved towards non-graphitic disordered carbon structures that can intercalate Na ions, typically with a sloping voltage curve below 1 V [31, 34, 59, 63], as can be appreciated from Fig. 1.10. Among those, hard carbons show an additional plateau below 100 mV. These two regions, the slope and the plateau, are usually ascribed to the intercalation of sodium ions assisted by the presence of defects, the filling of micropores

or reactions in the edges of graphene layers. To this day, there is not a clear consensus in the scientific community about which process corresponds to which region [31, 72].

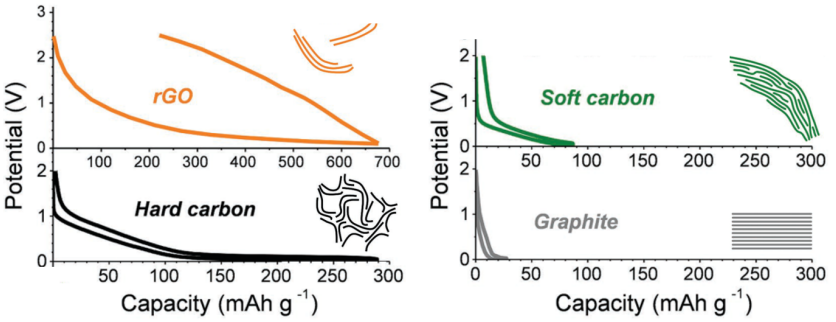

Figure 1.10: Different carbon structures representation and their corresponding typical voltage profile in sodium-ion batteries: graphite (grey), soft carbon (green), hard carbon (black) and reduced graphene oxide (rGO, orange) [71].

Hard carbons are the main candidates to be used as anode material in SIBs due to the combination of low operating voltage and fairly large capacity (see Figs. 1.9 and 1.10), although their performance is yet far from that obtained in LIBs with graphite [34]. However, since synthesis conditions and precursors have a huge impact in the electrochemical response, there is still room to improve their performance. Moreover, they can be synthesized from a wide variety of cheap and abundant precursors (biomass or fossil fuel derivatives for example) and they have already been used in the first generation of LIBs, and therefore, the technology is mature for its implementation into Na-ion battery technology.

Titanium oxides, alloys or organic compounds with higher insertion voltage values than carbon materials, can also be used as anode materials for SIBs.

Titanium oxide based materials have attracted interest due to the high reversible capacity at low voltage: $\approx$ 170 mA h g^{-1} at 1.0 V vs. Na^+/Na for sodium titanium oxide can be reached [73]. Nevertheless, titanates generally present poor electronic conductivity, so conductive coatings or improved architectures are required to obtain acceptable electrochemical activity.

Alloy materials have in general very high capacity values and low redox potentials. One of the main disadvantages of these materials is the high volumetric change upon cycling which tends to compromise their structural stability and leads to a rapid capacity fading. Tin for example, has a high theoretical capacity (850 mA h g^{-1}) with the redox potential at 0.3 V vs. Na^+/Na, but a volume expansion of 420% [74, 75]. A strategy to cope with the volume expansion has been to embed these materials within a carbon matrix, such as graphite, but this strategy results in a lower capacity and a low initial Coulombic efficiency, which continues to be an issue [76].

1.4.3 Cathode materials

Various families of cathode materials are being studied for SIBs, the principal being polyanionic compounds, Prussian blue analogs, organic compounds and layered oxides. As can be appreciated in Fig. 1.11, they spread over a large range of potential and capacity values. Beyond these parameters, the structural stability and the reversibility of the reaction is of mayor importance to ensure a good cyclability since, due to the big size of Na ion, these factors tend to be poorer than for LIB materials.

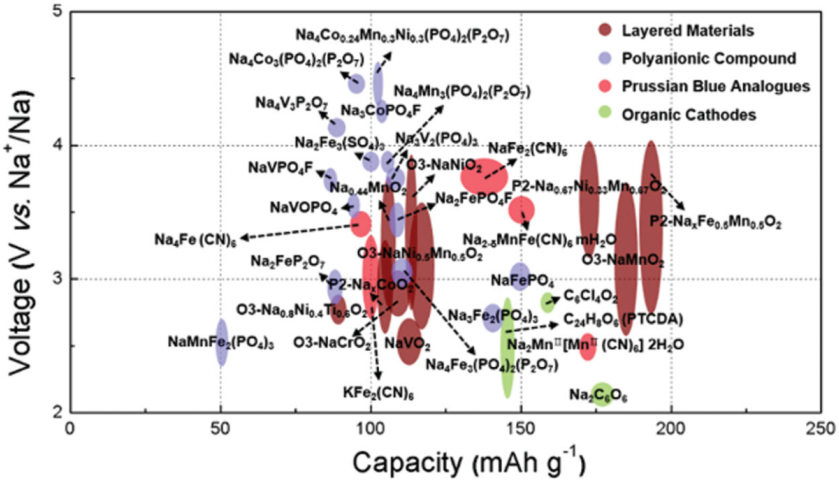

Figure 1.11: Statistical specific capacity and operating potentials of representative cathode materials for sodium-ion batteries [68].

1.4.3.1 Polyanionic compounds

The polyanionc compounds are robust structures, where XO_4 tetahedra (X = P, S, Si, As, Mo, or W) and TMO_n polyedra creating a 3D framework. The alkali ions can diffuse through the empty channels between them. A few examples of polyanionic crystal structures are presented in Fig. 1.12. There are several families among the polyanionic compounds, such as phosphates, pyrophosphates, fluorophosphates, sulfates or their mixtures.

Polyanionic compounds present several advantages, such as structural diversity with channels for Na ions, high thermal stability and structural stability even at high voltages, which results in a good cycle life. Their open framework structures allow Na ion migration through low-energy pathways. Moreover, the operational voltage can be tuned by changing the local environment [34, 63, 78–80]. Nevertheless, the presence of heavy polyanion groups results in poor gravimetric capacity values compared to other cathode families [33]. They also tend to have poorer electronic conductivities, which results in a poor rate performance; a carbon coating is required to ensure a good rate performance.

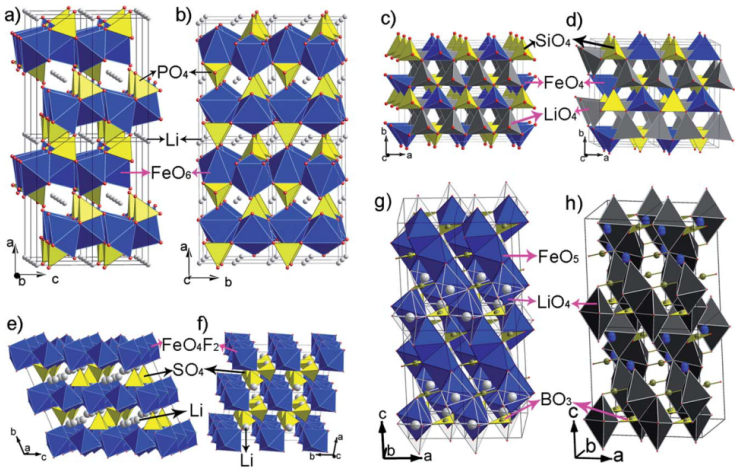

Figure 1.12: Example crystal structures of several polyanionic compounds: **(a)** and **(b)** Phosphate structures: yellow tetrahedral represent PO_4 groups and blue octahedra are TMO_6. **(c)** and **(d)** Silicate structures: grey tethahedral represent LiO_4 and yellow ones are SiO_4. **(e)** and **(f)** Fluorosulfate structure: yellow tetrahedral for SO_4 and blue octahedra for TMO_4F_2. **(g)** and **(h)** Borate structures: face shared LiO_4 tetrahedra in gray, trigonal TMO_5 bipyramides in blue and BO_3 triangles in yellow [77].

The phosphates presenting the NASICON (Sodium Super Ionic Conductor) structure have attracted interest thanks to the three-dimensional framework with large interstitial spaces allowing facile Na diffusion. The best working NASICON compounds rely on vanadium redox activity, resulting in a high operational voltage [81]. As an example, the electrochemical response of the carbon coated $NaVPO_4F$ is presented in Fig. 1.13a, where the different plateaus upon charge (discharge) correspond to the extraction (insertion) of the sodium in the two different positions in the structure.

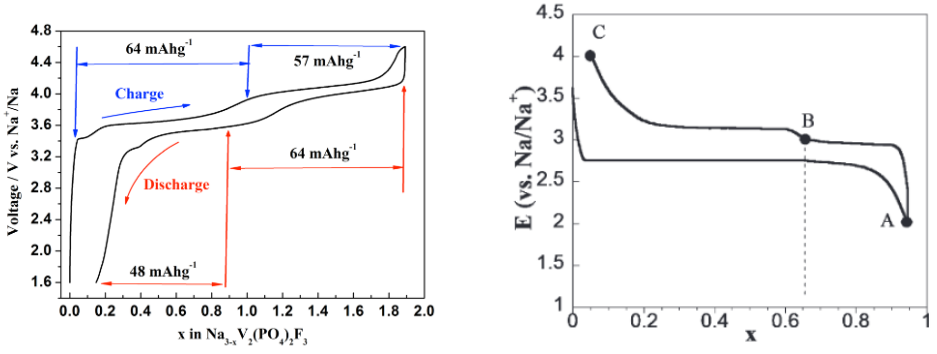

Figure 1.13: Examples of the electrochemical response of polyanionic compounds, **(a)** vanadium fluorophosphate ($Na_3V_2(PO_4)_2F_3$) [82] and **(b)** sodium phosphate ($NaFePO_4$) [83].

Nevertheless, more abundant and environmentally friendly elements are desirable although they may induce a lower operating potential compared to vanadium based polyanionic compounds. In this context, the iron based olivine $NaFePO_4$ phosphate is a very interesting compound. It is a well-known cathode thanks to its lithium analogue $LiFePO_4$. As opposed to its lithium analogue, that reaches 100% of the theoretical capacity, in $NaFePO_4$ only up to 80% is obtained reversibly ($\approx$ 125 mA h g^{-1}), as it can be appreciated in Fig. 1.13b. However, $NaFePO_4$ shows high capacity retention, of over 90% after 50 cycles at C/20 rate [84]. It has been shown also that structural evolution is different for both materials, $NaFePO_4$ and $LiFePO_4$ [85], highlighting the fact that although Li and Na are very similar elements, Na- and Li-compounds may present strong differences.

1.4.3.2 Prussian blue analogues

Materials analogs to Prussian blue, also called hexacyanometallates, present a robust structure, depicted in Fig. 1.14a. These materials present open channels that allow the rapid diffusion of the alkali ions. The general formula can be written as $ATM^1[TM^2(CN)_6]\cdot H_2O$, where A is the alkali ion and TM^1 and TM^2 are transition metal elements, and generally TM^2 is iron. One of the most advantageous properties of this family of materials is its easy synthesis at low temperatures in aqueous media and the abundance of the elements that compose these materials [86].

The robustness of the structure, similarly to the polyanionic compounds, provides these materials with a good cycling stability. Moreover, the easy diffusion of alkali ions results in good rate performing materials [87]. On the other hand, as in the case of the polyanionic compounds and as reflected in the voltage profile in Fig. 1.14b, the gravimetric energy densities are quite low due to the heavy hexacyanide groups.

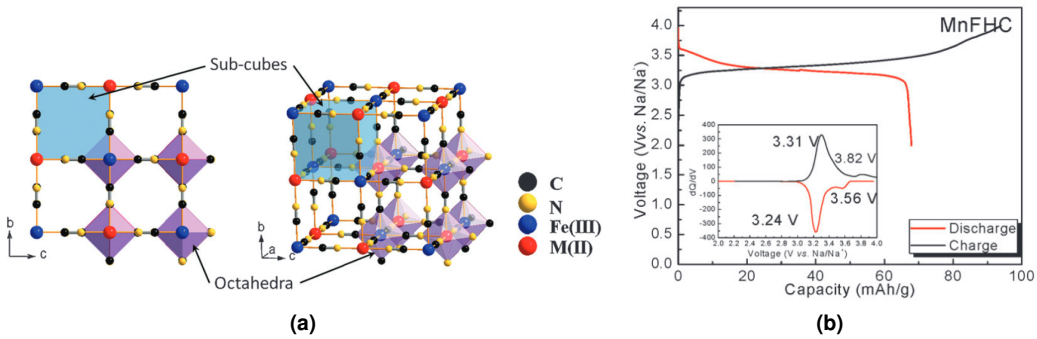

Figure 1.14: **(a)** Schematic structure of Prussian blue analogues [86] and **(b)** electrochemical response of $KMnFe(CN)_6$–Na cell [86].

1.4.3.3 Layered oxides

Transition metal layered oxides (TMLOs) are relatively easy to synthesize, versatile and have the highest specific energies among the different cathode families (see Fig. 1.11). These materials in

sodium based batteries have not reached the values that LIBs provide, but for SIBs more stable phases have been reported. More importantly, while Li analogues are limited to combinations of Co, Ni and Mn, layered Na compounds can be synthesized from a broad choice of transition metal (TM) elements, and thus, toxic elements can be avoided and abundant elements (such as Fe and Mn) favored. Great effort is being made to improve their electrochemical performance at competitive prices, because they are considered as the most promising cathode materials in terms of capacity, energy density and rate capability [88]. Nevertheless, they show the drawback of being hygroscopic, which requires moisture free conditions for their preparation and manipulation [89].

The generic formula for sodium layered oxides is Na_xTMO_2, where TM stands for transition metal element. These materials are composed of Na layers and transition metal layers, that consist of edge sharing TMO_6 octahedra. They can be classified according to the stacking order of the oxygen atoms and are denoted as Xn, where X refers to the alkali coordination (P: *trigonal prismatic*, O: *octahedral*) and n to the number of TMO_2 layers in the unit cell [90]. According to this nomenclature and as shown in Fig. 1.15, O3 polymorph's oxygen atoms are stacked as …ABCABC… and P2's as …ABBA… Transition between polymorphs can occur via gliding of TMO_2 layers.

Throughout this work, the interlayer distance of layered oxides will be considered as the distance between the center of transition metal layers (or the equivalent distance between Na-ion layers), as shown in Fig. 1.15 with the letter d.

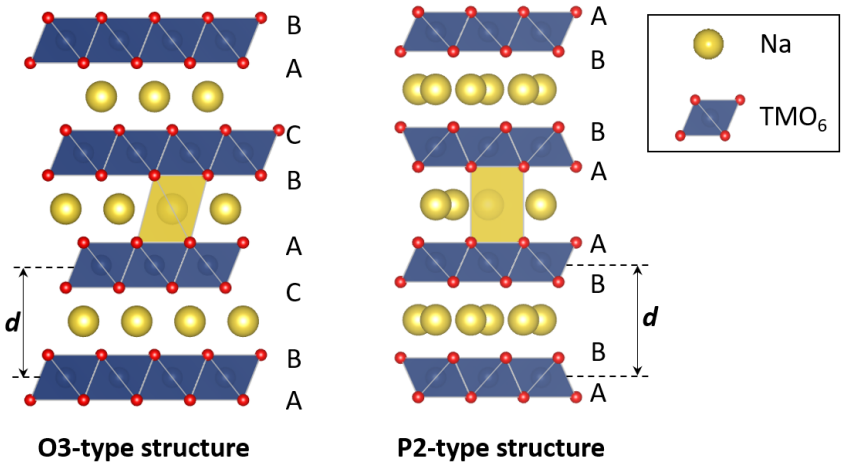

Figure 1.15: Classification of $NaTMO_2$ layered oxide materials, with the examples of O3- and P2-type structures, where TMO_6 are represented as blue octahedrons. Na environment, octahedral or prismatic, is highlighted in each case. Oxygen layers are labeled according to their stacking position. The interlayer distance d is defined as the distance between the TM or Na layers.

The general redox reaction of a sodium layered oxide can be described as:

$$NaTM^{3+}O_2 \underset{discharge}{\overset{charge}{\rightleftharpoons}} (1-x)\,Na^+ + Na_xTM_{1-x}^{(4-x)+}O_2 + (1-x)\,e^-$$

taking into account that TM can be a single type or a mixture of various transition metal elements, and that the oxidation state indicated is an average for all the TM ions.

As opposed to the polyanionic compounds, which tend to present lower capacity values but good cycling stability, the layered oxides generally show considerable capacities but are less stable upon cycling. This stability depends on the depth of charge and discharge processes. Indeed, the layered arrangement makes them prone to structural transformation at high and low sodium contents [91].

The P2-type structures usually show better cycling performance than the O3 phases due to the better diffusion in the larger prismatic sites [92]. This can be seen by comparing the voltage curve examples in Fig. 1.16, where the voltage curves of the O3-type structures are shown in Fig. 1.16a and those of the P2-type ones in Fig. 1.16b. It can be seen, for example, that the P2 structured Na_xMnO_2 and $Na_xFe_{1/2}Mn_{1/2}O_2$ materials have higher reversible capacities than the O3 analogues. Nevertheless, as opposed to the O-type structures, they are usually synthesized with a sodium deficiency of about 30%, which is a concern for the use of these materials in real full cells, as it decreases the initial Coulombic efficiency. Note that the first cycle is not presented in Fig. 1.16. Some strategies have been proposed to circumvent this issue by the use of additives such as sacrificial salts [93–95] or by precycling the material before it can be used in a full cell. However, these methods increase the final price or complicate the manufacturing process, reducing their commercial viability.

Nowadays, a wide variety of transition metal layered oxides are studied, depending on the desired property, such as increasing the average voltage or suppressing harmful phase transitions. Generally, widely available $3d$ TM elements are chosen (Fe, Mn, Ni, Cr) [96–100]. The use of a single TM layered oxide generally results in poor electrochemical performance, with rather low reversible capacities and retention. Depending on the required properties, binary [101–105], ternary [106–108] or quaternary [109, 110] mixtures have been proposed. For example, Ni increases the average of the reaction [111] (in Fig. 1.16 it can be seen how the Ni containing samples have higher average voltage curves), and Ti can stabilize the layered structure [112]. Other route to improve the structural stability, and hence, the electrochemical stability, has been the material doping with non-active elements (such as Ca, Zn, Al, Mg) [113–117], which act as pillars to keep the original structure while removing the sodium.

It is worth noting that all the cycling tests presented in Fig. 1.16 have been done within a limited voltage window, keeping the upper voltage limit close to the reaction voltage to avoid electrochemical irreversibility resulted from deep desodiation states. In the examples presented, the observed plateaus are of different nature depending on the sample. For example, Na_xCO_2 shows various steps due to structural changes upon cycling [118]. In $Na_xFe_{1/2}Mn_{1/2}O_2$ samples two plateaus can be seen that correspond to the redox reaction of the two redox active elements in the material: Fe and Mn [119].

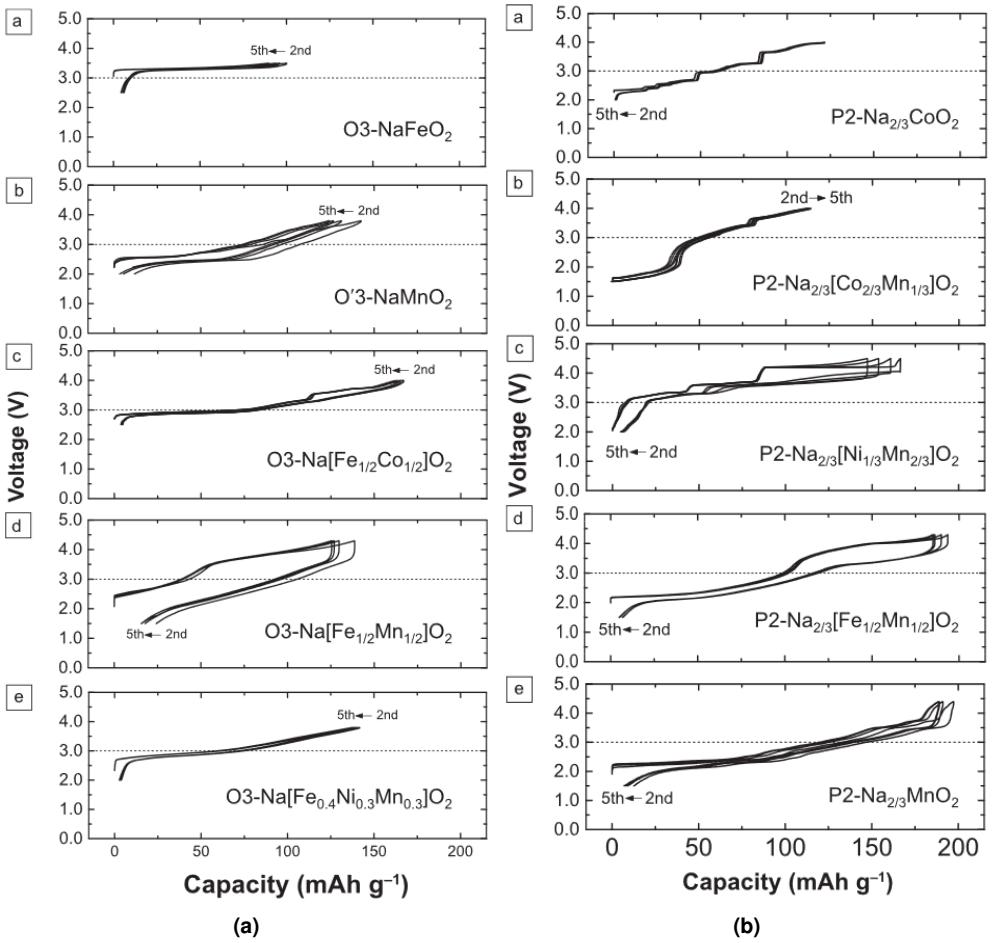

Figure 1.16: Examples of the electrochemical response of various **(a)** O-type and **(b)** P-type layered oxides [96].

Recently, and more focused on an academic point of view (due to their scarcity and high price), layered oxides based on $4d$ metals, such as Ru, Mo, Rh or Sn, have also been studied with acceptable electrochemical properties [120–124].

1.5 Structural degradation mechanisms in TM layered oxides as cathode materials for SIBs

1.5.1 General overview of the degradation mechanisms in Li and Na TM layered oxides

As explained earlier, layered oxides are very promising materials as cathodes for sodium ion batteries. However, their electrochemical irreversibility is one their main drawbacks, which is usually ascribed to structural or chemical changes occurred upon cycling, such as transition towards a spinel structure [125–128], TM migration to the alkali-metal layers [51, 100, 129–131] or oxygen redox activity [130, 132, 133].

The instability of the layered structure is a very well-known issue in Li- and Na-based layered oxides [134, 135]. Indeed, when cycling a battery, large amounts of alkali ions are (de)intercalated in the host structure of the electrode's active material. Some 3D interconnected structures, such as phosphates or Prussian blue analogs, are very robust and hence stable even after full removal of the alkali ions. On the other side, within the TMLO's layered structure, the removal of all the alkali ions would result in emptying complete structural layers, which may lead to a structure that is no longer stable.

The general trend of the structural changes upon alkali ion removal has been reported in the literature. It has been shown that the interlayer distance d increases upon alkali ion removal due to an increased repulsion between oxygen atoms in the TM oxide layers [131, 136–140]. Some phase transitions can be observed towards polymorph layered structures through layer gliding [140–144]. In this sense, the most common transitions are the O3 towards the P3 and the P2 towards the OP4 structures as named by Delmas et al. [90]. When too many alkali ions are removed, a reduction in the interlayer distance can be observed. The onset point of this d distance shrinking and its rate vary with the sample composition and structure. If the alkali ion is further extracted irreversible transitions tend to be observed, such as TM migration or transition to spinel-like structure. Indeed, although the layered structure is stable or metastable at high concentration of alkali ions, when the composition approaches TMO_2 ($x_A = 0$, being A Li or Na) the layered structure may spontaneously experience an atomic rearrangement towards a lower energy structure, typically with a 3D structure, such as the spinel. An example is shown in Fig. 1.17, where the Li-rich $Li(Li_{0.2}Mn_{0.55}Ni_{0.15}Co_{0.1})O_2$ transforms into the spinel structure when charged (upon Li removal) above 4.5 V. Many works try to overcome these structural instabilities by substitution of alkali or TM ions with electrochemically inactive ions or by TM substitution with electroactive species [145–148]. Moreover, several works have studied the structural evolution of layered

oxides to try to understand the structural properties at charged state and the reversibility of the structural transition.

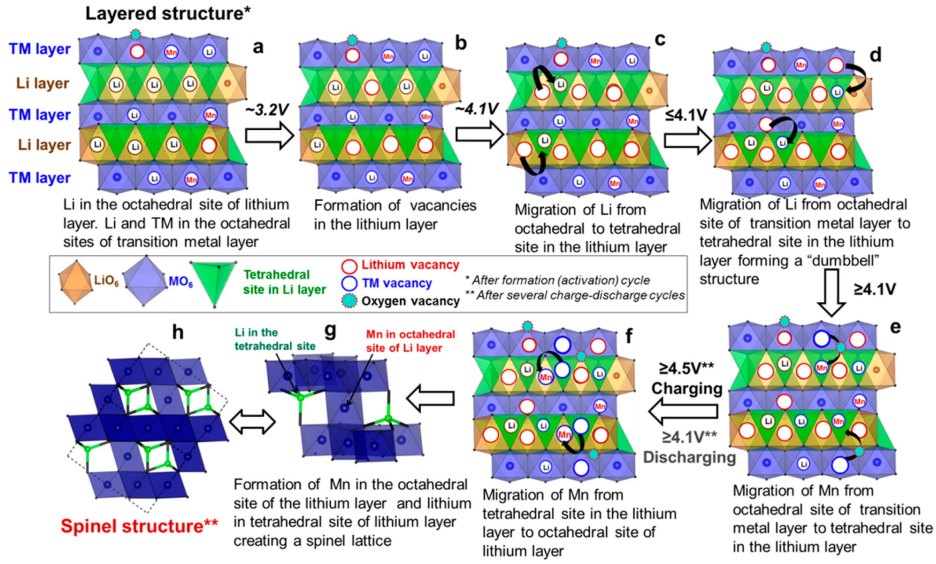

Figure 1.17: Layered to spinel structure transformation proposal using $Li_{1.2}Mn_{0.55}Ni_{0.15}Co_{0.1}O_2$ as an example by Mohanty et al. via formation of tetrahedral lithium in the lithium layer and migration of Mn from octahedral TM layer to octahedral site of lithium layer [127].

Two examples of structural evolution upon cycling (charge and discharge, that is, Na removal and insertion) of Na-based transition metal layered oxides (TMLOs) are presented in Fig. 1.18, for O3-type ternary (Fig. 1.18a) and for P2-type binary Na-TMLOs (Fig. 1.18b), which illustrate well the first steps of this sequence. When Na ions are extracted, the interlayer distance first increases (the $(0\,0\,\ell)$ reflections shift to lower angles), then, at about half charge a change in the trend can be seen, and the interlayer distance starts to collapse.

When this thesis work was initiated in 2016, few reported research works were focused on the study of this phenomenon in Na-TMLOs, although the stability of these compounds when deintercalated, compared to Li-TMLOs, was known to be more problematic. In recent years several publications have shown TM migration into the alkali layers, for both, lithium- [129, 130] and sodium-based [51, 131] layered oxides, that could be related with the interlayer distance collapse. Indeed, when the structure transformation by layer gliding can no longer accommodate the sodium extraction, further structural rearrangements are expected. The TM migration generally is described to result in local distortions [100, 130, 131]. Nevertheless, a layered to spinel transformation can occur via TM migration from the TM layers to the Na layers in the structure [125, 126, 128, 149]. Mohanty et al., for instance, described in detail the necessary steps for that complete transformation process from a Li-rich TMLO to spinel (see Fig. 1.17), in which TM migration into the Li layer appears as a key step [127].

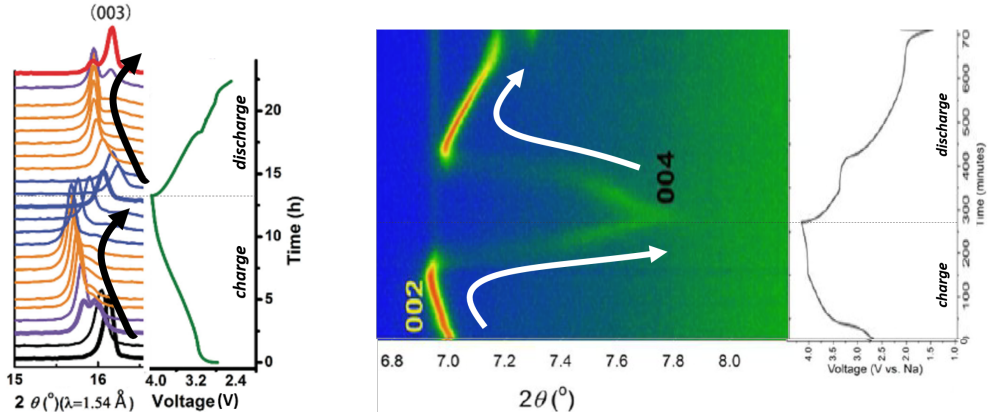

(a) O-type structure **(b)** P-type structure

Figure 1.18: Examples of the $(0\,0\,\ell)$ reflection shift in the X-ray diffraction (XRD) patterns upon cycling of iron and manganese based layered oxides. **(a)** O3-$Na_xFe_{0.30}Mn_{0.48}Cu_{0.22}O_2$ (adapted from Ref. [143]) and **(b)** P2-$Na_xFe_{1/2}Mn_{1/2}O_2$ (adapted from Ref. [144]). The shift of the $(0\,0\,\ell)$ reflection, which is directly related with the interlayer distance has been highlighted with arrows: higher 2θ angle means shorter distance and vice versa.

The higher instability of the O-type phases compared to the P-type ones has been proposed to be related to the TM migration. This appears in many layered oxides, both for LIBs and SIBs, due to the low activation barrier for TM ions to migrate as a consequence of the electrostatic repulsion between neighboring atoms in the TM layer [100, 127, 150, 151]. It has been proposed that this migration occurs to the tetrahedral vacancies in the TMO_2 layers [98, 100, 127], which are only available in O-type structures, and not in P-type ones.

Various strategies have been followed to address this issue. TM substitution has been found to mitigate this effect. Nevertheless, the price and the toxicity of binary, ternary or quaternary compounds can increase due to the reduced use of the abundant and non-toxic Fe and Mn by more expensive and sometimes toxic Ni, Mg, Ti or Co [109, 129, 152, 153].

This migration is believed to be detrimental. Indeed, it is the first step towards the layered to spinel structure, in which the reversible alkali ion reaction is not always possible, hence, resulting in the transformation to an electrochemically inactive material. Moreover, even when the complete transformation towards an spinel-like structure is not fulfilled, the TM ions in the sodium layers would block the Na diffusion [100, 127].

Oxygen reduction is another change in the material that might be detrimental to the reversibility of the electrochemical reaction. Oxygen redox activity has been mainly observed in Li-rich layered oxides, which is usually seen in the electrochemical curve by a plateau at high voltages [154–156]. This leads to an increase of the available capacity and energy density values. However, in some cases the oxygen redox is irreversible, and thus, the Coulombic efficiency is reduced, when oxygen gas irreversibly leaves the active material surface. In some cases, the oxygen

redox has been related to the TM migration [132]. This seems to occur in Li-rich TMLOs when the oxygen forms peroxo-like species by shortening the O-O bonds, which might decrease the energy barrier for the TM to migrate to the alkali ions layers [130, 133], and hence, promoting the structural transformation.

1.5.2 The specific case of $Na_x(Fe,Mn)O_2$ layered oxides

The first time that sodium deintercalation from $NaFeO_2$ was reported in 1985 by Kikkawa et al. [157], the desodiation was carried out by chemical oxidation of the sample. It was not until 1994 that the first electrochemical desodiation reaction was published by Takeda et al. [158], when it was considered as a possible cathode candidate for SIBs. At that time it was charged versus metallic lithium, and no discharge process was shown. The first full cycle versus Na was reported in 2006 by Okada et al. [159]. Since then and until the beginning of this thesis, few works have been published on $NaFeO_2$ as cathode material for SIBs [150, 160–162]. Although the theoretical capacity of this material is relatively high, 241 mA h g^{-1}, the reported reversible capacity values lie around 80 mA h g^{-1} as the material suffers from irreversible structural changes when the extracted sodium content exceeds the 50%. This can be seen in Figs. 1.19a and b, where the structural reversibility is observed when discharged from 3.4 V, that corresponds to 33% of Na removal upon charge, but irreversible structural changes are observed on the samples discharged from 4.0 V and 4.5 V, that correspond to a sodium extraction upon charge of 58% and 70% respectively [150, 158]. Contrary to the previous *ex-situ* XRD research works, shown in Fig. 1.19b, where the whole phase transformed into a monoclinic distorted O'3 structure with a change in the cell parameters of about 5% in z direction [158], in the *operando* XRD study of Lee et al. only the apparition of secondary distorted phases were shown, with little or no changes in the main structure (see Fig. 1.19c). Although *ex-situ* and *operando* results can differ due to the sample manipulation and relaxation times, both results do not seem to be consistent. Moreover, the structural evolution of $NaFeO_2$ reported by Lee et al. [151] is very different to other isostructural layered oxides, such as the O3-$Na_xFe_{0.30}Mn_{0.48}Cu_{0.22}O_2$ shown in Fig. 1.18a by Mu et al. [143].

This inconsistency has not been further investigated, and a full understanding of the structural evolution and electrochemical degradation mechanism in $NaFeO_2$ is still missing, as most reported works are mainly focused on compounds with Fe substituted by other non-toxic and cheap elements, such as manganese. Although the $Mn^{3+/4+}$ redox potential is lower than that of the $Fe^{3+/4+}$, Mn has attracted a lot of interest in cathode materials because its presence seems to help to stabilize the structure during cycling [163].

One of the peculiarities of iron and manganese cations is that they show Jahn-Teller (JT) distortion at a certain oxidation state. The JT distortion is a spontaneous symmetry break derived from an energy degeneracy that results in a lower energy for the system [164]. The Jahn-Teller effect occurs when the system has unevenly occupied degenerated energy levels [165].

The orbital splitting of Fe^{3+}, Fe^{4+}, Mn^{3+} and Mn^{4+} ions is presented in Fig. 1.20: with an electron configuration of [Ar]$3d^5$, Fe^{3+} in Fig. 1.20a; with an electron configuration of [Ar]$3d^4$, Fe^{4+}

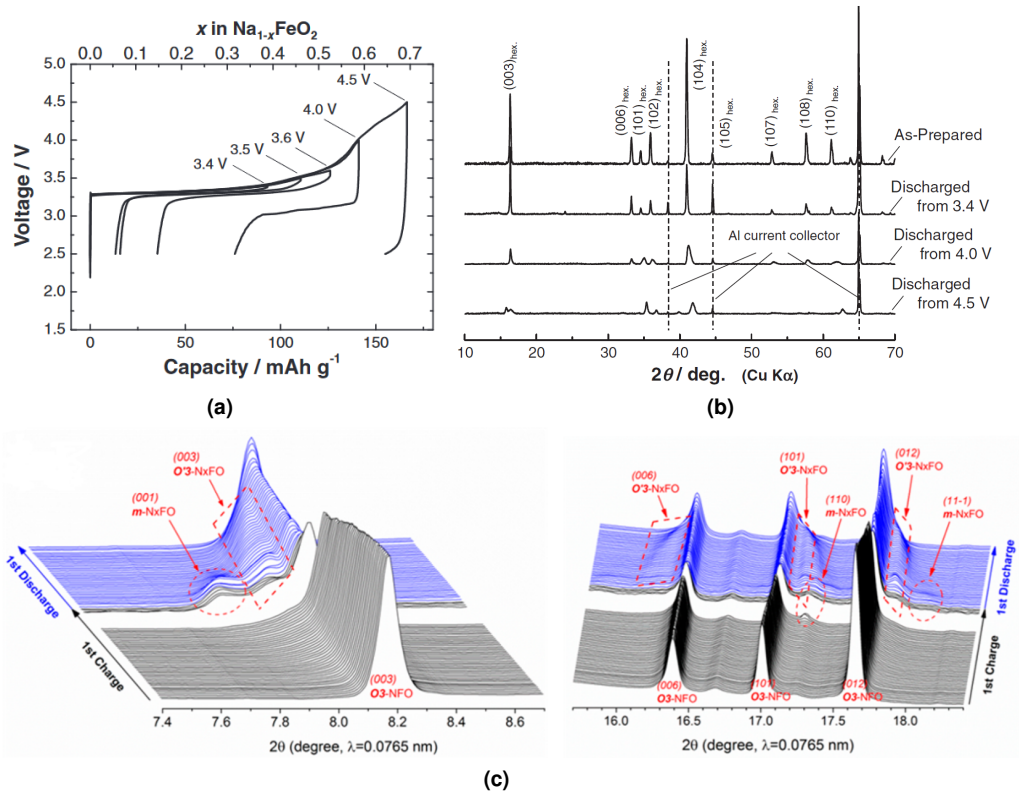

Figure 1.19: **(a)** Electrochemical response of $NaFeO_2$ with various upper voltage limits [150]. **(b)** *Ex-situ* XRD patterns of $Na_{1-x}FeO_2$ before and after cycling with different cut-off voltage by Yabuuchi et al. [150]. **(c)** *Operando* XRD results of $NaFeO_2$ by Lee et al. [151].

or Mn^{3+} in Fig. 1.20b and c; and with an electron configuration of $[Ar]3d^3$, Mn^{4+} in Fig. 1.20d. Note that these configurations correspond to the high spin (HS) state. As can be seen from Fig. 1.20, both Fe^{3+} and Mn^{4+} have evenly occupied energy levels and therefore, do not present any JT distortion. In Figs. 1.20a and d, the orbital splitting in the octahedral and the tetrahedral environment are shown. It can be seen that Fe^{3+} is equally stable in octahedral and tetrahedral environments ($\Delta|_{Fe^{3+}} = \Delta_{tet} - \Delta_o = 0$). On the other hand, Mn^{4+} is more stable in an octahedral environment ($\Delta|_{Mn^{4+}} = 0.85\Delta_o > 0$). This is also the case for Fe^{4+} and Mn^{3+}, where $\Delta = 0.42\Delta_o > 0$. The possible JT distorted octahedra of Fe^{4+} and Mn^{3+}, in Figs. 1.20b and 1.20c, show the elongated and compressed D_{4h} respectively. For this $[Ar]3d^4$ electron configuration, the lowest energy corresponds to the elongated D_{4h} distortion (Fig. 1.20b).

Thus, the compound $Na_x(Fe,Mn)O_2$ will suffer from JT distortion from Fe^{4+} and Mn^{3+} ions. These distortions are believed to be associated with structural degradations due to the anisotropy of the distortion [131].

A very clear example of the JT effect in the electrochemistry can be seen in $NaMnO_2$. While

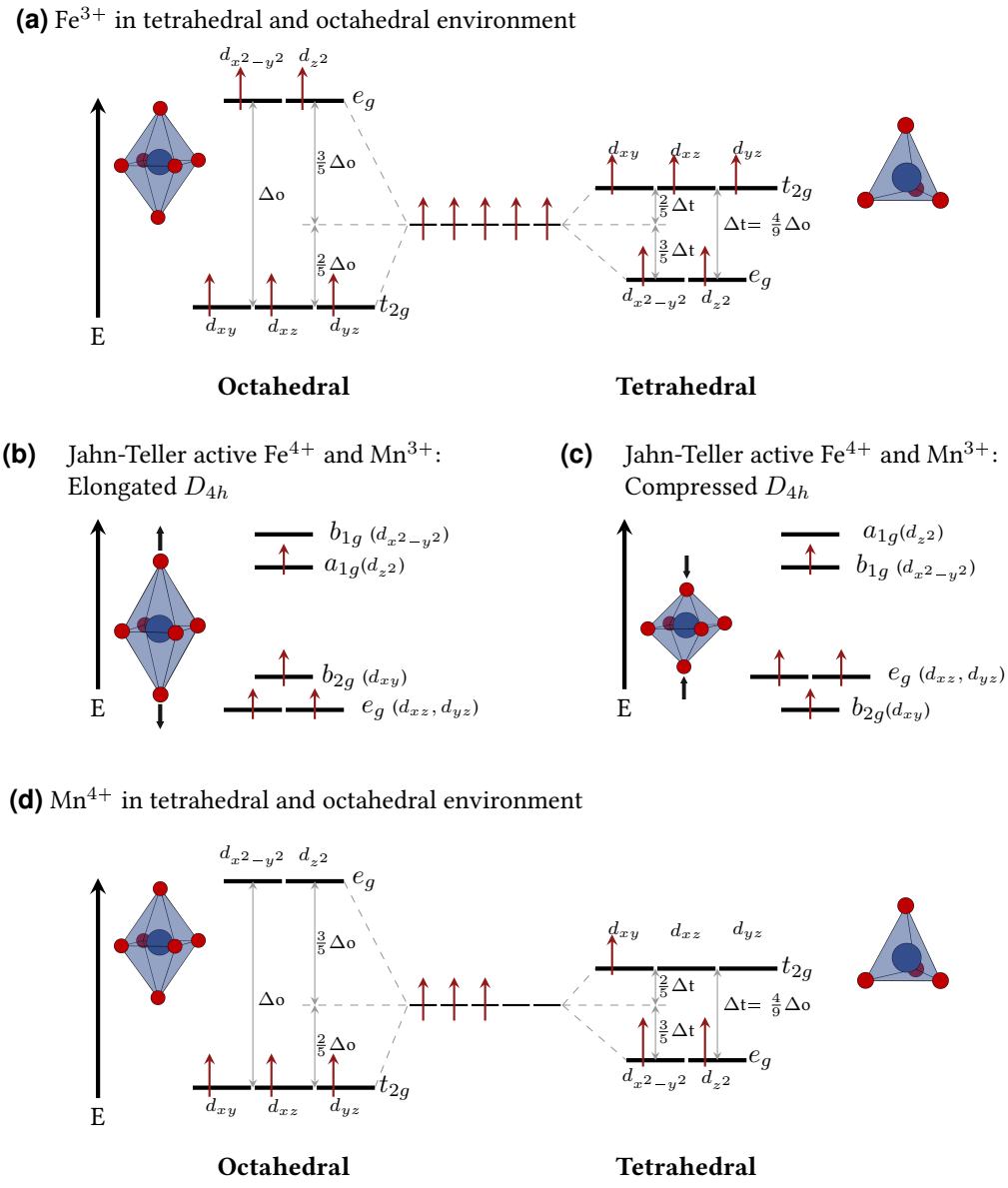

Figure 1.20: Crystal field diagram $3d$ orbital splitting comparison of **(a)** HS Fe^{3+} ([Ar]$3d^5$) in an octahedral (left) and a tetrahedral (right) environment. The electrons are represented as red arrows. Jahn-Teller active Fe^{4+} or Mn^{3+}, both with an electronic state of [Ar]$3d^4$, **(b)** for elongated D_{4h} **(c)** for compressed D_{4h} [164]. **(d)** Orbital splitting of HS Mn^{4+} ([Ar]$3d^3$) in the octahedral (left) and tetrahedral environment (right). The schematic octahedra and tetrahedra represent the TM ion with blue spheres and oxygen ions with red spheres.

Na ions are extracted from the structure, a cooperative JT distortion of the Mn^{3+} ions results in metastable structures that are reflected as plateaus in the electrochemical curve (see Fig. 1.21a) [166–168]. Billaud et al. increased the average oxidation state of Mn towards Mn^{4+} by partial substitution of Mn^{3+} with Mg^{2+}. It can be seen in Fig. 1.21, that adding 5 or 10% (Figs. 1.21b and c respectively) helps reducing the cooperative JT distortions of Mn^{3+}, which is reflected in a smoothing of the voltage profile [167].

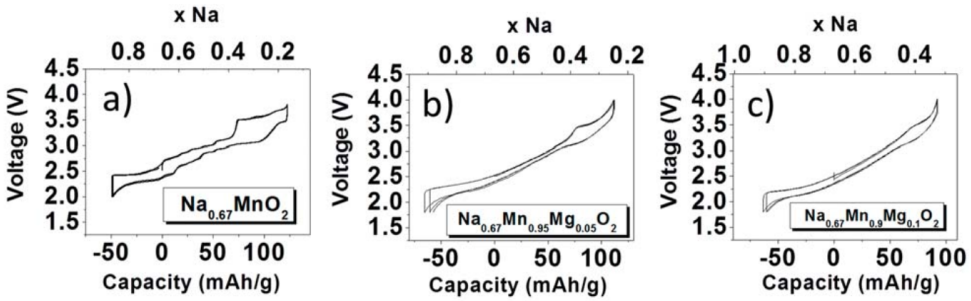

Figure 1.21: Voltage profile of $Na_xMn_{1-y}Mg_yO_2$ ($y = 0, 0.05, 0.1$) upon cycling (charge-discharge). In Na_xMnO_2 several voltage plateaus can be observed, although the material contains a single redox center, and the steps are smoothed out as the Mg content is creased [167].

Layered structures with mixed iron and manganese content have been widely studied, with different Fe : Mn ratios, as well as with different initial structures. In 2012 Yabuuchi et al. described the electrochemical response of P2- and O3-$Na_xFe_{1/2}Mn_{1/2}O_2$, where reversible capacities of about 150 mA h g^{-1} and 75 mA h g^{-1} where obtained respectively after 30 cycles at C/20 when cycled in the voltage range between 1.5 V and 4.3 V [169]. Thorne et al. reported in 2013 a whole series of $Na_{1-y}Fe_{1-y}Mn_yO_2$ compounds for $0 \leqslant y \leqslant 0.5$ where they showed that, when cycling up to 4.0 V, the voltage hysteresis was reduced with increasing Mn amount [163]. They also showed an increased capacity retention for the samples in which less Fe^{3+} was oxidized to Fe^{4+}.

However, the $Mn^{3+/4+}$ redox potential ($V_{Mn^{3+/4+}} \approx 2.5$ V) is lower than that of $Fe^{3+/4+}$ ($V_{Fe^{3+/4+}} \approx 3.3$ V). So even if capacity is improved, the average voltage is reduced, and therefore, the impact in the energy density is not that evident. Thus, a compromise has to be found, where relatively good capacity values and stability are matched with a high average voltage. Other stoichiometries with higher Fe content, such as $Na_{2/3}Fe_{2/3}Mn_{1/3}O_2$, have also been reported with different structures (O3 and P2) [138, 140, 170]. It is worth noting that at this composition, the transition metal oxidation states are Fe^{3+} and Mn^{4+}, and thus, no Jahn-Teller distortion is present in the pristine state. Although it is believed that the sodium diffusion is facilitated in P-type structures due to the larger prismatic sites [171], the reported results show that both structures show similar electrochemical properties.

Gonzalo et al. have published a qualitative description of the structural evolution of $Na_{2/3}Fe_{2/3}Mn_{1/3}O_2$ in two different polymorphs: P2 and O3 (see Fig. 1.22a and b respectively),

based on *operando* XRD [138]. Mortemard de Boisse et al. also reported the *operando* evolution of the O3-$Na_xFe_{2/3}Mn_{1/3}O_2$ polymorph (see Fig. 1.22c) [170]. The evolution of the interlayer distance, reflected by the shift of the $(0\,0\,\ell)$ reflection ($15° < 2\theta < 20°$) is very similar to that observed in most of the layered oxides, with an initial increment followed by a shrinking. Mortemard de Boisse et al. described various transitions between layered polymorphs through layer gliding. At charged state, above 3.8 V, an unknown structure was described (*X* in Fig. 1.22c), which was believed to appear through stacking faults and to be related with the electrochemical degradation of the material.

In summary, it has been seen that iron and manganese based TMLOs show promising results in terms of capacity, despite the degradation that they suffer especially at high voltages. A compromise has to be found in their relative presence, as a higher Mn content will increase the capacity while a higher Fe content will increase the average voltage. Understanding the degradation mechanisms of these materials could help the development of better performing materials.

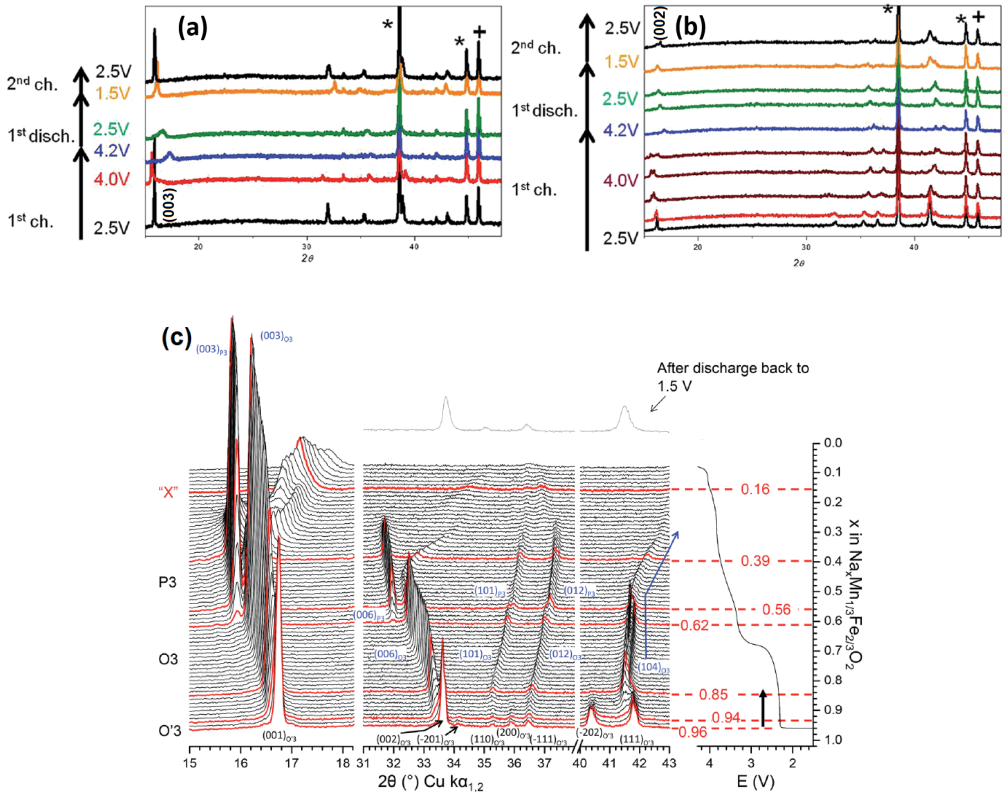

Figure 1.22: Structural evolution of **(a)** P2-$Na_xFe_{2/3}Mn_{1/3}O_2$ and **(b)** O3-$Na_xFe_{2/3}Mn_{1/3}O_2$ by Gonzalo et al. [138], and **(c)** of O3-$Na_xFe_{2/3}Mn_{1/3}O_2$ by Mortemard de Boisse et al. [170].

1.6 Objectives and methodology

The main objective of this work is to get insight on the mechanism of TM migration and its influence on the electrochemical properties of TM layered oxides, which is one of the main bottleneck issues for this family of materials to become the cathodes for commercial sodium-ion batteries.

For this purpose, the structural changes occurring upon cycling will be thoroughly studied in a selection of model systems in order to relate them with their electrochemical properties, with special focus in the behavior at high potentials.

As system of study, a series of iron-rich O3-$Na_xFe_{1-y}Mn_yO_2$ compounds, with $0 \leqslant y \leqslant 1/3$, which will be complemented by P2-$Na_{2/3}Fe_{2/3}Mn_{1/3}O_2$ provided by collaboration from CIC Energigune. A deep study of the chemical and structural evolution of these materials upon cycling will be done through advanced *in-situ* techniques (*in-situ* and *operando* lab-scale and synchrotron XRD and Mössbauer spectroscopy for example). In order to try to relate the structural changes produced upon cycling with their electrochemical response, in addition to the traditional electrochemical cycling tests, a study of the internal resistance and Na diffusion coefficient evolution upon cycling will also be presented, based on coupled potentiostatic intermittent titration and electrochemical impedance spectroscopy measurements.

Bibliography

[1] Statistical Review of World Energy | Energy economics | BP. https://www.bp.com/en/global/corporate/energy-economics/statistical-review-of-world-energy/downloads.html, (Accessed: 2018-11-07).

[2] U.S. Energy Information Administration (EIA). https://www.eia.gov/todayinenergy/detail.php?id=32912, (Accessed: 2018-11-07).

[3] I. P. on Climate Change and O. Edenhofer, editors. *Climate change 2014: mitigation of climate change: Working Group III contribution to the Fifth Assessment Report of the Intergovernmental Panel on Climate Change*. Cambridge University Press, New York, NY, 2014.

[4] Statistical Review of World Energy | Energy economics | Home. https://www.bp.com/en/global/corporate/energy-economics/statistical-review-of-world-energy.html, (Accessed: 2020-01-03).

[5] P. A. Owusu and S. Asumadu-Sarkodie. *Cogent Engineering*, 3(1):1167990, 2016.

[6] Paris Agreement | Climate Action. https://ec.europa.eu/clima/policies/international/negotiations/paris_en, (Accessed: 2019-11-28).

[7] UNITED NATIONS UN Climate Change Summit 2019. https://www.un.org/en/climatechange/un-climate-summit-2019.shtml, (Accessed: 2019-12-05).

[8] J. B. Goodenough. *Energy Storage Materials*, 1:158–161, 2015.

[9] Electricity storage and renewables: Costs and markets to 2030. https://www.irena.org/publications/2017/Oct/Electricity-storage-and-renewables-costs-and-markets, (Accessed: 2019-10-31).

[10] B. Dunn, H. Kamath, and J.-M. Tarascon. *Science*, 334(6058):928–935, 2011.

[11] Y. Huang, Y. Zheng, X. Li, F. Adams, W. Luo, Y. Huang, and L. Hu. *ACS Energy Letters*, 3(7):1604–1612, 2018.

[12] M. Armand and J.-M. Tarascon. *Nature*, 451(7179):652–657, 2008.

[13] S. Sabihuddin, A. Kiprakis, and M. Mueller. *Energies*, 8(1):172–216, 2014.

[14] H. Chen, T. N. Cong, W. Yang, C. Tan, Y. Li, and Y. Ding. *Progress in Natural Science*, 19(3):291–312, 2009.

[15] S. Soylu. *Electric Vehicles: The Benefits and Barriers*. IntechOpen, 2011.

[16] M. T. Arif, A. M. T. Oo, A. B. M. S. Ali, and G. M. Shafiullah. *Smart Grid and Renewable Energy*, 04(02):167–180, 2013.

[17] Advantages and limitations of the Different Types of Batteries - Battery University. https://batteryuniversity.com/learn/archive/whats_the_best_battery, (Accessed: 2020-03-26).

[18] A. Volta. *Philosophical Transactions*, 90:403–431, 1800.

[19] G. Plante. *The Storage of Electrical Energy*. Paul Bedford, 1859.

[20] K. Mizushima, P. C. Jones, P. J. Wiseman, and J. B. Goodenough. *Materials Research Bulletin*, 15(6):783–789, 1980.

[21] R. Yazami and P. Touzain. *Journal of Power Sources*, 9(3):356–371, 1983.

[22] A. K. Padhi, K. Nanjundaswamy, and J. B. Goodenough. *Journal of The Electrochemical Society*, 144(4):1188–1194, 1997.

[23] B. Scrosati. *Journal of Solid State Electrochemistry*, 15(7-8):1623–1630, 2011.

[24] Faradion – The world leader in non-aqueous sodium-ion cell technology. https://www.faradion.co.uk/, (Accessed: 2020-01-29).

[25] Keywords to understanding Sony Energy Devices, Sony Energy Devices Corporation. http://www.sonyenergy-devices.co.jp/en/keyword/, (Accessed: 2016-06-22).

[26] M. A. P. Mahmud, N. Huda, S. H. Farjana, and C. Lang. *Batteries*, 5(1):22, 2019.

[27] P. Bruce, B. Scrosati, and J.-M. Tarascon. *Angewandte Chemie International Edition*, 47(16):2930–2946, 2008.

[28] B. L. Ellis, K. T. Lee, and L. F. Nazar. *Chemistry of Materials*, 22(3):691–714, 2010.

[29] Battery markets and charging infrastucture -BloombergNEF. https://bnef.turtl.co/story/evo2019/, (Accessed: 2020-03-26).

[30] Energy Storage Investments Boom As Battery Costs Halve in the Next Decade - BloombergNEF. https://about.bnef.com/blog/energy-storage-investments-boom-battery-costs-halve-next-decade/, (Accessed: 2020-03-26).

[31] M. n. Muñoz-Márquez, D. Saurel, J. L. Gómez-Cámer, M. Casas-Cabanas, E. Castillo-Martínez, and T. Rojo. *Advanced Energy Materials*, 7(20):1700463, 2017.

[32] M. D. Slater, D. Kim, E. Lee, and C. S. Johnson. *Advanced Functional Materials*, 23:947–958, 2013.

[33] S.-W. Kim, D.-H. Seo, X. Ma, G. Ceder, and K. Kang. *Advanced Energy Materials*, 2(7):710–721, 2012.

[34] V. Palomares, M. Casas-Cabanas, E. Castillo-Martínez, M. H. Han, and T. Rojo. *Energy & Environmental Science*, 6(8):2312, 2013.

[35] S. Kuze, J.-i. Kageura, S. Matsumoto, T. Nakayama, M. Makidera, M. Saka, T. Yamaguchi, T. Yamamoto, and K. Nakane. *Sumitomo Kagaku*, 2013:1–13, 2013.

[36] H. Reiss. *The Journal of Physical Chemistry*, 89(18):3783–3791, 1985.

[37] J. B. Goodenough and Y. Kim. *Chemistry of Materials*, 22(3):587–603, 2010.

[38] C. Liu, Z. G. Neale, and G. Cao. *Materials Today*, 19(2):109–123, 2016.

[39] O. Pecher, J. Carretero-González, K. J. Griffith, and C. P. Grey. *Chemistry of Materials*, 29(1):213–242, 2017.

[40] M. A. Muñoz-Márquez, M. Zarrabeitia, E. Castillo-Martínez, A. Eguía-Barrio, T. Rojo, and M. Casas-Cabanas. *ACS Applied Materials & Interfaces*, 7(14):7801–7808, 2015.

[41] M. Zarrabeitia, F. Nobili, M. n. Muñoz-Márquez, T. Rojo, and M. Casas-Cabanas. *Journal of Power Sources*, 330:78–83, 2016.

[42] J. M. Tarascon, C. Delacourt, A. S. Prakash, M. Morcrette, M. S. Hegde, C. Wurm, and C. Masquelier. *Dalton Transactions*, 19:2988, 2004.

[43] M. R. Palacín. *Chemical Society Reviews*, 38(9):2565, 2009.

[44] Y. Ren, T. Zhao, P. Tan, Z. Wei, and X. Zhou. *Applied Energy*, 187:706–716, 2017.

[45] N. Imanishi and O. Yamamoto. *Materials Today Advances*, 4:100031, 2019.

[46] G. Kreysa, K.-i. Ota, and R. F. Savinell, editors. *Encyclopedia of Applied Electrochemistry*. Springer New York, New York, NY, 2014.

[47] J. Molenda. In *Lithium-ion Batteries - Thin Film for Energy Materials and Devices*. IntechOpen, 2019. doi:10.5772/intechopen.83606.

[48] G. Ceder, M. Aydinol, and A. Kohan. *Computational Materials Science*, 8(1-2):161–169, 1997.

[49] K. Yamamoto, Y. Iriyama, T. Asaka, T. Hirayama, H. Fujita, C. Fisher, K. Nonaka, Y. Sugita, and Z. Ogumi. *Angewandte Chemie International Edition*, 49(26):4414–4417, 2010.

[50] N. Yabuuchi and S. Komaba. *Science and Technology of Advanced Materials*, 15(4):043501, 2014.

[51] N. Yabuuchi, K. Kubota, M. Dahbi, and S. Komaba. *Chemical Reviews*, 114(23):11636–11682, 2014.

[52] P. K. Nayak, L. Yang, W. Brehm, and P. Adelhelm. *Angewandte Chemie International Edition*, 57(1):102–120, 2018.

[53] M. S. Islam and C. A. J. Fisher. *Chemical Society Reviews*, 43(1):185–204, 2014.

[54] S. P. Ong, V. L. Chevrier, G. Hautier, A. Jain, C. Moore, S. Kim, X. Ma, and G. Ceder. *Energy & Environmental Science*, 4(9):3680, 2011.

[55] J.-Y. Hwang, S.-T. Myung, and Y.-K. Sun. *Chemical Society Reviews*, 46(12):3529–3614, 2017.

[56] Tiamat. `http://www.tiamat-energy.com/`, (Accessed: 2020-01-29).

[57] Natron Energy - Prussian Blue Sodium Ion Battery Technology. `https://natron.energy/`, (Accessed: 2020-01-29).

[58] HiNa Battery Technology Co., Ltd. `http://www.hinabattery.com/en/`, (Accessed: 2020-01-29).

[59] K. Kubota and S. Komaba. *Journal of The Electrochemical Society*, 162(14):A2538–A2550, 2015.

[60] M. Chen, Q. Liu, S. Wang, E. Wang, X. Guo, and S. Chou. *Advanced Energy Materials*, 9(14):1803609, 2019.

[61] A. Ponrouch, E. Marchante, M. Courty, J.-M. Tarascon, and M. R. Palacín. *Energy & Environmental Science*, 5(9):8572, 2012.

[62] X. Xia, M. N. Obrovac, and J. R. Dahn. *Electrochemical and Solid-State Letters*, 14(9):A130, 2011.

[63] D. Kundu, E. Talaie, V. Duffort, and L. F. Nazar. *Angewandte Chemie International Edition*, 54(11):3431–3448, 2015.

[64] K. Vignarooban, R. Kushagra, A. Elango, P. Badami, B.-E. Mellander, X. Xu, T. Tucker, C. Nam, and A. Kannan. *International Journal of Hydrogen Energy*, 41(4):2829–2846, 2016.

[65] H. Che, S. Chen, Y. Xie, H. Wang, K. Amine, X.-Z. Liao, and Z.-F. Ma. *Energy & Environmental Science*, 10(5):1075–1101, 2017.

[66] B. Wang, X. Wang, C. Liang, M. Yan, and Y. Jiang. *ChemElectroChem*, 6(18):4848–4853, 2019.

[67] Q. Liu, C. Du, B. Shen, P. Zuo, X. Cheng, Y. Ma, G. Yin, and Y. Gao. *RSC Advances*, 6(91):88683–88700, 2016.

[68] H. Kim, H. Kim, Z. Ding, M. H. Lee, K. Lim, G. Yoon, and K. Kang. *Advanced Energy Materials*, 6(19):1600943, 2016.

[69] B. Jache and P. Adelhelm. *Angewandte Chemie International Edition*, 53(38):10169–10173, 2014.

[70] B. Jache, J. O. Binder, T. Abe, and P. Adelhelm. *Physical Chemistry Chemical Physics*, 18(21):14299–14316, 2016.

[71] D. Saurel, B. Orayech, B. Xiao, D. Carriazo, X. Li, and T. Rojo. *Advanced Energy Materials*, 8(17):1703268, 2018.

[72] C. Bommier, T. W. Surta, M. Dolgos, and X. Ji. *Nano Letters*, 15(9):5888–5892, 2015.

[73] L. Zhao, H.-L. Pan, Y.-S. Hu, H. Li, and L.-Q. Chen. *Chinese Physics B*, 21(2):028201, 2012.

[74] S. Komaba, Y. Matsuura, T. Ishikawa, N. Yabuuchi, W. Murata, and S. Kuze. *Electrochemistry Communications*, 21:65–68, 2012.

[75] J. W. Wang, X. H. Liu, S. X. Mao, and J. Y. Huang. *Nano Letters*, 12(11):5897–5902, 2012.

[76] C.-H. Lim, T.-Y. Huang, P.-S. Shao, J.-H. Chien, Y.-T. Weng, H.-F. Huang, B. J. Hwang, and N.-L. Wu. *Electrochimica Acta*, 211:265–272, 2016.

[77] Z. Gong and Y. Yang. *Energy & Environmental Science*, 4(9):3223, 2011.

[78] V. Palomares, P. Serras, I. Villaluenga, K. B. Hueso, J. Carretero-González, and T. Rojo. *Energy & Environmental Science*, 5(3):5884, 2012.

[79] C. Masquelier and L. Croguennec. *Chemical Reviews*, 113(8):6552–6591, 2013.

[80] M. Reynaud, A. Wizner, N. A. Katcho, L. C. Loaiza, M. Galceran, J. Carrasco, T. Rojo, M. Armand, and M. Casas-Cabanas. *Electrochemistry Communications*, 84:14–18, 2017.

[81] B. L. Cushing and J. B. Goodenough. *Journal of Solid State Chemistry*, 162(2):176–181, 2001.

[82] W. Song, X. Cao, Z. Wu, J. Chen, Y. Zhu, H. Hou, Q. Lan, and X. Ji. *Langmuir*, 30(41):12438–12446, 2014.

[83] P. Moreau, D. Guyomard, J. Gaubicher, and F. Boucher. *Chemistry of Materials*, 22(14):4126–4128, 2010.

[84] S.-M. Oh, S.-T. Myung, J. Hassoun, B. Scrosati, and Y.-K. Sun. *Electrochemistry Communications*, 22:149–152, 2012.

[85] M. Galceran, D. Saurel, B. Acebedo, V. V. Roddatis, E. Martin, T. Rojo, and M. Casas-Cabanas. *Physical Chemistry Chemical Physics*, 16(19):8837, 2014.

[86] Y. Lu, L. Wang, J. Cheng, and J. B. Goodenough. *Chemical Communications*, 48(52):6544, 2012.

[87] C. D. Wessells, R. A. Huggins, and Y. Cui. *Nature Communications*, 2(1):550, 2011.

[88] X. Li, Y. Wang, D. Wu, L. Liu, S.-H. Bo, and G. Ceder. *Chemistry of Materials*, 28(18):6575–6583, 2016.

[89] M. H. Han, E. Gonzalo, G. Singh, and T. Rojo. *Energy Environ. Sci.*, 8(1):81–102, 2015.

[90] C. Delmas, C. Fouassier, and P. Hagenmuller. *Physica B+C*, 99(1):81–85, 1980.

[91] R. J. Clément, P. G. Bruce, and C. P. Grey. *Journal of The Electrochemical Society*, 162(14):A2589–A2604, 2015.

[92] J. W. Choi and D. Aurbach. *Nature Reviews Materials*, 1(4):16013, 2016.

[93] G. Singh, B. Acebedo, M. C. Cabanas, D. Shanmukaraj, M. Armand, and T. Rojo. *Electrochemistry Communications*, 37:61–63, 2013.

[94] B. Zhang, R. Dugas, G. Rousse, P. Rozier, A. M. Abakumov, and J.-M. Tarascon. *Nature Communications*, 7(1):10308, 2016.

[95] M. Sathiya, J. Thomas, D. Batuk, V. Pimenta, R. Gopalan, and J.-M. Tarascon. *Chemistry of Materials*, 29(14):5948–5956, 2017.

[96] K. Kubota, N. Yabuuchi, H. Yoshida, M. Dahbi, and S. Komaba. *MRS Bulletin*, 39(05):416–422, 2014.

[97] S. Miyazaki, S. Kikkawa, and M. Koizumi. *Synthetic Metals*, 6:211–217, 1983.

[98] S. Komaba, C. Takei, T. Nakayama, A. Ogata, and N. Yabuuchi. *Electrochemistry Communications*, 12(3):355–358, 2010.

[99] D. Hamani, M. Ati, J.-M. Tarascon, and P. Rozier. *Electrochemistry Communications*, 13(9):938–941, 2011.

[100] K. Kubota, I. Ikeuchi, T. Nakayama, C. Takei, N. Yabuuchi, H. Shiiba, M. Nakayama, and S. Komaba. *The Journal of Physical Chemistry C*, 119(1):166–175, 2015.

[101] H. Wang, Y. Xiao, C. Sun, C. Lai, and X. Ai. *RSC Advances Journal*, 5(129):106519–106522, 2015.

[102] Y.-T. Zhou, X. Sun, B.-K. Zou, J.-Y. Liao, Z.-Y. Wen, and C.-H. Chen. *Electrochimica Acta*, 213:496–503, 2016.

[103] P.-F. Wang, Y. You, Y.-X. Yin, Y.-S. Wang, L.-J. Wan, L. Gu, and Y.-G. Guo. *Angewandte Chemie International Edition*, 55(26):7445–7449, 2016.

[104] P.-F. Wang, H. Xin, T.-T. Zuo, Q. Li, X. Yang, Y.-X. Yin, X. Gao, X. Yu, and Y.-G. Guo. *Angewandte Chemie International Edition*, 57(27):8178–8183, 2018.

[105] S. Guo, Y. Sun, P. Liu, J. Yi, P. He, X. Zhang, Y. Zhu, R. Senga, K. Suenaga, M. Chen, and H. Zhou. *Science Bulletin*, 63(6):376–384, 2018.

[106] H. Wang, X.-Z. Liao, Y. Yang, X. Yan, Y.-S. He, and Z.-F. Ma. *Journal of The Electrochemical Society*, 163(3):A565–A570, 2016.

[107] Y. Xie, H. Wang, G. Xu, J. Wang, H. Sheng, Z. Chen, Y. Ren, C.-J. Sun, J. Wen, J. Wang, D. J. Miller, J. Lu, K. Amine, and Z.-F. Ma. *Advanced Energy Materials*, 6(24):1601306, 2016.

[108] H. Van Nguyen, H. T. N. Nguyen, N. L. T. Huynh, A. L. B. Phan, M. Van Tran, and P. M. L. Le. *Journal of Solid State Electrochemistry*, 24(1):57–67, 2020.

[109] X. Li, D. Wu, Y.-N. Zhou, L. Liu, X.-Q. Yang, and G. Ceder. *Electrochemistry Communications*, 49:51–54, 2014.

[110] J.-L. Yue, Y.-N. Zhou, X. Yu, S.-M. Bak, X.-Q. Yang, and Z.-W. Fu. *Journal of Materials Chemistry A*, 3(46):23261–23267, 2015.

[111] N. Ortiz-Vitoriano, N. E. Drewett, E. Gonzalo, and T. Rojo. *Energy Environ. Sci.*, 10:1051–1074, 2017.

[112] Z. Cao, L. Li, C. Zhou, X. Ma, and H. Wang. *Functional Materials Letters*, 13(3):2051010, 2020.

[113] S. C. Han, H. Lim, J. Jeong, D. Ahn, W. B. Park, K.-S. Sohn, and M. Pyo. *Journal of Power Sources*, 277:9–16, 2015.

[114] M. Matsui, F. Mizukoshi, and N. Imanishi. *Journal of Power Sources*, 280:205–209, 2015.

[115] X. Wu, G.-L. Xu, G. Zhong, Z. Gong, M. J. McDonald, S. Zheng, R. Fu, Z. Chen, K. Amine, and Y. Yang. *ACS Applied Materials & Interfaces*, 8(34):22227–22237, 2016.

[116] Y. Kee, N. Dimov, S. Champet, D. H. Gregory, and S. Okada. *Ionics*, 22(11):2245–2248, 2016.

[117] G. Singh, N. Tapia-Ruiz, J. M. Lopez del Amo, U. Maitra, J. W. Somerville, A. R. Armstrong, J. Martinez de Ilarduya, T. Rojo, and P. G. Bruce. *Chemistry of Materials*, 28(14):5087–5094, 2016.

[118] R. Berthelot, D. Carlier, and C. Delmas. *Nature Materials*, 10(1):74–80, 2011-01.

[119] N. Yabuuchi and S. Komaba. *Science and Technology of Advanced Materials*, 15(4):043501, 2014.

[120] P. Rozier, M. Sathiya, A.-R. Paulraj, D. Foix, T. Desaunay, P.-L. Taberna, P. Simon, and J.-M. Tarascon. *Electrochemistry Communications*, 53:29–32, 2015.

[121] D. Mikhailova, O. M. Karakulina, D. Batuk, J. Hadermann, A. M. Abakumov, M. Herklotz, A. A. Tsirlin, S. Oswald, L. Giebeler, M. Schmidt, J. Eckert, M. Knapp, and H. Ehrenberg. *Inorganic Chemistry*, 55(14):7079–7089, 2016.

[122] B. Mortemard de Boisse, G. Liu, J. Ma, S.-i. Nishimura, S.-C. Chung, H. Kiuchi, Y. Harada, J. Kikkawa, Y. Kobayashi, M. Okubo, and A. Yamada. *Nature Communications*, 7(1):11397, 2016.

[123] A. J. Perez, D. Batuk, M. Saubanère, G. Rousse, D. Foix, E. McCalla, E. J. Berg, R. Dugas, K. H. W. van den Bos, M.-L. Doublet, D. Gonbeau, A. M. Abakumov, G. Van Tendeloo, and J.-M. Tarascon. *Chemistry of Materials*, 28(22):8278–8288, 2016.

[124] B. Mortemard de Boisse, M. Reynaud, J. Ma, J. Kikkawa, S.-i. Nishimura, M. Casas-Cabanas, C. Delmas, M. Okubo, and A. Yamada. *Nature Communications*, 10(1):2185, 2019.

[125] J. Reed, G. Ceder, and A. Van Der Ven. *Electrochemical and Solid-State Letters*, 4(6):A78, 2001.

[126] J. Lee, A. Urban, X. Li, D. Su, G. Hautier, and G. Ceder. *Science*, 343(6170):519–522, 2014.

[127] D. Mohanty, J. Li, D. P. Abraham, A. Huq, E. A. Payzant, D. L. Wood, and C. Daniel. *Chemistry of Materials*, 26(21):6272–6280, 2014.

[128] J. Zheng, P. Xu, M. Gu, J. Xiao, N. D. Browning, P. Yan, C. Wang, and J.-G. Zhang. *Chemistry of Materials*, 27(4):1381–1390, 2015.

[129] M. Sathiya, K. Hemalatha, K. Ramesha, J.-M. Tarascon, and A. S. Prakash. *Chemistry of Materials*, 24(10):1846–1853, 2012.

[130] J. R. Croy, M. Balasubramanian, K. G. Gallagher, and A. K. Burrell. *Accounts of Chemical Research*, 48(11):2813–2821, 2015.

[131] E. Talaie, V. Duffort, H. L. Smith, B. Fultz, and L. F. Nazar. *Energy & Environmental Science*, 8(8):2512–2523, 2015.

[132] A. R. Armstrong, M. Holzapfel, P. Novák, C. S. Johnson, S.-H. Kang, M. M. Thackeray, and P. G. Bruce. *Journal of the American Chemical Society*, 128:8694–8698, 2006.

[133] E. McCalla, A. M. Abakumov, M. Saubanère, D. Foix, E. J. Berg, G. Rousse, M.-L. Doublet, D. Gonbeau, P. Novák, G. V. Tendeloo, R. Dominko, and J.-M. Tarascon. *Science*, 350(6267):1516–1521, 2015.

[134] A. R. Armstrong, N. Dupre, A. J. Paterson, C. P. Grey, and P. G. Bruce. *Chemistry of Materials*, 16(16):3106–3118, 2004.

[135] J. Cabana, S.-H. Kang, C. S. Johnson, M. M. Thackeray, and C. P. Grey. *Journal of The Electrochemical Society*, 156(9):A730, 2009.

[136] J. N. Reimers and J. R. Dahn. *Journal of The Electrochemical Society*, 139(8):2091, 1992.

[137] T. Ohzuku and A. Ueda. *Journal of The Electrochemical Society*, 141(11):2972, 1994.

[138] E. Gonzalo, M. H. Han, J. M. López del Amo, B. Acebedo, M. Casas-Cabanas, and T. Rojo. *Journal of Materials Chemistry A*, 2:18523–18530, 2014.

[139] Y. H. Jung, A. S. Christiansen, R. E. Johnsen, P. Norby, and D. K. Kim. *Advanced Functional Materials*, 25(21):3227–3237, 2015.

[140] N. Sharma, E. Gonzalo, J. C. Pramudita, M. H. Han, H. E. A. Brand, J. N. Hart, W. K. Pang, Z. Guo, and T. Rojo. *Advanced Functional Materials*, 25(31):4994–5005, 2015.

[141] R. J. Gummow, N. Sharma, R. Feng, G. Han, and Y. He. *Journal of The Electrochemical Society*, 160(10):A1856–A1862, 2013.

[142] B. Mortemard de Boisse, D. Carlier, M. Guignard, L. Bourgeois, and C. Delmas. *Inorganic Chemistry*, 53(20):11197–11205, 2014.

[143] L. Mu, S. Xu, Y. Li, Y.-S. Hu, H. Li, L. Chen, and X. Huang. *Advanced Materials*, 27(43):6928–6933, 2015.

[144] W. K. Pang, S. Kalluri, V. K. Peterson, N. Sharma, J. Kimpton, B. Johannessen, H. K. Liu, S. X. Dou, and Z. Guo. *Chemistry of Materials*, 27(8):3150–3158, 2015.

[145] Y. Gao, M. V. Yakovleva, and W. B. Ebner. *Electrochemical and Solid-State Letters*, 1(3):117–119, 1998.

[146] A. Van der Ven and G. Ceder. *Electrochemistry Communications*, 6(10):1045–1050, 2004.

[147] K. Kang, Y. S. Meng, J. Bréger, C. P. Grey, and G. Ceder. *Science*, 311(5763):977–980, 2006.

[148] D. Buchholz, C. Vaalma, L. G. Chagas, and S. Passerini. *Journal of Power Sources*, 282:581–585, 2015.

[149] J. Reed and G. Ceder. *Chemical Reviews*, 104(10):4513–4534, 2004.

[150] N. Yabuuchi, H. Yoshida, and S. Komaba. *Electrochemistry*, 80(10):716–719, 2012.

[151] E. Lee, D. E. Brown, E. E. Alp, Y. Ren, J. Lu, J.-J. Woo, and C. S. Johnson. *Chemistry of Materials*, 27:6755–6764, 2015.

[152] J. S. Thorne, S. Chowdhury, R. A. Dunlap, and M. N. Obrovac. *Journal of The Electrochemical Society*, 161(12):A1801–A1805, 2014.

[153] J. Billaud, G. Singh, A. R. Armstrong, E. Gonzalo, V. Roddatis, M. Armand, T. Rojo, and P. G. Bruce. *Energy Environ. Sci.*, 7(4):1387–1391, 2014.

[154] N. Tran, L. Croguennec, M. Ménétrier, F. Weill, P. Biensan, C. Jordy, and C. Delmas. *Chemistry of Materials*, 20(15):4815–4825, 2008.

[155] B. Xu, C. R. Fell, M. Chi, and Y. S. Meng. *Energy & Environmental Science*, 4(6):2223, 2011.

[156] N. Yabuuchi, R. Hara, M. Kajiyama, K. Kubota, T. Ishigaki, A. Hoshikawa, and S. Komaba. *Advanced Energy Materials*, 4(13):1301453, 2014.

[157] S. Kikkawa, S. Miyazaki, and M. Koizumi. *Materials research bulletin*, 20(4):373–377, 1985.

[158] Y. Takeda, K. Nakahara, M. Nishijima, N. Imanishi, and O. Yamamoto. *Materials Research Bulletin*, 29(6):659–666, 1994.

[159] S. Okada, Y. Takahashi, T. Kiyabu, T. Doi, J.-I. Yamaki, and T. Nishida. In *Meeting Abstracts*, pages 201–201. The Electrochemical Society, 2006.

[160] J. Zhao, L. Zhao, N. Dimov, S. Okada, and T. Nishida. *Journal of The Electrochemical Society*, 160(5):A3077–A3081, 2013.

[161] X. Wang, G. Liu, T. Iwao, M. Okubo, and A. Yamada. *The Journal of Physical Chemistry C*, 118(6):2970–2976, 2014.

[162] R. Kataoka, K. Kuratani, M. Kitta, N. Takeichi, T. Kiyobayashi, and M. Tabuchi. *Electrochimica Acta*, 182:871–877, 2015.

[163] J. S. Thorne, R. A. Dunlap, and M. N. Obrovac. *Journal of The Electrochemical Society*, 160(2):A361–A367, 2013.

[164] M. A. Halcrow. *Chemical Society Reviews*, 42(4):1784–1795, 2013.

[165] H. A. Jahn and E. Teller. *Proceedings of the Royal Society A*, 159A:220–235, 1937.

[166] X. Ma, H. Chen, and G. Ceder. *Journal of The Electrochemical Society*, 158(12):A1307–A1312, 2011.

[167] J. Billaud, G. Singh, A. R. Armstrong, E. Gonzalo, V. Roddatis, M. Armand, T. Rojo, and P. G. Bruce. *Energy & Environmental Science*, 7(4):1387, 2014.

[168] X. Li, X. Ma, D. Su, L. Liu, R. Chisnell, S. P. Ong, H. Chen, A. Toumar, J.-C. Idrobo, Y. Lei, J. Bai, F. Wang, J. W. Lynn, Y. S. Lee, and G. Ceder. *Nature Materials*, 13(6):586–592, 2014.

[169] N. Yabuuchi, M. Kajiyama, J. Iwatate, H. Nishikawa, S. Hitomi, R. Okuyama, R. Usui, Y. Yamada, and S. Komaba. *Nature Materials*, 11(6):512–517, 2012.

[170] B. Mortemard de Boisse, J.-H. Cheng, D. Carlier, M. Guignard, C.-J. Pan, S. Bordère, D. Filimonov, C. Drathen, E. Suard, B.-J. Hwang, A. Wattiaux, and C. Delmas. *Journal of Materials Chemistry A*, 3(20):10976–10989, 2015.

[171] Y. Mo, S. P. Ong, and G. Ceder. *Chemistry of Materials*, 26(18):5208–5214, 2014.

2 | Experimental methodology

Contents

2.1 Synthesis of the active material

All the samples presented in this work have been prepared via ceramic method. This synthesis method consists of direct reaction of solid components at high temperature [1]. In most cases for this work, sodium carbonate and transition metal oxides have been used as precursors, but specific precursors for each synthesized material will be presented in Synthesis and Characterization chapter (Chapter 3). The reagents have been hand mixed together in stoichiometric amounts as powder using an agate mortar and a pestle. If any of the material elements is prone to evaporation, an excess of its precursor has been added.

The mixture has been pressed into a pellet (125 MPa pressure) and has been heat treated in an alumina crucible. Depending on the needed atmosphere for the reaction, different furnaces have been used. When the material can be heated under air atmosphere, box furnaces, also called muffle furnaces, have been used (Fig. 2.1a). When oxygen atmosphere is needed, a tubular oven has been used (Fig. 2.1b). It consist of an alumina tube that is drained with the appropriate gas before the sample is introduced. The experimental details for the synthesis of each material will be presented in Chapter 3.

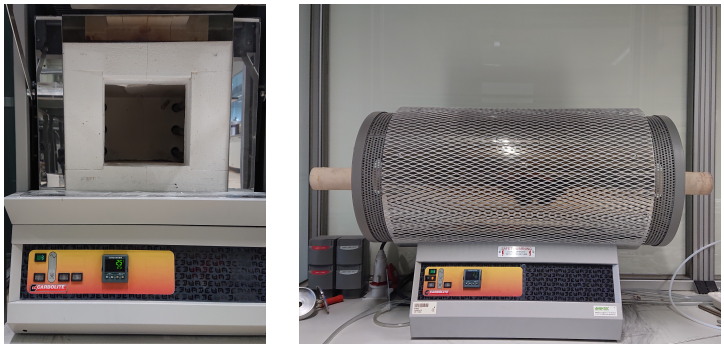

(a) (b)

Figure 2.1: **(a)** Box and **(b)** tube furnaces used for the synthesis of the layered oxides.

2.2 Physicochemical characterization

2.2.1 X-ray diffraction (XRD)

2.2.1.1 Basic principles

The X-ray diffraction (XRD) technique is used to determine the crystallographic structure of a solid. The electron cloud of the atoms constituting the sample elastically scatter the incident X-ray beam, creating constructive or destructive interferences, depending on the relation of emitted wavelength λ and the position of the scattering atoms. Constructive interferences will occur when

Bragg's condition is respected (equation 2.1 and Fig. 2.2), where θ is the incident and reflected X-ray angle in the plane perpendicular to the atomic reflection planes, $d_{hk\ell}$ is the distance between $(h\,k\,\ell)$ reflection planes as defined by Miller indexes and n is an integer.

$$2d_{hk\ell}\sin\theta = n\lambda \tag{2.1}$$

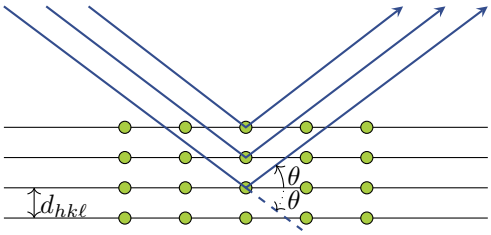

Figure 2.2: X-ray diffraction geometry on $(h\,k\,\ell)$ plane of a crystalline solid. Blue arrows represent X-rays, green dots represent electron clouds and black lines help visualize crystalline $(h\,k\,\ell)$ planes.

This can also be defined in the reciprocal space Q:

$$Q = \frac{4\pi}{\lambda}\sin\theta = \frac{2n\pi}{d_{hk\ell}} \tag{2.2}$$

In this case, the result does not depend on the wavelength of the source.

The Ewald construction, which is schematically presented in Fig. 2.3, combines the real and reciprocal space concepts. Ewald's sphere has a radius equal to the wavelength λ, and it is centered at the position of the sample. Whenever Bragg's equation is satisfied, a lattice point in reciprocal space (k_i in Fig. 2.3) will coincide with the surface of the sphere. In a sample with randomly oriented particles (as in a powder sample), the different crystallites will be projected in a way that they will diffract in every direction creating a cone with a semiaperture of 2θ. Concentric cones will be created for all the reflecting configurations. In a 2D detector, as the one represented in Fig. 2.3, the intensity at each aperture is homogeneously distributed in the base of the cone, creating the so called Debye rings, as in the example presented in Fig. 2.4 (left side) [2]. However, it is easier, and hence more common, to obtain 1D patterns (see the right side of Fig. 2.4) with the use of linear detectors, where a limited angular aperture of the ring is measured.

The intensity of the diffracted ray depends in the atomic arrangement inside the unit cell [3], but also on various instrumental or extrinsic factors, such as the multiplicity of Bragg planes, the Lorentz-Polarization factor, extinction, absorption and microabsorption or the monochromator polarization. See Section 2.6.2.1 and its Table 2.1 for more details on these parameters. If the particles present a preferred orientation, as it can occur in the case of platelet-like samples, the intensity of certain Debye rings will not be homogeneously distributed in the whole circumference, and therefore, the intensity of these peaks in a 1D detector will be altered.

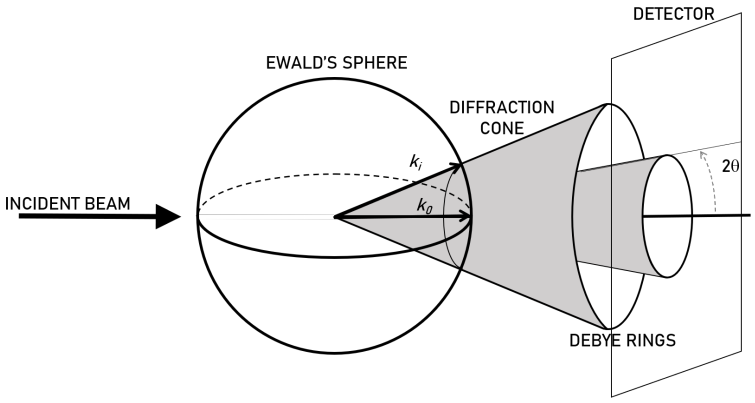

Figure 2.3: Schematic representation of Ewald's sphere and the formation of diffraction cones.

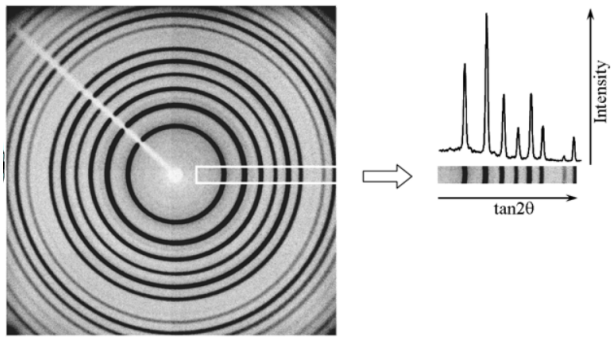

Figure 2.4: Example of LaB_6 diffraction pattern. Debye rings in a 2D detector (left) and its aspect in the most common representation form of 1D plot (right) [2].

The XRD analysis has been carried out using FullProf Suite software [4], a program developed for the description of crystalline structures. This software can be used for Le Bail (or profile matching) or Rietveld refinements. In the later, the crystalline structure parameters are refined. Some of the most commonly refined parameters include space group, cell parameters, atomic positions and occupancies, thermal factors or texture parameters (such as preferred orientation). In Le Bail type refinements on the other hand, only the symmetry operations of the crystalline structure are considered (space group and cell parameters). This allows defining the aperture of the Debye ring, but their intensity is empirically calculated by minimum square fitting, without any physical meaning. This program also allows the refinement of the peaks shape (mathematical description, width and asymmetries) or background among others.

2.2.1.2 Pristine powder sample diffraction

2.2.1.2.1 Lab-scale diffractometer

In the realization of this work Bruker diffractometers have been used at CIC Energigune (see Fig. 2.5b), equipped with copper or cobalt X-ray tube source and a Bragg-Brentano geometry (see Fig. 2.5a). The Advance D8, dedicated to *in-situ* studies uses a Cu K-α_1 ($\lambda = 1.5406$ Å) and Cu K-α_2 ($\lambda = 1.5444$ Å) tube for copper and Co K-α_1 ($\lambda = 1.78896$ Å) and Co K-α_2 ($\lambda = 1.7928$ Å) tube for the cobalt (the tube was substituted from Cu to Co during the course of this thesis). The Discover D8, dedicated to routine powder diffraction, has a monochromator in order to emit only with Cu K-α_1 wavelength. In both cases the reflected ray is focused in the detector, which uses an electronic discrimination to avoid iron fluorescence. The photons travel through a slit (axial soller slit) to control the divergence of the incident beam and a pinhole to get a round beam shape. The reflected beam scattered by the sample passes through a Ni filter to avoid Cu K-β wavelength.

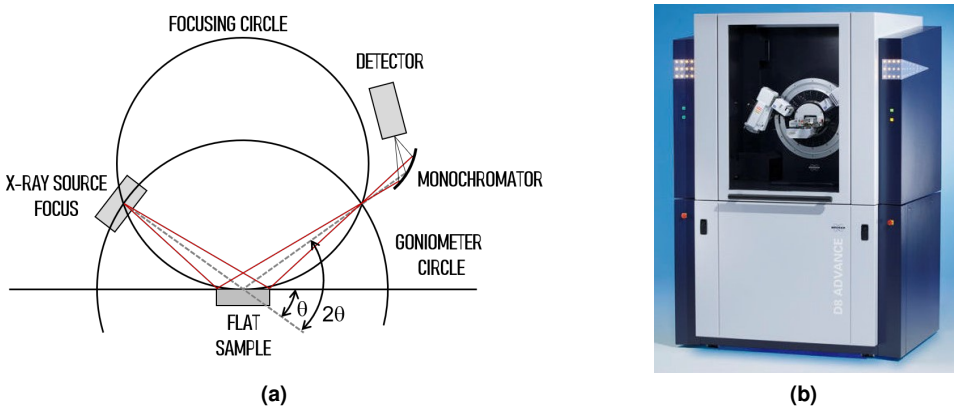

Figure 2.5: **(a)** Schema of the Bragg-Brentano geometry, where the X-ray source (X-ray tube), the flat powder sample and the detector are highlighted [5]. **(b)** Bruker D8 diffractometer.

The holders used to measure the samples in Bruker D8 diffractometers are presented in Fig. 2.6. To avoid moisture contamination the samples are mounted inside a glove box and are covered with Kapton film.

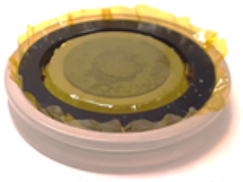

Figure 2.6: XRD sample holder for Bruker D8 diffractometers. The air sensitive sample is protected with Kapton film.

2.2.1.2.2 Synchrotron HRXRD at ALBA's MSPD

High resolution X-ray diffraction (HRXRD) has been performed for several samples at the Material Science and Powder Diffraction (MSPD) beamline at ALBA synchrotron (Barcelona) (see Fig. 2.7, where the main components of the MSPD beamline have been highlighted). Although the X-ray source is very different to lab-scale diffractometer, the measurement follows the same principle. At ALBA synchrotron, the electrons are accelerated in a ring to 3 GeV and are released to the different beamlines, where the energy of the beam can be tuned. For this work, the chosen energy has been 15 keV ($\lambda = 0.8266$ Å). The X-ray flux is higher, and thus, acquisition time is reduced, and resolution is usually higher. The measurements are done in transmission geometry, and the transmitted scattered signal is detected with a linear Mythen detector.

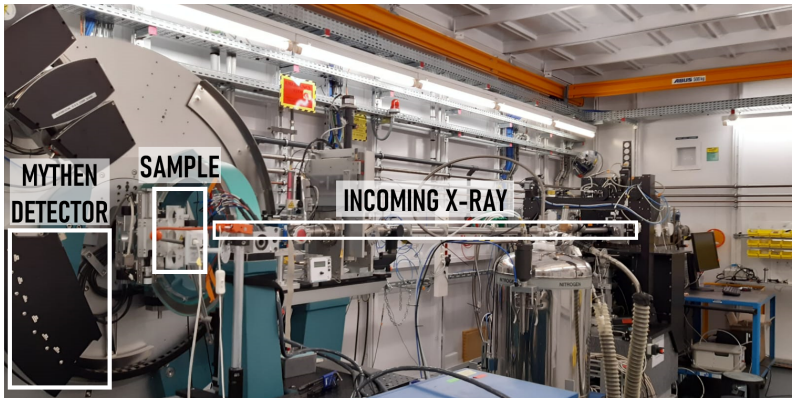

Figure 2.7: MSPD beamline at ALBA synchrotron. The incoming beam tube, the position of the sample and the detector have been highlighted.

Samples for synchrotron measurements have been air tight sealed inside an Argon glove-box in 0.25 mm radius capillaries, which are placed in the holders with the help of vacuum grease as shown in Fig. 2.8. Borosilicate (for room temperature measurements) and quartz capillaries (for high temperature measurements) have been used during the realization of this work.

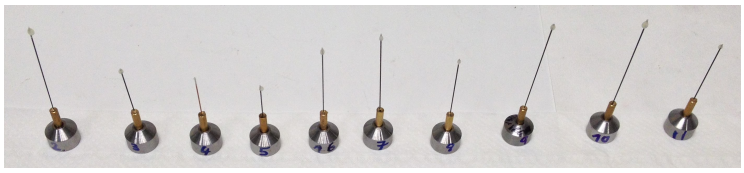

Figure 2.8: Borosilicate capillaries mounted in the appropriate holders for synchrotron measurements.

2.2.2 Small angle X-ray scattering (SAXS)

Small angle X-ray scattering (SAXS) is a non-destructive method for analyzing particle size, shape and surface. The zero-angle diffraction contains morphological information in angstrom to micro size region, depending on the measured angle. In order to estimate the surface area of the powder material, the Porod region is analyzed. The Porod regime is given for $Q \gg 2\pi/D$ where D is the characteristic scale of the object being investigated (around 10^2 nm grain size) and Q is the reciprocal space. The slope of the transmitted intensity depends on the specific surface S of the particles. Considering that the interface between two medias is sharp, Porod's law can be described as [6]:

$$I(Q) = 2\pi \frac{S}{Q^4} \Delta\rho^2 \tag{2.3}$$

where $\Delta\rho$ is the scattering length density contrast between two medias, in this case, the material to be measured and vacuum, which depends on their electronic densities.

Assuming spherical particles, the radius of the particles can be estimated using the following expression:

$$R = \frac{3}{Sd} \tag{2.4}$$

where d is the theoretical density of the material.

As shown in Fig. 2.9a the sample is illuminated by a collimated X-ray beam and a 2D detector registers the scattered radiation in transmission geometry, which is more appropriate than the reflection geometry for small angle scattering. In order to avoid the scattering by the air, the entire path is under vacuum.

The equipment used is a Bruker Nanostar U equipped with a Cu K-α X-ray source and a VÅNTEC-2000 2-D detector (see Fig. 2.9a). The sample to detector distance has been set to its maximum value of 108 cm. The intensities were corrected for black noise, background scattering noise, transmission, spatial distortion, and spherical distortion. The incident beam has been calibrated in order to obtain absolute intensities in cm^{-1}, which have been then transformed into specific values by dividing by the density of the samples.

The sample in powder form has been packed in a 0.15 mm thick Cu holder with a cavity of 2.45 mm. A low absorbing tape has been used to encapsulate and seal the sample, which has been filled into the sample holder inside an Argon filled glove-box and transferred into the SAXS chamber in an airtight container.

The SAXS measurements presented in this work have been carried out and processed by M. Jauregui.

2.2.3 Electronic microscopy

Electron microscopies work in a similar way to X-ray diffraction, but instead of the X-ray beam, an electron beam is used, which is focused using magnetic lenses. The shorter wavelength of the electrons compared to the X-rays allows a higher spatial resolution according to Bragg's law (see equation 2.1).

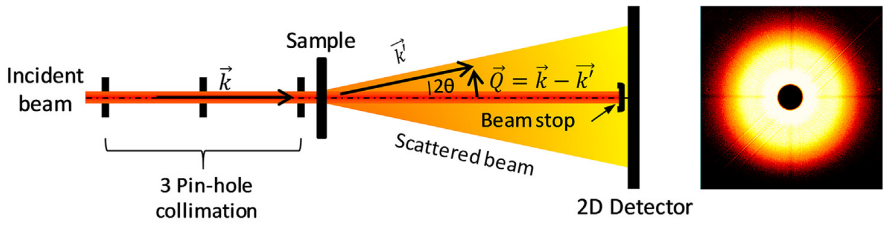

(a)

(b)

Figure 2.9: **(a)** Schematic representation of the geometry of the SAXS instrument [7]. **(b)** SAXS Nanostar instrument.

2.2.3.1 Scanning electron microscopy (SEM)

A topographic analysis has been done using scanning electron microscopy (SEM) (FEI Quanta 200FEG model) imaging to measure the particle sizes and morphology.

SEM microscopy uses an electron beam to create the image, therefore, the sample must be conductive so that the sample does not get charged. In SEM microscopies, the beam scans the surface of the sample and interactions occur between the beam and the sample; backscattered and secondary electrons, photons (X-rays and visible) and heat are created (see Fig. 2.10) [8].

To create topographic images, secondary electrons (electrons from valence band) are used. Their relative direction to the surface produces a contrast of roughness in the detector.

The powder sample has been dispersed on top of a conducting carbon tape. Since the materials studied in this work are bad electronic conductors, finely dispersed powder has been characterized, particularly focusing on smaller aggregates facilitating the electron escape to the carbon tape substrate and thus avoiding charging the particles.

The SEM images presented in this work have been taken with the help of B. Acebedo and M. Echeverría.

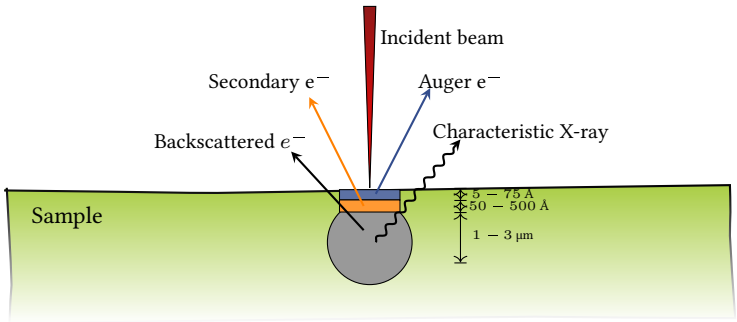

Figure 2.10: Schema of the interaction between sample and electron beam in scanning electron microscopy.

2.2.3.2 Transmission electron microscopy (TEM)

When the sample is small enough, electrons can be collected in transmission mode, with the so called transmission electron microscopy (TEM) technique. The equipment used for TEM imaging is a FEI Tecnai F20 electron microscope, operating at 200 kV. The beam is more energetic than that of the SEM, that is, the wavelength is shorter, and atomic resolution images can be collected. However, the sample's thickness needs to be smaller than 100-200 nm for the beam to be able to transmit through the particles.

The orientation of the particles is very important, since the electron beam is transmitted through the sample. When the crystal has been oriented in a particular crystallographic orientation it results in a neat projected image of atomic columns [9].

TEM microscopies can also function in scanning transmission electron microscopy (STEM) mode, where the beam is focused on a fine spot and the sample is scanned, that is, STEM combines the principles of transmission electron microscopy and scanning electron microscopy [10]. STEM imaging enables the use of other signals that cannot be correlated in TEM, like characteristic X-rays, which are sensitive to the composition.

Besides the higher resolution compared with SEM imagining, one of the main advantages of the TEM imaging is the possibility to do local electron diffraction patterns. It is the same working principle as the X-ray diffraction presented in Section 2.2.1, according to Bragg's law. In this case, since the beam is focused in a single crystal oriented in a particular way, the diffracted electrons are seen as bright spots instead of rings.

In Fig. 2.11 the principal components and ray diagrams in TEM, diffraction and STEM modes are shown.

For TEM sample preparation, the dry powder has been placed on top of a 400 mesh copper grid with a Lacey carbon layer inside the glove box. The sample has then been transferred to the microscope without air exposure.

The TEM images presented in this work have been carried out by Dr. F. Bonilla.

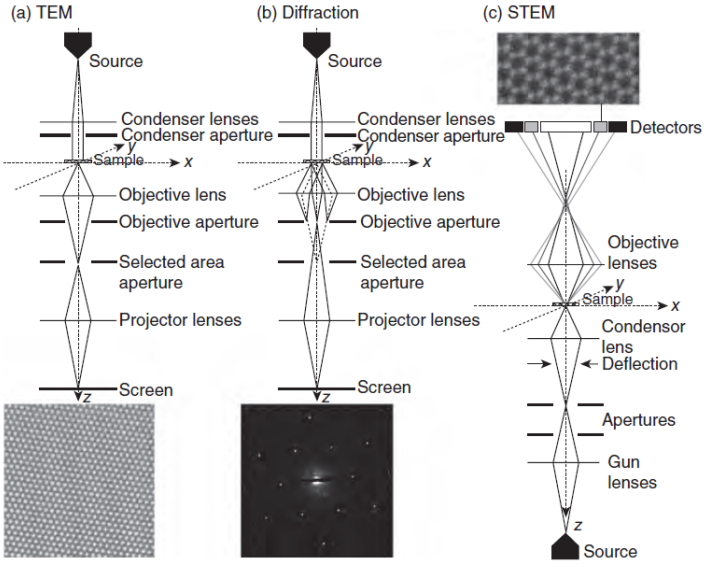

Figure 2.11: Schema of the principal components and ray diagrams in **(a)** TEM, **(b)** diffraction and **(c)** STEM modes [11].

2.2.3.3 Energy dispersive X-ray spectroscopy (EDX)

Atoms in the material are ionized with the electron beam, and they can relax by electron shell-to-shell transitions. This leads to Auger electron ejection or X-ray emission (see Fig. 2.10). The last are characteristic of the elements excited, in the surface of the sample. With this technique the energy of the emitted X-rays is analyzed by spectroscopy to detect the elements and do a semi-quantitative composition analysis. The energy dispersive X-ray spectroscopy (EDX) technique can be used in SEM and TEM microscopies.

2.2.4 Inductively coupled plasma optical emission spectrometry (ICP-OES)

In order to perform a quantitative elemental analysis in our samples, this is, to determine the concentrations of specific elements in the sample, inductively coupled plasma optical emission spectrometry (ICP-OES) measurements have been performed with a Horiba Ultima 2 Sequential ICP-OES equipment.

A solution of the sample is injected as an aerosol into a high temperature chamber where the sample is decomposed into its ionized constituent elements. These excited ions go to ground state emitting radiation, characteristic of each element. Relative intensity of the measured spectra is related with the concentration of each element. To determine relative concentrations, the instrument has to be previously calibrated.

In order to measure the sample it has to be diluted. In this work, the samples have been diluted in a 20% HNO_3 solution with the help of a heat treatment in a polytetrafluoroethylene reactor. Two

different methods have been used for the solvation, depending on the solubility constant K_s. The samples with a low K_s, that are easily dissolved, have been heated in a microwave during 15 minutes at 180°C. The samples with a high K_s have been heated in a muffle furnace during 10 hours at 180°C. Afterwards, the solution has been further dissolved with ICP grade H_2O (Chem-Lab ultra-pure water, LF < 1 µS/cm - 0.4 µm, UV filtrated) until a maximum of 20 mg/L of the most concentrated element is obtained.

This technique does not allow the quantification of oxygen in the samples. The results only compare the relative presence of alkali and transition metal elements. In this work, the obtained values have been normalized to the heaviest element present.

The ICP-OES measurements presented in this work have been carried out by N. Gomez and G. Liendo.

2.3 Magnetic characterization

The magnetic properties have been performed using the AC/DC magnetometry system (ACMS) option of a Quantum Design physical property measurement system (PPMS) equipment. The ACMS option, represented in Fig. 2.12, allows to perform AC susceptibility and DC magnetization measurements with an applied magnetic field up to 9 T, and an Evercool II system, allowing measurements at temperatures as low as 2 K.

The DC measurements are done using a technique called *extraction magnetometry*, which consists of moving a magnetized sample through the detection coils inducing a voltage in the coil set. The amplitude of the signal is proportional to the movement speed and magnetic moment of the sample. During the AC magnetic measurements, the PPMS applies an AC field on the sample of the desired intensity and frequency, and measures the induced current in the pick-up coils without sample motion.

The air sensitive samples have been mounted on the sample holder inside an Ar glove-box and have been transferred to the PPMS sample chamber in an airtight container with minimum air exposure. The holder is attached at the end of a rod that is inserted in the coil set. It packs the powder sample and keeps it in place relatively to the rod.

The zero field cool (ZFC) susceptibility measurements have been recorded while heating from 2.5 K to 300K in AC mode, with an oscillating applied field of 10 Oe and a frequency of 1000 Hz, and without any continuous external field. The field cool (FC) susceptibility measurements have been measured in the same way as the ZFC, after cooling down to 2.5 K with an applied DC field of 0.1 T.

The susceptibility is the relation between an applied magnetic field and the magnetic response of the material. χ susceptibility and χ^{-1} inverse susceptibility measurements can give information about the magnetic ordering type as the materials can be classified in four main magnetic groups depending on the behavior of the susceptibility: diamagnetic, paramagnetic, ferromagnetic and antiferromagnetic. Fig. 2.13 shows the typical susceptibility and inverse susceptibility response of

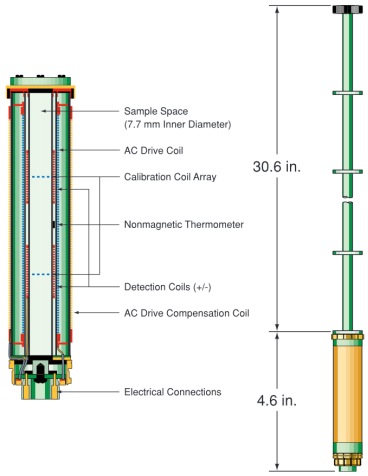

Figure 2.12: Coil set of PPMS ACMS from Quantum Design [12].

paramagnetic (with randomly oriented spins), ferromagnetic (with parallel aligned spins) and antiferromagnetic (with antiparallel aligned spins) materials. Ferromagnetic and antiferromagnetic samples show a transition temperature (T_C Curie and T_N Néel temperatures respectively) above which the thermal agitation is stronger than the spin alignment strength, and thus, paramagnetic behavior is observed. When the paramagnetic region of the inverse susceptibility is fitted with a linear curve, the temperature at which the line cuts the x axis reflects the nature of the sample:

- $T = 0$ for paramagnetic samples,
- $T = T_C > 0$ for ferromagnetic samples, and
- $T = \theta < 0$ for antiferromagnetic samples, where θ is the Weiss temperature.

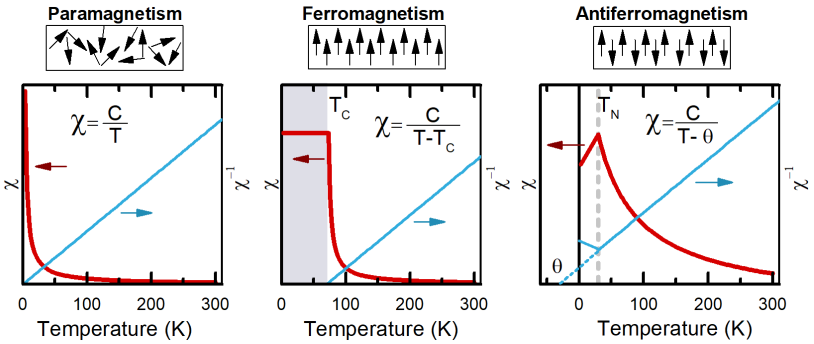

Figure 2.13: Temperature dependent susceptibility (χ, red) and inverse susceptibility (χ^{-1}, blue) of paramagnetic, ferromagnetic and antiferromagnetic solids.

Diamagnetism (not presented in Fig. 2.13) is a form of magnetism that only exists in the presence of an external magnetic field, in whose presence the orbital motion of the electron changes creating a weak magnetic field opposing the applied one. That is, diamagnetic samples present weak and negative susceptivility values in the presence of an external magnetic field. The holder used for the measurements has a diamagnetic response, but its influence in the total magnetic response is negligible.

2.4 Mössbauer spectroscopy

The Mössbauer spectroscopy is based in the energy level transitions that nuclei in atoms undergo. These energy levels depend on the electronic and magnetic environment, thus, energy level transition can provide information on the atom's local environment. The Mössbauer effect relies on the recoil-free emission of a γ-ray from a nucleus (source) in the excited state and the resonant absorption by an identical nucleus (absorber or sample) [13].

Most typically Mössbauer spectroscopy relies in ^{57}Fe instability, which decays giving off a gamma-ray (γ-ray) together with other types of energy. The source consist of ^{57}Co that decays on excited ^{57}Fe by electron capture, which then decays to ground state by γ-ray emission. In order to tune the emitted energy, Doppler Effect is used. The source is moved at a certain speed v, so that the change in energy can be written as:

$$\Delta E = E_\gamma v c^{-1} \tag{2.5}$$

Three main types of nuclear interactions are typically observed:

Isomer shift. A change in the s-electron density (e.g. produced by a change in valence) will result in a change of the Coulombic interactions, and consequently, in a change in nuclear levels. The difference in the nuclear radii of the ground and excited states results in the isomer shift (IS). The isomer shift can be used to determine the oxidation state among others. In high temperature studies, the IS will be affected by the second order Doppler shift, that adds to IS, resulting in a measured total **center shift** (CS) [14].

Quadrupole coupling. The electrostatic interaction of the nucleus with surrounding electronic charge splits the nuclear levels and gives rise to quadrupole coupling, and reflects the deviation of the spherical symmetry of the nucleus. Splitting can arise from charges in distant ions and the electrons in incompletely filled shells. Quadrupole coupling or quadrupole splitting (QS) can be used to determine spin state or site symmetry among others.

Magnetic hyperfine structure. The interaction between the nuclear magnetic dipole and the magnetic field coming from the atom's electrons is known as Zeeman Effect. The strength of the magnetic field is directly related to splitting energy, and thus, magnetic hyperfine splitting can be used to determine the magnetic field.

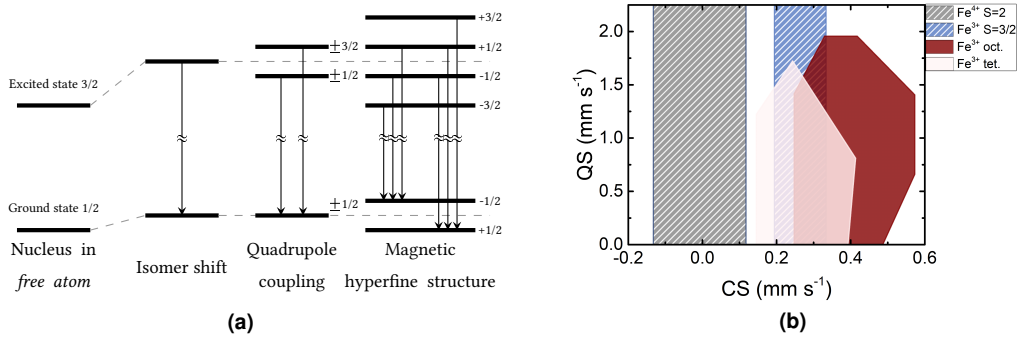

Figure 2.14: **(a)** Schema of decay of ^{57}Fe that gives rise to Mössbauer spectra. **(b)** Expected Mössbauer signals for Fe^{3+} and Fe^{4+} ions as a function of central shift (x axis) and quadrupole splitting (y axis). Values taken from Ref. [14] (lined color) and Ref. [15] (solid color).

A schema of the possible decay modes can be seen in Fig. 2.14a.

The expected center shift (CS) and quadrupole splitting (QS) values for Fe^{3+} and Fe^{4+} ions are presented in Fig. 2.14b. It is worth noting that there are very few compounds with iron (IV) oxidation state, and there is thus not a lot of information on Mössbauer spectroscopy of these compounds [16].

When preparing the powder samples for Mössbauer measurements in transmission mode two main considerations have to be taken into account: (i) low concentration of absorbing nuclei will cause low signal or long acquisition times and (ii) Mössbauer γ-rays are soft and are easily absorbed by heavy atoms. Material powder with Fe absorbing nuclei has been diluted with boron nitride (BN) powder to obtain a Fe nuclei concentration of $\approx$ 150 µmol cm^{-2}, which generally allows a good signal to noise ratio within a limited measuring time. The powder has been pressed in a 13 mm diameter pellet between adhesive tape and sealed under vacuum inside a polymeric bag to avoid contact with air. The sample has been flushed with nitrogen gas during the measurements. In order to avoid any possible preferred orientation contribution, the measurement has been done at magic angle, 54.7° perpendicular to the source and the detector, as it can be seen in Fig. 2.15. The calibration has been done with a Fe foil, and the presented central shifts are given with respect to α-Fe.

All the Mössbauer experiments have been carried out at Uppsala University, Sweden, at the Ångström Advanced Battery Center (ÅABC).

2.5 Electrochemical performance

2.5.1 Electrode preparation

Redox reactions must be favored in the electrodes. To this purpose carbon black (Super C65, IMERYS) has been used as conducting additive, which helps the electrons to move in the electrode.

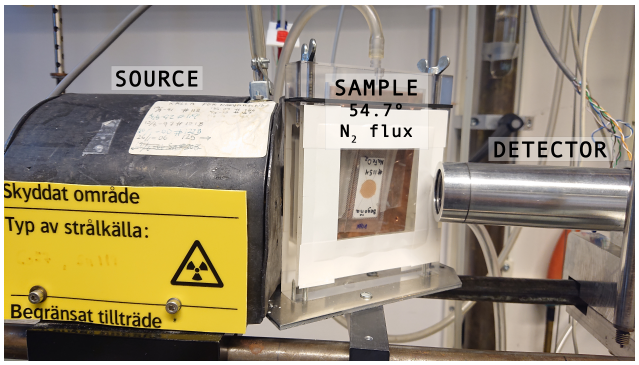

Figure 2.15: Set-up of the Mössbauer spectroscopy in transmission mode at Ångström Advanced Battery Center (ÅABC), Uppsala University, Sweden.

Polyvinylidene fluoride (PVdF) has been used as binder to increase the adhesion of the electrode composite and to the aluminum foil onto which it is attached. Active material and additives have been mixed inside an Argon glove-box using N-Methyl-2-pyrrolidone (NMP) as solvent. PVdF has been firstly dissolved in NMP, and carbon and active material (AM) have then been added and mixed with the magnetic stirrer until an homogeneous slurry has been obtained. An equilibrium has to be found in the amounts of non-active and active materials added, because the cell loses capacity per mass content as more additives are included [17]. The slurries prepared for this work consist of 80% of active material, 10% of conducting additive and 10% of binding polymer. The slurry has been poured on an aluminum foil (20 µm, Hohsen) and cast using a minicoater inside a glove-box. The roller height for the casting has been set to 250 µm, which includes the height of the slurry and of the aluminum foil. The laminates have been dried under vacuum over night at 80°C and electrodes have been cut to the appropriate size and pressed with $\approx$ 350 MPa pressure. A schema and a picture of the resulting composite are shown in Fig. 2.16.

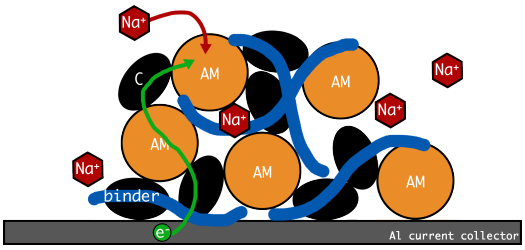

(a)

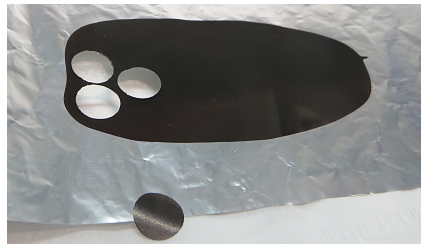

(b)

Figure 2.16: **(a)** Schematic illustration of an electrode: big orange spheres represent the active material (AM), black ellipses represent carbon black (C), binder is represented as blue lines, Na^+ ions are shown as red hexagons and electrons (e^-) as green spheres. **(b)** Picture of a laminate from where the electrodes are cut and a pressed electrode.

2.5.2 Half-cell assembly

For the study of the cathode materials half-cells have been assembled, where cathodic electrode is assembled vs. a constant voltage material. In this work, metallic sodium has been used as counter electrode. Metallic sodium has also been used as reference electrode in three electrode cells.

Cathode material and metallic Na are separated with an electrolyte soaked separator (Whattman glass fiber unless otherwise indicated). 1M $NaClO_4$ EC : PC 1:1 w.% (ethylene carbonate : propylene carbonate) has been used as standard electrolyte unless otherwise indicated.

In this work, two electrode and T-shaped three electrode Swagelok type cells have been used. In Fig 2.17 a schematic view of the used cells are presented. The connections with the exterior are done with stainless steel plungers. The cell has a diameter of 13 mm. The electrodes (cathode, and counter and reference electrodes) have been cut to 12 mm to fit without problems inside the cell, and the separator has been cut to 13 mm, slightly larger than the electrodes to avoid short-circuiting the cell.

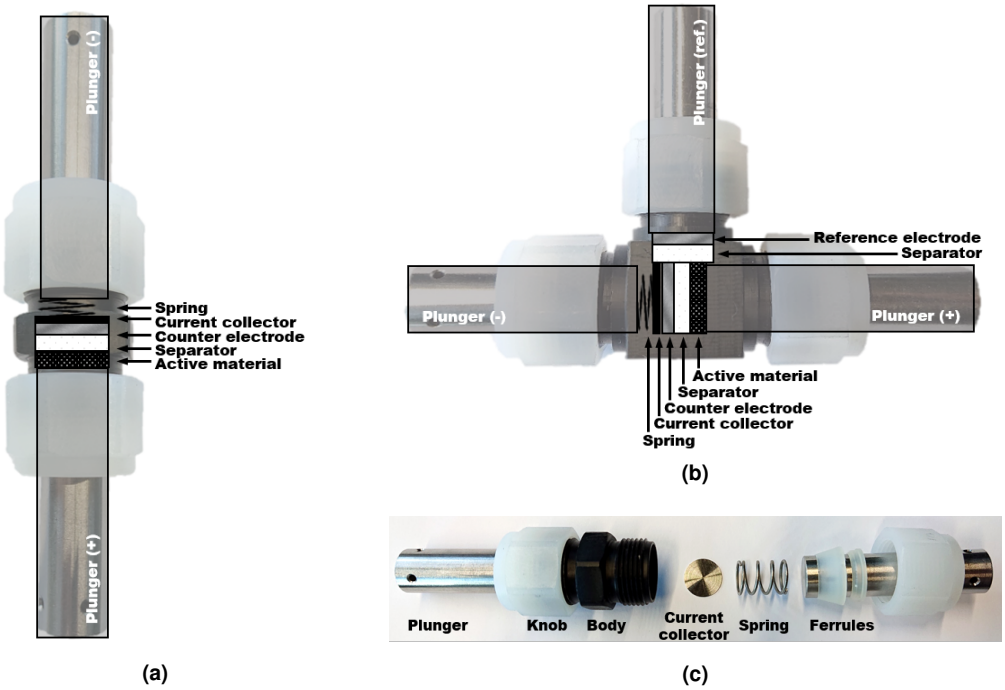

Figure 2.17: Swagelok cells used for the electrochemical characterization. **(a)** Two electrode **(b)** three electrode swagelok cell with interior schema. The positive and negative plungers have been labeled considering a cathodic active material (generally an electrode cast in aluminum foil) and a metallic sodium counter electrode. **(c)** A disassembled two electrode swagelok cell.

2.5.3 Galvanostatic cycling

The electrochemical properties of the cells have been tested with a galvanostatic cycling, where a constant current is applied with potential limitations. This way, the amount of exchanged charges can be quantified, and compared with the theoretical capacity Q_0 (equation 1.2).

As shown in the introduction chapter (Chapter 1), the voltage curve of a battery depends on the band energy of the active materials. Moreover, the voltage of the battery V_0 will depend on the chemical potentials of the positive and negative electrodes. In Fig. 2.18a it is shown that the experimental voltage differs from V_0 by the overpotential OP, which depends on the internal battery resistance.

The differences in the voltage profile of a biphasic or a solid solution mechanism are presented in Fig. 2.18b: while a two-phase mechanism is generally reflected as a flat voltage profile, the solid solution mechanism shows a slopping profile. In Fig. 2.18c, a curve with voltage plateaus can be seen, which are related to different processes. These plateaus are easily distinguished with the corresponding $\mathrm{d}Q/\mathrm{d}V$ derivative curve. Moreover, the integral of the derivative curve can provide quantitative values for the charge involved in each process. However, the cycling conditions and particle morphology also affect the voltage profile shape [18–20].

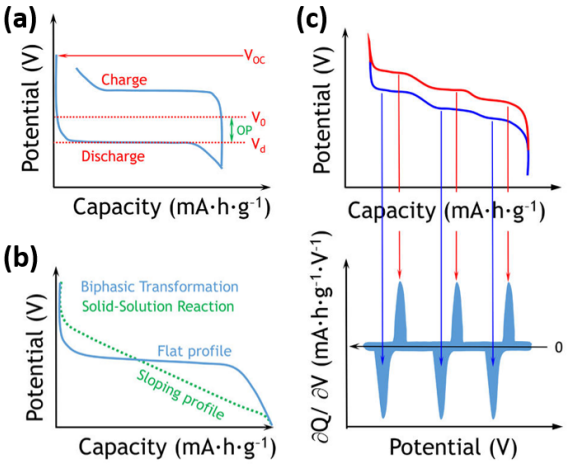

Figure 2.18: Typical features of galvanostatic cycling curves. **(a)** Identification of open circuit voltage (V_{OC}), overpotential (OP), equilibrium voltage (V_0) and discharge voltage (V_d); **(b)** biphasic vs. solid solution reaction mechanisms; and **(c)** galvanostatic profile (discharge in red, charge in blue) with various processes occurring and the corresponding $\mathrm{d}Q/\mathrm{d}V$ derivative curve. Figure modified from [21].

The standard galvanostatic measurements have been performed at C/10 rate, that is, at a theoretical charge or discharge time of 10 hours.

The gravimetric capacities presented in this work have been calculated considering only the weight of the active material.

In rate capability tests, a series of galvanostatic cycles are performed at various rates. Here, 5 cycles have been done at each rate, that generally comprises the following rates: C/10, C/5, C/2.5, 1C, 2C and back to C/10.

Electrochemical properties have been measured with Bio-Logic potentiostats (SP-50, SP-150 and VMP3).

2.5.4 Electrochemical Impedance Spectroscopy (EIS)

The working principle of a Na-ion battery consists of the transport of Na ions from one electrode to another: Na^+ ions are extracted from an electrode, move to the electrolyte, pass through it and diffuse in the other electrode. All these processes of electrical flow show a resistance that can be measured with electrochemical impedance spectroscopy (EIS) measurements.

The EIS is a technique in which a sinusoidal perturbation is applied, a potential perturbation ($V(t)$) in the case of potentiostatic electrochemical impedance spectroscopy (PEIS). The electrochemical impedance Z can be defined as the ratio of the input potential $V(t)$ and the output current $I(t)$:

$$Z = \frac{V(t)}{I(t)} \tag{2.6}$$

The response current will present an amplitude as well as a phase shift that depends on the amplitude and frequency of the input signal, and on the mechanism inducing the cell impedance. The impedance can be expressed in terms of real and imaginary components:

$$Z = Z_0 \exp(j\phi) = Z_0 \cos\phi + jZ_0 \sin\phi = \mathrm{Re}(Z) + j\,\mathrm{Im}(Z) \tag{2.7}$$

where Z_0 is the amplitude and ϕ is the phase shift of the response with respect to the perturbation.

The real part corresponds to the resistances and the imaginary part to the capacitors and inductors. A common way to represent the data is with Nyquist plots, where the real part is plotted in the x axis and the negative of the imaginary part in the y axis. Each of the phenomena occurring in the cell (ionic and electronic transportation, redox reactions occurring at the surface of the particles...) have different characteristic times, which are discerned by measuring the impedance at different frequencies. In the Nyquist plot the high frequency region lies to the left and the low frequency region to the right.

The EIS spectra are commonly analyzed by fitting the Nyquist plots to equivalent circuits, with resistances and capacitor elements combined in serial or parallel mode, which can be simulated with mathematical methods. A simple model was presented by Randles in 1947 [22], and is shown in Fig. 2.19a. The Randles circuit, as it is known, contains the most common equivalent circuit elements [23, 24]:

Electrolyte resistance. The resistance of the solution depends on its concentration, type of ions, temperature and geometry of the current carrying volume. Most of the cells do not have

uniform current distribution through the electrolyte area so it is laborious to calculate theoretical electrolyte resistance. This resistance is generally found at high frequencies. It is shown as R_S in Fig. 2.19a.

Charge transfer resistance. When the metal and the electrolyte are in contact, electrons and ions can be transferred between metal diluted in the electrolyte and electrode at certain voltages. The charge transfer resistance accounts for the migration of A^+ ions and e^- electrons to the surface of the particles and for the resistance needed for the transfer to occur. This resistance is generally found at medium to low frequencies. It is shown as R_{CT} in Fig. 2.19a.

Double layer capacitor. A capacitor appears at the interface between the electronic conductive particles and the insulator media (electrolyte). The solvated ions of the electrolyte adsorb at the surface of the electrode while electrons get at the surface of the electrode. The boundary is generally separated by a thin insulating surface of the order of angstroms. It is shown as C_{DL} in Fig. 2.19a.

Warburg impedance. When the ions diffuse into the bulk of the electrode to reduce concentration gradients in the particles, then a constant phase impedance -Warburg impedance- appears, and it depends on the frequency of the perturbation. Usually Warburg impedance appears at low frequencies, when active ions have to diffuse long distances. Warburg impedance is presented as Z_D in Fig. 2.19a.

Mathematically, resistances are real components of the impedance ($R = \mathrm{Re}(Z_R)$) and do not depend on the frequency. The capacitors are imaginary ($C = \frac{1}{j\omega Z_C}$) and are reflected as vertical positive straight lines in Nyquist plots. The combination of a resistance and a capacitor in parallel ($R||C$) corresponds to a semicircle of diameter R in a Nyquist plot.

In real systems, the surfaces and interfaces are not ideal, and in order to account for surface irregularities or roughness, the capacitors (C) are substituted by constant phase element (CPE) components. A CPE is an imperfect capacitor with an impedance value of:

$$Z_{CPE} = \frac{1}{C_0(j\omega)^a} \tag{2.8}$$

where ω corresponds to the angular frequency ($\omega = 2\pi f$, where f is the frequency) and a is the argument ($-1 \leqslant a \leqslant 1$). In a Nyquist plot the CPE is reflected by a segment with a phase angle of $-(90 \times a)^\circ$. A resistor corresponds to $a = 0$ (frequency independent value), a perfect inductor corresponds to $a = -1$ (negative straight vertical line) and a perfect capacitor corresponds to $a = 1$ (positive straight vertical line). The semicircles formed by a $R||CPE$ look like depressed semicircles. The CPE element is commonly used in battery research to simulate imperfect capacitors as well as diffusion processes [24].

Indeed, mass diffusion in semi-infinite linear diffusion (SILD) conditions is reflected as a Warburg impedance, which corresponds in Nyquist plots to a 45° slope (CPE with $a = 0.5$). SILD

conditions are fulfilled when the diffusion path is short compared with the radius of the diffusing phase, that is, when the diffusing species do not reach the end of the diffusing phase. The SILD diffusion can be described as [25]:

$$Z_w = \frac{A_w}{\sqrt{\omega}} - j\frac{A_w}{\sqrt{\omega}} \tag{2.9}$$

where ω is the angular frequency in radians and A_w is the Warburg coefficient.

However, a cell can rarely be described with such a simple model due to the numerous processes taking place upon cycling. In Fig. 2.19b an example of a Nyquist plot of a real battery is presented, where the contributions from various processes are highlighted [24]. Note that since several processes can occur at similar time scales, it is common for the semicircles to overlap in Nyquist plots.

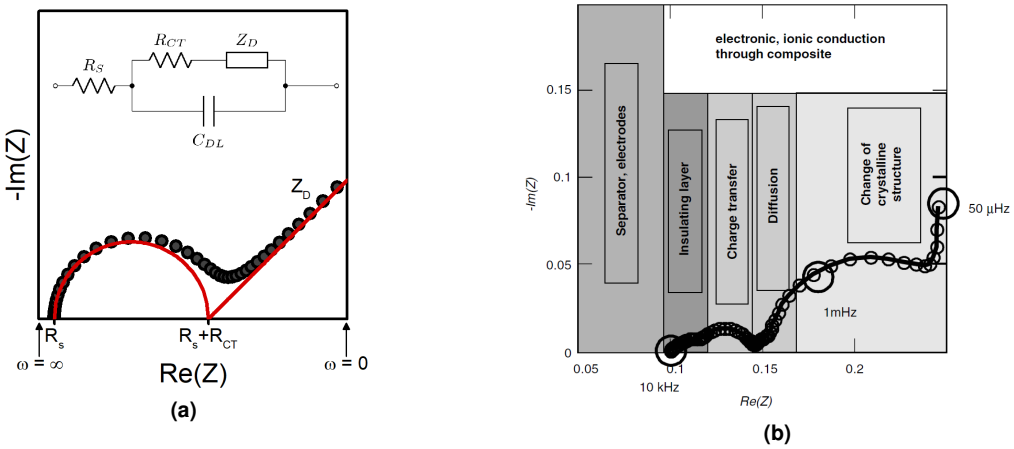

Figure 2.19: **(a)** The Randles equivalent circuit, that describes the charge-transfer and diffusion process [22, 24], and the resulting Nyquist plot. **(b)** Typical Nyquist spectra of an intercalation material [24].

Apart from the phase transitions or changes in the crystalline structure, as shown in Fig. 2.19b, deviation from the Warburg impedance can be modelled when the diffusing lengths are physically limited, where $t \approx {}^{r^2}/_{D}$, where r is the diffusion length and D is the diffusion coefficient [26]. The limiting boundary can be reflective (finite space diffusion) or transmissive (finite length diffusion) [24]. In Fig. 2.20 the typical response of the different models are presented. The diffusion signal is reflected as a capacitor (positive imaginary impedance) in the finite space case, and it transforms into a semicircle in the finite length case [24].

The Warburg coefficient in the finite length impedance can be mathematically described as [27]:

$$A_{w\,FL} = R_d \frac{\tanh\sqrt{2\pi j f \tau}}{\sqrt{2\pi j f \tau}} \tag{2.10}$$

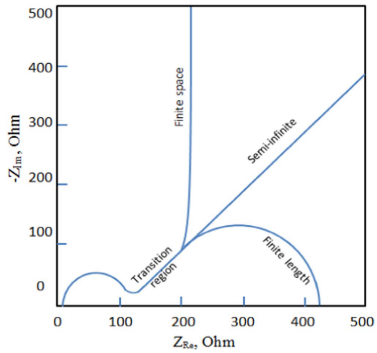

Figure 2.20: Different types of Warburg impedance Nyquist models: finite space, semi-infinite linear diffusion and finite length [26].

2.5.5 Potentiostatic Intermittent Titration Technique (PITT)

As it has been previously explained, the working principle of a Na-ion battery consists of the transport of Na ions from one electrode to another, with the resulting changes in Na ion concentration. Fick's second law of diffusion (equation 2.11) explains the change in diffusion coefficient (D) as a function of concentration, and it can model the way that charge carrier ions (Na^+ ions in this particular case) diffuse in the active material.

$$\frac{\partial C_{Na^+}}{\partial t} = D_{Na^+} \frac{\partial^2 C_{Na^+}}{\partial x^2} \tag{2.11}$$

where t is time, x is the distance from the electrolyte/electrode interface and C_{Na^+} is the concentration of Na^+ ions at x. Some boundary conditions can be applied to solve the equation. For a particle of radius r, for example [28]:

- Equilibrium concentration of mobile species at different potential values for a distance $0 \leqslant x \leqslant r$ at $t = 0$.
- Equilibrium of concentration of mobile species at the electrode/electrolyte interface at $t > 0$.
- Impermeable phase boundary at $x = r$.

When a potential step is applied at equilibrium state, the concentration of the mobile species in the surface will be modified creating a concentration gradient. The response current of the cell to the potential step is proportional to the gradient. It can be approximated in the short time (equation 2.12) and the large time (equation 2.13) regions [28]:

$$I(t) = zFS(c_s - c_0)\left(\frac{D}{\pi t}\right)^{1/2} \qquad t \ll \frac{r^2}{D} \tag{2.12}$$

$$I(t) = zFS(c_s - c_0)\frac{D}{r}\exp\left(-\frac{-\pi^2 Dt}{4r^2}\right) \qquad t \gg \frac{r^2}{D} \tag{2.13}$$

where z is the charge number of electroactive species, F is Faraday's constant, S is the cross sectional area and $(c_s - c_0)$ denotes de concentration difference at the surface at time t. Since it is experimentally impossible to measure $c_s(t)$, it is estimated from the total charge transferred until the system is equilibrated at the potential step [29]. The transferred charge can be calculated by integrating potentiostatic current over time or by direct measurement using a coulometer.

When the diffusion path of the mobile specie is short compared with the radius of the particle, the Cottrellian or semi-infinite linear diffusion (SILD) conditions are fulfilled. A short excitation time, a low diffusivity or a short diffusion depth compared to the overall depth of the insertion material are thus required. In the Cottrell region, and on the basis of equation 2.12, equation 2.14 can be applied [28, 30]:

$$I(t) = zFS\frac{\Delta Q}{V_M}\sqrt{\frac{D}{\pi t}} \tag{2.14}$$

where D is the diffusion coefficient, ΔQ is the diffusion related change of charge during the potential step and V_M is the molar volume. That is, in the Cottrellian or SILD region, the current is proportional to the inverse of the square root of time.

However, one needs to take into account the limitations of the method. The potential step is considered to be small enough so that the diffusion coefficient is constant throughout the step, and that the current during the step is mainly controlled by mass diffusion. It neglects the additional limitation of the current from surface processes (such as charge transfer or surface layers) as well as additional contributions to the current (and as a consequence of ΔQ) such as phase transitions. Moreover, the particles are assumed large enough so that the finite size effects of the geometry are negligible [29]. Part of these limitations are taken into account by applying the formula only in the time range where the current actually evolves as the inverse of the squares time (Cottrellian behavior indicating SILD conditions), but the possible error in ΔQ can remain to be an issue especially when phase transitions are present.

2.5.6 Coupled PITT-PEIS measurements

During the coupled PITT-PEIS measurements the cells have been cycled (charge and discharge) on 25 mV potentiostatic steps, where the current has been allowed to relax to a value of C/500 (≈ 0.48 mA g^{-1}). However, and due to the very long relaxation times, the time has been limited to a maximum of 20 hours per step. After every step, at semi-equilibrium state, an impedance spectrum is measured by applying a sinusoidal voltage of 10 mV amplitude around the equilibrium value and a frequency ranging from 200 kHz to 2 mHz. An example of the applied potential steps can be seen in Fig. 2.21

The cells have been charged and discharged within several potential windows to observe the evolution of the measured parameters within the reversible and the irreversible electrochemical activity windows as defined with galvanostatic cycling measurements.

All the PEIS and PITT measurements have been carried out in three electrode swageloks using metallic Na as counter electrode and as reference electrode. A VMP3 Bio-Logic potentiostat has

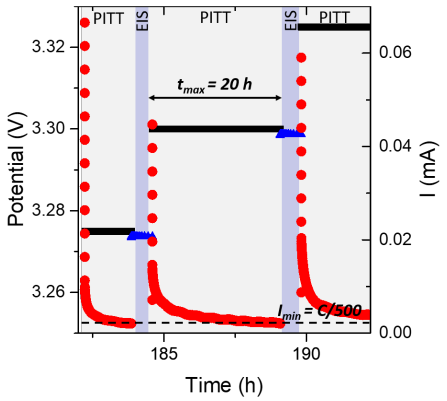

Figure 2.21: An example of a PEIS-PITT coupled potential step. During PITT steps (black squares, highlighted in gray) the potential is maintained and the current (red circles) is allowed to relax for a maximum of 20 hours or until the current C/500 is reached. During EIS measurements (blue triangles) a sinusoidal potential is applied with an amplitude of 10 mV and varying frequency and the potential to current relation is measured.

been used for the measurements. The Nyquist spectra have been fitted using Z Fit software (Bio-Logic) [27].

2.6 *In-situ* and *operando* battery characterization

The materials have been studied at different states of charge, and depending on the measurement method, three different categories can be distinguished:

***Ex-situ* measurements.** The material under study is removed from the cell for its study. When the material to study is, as in this work, the active material, it has to be cleaned before being analyzed.

***In-situ* measurements.** The material under study is cycled inside a specifically designed cell container that allows its measurement without further manipulation. In *in-situ* measurements the materials are under static conditions, that is, no current nor voltage is applied during measurements. During *in-situ* characterizations the voltage and current evolution can be measured.

***Operando* measurements.** The material under study is cycled inside a specifically designed cell container, generally the same as the one used for *in-situ* measurements. In this case, the measurements are performed while cycling the material, that is, while current or voltage is applied. A compromise has to be found between the cycling rate and the acquisition time: standard measuring techniques usually require low cycling rates in order to obtain quality data with enough time resolution.

2.6.1 Oxidation of samples

2.6.1.1 Electrochemical oxidation of samples

The *ex-situ* measurements in this work have been carried out for electrochemically oxidized samples. The active material is electrochemically desodiated for its subsequent analysis. The electrode or active material mixture is washed with the same solvent as the one used in the electrolyte to remove any electrolyte salt trace. In this work PC solvent (propylene carbonate) has been used for washing. The clean material is then dried under vacuum without any exposure to air atmosphere. The material has to be treated for its study, and the preparation will depend on the technique to be used.

2.6.1.2 Chemical oxidation of samples

Although it is not technically an *ex-situ* measurement, as the material is not electrochemically cycled, a chemical oxidation treatment has been performed on the active material to mimic the electrochemical oxidation. As cycling the active material without the addition of conductive additive carbon has not been possible, the only way to solely obtain the oxidized material has been via chemical treatment.

For the chemical oxidation, an oxidative reagent, nitronium tetrafluoroborate (NO_2BF_4, Sigma Aldrich, $\geqslant$95%), has been dissolved in acetonitrile (CH_3CN, $\geqslant$99.90%, Scharlau). The layered oxide has then been added and stirred for several hours. The amounts of oxidative agent and stirring hours depend on the desodiation degree sought. The reaction can be described with equation 2.15:

$$NaTM^{III}O_2 + NO_2BF_4 \rightarrow TM^{IV}O_2 + NaBF_4 + NO_2 \tag{2.15}$$

where the roman numerals represent the oxidation state of the transition metal element. The layered oxides are not dissolved in acetonitrile, but $NaBF_4$ and NO_2 are, so the oxidized material is left to precipitate and is washed several times until only TMO_2 powder is left.

However, the reaction is usually not complete, so NO_2BF_4 has to be added in excess. Based on previous attempts by colleagues with similar materials, a twofold NO_2BF_4 excess has been used to obtain a fully desodiated state.

In this work, batches of about 1 g of active material have been desodiated using about 20 mL of solvent. The stirring times have been set above 24 hours, where the reaction has already reached its limit, and the material has been washed at least 5 times.

All the reactants and solvents used for the chemical desodiation are water free, in order to avoid water or proton intercalation upon sodium extraction. The reaction has been carried out in an oxygen and water free atmosphere, inside an argon filled glove-box.

2.6.2 *In-situ* and *operando* techniques

2.6.2.1 *In-situ* and *operando* X-ray diffraction

Operando XRD is a very powerful technique to elucidate metastable structures formed during charge and discharge, but its use was limited until 1990 [31, 32]. *Operando* techniques allow the study of the fundamental mechanisms by which these materials operate, together with the kinetics of the processes [33]. As many *operando* techniques, XRD is not without challenges. The system to study needs not to react with the container while allowing X-rays to reach the sample. Since the first *operando* XRD measurements in 1978 [34], many different designs have been reported, both for diffraction and transmission mode. The X-ray window generally consists of a Be-window, which besides being electronically conductive, has a low X-ray absorption coefficient [31, 35–39]. Beryllium is however unstable at high voltages. For the study of cathode materials Be window has generally to be protected with an aluminum layer that will also generate reflections as well as X-ray absorption. One of the most used alternatives are Kapton film windows [40–45]. In 2015 Borkiewicz et al. [46] showed that using flexible windows can affect the homogeneity of the reaction in the electrode surface due to the lower pressure in the window region. For this reason, other alternatives have been investigated, such as glassy carbon [47] or sapphire [48] windows, where rigid and non-toxic materials are used. In this work Al covered Be window has been used as current collector.

Operando measurements have been carried out in the Bruker Advance D8 diffractometer using a 9 mm radius cell designed at the CIC Energigune (see Fig. 2.22). The electrochemical properties have been measured with a mobile Bio-Logic potentiostat. The active material and additive mixture have been placed uniformly in powder form over the aluminum covered beryllium window and separated from metallic sodium with separators to avoid possible short-circuits. Two glass fiber separators have been used in every cell.

Super C65 and PVdF binder additives used for electrode preparation have been substituted by Ketjenblack (KB) carbon, because the last has a larger specific surface and it tends to better cover the particles. Approximately 100 mg of material have been used to assemble the cell in 80 to 20 weight proportion of AM to KB. This amount is generally enough to uniformly cover the beryllium window and to have enough intensity in reflected X-rays without deteriorating electrochemical performance. Separators have been soaked with 1M $NaClO_4$ EC:PC electrolyte.

Typically a first diffraction pattern has been taken before cycling for a couple of hours in the whole angle range in order to be able to discern reflections from the active material and contributions from other components of the cell (e.g. beryllium window, aluminum foil, carbon or electrolyte). During the cycling a compromise has to be found between time resolution and signal to noise ratio. The measured angle range has been selected to include reflections of interest trying to reduce acquisition time (i.e. increase time resolution) taking into account the intensity of reflected peaks. Cycling of the cell has been done at a low rate in order to see structural changes in a quasistatic state. Typically, the measurement has been set to record about 60 XRD patterns during charge or discharge considering that theoretical capacity can be reached.

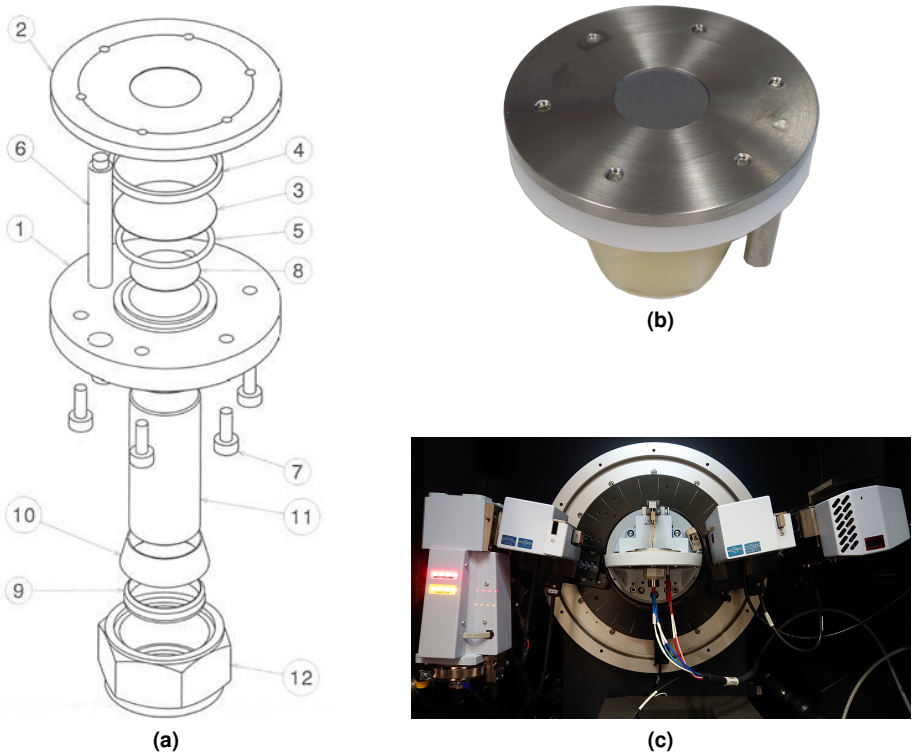

Figure 2.22: **(a)** Design and **(b)** bottom view of the in-situ cell used for this work, where beryllium window is visible. **(c)** *Operando* XRD set up in Bruker D8 Advance diffractometer, with Be window looking upwards, connected to Bio-logic potentiostat.

In-situ and *operando* synchrotron measurements have been taken using the same cell shown in Fig. 2.22, as it can be appreciated in Fig. 2.23, where the experimental set-up at the MSPD (ALBA synchrotron) beamline is shown. The beamline can be see at the back of the cell in Fig. 2.23a, and the detector at the back of Fig. 2.23b. Since synchrotron measurements are done in transmission mode, the plunger has been modified, and it includes a beryllium covered hole that allows X-ray transmission through it (see Fig. 2.23b). The stainless steel current collector has also been modified with a 2 mm hole. In some cases the sodium counter electrode has also been punctured in the measuring region to avoid the reflections and absorption. However, since the material is not a good electronic conductor and a low pressure in the measuring region might delay the electrochemical activity, in other cases the whole electrode area has been covered with Na metal to try to reduce any pressure inhomogeneity.

During the analysis of the *operando* XRD data, the intensity of certain angle zones will be integrated. However, it has to be taken into account that there are several angle dependent factors that affect the intensity of the diffracted pattern, for which it needs to be corrected before the integration. These factors are presented below, and their mathematical expressions can be found

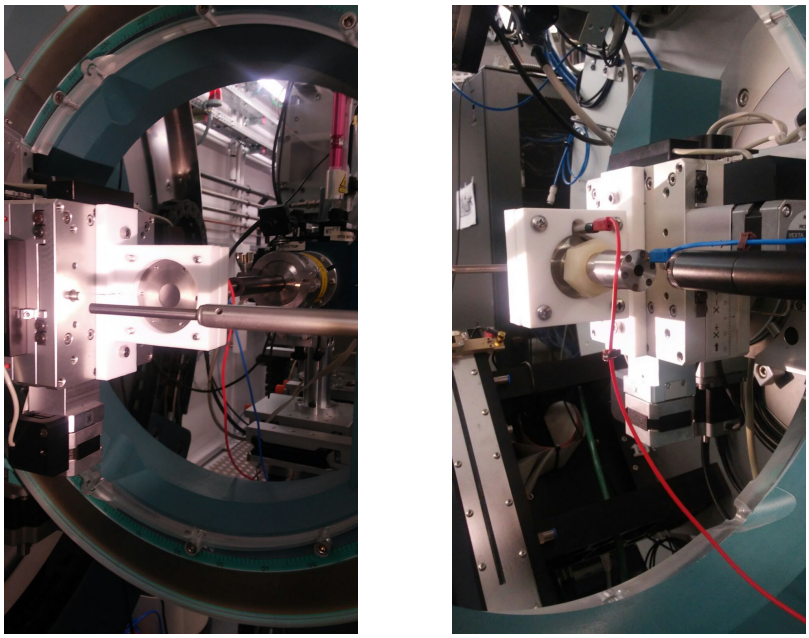

(a) (b)

Figure 2.23: Experimental set-up for the *in-situ* and *operando* measurements carried out at ALBA synchrotron, from **(a)** bottom or Be window side and **(b)** top or plunger side. The wiring for the connection of the cell with the potentiostat can be appreciated.

in Table 2.1:

- The X-ray has to transmit through the beryllium window and the protective aluminum foil, before it reaches the sample. In addition, the diffracted ray also has to transmit through the Be and Al layers. Both the incident and the diffracted rays will be attenuated. The attenuation will depend on the distance that the ray has to travel through each material, that depends at the same time on the angle [3].
- The intensity of a diffraction pattern depends on the temperature of the sample due to the atomic vibrations [49]. The Debye-Waller thermal agitation factor accounts for the changes in the surface charge density induced by the thermal agitation [50].
- The polarization of the incident beam affects the scattered intensity. The expression in Table 2.1 corresponds to a non-polarized source [3].
- When a crystal is rotated under a beam, the various planes of the crystal do not occupy the reflection-satisfying conditions for equal lengths of time. The Lorentz factor, or irradiated volume change, is proportional to the time of reflection permitted to each reflection [51].
- The diffracted signal includes a whole ring, although the detectors are linear. Therefore, the finite width of the detector corresponds to a different angular range depending on the radius

of the diffracted ring [52, 53]. The expression in Table 2.1 is the correction for a randomly oriented powder sample.

Table 2.1: Angle dependent factors that affect the experimental XRD intensity during the operando XRD experiments, with which patterns have been corrected before integration to estimate I/I_0. The attenuation coefficient factors have been estimated using NIST online tool [54], and the Debye Waller factors have been extracted from Rietveld refinements of the pristine powder samples.

Factor	Formula	
Be window attenuation	$\exp\left[-\mu_{Be}\frac{2d_{Be}}{\sin\theta}\right]$	μ: attenuation coefficient $\mu_{Be}(Co) = 253.45\ \mathrm{m}^{-1}$ $\mu_{Be}(Cu) = 158.92\ \mathrm{m}^{-1}$ d: Be thickness $d_{Be} = 250 \times 10^{-6}$ m
Al foil attenuation	$\exp\left[-\mu_{Al}\frac{2d_{Al}}{\sin\theta}\right]$	μ: attenuation coefficient $\mu_{Al}(Co) = 20196\ \mathrm{m}^{-1}$ $\mu_{Al}(Cu) = 13600\ \mathrm{m}^{-1}$ d: Al thickness $d_{Al} = 6 \times 10^{-6}$ m
Thermal factor	$\left(\exp\left[-\frac{B\sin^2\theta}{\lambda}\right]\right)^2$	B: Debye Waller temperature factor $B(Co) = 1.8\ \text{Å}^2$ $B(Cu) = 1.7\ \text{Å}^2$ λ: wavelength $\lambda_{Co} = 1.78897$ Å $\lambda_{Cu} = 1.54053$ Å
Polarization	$\frac{1}{2}(1+\cos^2 2\theta)$	
Irradiated volume change	$\frac{1}{\sin 2\theta}$	
Powder ring distribution factor	$\frac{1}{\sin\theta}$	

2.6.2.2 *In-situ* Mössbauer spectroscopy

In-situ Mössbauer measurements have been done in pouch-cells. In this kind of cells, the battery stack (working electrode - electrolyte - counter electrode) is mounted inside a polymeric bag, which generally has an aluminum layer to protect the battery components. For this work an Al free polymer has been chosen, to avoid possible Fe signals from impurities in the aluminum from the polymer bag, as well as to reduce the absorbing elements. However, the aluminum foil helps the hermetic sealing of the battery component, and the lack of aluminum foil in the bag should not affect the performance of the battery. In this work, the *in-situ* measurements extend to a couple of weeks maximum, where the polymer should be hermetic enough to protect the inside from the

external atmosphere without the presence of Al foil. Moreover, the cells have been cycled under a constant nitrogen flux, and so, atmospheric humidity contamination is avoided. Between the composite electrode cast in Al foil and a thin self-standing sodium electrode, a Whattman glass fiber has been used as separator soaked in 1M $NaPF_6$ EC:DMC (1:1 volume %) electrolyte. The electrical connections with the exterior are done with Al foil tabs. A picture of a pouch cell used for *in-situ* measurements is presented in Fig. 2.24.

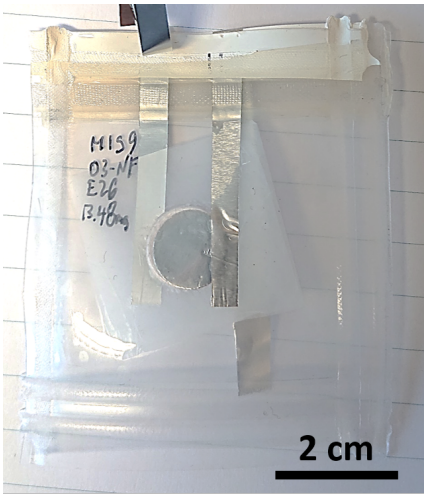

Figure 2.24: Pouch cell designed for *in-situ* Mössbauer measurements. The aluminum foil of the positive electrode and the wet glass fiber separators can be seen. Aluminum tabs have been used for the positive and negative electrodes.

The cells have been charged at constant current rate of C/10, and left to relax for several hours at different states of charge while the Mössbauer spectra were acquired, the acquisition time depending on the quality of the resulting spectrum. The data analysis has been done using MossA software [55].

Bibliography

[1] U. Schubert and N. Hüsing. *Synthesis of inorganic materials*. Wiley-VCH, 2 edition, 2005.

[2] L. Lutterotti. Introduction to Crystallography & Diffraction Techniques. Technical report.

[3] C. Giacovazzo, H. L. Monaco, G. Artioli, M. Viterbo, M. Milanesio, G. Ferraris, G. Gilli, G. Zanotti, and M. Catti. *Fundamentals of Crystallography*. Oxford University Press, 3 edition, 1992.

[4] J. Rodriguez-Carvajal. *Physica B*, 192:55, 1993.

[5] L. Aslanov, G. Fetisov, J. Howard, and I. U. of Crystallography. *Crystallographic Instrumentation*. IUCr monographs on crystallography. International Union of Crystallography, 1998.

[6] S. K. Sinha, E. B. Sirota, S. Garoff, and H. B. Stanley. *Physical Review B*, 38(4):2297–2311, 1988.

[7] D. Saurel, J. Segalini, M. Jauregui, A. Pendashteh, B. Daffos, P. Simon, and M. Casas-Cabanas. *Energy Storage Materials*, 21:162–173, 2019.

[8] R. F. Egerton. *Physical principles of electron microscopy: an introduction to TEM, SEM, and AEM*. Springer, New York, NY, 2005.

[9] A. L. Robinson. *Science*, 230(4723):304–306, 1985.

[10] An Introduction to Electron Microscopy - STEM | Thermo Fisher Scientific. `https://www.fei.com/introduction-to-electron-microscopy/stem/`, (Accessed: 2019-12-03).

[11] J. C. Meyer. In V. Skakalova and A. Kaiser, editors, *Graphene: properties, preparation, characterization and devices*, number 57 in Woodhead Publishing Series in Electronic and Optical Materials, pages 101–123. Woodhead Publ LTD, 2014.

[12] Products - Physical Property Measurement System PPMS ®. `https://www.qdusa.com/products/ppms.html`, (Accessed: 2017-10-05).

[13] G. Wertheim. *Mössbauer Effect: Principles and Applications*. Academic paperbacks: Physics. Elsevier Science, 1968.

[14] P. Gütlich, E. Bill, and A. Trautwein. *Mössbauer spectroscopy and transition metal chemistry: fundamentals and application*. Springer, 1978.

[15] E. Murad and J. Cashion. *Mössbauer Spectroscopy of Environmental Materials and Their Industrial Utilization*. Springer US, Boston, MA, 2004.

[16] N. N. Greenwood and T. C. Gibb. *Mössbauer Spectroscopy*. Springer Netherlands, 1971.

[17] P. K. Shen, C.-Y. Wang, S. P. Yiang, C. Sun, and J. Zhang, editors. *Electrochemical Energy: Advanced Materials and Technologies*. CRC Press, 2016.

[18] T. Drezen, N.-H. Kwon, P. Bowen, I. Teerlinck, M. Isono, and I. Exnar. *Journal of Power Sources*, 174(2):949–953, 2007.

[19] N. Nitta, F. Wu, J. T. Lee, and G. Yushin. *Materials Today*, 18(5):252–264, 2015.

[20] K. Minnici, Y. H. Kwon, M. M. Huie, M. V. de Simon, B. Zhang, D. C. Bock, J. Wang, J. Wang, K. J. Takeuchi, E. S. Takeuchi, A. C. Marschilok, and E. Reichmanis. *Electrochimica Acta*, 260:235–245, 2018.

[21] O. Pecher, J. Carretero-González, K. J. Griffith, and C. P. Grey. *Chemistry of Materials*, 29(1):213–242, 2017.

[22] J. E. B. Randles. *Discussions of the Faraday Society*, 1:11–19, 1947.

[23] A. Lasia. *Electrochemical Impedance Spectroscopy and its Applications*. Springer New York, 2014.

[24] E. Barsoukov and J. R. Macdonald, editors. *Impedance spectroscopy: theory, experiment, and applications*. Wiley-Interscience, Hoboken, N.J, 2nd ed edition, 2005.

[25] C. Ho, I. D. Raistrick, and R. A. Huggins. *Journal of the Electrochemical Society*, 127(2):343–350, 1980.

[26] T. Q. Nguyen and C. Breitkopf. *Journal of The Electrochemical Society*, 165(14):E826–E831, 2018.

[27] Zfit - Bio-Logic Science Instruments. `https://www.bio-logic.net/zfit/`, (Accessed: 2019-11-27).

[28] C. J. Wen, B. A. Boukamp, R. A. Huggins, and W. Weppner. *Journal of The Electrochemical Society*, 126(12):2258–2266, 1979.

[29] B. Han, A. Van der Ven, D. Morgan, and G. Ceder. *Electrochimica Acta*, 49(26):4691–4699, 2004.

[30] M. D. Levi, E. A. Levi, and D. Aurbach. *Journal of Electroanalytical Chemistry*, 421(1-2):89–97, 1997.

[31] M. Morcrette, Y. Chabre, G. Vaughan, G. Amatucci, J.-B. Leriche, S. Patoux, C. Masquelier, and J.-M. Tarascon. *Electrochimica Acta*, 47(19):3137–3149, 2002.

[32] J. Yang, S. Muhammad, M. R. Jo, H. Kim, K. Song, D. A. Agyeman, Y.-I. Kim, W.-S. Yoon, and Y.-M. Kang. *Chemical Society Reviews*, 45(20):5717–5770, 2016.

[33] C. P. Grey and J. M. Tarascon. *Nature Materials*, 16(1):45–56, 2017.

[34] R. R. Chianelli. *Journal of The Electrochemical Society*, 125(10):1563, 1978.

[35] J. B. Leriche, S. Hamelet, J. Shu, M. Morcrette, C. Masquelier, G. Ouvrard, M. Zerrouki, P. Soudan, S. Belin, E. Elkaïm, and F. Baudelet. *Journal of The Electrochemical Society*, 157(5):A606, 2010.

[36] R. Berthelot, D. Carlier, and C. Delmas. *Nature Materials*, 10(1):74–80, 2011-01.

[37] E. Gonzalo, M. H. Han, J. M. López del Amo, B. Acebedo, M. Casas-Cabanas, and T. Rojo. *Journal of Materials Chemistry A*, 2(43):18523–18530, 2014.

[38] J. Billaud, R. J. Clément, A. R. Armstrong, J. Canales-Vázquez, P. Rozier, C. P. Grey, and P. G. Bruce. *Journal of the American Chemical Society*, 136(49):17243–17248, 2014.

[39] S. Hartung, N. Bucher, R. Bucher, and M. Srinivasan. *Review of Scientific Instruments*, 86(8):086102, 2015.

[40] T. Gross, T. Buhrmester, K. Bramnik, N. Bramnik, K. Nikolowski, C. Baehtz, H. Ehrenberg, and H. Fuess. *Solid State Ionics*, 176(13):1193–1199, 2005.

[41] H. C. Shin, S. B. Park, H. Jang, K. Y. Chung, W. I. Cho, C. S. Kim, and B. W. Cho. *Electrochimica Acta*, 53(27):7946–7951, 2008.

[42] K. Rhodes, R. Meisner, Y. Kim, N. Dudney, and C. Daniel. *Journal of The Electrochemical Society*, 158(8):A890, 2011.

[43] J. Gao, M. A. Lowe, Y. Kiya, and H. D. Abruña. *The Journal of Physical Chemistry C*, 115(50):25132–25137, 2011.

[44] N. Sharma, E. Gonzalo, J. C. Pramudita, M. H. Han, H. E. A. Brand, J. N. Hart, W. K. Pang, Z. Guo, and T. Rojo. *Advanced Functional Materials*, 25(31):4994–5005, 2015.

[45] E. Lee, D. E. Brown, E. E. Alp, Y. Ren, J. Lu, J.-J. Woo, and C. S. Johnson. *Chemistry of Materials*, 27:6755–6764, 2015.

[46] O. J. Borkiewicz, K. M. Wiaderek, P. J. Chupas, and K. W. Chapman. *The Journal of Physical Chemistry Letters*, 6(11):2081–2085, 2015.

[47] O. J. Borkiewicz, B. Shyam, K. M. Wiaderek, C. Kurtz, P. J. Chupas, and K. W. Chapman. *Journal of Applied Crystallography*, 45(6):1261–1269, 2012.

[48] O. A. Drozhzhin, I. V. Tereshchenko, H. Emerich, E. V. Antipov, A. M. Abakumov, and D. Chernyshov. *Journal of Synchrotron Radiation*, 25(2):468–472, 2018.

[49] E. Menon and A. Fox. *Acta Materialia*, 44(6):2547 – 2555, 1996.

[50] J. R. Manson, G. Benedek, and S. Miret-Artes. *Journal of Physical Chemistry Letters*, 7:1016–1021, 2016.

[51] M. J. Buerger. *Proceedings of the National Academy of Sciences*, 26(11):637–642, 1940.

[52] R. C. Reynolds. *Clays and Clay Minerals*, 31(3):233–234, 1983.

[53] R. C. Reynolds. *Clays and Clay Minerals*, 34(4):359–367, 1986.

[54] X-Ray Mass Attenuation Coefficients | NIST. `https://www.nist.gov/pml/x-ray-mass-attenuation-coefficients`, (Accessed: 2019-06-25).

[55] C. Prescher, C. McCammon, and L. Dubrovinsky. *Journal of Applied Crystallography*, 45(2):329–331, 2012.

3 | Synthesis and physicochemical characterization of Na_xTMO_2 layered oxides

Contents

3.1 Introduction

In this chapter the synthesis procedure and the physicochemical characterization of the synthesized materials will be presented. The crystalline structure of those materials has been characterized by XRD, and analyzed by Rietveld refinement. Mössbauer spectroscopy has been used to verify the iron oxidation state and its environment, and to check the possible presence of iron containing secondary phases. The chemical composition of all the samples has been verified by ICP-OES. The sample morphology and surface area have been studied with SEM and SAXS respectively. Finally, magnetic properties have been measured to determine the effective magnetic moment and the type of magnetic ordering of the studied materials.

In all cases, the materials are analyzed in powder form. Since all the compounds studied in this work are moisture sensitive, the measurements have been done avoiding the air and moisture exposure.

3.2 Synthesis and physicochemical characterization of $NaFeO_2$

$NaFeO_2$ has been prepared by mixing anhydrous sodium carbonate (Na_2CO_3, $\geqslant$ 99%, Sigma Aldrich) and iron (II,III) oxide (Fe_3O_4, $\geqslant$ 97%, Alfa Aesar) stoichiometrically using an agate mortar and a pestle and afterwards heated at high temperature. The synthesis reaction can be written as follows:

$$\frac{1}{2}Na_2CO_3 + \frac{1}{3}Fe_3O_4 + \frac{1}{12}O_2 \xrightarrow{650^{\circ}C,15h\ air} NaFeO_2 + \frac{1}{2}CO_2$$

The precursors have been chosen based on literature, but instead of using Na_2O_2 as reported in most of the works [1–8], dehydrated sodium carbonate has been used [9, 10]. Sodium carbonate, unlike sodium peroxide, is stable under air atmosphere. Therefore, using the carbonate simplifies the precursor mixing step, as it can be done outside the glovebox. Heating temperature and time have been also chosen based on literature. However, some tests were done before the pure phase was obtained. In Table 3.1 some examples of the tested conditions are presented, together with the percentage of the observed secondary phase. In Fig. 3.1 the corresponding XRD patterns are shown. With vertical dashed lines, the reflections of the O3-$NaFeO_2$ phase are highlighted, and the reflections of the secondary phase have been marked with $*$ symbols. In all the cases the observed secondary phase is $\beta-NaFeO_2$. From these tests, it seems that the heating atmosphere or the cooling rate do not affect the final results as much as the heating temperature and time. The $\beta-NaFeO_2$ phase is formed at high temperatures, as its presence increases with increasing heating temperature and time. Final temperature was thus limited to 650°C.

The pure phase has been obtained by heating the pelletized material at 5°C/min rate and held at 650°C during 15 hours under air atmosphere. The sample has been removed from the furnace above 100°C and transferred into an argon glove-box to avoid moisture contamination. The XRD pattern of the pure phase collected at CIC EnergiGUNE and that collected at ALBA synchrotron

Table 3.1: Some of the synthesis methods tested before pure $NaFeO_2$ sample was obtained. *XRD pattern* label refers to Fig. 3.1.

XRD pattern	Synthesis condition	Secondary phase
A	Precursor mixing: by hand Dwell temperature, time and atmosphere: 750°C, 15 h, Ar Cooling: fast (submerged in liquid N_2)	$\beta-NaFeO_2$ 21(1) %
B	Precursor mixing: by hand Dwell temperature, time and atmosphere: 750°C, 18 h, air Cooling: fast (submerged in liquid N_2)	$\beta-NaFeO_2$ 25(2) %
C	Precursor mixing: by hand Dwell temperature, time and atmosphere: 700°C, 18 h, Ar Cooling: slow (left inside furnace to cool down)	$\beta-NaFeO_2$ 12(1)%

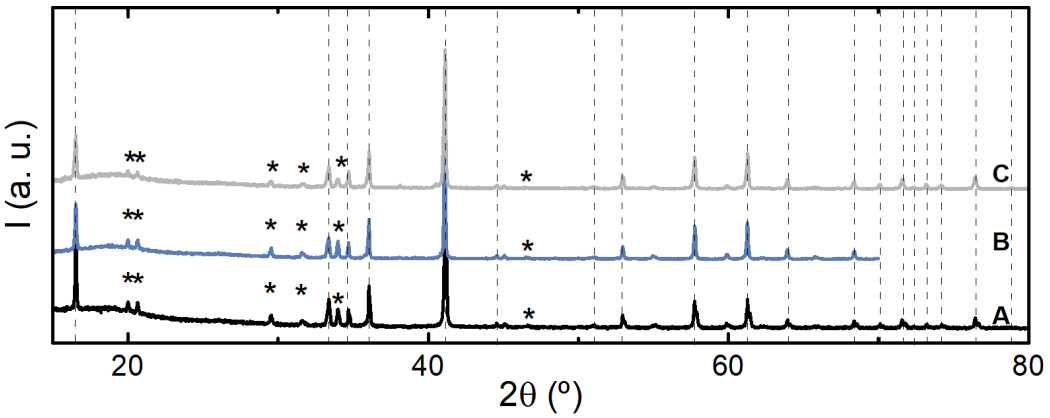

Figure 3.1: XRD patterns of several synthesis tests (see Table 3.1) before pure $NaFeO_2$ was obtained.

are shown in Fig. 3.2. Comparing both patterns it appears that synchrotron data present sharper peaks. The reflection $(1\,0\,4)$, zoomed in the red inset, has a full width at half maximum (FWHM) of 11.98×10^{-3} Å^{-1} in the measurement at CIC EnergiGUNE and almost the half, 6.61×10^{-3} Å^{-1}, in the measurement at ALBA synchrotron. A higher signal to noise ratio is also observed. In the same region, a signal to noise ratio of 14.3 is measured at CIC EnergiGUNE, while the value increases to 133.3 in the synchrotron measurement. Note that a higher Q range (0.05 Å$^{-1} \leqslant Q \leqslant 7.85$ Å^{-1}) has been measured at synchrotron, equivalent to $0.7° \leqslant 2\theta \leqslant 148.6°$ with Cu K-α_1 wavelength. In the XRD measurement taken at CIC EnergiGUNE a pure O3 phase has been detected, with the space group (SG) $R\bar{3}m$. A simulated O3-type structure can be seen in Fig. 3.3. In this structure, FeO_6 and Na layers are intercalated, and both Fe and Na ions occupy octahedral sites. However, and as a result of the better resolution of the synchrotron data, it has been possible

to detect 2% in weight of $\beta-NaFeO_2$ phase (SG $Pna2_1$). Nonetheless, its presence should not be relevant in regard of the electrochemical performance since the β phase has been demonstrated to be electrochemically inactive [11]. The measurement taken at ALBA synchrotron has been refined using FullProf Suite software [12]. A selected angle range of the refined pattern and the resulting parameters are presented in Fig. 3.4 and Table 3.2 respectively. The cell parameters and the atomic positions are in good agreement with previously reported values [1–10]. The occupancies for Na and Fe obtained with the XRD refinement, as seen in Table 3.2, are in good agreement with the expected values within the error bars. That is, the XRD data does not show any sign of Fe or Na vacancies or Fe/Na anti-site disorder. Moreover, the chemical composition of the synthesized material has been confirmed by ICP-OES. The results, normalized to iron content, confirm that the aimed composition has been obtained with only a slight sodium deficiency: $Na_{0.974}Fe_1O_2$, with an error of 1.5%. Although the ICP values differs slightly from the aimed composition, throughout the work all the compositions will be referred to with the aimed stoichiometric composition unless the exact composition is relevant.

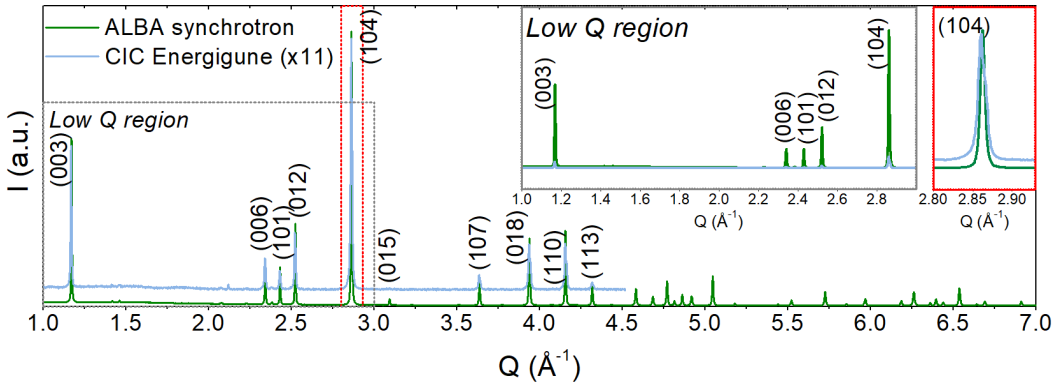

Figure 3.2: Comparison of $NaFeO_2$ powder XRD patterns taken at ALBA synchrotron for 30 seconds (green line) and Bruker D8 Discover diffractometer at CIC EnergiGUNE for 30 minutes (blue line) rescaled by $\times 11$. The red inset shows a zoom of the reflection $(1\,0\,4)$. The mayor reflections have been labeled with $(h\,k\,\ell)$ Miller indices. A low Q region is also shown in the gray inset without rescaling of the data. Note that measured Q range is higher in the measurement done at synchrotron.

The experimental Mössbauer spectrum is shown in Fig. 3.5 with open circles, together with the corresponding refinement with a continuous line. The refinement has been carried out using MossA software [13]. The refined parameters are presented in Table 3.3. A single doublet is observed, meaning that the sample is non-magnetic at room temperature, at which temperature the measurement has been carried out. Based on literature, the central shift (CS) (close to 0.35 mm s^{-1}) and quadrupole splitting (QS) (close to 0.5 mm $^{-1}$) combination corresponds to a six-coordinated Fe^{3+} [14]. This result is in good agreement with the O3 structure determined by XRD, where the iron (III) ions are in octahedral sites, surrounded by 6 oxygen ions. Moreover, the values are in good agreement with already reported values for O3-$NaFeO_2$ phase [2, 6, 15]. A unique contribution has

Table 3.2: Rietveld refinement parameters of the XRD pattern of $NaFeO_2$ measured at ALBA synchrotron: space group, cell parameters, atomic positions, occupancy (occ.), isotropic Debye-Waller factors (B_{iso}) and refinement agreement factors. Note that a high χ^2 value is generally obtained in high resolution (synchrotron) XRD measurements due to data point density, value is higher than that obtained in refinements of patterns measured in lab-scale diffractometers. The refinement of the 2% of the electrochemically inactive β-$NaFeO_2$ phase is not shown here.

Space group $R\bar{3}m$			**Cell parameters** $\boldsymbol{a}$ = $\boldsymbol{b}$ = 3.02379(5) Å	$\boldsymbol{c}$ = 16.0974(2) Å	
Atom	**Atomic position**			$\mathbf{B}_{iso}$ (Å^2)	**Occ.**
	x	**y**	**z**		
Na	0	0	0	0.5(2)	0.9(1)
Fe	0	0	0.5	0.5(3)	0.9(1)
O	0	0	0.2339(5)	0.5(2)	1
Agreement factors			$\chi^2 = 11.2$	$R_b = 2.01$	$R_p = 3.81$

been needed for the refinement, and a low agreement factor has been obtained ($\chi^2 = 3.8 \times 10^{-31}$), which indicates that no impurity is detected. The β phase detected with synchrotron diffraction is not seen in this measurement. In both structures, the O3- and $\beta-NaFeO_2$, the iron oxidation state is $3+$, so a similar central shift is expected for both samples. However, the iron environment is different: octahedral for the O3 phase and tetrahedral for the β phase. The tetrahedral environment should lead to a lower QS due to the shorter Fe-O bonds: 2.0538(5) Å in the octahedral environment, and 1.81(2) Å in average in the tetrahedral one. However, the β phase presence is low to induce a detectable asymmetry in this measurement.

As seen from the SEM images in Fig. 3.6 the sample consists of spheroid sub-micron sized homogeneous primary particles of 250 nm average diameter, which aggregate into secondary particles with sizes ranging from a few micrometers up to several tenths of micrometers. Some of the SEM images throughout the work are not correctly focused, especially those with high magnification, due to a charging effect of the particles. When the focusing process took more than a couple of minutes, the particles would charge and start to vibrate impeding taking more pictures.

The XRD technique shows the average diffraction pattern of a relatively large volume of the material. In order to check the local atomic ordering, TEM measurements of the pristine powder have been carried out. In Fig. 3.7, TEM and STEM micrographs, and electron diffraction patterns are presented perpendicular to c axis. It can be seen how the particles are mainly monocrystalline, and not formed by clusters of differently oriented crystals. It is though worth noting that TEM microscopy is only suitable for the characterization of nano-sized particles, smaller than $\approx$ 100 nm. Thus, it might occur that only the smallest particles have been characterized, and that bigger particles are polycrystalline.

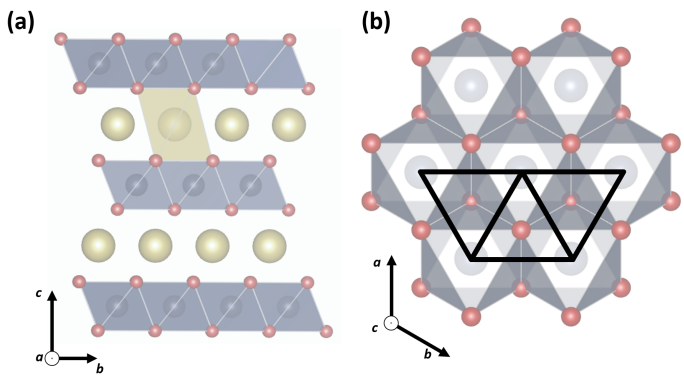

Figure 3.3: **(a)** Side view and **(b)** top view of the crystal structure of $NaFeO_2$. Triangular arrangement of transition metal atoms in O3 type structures has been highlighted with black in the top view, where the FeO_6 layer of $NaFeO_2$ sample is shown perpendicular to c axis. Na ions are shown as yellow spheres, Fe ions are shown with blue octahedra and oxygen ions with red spheres.

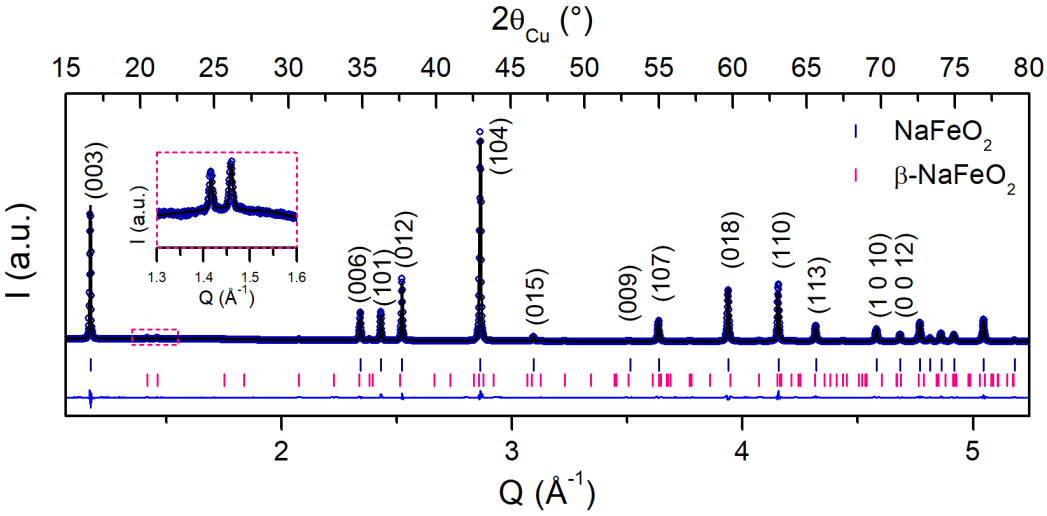

Figure 3.4: XRD Rietveld refinement of $NaFeO_2$ layered oxide. Open circles are used for the observed intensity, black line for the refined pattern, blue line for the difference and vertical marks for the reflection angle position. The $(h\,k\,\ell)$ indices of the O3 phase are written close to the mayor reflections. In the inset, highlighted with the pink dashed line, the reflections $(1\,1\,0)$ and $(0\,1\,1)$ of the β-$NaFeO_2$ phase. The high resolution XRD measurement from ALBA synchrotron is presented as function of Q reciprocal vector, with the equivalent 2θ angle to Cu source X-rays on top axis. With pink vertical marks the position of the reflections of the 2% β-$NaFeO_2$ impurity are shown.

Anyway, the atomic resolution TEM image (Fig. 3.7a) shows the series of Fe (light) and Na (dark) atoms with homogeneous interlayer spacing that agree with the XRD data. Some irregularities can be observed close to the surface, but the bulk of the particle shows no irregularities or the

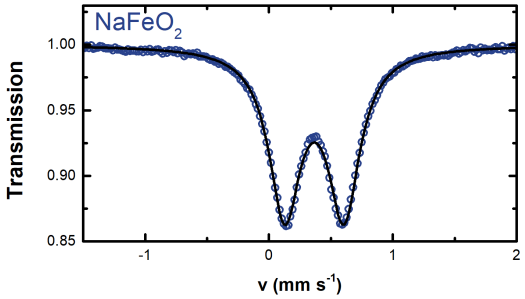

Figure 3.5: Experimental and refined Mössbauer spectra of pristine $NaFeO_2$ powder. The open circles correspond to normalized transmission, and the solid line to the fitted curve.

Parameter	Value
CS (mm s^{-1})	0.366(1)
FWHM (mm s^{-1})	0.311(2)
QS (mm s^{-1})	0.478(1)
χ^2	3.8×10^{-31}

Table 3.3: Refinement parameters of $NaFeO_2$ powder sample Mössbauer spectrum. Central shift (CS), full width at half maximum (FWHM) and quadrupole splitting (QS).

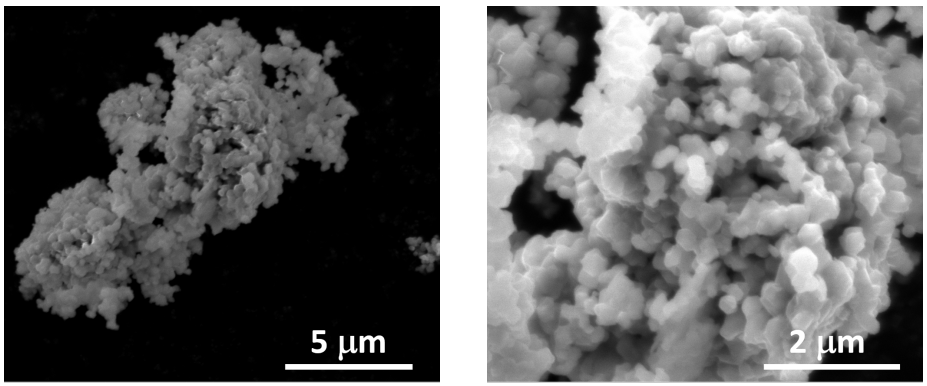

Figure 3.6: SEM images of $NaFeO_2$ powder with **(a)** $\times 15000$ and **(b)** $\times 40000$ magnification.

presence of stacking faults. These faults are planar defects, and can be defined as a misalignment in the stacking order in the structure, which are very common in layered oxides [16–19]. Although TEM imaging shows only a local ordering, the stacking faults can also be detected by asymmetries in the reflections of certain peaks in XRD measurements, which have not been observed in Fig. 3.4. Thus, it can be concluded that, if present, the amount of stacking faults is not significant.

As the STEM detector (Fig. 3.7b) is sensitive to the atomic composition, dark lines (highlighted with arrows) can be seen, that are not present in TEM images. Thus, it seems clear that the explanation is not because there are cracked particles, but a single layer with a different composition not altering the surrounding structure. These lines are also seen in the low magnification STEM image when the particle is oriented in a $(h\,k\,0)$ direction (Fig. 3.7d).

The electron diffraction image (Fig. 3.7c) is also in good agreement with the XRD data presented

earlier. The image is taken in the zone axis (z.a.) $[0\,1\,0]$. The interlayer distance obtained from the electron diffraction image is 16.11 Å, very close to the values obtained with the HRXRD diffraction pattern (16.0974(2) Å, see Table 3.2). The in-plane distance obtained here is 3.05 Å, slightly higher than the 3.02379(5)Å calculated from the HRXRD data. Considering that the HRXRD measures an average distance of all the illuminated particles and TEM diffraction is a local measurement, the values can be regarded as consistent.

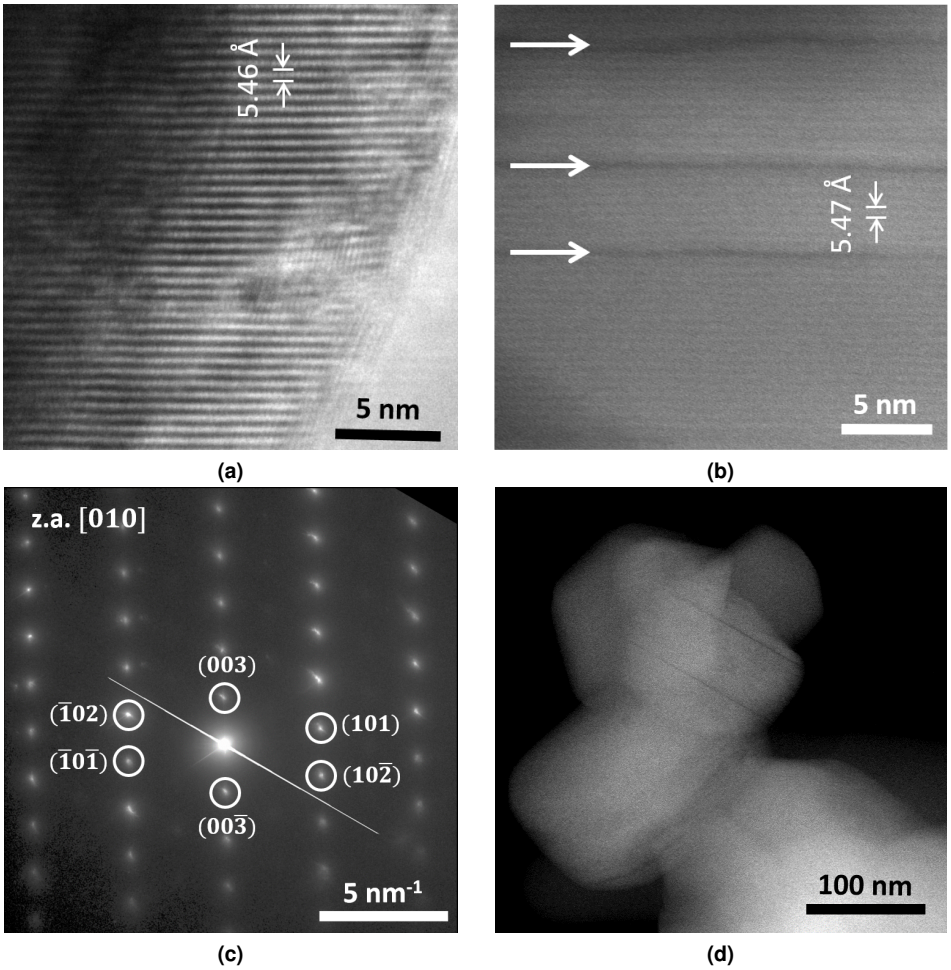

Figure 3.7: **(a)** High resolution TEM (HRTEM), **(b)** STEM, **(c)** electron diffraction and **(d)** low magnification STEM images of $NaFeO_2$ powder. All the pictures have been taken perpendicular to *c* axis.

The particle size and morphology of $NaFeO_2$ depends on the synthesis precursors and conditions. The particle size obtained in this work has been compared with those reported in the literature, which are gathered in Table 3.4. It can be seen that the synthesis conditions used in this work result in smaller particles than those reported in the literature. Although crystalline

structure is comparable, as reflected by the similar cell parameters, the differences in particle size can affect the electrochemical properties of the material [20].

Table 3.4: Comparison of the cell parameters (up to three significant figures) and average particle size depending on the synthesis conditions (sodium and iron precursors, and heating temperature and dwell time) between literature and this work.

Na prec.	Fe prec.	Heating temp.	Dwell time	Cell parameters		Average size	Ref.
				b (Å)	***c*** (Å)		
Na_2O_2	Fe_3O_4	630°C	10 h	3.023	16.084	2-10 µm	Kataoka et al. [7]
Na_2O_2	nano-Fe_3O_4	630°C	10 h	3.025	16.095	1-2 µm	Kataoka et al. [7]
Na_2O_2	Fe_3O_4	650°C	12 h	-	-	0.9-5 µm	Hwang et al. [8]
Na_2CO_3	Fe_3O_4	650°C	15h	3.023	16.097	250 nm	*This work*

The typical techniquie used for the particle specific surface area calculation is N_2 gas adsorption. However, due to the low expected surface area compared to the sensitivity of the instrument, SAXS has been chosen instead. The scattered intensity of SAXS is presented as a function of the reciprocal distance Q in Fig. 3.8.

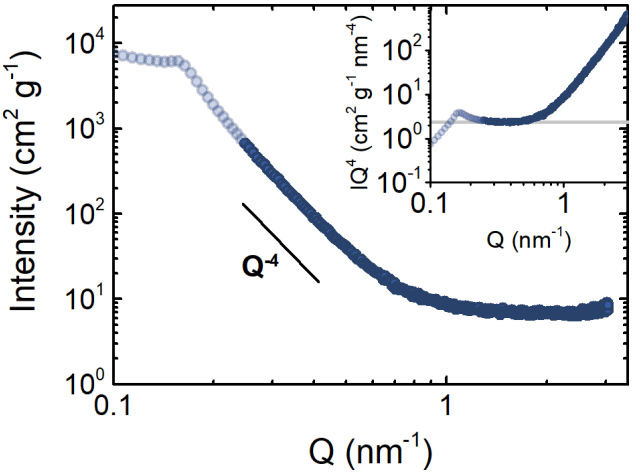

Figure 3.8: Scattered intensity of $NaFeO_2$ vs. reciprocal distance Q. In the inset, Porod plot IQ^{-4} vs. Q. The points that are shown in light color correspond to values affected by the beam stop.

Note that a trend change can be seen at values below $Q = 0.25$ nm^{-1}, shown with light color. The values at which the intensity stays approximately constant ($Q \leqslant 0.15$ nm^{-1}) correspond to the region where the beam stop is located, at the center of the detector, to block the direct beamlight and avoid its damage. The slight increment observed in IQ^4 in Porod plot (inset in Fig. 3.8) at 0.15 nm$^{-1} \leqslant Q \leqslant 0.20$ nm^{-1} is due to the light diffused at the beam stop.

The particle surface area S has been calculated from Porod region, shown in the inset with a gray line, applying equation 2.3 with a result of $S = 2.788$ m^2 g^{-1}. $\Delta\rho$ has been calculated using the theoretical density of the material and from the National Institute of Standards and Technology [21]. Considering spherical particles, this corresponds to particles with a radius of 250 nm according to equation 2.4, in good agreement with the SEM results shown above.

The magnetic properties of the material under study have been measured, by means of ZFC-FC measurements, and the results are shown in Fig. 3.9. A maximum in the χ susceptibility is observed at 10 K, for both ZFC and FC measurements. At higher temperatures χ decreases, and in the inverse susceptibility (χ^{-1}) a linear dependency with the temperature is seen, as observed for the paramagnetic samples. The maximum in ZFC-FC curves show that the sample is antiferromagnetic, with a Néel temperature of $T_N = 10(3)$ K.

The inverse susceptibility curve has been fitted using Curie-Weiss law (equation 3.1):

$$\chi^{-1} = \frac{T - \theta}{C} \tag{3.1}$$

where θ is the Weiss temperature and C is the Curie constant. The antiferromagnetic nature of the sample is confirmed by the negative Weiss temperature, $\theta = -28.6(8)$ K.

The effective magnetic moment μ_{eff} has been calculated from the Curie constant, according to expression 3.2:

$$C = \frac{N_A \mu_{eff}^2 \mu_B^2}{3k_B} \tag{3.2}$$

where N_A is Avogadro's number, μ_B is the Bohr magneton and k_B is Boltzmann's constant.

The obtained effective magnetic moment is $\mu_{eff} = 7.3(2)\mu_B$. This result is higher than the theoretical spin only moment of $\mu_{SO} = 5.92\mu_B$, considering high spin Fe^{3+}, this is spin $S = 5/2$, and a Landé factor $g = 2$. Higher experimental results than theoretically expected values have been previously reported for $NaFeO_2$ [4] and other layered structures [22]. This discrepancy has been associated with the spin-orbit coupling effects in similar structures. However, in the case of $NaFeO_2$, Fe^{3+} is a spin-only ion, that is, all *d* orbitals are occupied by a single electron, and the spin-orbital coupling should be zero. In this case it might be associated with short-range magnetic fluctuations that persist to high temperatures arising from the competing exchange interactions that frustrate the spins, as described by McQueen et al. [4].

The antiferromagnetic forces are quite weak given the high value of θ. This points to a probable antiferromagnetic ordering between far neighbors, that is, the antiferromagnetism comes from the coupling between Fe ions in adjacent layers instead of from the close neighbors within the plane. Indeed, O3 type structures have a triangular distribution of TM ions, which produces a geometrically frustrated antiferromagnet, and thus a complex spin arrangement [10]. The triangular arrangement of TM ions is shown and highlighted in Fig. 3.3b.

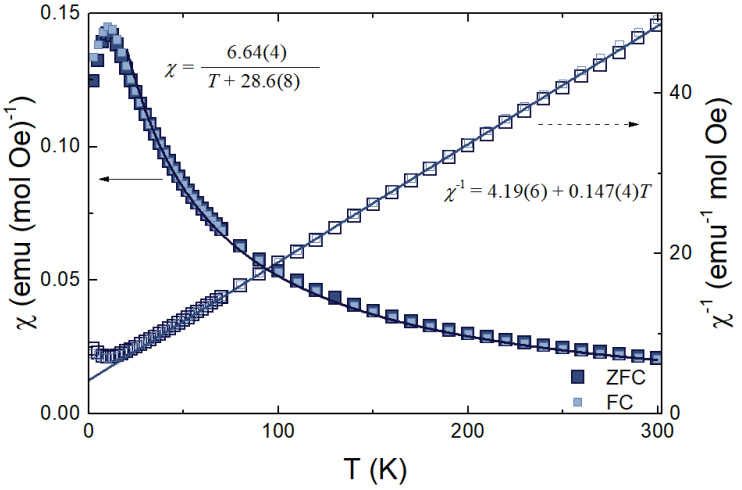

Figure 3.9: ZFC-FC measurement of $NaFeO_2$ in the temperature range between 2.5 K and 300 K. Susceptibility (left axis) is presented with solid squares and inverse susceptibility (right axis) with open squares as a function of temperature. Data has been fitted with Curie-Weiss law (solid lines).

3.3 Synthesis and physicochemical characterization of $NaFe_{0.9}Mn_{0.1}O_2$

$NaFe_{0.9}Mn_{0.1}O_2$ has been prepared mixing anhydrous sodium carbonate (Na_2CO_3, $\geqslant 99\%$, Sigma Aldrich), iron (II,III) oxide (Fe_3O_4, $\geqslant 97\%$, Alfa Aesar) and manganese oxide using an agate mortar and a pestle. Manganese (III) oxide (Mn_2O_3, $\geqslant 99\%$, Alfa Aesar) and manganese (IV) oxide (MnO_2, $\geqslant 99.99\%$, Sigma Aldrich) have been tested, as well as different proportions of sodium precursor excess in order to maximize the amount of sodium in the sample. The synthesis reactions, with both manganese precursors, can be described as follows:

$$\frac{1}{2}Na_2CO_3 + 0.3Fe_3O_4 + 0.05Mn_2O_3 + \frac{3}{40}O_2 \xrightarrow{650^{\circ}C,\ 2h,\ air} NaFe_{0.9}Mn_{0.1}O_2 + \frac{1}{2}CO_2$$

$$\frac{1}{2}Na_2CO_3 + 0.3Fe_3O_4 + 0.1MnO_2 + \frac{1}{20}O_2 \xrightarrow{650^{\circ}C,\ air} NaFe_{0.9}Mn_{0.1}O_2 + \frac{1}{2}CO_2$$

In literature, a whole series of O3-$Na_yFe_yMn_{1-y}O_2$ ($0.5 \leqslant y \leqslant 1$) have been reported, synthesized with MnO_2 precursor (manganese (IV) oxide) [23], with the same amount of sodium and iron content. However, one of the main advantages of the O3 structures is that, unlike P phases, they can usually be synthesized with higher sodium content. In the fully sodiated state, both Mn and Fe would be in 3+ oxidation state, so in order to maximize the Na content in the final structure, Mn(III) oxide has also been tested as a precursor. In the Table 3.5 the ICP-OES results for the two synthesis are shown, comparing the effect of using Mn(III) or Mn(IV) oxides as precursor in the final sodium content. Using Mn(III) leads to a higher sodium content, although a fully sodiated material has not been possible to synthesize.

Table 3.5: ICP-OES results of $Na_xFe_{1-y}Mn_yO_2$, with aimed composition of $x = 1$ and $y = 0.1$. XRD pattern refers to Fig. 3.10.

XRD pattern	Mn precursor oxidation state	Precursor proportion (Na:Fe:Mn)	ICP results (Na:Fe:Mn)
A	III	1 : 0.9 : 0.1	0.96 : 0.90 : 0.10
B	IV	1 : 0.9 : 0.1	0.90 : 0.90 : 0.10

The corresponding XRD patterns are presented in Fig. 3.10. The expected O3 structure is obtained with both precursors, although the cell parameters are slightly different as shown by the mismatch in the peaks positions. This has been highlighted in the insets where the reflections $(0\,0\,3)$ and $(1\,0\,4)$ of Fig. 3.10. The mismatch cannot be accounted only for a displacement in the sample height, as that will produce a shift of both peaks in the same direction, and not like the case observed here. It has been shown that the interlayer distance depends strongly on the sodium content, and not that much on the transition metal radii [23]. Moreover, both Fe^{3+} and Mn^{3+} ions have similar radii [24]. Although both structures share the same space group and Fe:Mn ratio, as shown with the ICP analysis, they have different sodium contents, and hence the difference in the cell parameters.

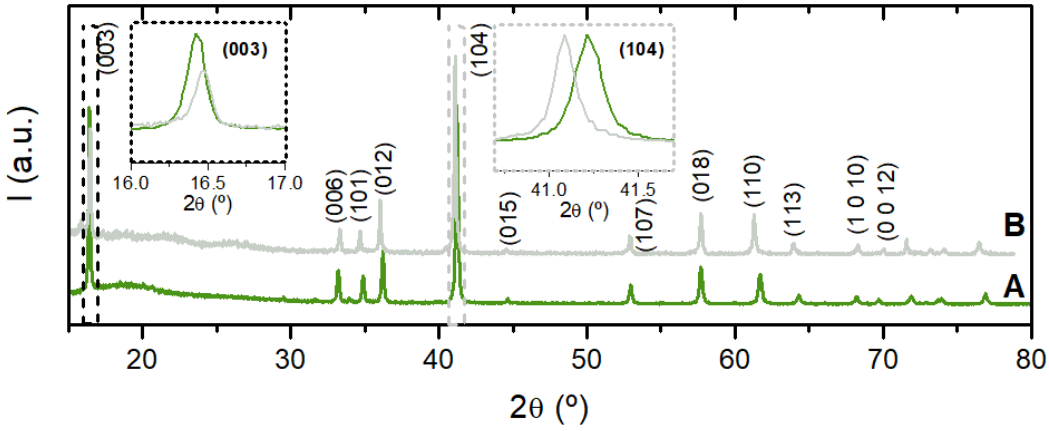

Figure 3.10: XRD patterns normalized to $(1\,0\,4)$ reflection of synthesis tests using different Mn precursors (see Table 3.5). In the inset, reflections $(0\,0\,3)$ and $(1\,0\,4)$ have been highlighted.

To obtain the best results, in terms of Na content and sample purity, manganese (III) oxide, iron (II,III) oxide and sodium carbonate have been mixed using a mortar and a pestle. The pelletized material has been heated at 5°C/min rate and hold at 650°C during 15 hours under air atmosphere. Sample has been removed from the furnace above 100°C and transferred into an argon glovebox to avoid moisture contamination. The c axis for this phase is between that of $NaFeO_2$ and that reported in literature for $Na_xFe_{0.9}Mn_{0.10}O_2$ for $x = 0.90$ [23]: $c = 16.10$ Å for $NaFeO_2$,

and $c = 16.21$ Å reported at $x = 0.90$ vs. 16.115(3) Å observed in this work at $x = 0.96$ for $Na_xFe_{0.9}Mn_{0.10}O_2$. As explained earlier, the difference most likely comes from the sodium content differences. With higher sodium content, the repulsion between the oxygen atoms of adjacent layers is reduced, and thus, interlayer distance will be shorter.

The refined XRD pattern of the sample with no impurities and maximized Na content (synthesis *B* in Table 3.5) can be seen in Fig. 3.11, and the refined parameters are summarized in Table 3.6. Iron and manganese occupancies have not been refined; both elements have a similar electronic structure, and thus, a similar response to X-ray diffraction making it not possible to refine the Fe:Mn occupancy ratio in a lab-scale diffractogram. $NaFe_{0.9}Mn_{0.1}O_2$ shares the O3 structure with $NaFeO_2$, the structure has been refined with the SG $R\bar{3}m$ and good agreement factors.

Table 3.6: Rietveld refinement parameters of the XRD pattern of $NaFe_{0.9}Mn_{0.1}O_2$ measured at CIC EnergiGUNE: space group, cell parameters, atomic positions, occupancy (occ.), isotropic Debye-Waller factors (B_{iso}) and refinement agreement factors.

Space group $R\bar{3}m$				**Cell parameters** $\boldsymbol{a}$ = $\boldsymbol{b}$ = 3.0215(3) Å	$\boldsymbol{c}$ = 16.115(3) Å
Atom	**Atomic position**			$\mathbf{B}_{iso}$ (Å^2)	**Occ.**
	x	**y**	**z**		
Na	0	0	0	0.6(5)	0.9(3)
Fe	0	0	0.5	0.4(5)	0.9
Mn	0	0	0.5	1.9(4)	0.1
O	0	0	0.235(8)	0.9(5)	1
Agreement factors			$\chi^2 = 1.69$	$R_b = 9.96$	$R_p = 14.8$

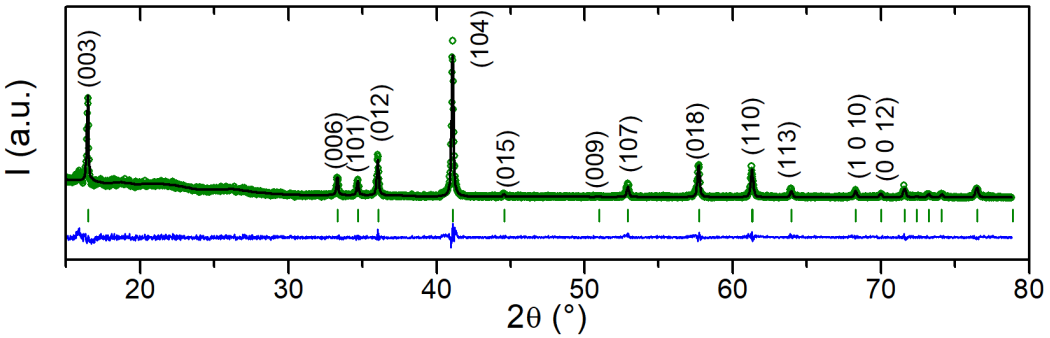

Figure 3.11: XRD Rietveld refinements of O3-$NaFe_{0.9}Mn_{0.1}O_2$ layered oxide. Open circles are used for the observed intensity, black line for the refined pattern, blue line for the difference and vertical marks for the reflection angle position. Corresponding refinement values are collected in Table 3.6.

The Mössbauer spectrum (Fig. 3.12) is very similar to that of $NaFeO_2$ sample. The fitting consists of a single doublet, with a good agreement factor ($\chi^2 = 3.92 \times 10^{-20}$). The refined parame-

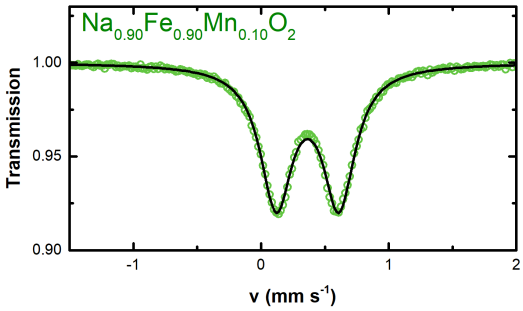

Figure 3.12: Mössbauer refinement of pristine $NaFe_{0.9}Mn_{0.1}O_2$ powder. Open circles correspond to normalized transmission, and solid line for the fitted curve.

Parameter	Value
CS (mm s^{-1})	0.364(1)
FWHM (mm s^{-1})	0.303(3)
QS (mm s^{-1})	0.491(2)
χ^2	3.92×10^{-20}

Table 3.7: Refinement parameters of $NaFe_{0.9}Mn_{0.1}O_2$ powder sample Mössbauer spectrum. Central shift (CS), full width at half maximum (FWHM) and quadrupole splitting (QS).

ters, summarized in Table 3.7, show that the doublet has a CS of 0.364 mm s^{-1} and a QS of about 0.5 mm s^{-1}. These values correspond to Fe^{3+} in an octahedral environment, as expected. The slightly increased QS value compared to that of $NaFeO_2$ reflects that the FeO_6 octahedra are less symmetric, i.e. are slightly distorted. The distortion can arise from either a sodium deficiency that locally affects the ions around the vacancies or due to the presence of mixed Fe and Mn ions in the layers.

The chemical composition has been confirmed with ICP-OES. The obtained formula, normalized to iron content, is $Na_{0.96}Fe_{0.90}Mn_{0.10}O_2$ ($\pm 1.5\%$).

The SEM images, presented in Fig. 3.13, show a similar morphology to the $NaFeO_2$ sample, with spheroid primary particles of 280 nm average diameter, aggregated into secondary particles with sizes ranging from a few micrometers to tenths of micrometers.

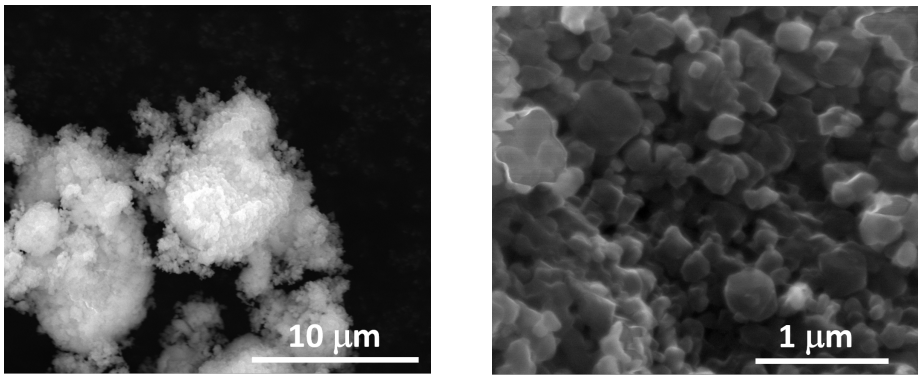

Figure 3.13: SEM images of $NaFe_{0.9}Mn_{0.1}O_2$ powder with **(a)** $\times 10000$ and **(b)** $\times 80000$ magnification.

Magnetic measurements, in Fig. 3.14, reveal that, as in the case of $NaFeO_2$, this material exhibits an antiferromagnetic behavior with a Néel temperature of $T_N = 10(3)$ K. The negative Weiss temperature of $\theta = -20.5(4)$ K confirms the antiferromagnetic nature of the sample. An effective magnetic moment of $\mu_{eff} = 5.9(2)\mu_B$ has been calculated from the Curie-Weiss fitting result, slightly higher than the theoretical spin only moment $\mu_{SO} = 5.74\mu_B$ considering high-spin Fe^{3+} and Mn^{4+}. As explained in the case of $NaFeO_2$ in the previous section, Fe^{3+} as well as Mn^{4+} are spin only ions, and therefore, no spin-orbital coupling is expected.

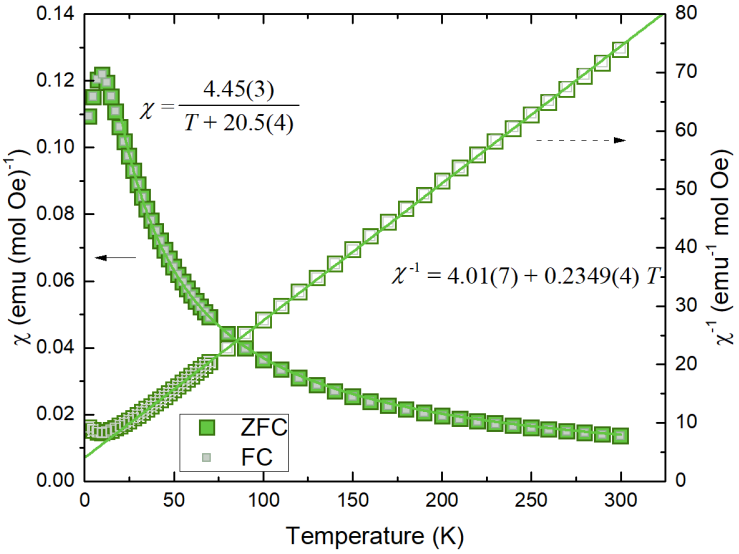

Figure 3.14: ZFC-FC measurement of $NaFe_{0.9}Mn_{0.1}O_2$ in the temperature range between 2.5 K and 300 K. Susceptibility (left axis) is presented with solid squares and inverse susceptibility (right axis) with open squares as a function of temperature. Data has been fitted with Curie-Weiss law (solid lines).

3.4 Synthesis and physicochemical characterization of O3-$Na_{2/3}Fe_{2/3}Mn_{1/3}O_2$

O3-$Na_{2/3}Fe_{2/3}Mn_{1/3}O_2$ sample has been prepared in a three step synthesis based on literature [25].

In the first step, from iron and manganese nitrates ($Fe(NO_3)_3 \cdot 9H_2O$, $\geqslant 98\%$, Sigma Aldrich and $Mn(NO_3)_2 \cdot 4H_2O$, $\geqslant 98\%$, Acros Organics) respective hydroxides have been obtained ($Fe(OH)_3$ and $Mn(OH)_2$). To this aim, sodium hydroxide (NaOH, $\geqslant 99.25\%$, Fisher Scientific) has been dissolved in distilled water with a concentration of 1M. With a constant stirring, the two solutions have been stoichiometrically mixed and a brown solid precipitate appears. The precipitate, consisting of an iron and manganese hydroxides mixture, has been filtered and washed with cold water. $NaNO_3$ side product is soluble in water, so it is not present in the filtered solid. The synthesis of the

hydroxides can be described as follows:

$$\frac{2}{3}Fe(NO_3)_3 \cdot 9H_2O + \frac{1}{3}Mn(NO_3)_2 \cdot 4H_2O + \frac{8}{3}NaOH \xrightarrow{H_2O} \frac{2}{3}Fe(OH)_3 + \frac{1}{3}Mn(OH)_2 + \frac{8}{3}Na^+NO_3^-$$

After drying at 100°C overnight, the hydroxide mixture has been mixed using an agate mortar and a pestle with the stoichiometric amount of sodium nitrate ($NaNO_3$, $\geqslant 99\%$, Alfa Aesar). Pelletized material has been heated in the second step at 700°C during 2h under pure O_2 flow.

After grinding inside an argon glove-box, the material has been pelletized again and heated in the third step at 900°C during 2h under pure oxygen flow. In both cases, heating has been applied at a 5°C/min rate and the material has been taken out of the furnace above 100°C to avoid moisture contamination.

These two steps can be described with the following equation:

$$\frac{2}{3}NaNO_3 + \frac{2}{3}Fe(OH)_3 + \frac{1}{3}Mn(OH)_2 + \frac{2}{3}O_2 \xrightarrow{\text{700°C, 2h, } O_2 \mid \text{900°C, 2h, } O_2} Na_{2/3}Fe_{2/3}Mn_{1/3}O_2 + \frac{4}{3}H_2O + \frac{2}{3}NO_2$$

A 5% excess of $NaNO_3$ precursor has been added to account for the possible Na evaporation during the synthesis reaction.

The crystallinity of the sample has been analyzed with HRXRD at ALBA synchrotron. Refined pattern and parameters can be seen in Fig. 3.15 and Table 3.8 respectively. The sample has the same O3 structure as the previously shown samples, it has been thus refined with the $R\bar{3}m$ space group. The sample has no impurities within the resolution of the diffracted pattern. The refined parameters are in good agreement with the previously reported values [25, 26], and the refined occupancies are in good agreement with the expected stoichiometry. The interlayer distance is larger than those of $NaFeO_2$ and $NaFe_{0.9}Mn_{0.1}O_2$ previously shown, presumably due to the lower Na content and the resulting increased repulsion between the oxygen ions in adjacent layers.

Chemical composition has been confirmed with ICP-OES. The nominal result obtained, normalized to iron content, is $Na_{0.81}Fe_{0.67}Mn_{0.32}O_2$, with an error of 4%. The transition metal proportion agrees with the aimed composition, and an excess of sodium has been detected, as shown with the XRD characterization (see Table 3.8).

The Mössbauer spectrum in Fig. 3.16 shows a single doublet. The refined parameters, in Table 3.9, are in good accordance, as in previous samples, with Fe^{3+} octahedral coordinated ion. CS is very similar to the values of $NaFeO_2$ and $NaFe_{0.9}Mn_{0.1}O_2$ (0.35 mm s^{-1}), but QS is higher (0.65 mm s^{-1}), due to the distortion of TM-O distances. As explained earlier, the distortion most likely comes from the sodium vacancies in the structure or the mixed transition metal elements in the TM layers, which are higher in this case than in the previously presented case of $NaFe_{0.9}Mn_{0.1}O_2$.

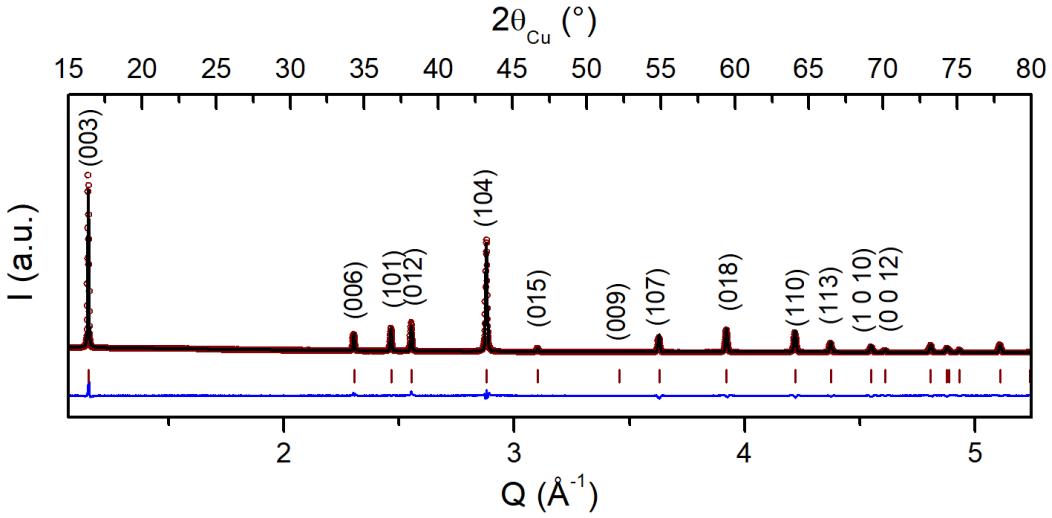

Figure 3.15: High resolution XRD Rietveld refinements of O3-$Na_{2/3}Fe_{2/3}Mn_{1/3}O_2$ layered oxide. Open circles are used for the observed intensity, black line for the refined pattern, blue line for the difference and vertical marks for the reflection angle position. Measurement from ALBA synchrotron as a function of Q reciprocal vector, and 2θ angle equivalent to Cu X-ray source on top axis. Corresponding refinement values are collected in Table 3.8.

Table 3.8: Rietveld refinement parameters of the XRD pattern of O3-$Na_{2/3}Fe_{2/3}Mn_{1/3}O_2$ measured at ALBA synchrotron: space group, cell parameters, atomic positions, occupancy (occ.), isotropic Debye-Waller factors (B_{iso}) and refinement agreement factors.

Space group $R\bar{3}m$			**Cell parameters** $\boldsymbol{a}$ = $\boldsymbol{b}$ = 2.97789(7) Å	$\boldsymbol{c}$ = 16.3519(7) Å
Atom	**Atomic position**			**Occ.**
	x	**y**	**z**	$\mathbf{B}_{iso}$ (Å^2)	
Na	0	0	0.0	0.7(6)	0.70(7)
Fe	0	0	0.5	0.8(5)	0.7(3)
Mn	0	0	0.5	0.5(5)	0.37(7)
O	0	0	0.229(1)	1.0(4)	1
Agreement factors		$\chi^2 = 3.49$	$R_b = 10.6$	$R_p = 7.40$	

The SEM images, presented in Fig. 3.17, reveal a similar morphology to $NaFeO_2$ sample, with small spheroid primary particles, aggregated into secondary particles with sizes ranging from a

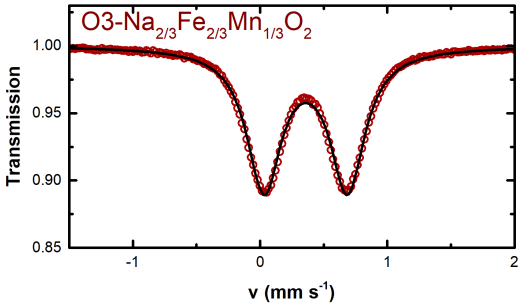

Figure 3.16: Mössbauer refinement of pristine O3-$Na_{2/3}Fe_{2/3}Mn_{1/3}O_2$ powder. Open circles correspond to normalized transmission, and solid line for the fitted curve.

Parameter	Value
CS (mm s^{-1})	0.359(1)
FWHM (mm s^{-1})	0.331(2)
QS (mm s^{-1})	0.655(2)
χ^2	2.8×10^{-187}

Table 3.9: Refinement parameters of O3-$Na_{2/3}Fe_{2/3}Mn_{1/3}O_2$ powder sample Mössbauer spectrum. Central shift (CS), full width at half maximum (FWHM) and quadrupole splitting (QS).

few micrometers to tenths of micrometers. However, the particles in this sample are less homogeneous and have a higher particle size than previous samples, with an average diameter of 800 nm. Moreover, the average aggregate size is also bigger for this sample.

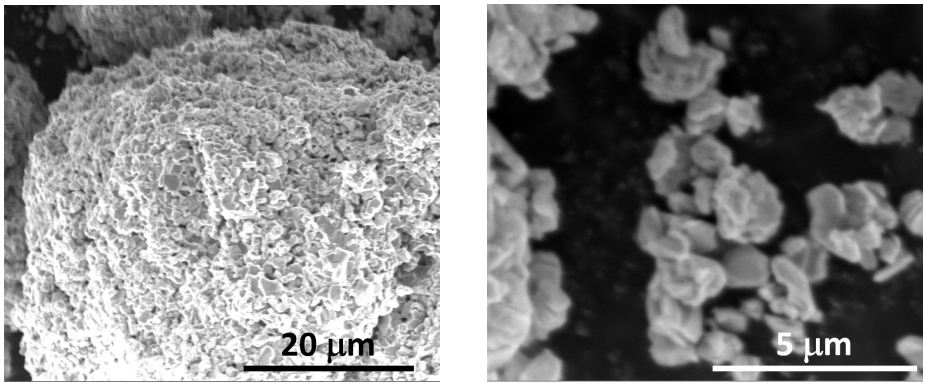

Figure 3.17: SEM images of O3-$Na_{2/3}Fe_{2/3}Mn_{1/3}O_2$ powder with **(a)** $\times 5000$ and **(b)** $\times 24000$ magnification.

The local atomic ordering has been studied with TEM imaging. Similarly to the analysis done for $NaFeO_2$ in Fig. 3.7, high resolution TEM, STEM and electron diffraction images are presented in Fig. 3.18. This sample, being partially desodiated at the pristine state, and having a mixture of two transition metal elements, can be expected to be more disordered or less homogeneous than the isostructural $NaFeO_2$. In Fig. 3.18a, the HRTEM image of a particle is presented, where Fe and Na layers can be distinguished. Unluckily, it has not been possible to perfectly orient the

particle in the $(1\,0\,0)$ or $(0\,1\,0)$ direction, but a mixture of both, $(h\,k\,0)$ and thus, atomic columns are not distinguished. Instead, atomic layers can be seen: light rows for TM layers and dark rows for sodium layers. Moreover, irregularities in the particle surface can be observed as bright and dark zones. Indeed, surface roughness will create thick and thin regions in the particle, that are reflected with different contrast in transmission mode.

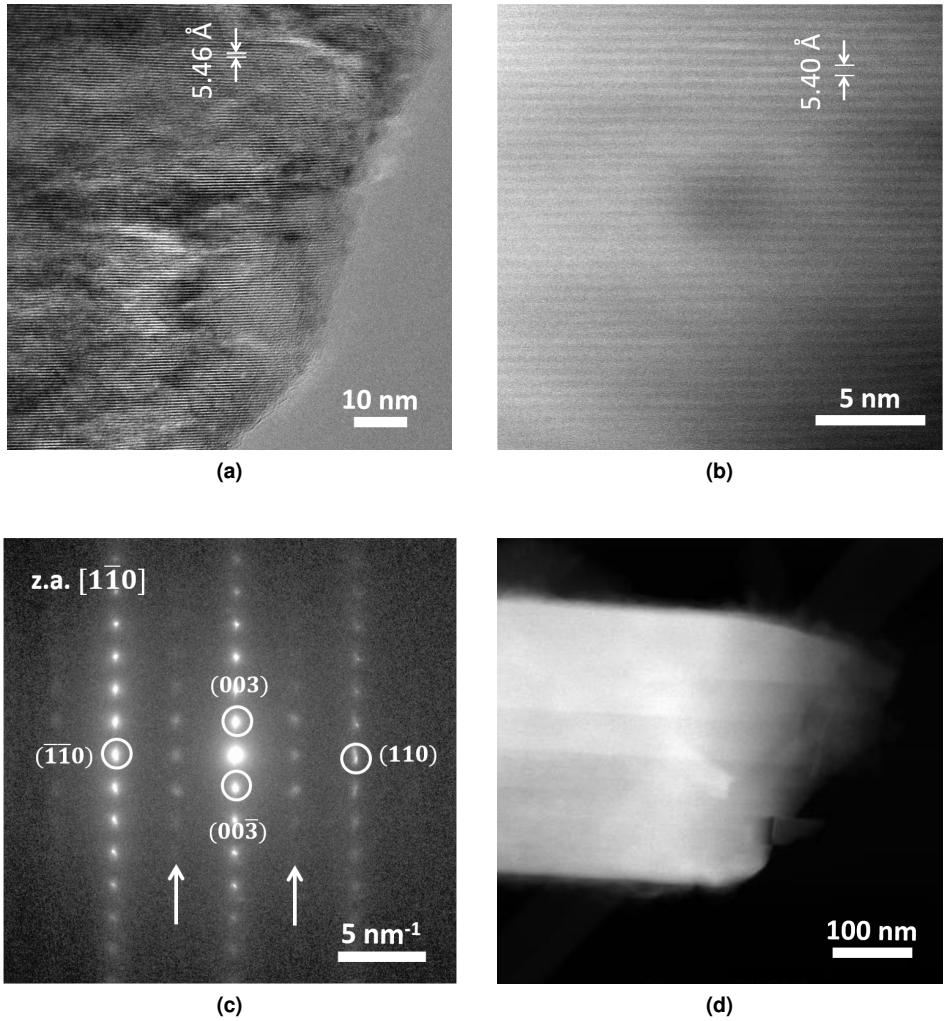

Figure 3.18: **(a)** High resolution TEM (HRTEM), **(b)** STEM, **(c)** electron diffraction and **(d)** low magnification STEM images of O3-$Na_{2/3}Fe_{2/3}Mn_{1/3}O_2$ powder. All the pictures have been taken perpendicular to *c* axis.

A similar image can be distinguished in the STEM image (Fig. 3.18b), where the contrast is related to the composition. As opposed to $NaFeO_2$ sample (see Fig. 3.7), here there are no apparent dark lines, although a dark spot can be seen in the high magnification STEM image (Fig. 3.18b).

More interestingly, in the low magnification STEM image (Fig. 3.18d), the particle seems to be divided in bands, with gradient composition ordering as reflected by the gradient color contrast by bands. Energy dispersive X-ray spectroscopy (EDX) analysis in different regions has shown that the Fe to Mn ratio is $^2/_3$: $^1/_3$ as expected, with an error of 2% in all the measured regions. The sodium content however differs from one region to another, ranging from values as low as 0.16 up to 0.96, and an average of 0.6. Thus, the differences in contrast seem to be related to an inhomogeneous distribution of Na ions in the structure. The electron diffraction image (Fig. 3.18c), shows that the interlayer distance is slightly larger than that obtained with HRXRD (see Table 3.8): 16.3519(7) Å in HRXRD vs. 16.471 Å in electron diffraction. The in-plane metal to metal distance obtained in electron diffraction is 2.92Å, compared to the 2.97789(7)Å calculated from HRXRD. The difference between the bulk XRD and electron diffraction is less than 2%, and considering that the electron diffraction is a local technique, while HRXRD gives an average result, both techniques are in good agreement. Indeed, the interlayer distance is closely related to the sodium content, and thus, depending on the area chosen for the electron diffraction, a low or a high sodiated area, different values will be obtained. Moreover, electron diffraction spots not considered in the as-synthesized structure can be seen, highlighted with arrows in Fig. 3.18c. These diffracted spots could be related to a superstructure formed by a sodium-vacancy ordering that is not manifested in the X-ray diffraction. It is worth reminding that the electron diffraction is a local measurement, and thus, the sodium-vacancy ordering can have a short range that is not revealed in the bulk XRD measurements.

The particle surface area has been calculated with SAXS scattering. In Fig. 3.19 scattered intensity is presented as a function of the reciprocal distance, and Porod plot is presented in the inset. Similarly to the results presented for $NaFeO_2$ in Fig. 3.8, for values $Q \leqslant 0.25\ \mathrm{nm}^{-1}$, the data are affected by the beam stop located at the center of the detector and the light diffused on it. The affected region is shown with light colors in Fig. 3.19.

In the Porod region shown with a gray line in the inset, applying equation 2.3, a particle surface area of $S = 0.707\ \mathrm{m}^2\ \mathrm{g}^{-1}$ has been estimated. Considering spherical particle, this value corresponds to particles with a radius of 970 nm, which is slightly larger than the results obtained with SEM (800 nm). However, and considering that SEM technique is a local technique, and the measured particles are limited, the results are in good agreement.

The ZFC-FC measurements show a similar behavior to the previous samples: it presents an antiferromagnetic ordering with a Néel temperature of $T_N = 8 \pm 3$ K. At $T = 120 \pm 10$ K a discontinuity can be seen. In the inverse susceptibility measurement is clear that the slope is the same before and after the step, but there is an offset of 30 mol Oe emu^{-1}. The curve has been separated in low temperature (LT: $T < 70$°C) and high temperature (HT: $T > 170$°C) regions.

Since the effective magnetic moment is defined by the slope of the inverse susceptibility and the slope is the same at high and low temperatures, a consistent value is obtained in both regions, $\mu_{eff} = 6.1(2)\ \mu_B$. This value, as for the case of $NaFeO_2$ and $NaFe_{0.9}Mn_{0.1}O_2$ presented earlier,

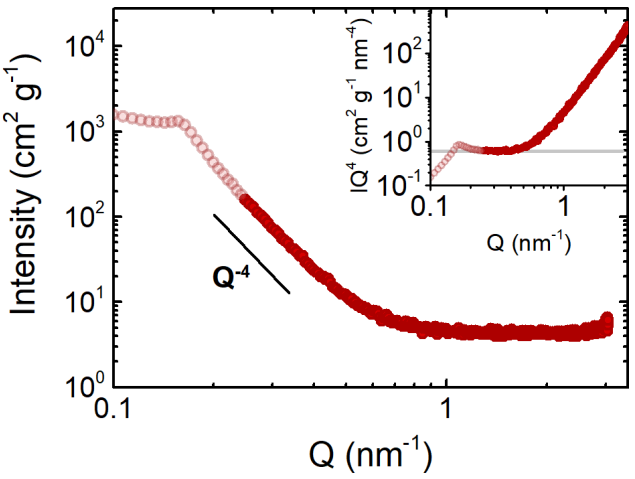

Figure 3.19: Scattered intensity of O3-$Na_{2/3}Fe_{2/3}Mn_{1/3}O_2$ vs. reciprocal distance Q. In the inset, Porod plot IQ^{-4} vs. Q. The points that are shown in light colors correspond to values affected by the beam stop.

is higher than the expected spin only moment, $\mu_{SO} = 5.33\mu_B$, considering HS Fe^{3+} ($S = 5/2$) and HS Mn^{4+} ($S = 3/2$).

In both curves the Weiss Temperature θ is negative: $\theta_{LT} = -24.0(3)$ K and $\theta_{HT} = -198(2)$ K, confirming the antiferromagnetic nature of the sample. However, two different antiferromagnetic forces seem to be present, with a stronger interaction at high temperatures as reflected by the lower θ value. Due to the triangular lattice of the structure, the sample is a frustrated antiferromagnet. At low temperatures the antiferromagnetism is most likely formed between different TM planes, as for the $NaFeO_2$ and $NaFe_{0.9}Mn_{0.1}O_2$ samples presented earlier. At high temperatures on the other hand, the antiferromagnetism nature is stronger and is probably present within the TM planes. Since the strong antiferromagnetic ordering at high temperature is not present in the samples with low or no manganese content, it seems reasonable to think that it is formed by the Mn spin arrangement. Indeed, Weiss constant of Na_xMnO_2 samples reported in the literature are very low, ranging from -650 K to -400 K [27–29]. This transition, although smoother has been observed in a different batch of the same structure and composition sample, as well as in a P2-structured $Na_{2/3}Fe_{2/3}Mn_{1/3}O_2$ sample, both synthesized in 2014 by E. Gonzalo and measured and analyzed by D. Saurel (see Section A.2 in Appendix A).

Another explanation for having two distinct Weiss Temperatures could be related to the presence of inhomogeneities in the structure as observed in the TEM imaging (see Fig. 3.18). Although in XRD a single phase could only be observed, TEM images has shown that there are sodium distribution inhomogeneities. A different sodium distribution could result in a different Fe/Mn ordering, and therefore in a different magnetic ordering. That is, different magnetic orderings could be expected in Na-rich and Na-poor phases. Nonetheless, further experiments would be required

to fully understand these results.

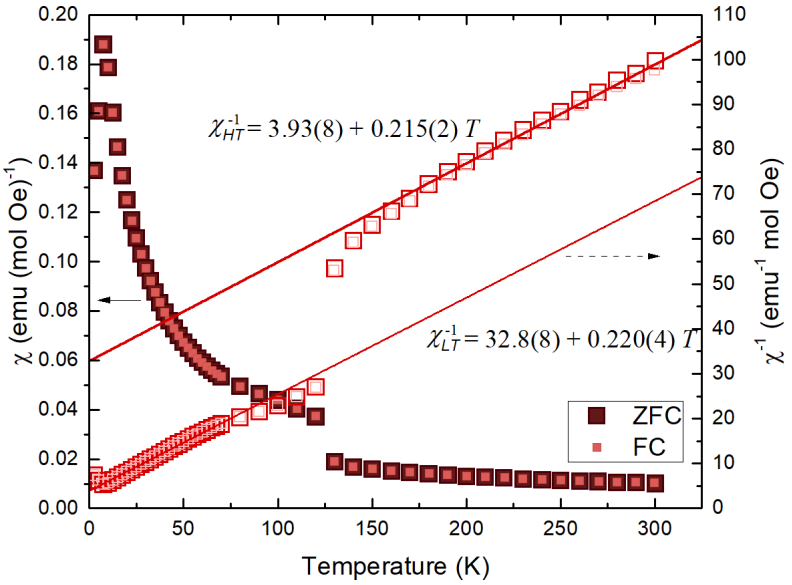

Figure 3.20: ZFC-FC measurement of O3-$Na_{2/3}Fe_{2/3}Mn_{1/3}O_2$ in the temperature range between 2.5 K and 300 K. Susceptibility (left axis) is presented with solid squares and inverse susceptibility (right axis) with open squares as a function of temperature. Data has been fitted with Curie-Weiss law (solid lines) in the low temperature region (LT, $T < 120$ °C) and high temperature region (HT, $T > 120$ °C) separately.

3.5 Comparison of $Na_xFe_{1-y}Mn_yO_2$ samples

As previously described in this chapter, several materials of the O3-$Na_xFe_{1-y}Mn_yO_2$ ($2/3 \leqslant y \leqslant 1$) family have been synthesized and structurally described. All of them show orange color due to the presence of Fe^{3+}, and the samples are darker as the amount of manganese is increased. This color variation can be seen in Fig. 3.21.

With SEM and SAXS data for some of the samples, the average particle size has been measured. The results are gathered in Table 3.10. The particles of the O3-type structure materials are spherical, and the particle size homogeneity is reduced as the heating temperature is increase. It can also be seen that increasing the heating temperature also increases the particle size.

The XRD analysis shows that the phases with O3 structure follow Vegard's law [38], where a linear change in molar volume can be observed with sodium content as measured with ICP-OES. In Fig. 3.22 the molar volume of the studied O3 phases is presented, including the linear regression of the volume with a gray line. Although more points would be desirable, it seems that interlayer distance is strongly dependent on the sodium content and not so much on the nature of the transition metal elements, as stated in the literature [23].

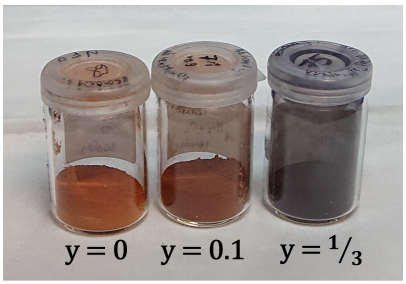

Figure 3.21: Synthesized series of $Na_xFe_{1-y}Mn_yO_2$ system, for $y = 0$ ($NaFeO_2$), $y = 0.1$ ($NaFe_{0.9}Mn_{0.1}O_2$) and $y = 1/3$ ($Na_{2/3}Fe_{2/3}Mn_{1/3}O_2$).

Table 3.10: Summary of the average particle size and morphology of the studied samples. The synthesis temperature (temp.), the shape, and the average radius r, are given.

Sample	**Temp.** (°C)	**Shape**	r_{SEM} (nm)	r_{SAXS}(nm)
O3-$NaFeO_2$	650	Spherical	250	250
O3-$NaFe_{0.9}Mn_{0.1}O_2$	650	Spherical	280	-
O3-$Na_{2/3}Fe_{2/3}Mn_{1/3}O_2$	800	Spherical	800	970

All the studied materials show the same antiferromagnetic ordering temperature, with a Néel temperature $T_N \approx 10(3)$ K. Weiss temperature however changes with the iron substitution by manganese as shown in Fig. 3.23a. Weiss temperature is above -30 K in all cases, and it increases with increasing manganese content with the exception of O3-$Na_{2/3}Fe_{2/3}Mn_{1/3}O_2$. Note that for the O3-$Na_{2/3}Fe_{2/3}Mn_{1/3}O_2$ sample, only the low temperature Weiss temperature (θ_{LT}) is presented, which seems to be related with iron spin arrangement, while the high temperature θ_{HT} seems to be more related to the manganese spin arrangement, as it has been described earlier in this chapter. The antiferromagnetic force of all these compounds is low at low temperatures, and it decreases with decreasing iron content. Due to the triangular lattice of the transition metal ions in the TMO_2 layers, the antiferromagnetic ordering is frustrated in the TM layers. Thus, the an-

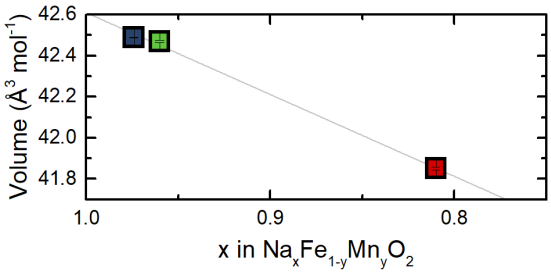

Figure 3.22: Molar volume of the $Na_xFe_{1-y}Mn_yO_2$ series as a function of sodium content. Gray line shows the linear dependency of the volume.

tiferromagnetic ordering seems to appear more easily between adjacent layers, that is, between distant ions, and hence the low antiferromagnetic force. However, O3-$Na_{2/3}Fe_{2/3}Mn_{1/3}O_2$ has an antiferromagnetic ordering transition, and at high temperatures a strong antiferromagnetic force can be seen with a low Weiss temperature value: $\theta = -198(2)$ K. The ordering in this case seems to come from the antiferromagnetic coupling between close neighbor Mn ions within the TMO_2 layers. Another explanation to describe the two distinct Weiss temperatures could be related to an inhomogeneous sodium distribution in the structure. The Mn/Fe ordering might differ in the sodium-rich and sodium-poor regions observed with TEM imagining, which would result in two distinct magnetic ordering.

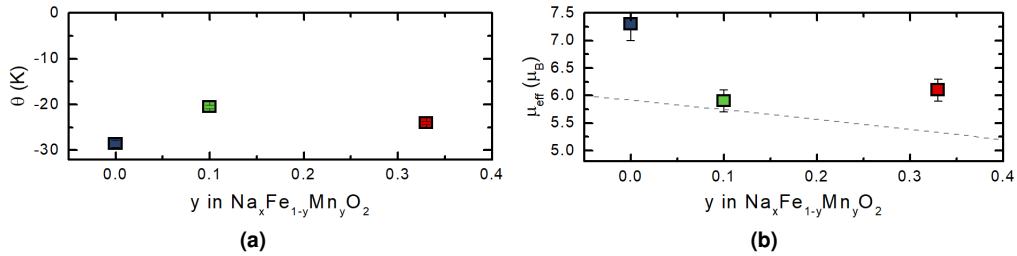

Figure 3.23: **(a)** Weiss temperature calculated at low temperatures and **(b)** effective magnetic moment of the $Na_xFe_{1-y}Mn_yO_2$ series as a function of Fe substitution by Mn. Dashed line shows calculated spin only moment, considering HS Fe^{3+}, HS Mn^{4+} and Landé factor of $g = 2$.

The experimentally calculated effective magnetic moment of the $Na_xFe_{1-y}Mn_yO_2$ system ($y = 0, 0.1, 0.33$) is shown in Fig. 3.23b with squares. The values are compared with the theoretically expected spin only moment (dashed line) calculated as:

$$\mu_{SO} = \sqrt{\sum x_i g_i^2 S_i(S_i+1)} \tag{3.3}$$

where g_i is the Landé g factor, S is the total spin quantum number and x_i is the relative amount of the contributing atom.

In all the measurements the experimental value is above the theoretically expected spin only moment. It is not uncommon to obtain higher values, and is generally ascribed to a spin-orbital coupling. It is however worth noting that both transition elements present in these structures, Fe^{3+} and Mn^{4+} are spin-only elements. That is, the d orbitals are filled with a single electron, and thus the orbital angular momentum should be zero, having therefore no spin-orbital coupling. The higher measured magnetic moment for $NaFeO_2$ compared to the expected one had also been associated by McQueen et al. to a short-range magnetic ordering fluctuation arisen from competing exchange interactions which frustrate the spins, suggested by a susceptibility that does not perfectly follow the Curie-Weiss law [4]. Nonetheless, in the present work the Curie-Weiss law was well respected where the effective moment values have been determined. Further investigation would be required to find an answer to this difference between experimental and theoretically expected values.

In addition, there are no excited states of the same spin multiplicity as the ground state (S=5/2), so second order spin orbit coupling contributions should also be zero. I am therefore not quite sure why the magnetic moment is higher than expected, but I would not think that this is due to spin-orbit coupling effects.

It is also worth mentioning that the Landé factor has not been measured for these samples, and the standard $g_s = -g_e \approx 2$ value has been used instead. However, it has been shown in previous publications that this factor depends on the sample and on the temperature [28].

The Mössbauer spectra parameters of all the samples are compared in Fig. 3.24. The central shift reflects the oxidation state of iron. In all these samples, with a central shift of CS $= 0.36$ mm s^{-1}, only Fe^{3+} is present. Quadrupole splitting, on the other hand, increases with increased Mn content. QS reflects the changes in the anisotropy of the electronic charge distribution. Increased quadrupole splitting can be related to changes TM-O distances and deformation of TMO_6 octahedron, as reflected by the changes in cell parameters. This deformations or distortions can be related to the increasing sodium vacancies or to the increasing iron and manganese mixing on the TMO_2 layers.

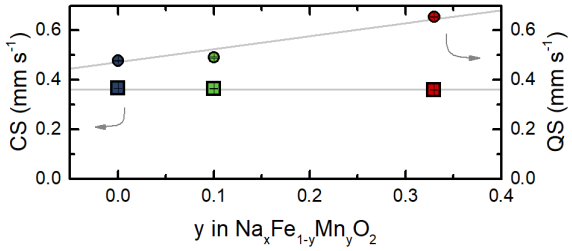

Figure 3.24: Mössbauer spectra parameters of the $Na_xFe_{1-y}Mn_yO_2$ series as a function of Fe substitution by Mn. Squares for central shift (CS) and circles for quadrupole splitting (QS).

3.6 Conclusions

A series of $Na_xFe_{1-y}Mn_yO_2$ materials has been synthesized, for $y = 0, 0.10, 0.33$ with an O3 structure. These layered oxides are based on the inexpensive and abundant iron and manganese transition metals. The used precursors, transition metal oxides and carbonates, are low cost and non-toxic. Moreover, the synthesis method is easily scalable.

All the obtained phases are crystalline and with a high purity. Only the high resolution XRD measurements done at ALBA synchrotron have allowed the detection of a minimum presence of a secondary phase (β-$NaFeO_2$) in the case of $y = 0$. In order to try to avoid the problems that a partially desodiated sample presents when the material is tested in a commercial cell, the sample with 10% on manganese has been attempted fully sodiated. The Na quantification by ICP-OES technique shows that the sample is highly sodiated, with less than 5% of sodium deficient. The O3-$Na_{2/3}Fe_{2/3}Mn_{1/3}O_2$ sample also shows higher sodium content than the $x = 2/3$ reported

in previous works. Mössbauer measurements have confirmed that the iron oxidation state and environment agree with the aimed structures.

The characterization of all the samples is in good agreement with the already reported values. Some minor differences with the reported results are expected, as the synthesis conditions differ slightly. For example, $NaFeO_2$ sample shows a smaller particle size than that reported in literature. Also, the $NaFe_{0.9}Mn_{0.1}O_2$ sample has been synthesized with a higher sodium content that those reported in literature, in order to minimize the sodium deficiency problem of the layered oxides, and thus differences in cell parameters are expected.

All the samples show an antiferromagnetic behavior, with a Neél temperature of $T_N \approx 10$ K. Although the transition metal presence changes for the different samples, all of them have equivalent TMO_2 transition metal oxides layers in the structure, where TM is a mixture of iron and manganese. Hence, the similar antiferromagnetic nature.

Bibliography

[1] S. Kikkawa, S. Miyazaki, and M. Koizumi. *Material Research Bulletin*, 20:373–377, 1985.

[2] Y. Takeda, K. Nakahara, M. Nishijima, N. Imanishi, and O. Yamamoto. *Materials Research Bulletin*, 29(6):659–666, 1994.

[3] M. C. Blesa, E. Moran, C. Leon, J. Santamaria, J. D. Tornero, and N. Menendez. *Solid State Ionics*, 126:81–87, 1999.

[4] T. McQueen, Q. Huang, J. W. Lynn, R. F. Berger, T. Klimczuk, B. G. Ueland, P. Schiffer, and R. J. Cava. *Physical Review B*, 76(2):024420, 2007.

[5] N. Yabuuchi, H. Yoshida, and S. Komaba. *Electrochemistry*, 80(10):716–719, 2012.

[6] E. Lee, D. E. Brown, E. E. Alp, Y. Ren, J. Lu, J.-J. Woo, and C. S. Johnson. *Chemistry of Materials*, 27:6755–6764, 2015.

[7] R. Kataoka, K. Kuratani, M. Kitta, N. Takeichi, T. Kiyobayashi, and M. Tabuchi. *Electrochimica Acta*, 182:871–877, 2015.

[8] J. Hwang and J. Kim. *Materials Letters*, 206:100–104, 2017.

[9] Y. Takeda, J. Akagi, A. Edagawa, M. Inagaki, and S. Naka. *Materials Research Bulletin*, 15(8):1167–1172, 1980.

[10] N. Terada, D. D. Khalyavin, J. M. Perez-Mato, P. Manuel, D. Prabhakaran, A. Daoud-Aladine, P. G. Radaelli, H. S. Suzuki, and H. Kitazawa. *Physical Review B*, 89(18), 2014.

[11] Y. Tian, T. Shi, W. D. Richards, J. Li, J. C. Kim, S.-H. Bo, and G. Ceder. *Energy & Environmental Science*, 10(5):1150–1166, 2017.

[12] J. Rodriguez-Carvajal. *Physica B*, 192:55, 1993.

[13] C. Prescher, C. McCammon, and L. Dubrovinsky. *Journal of Applied Crystallography*, 45(2):329–331, 2012.

[14] E. Murad and J. Cashion. *Mössbauer Spectroscopy of Environmental Materials and Their Industrial Utilization*. Springer US, Boston, MA, 2004.

[15] J. Zhao, L. Zhao, N. Dimov, S. Okada, and T. Nishida. *Journal of The Electrochemical Society*, 160(5):A3077–A3081, 2013.

[16] M. Casas-Cabanas, M. Reynaud, J. Rikarte, P. Horbach, and J. Rodríguez-Carvajal. *Journal of Applied Crystallography*, 49(6):2259–2269, 2016.

[17] R. Shunmugasundaram, R. S. Arumugam, and J. R. Dahn. *Journal of The Electrochemical Society*, 163(7):A1394–A1400, 2016.

[18] S. Bette, T. Takayama, V. Duppel, A. Poulain, H. Takagi, and R. E. Dinnebier. *Dalton Transactions*, 48(25):9250–9259, 2019.

[19] B. Mortemard de Boisse, M. Reynaud, J. Ma, J. Kikkawa, S.-i. Nishimura, M. Casas-Cabanas, C. Delmas, M. Okubo, and A. Yamada. *Nature Communications*, 10(1):2185, 2019.

[20] K. Minnici, Y. H. Kwon, M. M. Huie, M. V. de Simon, B. Zhang, D. C. Bock, J. Wang, J. Wang, K. J. Takeuchi, E. S. Takeuchi, A. C. Marschilok, and E. Reichmanis. *Electrochimica Acta*, 260:235–245, 2018.

[21] Neutron Activation and Scattering Calculator. `https://www.ncnr.nist.gov/resources/activation/`, (Accessed: 2019-07-08).

[22] M. Sofin and M. Jansen. *Zeitschrift fur Naturforschung section B-A Journal of Chemical Sciences*, 60(6):701–704, 2005.

[23] J. S. Thorne, R. A. Dunlap, and M. N. Obrovac. *Journal of the Electrochemical Society*, 160(2):A361–A367, 2013.

[24] Shannon Radii. `http://abulafia.mt.ic.ac.uk/shannon/ptable.php`, (Accessed: 2020-02-12).

[25] E. Gonzalo, M. H. Han, J. M. López del Amo, B. Acebedo, M. Casas-Cabanas, and T. Rojo. *Journal of Materials Chemistry A*, 2:18523–18530, 2014.

[26] B. Mortemard de Boisse, J.-H. Cheng, D. Carlier, M. Guignard, C.-J. Pan, S. Bordère, D. Filimonov, C. Drathen, E. Suard, B.-J. Hwang, A. Wattiaux, and C. Delmas. *Journal of Materials Chemistry A*, 3(20):10976–10989, 2015.

[27] C. Stock, L. C. Chapon, O. Adamopoulos, A. Lappas, M. Giot, J. W. Taylor, M. A. Green, C. M. Brown, and P. G. Radaelli. *Physical Review Letters*, 103(7):077202, 2009.

[28] R. Stoyanova, D. Carlier, M. Sendova-Vassileva, M. Yoncheva, E. Zhecheva, D. Nihtianova, and C. Delmas. *Journal of Solid State Chemistry*, 183(6):1372–1379, 2010.

[29] M. Chandra, R. Shukla, M. Rashid, A. Gupta, S. Basu, and R. Dhaka. *Materials Research Bulletin*, 105:178–183, 2018.

[30] C. Delmas, C. Fouassier, and P. Hagenmuller. *Physica B+C*, 99(1):81–85, 1980.

[31] B. Mortemard de Boisse, D. Carlier, M. Guignard, L. Bourgeois, and C. Delmas. *Inorganic Chemistry*, 53(20):11197–11205, 2014.

[32] F. Klein, B. Jache, A. Bhide, and P. Adelhelm. *Physical Chemistry Chemical Physics*, 15(38):15876, 2013.

[33] M. Fiore, G. Longoni, S. Santangelo, F. Pantò, S. Stelitano, P. Frontera, P. Antonucci, and R. Ruffo. *Electrochimica Acta*, 269:367–377, 2018.

[34] D. Li, J. Zhou, X. Chen, and H. Song. *ACS Applied Materials & Interfaces*, 8(45):30899–30907, 2016.

[35] G. D. Park, J. S. Cho, J.-K. Lee, and Y. C. Kang. *Scientific Reports*, 6(1):22432, 2016.

[36] B. Tian, J. Świątowska, V. Maurice, S. Zanna, A. Seyeux, L. H. Klein, and P. Marcus. *The Journal of Physical Chemistry C*, 117(42):21651–21661, 2013.

[37] J. Drbohlavova, R. Hrdy, V. Adam, R. Kizek, O. Schneeweiss, and J. Hubalek. *Sensors*, 9(4):2352–2362, 2009.

[38] A. R. Denton and N. W. Ashcroft. *Physical Review A*, 43(6):3161–3164, 1991.

[39] C. Kittel. *Introducción a la física del estado sólido*. Reverté, 3 edition, 1997.

[40] U. Müller. *Inorganic Structural Chemistry*. Inorganic Chemistry: A Textbook Series. Wiley, 2007.

4 | Electrochemical characterization of Na_xTMO_2 layered oxides

Contents

4.1 Introduction

This chapter will present the electrochemical characterization of the synthesized materials, where the electrochemical reversibility will be tested. This will be carried out by galvanostatic cycling within various voltage windows and rates

4.2 Electrochemical characterization of $NaFeO_2$

$NaFeO_2$ has been cycled at a rate of C/10 (that is, at a rate in which the nominal capacity would be obtained in 10 hours) in a conservative voltage window of $V = 2.5 - 3.5$ V, in two electrode half cells with Na metal counter electrodes. The results are presented in Fig. 4.1:, as voltage profile vs. capacity (Fig. 4.1a), discharge capacity and Coulombic efficiency vs. cycle number (Fig. 4.1b), and $\mathrm{d}Q/\mathrm{d}V$ derivative curve for selected cycles (Fig. 4.1c). A single voltage plateau is observed at $V = 3.3$ V upon charge (3.25 V upon discharge) in the voltage-capacity curves of Fig. 4.1a, corresponding to $Fe^{3+/4+}$ reversible redox reaction [1, 2]. The reaction voltage has been defined according to the position of the most intense peak in the derivative curve (Fig. 4.1c). The initial Coulombic efficiency is of about 90%, as seen in Fig. 4.1b (solid line). In most materials, during the first cycles, Coulombic efficiency losses are observed, often due to the formation of passivating and interface layers between at the material-electrolyte interface [3–5]. This value of 90% can be considered high compared to most cathode materials. After the first 5 cycles the Coulombic efficiency approaches 99%, which means that the redox reaction of Fe can be considered almost fully reversible. The slight Coulombic losses induce a loss of capacity that is not optimal, as after 50 cycles only 77% of the discharge capacity is retained (see scatter points in Fig. 4.1b), approximately 0.45% of the initial capacity is lost in average in each cycle. This corresponds to an efficiency of 99.55%, meaning that part of the CE loss is due to capacity loss, and part might be related to a side reaction. This is nevertheless a better figure that what has been previously reported for this material: 67% of initial capacity retention after 8 cycles [6] or 50% after 30 cycles [7] with the same upper voltage limit. The improved capacity retention of our material might be due to the smaller particle size obtained during the synthesis as shown in Chapter 3 (see Table 3.4) [8–12]. Indeed, as the particle size is reduced, the diffusion path of Na ions, as well as the electrons, is reduced, which generally results in a better electrochemical behavior [13].

In Fig. 4.1c the derivative $\mathrm{d}Q/\mathrm{d}V$ curves are shown for the 1^{st}, 5^{th}, 10^{th} and 50^{th} cycles. A sharp peak can be seen during the first charge, that is smoothed upon cycling. The derivative curve shows that the plateau consists of two different reactions, the first occurring at 3.32 V and the second at 3.36 V during charge (3.25 V and 3.31 V respectively on discharge), which have been previously associated with the reversible $Fe^{3+/4+}$ redox reaction [1, 2]. The voltage hysteresis increases upon cycling, as seen by the shift of the reaction peaks to higher potentials on charge and to lower potentials on discharge. That is, more energy is needed to charge the cell while less energy is provided on discharge. The increment of the hysteresis is however very small: considering the position of the sharpest peak of the derivative curve, the hysteresis increases from 71.3 mV in the

5^{th} cycle to 94.1 mV in the 50^{th}. Due to the very flat electrochemical profile upon charge, this could be enough to account for the loss of capacity upon cycling. The shape of the derivative curve is maintained, meaning that the mechanism is also maintained in this potential window at least for 50 cycles. There is however a broadening of the peaks upon cycling. The plateaus in the potential curve, and thus, the sharp peaks in $\mathrm{d}Q/\mathrm{d}V$ curves, are typical of biphasic transformations [14]. The broadening of the peaks might reflect a loss of crystallinity upon cycling, which can be due to the formation of defects upon the sodium extraction and insertion on the cycling process. Indeed, a disordered structure will present a variety of environments for the sodium, each having its own extraction and insertion potential [15].

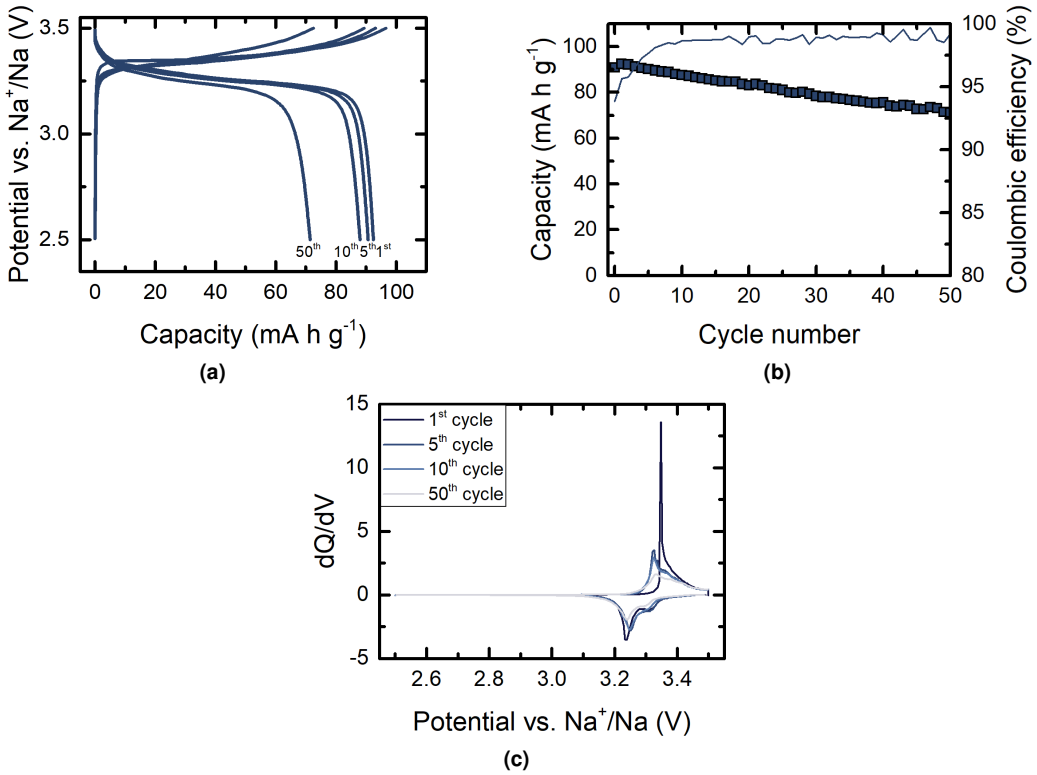

Figure 4.1: Galvanostatic cycling at C/10 of $NaFeO_2$ in a conservative voltage window between 2.5 and 3.5 V. **(a)** Voltage curves vs. capacity of 1^{st}, 5^{th}, 10^{th} and 50^{th} cycles, **(b)** discharge capacity (scatter) and Coulombic efficiency (solid line) vs. cycle number and **(c)** $\mathrm{d}Q/\mathrm{d}V$ derivative curves for selected cycles. Measurements done in a 2 electrode swagelok.

The rate capability test results are presented in Fig. 4.2. As seen in the voltage-capacity curves of Fig. 4.2a, the discharge capacity reduces from 95 mA h g^{-1} at C/10 to 45 mA h g^{-1} at 2C, corresponding to a loss of about 52% of the initial capacity. This can be ascribed to a voltage hysteresis increase from 0.09 V at C/10 to 0.33 V at 2C, which is a typical consequence of the kinetics of the

charge-discharge process. These results are quite good compared to the literature. As an example, Ni and Ti containing O3 layered oxides, presented as stable at high rates, have been reported to show at 2C 60% and 75% of the capacity available at C/10 [16, 17]. Moreover, after testing the $NaFeO_2$ material at high current, when cycling back at C/10, almost all the initial capacity (92%) is recovered, very close to the 94% shown in the best performing material of reference [17]. This is an especially good result considering that the studied material is based solely on iron, which is known to promote a fast capacity fading [7, 9].

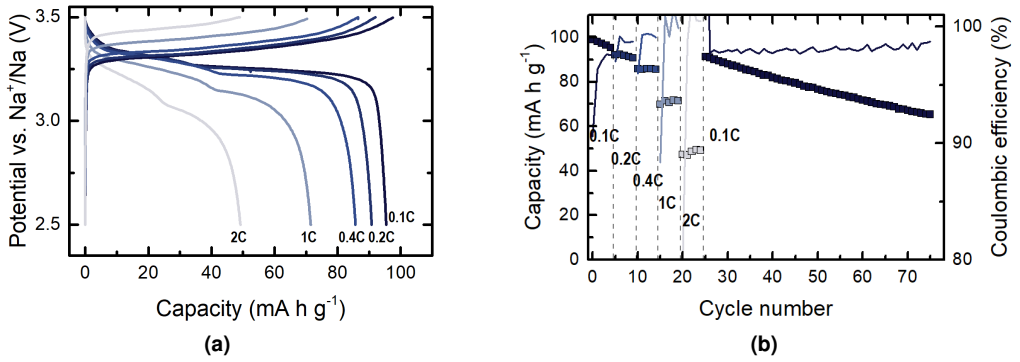

Figure 4.2: Rate capability test of $NaFeO_2$ at several rates, indicated in the graph. **(a)** Voltage curves vs. capacity of 5th cycle of each rate and **(b)** discharge capacity (scatter) and Coulombic efficiency (solid line) vs. cycle number. Measurements done in a two electrode swagelok.

The influence of the charge potential on the initial charge-discharge voltage-composition profile of $NaFeO_2$ at C/10 is presented in Fig. 4.3. It has been tested in different cells at C/10 with several upper voltage limits: 3.5 V, 4.0 V and 4.5 V. Fig. 4.3a presents the first cycle for each potential window and Fig. 4.3b shows the corresponding $\mathrm{d}Q/\mathrm{d}V$ derivative curves.

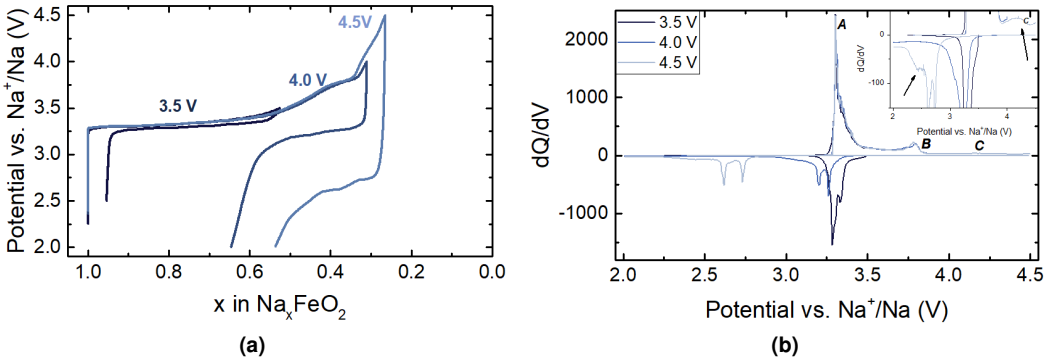

Figure 4.3: $NaFeO_2$ cycling at C/10 rate with several upper voltage window limits: 3.5 V, 4.0 V and 4.5 V. **(a)** Voltage vs. composition curves and **(b)** $\mathrm{d}Q/\mathrm{d}V$ derivative (zoom in the inset). Measurements done in two electrode swageloks.

When the upper voltage limit is increased the first charge capacity naturally increases from 104 mA h g^{-1} at 3.5 V up to 167 mA h g^{-1} at 4.0 V and 178 mA h g^{-1} when cycled to 4.5 V. There is, however, a reduction of the reversible Na re-intercalation, inducing a strong drop of the Coulombic efficiency from 90% at 3.5 V to 57% and 49% respectively, when the voltage limit is increased to 4.0 V and 4.5 V. Moreover, the voltage hysteresis is also affected: when the cell is charged to 3.5 V the hysteresis is lower than 0.02 V, meaning that the voltage profile is close to the thermodynamic equilibrium value. On the other hand, when charged to 4.0 V and 4.5 V, the voltage hysteresis increases to 0.15 V and 0.7 V respectively. As seen in Fig. 4.1c, the $\mathrm{d}Q/\mathrm{d}V$ derivative curves presented in Fig. 4.3b, show no significant change upon charge for the 3.3 V reaction plateau (reaction *A*): the curves during charge show the $Fe^{3+/4+}$ reaction at $V = 3.3$ V, as seen in Fig. 4.1c. When charged beyond 3.5 V a second reaction can be seen at 3.8 V (reaction *B*), indicated by a second peak in the derivative curve when charged to 4.0 V and 4.5 V. As can be seen in the inset of Fig. 4.3b, a third peak in the charge derivative curve can be seen at 4.2 V, indicating the presence of a third charge process (reaction *C*). While the charge profiles are very similar with a good overlap, the discharge profiles change strongly depending on the potential reached during charge, with a strong reduction of the capacity and reaction potential.

This behavior is similar to previous reports, although it is slightly less pronounced here. These changes were ascribed to irreversible structural changes occurring when charged beyond 3.5 V [2, 7, 9]. Indeed, when layered oxides are charged beyond a certain voltage , approaching total desodiation, the structure usually undergoes an irreversible structural evolution which degrades the electrochemical response [18–21].

Cycling stability has nevertheless been tested in the potential window $1.0 - 4.5$ V, and the results are presented in Fig. 4.4. As could be predicted, the discharge capacity drops fast during the first cycles. Surprisingly, the capacity stabilizes close to 30 mA h g^{-1} after about 10 cycles, and remain stable upon further cycling, with a Coulombic efficiency over 95% afterwards. Although the electrochemical response is indeed degraded when the material is charged to 4.5 V, contrary to the common belief the material remains electrochemically active with a good reversibility up to at least 30 cycles. This is, to our knowledge, the first time that reversible electrochemical activity is reported for $NaFeO_2$ when charged to such high potentials. Indeed, Li et al. claimed that $NaFeO_2$ is electrochemically inactive when more than 30% of the sodium content has been extracted from the structure [22]. Yabuuchi et al. also reported no reversible capacity when cycled to 4.5 V [7]. The difference between the reported measurements and the one presented in this work, besides the smaller particle size, can be related to the lower discharged potential limit. Indeed, the increased polarization lowers the discharge plateau below 2.5 V, potential at which Yabuuchi et al. stopped their measurements, while in this case, as shown in Fig. 4.4, the lower potential limit has been decreased to 1.0 V.

On the light of these results, the reversible upper potential limit to ensure reversible electrochemical response of the initial structure will be considered to be 3.5 V for $NaFeO_2$, as previously reported in the literature [2, 7].

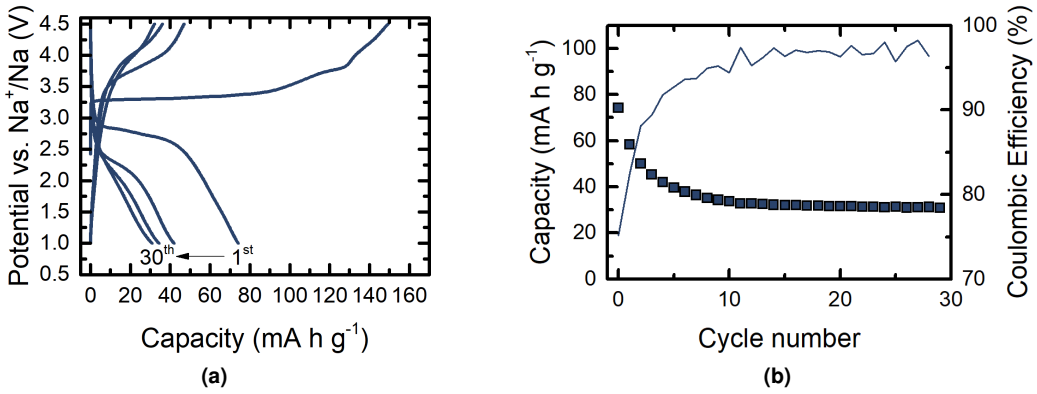

Figure 4.4: $NaFeO_2$ galvanostatic cycling at C/10 in the potential window 4.5-1.0 V. **(a)** Voltage curves vs. capacity of 1st, 5th, 10th and 30th cycle of each rate and **(b)** discharge capacity (scatter) and Coulombic efficiency (solid line) vs. cycle number. Measurements done in a three electrode swagelok.

4.3 Electrochemical characterization of $NaFe_{0.9}Mn_{0.1}O_2$

The the galvanostatic cycling of $NaFe_{0.9}Mn_{0.1}O_2$ sample is presented in Fig. 4.5. The upper voltage limit has been maintained at 3.5 V, but the lower limit has been decreased to 1.5 V to include the $Mn^{3+/4+}$ redox reaction, which is expected to be observed around 2.3 V according to previous reports [23]. The voltage-composition curve, shown in Fig. 4.5a, is very similar to that of $NaFeO_2$, with a plateau at 3.30 V on charge (3.25 V on discharge) due to the reversible $Fe^{3+/4+}$ redox reaction, and a fast decrease of voltage afterwards. During the first charge, highlighted with a dashed line in Fig. 4.5a, there are no signatures of any reacting manganese, which is further confirmed by the derivative curve of Fig. 4.5c: the voltage steadily increases up to $\approx$ 3.3 V where the iron redox reaction is expected and no peak is observed in the derivative curve near 2.3 V. The open circuit voltage (OCV) lies around 2.6 V, similar to what was observed for $NaFeO_2$, above the $Mn^{3+/4+}$ redox potential, suggesting that all the manganese is in Mn^{4+} in the pristine material. On discharge and on the subsequent charges, the manganese redox related step can be seen at $V \approx 2.5$ V on both, the voltage-composition profiles of Fig. 4.5a and in the derivative curves of Fig. 4.5c. This manganese redox related capacity is about a 3% of the total capacity delivered by the cell. The accident observed in the first discharge of Fig. 4.5a, highlighted with an arrow is ascribed to the formation of a passivation surface on the metallic sodium counter electrode [24]. The accident corresponds to minimum in the derivative curve of the 1st discharge peak (shadowed in gray and labelled as Na in Fig. 4.5c).

As it can be seen in Fig. 4.5a, both the initial discharge capacity (131 mA h g^{-1}) and the initial Coulombic efficiency (99%) are significantly larger that that of $NaFeO_2$, the former being a result of the manganese redox contribution. The later can be probably ascribed to the additional contribution of Mn during the discharge, not present during the charge. The second cycle, with a capacity of 129 mA h g^{-1}, has a lower Coulombic efficiency, of 95%, which is closer to the value

obtained for $NaFeO_2$, probably because Mn contributes both to charge and discharge in this case. The Coulombic efficiency increases above 98% during the first 5 cycles, similarly to what has been seen for $NaFeO_2$. The capacity suffers from a fading of $\approx 0.72\%$ each cycle, and after 50 cycles 64% of the initial capacity is retained, both figures being poorer than those observed for $NaFeO_2$.

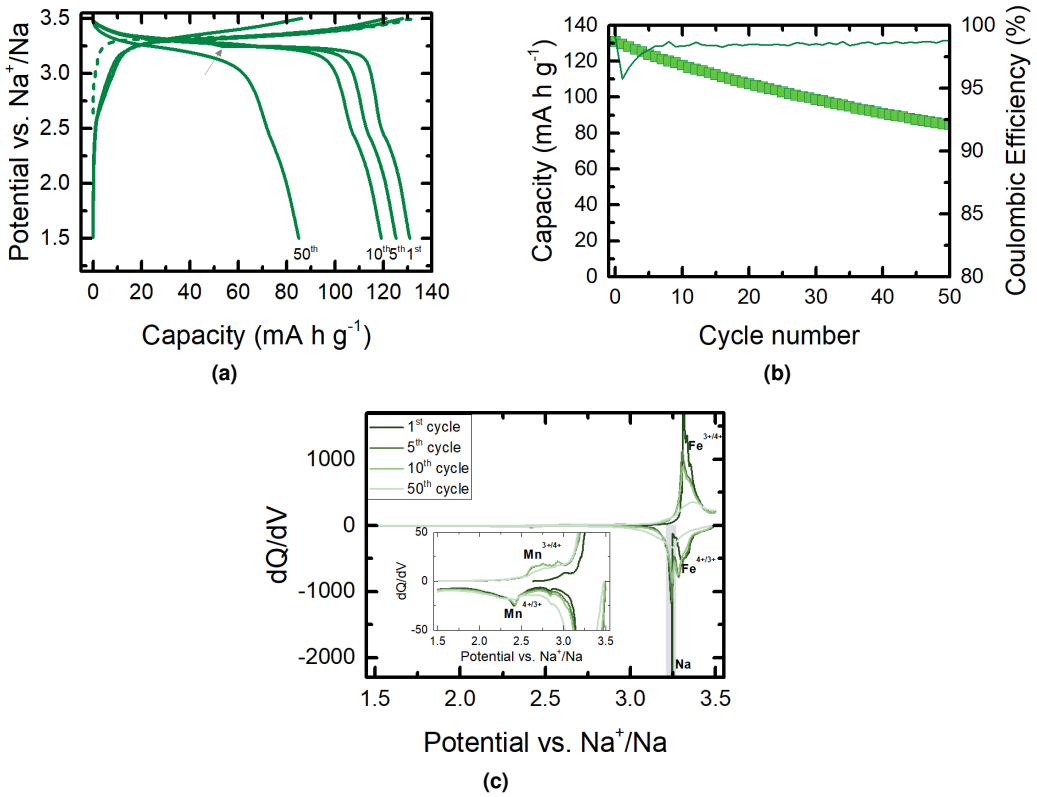

Figure 4.5: Galvanostatic cycling at C/10 of $NaFe_{0.9}Mn_{0.1}O_2$ in a conservative voltage window between 1.5 and 3.5 V. **(a)** Voltage curves vs. capacity of 1st, 5th, 10th and 50th cycles (first charge highlighted with a dashed line), **(b)** discharge capacity (scatter) and Coulombic efficiency (solid line) vs. cycle number, and **(c)** $\mathrm{d}Q/\mathrm{d}V$ derivative curves (zoom in the inset). Measurements done in 2 electrode swagelok.

The mechanism is not much affected upon cycling, as reflected by the derivative curves. As can be seen from Fig. 4.5a, both capacity and potential hysteresis are relatively steady during the initial ten cycles. There is however a notable change from the 10th to the 50th cycle, with an increase of hysteresis and decrease of capacity. This degradation of the electrochemical response suggests changes of the material. As can be seen from Fig. 4.5c, from cycle 10 to 50 the peaks get broader which suggest a loss of crystallinity according to similar processes observed previously in the literature [25, 26].

4.4 Electrochemical characterization of O3-$Na_{2/3}Fe_{2/3}Mn_{1/3}O_2$

The galvanostatic cycling results of O3-$Na_{2/3}Fe_{2/3}Mn_{1/3}O_2$, cycled with the same conditions as $NaFe_{0.9}Mn_{0.1}O_2$ (C/10 rate in the voltage range of $1.5 - 3.5$ V) are presented in Fig. 4.6. In these curves one can observe a low capacity during the first charge highlighted with a dashed line in Fig. 4.6a (8 mA h g^{-1}, about 3% of the theoretical capacity). Indeed, the $Fe^{3+/4+}$ oxidation reaction lies now outside the cycled potential range, above 3.5 V, and hence, the observed capacity corresponds to the manganese redox activity. However, the presence of Mn^{3+} is minor, as the composition is aimed to be fully Mn^{4+}, which cannot be further oxidized within this potential window. On discharge and following cycles on the other hand, as the potential allows the redox reaction of manganese, a reversible capacity of 86 mA h g^{-1} with a Coulombic Efficiency of 99% is observed (see Fig. 4.6b). The reaction plateau, lying at 2.35 V on charge (2.25 V on discharge), corresponds to the $Mn^{3+/4+}$ redox reaction. It can be seen that the reversibility of the material is good, as the capacity-voltage curves are not changing (Fig. 4.6a), and show a capacity retention of 85% after 50 cycles (Fig. 4.6b). It is worth noting that the obtained capacity values correspond to approximately one third of the theoretical capacity (260.58 mA h g^{-1}), reflecting the reversible redox reaction of all the manganese ions in the sample.

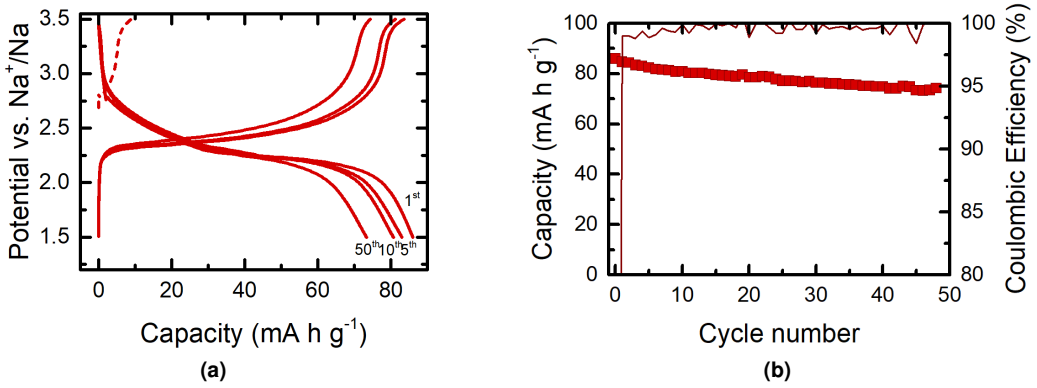

Figure 4.6: Galvanostatic cycling at C/10 of O3-$Na_{2/3}Fe_{2/3}Mn_{1/3}O_2$ in a conservative voltage window between 1.5 and 3.5 V. **(a)** Voltage curves vs. capacity of 1st, 5th, 10th and 50th cycles (first charge has been highlighted with a dashed line), **(b)** discharge capacity (scatter) and Coulombic efficiency (solid line) vs. cycle number, and **(c)** dQ/dV derivative curves. Measurements done in a 2 electrode swagelok.

However, one of the advantages of the iron and manganese containing material is the possibility to use the redox of both transition metals. Indeed, the iron redox reaction onset is visible in Fig. 4.6a as a tail at 3.5 V voltage curve. The redox reaction of iron is increased in this material compared to the previously presented $NaFeO_2$ and $NaFe_{0.9}Mn_{0.1}O_2$, leaving it outside this voltage window. To allow the iron redox reaction, $Na_{2/3}Fe_{2/3}Mn_{1/3}O_2$ has been cycled within an

increased voltage range of $1.5 - 4.2$ V (see Fig. 4.7). This voltage window has been chosen based on previous reports for this material [23, 27, 28]. In this case, the voltage curves, shown in Fig. 4.7a, are clearly different to the samples with lower manganese content presented earlier. They exhibit an S shape with two potential plateaus, the one corresponding to $Fe^{3+/4+}$ redox around 3.5 V on charge (3.2 V on discharge) and the one corresponding to $Mn^{3+/4+}$ around 2.5 V on charge (2.2 V on discharge). These plateaus are better defined on charge, and it can be seen how the iron redox related plateau is larger than the manganese one, as expected from their relative presence proportion. During the 1st charge (highlighted with a dashed line in Fig. 4.7a) the capacity comes mainly from the $Fe^{3+/4+}$ oxidation reaction, with only a slight contribution from the $Mn^{3+/4+}$ oxidation reaction. Indeed, manganese oxidation related capacity is only about 4% of the total initial charge capacity, as observed when cycled in the limited voltage window (Fig. 4.6a).

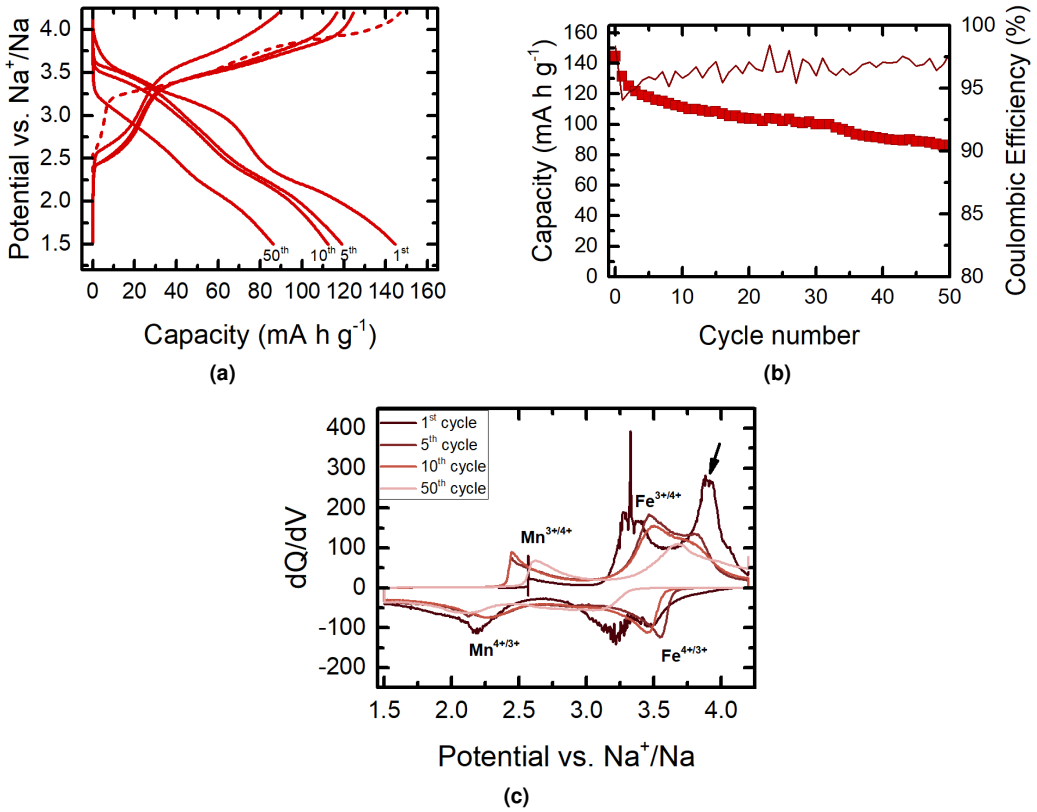

Figure 4.7: Galvanostatic cycling at C/10 of O3-$Na_{2/3}Fe_{2/3}Mn_{1/3}O_2$ in a voltage window between 1.5 and 4.2 V. **(a)** Voltage curves vs. capacity of 1st, 5th, 10th and 50th cycles (first charge has been highlighted with a dashed line), **(b)** discharge capacity (scatter) and Coulombic efficiency (solid line) vs. cycle number, and **(c)** dQ/dV derivative curves. Measurements done in a 2 electrode swagelok.

The first discharge of O3-$Na_{2/3}Fe_{2/3}Mn_{1/3}O_2$ has a capacity of 145 mA h g^{-1}. This corresponds to a Coulombic efficiency of 98% at the first cycle, despite the additional discharge capacity due

to the contribution of the Mn. This is due to the poor Coulombic efficiency of the Fe reaction: from 145 mA h g^{-1} during the first charge, it decreases down to around 80 mA h g^{-1} during the first discharge and continues decreasing upon further cycling. As a consequence, as can be seen in Fig. 4.7b, the total capacity decays fast, especially during the first cycles. After the initial 5 cycles, the capacity continues to decay but at a slower rate, with about a 0.7% of capacity loss per cycle. The Coulombic efficiency also oscillates around 96% upon cycling, which is lower than those observed for $NaFeO_2$ and $NaFe_{0.9}Mn_{0.1}O_2$ cycled in the voltage windows of $2.5-3.5$ V and $1.5-3.5$ V, respectively. The capacity retention of O3-$Na_{2/3}Fe_{2/3}Mn_{1/3}O_2$ is comparable to that reported in the literature: Gonzalo et al. reported a 76% of retention while in this work a 75% has been obtained after 15 cycles at C/10 rate and cycled in the same voltage range of 4.2-1.5 V [23]. After 50 cycles the 60% of the initial capacity still retained.

More insight on the evolution of the electrochemical processes can be reached from the $\mathrm{d}Q/\mathrm{d}V$ derivative curves, shown in Fig. 4.7c. The $Mn^{3+/4+}$ redox reaction in revealed by a broad peak at 2.5 V upon charge (2.2 V on discharge). The first $Fe^{3+/4+}$ reaction peak can be seen at $V \approx 3.3$ V during the 1st charge and $V \approx 3.2$ V during the 1st discharge, similar to the previous samples. It would correspond to reaction *A* identified for the $NaFeO_2$ sample. Another reaction can be seen at 3.8 V upon charge, which has been highlighted with an arrow, and that corresponds to reaction *B* identified for $NaFeO_2$. During the 1st discharge, these peaks can also be differentiated at 3.2 V and 3.5 V, but the shape of the curve in this voltage range changes on subsequent cycles. Indeed, the Fe reaction peak broaden, merge and become weaker. It can be seen how the overpolarization increases with cycling, as the peaks are shifted towards higher potentials during charge and towards lower potentials during discharge. This overpolarization increment is also visible in the manganese redox reaction potential. These observations suggest that, as for $NaFeO_2$ when cycled to 3.8 V and 4.2 V, some irreversible structural change occur when O3-$Na_{2/3}Fe_{2/3}Mn_{1/3}O_2$ is cycled in the usual voltage window of 1.5-4.2 V. This is most probably related to the triggering of reaction *B*. This demonstrate that, although its capacity is increased due to the Mn contribution, O3-$Na_{2/3}Fe_{2/3}Mn_{1/3}O_2$ suffers from the same degradation mechanism that $NaFeO_2$.

When the two tested voltage windows are compared, for example in terms of normalized capacity retention (see Fig. 4.8), it is clear that when cycled with a limited upper voltage (i.e. when cycled up to 3.5 V as opposed to 4.2 V), the electrochemical stability is improved. However, and as shown in the inset, the cell cycled up to 4.2 V still presents a higher reversible discharge capacity after 50 cycles.

A rate capability has been done in the voltage window $V = 1.5 - 4.2$ V and the results are presented in Fig. 4.9. The initial capacity values at C/10 reproduce the results of the galvanostatic cycling of Fig. 4.7, as expected. As seen in Fig. 4.9a, when increasing the rate, the Fe and Mn related plateaus are hardly distinguished, and at 1C, especially during discharge, a continuous slope can be seen. The $Fe^{3+/4+}$ oxidation reaction plateau during charge, initially at 3.5 V, is however visible at all rates, and the polarization increment is clear, as e.g. at 2C rate, this plateau is observed above 4.0 V, very close to the upper limit of the voltage window. This might be the reason for

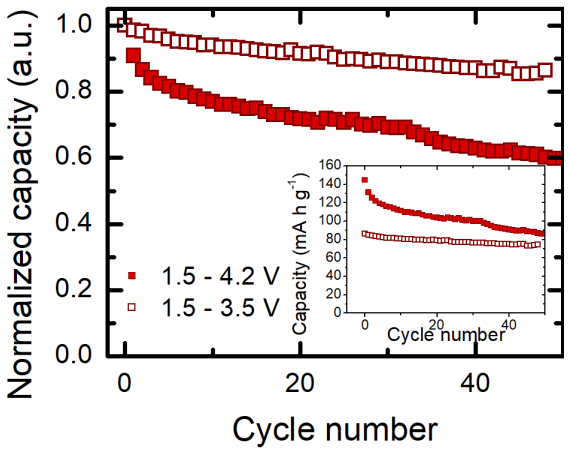

Figure 4.8: Normalized capacity of O3-$Na_{2/3}Fe_{2/3}Mn_{1/3}O_2$ cycled within different voltage windows: in the conservative window of 1.5-3.5 V (open squares) and in the commonly used extended voltage window 1.5-4.2 V (solid squares). In the inset the gravimetric capacity is shown.

the low capacity values obtained at this rate, which is about 20% of the initial capacity at C/10. On the other hand, there is no sign of any irreversible structural degradation, as the initial C/10 capacity is recovered when cycling back at slow rates, which means that the irreversible changes that progressively degrade the capacity at C/10 are not enhanced when the rate increases. As seen in Fig. 4.9b, the capacity retention from cycle 25 to 75 ar C/10 is very similar to that observed during the galvanostatic cycling, confirming that the higher rate had a negligible impact on the capacity loss.

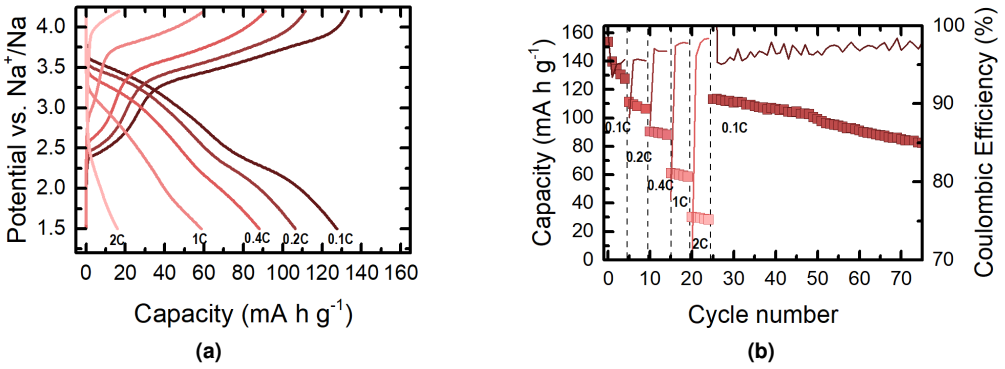

Figure 4.9: Rate capability test of O3-$Na_{2/3}Fe_{2/3}Mn_{1/3}O_2$ at several rates, indicated in the graph. **(a)** Voltage curves vs. capacity of 5th cycle of each rate and **(b)** discharge capacity (scatter) and Coulombic efficiency (solid line) vs. cycle number. Measurements done in a two electrode swagelok.

4.5 Comparison of the electrochemical performance of $Na_xFe_{1-y}Mn_yO_2$ samples

The capacity retention at C/10 of the different samples studied in the previous sections are gathered in Fig. 4.10, and the main indicators are presented in Table 4.1. For comparison purposes, the voltage windows that are presented are those commonly used in the literature that include the redox reaction of iron and manganese ions. That is, $NaFeO_2$ has been cycled in the voltage range of 2.5-3.5 V, $NaFe_{0.9}Mn_{0.1}O_2$ in 1.5-3.5 V and $Na_{2/3}Fe_{2/3}Mn_{1/3}O_2$ in 1.5-4.2 V, regardless of the better stability observed for this last sample when cycled in a limited voltage window. The initial reversible capacity is improved when the manganese content is increased, due to the combination of the contribution of Mn and the increase of the charge voltage compared to $NaFeO_2$, but the capacity retention is worsened. However, it should be noted that after 50 cycles, the $NaFe_{0.9}Mn_{0.1}O_2$ and $Na_{2/3}Fe_{2/3}Mn_{1/3}O_2$ compounds still present higher reversible capacity than $NaFeO_2$. On the other hand, the Coulombic efficiency is worsened with increased Mn content (see solid lines in Fig. 4.10). Looking at the redox potentials and voltage hysteresis of the different compounds in Table 4.1, there seems to be a relation between reaction potential and the different TM concentration.Indeed, when increasing the Mn content, the Fe redox potential increases and that of Mn decreases. These results are similar to those previously published for the lithium based iron and manganese olivine (Li(Fe,Mn)PO_4), were the changes in the reaction potential are related to the change in the covalency of the TM-O bonds with TM substitution [29, 30]. Moreover, the potential hysteresis of the Fe redox reaction increases while that of Mn decreases with increasing Mn content. As for the results upon cycling, the voltage hysteresis (for either Fe or Mn redox reactions) increases in various cases over 100% in 50 cycles.

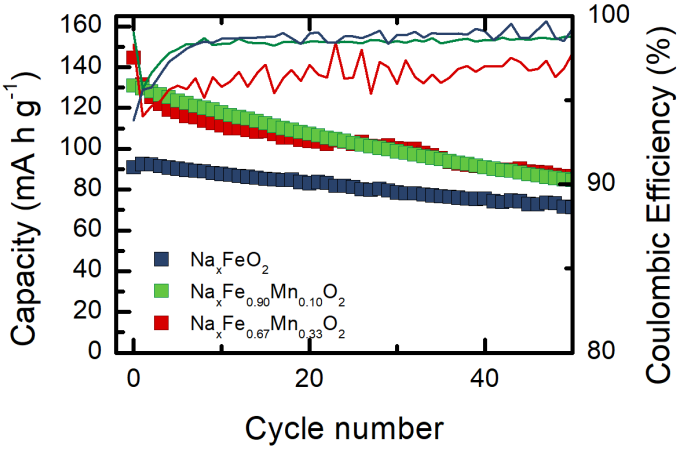

Figure 4.10: Comparison of the capacity retention of the $Na_xFe_yMn_{1-y}O_2$ series at C/10 rate (squares) and CE (lines). The voltage windows at which the cells have been cycled depend on the sample. $NaFeO_2$: $V = 3.5 - 2.5$ V; $NaFe_{0.9}Mn_{0.1}O_2$: $V = 3.5 - 2.0$ V; and $Na_{2/3}Fe_{2/3}Mn_{1/3}O_2$: $V = 4.2 - 1.5$ V.

Table 4.1: Summary of the electrochemical results of the $Na_xFe_{1-y}Mn_yO_2$ series cycled at C/10 cycling rate. Capacity values (Q) are taken during the 1st discharge, the capacity retention is considered after 50 cycles, redox voltage (V) for iron and manganese oxidation reactions are taken at the maximum of the derivative during the 2nd charge, and potential hysteresis (ΔV) for Fe and Mn redox processes is taken during with the maximum of the derivative peaks during the 2nd cycle.

Parameter	$\mathbf{Na_xFe_{1-y}Mn_yO_2}$				
	$\mathbf{y = 0}$	$\mathbf{y = 0.1}$	$\mathbf{y = 1/3}$	$\mathbf{y = 0}$	$\mathbf{y = 1/3}$
V_{window} (V)	3.5-2.5	3.5-2.0	4.2-1.5	4.5-1.0	3.5-1.5
Q (mA h g^{-1})	92	131	145	75	86
Q retention (%)	77	64	60	40*	86
V_{Fe} (V)	3.33	3.31	3.42	3.38	-
ΔV_{Fe} (mV), 2nd cycle	78	61	127	895	-
ΔV_{Fe} (mV), 50th cycle	94	115	$\approx$ 600	1890*	-
V_{Mn} (V)	-	2.65	2.44	-	2.35
ΔV_{Mn} (mV), 2nd cycle	-	239	216	-	118
ΔV_{Mn} (mV), 50th cycle	-	$\approx$ 406	$\approx$ 533	-	141

* After 30 cycles

The gravimetric energy density on discharge is presented in Fig. 4.11. In this figure is evident that, although the presence of manganese improves the capacity of the cells, the energy density improvement is not that high due to the lower voltage of the manganese redox reaction. It can be seen that, although the capacity was higher for $NaFe_{0.9}Mn_{0.1}O_2$ and O3-$Na_{2/3}Fe_{2/3}Mn_{1/3}O_2$ than for $NaFeO_2$ after 50 cycles (see Fig. 4.10), the energy density upon discharge is very similar for the three samples, due to the higher potential of Fe redox. In fact, $NaFeO_2$ presents the higher energy density values after about 30 cycles. Moreover, the energy efficiency is much worsened with the addition of manganese. The worse efficiency of the manganese containing samples can be ascribed mainly to the inclined plateaus in the voltage curves and the increasing hysteresis shown in Table 4.1.

It is worth mentioning that the initial gravimetric energy densities of the present materials are within or even above some commercial technologies [31]. However, the poor stability needs to be addressed before they can be commercially used.

The results performed in the less common voltage windows (4.5-1.0 for $NaFeO_2$ and 3.5-1.5 for $Na_{2/3}Fe_{2/3}Mn_{1/3}O_2$) have been included with open squares in Fig. 4.12. In Fig. 4.12a, where the upper voltage has been limited to 3.5 V, it can be seen that the best capacity retention is obtained for $Na_{2/3}Fe_{2/3}Mn_{1/3}O_2$, but it also presents the lowest capacity, because only the manganese is redox active. Moreover, and due to the lower reaction potential of Mn, the energy density (Fig. 4.12b) is much lower for $Na_{2/3}Fe_{2/3}Mn_{1/3}O_2$ than for $NaFeO_2$ or $NaFe_{0.9}Mn_{0.1}O_2$. On the other hand, when cycled in an extended potential window, the detrimental effects in the capacity are more

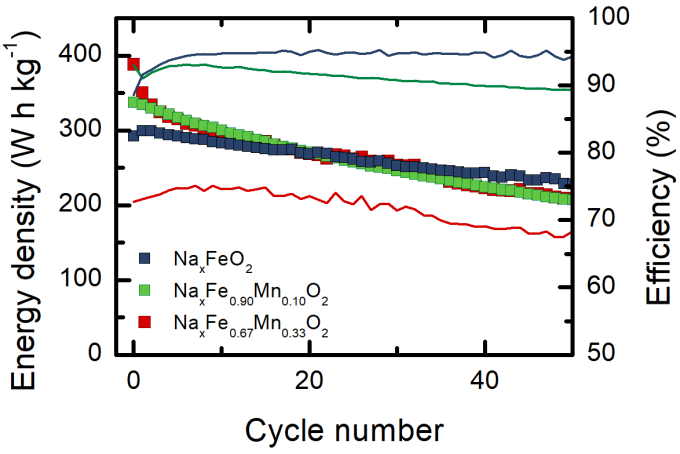

Figure 4.11: Comparison of the gravimetric energy density upon cycling of the $Na_xFe_yMn_{1-y}O_2$ series at C/10 (squares) and Round Trip Efficiency (lines). The voltage windows at which the cells have been cycled depend on the sample. $NaFeO_2$: $V = 3.5 - 2.5$ V; $NaFe_{0.9}Mn_{0.1}O_2$: $V = 3.5 - 2.0$ V; and $Na_{2/3}Fe_{2/3}Mn_{1/3}O_2$: $V = 4.2 - 1.5$ V.

evident in $NaFeO_2$ than in $Na_{2/3}Fe_{2/3}Mn_{1/3}O_2$ (Fig. 4.12d), although the capacity retention is decreased in both samples. Moreover, and due to the increment in the voltage hysteresis, the energy density (Fig. 4.12c) is also affected, especially for $NaFeO_2$. Indeed, the RTE value for $NaFeO_2$ and $Na_{2/3}Fe_{2/3}Mn_{1/3}O_2$ lies around 50% and 70% respectively due to the voltage hysteresis. It seems thus that although increasing the upper voltage limit can increase the reversible capacity (as in the case of $Na_{2/3}Fe_{2/3}Mn_{1/3}O_2$), the iron reaction at high potentials results in a worsened electrochemical activity, with a degrade capacity retention and an increase in the voltage hysteresis (see Table 4.1). Nonetheless, limiting the electrochemistry to Mn redox results in poor performance in terms of energy density due to the low average potential of the curves.

The rate capability results of $NaFeO_2$ and $Na_{2/3}Fe_{2/3}Mn_{1/3}O_2$, cycled within the common voltage windows reported in the literature, are compared in Fig. 4.13. The best results have been obtained for $NaFeO_2$. The most probable cause is the limited voltage window used in the case of $NaFeO_2$, which in the same manner, limits the reactions occurring at high potentials and that are detrimental for the electrochemical activity. Moreover, there are two other probable reasons to obtain a good rate capability test in $NaFeO_2$:

i. The smaller particle size of $NaFeO_2$ active material compared to others. The rate capability test requires a fast exchange of Na^+ ions and electrons in the particles. In smaller sized particles, the exchange tends to occur close to the surface, facilitating the process.

ii. The flatter voltage plateau of $NaFeO_2$. In the manganese containing samples, the reaction plateaus tend to be inclined, and especially that of Fe which is close to the edge of the voltage window.

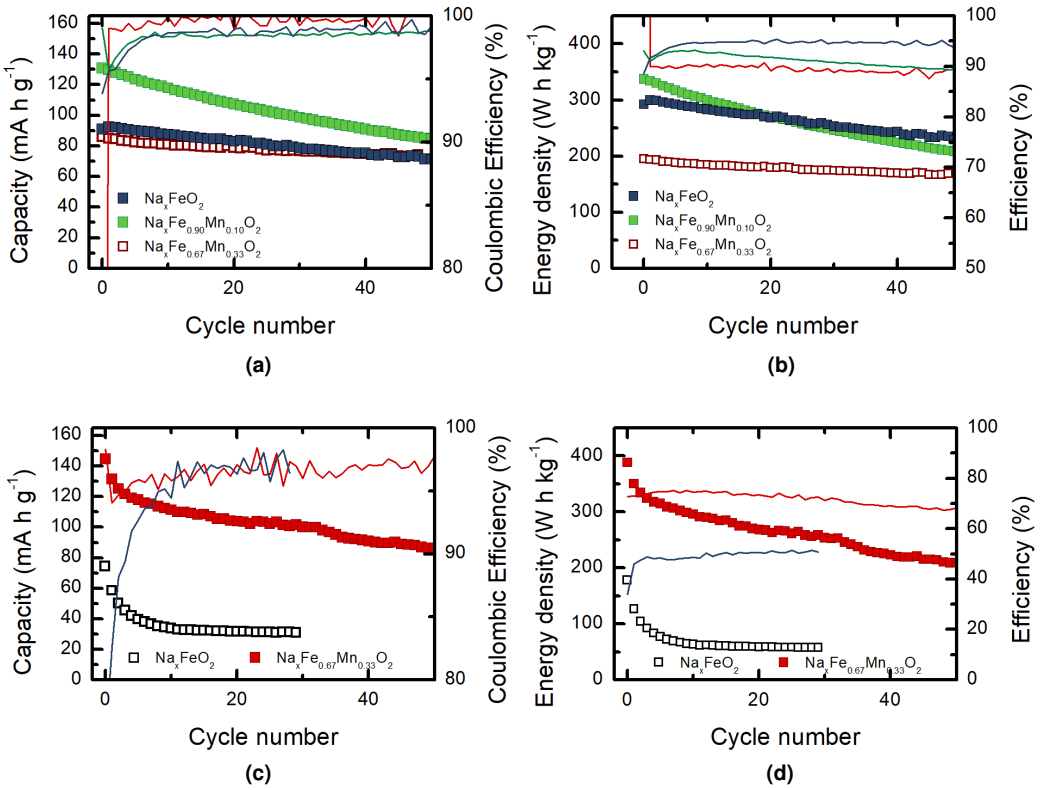

Figure 4.12: Comparison of of the electrochemical performance **(a,b)** when the upper voltage is limited to 3.5 V and **(c,d)** when cycled to high potentials. **(a,c)** Capacity retention (squares) and CE (lines), and **(b,d)** Energy density (squares) and RTE (lines). The samples cycled within the common voltage window as presented in the literature are shown with solid squares ($NaFeO_2$ in 2.5-3.5 V, $NaFe_{0.9}Mn_{0.1}O_2$ in 1.5-3.5 V and $Na_{2/3}Fe_{2/3}Mn_{1/3}O_2$ in 1.5-4.2 V), and those cycled in less common voltage windows with open squares ($NaFeO_2$ in 1.0-4.5 V and $Na_{2/3}Fe_{2/3}Mn_{1/3}O_2$ in 1.5-3.5 V).

4.6 Conclusions

The electrochemical performance, when cycled within the common potential window, shows for $NaFeO_2$ the lowest initial capacity among the studied samples ($NaFeO_2$, $NaFe_{0.9}Mn_{0.1}O_2$ and $Na_{2/3}Fe_{2/3}Mn_{1/3}O_2$), due to the lack of the Mn redox related capacity. On the other hand, it also shows the best capacity retention and Coulombic efficiency values. This is due to the detrimental effect of charging Fe containing samples to high potentials. Indeed, when $Na_{2/3}Fe_{2/3}Mn_{1/3}O_2$ is cycled in a limited voltage window where the redox reaction of Fe is not allowed, the capacity retention is improved significantly, but due to the low redox potential of Mn, the energy density is also low.

It is worth mentioning that, as opposed to the common believe, $NaFeO_2$ is electrochemically active when cycled to high potentials, as high as 4.5 V. However, the reversible capacity and RTE

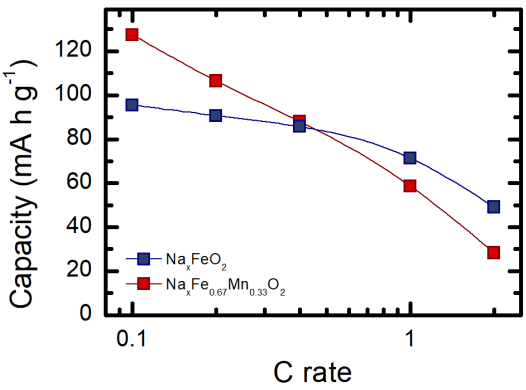

Figure 4.13: Comparison of the rate capability results of $NaFeO_2$ and $Na_{2/3}Fe_{2/3}Mn_{1/3}O_2$, cycled within the voltage windows of 2.5-3.5 V and 1.5-4.2 V respectively. The capacity presented corresponds to that of the fifth cycle at each rate.

are far from optimal, with a discharge capacity of 30 mA h g^{-1} on the 30th cycle and a capacity retention of 40% after 30 cycles, and an RTE of about 50%.

The reaction potentials of the iron and manganese depend on the TM concentration: with increasing Mn content the potential of Fe redox reaction increases and that of Mn decreases. Moreover, the reaction plateaus tend to incline with increasing TM mixture. That is the limiting factor for $Na_{2/3}Fe_{2/3}Mn_{1/3}O_2$ when cycled in a limited potential window, whose upper limit needs to be increased to take advantage of the capacity obtained from the iron. Moreover, the inclined plateaus of $Na_{2/3}Fe_{2/3}Mn_{1/3}O_2$ also results in a poorer capacity retention results compared to those of $NaFeO_2$, as part of the plateau lies outside of the cycling voltage window.

The cycling stability of these materials is not the best performing, but one should remember that they are based on cheap, clean and environmentally friendly precursors. Moreover, the electrode preparation has not been optimized, as it is beyond the scope of this work. The capacity and energy density values obtained are well within the state of the art for this kind of low cost and environmentally friendly materials. On the following chapters we will try to find the reasons behind the electrochemical degradation that these materials present. This way, it might be possible to avoid these detrimental effects to obtain better performing materials.

Bibliography

[1] J. Zhao, L. Zhao, N. Dimov, S. Okada, and T. Nishida. *Journal of The Electrochemical Society*, 160(5):A3077–A3081, 2013.

[2] Y. Takeda, K. Nakahara, M. Nishijima, N. Imanishi, and O. Yamamoto. *Materials Research Bulletin*, 29(6):659–666, 1994.

[3] M. Dubarry and B. Y. Liaw. *Journal of Power Sources*, 194(1):541–549, 2009.

[4] B. D. Adams, J. Zheng, X. Ren, W. Xu, and J.-G. Zhang. *Advanced Energy Materials*, 8(7):1702097, 2018.

[5] F. Yang, D. Wang, Y. Zhao, K.-L. Tsui, and S. J. Bae. *Energy*, 145:486–495, 2018.

[6] E. Lee, D. E. Brown, E. E. Alp, Y. Ren, J. Lu, J.-J. Woo, and C. S. Johnson. *Chemistry of Materials*, 27(19):6755–6764, 2015.

[7] N. Yabuuchi, H. Yoshida, and S. Komaba. *Electrochemistry*, 80(10):716–719, 2012.

[8] T. Drezen, N.-H. Kwon, P. Bowen, I. Teerlinck, M. Isono, and I. Exnar. *Journal of Power Sources*, 174(2):949–953, 2007.

[9] R. Kataoka, K. Kuratani, M. Kitta, N. Takeichi, T. Kiyobayashi, and M. Tabuchi. *Electrochimica Acta*, 182:871–877, 2015.

[10] N. A. Katcho, J. Carrasco, D. Saurel, E. Gonzalo, M. Han, F. Aguesse, and T. Rojo. *Advanced Energy Materials*, 7(1):1601477, 2017.

[11] M. Torabi, A. T. Neyshabouri, B. SoltanMohammad, S. H. Razavi, and M. K. Rad. *Journal of New Materials for Electrochemical Systems*, 20:039–042, 2017.

[12] K. Minnici, Y. H. Kwon, M. M. Huie, M. V. de Simon, B. Zhang, D. C. Bock, J. Wang, J. Wang, K. J. Takeuchi, E. S. Takeuchi, A. C. Marschilok, and E. Reichmanis. *Electrochimica Acta*, 260:235–245, 2018.

[13] J. Cui, C. Qing, Q. Zhang, C. Su, X. Wang, B. Yang, and X. Huang. *Ionics*, 20(1):23–28, 2014.

[14] R. Berthelot, D. Carlier, and C. Delmas. *Nature Materials*, 10(1):74–80, 2011.

[15] R. J. Clément, Z. Lun, and G. Ceder. *Energy & Environmental Science*, 13(2):345–373, 2020.

[16] J. Wang, Z. Zhou, Y. Li, M. Li, F. Wang, Q. Yao, Z. Wang, H. Zhou, and J. Deng. *Journal of Alloys and Compounds*, 792:1054–1060, 2019.

[17] C. Zhou, L. Yang, C. Zhou, B. Lu, J. Liu, L. Ouyang, R. Hu, J. Liu, and M. Zhu. *ACS Applied Materials & Interfaces*, 11(8):7906–7913, 2019.

[18] D. Kim, S.-H. Kang, M. Slater, S. Rood, J. T. Vaughey, N. Karan, M. Balasubramanian, and C. S. Johnson. *Advanced Energy Materials*, 1(3):333–336, 2011.

[19] D. D. Yuan, Y. X. Wang, Y. L. Cao, X. P. Ai, and H. X. Yang. *ACS Applied Materials & Interfaces*, 7(16):8585–8591, 2015.

[20] J.-L. Yue, Y.-N. Zhou, X. Yu, S.-M. Bak, X.-Q. Yang, and Z.-W. Fu. *Journal of Materials Chemistry A*, 3(46):23261–23267, 2015.

[21] Y. You, S. Xin, H. Y. Asl, W. Li, P.-F. Wang, Y.-G. Guo, and A. Manthiram. *Chem*, 4(9):2124–2139, 2018.

[22] X. Li, Y. Wang, D. Wu, L. Liu, S.-H. Bo, and G. Ceder. *Chemistry of Materials*, 28(18):6575–6583, 2016.

[23] E. Gonzalo, M. H. Han, J. M. López del Amo, B. Acebedo, M. Casas-Cabanas, and T. Rojo. *Journal of Materials Chemistry A*, 2(43):18523–18530, 2014.

[24] A. Rudola, D. Aurbach, and P. Balaya. *Electrochemistry Communications*, 46:56–59, 2014.

[25] R. J. Gummow, N. Sharma, R. Feng, G. Han, and Y. He. *Journal of The Electrochemical Society*, 160(10):A1856–A1862, 2013.

[26] K. Kubota, S. Kumakura, Y. Yoda, K. Kuroki, and S. Komaba. *Advanced Energy Materials*, 8(17):1703415, 2018.

[27] B. Mortemard de Boisse, J.-H. Cheng, D. Carlier, M. Guignard, C.-J. Pan, S. Bordère, D. Filimonov, C. Drathen, E. Suard, B.-J. Hwang, A. Wattiaux, and C. Delmas. *Journal of Materials Chemistry A*, 3(20):10976–10989, 2015.

[28] N. Sharma, E. Gonzalo, J. C. Pramudita, M. H. Han, H. E. A. Brand, J. N. Hart, W. K. Pang, Z. Guo, and T. Rojo. *Advanced Functional Materials*, 25(31):4994–5005, 2015.

[29] R. Malik, F. Zhou, and G. Ceder. *Physical Review B*, 79:214201, 2009.

[30] T. Muraliganth and A. Manthiram. *The Journal of Physical Chemistry C*, 114(36):15530–15540, 2010. Publisher: American Chemical Society.

[31] A. El Kharbachi, O. Zavorotynska, M. Latroche, F. Cuevas, V. Yartys, and M. Fichtner. *Journal of Alloys and Compounds*, 817:153261, 2020.

5 | Advanced structural characterization of O3-Na_xFeO_2 upon cycling

Contents

5.1 Introduction

Transition metal based sodium layered oxides suffer from structural changes upon sodium extraction and insertion, as previously reported in several research works [1–3].

In this chapter $NaFeO_2$ will be characterized as case study for O3 transition metal layered oxides. One of the most direct ways to observe these changes is *operando* XRD, which consists in the collection of consecutive XRD patterns while the cell is under operation. XRD data will be used to determine the structural changes upon cycling. Based on the assumption of TM migration to Na layers and with the help of simulations, an estimation of migrated Fe will be presented. The results obtained with the simulations will be confirmed with Mössbauer spectroscopy.

5.2 *Operando* structural characterization by X-ray diffraction

Before the *operando* measurements, a long XRD pattern of the pristine material in the cell has been done. This pattern can be compared with the pristine powder's pattern and then discern the contributions from the other cell components as well as calibrate the sample's height. Indeed, there will be reflections from the beryllium window and the aluminum foil. Moreover, the material is mixed with carbon and wet with electrolyte, that increases the background contribution. The beryllium and the aluminum contributions, being crystalline materials, can be added as static phases, and the background contribution from KetjenBlack carbon and electrolyte can be included as a constant background for the refinement. Furthermore, the instrument is calibrated for sample holders where the surface of the sample lies at the center of the goniometer. Since when the sample is placed inside the cell a slight displacement in the vertical axis is present, the height of the sample needs to be calibrated accordingly. The height, being related to the cell geometry, will stay constant throughout the whole measurement, and will create a displacement of the reflections. The shift can be clearly seen in Fig. 5.1, which compares the XRD pattern of the powder sample in a normal airtight sample holder (dark blue line) and the same sample within the cell before starting the *operando* measurement (light blue line).

To correct the height of the sample FullProf software has been used [4], since it allows refining it. The refinement of the initial pattern inside the cell and the refined parameters are presented in Fig. 5.2 and Table 5.1 respectively.

Table 5.1: Le Bail or pattern matching refinement parameters of an *in-situ* XRD pattern of $NaFeO_2$: space group, cell parameters, SYCOS (related to sample height) and agreement factors.

Space group	**Cell parameters**		**SYCOS**
$R\bar{3}m$	$\boldsymbol{a}$ = $\boldsymbol{b}$ = 3.029(9) Å	$\boldsymbol{c}$ = 16.14(8) Å	-0.011(3)
Agreement factors	$\chi^2 = 6.05$	$R_b = 4.72$	$R_p = 4.32$

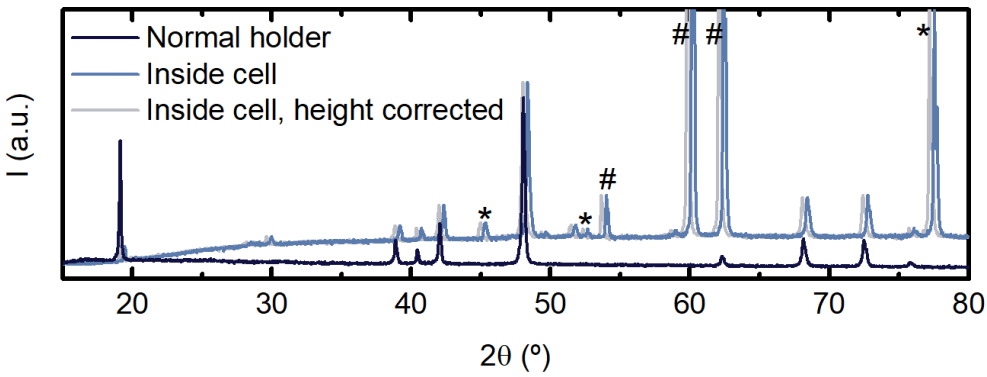

Figure 5.1: Comparison of the XRD patterns of powder sample in a normal airtight holder (dark blue) and inside the cell (light blue). A shift in the material's reflections is observed due to the difference in height. The measurement inside the cell with corrected height is shown in gray. The reflections from Be window are highlighted with a # symbol and from Al foil with a ∗ symbol.

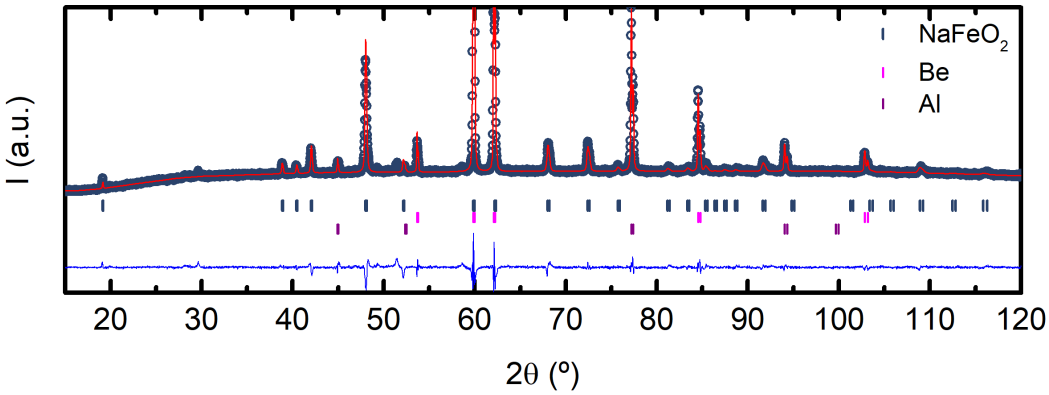

Figure 5.2: *In-situ* pattern of $NaFeO_2$ refined, including sample height. Three phases are refined: $NaFeO_2$, aluminum (from Al foil) and beryllium (from Be window). The experimental data are presented with dark blue scatter points, and the refinement with a red line, the difference between both with a blue line and the reflection angle position with vertical marks: from top to bottom, in blue for $NaFeO_2$, pink for Be and purple for Al.

The SYCOS parameter refined by FullProf is related to the sample height as [5]:

$$SYCOS = \frac{180}{\pi}\frac{s}{R} \tag{5.1}$$

where s is the displacement, R is the goniometer radius (280 mm for the instrument that has been used, a Bruker D8 Advance) and s is the sample's height displacement.

The 2θ angle can be corrected by the height of the shift according to [5]:

$$2\theta_{correc} = 2\theta_{meas} - \frac{2s}{R}\cos\theta_{meas} \tag{5.2}$$

The pattern of the measurement inside the cell corrected for the height displacement is presented in Fig. 5.1 in gray color, and its reflections' position perfectly overlap with those of the measurement done in a normal holder.

A 2D representation of XRD patterns evolution upon the *operando* measurement is presented in Fig. 5.3(a-c), in which the color depends on the intensity, the 2θ angle indicated by x axis and time in y axis. Reflections are indexed with $(h\,k\,\ell)$ Miller notation according to the initial phase with the $R\bar{3}m$ space group. The voltage and sodium content are presented as a function of time in Fig. 5.3d. This cell has been charged to 4.0 V, over the reversible voltage limit, to try to understand the degradation processes occurring at high voltage values. The voltage has been held at 4.0 V with the aim of maximizing the sodium extraction and the probable structural degradation. The voltage was not further increased to avoid parasitic reactions, such as electrolyte decomposition, that would bias the x value determined from the electrochemical reaction control. At the end of the measurement the sodium content is $x = 0.22$, which corresponds to 78% of the theoretical capacity (188 mA h g^{-1}).

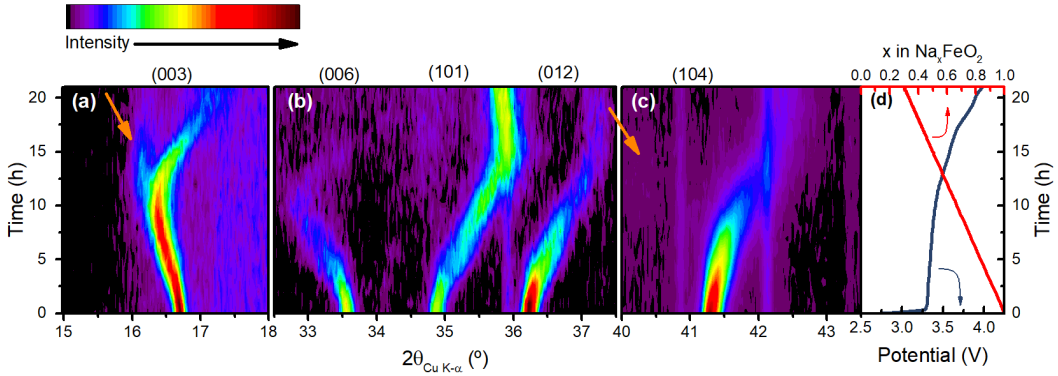

Figure 5.3: *Operando* XRD data of $NaFeO_2$ charged to high voltage (4.0 V). **(a-c)** 2D representation of *operando* XRD data as a function of 2θ in x axis and time in y axis. Highlighted with orange arrows, the presence of a secondary P3 phase. Reflections are labeled on top according to initial O3 phase. **(d)** Voltage (bottom) and sodium content (top) curves as a function of time.

There is a clear shift of all the reflections, meaning that the cell parameters change during sodium deintercalation. The reflection $(0\,0\,3)$ in Fig. 5.3a shifts to lower angles in the beginning of the charge, reflecting an increment in the interlayer distance d ($d = c/3$, where c is the cell parameter in z axis, see Fig. 1.15). This behavior is general and well known for layered oxides, as the repulsive forces between the oxygens in adjacent layers increase with sodium extraction [1, 2, 6–11]. On the other side, reflections with contribution from in-plane metal-metal distance $a = b$ $(1\,0\,1\,,\ 0\,1\,2\,,\ 1\,0\,4)$ shift to higher angles, which means that in-plane distance b decreases. This feature is also well known for layered oxides, and it has been ascribed to a decrease of electrostatic repulsion between sodium and transition metal ions [1, 2, 6, 11]. As in most layered oxides, at half charge there is a change in the shift trend, with the $(0\,0\,3)$ reflection shifting to higher angles,

indicating a shrinking of interlayer distance [2], and reflections with contributions of in-plane distance slightly shifting to lower angles. In Fig. 5.3a, close to the $(0\,0\,3)$ reflection and highlighted with an orange arrow, the presence of a secondary phase is visible. It is also visible in Fig. 5.3c, near the reflection $(1\,0\,4)$, although its relative intensity is much lower. This reflection might be an indicative of a phase transformation. Layered oxides are easily transformed from O to P phases by layer gliding, and in particular O3 to P3 transition has been reported for other Fe containing O3 layered oxides [12–15]. Both O3 and P3 phases share the same $R\bar{3}m$ space group, but with different atomic arrangement, and thus, share the reflections with different relative intensities. In particular, P3 structures have a lower relative intensity of the $(1\,0\,4)$ reflection compared to the O3 structure. Within the resolution of these measurements, besides the reflections close to the main $(0\,0\,3)$ and $(1\,0\,4)$ diffraction peaks, there are no extra reflections, indicating that the secondary phase probably belongs to the same space group as the main O3 phase. Also, due to the direct oxygen-oxygen stack between adjacent layers in P structures, as opposed to the diagonal stacking in O structures, d interlayer distance tends to be larger in P phases (reflection with weight in ℓ shifts to lower angles). All these observations seem to be indicative that the secondary phase observed here for $NaFeO_2$ near 3.40 V is a P3 phase.

In Fig. 5.4 representative examples of Le Bail refinements of *operando* XRD patterns are presented at various states of charge. A single $R\bar{3}m$ phase has been used, besides the static Be and Al from the cell components, since the low intensity of the P3 phase's reflections has not allowed its refinement. It appears clearly from Fig. 5.4 that the peaks get broader as the cell is charged indicating a loss in crystallinity. Changes in relative intensities are also appreciated, especially in the $32^\circ \leqslant 2\theta \leqslant 38^\circ$ region, where $(0\,0\,6\,,\ 1\,0\,1\,,\ 0\,1\,2)$ reflections can be seen.

The cell parameter evolution has been calculated with a sequential Le Bail refinement using FullProf Suite software [4]. In this kind of analysis, a first pattern is refined, similarly to the one shown in Fig. 5.2 and is used as an input to analyze several XRD patterns. The software will use the results of the i^{th} pattern to analyze the $(i+1)^{th}$. The refined parameters have to be carefully selected to allow a correct fitting of the patterns but trying to minimize the amount of variables to avoid deviations. The method does not allow the transformation of the space group, so the space group $R\bar{3}m$ has been considered for the whole measurement. In order to obtain a good compromise between signal to noise ratio and time resolution, the measured angular range has been limited to $14^\circ \leqslant 2\theta \leqslant 45^\circ$. This, together with the broadening of the peaks and overlapping of the signals coming from the cell components, complicate the Le Bail refinements. Nevertheless, as can be appreciated from Fig. 5.4 the Le Bail refinements of the various patterns is good enough.

However, and since Le Bail refinement of the P3 phase has not been possible, the interlayer distance and weight proportion of this secondary phase is unknown. For this reason, the interlayer distance has also been calculated by fitting the vicinity $(0\,0\,3)$ reflection with pseudo-Voigt functions, to estimate the peaks' integral intensity and the interlayer distance d of both O3 and P3 phases. In Fig. 5.5 a few examples of the pseudo-Voigt fitting of the low angle region ($15^\circ \leqslant 2\theta \leqslant 18^\circ$) is presented. Since the intensity of the secondary P3 phase is low, its position

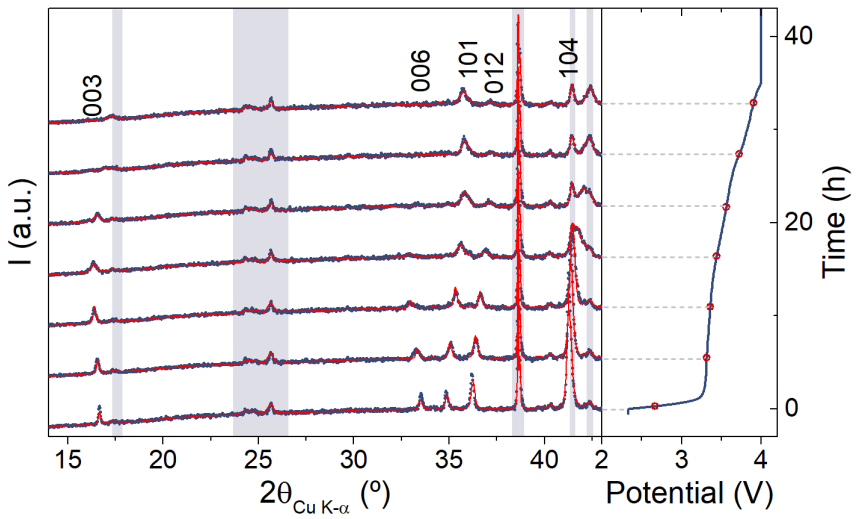

Figure 5.4: Le Bail refinement examples of $NaFeO_2$ at various states of charge. Experimental data are presented with blue points and Le Bail refinements with a red line. On top, $(h\,k\,\ell)$ Miller index according to the pristine sample. Reflections from cell components (aluminum, beryllium and beryllium oxide from the window's corrosion) have been highlighted in gray. In the right panel the voltage curve, and marked the points at which the diffraction patterns have been taken.

has been refined in the pattern where its intensity is maximum and it has been fixed for the following patterns. However, its width and intensity have been refined. The background has been refined for the first pattern and has been fixed for the followings. It consists of a linear background and a reflection coming from the corrosion of the beryllium window (BeO) in $2\theta \approx 17.4°$, fitted with a pseudo-Voigt peak (see dotted line in Fig. 5.5). As can be seen in Fig. 5.5, the fit is in good agreement with the experimental data in the studied region. The interlayer distance d has been calculated using Bragg's law (equation 2.1) taking into account the sample's height displacement.

The results from Le Bail and pseudo-Voigt analysis described above are presented in Fig. 5.6. The voltage and time evolution are presented in Fig. 5.6a. It appears clearly that both methods, Le Bail and pseudo-Voigt, give the same results for the interlayer distance (see Fig. 5.6b). However, each of the techniques gives an additional information: metal to metal b distance of the main O3 phase in the case of the Le Bail refinements (Fig. 5.6c), and interlayer distance of the secondary P3 phase (Fig. 5.6b) and the relative intensity of both phases (Fig. 5.6d) in the case of pseudo-Voigt function fittings.

It can be seen in Fig. 5.6b that the interlayer distance d increases (increased O-O repulsion between layers) from 5.37 Å in the initial state up to 5.47 Å at $x = 0.65$ ($V = 3.41$ V, $t = 11$ h), and then it starts to shrink down to 5.20 Å until the end of charge ($x = 0.23$, $V = 4.0$ V), lower than the initial distance. The P3 phase appears about when the maximum of the interlayer distance of the O3 phase is reached, and its interlayer distance stays constant on further desodiation. In Fig. 5.6c in-plane distance b of the O3 phase is presented. Note that in the definition of the hexagonal O3

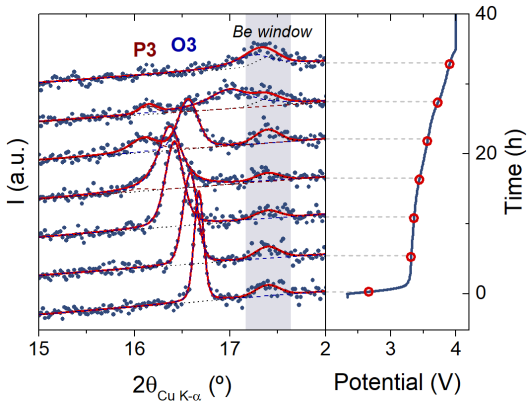

Figure 5.5: Pseudo-Voigt refinement examples of the $(0\,0\,3)$ reflection of $NaFeO_2$ at various states of charge. Experimental data are presented with blue points and pseudo-Voigt fittings with a red line. Reflection from cell components has been highlighted in gray. The right panel shows the voltage curve, and marked the points where the diffraction patterns have been taken.

structure the in-plane distances a and b are equivalent. It reduces from 3.02 Å at initial state down to 2.94 Å at 3.70 V ($x = 0.40$) where an inflexion point is observed. At the end of the charge it slightly increases and b reaches a value of 2.95 Å.

The intensity of the O3 phase (Fig. 5.6d) increases at first, and when its interlayer distance starts to shrink, a reduction of the intensity is observed. This reduction of intensity does not seem to be only due to the appearance of the P3 phase, as reflected by the global intensity decay (gray diamonds in Fig. 5.6d): the sum of the intensities of the O3 and the P3 phases continuously decreases until the end of charge.

A second cell has been run for two cycles to try to determine the reversibility of the above described processes. The *operando* XRD patterns are presented in Fig. 5.7(a-c). Similarly to the previous cell, the color depends on the intensity, 2θ angle is indicated in x axis and time in y axis. Note that this cell has been measured with a cobalt X-ray source, instead of the more common copper one. Due to its larger wavelength ($\lambda_{Co} = 1.78897$ Å vs. $\lambda_{Cu} = 1.54053$ Å), the reflections are shifted to higher angles compared to Figs. 5.3-5.5. Reflections are indexed with $(h\,k\,\ell)$ Miller notation according to the initial phase with the $R\bar{3}m$ space group. The voltage and sodium content are presented as a function of time in Fig. 5.7d. This cell has been cycled with various upper voltage limits in a galvanostatic regime at C/30 rate. During the first cycle, it has been charged to 3.6 V, within the reversible voltage window. It is slightly higher than the 3.5 V voltage considered in Chapter 4, to account for the polarization that the *operando* measurements will present. In house *operando* measurements do not allow the measurement of thin electrodes cast and pressed in Al foil (typically 3 mg cm^{-2}), because the beam is not intense enough to penetrate through the foil. Therefore, the measurements have been done on heavier electrodes in powder form (typically 30 mg cm^{-2}), where carbon and active material particles are simply mixed by hand and their

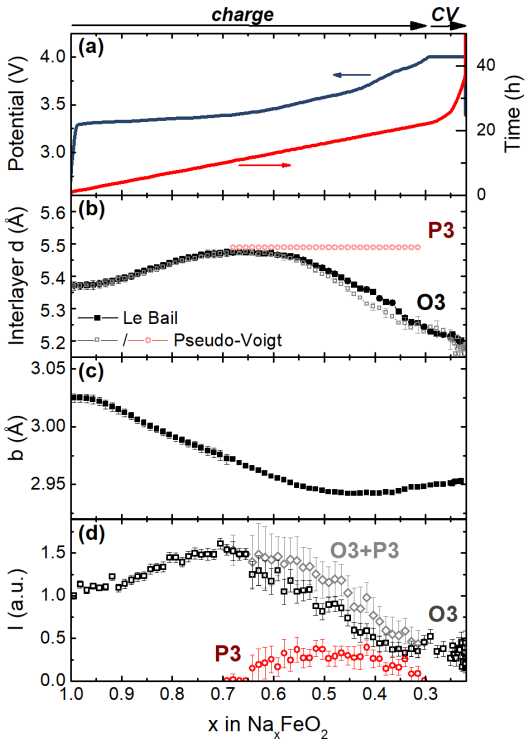

Figure 5.6: Analysis results of the *operando* XRD data shown in Figs. 5.3, 5.4 and 5.5 obtained by Le Bail refinements and pseudo-Voigt fitting. **(a)** Voltage (left) and time (right) as a function of composition. **(b)** Interlayer distance d of the main O3 phase (black) and secondary P3 phase (red) calculated by Le Bail refinements of the whole measured range (solid points) and pseudo-Voigt refinements at the vicinity of $(0\,0\,3)$ reflection (open points). **(c)** In-plane metal-metal b distance evolution obtained by Le Bail refinement. **(d)** Normalized intensity of the O3 (black) and P3 (red) phases obtained by integration of the pseudo-Voigt fits at the vicinity of the $(0\,0\,3)$ reflection. In gray, the sum of the intensities of the $(0\,0\,3)$ reflections of both O3 and P3 phases. The numerical results can be found in Table B.1.

interconnection is not optimized, resulting in a slightly overpolarized cycling. During the second cycle, the upper voltage limit has been increased to 3.8 V, to try to observe the structures formed at high voltages that are detrimental for the electrochemical activity. Although the plateau of $Fe^{3+/4+}$ redox reaction sits around 3.3 V, the discharge voltage has been lowered to 1.0 V to account for the polarization increment that can be expected when charged beyond 3.6 V. At the end of the two discharge processes, the discharge voltage (1.0 V) has been maintained constant until a limit equilibrium current of $I = C/300$ (0.80 µA g^{-1}) has been reached to try maximize the reinserted sodium amount.

The evolution of the reflections is very similar to those seen in the Fig. 5.3. Interlayer distance starts increasing with sodium extraction as reflected by the reduction of the $(0\,0\,3)$ reflection's angle, together with a reduction in the in-plane distance, as reflected by the shift to higher angles

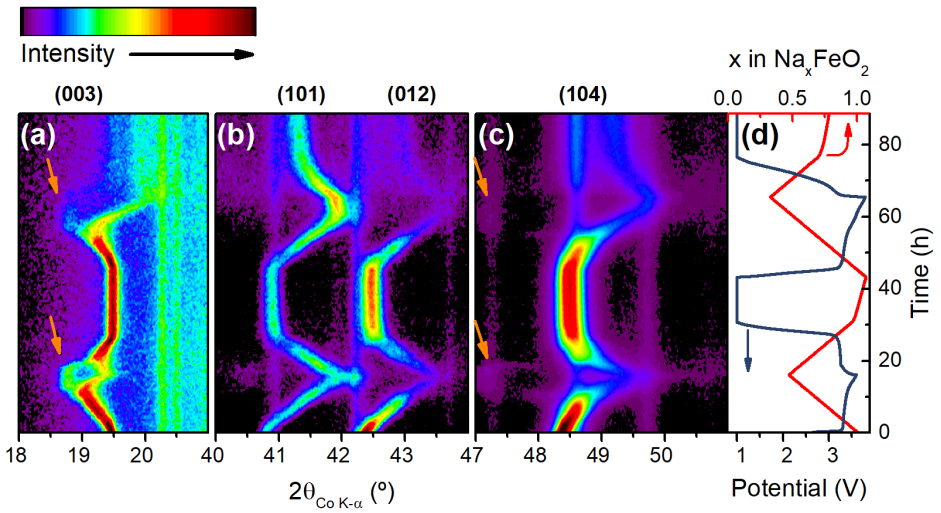

Figure 5.7: **(a-c)** 2D representation of *operando* XRD of $NaFeO_2$ for selected 2θ angle ranges measured with Co K-α source. Reflections are indexed with $R\bar{3}m$ space group according to initial O3 phase. Orange arrows in (a) and (c) indicate the presence of a secondary phase. **(d)** Voltage of the cell and sodium content evolution as a function of time.

of the reflections $(1\,0\,1\,,\ 0\,1\,2\,,\ 1\,0\,4)$. Moreover, the beginning of interlayer distance shrinking is also observed at half charge ($V = 3.36$ V, $t = 10$ h). When the O3 phase's interlayer distance starts to reduce, the P3 is distinguished, with an increasing interlayer distance. The trend is reversed on discharge from 3.6 V, therefore, the process seems reversible. The Coulombic efficiency reaches 97%, with a discharge capacity of 115 mA h g^{-1}. This reversibility is confirmed by the XRD reflections shifting back close to their original positions.

However, although reflections with in-plane distance contribution $(1\,0\,1\,,\ 0\,1\,2\,,\ 1\,0\,4)$ follow a symmetric path, an asymmetric path can be observed if looking closer at the $(0\,0\,3)$ reflection between the charge and the discharge. The O3 phase shifts back to low angles on discharge, but the shift is lower than that seen during charge. The P3 phase also seems to disappear in favor of the O3 phase.

Similarly to the previous cell, a quantitative analysis has been done by fitting the XRD patterns in the vicinity of the $(0\,0\,3)$ peak (angular range shown in Fig. 5.7a) to calculate the interlayer distance of the O3 and P3 phases, as well as their $(0\,0\,3)$ reflection's relative intensity. Pseudo-Voigt functions with fixed background (including the double peak from Be window at $2\theta \approx 20.5°$) have been used for that purpose.

The results, interlayer distance and normalized intensity, are presented in Fig. 5.8. As previously seen, the interlayer distance of the O3 phase starts increasing with sodium extraction from 5.39 Å up to 5.51 Å until the voltage at $V = 3.43$ V is reached ($x = 0.61, t = 12$ h), at which point the trend changes and it starts to decrease. The intensity, which was increasing upon Na extrac-

tion below 3.43 V, also changes its trend beyond that point and starts to decrease together with the interlayer distance reduction. At this point, the P3 phase is fully distinguishable. It is worth noting that the data are slightly noisy, due to short acquisition time (30 mins/pattern for a total 2θ range of 14° in two steps) considering that the diffraction patterns are attenuated by the cell components. Moreover, the background is curved and parasitic reflections from the cell components are very close to the active material's ones, producing some asymmetries in the peaks. In order to keep the refinements as reliable as possible, the fitting has been kept to the minimum amount of parameters as possible. That is, only when two series of peaks are completely distinguishable have been independently refined by introducing an additional phase.

Upon discharge from 3.6 V, the O3 phase's interlayer distance d increases slightly together with a fast shrinking of the P3's one. The intensity of both phases decreases fast at the beginning of the discharge, until the P3 phase is no longer distinguishable. Beyond the end of the discharge plateau ($V = 3.15$ V, $x = 0.85$, $t = 29.5$ h), no appreciable changes in cell parameter and intensity are observed. Values close to the initial ones are obtained, meaning the structural changes are very reversible when charged in the conservative voltage window.

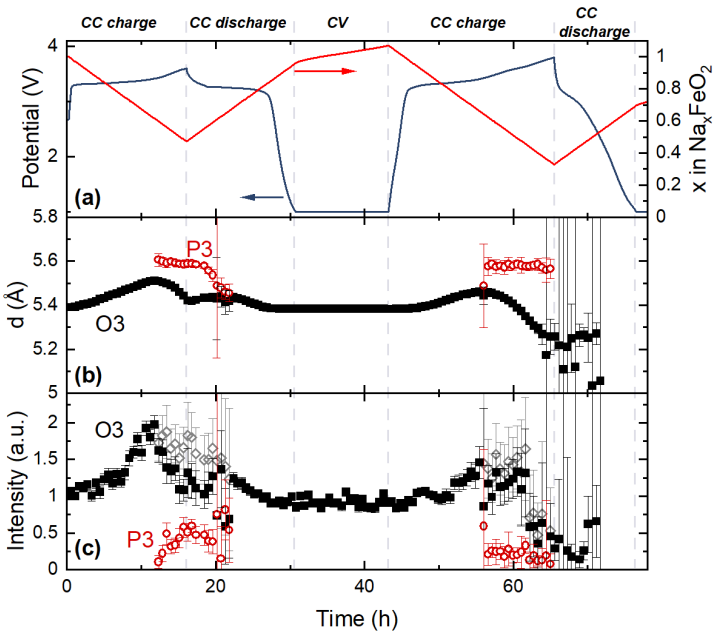

Figure 5.8: Pseudo-Voigt analysis results of the vicinity of the (003) reflection in Figure 5.7a. **(a)** Voltage and sodium content evolution, **(b)** interlayer distance evolution of the O3 (back solid squares) and the P3 (red open circles) phases and **(c)** intensity evolution of O3 (black solid squares) and P3 (red open circles) phases. In gray, intensity of both phases. The numerical results can be found in Table B.2.

When charged to 3.8 V, similar parameters evolution to those seen when charged to 3.6 V are observed: an increase of the interlayer distance of the O3 phase accompanied with an increase in its

peaks intensity, until an inflexion point is reached at 3.42 V ($x = 0.64$, $t = 56.5$ h). At this moment, O3 phases' interlayer distance d and $(0\,0\,3)$ peak's intensity decrease while the P3 phase appears with a larger interlayer distance ($d_{O3} = 5.45$ Å and $d_{P3} = 5.58$ Å). The interlayer distance of the main phase further drops below the initial value (5.39 Å), and reaches a minimum value of 5.20 Å at the end of charge. As can be seen in Fig. 5.8, the P3 phase disappears slightly before the 3.8 V limit is reached, without any noticeable change in the d parameter. It seems thus that the sodium is mainly extracted from the O3 phase, and the P3 phase disappears in favor of the O3. Note that the d parameter's error bars increase close to the end of charge at 3.8 V. This is because at this point, the $(0\,0\,3)$ reflection overlaps that of the Be window. The electrochemistry after reaching 3.8 V is also affected, the Coulombic efficiency lowers to 55% (88 mA h g^{-1} of discharge capacity). As can be seen from Fig. 5.7d, the polarization is increased in the following discharge, which also presents a sloping profile, while when discharged from 3.6 V a plateau followed by a fast voltage drop can be seen. These features are indicators of a degraded reaction kinetics, which, attending to literature, might be the effect of structural transformation [16–18] or iron migration from FeO_2 layers to Na layers [2, 10, 19–22].

5.2.1 Study of iron migration

In the previous section it has been shown that the interlayer distance drops down to values below the initial ones at high voltage values, which might be related to TM migration into Na layers [2, 10, 19]. Rietveld analysis would be required to determine the atomic positions inside the crystal structure. Unluckily, the experimental data do not allow this kind of analysis, and thus, an alternative method based on XRD patterns simulations has been developed.

According to previous works, two different sites are present in Na interslabs to which TM migration can occur: octahedral sites (already occupied by Na ions) and tetrahedral sites (empty) [2, 19], see orange and gray sites respectively in Fig. 5.9a. The XRD patterns of the O3 phase have been simulated with FullProf software suite [4], with Fe migrated to the two above mentioned sites of the Na layers (see Fig. 5.9b). It is clear from these simulations that the site where Fe sits has a huge impact in the final XRD pattern. When Fe is placed in the Na layers, the $(0\,0\,3)$ reflection's intensity decreases, and the relative intensities of the $(0\,0\,6\,,\ 1\,0\,1\,,\ 0\,1\,2)$ reflections change. While reflection $(1\,0\,1)$ has a lower intensity among the three reflections when Fe is in the octahedral sites of the Na layers, it is more intense when Fe migrates to the tetrahedral vacancies in the Na layers. The relative intensities of these reflections in the experimental pattern (blue line in Fig. 5.9b) resembles more to that in which Fe sits in tetrahedral vacancies.

In order to understand the effect of the migration in the intensity of the $(0\,0\,\ell)$ reflection a model has been developed based on the theory of the X-ray diffraction technique. The intensity of a certain $(h\,k\,\ell)$ reflection in a XRD pattern depends mainly on the atomic ordering of the crystalline structure. The amplitude S_{hlk} of the diffracted X-ray beam is the sum of the amplitudes

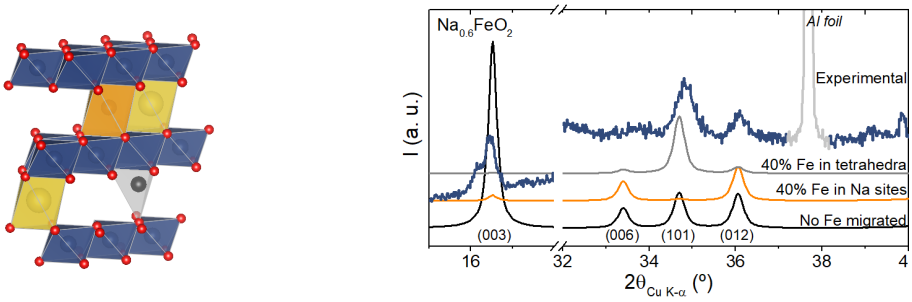

Figure 5.9: **(a)** Structure schema of partially desodiated Na_xFeO_2 with Fe migration. Yellow octahedra for Na atoms, blue octahedra for Fe atoms and migrated Fe in orange octahedra (Na sites) and gray tetrahedra. **(b)** Simulation XRD pattern with Cu K-α wavelength of $Na_{0.6}FeO_2$ for selected angle range, without Fe migration, with 40% of iron migrated to octahedral sites in Na layers (octahedral sites) and to tetrahedral sites in Na layers, together with an experimental pattern.

scattered from single atoms [23]:

$$S_{hk\ell} = \sum_j f_j \exp(-2\pi i \mathbf{h} \cdot \mathbf{r}_j) \tag{5.3}$$

where h, k and ℓ stand for Miller indices of the $(h\,k\,\ell)$ reflection, f_j for the atomic form factor (including the Debye-Weller thermal agitation factor), $\mathbf{h}$ for the scattering vector and $\mathbf{r}_j$ for the atomic coordinates of the j^{th} atom. In the $NaFeO_2$ structure, Na sites in the interlayer would have the position $\mathbf{r}_{Na} = (0,0,0)$, Fe in the FeO_2 layers would have the position $\mathbf{r}_{Fe} = (0,0,0.5)$, and the tetrahedral sites to which Fe are susceptible to migrate would have the position $\mathbf{r}_{tet} = (0,0,5/8)$. As a consequence, the contribution of the occupancy of these sites to the amplitude of the $(0\,0\,\ell)$ reflections, taking the FeO_2 layers as a reference, would be positive for the Fe atoms in the FeO_2 layers and negative for Na or migrated Fe present in the Na interlayer. This is the reason why the intensity increases while extracting Na and would on the contrary decrease if Fe migrates to the Na interlayers. For a given composition with x atoms of Na in the Na layers octahedral sites and z TM (Fe) atoms migrated into the octahedral or tetrahedral sites of the interlayer, corresponding to the formula $(Na_xFe_z)Fe_{1-z}O_2$, with $x + z \leqslant 1$, the amplitude of the $(0\,0\,\ell)$ reflections can be described as follows:

$$\begin{aligned} S_{00\ell} =& x f_{Na} + z f_{TM} - (1-z) f_{TM} + \sum f_O \exp(-2\pi i \mathbf{h} \cdot \mathbf{r}_j) = \\ & x f_{Na} + 2z f_{TM} - f_{TM} + \sum f_O \exp(-2\pi i \mathbf{h} \cdot \mathbf{r}_j) \end{aligned} \tag{5.4}$$

Taking into account that the oxygen atoms contribution (last term in equation 5.4) does not depend on x nor z, and assuming that the oxygen occupancy does not change upon cycling, it can be considered constant (K). The intensity, which is proportional to the square of the scattered amplitude, can hence be simplified as:

$$I_{00\ell} \propto (S_{00\ell})^2 \propto (x f_{Na} + 2z f_{TM} - f_{TM} + K)^2 \tag{5.5}$$

From this equation it can be concluded that the intensity can be described as a two variable 2nd order polynomial function of Na content x and migrated Fe content z.

The evolution of the intensity of the $(0\,0\,3)$ reflection of the O3 structure of $(Na_xFe_z)Fe_{1-z}O_2$, the most intense of the $(0\,0\,\ell)$, has been simulated using the FullProf software suite [4] for different values of x, z, and interlayer distance d, z being the concentration of Fe atoms that have migrated to Na layer's tetrahedral sites. The results of the simulations are presented in Fig. 5.10 as square symbols. The simulated dependence of the $(0\,0\,3)$ intensity on x and z has been parametrized by finding the best fit with equation 5.5 (lines in Figs. 5.10a and b) in order to determine the arguments. Finally, the influence of the interlayer distance d on the intensity, represented in Figure 5.10c, has been adequately fitted with a straight line, denoting a linear dependency, whose parameters depend only on I_0, but not on x nor z. Simulations with varying in-plane distances *a* or *b* have also been carried out with values varying from 2.90 Å to 3.05 Å, above and below the values estimated from the analysis presented in Fig. 5.6c. The simulations showed no appreciable changes in the resulting $(0\,0\,3)$ integrated peak intensity, therefore it has not been included in the equation, and its influence has hence been neglected. As a result of this parametrization of the simulations, the intensity of $(0\,0\,3)$ reflection has been established as equation 5.6, with a dependency of the on x (sodium content), z (Fe atoms migrated to tetrahedral sites of Na layers) and d (interlayer distance).

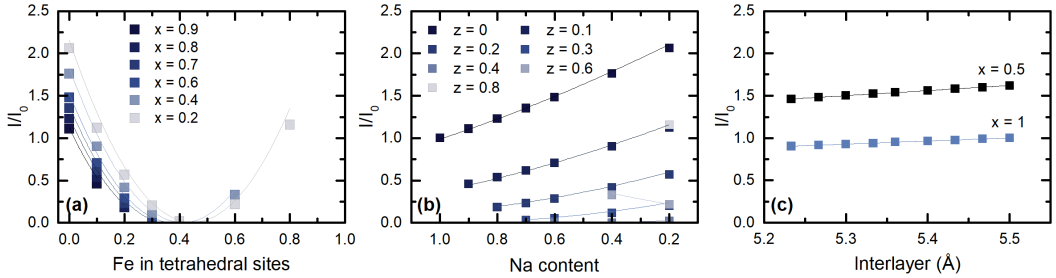

Figure 5.10: Intensity of the reflection $(0\,0\,3)$ of the simulated patterns, **(a)** as a function of the content z of migrated Fe for different Na contents x, **(b)** as function of the Na content x for different amounts z of migrated Fe, and **(c)** as function of the interlayer distance d for $z = 0$ and two different sodium contents x. In all cases the intensity has been normalized by I_0, the intensity simulated with $x = 1$, $z = 0$ and $d = 5.37$ Å, which corresponds to the pristine $NaFeO_2$ phase. The simulations have been run considering the migration of Fe to tetrahedral sites in Na layers.

$$\left.\frac{I(x,z,d)}{I(x_0,z_0,d_0)}\right|_{tetr} = ((2.517 - 1.867x + 0.349x^2) + z(-10.402 + 3.846x - 0.0134x^2) + z^2(10.781 + 0.0213x - 0.0306x^2))(1 - 0.260(d - d_0)) \tag{5.6}$$

where $x_0 = 1$, $z_0 = 0$ and $d_0 = 5.37$ Å are the parameters corresponding to the pristine $NaFeO_2$ phase. The same analysis has been done considering Fe migration to the octahedral sites of the

Na layers (those occupied by Na and Na vacancies), and the parametrization of the curve has been established as:

$$\begin{aligned}\left.\frac{I(x,z,d)}{I(x_0,z_0,d_0)}\right|_{oct} =&((2.517-1.867x+0.349x^2)\\ &+z(-8.225+2.894x+0.0129x^2)\\ &+z^2(6.722+0.019x-0.032x^2))(1-0.260(d-d_0))\end{aligned} \tag{5.7}$$

All the parameters, except the amount of migrated Fe z, have been determined experimentally: d from the refinement of the XRD data (Figs. 5.6b and 5.8b), I/I_0 from the integrated intensity of the reflection $(0\,0\,3)$ and x from the chronoamperometric curves recorded during *operando* measurements. As a consequence, the expressions 5.6 and 5.7 constitute second order degree equations that depend only on z: they can be analytically solved to obtain z at any state of charge.

The intensity of the O3 and P3 phases has been previously calculated with the pseudo-Voigt fittings. This measurements will be validated by integrating an angular range around the reflection $(0\,0\,3)$. A constant background has been subtracted from the patterns, the same as the one used for the pseudo-Voigt refinements and shown in Fig. 5.5 with a dotted line. Moreover, the patterns have been corrected by the angle dependent intensity affecting factors gathered in Table 2.1, which include Be window and Al foil attenuation, thermal factor, Lorentz polarization factor, irradiated sample volume change and powder ring distribution factor. In Fig. 5.11 the effect of the different factors is presented. In the region of the $(0\,0\,3)$ reflection, between $2\theta = 16^\circ$ and $2\theta = 17.5^\circ$ where the reflections in Fig. 5.3a can be seen, the intensity varies less than 5%. The integrated angular range has been chosen broad enough to include the $(0\,0\,3)$ peak of both phases, O3 and P3: $15^\circ \leqslant 2\theta \leqslant 18^\circ$ for the cell charged to 4.0 V (Fig. 5.3) and $18^\circ \leqslant 2\theta \leqslant 21^\circ$ for the cell charged to different upper voltage limits (Fig. 5.7). This allows to compensate the intensity loss of the O3 phase due to the onset of the O3-P3 transition, and hence, avoiding any bias that it might have on the estimated amount of migrated Fe. The integrated intensity, as opposed to the one obtained from the pseudo-Voigt refinements, does not depend on the quality of the refinements (especially when the peaks get broader and their detection is difficult), and offers a more systematic method, which allows to obtain fast and reliable information.

The orange dots in Fig. 5.12b show the evolution of the intensity I/I_0 of the $(0\,0\,3)$ reflection vs. the sodium content x, calculated as described above from the integration of the angular range shown in Fig. 5.3a. Together, and as open gray diamonds, the values obtained with the pseudo-Voigt refinements are shown for comparison. The values obtained with both methods agree, which corroborates their validity. The normalized intensity I/I_0 simulated without iron migration as calculated from equation 5.6 (or equation 5.7) with $z = 0$ and x and d as shown in Fig. 5.6 is also presented in 5.12b as a dashed line. Both simulated and experimental intensities are in good agreement until $x \approx 0.6$ ($V = 3.40$ V). This confirms that the intensity increase can be ascribed to the increased contrast between Na and FeO_2 layers as a consequence of the Na extraction from the Na layers without the need to consider any other change in the occupancies. However, before the end

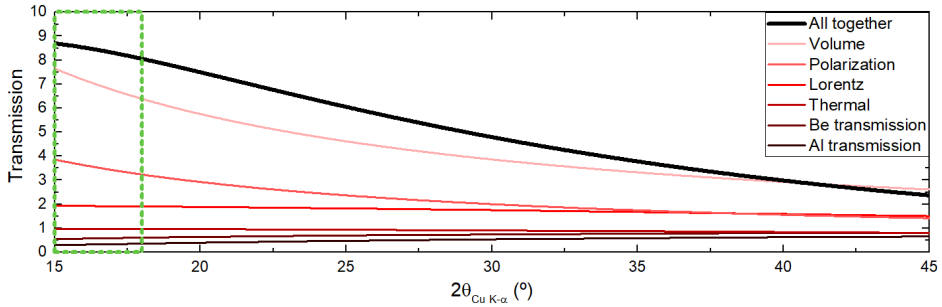

Figure 5.11: Transmission of XRD intensity in the whole measured angular range during *operando* measurements, considering the attenuation factors gathered in Table 2.1. Marked with a dashed rectangle, the area corresponding to the vicinity of the $(0\,0\,3)$ reflection.

of the charge is reached the experimental intensity evolution starts to depart from the simulation to finally decrease for sodium contents below 0.55 ($V = 3.52$ V) until the end of charge, reaching intensity values well below the pristine one. This means that additional atomic arrangement or occupancy changes are occurring, besides sodium extraction.

Since the reflection studied here is $(0\,0\,3)$, the changes in occupancies revealed by the difference between the simulated and the experimental intensities must be occurring in the c direction, and it cannot be caused by Na alone. A change in the oxygen occupancy is unlikely, since the oxygen evolution for this compound has been detected at significantly higher voltage values, $V \geqslant 4.0$ V [24]. Changes in Fe occupancy, and more precisely Fe migration into the Na layers, appears to be the most likely source of difference between simulated and experimental intensities. The experimental XRD patterns and simulations are compared in Fig. 5.9b. Comparing the relative intensities of the $(1\,0\,1)$ and $(0\,1\,2)$ reflections between the experimental and the simulated patterns, the charged state resembles more to the pattern in which the Fe migration has been simulated to the tetrahedral sites in the Na layers (gray tetrahedra in Fig. 5.9a). Furthermore, transition metal migration to tetrahedral vacancies has been previously reported for this and other layered oxides [2, 10, 19–22]. Therefore, the difference between the simulation and the experimental intensities has been considered to come from the migration of iron ions in the tetrahedral sites. Thus, the amount of migrated Fe z has been estimated using the equation 5.6 and the results are plotted in Fig. 5.12c with solid up triangles. In order to compare the effect that the iron would have when it migrates to different sites, Fe migration to octahedral sites has also been estimated using equation 5.7, and the results are plotted in Fig. 5.12c with down open triangles.

At half charge, around $x = 0.6$, the experimental and simulated intensities start to depart, indicating the onset in the iron migration. The results, in Fig. 5.12c, show that the migration to the two distinct sites affect the intensity in similar ways, and thus, the estimated Fe migration is similar in both sites. The migrated iron z linearly increases until the end of charge, where a maximum of $\approx 35\%$ of migrated Fe to tetrahedral vacancies ($\approx 40\%$ to octahedral sites) has been estimated. Interestingly, as can be seen by comparing Figs. 5.6 and 5.12, this migration initiates

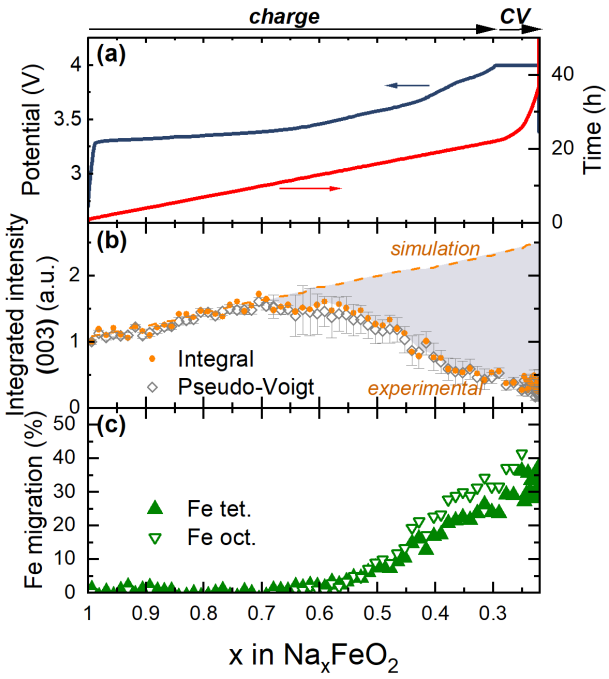

Figure 5.12: Analysis of the intensity evolution of the $(0\,0\,3)$ reflection of the *operando* XRD data of $NaFeO_2$ charged to high voltage (4.0 V) of Fig. 5.3 as a function of sodium content. **(a)** Voltage (left axis) and time (right axis) evolution. **(b)**Simulated intensity considering that no atomic rearrangement occurs besides the sodium extraction (dashed line) and experimental intensity of $(0\,0\,3)$ reflection: integrated intensity (orange points) and the sum of the intensities obtained for O3 and P3 phases from pseudo-Voigt refinements (gray diamonds, see Fig. 5.6d). The difference between simulated and experimental intensities has been shadowed in gray for clarity. **(c)** The estimated Fe migration to the tetrahedral (solid up triangles) or octahedral (open down triangles) vacancies in the Na layers calculated with equation 5.6. The numerical results can be found in Table B.1.

simultaneously with the collapse of the interlayer distance. The two phenomena appear thus to be intimately correlated. This could be explained by a screening of the oxygen-oxygen repulsion and the creation of O-Fe-O bonds when Fe migrates to the depleted Na interlayers. The formed covalent O-Fe-O bond will be stronger than the initial ionic O-Na-O bond [18], and it will thus result in a shorter interlayer distance. Nonetheless, a reduction in the interlayer distance has also been described as a change in the balance between the repulsive Coulombic forces and attractive Van der Waals. As such, the actual reason for the shrinking is still unknown. It is worth noting that since the beginning of the Fe migration at $x \approx 0.55$ until the end of charge at $x \approx 0.2$, approximately 35% of the iron ions have migrated to the tetrahedral sites. Thus, for each sodium extracted, one iron moves to the Na layer.

A similar analysis has been carried out for the *operando* XRD patterns of Fig. 5.7. The corrected and normalized experimental intensity of the low angle region (Fig. 5.7a) is presented in Fig. 5.13b

as dots. The expected intensity without TM migration, as a dashed line in 5.13b, has been estimated from the expression 5.6 for $z = 0$. As in the previous case, both simulated and experimental values agree well until $V = 3.42$ V ($x = 0.60$, $t = 12.25$ h). At larger voltages the experimental intensity is lower than the calculated for $z = 0$, which indicates iron migration to Na layers. Fe migration to tetrahedral sites has been estimated according to expression 5.6, and the results are presented in 5.13c.

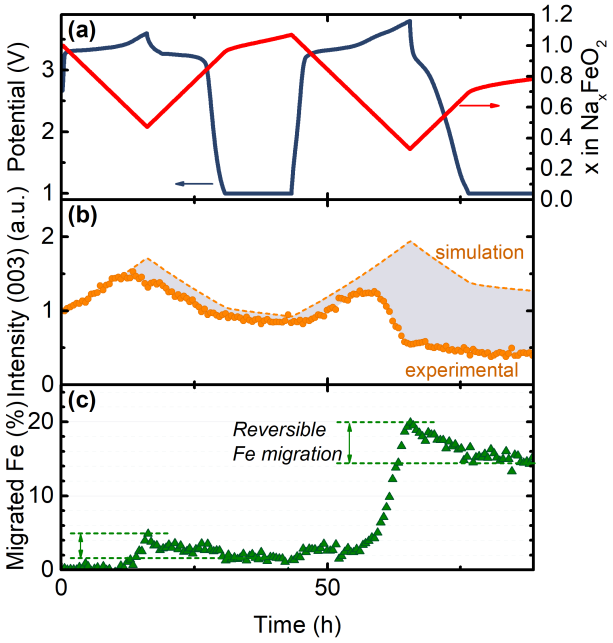

Figure 5.13: Estimation of Fe migration of $NaFeO_2$ upon cycling. **(a)** Voltage and sodium content profile as a function of time. **(b)** Experimental integrated intensity (scatter data) and intensity from simulations considering no Fe migration (dashed line) of $(0\,0\,3)$ reflection. The difference has been shadowed in gray for clarity. **(c)** Estimated Fe migration to tetrahedral vacancies in Na layers calculated with equation 5.6. The numerical results can be found in Table B.2.

During the first cycle the maximum migrated Fe reaches 5% at the end of charge to 3.6 V. Surprisingly, this migration appears to be partially reversible upon discharge, as migrated Fe is reduced down to less than 2% at the end of the first discharge; this corresponds to almost 67% of the migrated iron moving back to its original site. During the second charge to 3.8 V, the amount of migrated iron reaches 20%, and after the subsequent discharge only 14.5% remains in Na layers, corresponding to 27.5% of the migrated iron moving back to its original site. As has been observed for the previous cell, it can be seen by comparing Figs. 5.8 and 5.13 that the iron migration starts upon charge concomitantly with the decrease of the interlayer distance, which confirms the intimate correlation between both phenomena.

Although Fe migration has been found to be surprisingly partially reversible, this reversibility depends on the upper voltage limit, and the remaining migrated Fe is progressively accumulated in successive charges. When cycled in the conservative voltage window, as shown in Fig. 4.1, the Fe migration is low and mostly reversible so that there is a slow capacity decay and polarization is only slightly increased in each cycle. However, increasing the upper voltage limit results in an increase of Fe migration and a decrease of its reversibility, inducing an increased polarization upon cycling, and as a consequence, a decaying capacity, as seen in Fig. 4.3. The migration of Fe into the Na layers appears thus to be intimately related with the structural evolution occurring above 3.4 V which induces the poor capacity retention of the material when charged beyond $x \approx 0.6$.

5.3 *In-situ* structural characterization by Mössbauer spectroscopy

Mössbauer spectroscopy measurements should allow to distinguish between the initial Fe^{3+} and Fe^{4+} in octahedral sites of the FeO_2 layers as well as to which sites Fe migrates and with which oxidation state (Fe^{3+} or Fe^{4+}). Since good quality Mössbauer spectra require several hours acquisition time, *operando* measurements have been discarded, as the cell would have required a very slow cycling rate or it would cover a large composition range. *In-situ* measurements have been done instead, this is, the charge-discharge process has been done by successive galvanostatic charge and discharge steps, followed by open circuit voltage relaxation prior to the Mössbauer data acquisition. More details can be found in the Section 2.4 in the experimental chapter (Chapter 2).

Fig. 5.14 presents the *in-situ* Mössbauer absorption spectra and corresponding refinements at several states of charge, together with the electrochemical curve at which the spectra have been taken: left hand side for the measurements done during charge and right hand side for the discharge. The patterns refined with various signals are shown in Fig. 5.14(b-i), and the corresponding relative intensities are shown with columns in Fig. 5.14a, labeled with the panel name of the corresponding spectrum. Up to four different iron environments have been detected. The refinements have been done using MossA software [25]. The numeric results of these measurements are gathered in Table B.4.

In the initial measurement, in Fig. 5.14b, a main doublet corresponding to Fe^{3+} in an octahedral site can be seen (from now on, oct. *A*). Its central shift, of CS ≈ 0.35 mm s^{-1}, indicates the iron (III) oxidation state, and together with the quadrupole splitting of QS ≈ 0.5 mm s^{-1} corresponds well with the values expected for a octahedral coordinated Fe^{3+} (see Fig. 2.14b for the values expected for the different Fe signals). Indeed, the values obtained for this initial spectrum are in good agreement with those shown in Fig. 3.5 for the pristine sample in powder form. This signal has been drawn in black in Figs. 5.14 and 5.15. The Fig. 5.15 shows the parameters of each signal as a function of CS (x axis) and QS (y axis). It can be seen that the different signals observed and that will be described below, are gathered in different regions, depending on the environment and the oxidation state of iron.

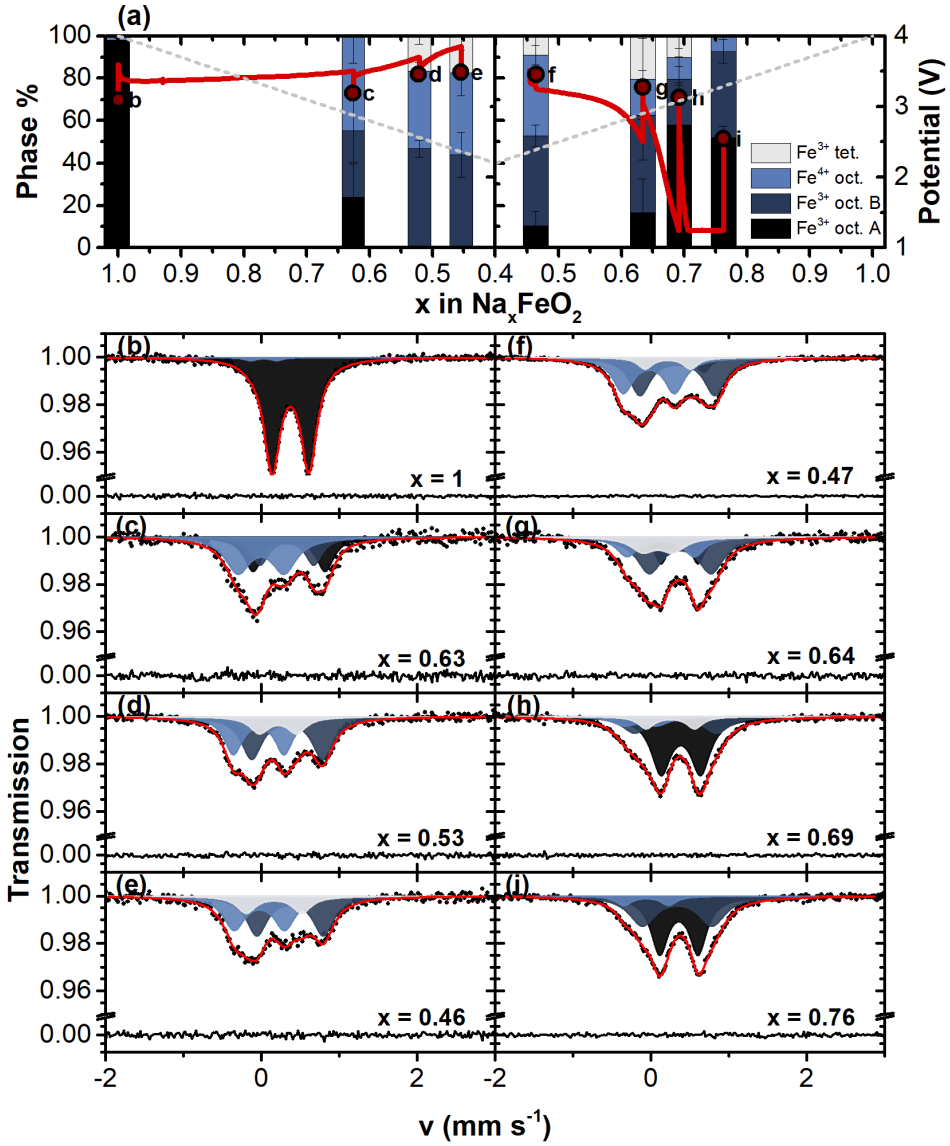

Figure 5.14: **(a)** Electrochemical curve (red line, right axis) and phase percentage of the different Fe environments. From dark to light: Fe^{3+} in octahedral site as in pristine sample (oct. A), Fe^{3+} in distorted octahedral site (oct. B), Fe^{4+} in octahedral site and Fe^{3+} in tetrahedral site. With a dashed gray line the expected Fe^{3+} content assuming no parasitic reactions, this is, that each extracted (inserted) Na corresponds to an oxidized (reduced) iron ion. **(b-i)** Refined Mössbauer spectra at several states of charge, indicated in panel (a). Scatter points corresponds to experimental absorption data after normalization, red and black solid lines correspond to the fitting and the difference respectively and different iron environment signals have been shadowed with the same color code as in the panel (a).

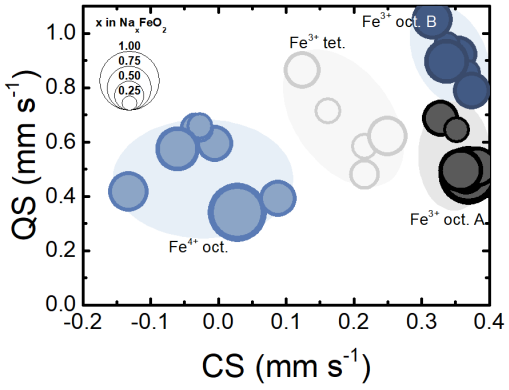

Figure 5.15: Refinement results of the *in-situ* Mössbauer measurements of $NaFeO_2$ shown in Fig. 5.14. Data is gathered as a function of CS (x axis) and QS (y axis). Different Fe environments are colored differently, and sodium content of each point is reflected with the symbol size.

A slight asymmetry in the initial Mössbauer spectrum (Fig. 5.14b) required the addition of a second doublet. It shows a lower central shift, around 0 mm s^{-1}, which corresponds to Fe^{4+} signal, because the shielding effect for the s-electrons is weak in Fe^{4+} [26]. The quadrupole splitting value, around 0.5 mm s^{-1}, indicates that Fe^{4+} sits in an octahedral environment. Its presence is quite low in this initial spectrum, about $2 \pm 2\%$ (see the column graph in Fig. 5.14a), indicating a slight sodium deficiency which might come from the synthesis or the manipulation of the material (during electrode preparation or cell assembly). The value is very low, within the error of the ICP-OES measurement, and too low to induce any detectable change in the XRD patterns. This highlights the high detection capability of the Mössbauer technique. This signal is presented in light gray color in Figs. 5.14 and 5.15. It appears clearly from 5.14a that when sodium is extracted (introduced) from the structure the Fe^{4+} content increases (decreases). The amount of Fe^{4+} detected with the Mössbauer technique matches within the error bars, with the values expected for the electrochemical reaction based only on the iron redox reaction. The expected value is presented in Fig. 5.14a as a gray dashed line. This confirms that no other redox or side reaction is occurs, at least in significant amounts, besides the expected $Fe^{3+/4+}$ reaction, and that it is reversible.

When $\approx 40\%$ of sodium is extracted from the structure, besides the previously described Fe^{3+} oct. *A* and Fe^{4+} oct. sites, a third doublet is needed to correctly refine the spectrum (Fig. 5.14c). This doublet has a central shift of CS ≈ 0.35 mm s^{-1}, close to the Fe^{3+} oct. *A* signal. Its quadrupole splitting is however larger, QS ≈ 0.90 mm s^{-1}. From this values it can be deduced that it corresponds to a Fe^{3+} ion in a distorted octahedral environment (from now on, oct. *B*). Indeed, the higher QS value compared to the oct. *A* site comes from a lower symmetry of the electric field, which might come from an inhomogeneous sodium extraction that distorts the surrounding octahedra. This oct. *B* site is presented in dark blue color in Figs. 5.14 and 5.15. The presence of two Fe^{3+} oct. sites, one of them showing a lower symmetry, has been previously reported for

other layered oxides [15]. In Fig. 5.14a it can be seen how Fe^{3+} oct. *A* decreases fast in favor of the oct. *B* signal upon charge, and already when charged to 3.7 V ($x = 0.53$) (Fig. 5.14d) the site oct. *A* is no longer detected. It is partially reverted on discharge, suggesting a partial structural reversibility. It confirms thus the structural changes described with *operando* XRD. At the end of discharge still close to 40% of the octahedral site remain as distorted *B* sites, which indicates that the original structure is not completely recovered on discharge, as observed in the *operando* XRD measurement after charging to high voltage values (see the end of discharge from 3.8 V in Figs. 5.7 and 5.8).

The distorted Fe^{3+} octahedra (Fe^{3+} oct. *B*) can be explained as the proximity of distorted Fe^{4+} octahedra and sodium vacancies. Indeed, as shown in the introduction (Fig. 1.20), Fe^{4+} ion is JT active, that is, it is a distorted octahedra.

On further desodiation, when close to 50% of the sodium has been extracted (Fig. 5.14d) a fourth signal is required for a correct fitting of the spectra. This signal has an intermediate central shift value between the already presented Fe^{3+} and Fe^{4+} octahedral signals, CS $= 0 - 0.3$ mm s^{-1}. It has been assigned to Fe^{3+} in a tetrahedral environment. Indeed, in a tetrahedral site the iron is four-coordinated, while it is six-coordinated in an octahedral site. Since metal-ligand bonds are shorter when coordination number is lower, there is less overlap of antibonding t_{2g} orbitals, resulting in lower central shift [27]. Thus, a lower central shift is expected for an iron lying in a tetrahedral environment than for one migrated to octahedral site or remaining in the initial site. This iron in the tetrahedral site corresponds to the migrated iron described based on *operando* XRD data (Section 5.2.1). In Fig. 5.14a it can be seen that iron migration is reversible on discharge. In this case, differently to what has been described in previous section, the reversibility is complete and not partial. However, and considering the approximations used during the *operando* XRD data analysis, the mechanism is confirmed. Moreover, the absolute values of migrated iron at 3.8 V obtained with the two techniques are very similar: $\approx 20\%$ for *operando* XRD (end of second charge in Fig. 5.13) and $17 \pm 15\%$ for Mössbauer data (Fig. 5.14e).

The fact that the migrating Fe ion is Fe^{3+} and not Fe^{4+} has some implications. If Fe in tetrahedral site has its oxidation state fixed to Fe^{3+}, capacity from $Fe^{3+/4+}$ redox will be limited by the ions in the tetrahedral sites. In the case presented in Fig. 5.12, for example, as 35% of the iron is migrated, and thus, if its oxidation state is fixed to 3+, only 65% of the theoretical capacity ($\approx$ 157 mA h g^{-1}) is accessible. However, this alone should not be a major issue if reversible. Based on Mössbauer measurements, the migration seems to be fully reversible on discharge, but the structural transformation is not as seen by *operando* XRD and confirmed by the presence of Fe^{3+} oct. *B* sites on discharge in the Mössbauer measurements. The structural transformation might be cumulative upon cycling, as well as the iron migration. Indeed, *operando* XRD results show that the reversibility is decreased as the charge voltage is increased causing a deterioration in its electrochemical performance (see Figs. 5.7, 5.8 and 5.13).

From these measurements, it seems that the major issue with the electrochemical irreversibility observed in $NaFeO_2$, is related to structural irreversibilities, as observed with *operando* XRD, and

not so much with the irreversibility of iron migration. However, although the iron migration seems to be reversible according to Mössbauer spectroscopy, the intensity of the $(0\,0\,3)$ reflection was not recovered on discharge as shown during the *operando* XRD measurements. The difference in the reversibility can be related to the difference between *in-situ* and *operando* measurements. In this scenario, allowing the material to relax seems to help with the reversibility of the migration. It is worth noting that the reversibility is high when the upper voltage is limited to about 3.5 V, and is decreased when charged to higher voltage values. It might occur that at high voltages other reactions occur, such as oxygen redox or electrolyte decomposition. In the following section, a characterization of the charged state to high voltages will be presented.

5.4 Structural characterization at high voltage charge state

As seen in the charged state XRD patterns in Figs. 5.3 and 5.7, the crystallinity of the material is reduced as a consequence of the sodium extraction and iron migration. This is also reflected in the increment of the Fe^{3+} oct. *B* site in Mössbauer measurements. Thus, the diffracted peaks in XRD patterns become broader and harder to detect. Moreover, *operando* and *in-situ* measurements have the added difficulty of the signals from the cell components, such as Be window, Al foil, conductive carbon and electrolyte, that difficult the detection of low intensity or broad signals appearing upon cycling. Therefore, and in order to avoid these difficulties, *ex-situ* measurements will be carried out in desodiated samples.

5.4.1 *Ex-situ* characterization

High resolution *ex-situ* XRD measurements have been carried out in powder form inside quartz capillaries at ALBA synchrotron. Electrochemically and chemically desodiated Na_xFeO_2 samples have been prepared, with a sodium content of $x \approx 0.20$.

The main advantages of the chemical desodiation are the absence of additives (the material is not mixed with carbon) or electrolyte traces, although rests of oxidizing agent could be present if the washing is not done properly. Also, the chemical desodiation tends to be less aggressive for the material, as it is done on the event of several hours with a good wetting of all the particles, and thus, the desodiation is done over the whole surface of the particles in a uniform way [28]. The preparation of the electrochemically and chemically desodiated materials is explained in the experimental Sections 2.6.1.1 and 2.6.1.2 respectively.

The XRD patterns of the chemically and electrochemically desodiated samples are presented in Fig. 5.16. The electrochemically desodiated sample presents a broad background at $5^\circ \leqslant 2\theta \leqslant 17^\circ$, which has been highlighted in gray, that corresponds to the signal of conductive carbon additive. Traces of electrolyte salt ($NaClO_4$) are also present in this sample, which have been highlighted with $*$ symbols. The reflections corresponding to the sample are very similar in both cases. Nonetheless, several differences can be noticed between the two samples, mainly in the relative intensities of the reflections. The inset of Fig. 5.16 shows a zoom of the region where the

reflections $(0\,0\,\ell)$ corresponding to the interlayer distance should appear. In both samples two different reflections can be seen, but with differences in their positions and relative intensities.

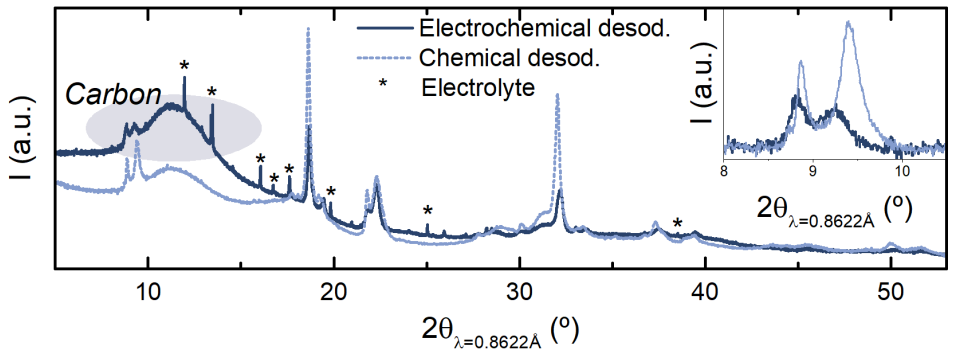

Figure 5.16: *Ex-situ* high resolution XRD patterns of electrochemically (dark blue) and chemically (light blue) desodiated Na_xFeO_2 samples. Electrolyte salt traces are highlighted with $*$ symbols. In the inset, a zoom in the low angle region of the patterns whose background has been removed. Measurements done in quartz capillaries and with a wavelength $\lambda = 0.8622$ Å. Highlighted in gray, the background increment due to the carbon present in the electrochemically desodiated sample.

Despite the structural differences between the desodiated samples with the two methods, Le Bail XRD refinements have been carried out in the chemically desodiated sample in order to try to understand the crystalline structures formed upon desodiation. The chemically desodiated sample was chosen due to the lack of reflections of electrolyte salt and lower background signal.

Layered oxides tend to suffer from layer gliding, transforming into distorted or different layered oxides [8, 14, 29–34], but due to TM migration, they can also transform into spinel-like structures [2, 18, 35–37]. In this case, the lack of reflections in the $12° \leqslant 2\theta \leqslant 17°$ region, discards the option of an ordered spinel-like structure. Also, only two reflections can be distinguished around $2\theta \approx 9°$, thus, two different layered oxides are expected. Several layered structures have been tested, such as O3 and P3 (space group $R\bar{3}m$), P2 ($P6_3/mmc$), monoclinic distorted O'3 and P'3 ($C2/m$) or OP4 ($P\bar{6}m2$). The monoclinic distorted phases are defined with different crystal space groups than the original structures, but they can be described as inclined phases. The distortion can be detected in XRD measurements by the splitting of several reflections. In Fig. 5.17 an example of an O3 structure distortion is shown.

Examples of refinements consisting of a combination of O3, P3 and monoclinic distorted phases are shown in Fig. 5.18, and the refined parameters are presented in Table 5.2. Unluckily, a good refinement could not be obtained: peak shape is not correct and many peaks remain unidentified. However it can be seen how at least one of the present phases has a monoclinic distortion. The refinement done with non-distorted O3 and P3 phases (Fig. 5.18a) can correctly determine the position of the peaks at $2\theta \approx 22°$ (green inset), but then the position of the peaks at $2\theta \approx 9°$ (blue inset) is not correctly determined. This does not happen in the other refinements, where at least one of the phases presents a monoclinic distortion. Indeed, the monoclinic structure, and thus the

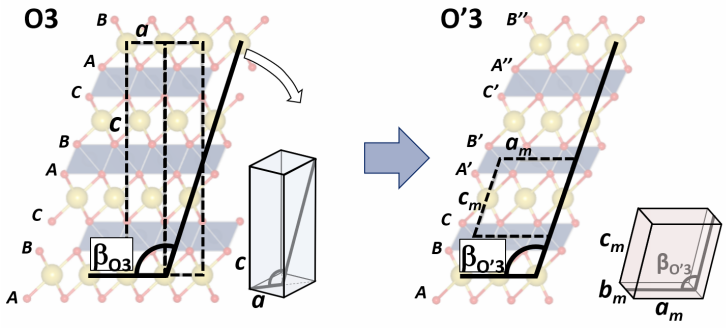

Figure 5.17: Schematic description of a monoclinic distortion from O3 (space group $R\bar{3}m$) to O'3 (space group $C2/m$). The yellow spheres represent the sodium ions, the blue octahedra the iron ions and the red spheres the oxygen ions. An increment in the inclination of the structure results in a change in the symmetry and the need to change the space group definition. The ABCABC stacking of the O3 is transformed into an ABCA'B'C' stacking, where the prime symbol represents a horizontal displacement. A representation of the unit cell (not to scale) is shown to the right of each structure, where the free cell parameters are presented.

position of the reflections, is more flexible: while in the monoclinic distorted phases a, b, c and β can be independently refined, only a and c can be refined in the non-distorted phases. The best refinement has been obtained with both monoclinic distorted phases (Fig. 5.18). Nonetheless, it has to be taken into account that Le Bail refinements tend to be improved with increased amount of reflections because each reflection's intensity is individually calculated. One needs to be cautious with the amount of phases and free variables in this kind of refinements. Here we have focused in two distinct zones, shown in the insets of Fig. 5.18: in the $8^\circ \leqslant 2\theta \leqslant 10^\circ$ region where the $(0\,0\,3)$ peak is present in the pristine phase; and in the $21^\circ \leqslant 2\theta \leqslant 23^\circ$, where the $(1\,0\,4)$ peak is present in the pristine phase. The width and shape of the peaks have been fitted attending to the results in the low angle region. It seems that at least one of the phases has suffered from a monoclinic distortion, although the fits presented here are not sufficient to determine whether is the main phase, the secondary or both.

Based on the previously presented results and on the literature [32, 38, 39], the most likely scenario seems to correspond to the initial O3 phase plus a monoclinic distorted P'3 phase, and during further analysis, this situation will be considered.

The stability of the charged material has been studied by means of operando HRXRD under a thermal treatment. For this measurement the chemically desodiated sample sealed in a quartz capillary has been heated up to 300 K while recording XRD patterns. The results are presented in Fig. 5.19. Although the description of the material is complex, this measurement under thermal treatment can give an insight of the present structures.

It can be seen that the structures are stable up to 190°C, maximum temperature reached during this measurement. Indeed, the reflections shift, but there are no appearing or disappearing

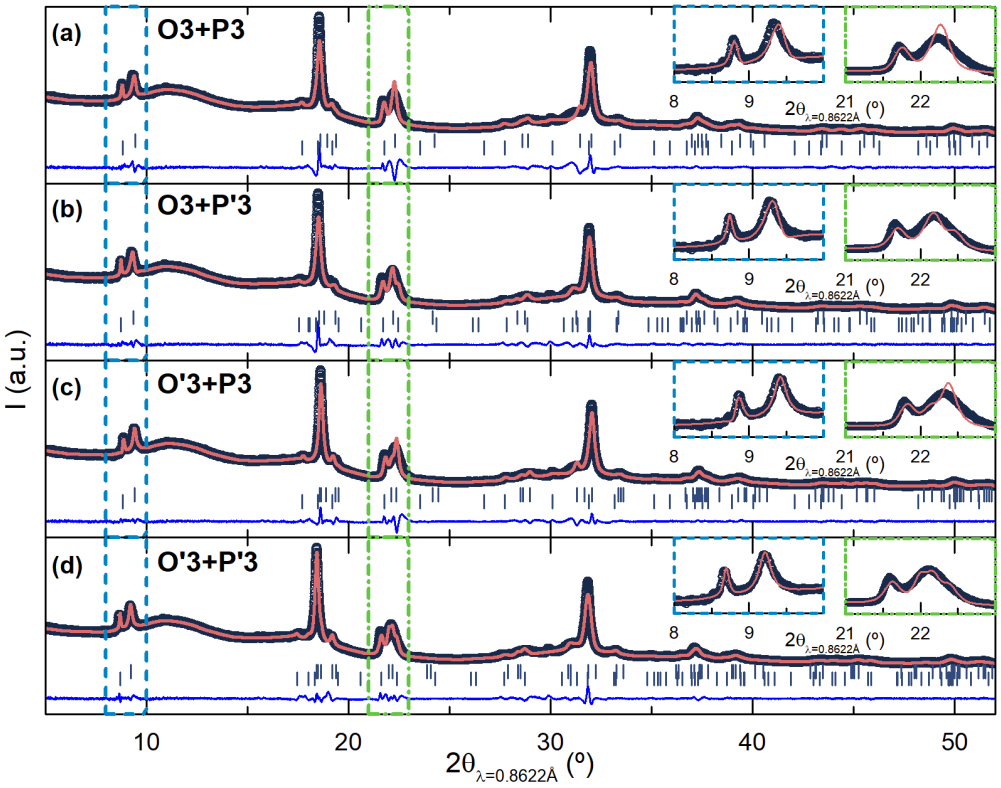

Figure 5.18: Le Bail refinements of chemically desodiated Na_xFeO_2 high resolution XRD pattern. The refinements have been done with the following phase combinations: **(a)** O3 + P3, **(b)** O3 + P'3, **(c)** O'3 + P3 and **(d)** O'3 + P'3. The results of the refinements are gathered in Table 5.2.

peaks, meaning that the cell parameters do change, but the space groups to which these structures belong are not. The reflections have been labeled according to the O3 and P'3 phase as refined in Fig. 5.18b. Up to 100°C only a slight shift of all the reflections to lower angles can be seen, which reflects that the material expands due to the increased temperature. That is, the present structures are stable. Above 100°C two different behaviors are observed for these two structures: while the thermal expansion of the P'3 phase continues linearly, the O3 structure changes the trend. The reflections shift to higher angles, reflecting a decrease of the cell parameters (both in-plane and interlayer). It can also be seen that the intensity of the $(0\,0\,3)_{O3}$ reflection decreases with increasing temperature, which together with the interlayer distance shrinking, points to a thermally activated Fe migration to the Na interslabs. However, as reflected by the shift of the $(1\,1\,0)_{O3}$ reflection, the in-plane distance is also decreased, as opposed to what has been observed in the *operando* XRD measurements earlier in this chapter. It seems therefore that the thermally activated Fe migration is related to a instability of the structure. However, it can be seen that the space group is not changing as the present reflections shift, but there are no new or disappearing

Table 5.2: Le Bail or pattern matching refinement parameters of the different fittings of an *ex-situ* high resolution XRD pattern of charged Na_xFeO_2: space group (S.G.), cell parameters and agreement factors. The name *Patt.* refers to the refinements presented in Fig. 5.18.

Patt.	Phase	S.G.	Cell parameters				Agreement factors		
			a	b	c	β	R_b	R_p	χ^2
(a)	O3	$R\bar{3}m$	2.99(7)	-	15.05(6)	-	0.392	2.24	6.55
	P3	$R\bar{3}m$	3.01(8)	-	16.08(6)	-	2.09	27.6	
(b)	O3	$R\bar{3}m$	3.00(2)	-	15.18(3)	-	0.176	1.89	3.78
	P'3	$C2/m$	5.28(2)	3.15(1)	5.87(1)	112.7(1)	0.700	23.2	
(c)	O'3	$C2/m$	5.182(4)	2.992(4)	5.345(5)	109.77(6)	0.235	1.74	3.63
	P3	$R\bar{3}m$	3.005(5)	-	16.08(3)	-	0.842	21.4	
(d)	O'3	$C2/m$	5.230(5)	2.975(3)	5.429(6)	108.73(7)	0.130	1.66	2.85
	P'3	$C2/m$	5.286(4)	3.132(4)	5.897(7)	112.55(7)	0.150	1.88	

reflections.

The in-plane ordering should be similar for the two phases in order to coexist in a single particle without strains. It seems that in this case, above 100°C the evolution of both phases diverges, and the in-plane distance of the two phases dissociate. One way that could explain this behavior is that cracks might be formed between the two structures, and with increasing temperature, these cracks open completely breaking the particles in two. At this point, the strains would be avoided, allowing further evolution of the O3 structure while the P'3 stays stable.

When the material is cooled back to 30°C the changes occurred during the heating are not reverted, reflecting that the structural changes, although thermally activated, are stable. Within the previously described scene, where O3-type and P'3 type particles are separated, it is reasonable to think that these changes would not be reverted upon cooling.

A better knowledge of the present phases can be obtained with *operando* measurements, as the evolution of the different reflections can be followed from the beginning. Reflections from possible impurities can be easily discarded, as they will not react during the electrochemical tests and they will remain static throughout the measurement. New reflections can also be described as the splitting of a peak (for example, due to a distortion of the structure) as in a solid solution reaction or as the appearance of a new phase due to a biphasic reaction mechanism.

5.4.2 *In-situ* characterization

To overcome the difficulty in identifying new peaks appearing in *ex-situ* measurements and to be able to follow the reactions occurring during the electrochemical cycling, an *operando* synchrotron XRD measurement was carried out at Australian Synchrotron by N. Sharma and L. Dujandhi. In this case, a laminated electrode was cycled inside a modified coin cell, which has flexible Kapton

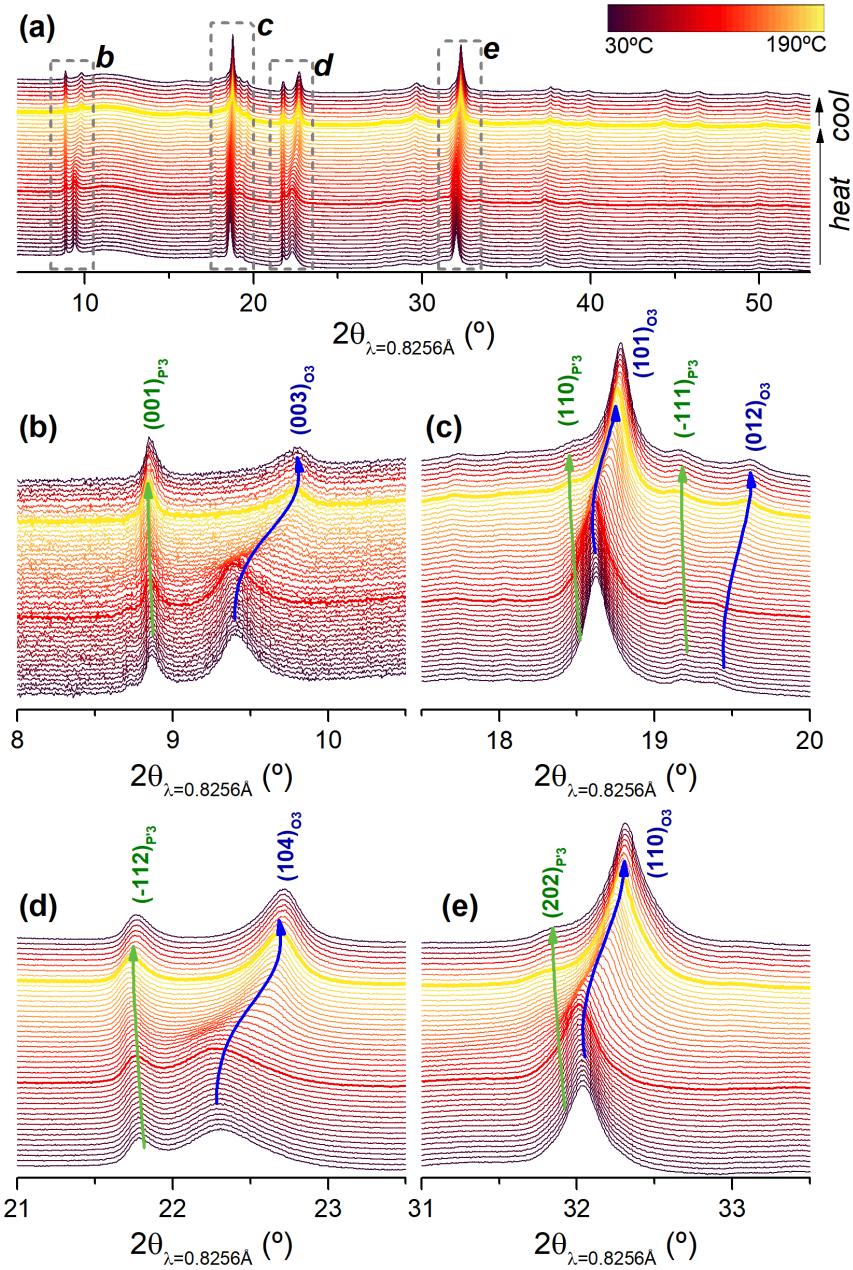

Figure 5.19: High resolution XRD patterns of chemically desodiated $NaFeO_2$ under a heat treatment. Patterns collected from 30°C up to 190°C and cooled back to 30°C. **(a)** A general overview of the patterns under a heat treatment. **(b-e)** Zoomed regions of representative reflections, areas highlighted in panel (a) with gray dashed rectangles. The patterns at 100°C and 190°C are highlighted with a thick red and yellow line respectively. The reflections have been labeled according to the fitting presented in Fig. 5.18b, with the shift of the O3 and P'3 phase's reflections highlighted with blue and green arrows respectively. Measurements carried out at ALBA synchrotron by M. Reynaud, C. Berlanga, A. Bustinza and M. Galceran.

windows in the anode and the cathode sides. The results are shown as 2D XRD in Fig. 5.20(a-c). Although the electrochemical curve (Fig. 5.20d) seems to be appropriate with the 50% of the theoretical capacity and without any appreciable polarization upon charge, the XRD patterns do not show any structural changes, as if no reaction was occurring at all. A similar *operando* XRD measurement of $NaFeO_2$ was published by Lee et al. in 2015 [32]. However, in-lab *operando* measurements presented earlier in this chapter, showed that structural changes do occur upon cycling. The lack of structural changes seem to be the result of a delayed reaction in the measured zone, due to the lack of pressure that the flexible windows put in the region, as it has been reported previously [40, 41].

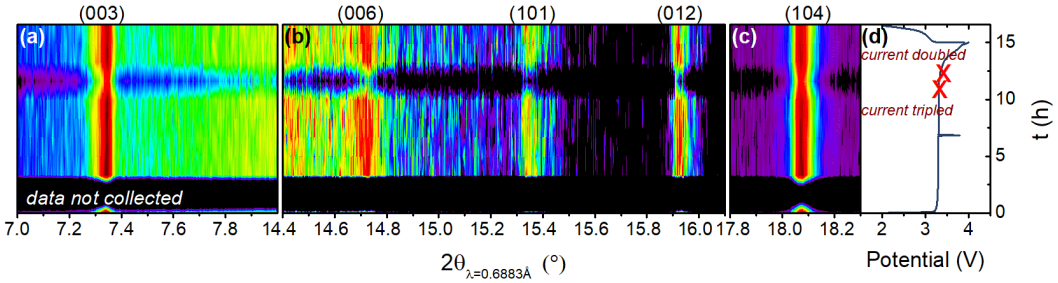

Figure 5.20: **(a-c)** *Operando* XRD measurements in a modified coin-cell for selected angular ranges. **(d)** Voltage evolution as a function of time. Measurements carried out at the Australian Synchrotron by L. Djuandhi and N. Sharma.

Thus, the same swagelok type cell used for the *operando* measurements presented earlier (see for example Figs. 5.3 and 5.7) has been used for synchrotron measurements. However, to allow the transmission mode, the current collector of the anode side has a 2 mm hole to allow the beam to go through the cell. The powder material is located between the rigid Be window cathode side current collector, and separator and metallic Na.

An *operando* XRD measurement has been done upon charge at CIC Energigune, after which the cell has been taken to ALBA synchrotron for a high resolution XRD snapshot at charged state. The cell has been allowed to relax several hours after the charge to try to homogenize the reaction in the whole electrode area, and avoid any possible delay in the measurement region.

The Fig. 5.21(d-f) shows a 2D representation of the *operando* XRD patterns of the cell charged to 4.0 V and hold at that voltage for 15 h to maximize the sodium extraction and iron migration. The structural evolution is very similar to those presented in Figs. 5.3 and 5.7. Interlayer distance increases up to $x \approx 0.62$ ($V = 3.40$ V), and shrinks afterwards to values below the initial ones, as reflected by the shift of the $(0\,0\,3)$ reflection. The in-plane distance reduces continuously as reflected by the shift to higher angles of the $(1\,0\,1\,,\ 0\,1\,2\,,\ 1\,0\,4)$ reflections. The presence of the secondary phase can also be seen to the right of the $(0\,0\,3)$, as shown with the orange arrow in Fig. 5.21d and f.

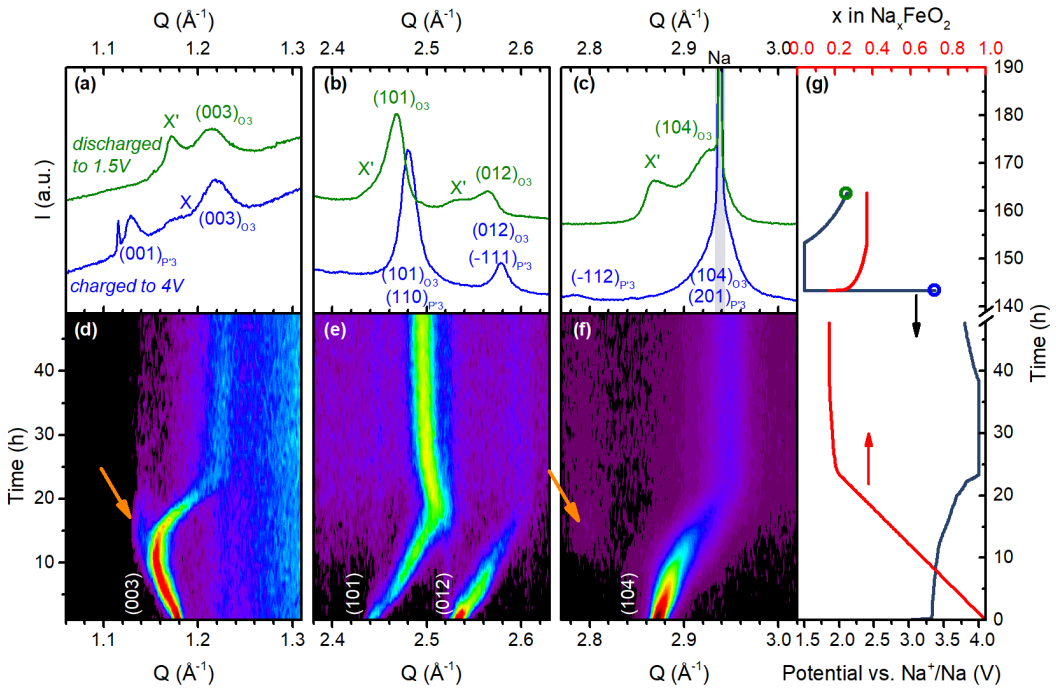

Figure 5.21: XRD patterns of $NaFeO_2$ for selected angle ranges. **(a–c)** High resolution XRD patterns recorded at ALBA synchrotron when charged to 4.0 V (blue) and discharged to 1.5 V (green) states. Na reflection is shaded in gray in panel (c). Reflections are indexed as $R\bar{3}m$ and $C2/m$ space groups, for O3 and P'3 phases respectively. A third phase, named as "X", is visible in charged and discharged states. **(d–f)** Operando powder XRD 2D data plots recorded at CIC Energigune. Note that metallic Na reflection is only visible in patterns taken at ALBA synchrotron in panel (c) due to the transmission geometry used, as opposed to the reflection geometry in other measurements. **(g)** Voltage profile and sodium content as a function of time. The blue and green open circles indicate when the HRXRD patterns of (a–c) were taken at charged and discharged state, respectively.

The blue line in Fig. 5.21(a-c) shows a high resolution XRD pattern of the charged material. In the small angle region ($1.1\ \text{Å}^{-1} \leqslant Q \leqslant 1.3\ \text{Å}^{-1}$) three different reflections can be seen, while only two reflections could be seen in the ex-situ measurements (Fig. 5.16). Based on the *operando* and *ex-situ* XRD analysis done previously, O3 and P'3 phases have been identified with a short and a large d interlayer distance respectively. The third reflection, with an intermediate d distance is an unknown phase, labeled as "X", that is not present in the *ex-situ* measurements in Fig. 5.16. A three phase system has been previously reported for O3-$Na_xFe_{2/3}Mn_{1/3}O_2$ phase near the fully desodiated state [1, 15]. The absence of the pristine phase's reflections at higher angles confirms that it is a new phase and not unreacted material, regardless of the proximity of this reflection to the initial phase's $(0\,0\,3)$ reflection. Mortemard de Boisse et al. [15] suggested that the unknown phase is formed via stacking faults and layer gliding. Furthermore, Somerville et al. [42] described a similar phase, labeled as "Z", as the intermediate between a P- and an O-type structure, with a

random ordering of the O- and P-type interlayers. The present work suggests that TM migration towards Na layers also contributes to the increased disorder of the crystalline structure. Unluckily, the broad and weak reflections prevent a proper refinement of the structure.

Interestingly, the secondary P'3 phase's $(0\,0\,\ell)$ reflection can be seen in the high resolution pattern in Fig. 5.21a, although it was not visible the lab scale measurements at charged state (see Figs. 5.3a and 5.7a). It can be due to (a) the higher resolution of the synchrotron measurements, or (b) the long relaxation process before the high resolution XRD pattern was done that helped the formation of a kinetically slow process to form phase. This second case is further supported by the increment of the P'3 phase's presence after heating due to the improved kinetics.

The cell was then discharged from 4.0 V down to 1.5 V in CCCV (constant current, constant voltage) mode in order to evaluate the structural reversibility after being charged to high voltage values. The discharged pattern is shown in Fig. 5.21(a-c) with the green line. The peaks of the O3 phase appear slightly shifted towards lower angles compared to the charged state pattern (blue line in Fig. 5.21(a-c)). This, together with the reintercalation of about 20% sodium content, suggests that the iron migration and sodium extraction are still partially reversible even in a deeply deintercalated Na_xFeO_2, although the reversibility seems to be lower than that shown for the cell charged to 3.8 V (Fig. 5.7).

One can conclude that the secondary P'3 phase has slow kinetics, and it cannot be detected during *operando* measurements, while it can be seen in *ex-situ* and *in-situ* measurements. This is also true for the disordered "X" phase. Moreover, the disordered phase is not only not reversible on discharge, but its proportion seems to increase at the cost of the P'3 phase, while sodium is at least partially reinserted in the O3 structure.

5.5 Comparison with the state of the art

Operando XRD results of this material has been previously reported by Lee et al. [32]. It can be seen in Fig. 5.22a that there is a big discrepancy between the reported values and the ones presented in this work. Indeed, in the measurements by Lee et al. [32], very little changes can be seen in the interlayer distance. Considering that they report almost half of the theoretical capacity, i.e. 50% of sodium extracted from the structure, it seems reasonable to think that they are measuring a region or particle with none or little electrochemical activity. It is most probably related to a problem of pressure in the measured region due to the cell configuration: a modified coin cell with flexible Kapton windows. That is, the measurement is similar to that presented in Fig. 5.20, measured with a cell of similar characteristics at the Australian Synchrotron.

Li et al. [24] also published an *operando* XRD measurement, although the interlayer distance values are not explicitly presented in the publication. The results are presented in Fig. 5.22b. In their measurement a continuous increment of the interlayer distance can be seen (continuous shift of the $(0\,0\,3)$ reflection to lower angles), without any significant biphasic region.

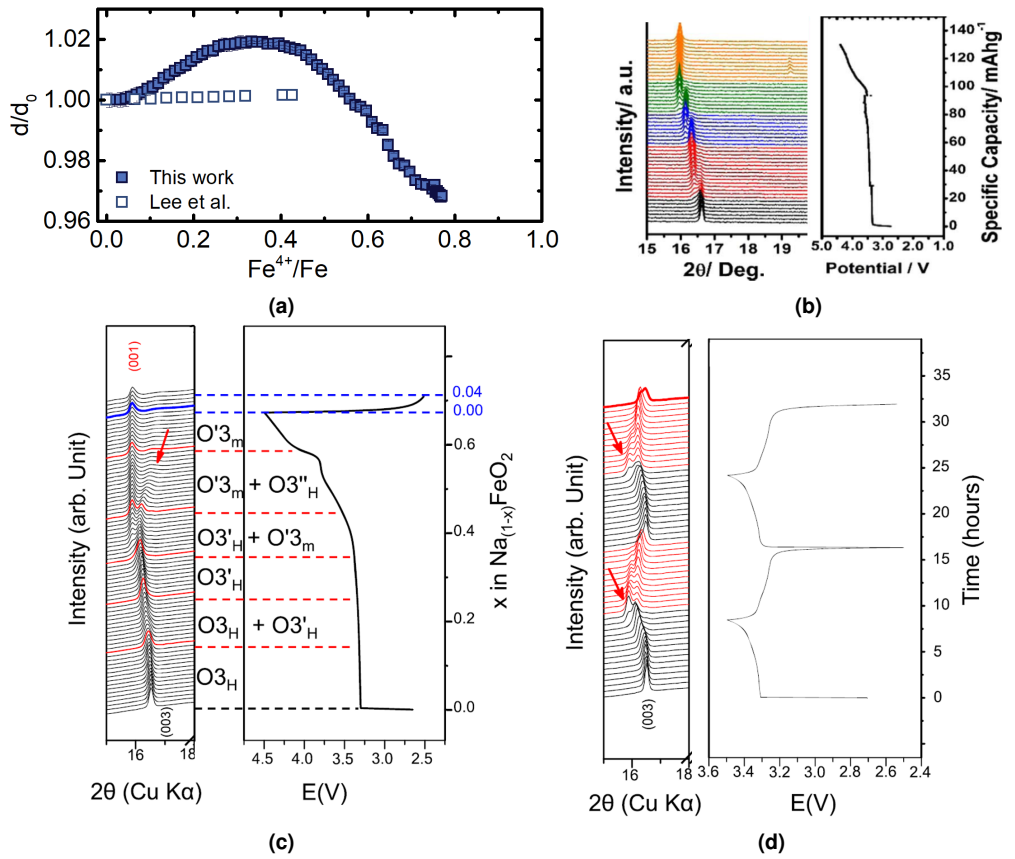

Figure 5.22: **(a)** Evolution of the normalized interlayer distance of O3-$NaFeO_2$ as a function of oxidized iron. Results obtained within this work (solid blue squares) are compared with those reported in the literature by Lee et al. [32] (open blue squares). Evolution of the $(0\,0\,3)$ reflection during *operando* XRD measurements by **(b)** Li et al. [24], and by Susanto et al. [43] **(c)** in the irreversible voltage window (up to 4.5 V) and **(d)** within the reversible voltage window (up to 3.5 V).

Other reports on $NaFeO_2$ structural evolution based on *ex-situ* XRD measurements show a complete transformation from O3 to monoclinic distorted O'3 phase [38, 44]. The difference in the results between the *operando* and *ex-situ* measurements can be related as explained earlier to kinetic limitations. If the formation of monoclinic O'3 phase is slow, its appearance will be limited during *operando* measurements. On the other hand, when the material is allowed to relax, as it happens during the preparation of *ex-situ* samples, the monoclinic phase has time to grow until the whole sample is converted. Indeed, *operando* XRD patterns do not present the peak splitting associated to the monoclinic distortion (see Figs. 5.3, 5.7 or 5.21 in Chapter 5), but *in-situ* and *non-operando* synchrotron data, where the material has been allowed to relax several hours before the measurement (see Fig. 5.18), show that at least a monoclinic distorted phase is required for a correct description of the patterns.

In 2019 Susanto et al. [43] reported *operando* XRD measurements at C/20, cycled between 4.5-2.5 V and 3.5-2.5 V (see Figs. 5.22c and d respectively). These results are more similar to the ones observed in this work, with the interlayer distance increment followed by a shrinking, as well as the apparition of a secondary P'3 phase (identified as O'3_m in Fig. 5.22c). They also claimed the formation of Fe_3O_4 oxide at the surface of the particles driven by oxygen release. However, in the results presented in this work it has not been possible to observe it.

Li et al. [2] showed in 2016 by means of high-resolution TEM and electron diffraction a transformation towards a spinel-like 3D structure when $NaFeO_2$ was charged as high as 4.5 V at C/10. In their experiments, $NaFeO_2$ was measured both, in pristine state and after a cycle, in which the cell was charged and discharged between 4.5 V and 2.0 V. *Ex-situ* TEM pictures allowed the direct observation of Fe ions migrated to tetrahedral and octahedral vacancies of the Na layers (see respectively green and blue dots in Fig. 5.23a) after the compound had been cycled to high potentials. This finding was supported with synchrotron *ex-situ* XRD, although the low crystallinity of the charged sample did not allow a proper refinement. Indeed, multiple refinements of layered and spinel structures were attempted with similar agreement factors.

From these results it can be seen that the experimental set up is very important in the measured results. One needs to make sure that the measured region shows a behavior significant of the whole studied material. Moreover, one needs to consider the possible experiments and the limitations of each technique, such as the difference between *operando* or *ex-situ* measurements, that will allow or not the formation of kinetically slow forming phases. For example, it can be seen that the pattern charged to 4.5 V reported *ex-situ* by Li et al. [2], in Fig. 5.23b, is quite different to that reported *in-situ* by Susanto et al. [43] (only peak $(0\,0\,3)$ presented in Fig. 5.22c), where there are no signs of any spinel-like structure. It is important to notice that the kinetics of each material will be an important parameters when deciding which technique or experimental set-up should be used, that each material will present its own limitations. Anyway, the results observed in this Chapter are very similar to those presented by Susanto et al. for this compound [43] and those reported by Li et al. for other layered oxides [2], which let us think that the presented results are significant.

5.6 Conclusions

In this chapter the structural and electrochemical reversibility of the material when cycled in a conservative voltage window (below 3.6 V) has been confirmed, as well as the structural irreversibility when charged above 3.8 V. The structural irreversibility is most likely the source of polarization and capacity loss.

The XRD technique has revealed a solid solution evolution of the main O3 phase throughout the cycling process. A biphasic O3-P'3 phase has been seen, with the P'3 phase appearing at half charge, but disappearing on further charging in favor of the O3 during *operando* measurements. However, in *ex-situ* and *in-situ* measurements at charged state the secondary phase can be seen,

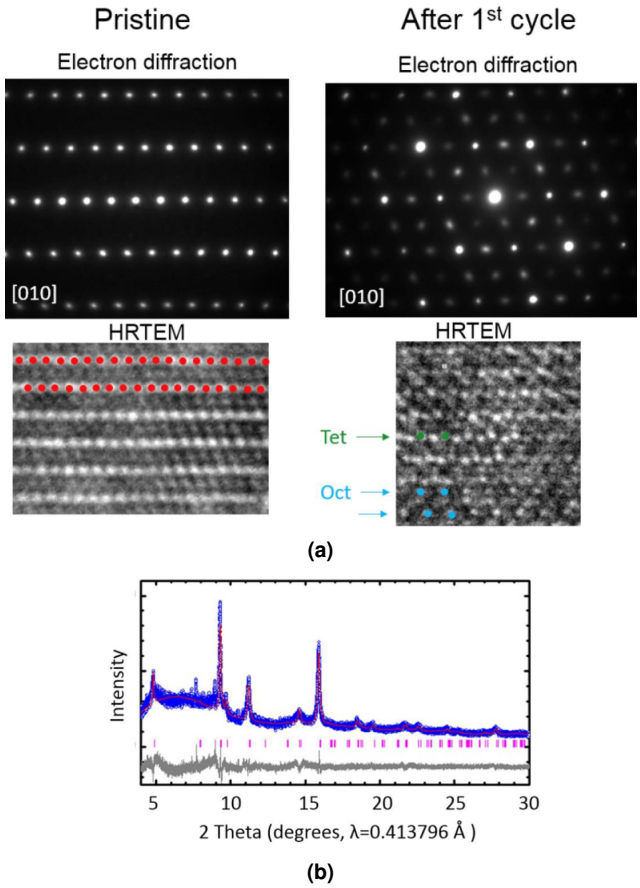

Figure 5.23: **(a)** Electron diffraction (top) and high-resolution TEM (bottom) images of $NaFeO_2$ in pristine state (left) and after being charged to 4.5 V (right). The blue and green dots in the cycled HRTEM image correspond to Fe ions migrated to octahedral and tetrahedral sites in Na layers respectively. **(b)** Pawley fit of the diffraction pattern of $NaFeO_2$ charged to 4.5 V with a spinel structure (space group $I4_1/amd$). Results by Li et al. [2].

reflecting that this P'3 phase might have slow kinetics, hence its disappearance during *operando* measurements and its presence otherwise. However, the P3 phase seems to be energetically favorable, hence its presence after a relaxation process as in the *ex-situ* and *in-situ* measurements.

Unluckily, atomic occupancy analysis (Rietveld refinement) of the XRDs of the desodiated structures has not been possible. Nevertheless, the evolution of $(0\,0\,3)$ reflection's intensity has been used to elucidate atomic occupancy and position based on the TM migration assumption. The method has allowed to estimate the amount of migrated iron, which has been confirmed with Mössbauer spectroscopy technique. It has been possible to set the onset of iron (III) migration to tetrahedral vacancies in Na layers at $x \approx 0.6$. Moreover, it has been seen that after iron migration onset, an iron ion migrates to the Na interslab for each extracted sodium.

Surprisingly, it has been found that the iron migration is highly reversible when cycled within a conservative voltage window, although the reversibility is decreased when the upper voltage window is increased.

Bibliography

[1] E. Gonzalo, M. H. Han, J. M. López del Amo, B. Acebedo, M. Casas-Cabanas, and T. Rojo. *Journal of Materials Chemistry A*, 2(43):18523–18530, 2014.

[2] X. Li, Y. Wang, D. Wu, L. Liu, S.-H. Bo, and G. Ceder. *Chemistry of Materials*, 28(18):6575–6583, 2016.

[3] N. Sharma, O. K. A. Bahri, M. H. Han, E. Gonzalo, J. C. Pramudita, and T. Rojo. *Electrochimica Acta*, 203:189–197, 2016.

[4] J. Rodriguez-Carvajal. *Physica B*, 192:55, 1993.

[5] J. Rodríguez-Carvajal. AN INTRODUCTION TO THE PROGRAM. FullProf Manual, 2001.

[6] J. N. Reimers and J. R. Dahn. *Journal of The Electrochemical Society*, 139(8):2091–2097, 1992.

[7] T. Ohzuku and A. Ueda. *Journal of The Electrochemical Society*, 141(11):2972, 1994.

[8] Y. H. Jung, A. S. Christiansen, R. E. Johnsen, P. Norby, and D. K. Kim. *Advanced Functional Materials*, 25(21):3227–3237, 2015.

[9] N. Sharma, E. Gonzalo, J. C. Pramudita, M. H. Han, H. E. A. Brand, J. N. Hart, W. K. Pang, Z. Guo, and T. Rojo. *Advanced Functional Materials*, 25(31):4994–5005, 2015.

[10] E. Talaie, V. Duffort, H. L. Smith, B. Fultz, and L. F. Nazar. *Energy & Environmental Science*, 8(8):2512–2523, 2015.

[11] K. Kubota, T. Asari, H. Yoshida, N. Yaabuuchi, H. Shiiba, M. Nakayama, and S. Komaba. *Advanced Functional Materials*, 26(33):6047–6059, 2016.

[12] M. Sathiya, K. Hemalatha, K. Ramesha, J.-M. Tarascon, and A. S. Prakash. *Chemistry of Materials*, 24(10):1846–1853, 2012.

[13] X. Li, D. Wu, Y.-N. Zhou, L. Liu, X.-Q. Yang, and G. Ceder. *Electrochemistry Communications*, 49:51–54, 2014.

[14] M. H. Han, E. Gonzalo, M. Casas-Cabanas, and T. Rojo. *Journal of Power Sources*, 258:266–271, 2014.

[15] B. Mortemard de Boisse, J.-H. Cheng, D. Carlier, M. Guignard, C.-J. Pan, S. Bordère, D. Filimonov, C. Drathen, E. Suard, B.-J. Hwang, A. Wattiaux, and C. Delmas. *Journal of Materials Chemistry A*, 3(20):10976–10989, 2015.

[16] A. Maazaz, C. Delmas, and P. Hagenmuller. *Journal of inclusion phenomena*, 1(1):45–51, 1983.

[17] D. Mohanty, J. Li, D. P. Abraham, A. Huq, E. A. Payzant, D. L. Wood, and C. Daniel. *Chemistry of Materials*, 26(21):6272–6280, 2014.

[18] S.-H. Bo, X. Li, A. J. Toumar, and G. Ceder. *Chemistry of Materials*, 28(5):1419–1429, 2016.

[19] K. Kubota, I. Ikeuchi, T. Nakayama, C. Takei, N. Yabuuchi, H. Shiiba, M. Nakayama, and S. Komaba. *The Journal of Physical Chemistry C*, 119(1):166–175, 2015.

[20] P. Yan, L. Xiao, J. Zheng, Y. Zhou, Y. He, X. Zu, S. X. Mao, J. Xiao, F. Gao, J.-G. Zhang, and C.-M. Wang. *Chemistry of Materials*, 27(3):975–982, 2015.

[21] C. Genevois, H. Koga, L. Croguennec, M. Ménétrier, C. Delmas, and F. Weill. *The Journal of Physical Chemistry C*, 119(1):75–83, 2015.

[22] S. Guo, Y. Sun, P. Liu, J. Yi, P. He, X. Zhang, Y. Zhu, R. Senga, K. Suenaga, M. Chen, and H. Zhou. *Science Bulletin*, 63(6):376–384, 2018.

[23] C. Giacovazzo, H. L. Monaco, G. Artioli, M. Viterbo, M. Milanesio, G. Ferraris, G. Gilli, G. Zanotti, and M. Catti. *Fundamentals of Crystallography*. Oxford University Press, 3 edition, 1992.

[24] Y. Li, Y. Gao, X. Wang, X. Shen, Q. Kong, R. C. Yu, G. Lu, Z. Wang, and L. Chen. *Nano Energy*, 47:519–526, 2018.

[25] C. Prescher, C. McCammon, and L. Dubrovinsky. *Journal of Applied Crystallography*, 45(2):329–331, 2012.

[26] P. Gütlich and C. Schröder. *Mössbauer Spectroscopy*. Wiley-VCH Verlag GmbH & Co. KGaA, Weinheim, Germany, 2012.

[27] P. Gütlich, E. Bill, and A. Trautwein. *Mössbauer spectroscopy and transition metal chemistry: fundamentals and application*. Springer, 1978.

[28] Y. Zhang, Z. Yang, and C. Tian. *Journal of Materials Chemistry A*, 7:23628–23661, 2019.

[29] C. Delmas, J.-J. Braconnier, C. Fouassier, and P. Hagenmuller. *Solid State Ionics*, 3-4:165–169, 1981.

[30] D. Carlier, I. Saadoune, L. Croguennec, M. Menetrier, E. Suard, and C. Delmas. *Solid State Ionics*, 144(3):263–276, 2001.

[31] R. Berthelot, M. Pollet, D. Carlier, and C. Delmas. *Inorganic Chemistry*, 50(6):2420–2430, 2011.

[32] E. Lee, D. E. Brown, E. E. Alp, Y. Ren, J. Lu, J.-J. Woo, and C. S. Johnson. *Chemistry of Materials*, 27:6755–6764, 2015.

[33] N. Bucher, S. Hartung, J. B. Franklin, A. M. Wise, L. Y. Lim, H.-Y. Chen, J. N. Weker, M. F. Toney, and M. Srinivasan. *Chemistry of Materials*, 28(7):2041–2051, 2016.

[34] P. Barpanda. *Chemistry of Materials*, 28(4):1006–1011, 2016.

[35] A. R. Armstrong, N. Dupre, A. J. Paterson, C. P. Grey, and P. G. Bruce. *Chemistry of Materials*, 16(16):3106–3118, 2004.

[36] S. Kim, X. Ma, S. P. Ong, and G. Ceder. *Physical Chemistry Chemical Physics*, 14(44):15571, 2012.

[37] P. He, H. Yu, D. Li, and H. Zhou. *Journal of Materials Chemistry*, 22(9):3680, 2012.

[38] Y. Takeda, K. Nakahara, M. Nishijima, N. Imanishi, and O. Yamamoto. *Materials Research Bulletin*, 29(6):659–666, 1994.

[39] N. Yabuuchi, H. Yoshida, and S. Komaba. *Electrochemistry*, 80(10):716–719, 2012.

[40] G. Ouvrard, M. Zerrouki, P. Soudan, B. Lestriez, C. Masquelier, M. Morcrette, S. Hamelet, S. Belin, A. M. Flank, and F. Baudelet. *Journal of Power Sources*, 229:16–21, 2013.

[41] O. J. Borkiewicz, K. M. Wiaderek, P. J. Chupas, and K. W. Chapman. *The Journal of Physical Chemistry Letters*, 6(11):2081–2085, 2015.

[42] J. W. Somerville, A. Sobkowiak, N. Tapia-Ruiz, J. Billaud, J. G. Lozano, R. A. House, L. C. Gallington, T. Ericsson, L. Häggström, M. R. Roberts, U. Maitra, and P. G. Bruce. *Energy & Environmental Science*, 12(7):2223–2232, 2019.

[43] D. Susanto, M. K. Cho, G. Ali, J.-Y. Kim, H. J. Chang, H.-S. Kim, K.-W. Nam, and K. Y. Chung. *Chemistry of Materials*, 31(10):3644–3651, 2019.

[44] R. Kataoka, K. Kuratani, M. Kitta, N. Takeichi, T. Kiyobayashi, and M. Tabuchi. *Electrochimica Acta*, 182:871–877, 2015.

6 | Advanced structural characterization of O3-$Na_xFe_{2/3}Mn_{1/3}O_2$ upon cycling

Contents

6.1 Introduction

A structural evolution study has been done for O3-$Na_{2/3}Fe_{2/3}Mn_{1/3}O_2$, similar to that shown in Chapter 5 for $NaFeO_2$. In Chapter 4 it has been shown that the presence of Mn in the structure results in reversible electrochemistry to higher potentials. Indeed, is generally possible to reversibly cycle binary and ternary TM layered oxides to higher potentials [1, 2]. In this chapter the relation between better electrochemical stability and TM migration will be studied.

6.2 *Operando* structural characterization by X-ray diffraction

The measurements of the lab-scale *operando* XRD evolution of O3-$Na_{2/3}Fe_{2/3}Mn_{1/3}O_2$ was carried out by E. Gonzalo, M. Han, D. Saurel, M. Casas-Cabanas and E. Martin in 2014, and preliminary results were published in *Journal of Materials Chemistry A* [3]. Within the scope of this work this measurement has been analyzed following the same methodology used for $NaFeO_2$ and presented in Chapter 5.

Before the operando XRD patterns are analyzed, an initial *in-situ* XRD pattern has been refined. This way, the patterns can be corrected for the height and for the intrinsic parasitic reflections of *in-situ* and *operando* measurements. In Fig. 6.1 the refined initial *in-situ* XRD pattern is presented, and in Table 6.1 the corresponding refined parameters. The refinement includes the parameter SYCOS, related to the deviation of the sample height s from the center of the diffractometer with equation 5.1.

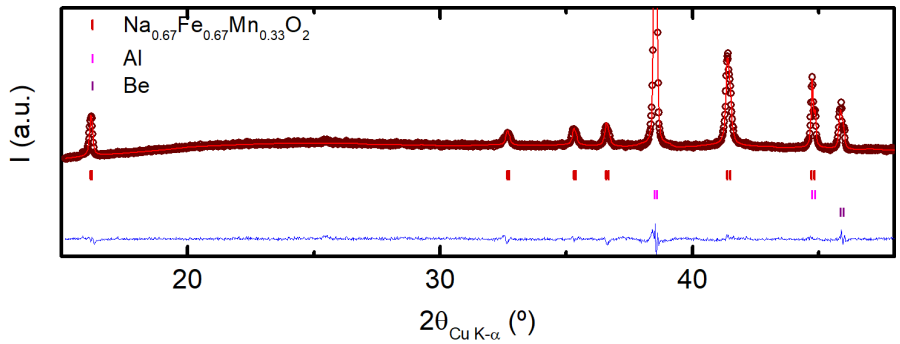

Figure 6.1: Pattern matching refinement of the initial *in-situ* XRD pattern of the O3-$Na_{2/3}Fe_{2/3}Mn_{1/3}O_2$ sample, including sample height. Three phases are refined: O3-$Na_{2/3}Fe_{2/3}Mn_{1/3}O_2$, aluminum (from Al foil) and beryllium (from Be window). The experimental data is presented with open circles, and the refinement with a red line, the difference in blue and the reflection angle position with vertical marks: from top to bottom, in red for O3-$Na_{2/3}Fe_{2/3}Mn_{1/3}O_2$, pink for Be and purple for Al.

Table 6.1: Le Bail or pattern matching refined parameters of a pristine *in-situ* XRD pattern of O3-$Na_{2/3}Fe_{2/3}Mn_{1/3}O_2$: space group, cell parameters, sample height and agreement factors. The refined pattern can be seen in Fig. 6.1.

Space group	**Cell parameters**		**SYCOS**
$R\bar{3}m$	$\boldsymbol{a}$ = $\boldsymbol{b}$ = 2.969(2) Å	$\boldsymbol{c}$ = 16.43(3) Å	-0.11(9)
Agreement factors	$\chi^2 = 4.66$	$R_b = 0.796$	$R_p = 0.596$

The *operando* XRD experiment of O3-$Na_{2/3}Fe_{2/3}Mn_{1/3}O_2$ is presented in Fig. 6.2. 2D plots for selected angle ranges (Fig. 6.2(a-c)) are shown as a function of time in y axis, angle in x axis and the diffracted intensity with the color code. The time evolution of the voltage curve and sodium content of the electrochemical control are represented in Fig. 6.2d. The cell has been cycled at constant current with a C/50 rate. The upper voltage limit is 4.2 V, which is within the reversible voltage window for this material as described in Chapter 4. It has been cycled for one full cycle, that is, charge and discharge. It shows a Coulombic efficiency of 96.5%, with a discharge capacity of 140 mA h g^{-1}. During charge three different reactions can be distinguished, corresponding to the three plateaus in the voltage evolution curve of Fig. 6.2d. At 2.5 V, at the beginning of the measurement, the end of a plateau can be seen, corresponding to $Mn^{3+/4+}$ oxidation reaction; this suggests the presence of Mn^{3+} in the pristine state. At 3.60 V and 3.85 V two potential plateaus can be seen, corresponding to $Fe^{3+/4+}$ oxidation reaction [3–6], corresponding to reactions *A* and *B* as presented in Chapter 4. However, on discharge the potential curve shows a pronounced slope, which could be of thermodynamic origin due to irreversible structural changes, or the consequence of an overpolarization related to slower kinetics. It is worth noting that on discharge the reaction has been pushed further than the initial state. The pristine material synthesis is aimed with manganese in its Mn^{4+} state, while the discharge has been done down to potentials where $Mn^{4+/3+}$ reduction is expected.

The structural evolution is qualitatively very similar to that of $NaFeO_2$ (see Figs. 5.3, 5.7 and 5.21). In order to study the evolution of the cell parameters, sequential Le Bail refinements have been carried out using FullProf Suite software [7]. Some examples of these refinements are presented in Fig. 6.3, together with the voltage evolution and the points at which the patterns have been taken.

A secondary phase is observed in the vicinity of the $(0\,0\,\ell)$ reflections after 5 hours ($2\theta \approx 15°$). As shown for the $NaFeO_2$ sample in Chapter 5, the lack of other additional reflections suggest that it belongs to the same space group as the main phase, that is, space group $R\bar{3}m$. Moreover, the fact that it has a bigger interlayer distance (its reflection appears at lower angles than the main phase's $(0\,0\,\ell)$ reflection) suggests that it might be a P-type phase, whose interlayer distance tends to be larger than those of the O-type phases. Indeed, in previous publications of this materials, the reflection has been assigned to a P3 phase [3, 5]. Both the initial O3 and the secondary P3 phases have been defined with $R\bar{3}m$ space group in the Le Bail refinements.

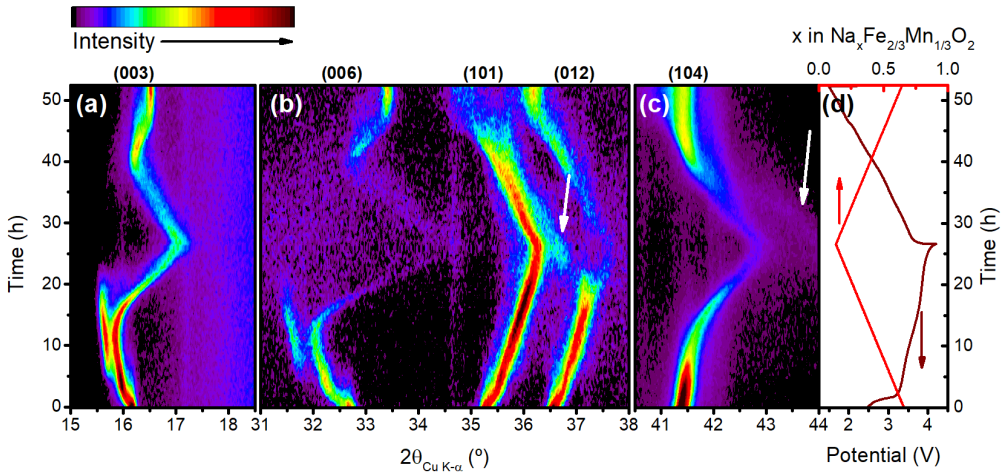

Figure 6.2: *Operando* XRD data of O3-$Na_{2/3}Fe_{2/3}Mn_{1/3}O_2$ cycled in $V = 4.2 - 1.5$ V voltage range. **(a-c)** 2D representation of *operando* XRD of O3-$Na_{2/3}Fe_{2/3}Mn_{1/3}O_2$ for selected 2θ angle ranges. Reflections are indexed with $R\bar{3}m$ space group according to initial O3 phase. White arrows in panels (b) and (c) highlight the splitting of the reflections due to a monoclinic distortion.**(d)** Voltage (bottom) and sodium content (top) evolution curves as a function of time. Measurements carried out by E. Gonzalo, M. Han, D. Saurel, M. Casas-Cabanas and E. Martin.

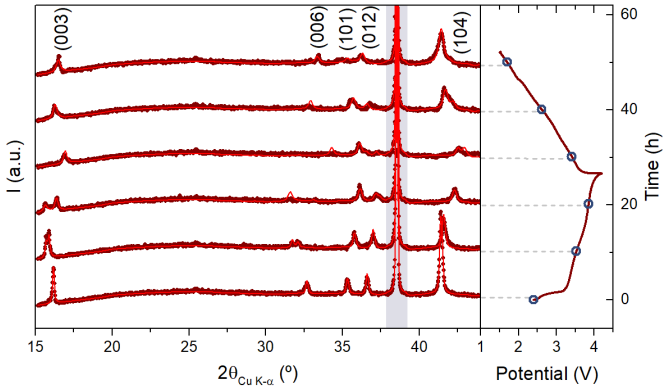

Figure 6.3: Le Bail refinement examples of O3-$Na_xFe_{2/3}Mn_{1/3}O_2$ at various states of charge. Experimental data is presented with points and Le Bail refinements with a red line. On top, $(h\,k\,\ell)$ Miller index according to the pristine sample. The reflection from the aluminum foil of the cell has been highlighted in gray. In the right panel the voltage curve with the points at which the diffraction patterns have been taken are marked.

Close to the end of the charge, the reflection $(1\,0\,2)$ splits in two, which has been highlighted with a white arrow in Fig. 6.2b. This splitting is a common signal for a monoclinic distorted O'3 phase [5], and comes from a gliding between the transition metal oxide layers resulting in an increment of β angle (see Fig. 6.4a and b). The monoclinic structure can be indexed with the space

group $C2/m$, and the split $(0\,1\,2)$ reflection would then be indexed as $(\bar{1}\,1\,1)$ and $(2\,0\,0)$. In Fig. 6.4c the simulated diffraction patterns of a pure O3 and a distorted O'3 phases have been simulated. Close to $(1\,0\,4)$ reflection, and to higher diffraction angle, a low intensity split can also be seen (see the white arrow in Fig. 6.2c). Indeed, in the monoclinic distorted phase, $(1\,0\,4)$ reflection of the O3 phase splits in $(\bar{2}\,0\,2)$ and $(1\,1\,1)$ reflections.

The β angle of the O3 phase described with the space group $R\bar{3}m$ can be defined as:

$$\beta_{O3} = 180 - \text{atan}\frac{c}{2b\sin 60^\circ} \tag{6.1}$$

where c and $b\,(=a)$ are the cell parameters. Therefore, β depends on the unit cell parameters, and not only on the distortion. The monoclinic distortion (MD) has been defined as the offset of the fourth layer relative to the first one, and has been calculated with expression 6.2. That is, the distortion reflects the horizontal distance of the equivalent atom in the 4$^{\text{th}}$ layer, see Fig. 6.4b. In a pure O3 phase, the fourth layer is equivalent to the first, and thus, the offset is zero.

$$MD = 1 - \frac{3c_m}{a_m}\cos(180 - \beta_{O'3}) \tag{6.2}$$

where c_m, a_m and $\beta_{O'3}$ are the cell parameters in the $C2/m$ space group.

In the XRD patterns shown in Fig. 6.3, it can be seen that the reflections lose intensity as the cell is being charged. It is especially true for the less intense $(0\,0\,6\,,\ 1\,0\,1\,,\ 0\,1\,2)$ reflections. Indeed, their intensity is comparable to the background noise at charged state. The FullProf Suite software [7], when performing Le Bail or pattern matching refinements, refines the intensity of each reflection individually. In some patterns the software detected background noise and integrated the intensity accordingly, hence the reflection peaks appearing in the refinements of Fig. 6.3 while no reflection is appreciable in the experimental data (see e.g. the reflection at $2\theta \approx 31.6^\circ$ in the pattern taken at $t = 20$ h, $V = 3.85$ V). Indeed, slightly changing the background curve in the input file can change the way the software refines the intensity of these peaks, although their position remains constant. However, special attention has been paid to the position of the $(0\,0\,3)$, $(1\,0\,1)$ and $(1\,0\,4)$ reflections during the refinements, whose intensities remain higher at all states of charge. Moreover, and for the sake of simplicity, the background has been kept constant during the sequential refinements.

Unlike in the $NaFeO_2$ measurements in Chapter 5, it has been possible to individually refine the main O3 and the secondary P3 phases for this sample. Moreover, the monoclinic distortion seen with reflection splitting has also been included in the Le Bail refinements. Thus, the sequential Le Bail analyses have been done in several blocks, separated by the addition or transformation of the phases included in the refinements.

As shown for $NaFeO_2$ in Chapter 5, pseudo-Voigt refinements of the $(0\,0\,3)$ reflection's vicinity has also been done, in order to determine the relative intensities of the reflections of each phase. A few significant examples are presented in Fig. 6.5. A constant background has been set for all the patterns, consisting of a linear slope with a small bump at $2\theta \approx 15.8^\circ$ assigned to beryllium oxide

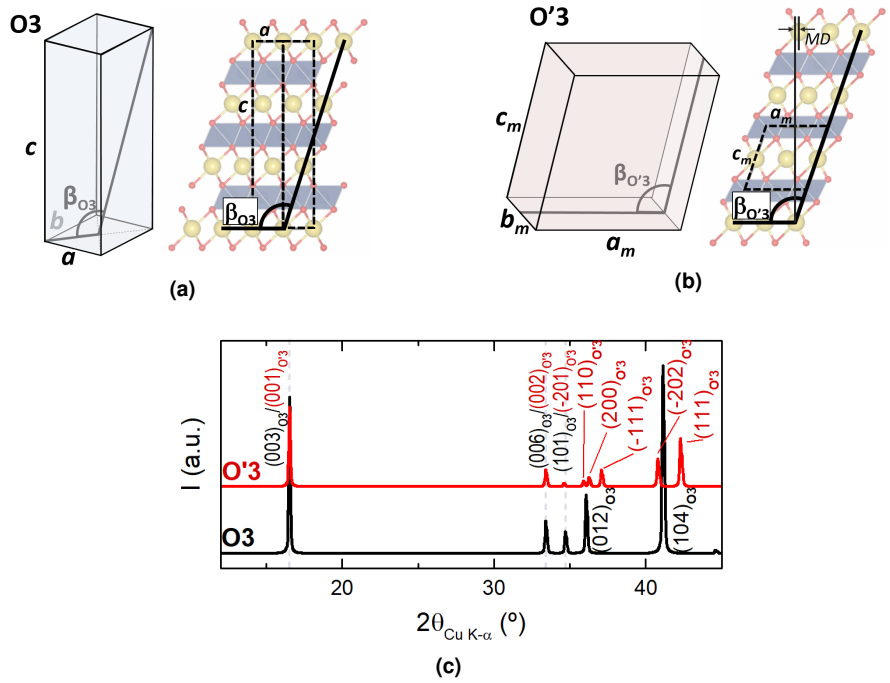

Figure 6.4: Comparison of the O3 and the monoclinic distorted O'3 structures. **(a)** A representation of the crystallographic unit cell (left, not to scale) and structure (right) of the O3 phase (space group $R\bar{3}m$). The yellow spheres represent the sodium ions, the blue octahedron represent the Fe ions and the red spheres represent the oxygen ions. Note that in the structural representation a cell parameter is out of plane. **(b)** A representation of the crystallographic unit cell (left, not to scale) and structure (right) of the distorted O'3 phase (space group $C2/m$). In this particular example $\beta_{O3} = 110.60°$ and $\beta_{O'3} = 106.31°$. The monoclinic distortion (MD) is explicitly shown. **(c)** The XRD pattern simulation of the O3 (black line) and the O'3 (red line) phases drawn in panel (a) and (b) respectively, with the corresponding Miller index labels.

from the window corrosion (see dotted back line). One or two additional pseudo-Voigt peaks have been used to refine the O3 (dashed blue line) and P3 (dashed red line) phases' $(0\,0\,3)$ reflection. The position of the peaks has afterwards been corrected to account for the shift in the sample height due to the *operando* XRD set-up geometry. The correction has been done according to equation 5.2 and the displacement obtained with the refinement presented in Fig. 6.1 and Table 6.1.

The results of the refinements are gathered in Fig. 6.6. The voltage and sodium content evolution are presented as a function of time in Fig. 6.6a, and d interlayer distance (from Le Bail and pseudo-Voigt refinements) and b in-plane distance (from Le Bail refinements) have been plotted in Fig. 6.6b and c respectively. The interlayer distance of the O3 and the P3 phases obtained with Le Bail and pseudo-Voigt fittings overlap perfectly, which confirms the validity of the methods. The monoclinic distortion percentage, as defined with equation 6.2, is presented in Fig. 6.6c (right axis). The relative intensities of the two phases, obtained from the pseudo-Voigt fittings are shown

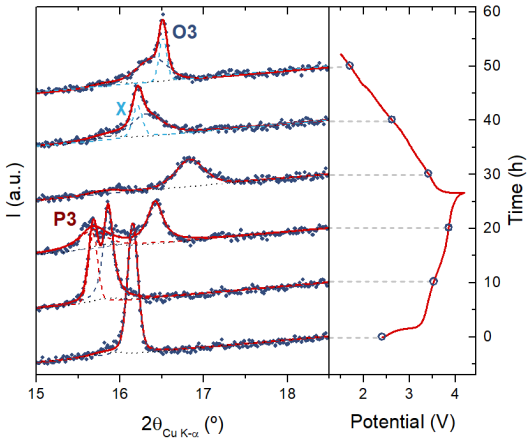

Figure 6.5: Pseudo-Voigt refinement examples of the low angle region of O3-$Na_{2/3}Fe_{2/3}Mn_{1/3}O_2$ at various states of charge. Experimental data is presented with points and pseudo-Voigt fittings with a red line. In the right panel the voltage curve, and marked the points where the diffraction patterns have been taken.

in Fig. 6.6d.

During the first 12 hours the main phase evolves continuously, an indicative of solid solution. The interlayer distance d increases with sodium extraction as reflected by the shift to lower angles of the $(0\,0\,\ell)$ reflections due to the increased O-O repulsion between adjacent layers (Fig. 6.2). The Le Bail and pseudo-Voigt refinements (Fig. 6.6b) show that it corresponds to an increase of d from 5.48 Å to 5.59 Å. Afterwards it starts to decrease until values lower than the initial one are reached at the end of charge ($d = 5.20$ Å), as seen for $NaFeO_2$ compound in Chapter 5. During the whole charge the metal to metal distance b reduces as reflected by the shift to higher angles of the reflections with contributions from h and k of the $(h\,k\,\ell)$ reflections (Fig. 6.2), due to decreased repulsion between transition metal and sodium ions. In-plane distance b reduces from 2.97 Å down to 2.89 Å at the end of charge (Fig. 6.6c). Close to the end of discharge however, when the O3 phase distorts and forms the monoclinic phase, the decrease in b gets slower and remains close to constant.

After the first 5 hours, at 3.35 V ($x = 0.57$), close to the main O3 phase a secondary P3 phase appears. Simultaneously with its appearance, a plateau in the voltage curve can be seen, as expected for a biphasic reaction [8]. The interlayer distance of the P3 phase increases linearly, yet slightly, from 5.63 Å up to 5.68 Å until it disappears at $V = 3.95$ V, close to the end of the charge. The evolution of the O3 and P3 phases' in-plane distances b evolve in parallel during charge until the monoclinic onset of the O3 phase at $t = 18$ h. At this moment, b of the O3 phase continues reducing, but that of the P3 phase stays stable at 2.91 Å until the phase is not detected anymore. It is worth noting that this P3 phase transformation is more advanced in this sample than in $NaFeO_2$ presented in the previous chapter. The interlayer distance is more separated in

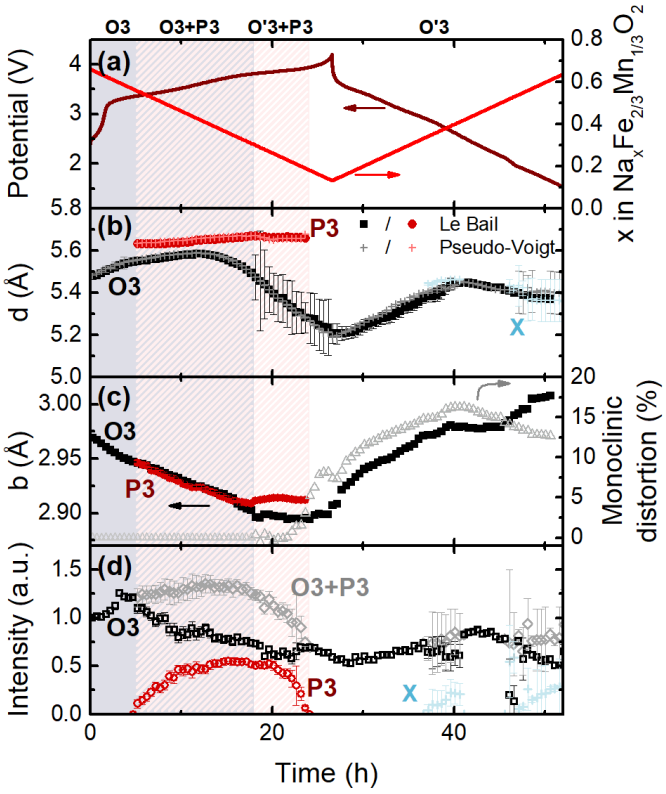

Figure 6.6: Analysis of the operando XRD patterns of O3-$Na_{2/3}Fe_{2/3}Mn_{1/3}O_2$ of Fig. 6.2. **(a)** Voltage and sodium content evolution, **(b)** interlayer distance evolution of O3 (black), P3 (red) and an unknown "X" (light blue) phases, analyzed with Le Bail (squares and circles) and pseudo-Voigt refinements (crosses), **(c)** in-plane distance values obtained from Le Bail refinements (left axis) and the monoclinic distortion (right axis), and **(d)** integrated intensity evolution of O3, P3 and "X" phases, obtained from pseudo-Voigt refinements, and in gray the summed intensity. The numerical results can be found in Table B.3.

this case, and the P3 to O3 intensity ratio is higher. Moreover, the P3 phase appearance occurs earlier in $Na_{2/3}Fe_{2/3}Mn_{1/3}O_2$. Note that the error bars get larger in the biphasic region with O'3 and P3 phases, especially in d (Fig. 6.6b). Indeed, the interlayer distance depends on the β angle that is also refined.

Upon discharge the process is partially reversible. The in-plane distance b of the O3 phase is very reversible (see Fig. 6.6c). However, the monoclinic distortion is not reverted. It continues to increase (see Fig. 6.6c, right axis) until half discharge is reached ($t = 40$ h), with a maximum distortion of 16%, and then it only decreases slightly. This event is concomitant with the offset of the interlayer distance reduction (Fig. 6.6b) and the intensity decrease (Fig. 6.6d). Despite the asymmetric charge-discharge process, especially reflected by the asymmetry of the evolution of the $(0\,0\,3)$ reflection, the reaction presents a large degree of reversibility. Interlayer distance increases

back during the first part of the discharge from 5.19 Å up to 5.45 Å at 2.57 V. The maximum is however smaller than the maximum *d* obtained on charge at 12 h, 5.58 Å, and even slightly smaller than the pristine value, 5.48 Å. Moreover, the P3 phase does not appear on discharge. Below 2.57 V ($t = 40$ h), interlayer distance starts to shrink back. An increase of the maximum intensity is observed in Fig. 6.2a, but the intensity obtained from pseudo-Voigt refinements is not increased notably. In the patterns during discharge of Fig. 6.5 two different peaks are distinguished, a broad one corresponding to the O3 phase and a sharp one that has been labeled as "X" (see Fig. 6.6b and d). This sharp reflection does not correspond to the P3 phase. It can be seen in Fig. 6.6b how it appears to the left and the right of the main O3 phase's $(0\,0\,3)$ reflection, suggesting that it probably belongs to inhomogeneous reaction and not to the presence of a secondary phase. It is most probably related to the change in the redox active transition metal. Indeed, the unknown "X" phase appears at $V \approx 2.8$ V, between the potentials at which $Fe^{4+/3+}$ and $Mn^{4+/3+}$ redox reactions occur.

The intensity (Fig. 6.6d) starts increasing during charge, as expected for sodium extraction as seen in the previous chapter (Section 5.2.1). Moreover, and similarly to what happens in $NaFeO_2$, concomitantly with the interlayer distance decrease, the intensity is also reduced. On discharge however the intensity is not completely recovered. A slight increment of the intensity can be seen, but it does not reach the values of the initial pattern. Moreover, at half discharge, simultaneously with the maximum of the interlayer distance and monoclinic distortion, the intensity has an inflexion point after which it stays constant.

6.2.1 Study of iron migration

The similarities with $NaFeO_2$ sample in Chapter 5, seem to indicate that O3-$Na_{2/3}Fe_{2/3}Mn_{1/3}O_2$ also suffers from TM migration to Na interlayer. At half charge the interlayer distance increment reverses and reduces to values lower than the initial one, and is not recovered in discharge. Moreover, the intensity of the $(0\,0\,3)$ reflection also decreases below the initial values at the end of charge and is only partially reversible on discharge.

Similarly to what has been done for $NaFeO_2$, the intensity of the $(0\,0\,3)$ reflection has been parametrized for the manganese containing sample. The migrating TM ion has been considered to be Fe and not Mn, since previous works indicate that Fe is the most prone element to suffer from migration [9]. However, Fe and Mn diffraction signals should not differ much, as they both have similar electron densities. The compound formula for z ions of Fe moving to Na interlayers can be written as $(Na_xFe_z)(Fe_{2/3-z}Mn_{1/3})O_2$. Due to the similarities with $NaFeO_2$, iron has been assumed to migrate to tetrahedral vacancies in Na layers, although the results should not change much in the event of the migration occurring to octahedral vacancies as seen in previous chapter. As done in Section 5.2.1 of the previous chapter, the intensity will be described as a two variable 2^{nd} order polynomial.

The simulated dependence of the $(0\,0\,3)$ reflection's intensity on the migrated Fe z and the sodium content x has been plotted with squares in Fig. 6.7a and b respectively. The best fits with a

second degree polynomial (equation 5.5, lines in Fig. 6.7a and b) have been used to determine the arguments of the polynomial. As in the $NaFeO_2$ sample, the intensity shows a linear dependency with the interlayer distance, as denoted by the linear fit of the data in Fig. 6.7c.

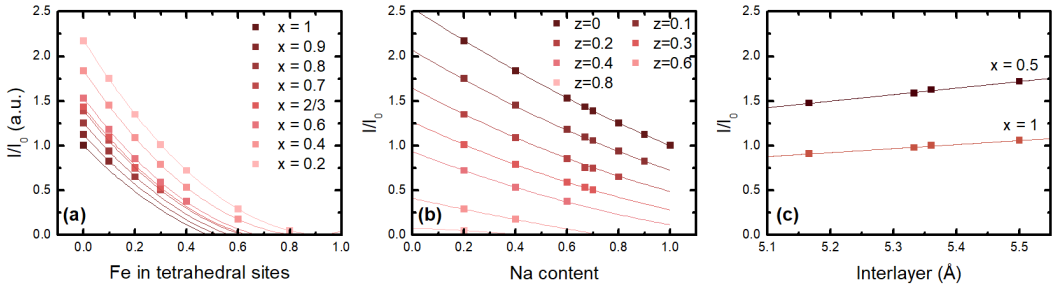

Figure 6.7: Intensity of the reflection $(0\,0\,3)$ of the simulated patterns, **(a)** as a function of the content z of migrated Fe for different Na contents x, **(b)** as function of the Na content x for different amounts z of migrated Fe, and **(c)** as function of the interlayer distance d for $z = 0$ and two different sodium contents x. In all cases the intensity has been normalized by I_0, the intensity simulated with $x = 1$, $z = 0$ and $d = 5.36$ Å, which corresponds to O3-$Na_1Fe_{2/3}Mn_{1/3}O_2$. The simulations have been run considering the migration of Fe to tetrahedral sites in Na layers.

The parametrized and normalized curve is written as:

$$\left.\frac{I(x,z,d)}{I(x_0,z_0,d_0)}\right|_{tetr} = ((1.762 - 1.309x + 0.239x^2) + z(-3.440 + 1.114x + 0.312x^2) + z^2(1.627 + 0.569x - 0.997x^2))(1 - 0.266(d - d_0)) \quad (6.3)$$

The parameters are defined in the same way as in Chapter 5: x for the sodium content, d for interlayer distance, and z for the migrated Fe, in this case to tetrahedral vacancies in Na layers. The way that z has been calculated is the proportion of migrated Fe vs. total Fe, ($z = \frac{Fe_{mig}}{Fe}$). This is, the chemical formula could be presented as $(Na_xFe_z)(Fe_{2/3-z}Mn_{1/3})O_2$.

The intensity has been calculated by the integration of the 2θ range shown in Fig. 6.2a considering all the present phases in a similar way at which it has been done for $NaFeO_2$. Before integration the background has been subtracted and the intensity corrected by factors that affect to it as a function of θ, presented in Table 2.1. By doing so, the values obtained with the pseudo-Voigt refinements will be validated. The results are presented as scatter points in Fig. 6.8b, together with the voltage and sodium content evolution in Fig. 6.8a. It is clear from Fig. 6.8b that the intensity values obtained from pseudo-Voigt refinements (open gray diamonds) and from signal integration (solid orange points) are in good agreement, although the pseudo-Voigt data is noisier close to the end of the discharge and it has large error bars in the biphasic regions. The expected intensity without iron migration based on simulations is also presented with a dashed line, calculated from equation 6.3 with $z = 0$, and x and d taken from Fig. 6.6a and b. The difference between the experimental and the expected simulated intensities has been plotted with open orange points in Fig. 6.8b (right axis).

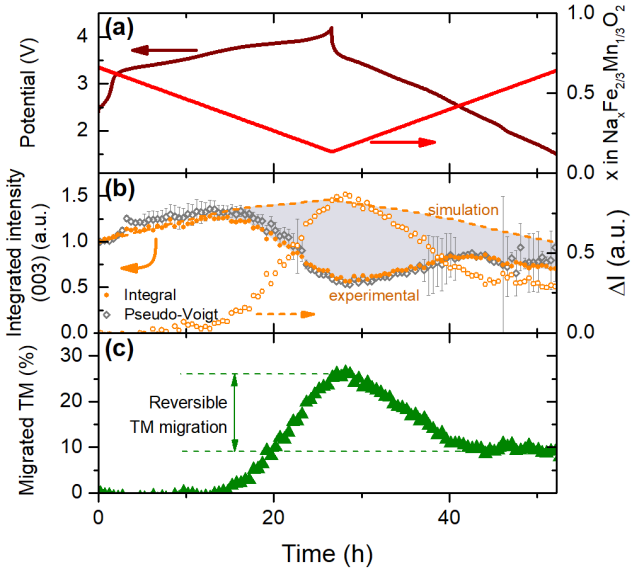

Figure 6.8: Estimation of Fe migration of O3-$Na_{2/3}Fe_{2/3}Mn_{1/3}O_2$ upon cycling. **(a)** Voltage and sodium content profile as a function of time. **(b)** Experimental integrated intensity (orange solid scatter data) and intensity from simulations considering no Fe migration (dashed line) of $(0\,0\,3)$ reflection. The difference has been shadowed in gray for clarity, and is shown with open scatter data in the right axis. The intensity obtained from pseudo-Voigt fittings is presented with open gray diamonds. **(c)** Estimated Fe migration to tetrahedral vacancies in Na layers calculated with equation 6.3. Migrated Fe has been calculated as a function of total TM ($\frac{Fe_{mig}}{Fe+Mn}$). The numerical results can be found in Table B.3.

It can be seen in Fig. 6.8b that the experimental and the expected simulated intensities are in good agreement in the beginning of charge. However, the experimental intensity starts to decrease at half charge, until $t = 12$ h, concomitant with the reduction in interlayer distance (see Fig. 6.6b). The decrease in intensity, related to an atomic rearrangement other than sodium extraction, is most likely related to iron migration into Na layers, and more specifically, to tetrahedral vacancies. Indeed, the relative intensities of the $(0\,0\,6\,,\ 1\,0\,1\,,\ 0\,1\,2)$ reflections show that the most intense peak corresponds to reflection $(1\,0\,1)$ (see Fig. 6.2b), and as seen in previous Chapter 5, this case resembles more to the migration to tetrahedral vacancies in Na layers (see Fig. 5.9b). The Fig. 6.8c shows the estimated migrated iron over the total of the transition metal elements ($\frac{Fe_{mig}}{Fe+Mn}$) calculated with equation 6.3. Once the experimental and simulated intensities start to differ ($V = 3.75$ V, $x = 0.36$), iron starts to migrate linearly until a maximum of 26% is reached at the end of charge at 4.2 V, which is surprisingly high giving the electrochemical reversibility of the material after having it charged to this voltage (see Fig. 4.7b). Nevertheless, unlike for the $NaFeO_2$ sample, O3-$Na_{2/3}Fe_{2/3}Mn_{1/3}O_2$ can be sodiated back. During the discharge and according to the simulations, iron partially migrates back to its original site, and at the end of discharge, transition metal in Na layers is estimated to be only 9%. On discharge from 4.2 V, 65% of the TM migration

is reversible. It seems thus that the back migration of iron to its original site is enhanced by the presence of Mn ions in the structure.

6.3 *In-situ* structural characterization by Mössbauer spectroscopy

In the previous chapter Mössbauer spectroscopy has been used to confirm the reversible migration of Fe^{3+} to tetrahedral sites in Na layers. A similar *in-situ* experiment has been carried out for O3-$Na_{2/3}Fe_{2/3}Mn_{1/3}O_2$, where a cell has been charged to 3.8 V and discharged and hold at 1.25 V. A second cell has also be measured at 4.2 V, but this cell has only been measured at charged state and it has not been discharged.

As done for $NaFeO_2$, the measurements have been done *in-situ*, but *non-operando*. That is, the cell is under relaxation while the measurement is being done. This has been of particular importance for this sample because of the low absorption in this case, lower than 1%. Indeed, the absorbing Fe element presence is lower in these measurements, due to two main reasons. First, O3-$Na_{2/3}Fe_{2/3}Mn_{1/3}O_2$ sample has a lower iron content, substituted by Mn that will partially block the signal. This is, a lower content of absorbing element together with a higher signal-blocking element is present. Second, the O3-$Na_{2/3}Fe_{2/3}Mn_{1/3}O_2$ available electrodes had a lower mass loading, of about 1 mg cm^{-2}, compared to the 3 mg cm^{-2} loading of the measured $NaFeO_2$ electrodes.

The voltage curves of the two measured cells are presented in Fig. 6.9a: with the dark blue line the cell that has been cycled in the $3.8 - 1.25$ V voltage window and with the light blue line the cell that has been charged to 4.2 V. The absorption spectra corresponding to the cell charged and discharged are shown at different state of charge in Fig. 6.9(b-g): left hand side for the measurements done during charge and right hand side for the measurements done during discharge. The spectra are presented together with their corresponding refinements, than have been done using MossA software [10]. In Fig. 6.9a the relative intensities of the refined signals are shown in columns, and they have been labeled with the corresponding spectra's panel name. The numeric results of these measurements are gathered in Table B.5.

Due to the low absorption of these samples, and despite the long acquisition times, above 24 h for each pattern, only two signals have been identified. These signals are already present in the initial measurement (Fig. 6.9b). The first signal, with a central shift of CS ≈ 0.35 and a quadrupole splitting of QS ≈ 0.7, is in good agreement with the expected HS Fe^{3+} in octahedral site (see Fig. 2.14b for the expected Mössbauer results for the different iron signals) and the pristine powder measurement (Fig. 3.16). As shown in the pristine powder measurements in Chapter 3, the quadrupole splitting of this sample is higher than that of $NaFeO_2$, and it can be attributed to a distortion of the FeO_6 octahedra, either due to the presence of mixed TM elements in the layers or the Na vacancies of the synthesized material. This signal is shown in dark red color in Figs. 6.9

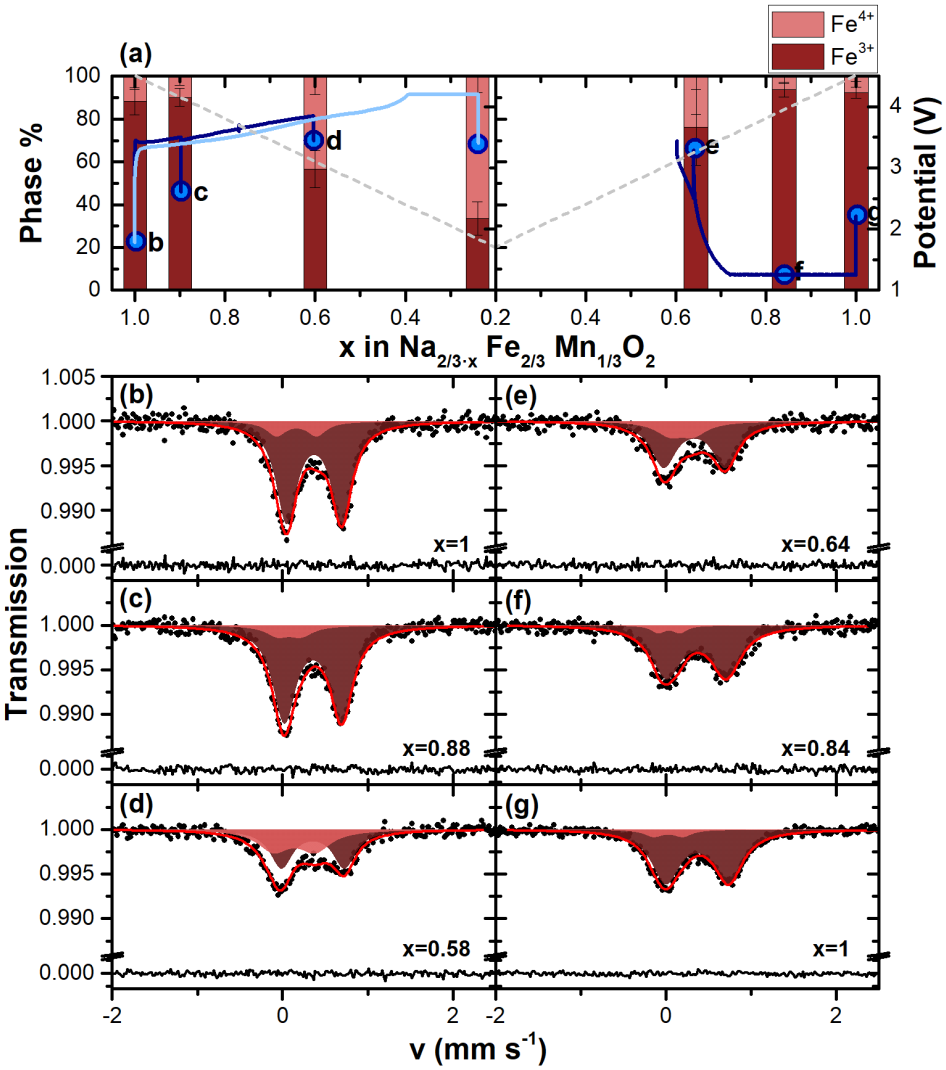

Figure 6.9: **(a)** Electrochemical curve (blue lines, right axis) and phase percentage of the different Fe environments. From dark to light: Fe^{3+} in octahedral site as in pristine sample and Fe^{4+} in octahedral site. With a dashed gray line the expected Fe^{3+} content assuming no parasitic reactions, this is, that each extracted (inserted) Na corresponds to an oxidized (reduced) iron ion. **(b-g)** Refined Mössbauer spectra at several states of charge, indicated in panel (a). Scatter data corresponds to experimental absorption data after normalization, red and black solid lines correspond to fitting and difference respectively and different iron environments have been shadowed with the same color code as in panel (a).

and 6.10. In Fig. 6.10 the refined signals' results are shown as a function of central shift (x axis) and quadrupole splitting (y axis).

The second detected signal has a lower central shift, which indicates a higher oxidation state,

due to the change in the effective nuclear charge with the removal of a d electron. The values sit between 0 and 0.17 mm s^{-1}, although the errors are quite large due to the noisy data. According to literature (see Fig. 2.14b), this signal corresponds well with HS Fe^{4+}. This signal is shown in light red in Figs. 6.9 and 6.10.

In Fig. 6.9a the relative intensity of the two signals has been plotted with columns. With a dashed gray line, the expected value for Fe^{3+} is shown, considering that there are no parasitic reactions, that is, that each sodium extracted (inserted) from the structure corresponds to an oxidized (reduced) TM, and more specifically, to $Fe^{3+/4+}$ oxidation (reduction) reaction. Already from the 1st measurement in the initial state, Fe^{4+} signal is observed, with a $12 \pm 7\%$ presence, reflecting either a sodium deficiency of about 12% (this is, initial formula is $Na_{0.55}Fe_{2/3}Mn_{1/3}O_2$), a Fe:Mn proportion that does not correspond to the expected $\frac{2}{3} : \frac{1}{3}$, a mixed iron and manganese (III) and (IV) valence states from the pristine state or a combination of the above. The ICP-OES results shown in Chapter 3, the pristine material has a sodium excess and a correct Fe:Mn stoichiometry. Thus, either a sodium decrease occurs during the material manipulation (electrode preparation or cell assembly), or a combination of iron and manganese (III) and (IV) oxidation states is present. It is though worth noting the large error bars due to the noisy data. However, the trend of the measured values is in good agreement with the expected values. These measurements also show that the $Fe^{3+/4+}$ redox reaction is highly reversible. The calculated iron (III) and (IV) proportions agree well within the error with the values expected from the electrochemical curve both in charge and discharge.

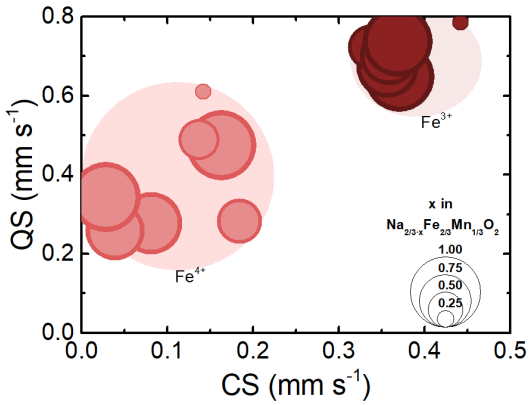

Figure 6.10: Refinement results of the *in-situ* Mössbauer measurements of O3-$Na_{2/3}Fe_{2/3}Mn_{1/3}O_2$ shown in Fig. 6.9. Data is gathered as a function of CS (x axis) and QS (y axis). Different Fe environments are colored differently, and sodium content of each data point is reflected with the symbol size.

6.4 Comparison with the state of the art

The structural evolution of this material has been previously reported by Sharma et al. [6, 11] at rates as high as 1C. That is 50 times the rate at which the cell studied *operando* in this work has been cycled, and so, is not suitable for comparison. Indeed, as it has been already shown in Chapter 4, that the kinetic limitations at high rates will limit the capacity. The structural evolution will also be altered [12–14].

Mortemard de Boisse et al. [5], on the other hand, published an *operando* XRD measurement performed in quasiequilibrium conditions, under PITT regime, that is, by charging the cell by small potential steps and allowing the material to relax during measurements. Rather than *operando*, they report an *in-situ* measurement. In Fig. 6.11 the normalized interlayer distance evolution obtained in this work (results from Fig. 6.6) and that reported by Mortemard de Boisse et al. [5] are compared. The results are very similar, although a slight offset can be seen between both measurements. The difference could be related to the preconditioning of the material. While the measurements reported in this work start on charge from the partially desodiated as-synthesized material ($Na_{2/3}Fe_{2/3}Mn_{1/3}O_2$) without any previous preconditioning, Mortemard de Boisse et al. start their measurements close to the fully sodiated state ($Na_{0.96}Fe_{2/3}Mn_{1/3}O_2$) after an initial discharge process. Note that the values in the composition range $0.96 \geqslant x \geqslant 2/3$ are shown as $Fe^{4+}/Fe = 0$. Moreover, the measurements by Mortemard de Boisse et al. were done under quasiequilibrium conditions, and thus, equilibrium state will be reached at an earlier Fe^{4+}/Fe state. The evolution is however similar in both cases, with an increase of d at the beginning of charge and a reduction starting at half charge approximately.

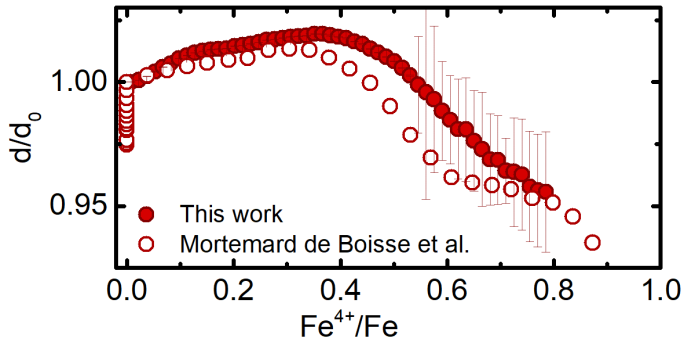

Figure 6.11: Evolution of the normalized interlayer distance of O3-$Na_{2/3}Fe_{2/3}Mn_{1/3}O_2$ as a function of oxidized iron. Results obtained within this work (solid points) are compared with those reported in the literature by Mortemard de Boisse et al. [5] (open points).

6.5 Conclusions

In this chapter the structural evolution of O3-$Na_{2/3}Fe_{2/3}Mn_{1/3}O_2$ upon cycling has been studied. It has been confirmed the O3-P3 biphasic mechanism upon charge reported for this material [3, 5]. It has also been possible to determine the extent of the monoclinic distortion suffered by the material. The discharge process has also been characterized at slow rates and it has been possible to determine the reversibility of the cell parameters. However, the monoclinic distortion is not reverted, as is not the biphasic mechanism. Mössbauer measurements have allowed to observe the high reversibility of the $Fe^{3+/4+}$ redox process.

The TM migration has been studied by analyzing the evolution of the $(0\,0\,3)$ reflection's intensity, although the atomic occupancy analysis have not been possible for the desodiated structures. The onset of Fe migration to tetrahedral vacancies in Na layers has been set at $x \approx 0.36$, linearly increasing until the end of charge. The migration is highly reversible even when cycled to high potentials. Unluckily, the low absorption of the sample for Mössbauer spectroscopy measurements has not allowed confirming the oxidation state or the site at which Fe migrates. Nonetheless, and due to the similarities with $NaFeO_2$ sample in Chapter 5, it has been assumed that iron (III) migrates to tetrahedral vacancies.

These results show that the presence of manganese in the structure does not reduce the amount of migrated iron into the Na layers, but it makes it more reversible.

Bibliography

[1] R. J. Clément, P. G. Bruce, and C. P. Grey. *Journal of The Electrochemical Society*, 162(14):A2589–A2604, 2015.

[2] M. H. Han, E. Gonzalo, G. Singh, and T. Rojo. *Energy and Environmental Science*, 8(1):81–102, 2015.

[3] E. Gonzalo, M. H. Han, J. M. López del Amo, B. Acebedo, M. Casas-Cabanas, and T. Rojo. *Journal of Materials Chemistry A*, 2(43):18523–18530, 2014.

[4] B. M. de Boisse, D. Carlier, M. Guignard, and C. Delmas. *Journal of The Electrochemical Society*, 160(4):A569–A574, 2013.

[5] B. Mortemard de Boisse, J.-H. Cheng, D. Carlier, M. Guignard, C.-J. Pan, S. Bordère, D. Filimonov, C. Drathen, E. Suard, B.-J. Hwang, A. Wattiaux, and C. Delmas. *Journal of Materials Chemistry A*, 3(20):10976–10989, 2015.

[6] N. Sharma, O. K. A. Bahri, M. H. Han, E. Gonzalo, J. C. Pramudita, and T. Rojo. *Electrochimica Acta*, 203:189–197, 2016.

[7] J. Rodriguez-Carvajal. *Physica B*, 192:55, 1993.

[8] O. Pecher, J. Carretero-González, K. J. Griffith, and C. P. Grey. *Chemistry of Materials*, 29(1):213–242, 2017.

[9] X. Li, Y. Wang, D. Wu, L. Liu, S.-H. Bo, and G. Ceder. *Chemistry of Materials*, 28(18):6575–6583, 2016.

[10] C. Prescher, C. McCammon, and L. Dubrovinsky. *Journal of Applied Crystallography*, 45(2):329–331, 2012.

[11] N. Sharma, E. Gonzalo, J. C. Pramudita, M. H. Han, H. E. A. Brand, J. N. Hart, W. K. Pang, Z. Guo, and T. Rojo. *Advanced Functional Materials*, 25(31):4994–5005, 2015.

[12] N. Sharma, N. Tapia-Ruiz, G. Singh, A. R. Armstrong, J. C. Pramudita, H. E. A. Brand, J. Billaud, P. G. Bruce, and T. Rojo. *Chemistry of Materials*, 27(20):6976–6986, 2015.

[13] N. Sharma, M. H. Han, J. C. Pramudita, E. Gonzalo, H. E. A. Brand, and T. Rojo. *Journal of Materials Chemistry A*, 3(42):21023–21038, 2015.

[14] D. Goonetilleke, S. Wang, E. Gonzalo, M. Galcerán, D. Saurel, S. J. Day, F. Fauth, T. Rojo, and N. Sharma. *Journal of Materials Chemistry A*, 7(19):12115–12125, 2019.

7 | Advanced electrochemical characterization of Na_xFeO_2 upon cycling

Contents

7.1 Introduction

In previous chapters the expected relation between the transition metal migration into Na layers and the electrochemical properties degradation has been confirmed, reflected as a reduced reversible capacity and increased polarization. This behavior has been proposed to be due to a reduced ionic diffusion as a consequence of TM migration to the alkali ion layers [1–6].

In this chapter, advanced electrochemical characterizations will be used to determine the internal resistances and ionic diffusion coefficient. They consist in potentiostatic intermittent titration technique (potentiostatic intermittent titration technique (PITT)) coupled with PEIS, performed on three electrode Swagelok cells in order to avoid any contribution from the metallic sodium counter electrode.

7.2 Coupled PITT and PEIS

The voltage and current evolution as a function of time during charge-discharge coupled PITT-PEIS measurements is shown in Figs. 7.1a, b, and c for the 1st, 2nd and 3rd cycles respectively. The voltage is shown in black during the PITT steps and in blue during PEIS steps. The current, in red, corresponds to the relaxation during PITT steps. The DC current decay during PITT as well as the AC current during PEIS measurement will both depend on the kinetic response of the material upon Na insertion and extraction, such as related to sodium diffusion or surface resistivity. More details on the theoretical aspects and on the experimental set-up can be found in the experimental chapter (Sections 2.5.4-2.5.6).

The equilibrium potential (E_0) as a function of the composition is shown in Fig. 7.1d, that is, the voltage and composition after relaxation, at the end of each step. The sodium content change has been calculated as the integral of the current over time ($\Delta x = \int I \mathrm{d}t$). The first cycle (Fig. 7.1a), charged to 3.4 V, shows a low voltage hysteresis between charge and discharge ($\Delta V = 40$ mV). The hysteresis is less than half than that seen on the first cycle during galvanostatic measurements in Chapter 4 (see Fig. 4.1c and Table 4.1, where $\Delta V = 108$ mV in the first cycle at C/10 rate). During PITT technique, kinetic related hysteresis should be negligible due to the quasi-equilibrium nature of the measurement. The voltages at which the plateaus are present can be seen easier in the $\mathrm{d}x/\mathrm{d}E_0$ derivative curve, presented in Fig. 7.1e. The $Fe^{3+/4+}$ redox reaction occurs at 3.33 V (process *A* in Fig. 7.1e) on charge and 3.29 V on discharge during the 1st cycle. The upper voltage has been limited to 3.4 V to avoid to the possible extent the irreversible reactions and iron migration observed above 3.5 V in the galvanostatic cycling of Chapter 5. This also limits the reaction, as only 15% of the theoretical capacity is reached during the discharge, with a Coulombic efficiency of 85%.

During the second cycle (Fig. 7.1b), the charge voltage has been increased to 3.8 V. This potential has been chosen to induce iron migration while still reversible to some extent as shown in the advanced structural characterization chapter (see Figs. 5.13 and 5.14a in Chapter 5). During charge, almost half of the theoretical capacity is reached. The two plateaus observed here are very similar

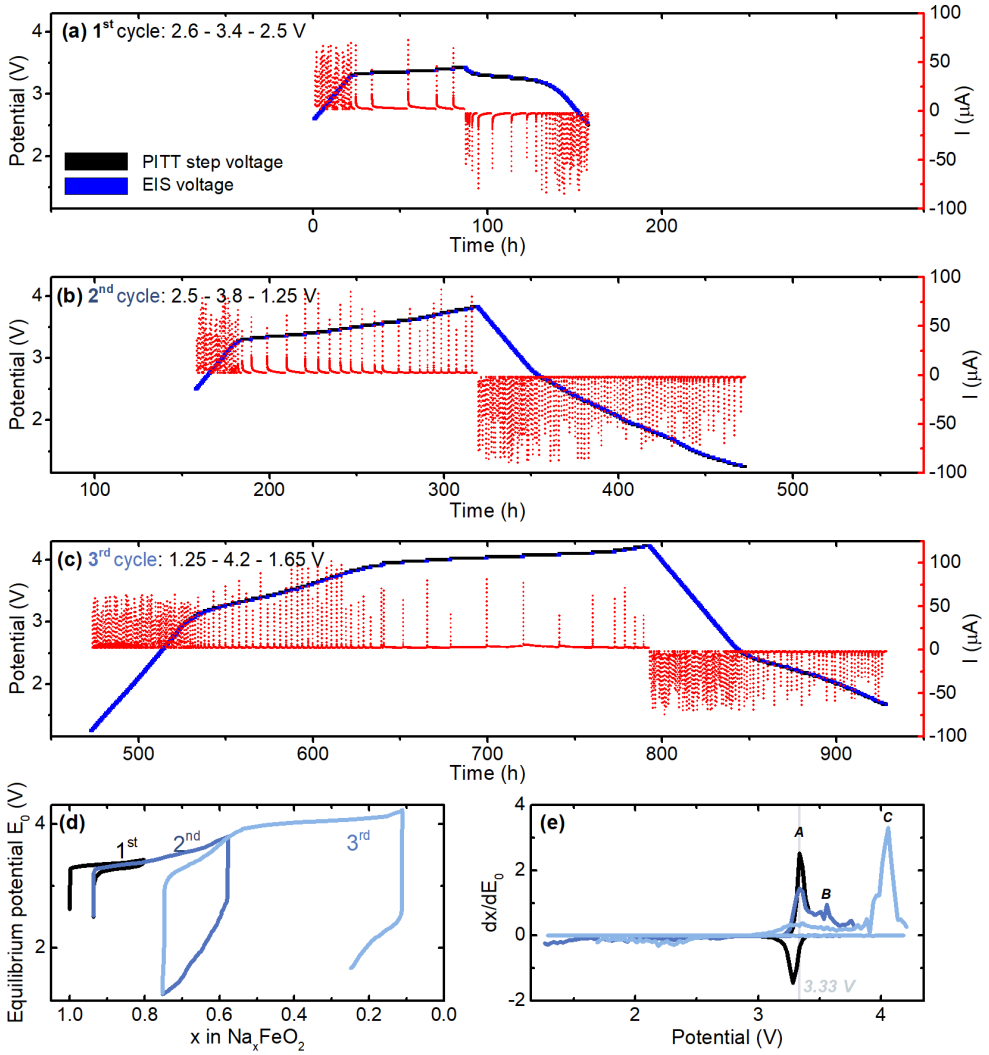

Figure 7.1: Voltage and current evolution of Na_xFeO_2 during coupled PITT and PEIS measurements. Voltage (black during PITT and blue during PEIS) and current (red) evolution during **(a)** 1st cycle ($V = 2.6 - 3.6 - 2.5$ V), **(b)** 2nd cycle ($V = 2.5 - 3.8 - 1.25$ V) and **(c)** 3rd cycle ($V = 1.25 - 4.2 - 1.65$ V). **(d)** Equilibrium potential and **(e)** $\mathrm{d}x/\mathrm{d}E_0$ derivative curves. The different processes observed in the derivative curves as peaks have been labeled.

to those seen during galvanostatic cycling (Fig. 4.3): a first process is observed at 3.3 V, process A already observed during the previous charge, and a second process can be seen at $V = 3.55$ V, that has been labeled as B in Fig. 7.1e, which indicate the succession of two distinct redox processes. According to the observations done in Chapter 5, it seems that the process B might be related to the onset of iron migration. On discharge, as seen during the galvanostatic measurements, an incre-

ment in the potential hysteresis can be seen, and the *A* and *B* processes are hardly distinguished merging into a sloppy region below 2.7 V, introducing a broad peak in the derivative curve in Fig. 7.1e. The fact that the potential hysteresis is observed in the quasi-equilibrium conditions of the PITT means that it is not a kinetics related polarization, but a thermodynamic one. Indeed, the relaxation current limit of $I = \text{C}/500$ is reached before the limiting time of $t = 20$ h, suggesting that the reaction has reached the thermodynamic equilibrium. The lower voltage limit has been decreased to 1.25 V in order to account for the observed potential hysteresis. In this 2$^{\text{nd}}$ cycle a 36% of the theoretical capacity is reached with a Coulombic efficiency of 48%. The irreversibility of the electrochemical properties might be related to an irreversible structural change. As shown in Chapter 5, when the material is charged to 3.8 V the structure suffers from irreversible changes (see Fig. 5.8): the interlayer distance is not recovered and crystallinity of the material is reduced. After these changes, the material presents a large potential hysteresis, as seen in this measurement.

Finally, the cell has been charged to 4.2 V during the third cycle (Fig. 7.1c). In this cycle, process *A* can be seen again close to 3.3 V, although the plateau is shorter and sloppier, as reflected by the broader and less intense peak in the derivative curve. The fact that the redox potential is not increasing on charge suggests that the corresponding reaction occurs at its equilibrium potential as expected in PITT measurements, even if during discharge the reaction is affected. In this case, where the reaction is pushed to a deeply desodiated state ($x \approx 0.1$), an additional high potential plateau can be seen at 4.0 V (process labeled as *C* in Fig. 7.1e). This process *C* seems to be kinetically slow. Indeed, the PITT steps around 4.0 V (steps at 4.0 V, 4.025 V, 4.05 V and 4.075 V, $t \approx 700$ h in Fig. 7.1c) reach the limiting relaxation time (20 h per step) before the limiting relaxation current ($I = \text{C}/500$). This plateau has been previously assigned to oxygen redox reaction in this and other similar layered oxides ($O^{2-} \rightleftharpoons O^{(2-n)-} + ne^-$) [7–9], but it has not been seen during galvanostatic cycling at C/10 (see Fig. 4.3). The fact that it is not observed in galvanostatic cycling can be related to the slow kinetics of the reaction, the material needs very long relaxation times that are not reached upon galvanostatic cycling. As for the second discharge from 3.8 V, here the capacity is not recovered on discharge, despite the low discharge potential of 1.65 V and the quasi-equilibrium conditions under which the cell has been discharged in PITT mode. This reflects that the material here also has undergone an irreversible change, probably related to the irreversible oxygen redox as stated in the literature for other layered oxide materials [7, 10–12]. The low cycling rate of the PITT measurements generally allows the reversible extraction and insertion of high amounts of sodium into the structure with low polarization, as the limiting effect of the kinetics related polarization is avoided by the relaxation at each PITT step. However, it also allows for slow response reactions to occur. In this case, it seems that already at 3.8 V there is some irreversible reaction allowed by the slow cycling of the cell that increases the thermodynamic polarization of the cell and reduces the reversible capacity. Process *C* seems to be a non-desired reaction that increases the voltage hysteresis to $\Delta V \approx 2$ V reducing the Coulombic efficiency to below 25%. The measurement had to be stopped at 1.65 V for technical reasons (potentiostat

maintenance), so before the 1.25 V limit was reached, but still 15% of the theoretical capacity was obtained upon discharge to 1.65 V, although with a low Coulombic efficiency (23%).

7.2.1 Analysis of the impedance spectra

A few examples of PEIS spectra are presented in Fig. 7.2 as Nyquist plots (imaginary vs. real impedances), in which the frequency increases from right to left. Medium-high and high frequency regions are zoomed in second and third columns respectively.

Two semicircles are distinguished, that correspond to at least two different reactions. The semicircle at high frequencies, above 2 Hz (third column in Fig. 7.2), remains stable at all states of charge. The semicircle at low frequencies on the other hand (first and second columns in Fig. 7.2), changes with the charge state of the material, especially during the cycling within the reversible potential window, this is, during 1st charge and discharge and 2nd charge. Note that only the beginning of the low frequency semicircle can be seen for some potentials in the first column of Fig. 7.2. Lower frequencies than 2 mHz would be required to see the complete semicircle. However, decreasing the measured frequency increases the total measurement time and much longer times would be required for the system to be considered at equilibrium at these frequencies. Thus, measuring lower frequencies is impractical. At around 1 Hz, a region with constant slope of about 45° can be seen to the left of the high frequency semicircles in the third column in Fig. 7.2, suggesting a diffusion-related Warburg type contribution to the impedance. This contribution does not seem to change significantly with the voltage, charge-discharge alternation and number of cycles.

Different equivalent models have been tested to refine the spectra. All the tested models (see Fig. 7.3 to see some example models) are derived from Randles equivalent circuit (see Fig. 2.19a), to which additional semicircles ($R||C$ components) have been added. Moreover, all the capacitors have been substituted by CPE elements to account for the depressed semicircles in the experimental Nyquist spectra (see equation 2.8 for its mathematical description). The tested models include three semicircles and a Warburg type semi-infinite linear diffusion impedance (Z_W) placed at different positions. The refinements with the model presented in Fig. 7.3a fits correctly, but considers the diffusive-like response at $\approx$ 1 Hz like a semicircle (namely $R_2||CPE_2$). The refinements done with the equivalent circuits from Fig. 7.3b and c do not fit correctly the experimental data at frequencies above 1 Hz, where Warburg impedance and a $R||CPE$ semicircle would be overlapped.

In order to obtain a correct fit taking into account the diffusive response at 1 Hz, the equivalent circuit from Fig. 7.4 has been used. This model includes two $R||CPE$ components to account for the two observed semicircles: $R_1||CPE_1$ for the high frequency semicircle (right column in Fig. 7.2) and $R_2||CPE_2$ for the low frequency semicircle (first and second columns in Fig. 7.2). A finite length diffusion impedance ($Z_{W\,FL}$) has been included in series with R_1 to account for the diffusion like response at mid frequencies ($f \approx 1$ Hz). This type of diffusion presents a 45° slope, as in the SILD Z_W, but it decays into a semicircle at low frequencies (see equation 2.10 for its mathematical description). A semi-infinite length diffusion impedance $Z_{W\,SILD}$ has been added in series with R_2 to account for the diffusive like response at low frequencies.

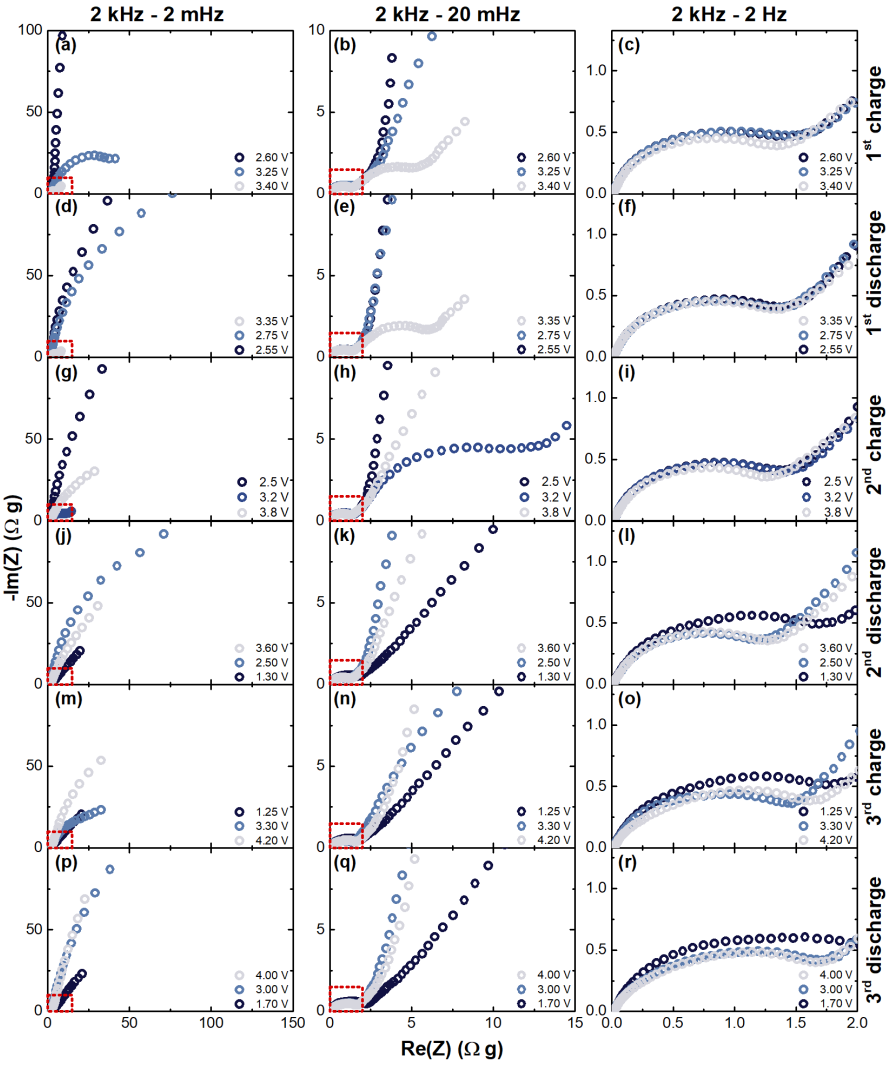

Figure 7.2: Examples of Nyquist spectra at different voltages during **(a-c)** 1st charge ($V = 2.6 - 3.4$ V), **(d-f)** 1st discharge ($V = 3.4 - 2.5$ V), **(g-i)** 2nd charge ($V = 2.5 - 3.8$ V), **(j-l)** 2nd discharge ($V = 3.8 - 1.25$ V), **(m-o)** 3rd charge ($V = 1.25 - 4.2$ V) and **(p-r)** 3rd discharge ($V = 4.2 - 1.65$ V). Each spectra is shown three times, with different zooms to show the details at high frequencies: the first column shows the whole spectra, the second is zoomed to show the mid frequency region and the third column shows the high frequency region. The approximate frequency range shown in each panel is written on top, although the exact range varies with the spectrum.

A few examples of the refinements are shown in Fig. 7.5 as a solid line. These spectra are the same as those shown in Fig. 7.2(g-i), during the second charge. The numerical results of one every five refinements are presented in Tables B.6-B.11, and are graphically presented in Fig. 7.7. For

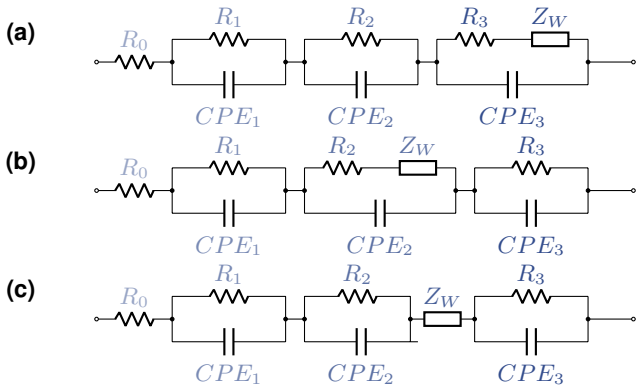

Figure 7.3: Different equivalent circuits tested for fitting the Nyquist plots.

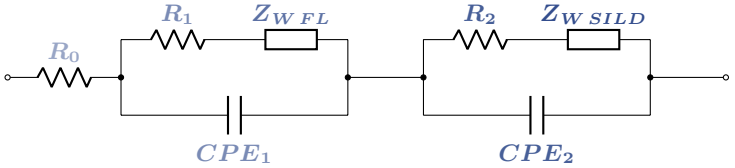

Figure 7.4: Equivalent circuit used for fitting the Nyquist plots. A few examples can be seen in Fig. 7.5 with solid lines.

the sake of simplicity, only when the diffusion related Warburg element is clearly seen as a 45° at low frequencies has $Z_{W\,SILD}$ been refined, as in the spectrum at 3.2 V in Fig. 7.5 or the spectra at 3.40 V and 3.35 V in Fig. 7.2b and e respectively. Otherwise, the impedance value has been set to $Z_{W\,SILD} = 0\,\Omega\ \mathrm{s}^{-1}$. Moreover, when the $R_2||CPE_2$ semicircle and the diffusive response are overlapped and not easily distinguished, the data has been cut to refine only the $R_2||CPE_2$ response. Elseways, the Z-fit software used for the refinements [13] is not able to correctly separate both processes and the result largely depends on the starting values. The resistance R_0 is negligible in these measurements, so it has been fixed to $R_0 = 0\,\Omega$ g. The equivalent circuit fits well the experimental spectra at all states of charge which confirms the applicability of the model. In some spectra the radius of the low frequency semicircle is too big to notice a clear curvature (see for example the spectrum at 2.60 V in Fig. 7.2a). In those cases, the Z-fit software refined the spectrum with a value close to $10^{20} \pm 10^{300}\ \Omega$ g, values that have not been considered.

It can be seen from Fig. 7.7b that the values of R_1 vary very little during the three charge-discharge cycles. Its value lies between 1.0-2.6 Ω g regardless of the charge state.

The value of R_2 on the other hand, varies by several orders of magnitude with the charge state of the material. During the first charge and at the beginning of the 3.3 V plateau R_2 reaches values above $7 \times 10^4\ \Omega$ g, while on the plateau the value drops by four orders of magnitude ($R_2 = 5\,\Omega$ g). The high R_2 value at the beginning of charge can be related to a reduced electronic conductivity,

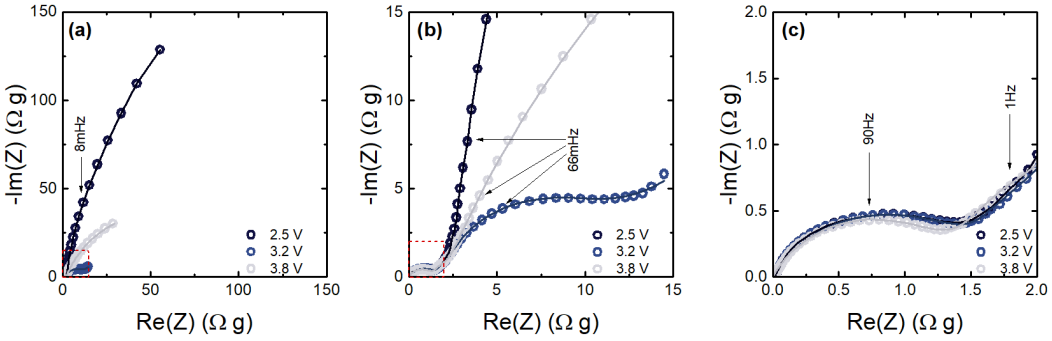

Figure 7.5: **(a)** Potentiostatic electrochemical impedance spectra at various potentials during 2nd charge (2.5 V, 3.2 V and 3.8 V), corresponding to Fig. 7.2 (g-i). Scatter points for the experimental data and solid lines for the simulated Nyquist spectra, using equivalent circuit from Fig. 7.4. **(b)** and **(c)** show zoomed areas of the same spectra.

as it is known that $NaFeO_2$ in its sodiated state is an electronic insulator [14–17]. Indeed, pristine $NaFeO_2$ shows high spin Fe^{3+} (with an electron configuration of $[Ar]3d^5$), which has an electron in every orbital. Fig. 7.6a shows the orbital splitting diagram of HS Fe^{3+}. The lack of electron vacancies hinders the electron hoping. When iron is oxidized to Fe^{4+} and loses one of its electrons (electron configuration $[Ar]3d^4$), one of the orbitals is emptied (see the orbital splitting diagram in Fig. 7.6b). The decrease of R_2 would be related to the increment of electronic conductivity due to the partial emptying of the Fe energy band as a consequence of the $Fe^{3+/4+}$ oxidation reaction [18], as electron hoping through the empty orbitals would be favored. As an example, the electronic conductivity in the isostructural $LiCoO_2$ has been proposed to occur through moving electron holes [19, 20], which would be enhanced with the oxidation of Co ions. Moreover, the increase of electronic conductivity with anion extraction (and the associated TM oxidation) has been previously described for Li based layered oxides and anode materials [20–22].

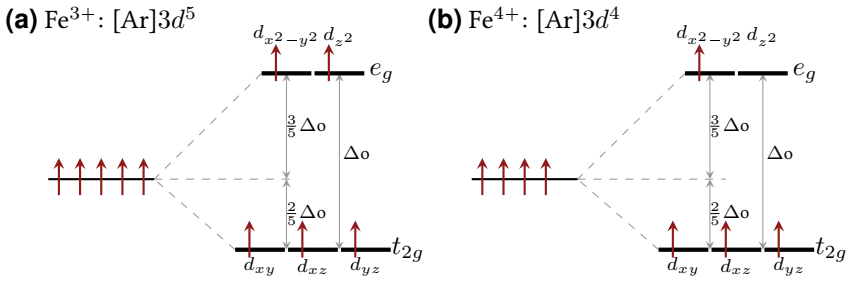

Figure 7.6: Crystal field diagram $3d$ orbital splitting comparison of **(a)** HS Fe^{3+} and **(b)** HS Fe^{4+} in an octahedral environment. Electrons are represented as red arrows.

On 1st discharge, the evolution of R_2 is very reversible: its value stays low, around 5 Ω g during process *A*, but it increases up to 5×10^2 Ω g at the end of the reaction, probably due to the

reduced electronic conductivity in the sodiated state as a consequence of the reversible $Fe^{3+/4+}$ redox reaction.

During the second charge a similar evolution can be seen, where R_2 is high at the sodiated state and decreases during the $Fe^{3+/4+}$ plateau. However, it starts to increase again near $x = 0.7$, when the potential starts to increase beyond 3.4 V (process *A*). At the end of the 2nd charge (3.8 V, $x = 0.58$) the value of R_2 reaches 125 Ω g, which corresponds to a two orders of magnitude increase from $x = 0.7$, and it stays high during discharge and subsequent cycling. The high R_2 value could be related to a crystalline structure transformation process [23]. Moreover, a change in the crystalline structure could lead to a lower electronic conductivity or an increased charge transfer resistance.

The results of the CPE elements' refinements are presented in Fig. 7.7c (C admittance) and Fig. 7.7d (a argument). It can be seen how the admittance value remains close to constant at all states of charge in both processes: $C_1 \approx 40$ µF s^{a-1} and $C_2 \approx 2$ mF s^{a-1}. However, the evolution of a argument differs in both processes. While a_1 remains close to constant at $a_1 \approx 0.65$ in the high frequency semicircle, a_2 in the low frequency region changes with the charge state of the material. The constant value of a_1 suggests that the roughness or inhomogeneities of the surface remain stable upon cycling. On the other hand, the changes in a_2 indicate the opposite, that the particle's morphology changes upon cycling. During the process *A* at 3.3 V a_2 decreases from 0.95 (close to a perfect capacitor) down to 0.6, suggesting an increase of the irregularities of the phase. The process seems to be reversible, as high a_2 values, close to the initial 0.95 value, are obtained at the end of the 1st discharge, although this increase upon discharge is slower and takes a larger range of potential than the drop upon charge. A similar behavior is observed during the 2nd cycle, where the value of a_2 drops around 3.3 V down to 0.65, and is only slightly increased on further cycling. During the 2nd discharge, and as a seen during the 1st cycle, a_2 increases until a maximum of $a_2 = 0.9$ is obtained at $V = 2.5$ V. However, when the potential is lowered below 2.5 V the value of a_2 is further decreased down to 0.5 at the end of the discharge. Again, the process seems to be partially reversible, and is increased during the 3rd charge, although the values remain below 0.85. At the end of the 3rd discharge the value of a_2 decreases again. Thus, it seems the surface of the particles become rougher during reaction *A* and at low potentials, but it is at least partially reversible.

The process at high to mid frequencies (block $(R_1 + Z_{w\,FL})||CPE_1$ in the equivalent circuit) seems to be related to a thin surface layer, given the finite length diffusion. A possible explanation for this, is the formation of a solid permeable interface (SPI) layer at the surface of the particles upon electrode lamination preparation, or upon contact with the electrolyte and the rest of the cell components, before any current or potential excitation are applied, which remains very stable upon cycling. Indeed, decomposition of the active material has been previously reported for lithium based materials [24]. The species forming the surface layer and its morphology depend on the electrode material type, temperature and storing time [25]. In this particular case, the layer seems to be electronic and ionic conductor.

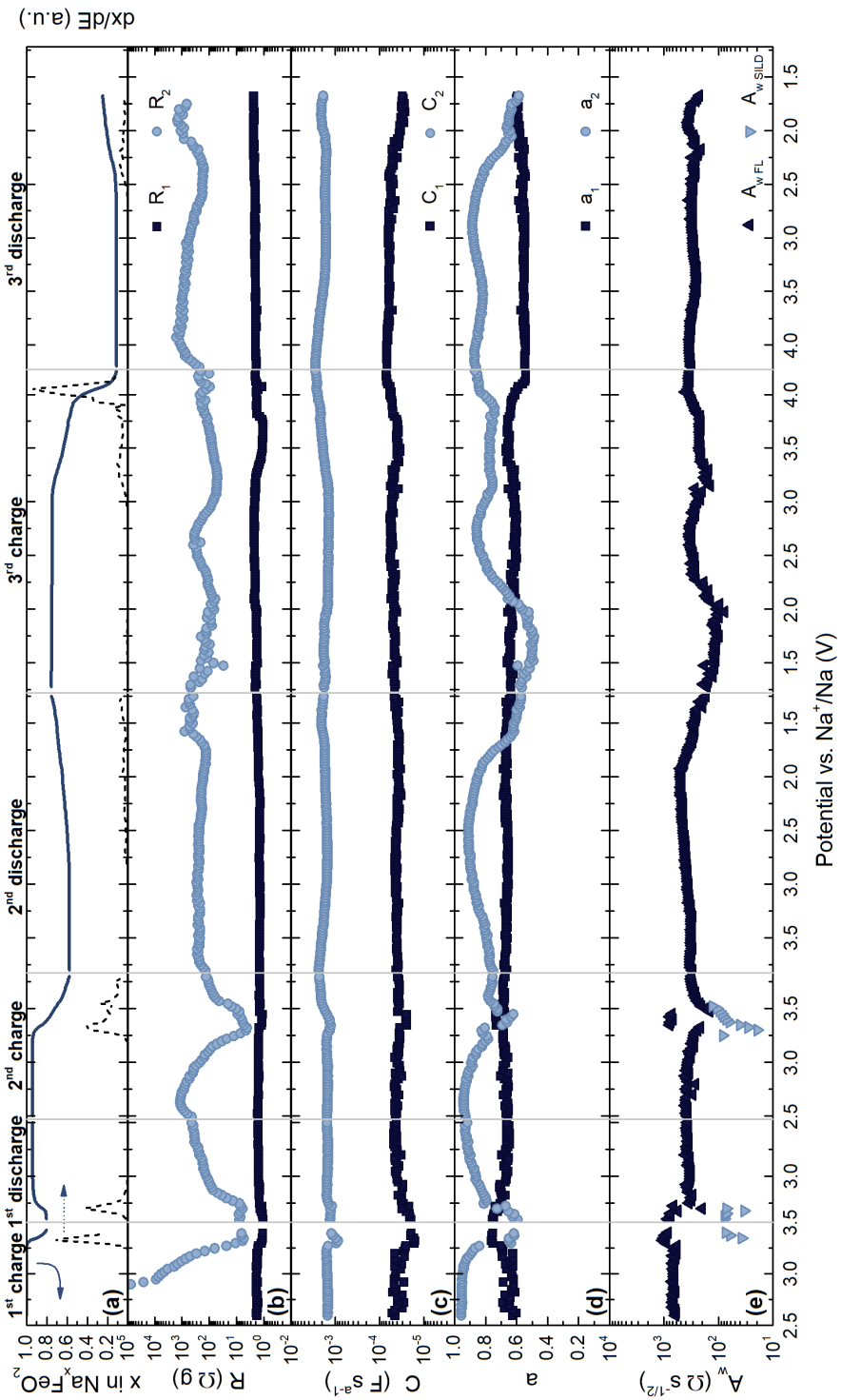

Figure 7.7: Results of the Nyquist spectra fitting with the equivalent circuit from Fig. 7.4 as a function of potential. **(a)** Sodium content (solid line, left) and derivative curve (dashed line, right), **(b)** resistance values, **(c)** admittance of the CPE component, **(d)** argument of the CPE component and **(e)** Warburg coefficient A_w. The components of the high frequency region $(R_1 + Z_{w\,FL})||CPE_1$ are shown in dark colors and the low frequency region components $(R_2 + Z_{w\,SILD})||CPE_2$ are shown with light colors.

On the other hand, the mid to low frequency process seems to be related to a process in the bulk of the particle where the end of the diffusing phase is not reached, and hence the semi-infinite linear diffusion. This process has been fitted with the $(R_2 + Z_{w\,SILD})||CPE_2$ block of the equivalent circuit. The formation of new structures in the bulk of the particle at potentials above 3.4 V could explain the increase in R_2 and its irreversibility, if the charge transfer or the electronic conductivity of the formed structure are worse than those of the original phase for example.

From these refinements it can be seen that the diffusion related Warburg coefficient $A_{w\,FL}$ obtained at mid frequencies (up triangles in Fig. 7.7e) changes very little throughout cycling, regardless of the potential or the cycle number. In most of the spectra, the semicircle formed by $R_2||CPE_2$ is too big to be able to observe the Warburg type response at low frequencies, and the impedance has been set to $Z_{W\,SILD} = 0\ \Omega\ s^{-1/2}$. However, during the first cycle and second charge, several spectra show a second 45° slope, and these spectra have been refined including $Z_{W\,SILD}$ (down triangles in Fig. 7.7e). The Warburg coefficient at low frequencies is about one order of magnitude lower than that estimated at 1 Hz. Nonetheless, it is reversible, and the observable Warburg coefficient is mainly constant.

This is a surprising result, because according to literature the electrochemical degradation has been related to a reduced ionic diffusion of the material [4], although it was not confirmed experimentally. However, at several states of charge, when a_2 gets close to 0.5, the diffusive response and the $R_2||CPE_2$ elements are hard to distinguish, as they both show similar inclinations. Moreover, the quality of the refinements can affect the final values. Thus, the Warburg coefficient has been otherwise calculated to validate the refinements.

7.2.2 Conventional methods to determine ionic diffusion

The ionic diffusion can be calculated from the response of the material to an electrochemical perturbation, assuming that the relaxation current is essentially limited by the Na mass diffusion. The electrochemical excitation can be of different nature, as the overpotential at the beginning of a constant current step (galvanostatic intermittent titration technique (GITT)), a potential step (PITT) or an oscillating potential (PEIS) or current (galvanostatic electrochemical impedance spectroscopy (GEIS)) around an equilibrium state. The excitation will create an ionic concentration gradient. According to Fick's laws of diffusion, the gradient will tend to homogenize through the diffusion of the mobile species (Na^+) from the high concentrated region to the low concentrated region. Biphasic and phase transformation regions are not considered in the theory [26], as it intrinsically assumes a solid solution mechanism, that is, a change of Na concentration without any other structural change in the material besides changes in unit cell parameters. Thus, the results analyzed in biphasic or phase transforming regions have to be carefully considered.

When the diffusion path of the mobile species is short compared with the radius of the particles, the Cottrellian or SILD conditions are fulfilled (see Section 2.5.6 for more details).

The diffusion coefficient D, on the basis of equation 2.14, can be expressed in terms of morphological factor (MF), thermodynamic factor (TF) and dynamic factor (DF) as in equation 7.1:

$$D = MF \times TF \times DF = \left(\frac{V_m}{zmFS}\right)^2 \left(\frac{\partial E}{\partial x}\right)^2 \left(\frac{1}{\sqrt{2}A_w}\right)^2 \tag{7.1}$$

These factors will be explained below.

7.2.2.1 Morphological factor

The morphological factor (MF) is a prefactor that accounts for the sample mass, surface, molar volume and transferred electrons:

$$MF = \left(\frac{V_m}{zmFS}\right)^2 \tag{7.2}$$

where V_m is the molecular volume, z is the amount of electrons transferred per formula unit ($z = 1$ in this case), F is the Faraday's constant, S is the effective surface area and m is the mass of the active material. V_m has been calculated according to the cell parameters of the pristine material, according to expression 7.3, given that it is an hexagonal unit cell which contains three formula units.

$$V_m = \frac{1}{3}a^2 c \sin\frac{\pi}{6} \tag{7.3}$$

In this case $V_m = 42.49$ Å^3. S has been estimated to be approximately two thirds of the surface area calculated by SAXS (see Fig. 3.8 in Chapter 3): $S = 1.859$ m^{2}g^{-1}. This $^2/_3$ factor is due to the anisotropy of the layered structure, as sodium ions are expected to insert only in the (a, b) plane, but not in z direction. The value obtained for this sample is MF= 8.93×10^{-16} m^{2}C^{-2}.

Both molar volume and specific surface area will depend on structural volume change upon cycling. However, according to the structural unit cell volume deduced from the analysis of the *operando* XRD experiments in Chapter 5, the maximum change in $^{V_m}/_S$ has been estimated to be about 2%. Diffusion coefficient can differ several orders of magnitude on a cycling process [26–29], so a change in MF of 2% should be negligible and it has thus been considered to stay constant throughout the cycling for the sake of simplicity.

7.2.2.2 Thermodynamic factor

The thermodynamic factor (TF) is obtained from the derivative of the equilibrium potential curve, as shown in equation 7.4:

$$TF = \left(\frac{\partial E_0}{\partial x}\right)^2 \approx \left(\frac{\Delta E_0}{\Delta x}\right)^2 \tag{7.4}$$

where E_0 represents the equilibrium potential during the PITT step. The equilibrium potential curves, composition vs. equilibrium potential, are shown in Fig. 7.1d. It is important to notice that biphasic regions will be reflected as a plateau in the potential curve, according to Gibbs phase rule

[30, 31]. As a consequence, $\mathrm{d}x/\mathrm{d}E_0$ will diverge inducing an artificial drop of the thermodynamic factor and, by extension, of the diffusion coefficient value. Indeed, the evolution of TF is related to the equilibrium voltage curve (Fig. 7.1d), as it is the squared inverse of its derivative. Thus, the reaction plateaus in the equilibrium potential curve will be reflected as low TF values, and the regions between the plateaus will be reflected as high TF values. One has thus to be cautious when applying this method in materials with biphasic transformations, such as during the O3-P3 transformation in the present case. The obtained TF values at all states of charge are presented with gray squares in Fig. 7.8b, together with the $|\mathrm{d}x/\mathrm{d}E_0|$ derivative curve in Fig. 7.8a.

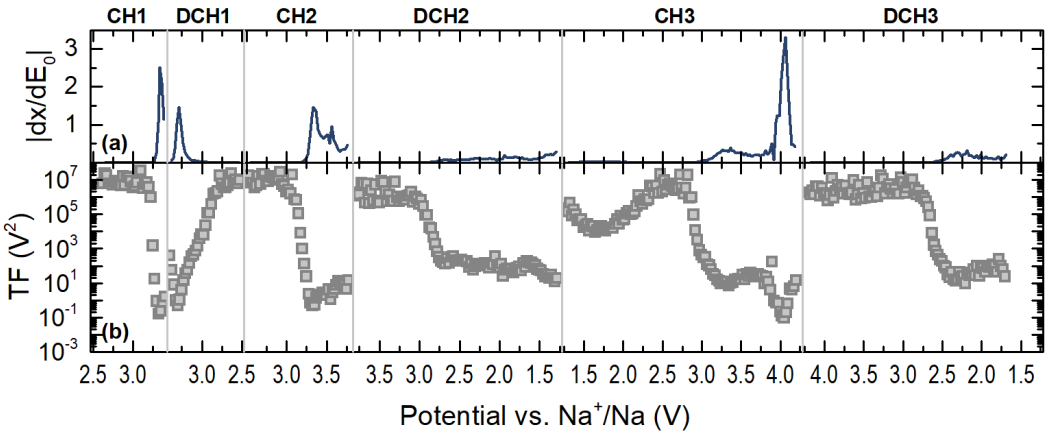

Figure 7.8: **(a)** Derivative curve $|\mathrm{d}x/\mathrm{d}E_0|$ and **(b)** thermodynamic factor evolution of $NaFeO_2$ as a function of potential. On top the cycle state is shown, CH for charge and DCH for discharge, and the number representing the cycle number.

At the beginning of the first charge ($V = 2.6{-}3.3$ V) a constant value is observed, TF $= 10^7$ V^2. During the plateau at 3.3 V (process A) reflected as a peak in the $\mathrm{d}x/\mathrm{d}E_0$ derivative curve, where the majority of the sodium extraction occurs, a drop of the thermodynamic factor down to less than 1 V^2 can be seen, which corresponds to a decrease in more than seven orders of magnitude. On discharge the evolution of TF is reversible, with a minimum at 3.3 V, below which the TF gradually increases until values close to the initial ones are reached at the end of the discharge, confirming the same level of reversibility observed for R_2 evolution from PEIS Nyquist plots refinements. This is reflected in the reversibility of the voltage curve during the 1st cycle in Fig. 7.1d.

During the second charge the behavior is similar to the first one, with a drop of seven orders of magnitude of TF at 3.3 V. Then, and as seen in Fig. 7.1d, the equilibrium potential increases slowly, which corresponds to only a slight increment in the $|\mathrm{d}E_0/\mathrm{d}x|$ derivative, reaching values of TF $= 10$ V^2 at the end of the charge. On discharge however, and due to the polarization observed in 7.1d, TF suffers a discontinuity as it increases back to 10^7 V^2.

This tendency is repeated on further cycling: a high TF value is observed at the beginning of the charge and discharge processes, where the polarization of the cell can be seen (see Fig. 7.1d) and

the $\mathrm{d}x/\mathrm{d}E_0|$ derivative is negligible, and it drops several orders of magnitude during the reaction plateaus where the $|\mathrm{d}x/\mathrm{d}E_0|$ derivative is no longer negligible. The potential hysteresis of the cell is thus reflected as a discontinuous TF evolution.

7.2.2.3 Dynamic factor

As explained in Section 2.5.5 in Chapter 2, the dynamic factor is inversely proportional to the squared Warburg coefficient (A_w).

$$DF = \left(\frac{1}{\sqrt{2}A_w}\right)^2 \tag{7.5}$$

The kinetic response change of the material to the external electric field will be reflected in changes of the Warburg coefficient, which can be calculated according to the applied excitation. Two different methods, based on an oscillating potential excitation at equilibrium state (PEIS) and current relaxation, both measured after each PITT potential step excitation, have been used and will be explained below.

7.2.2.3.1 From potentiostatic electrochemical impedance spectroscopy

Since the Warburg impedance is generally visible at low frequencies [23, 32], a common way to extract the Warburg element is to use the impedance value at the lowest measured frequency, according to [32]:

$$A_w = -\operatorname{Im}[Z(\omega_{min})]\sqrt{\omega_{min}} \tag{7.6}$$

Nonetheless, and as seen in the Nyquist plots of the impedance measurements in Section 7.2.1, the low frequency values correspond in many cases to the semicircle $R_2||CPE_2$.

A 45° slope is nevertheless seen between the $R_1||CPE_1$ and $R_2||CPE_2$ semicircles, around 1 Hz, that has been previously fitted with a finite length diffusion impedance, Z_{FL}. In Fig. 7.9a the imaginary part of the impedance has been plotted as a function of the frequency. It can be seen that around 1 Hz, the imaginary part evolves as the square root of the frequency, this is, it behaves as the Warburg impedance according to equation 2.9. In Fig. 7.9b the imaginary part of the impedance has been multiplied by the square root of the frequency, and the region at which the Warburg relation can be seen is reflected now as a constant value and a local minimum. Warburg coefficient can be calculated graphically as the local minimum:

$$A_w = \min[-\operatorname{Im}(Z)\sqrt{\omega}] \tag{7.7}$$

In Fig. 7.10 the results obtained with the three aforementioned methods are compared: with gray up and down triangles, from the Nyquist plots' refinements at mid and low frequencies respectively as shown in Fig. 7.7e; with blue circles the values obtained with equation 7.6 (calculated at the minimum frequency); and with dark blue squares the values obtained from equation 7.7 (the

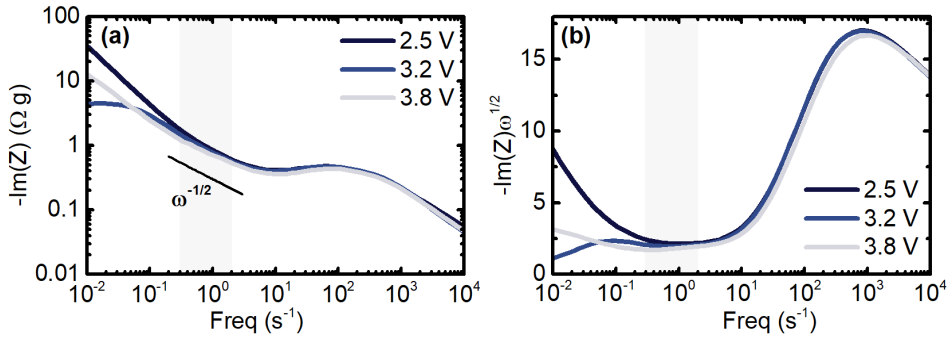

Figure 7.9: Graphical method for the Warburg coefficient calculation from PEIS data according to equation 7.7. **(a)** Imaginary part of impedance and **(b)** imaginary part of impedance times the square root of the frequency as a function of frequency. The frequency region where the diffusion-like conditions are fulfilled has been highlighted in gray.

graphical method). The graphical method and the Nyquist refinements at mid frequencies are in good agreement, with the same evolution although values from Nyquist refinements are about 4 times higher at most states of charge. Considering the changes of about seven orders of magnitude in the thermodynamic factor, a change of less than one order of magnitude between the values obtained with the two different methods should be negligible. The results obtained at the minimum frequency on the other hand show clear changes upon cycling. Moreover, these changes are very close to the changes observed for R_2 in Fig. 7.7b. It is worth noting that the value of a_2 argument of the CPE_2 element is in this region below 0.6 (see Fig. 7.7d), making it difficult to separate the diffusive response and the onset of the $R_2||CPE_2$ semicircle. It seems thus that the method were A_w is extracted from the minimum frequency value is reflecting the changes in R_2 rather than the Warburg coefficient. However, at some spectra the Warburg impedance at low frequencies can be seen, around 3.3 V during the first cycle and a half (1st cycle and 2nd charge). In these regions, highlighted in gray, indeed, the values obtained at the minimum frequency are in good agreement to the refinements done considering $Z_{W\,SILD}$ at low frequencies.

In conclusion, two dynamic factors can be observed at mid and low frequencies respectively. The mid frequency region values have been obtained by Nyquist plot fitting and with a graphical method. In both cases, a near constant value has been obtained close to DF $= 10^{-6}$ s Ω^{-2}. The low frequency region values have been obtained by Nyquist plot fitting and taking the values at the minimum frequency. However, the diffusive response at low frequencies is only appreciable in a few spectra due to the growth of the $R_2||CPE_2$ semicircle. The dynamic factor at low frequencies shows a maximum of DF $= 10^{-3}$ s Ω^{-2} at the reaction potential of process *A* as shown in Fig. 7.1e.

Taking into account that only the mid frequency Warburg could be obtained in the whole potential range, and bearing in mind that the values obtained from the Nyquist plot fittings are more susceptible to error because they depend on the goodness of the fitting, the results obtained from the graphical method will be used from now on.

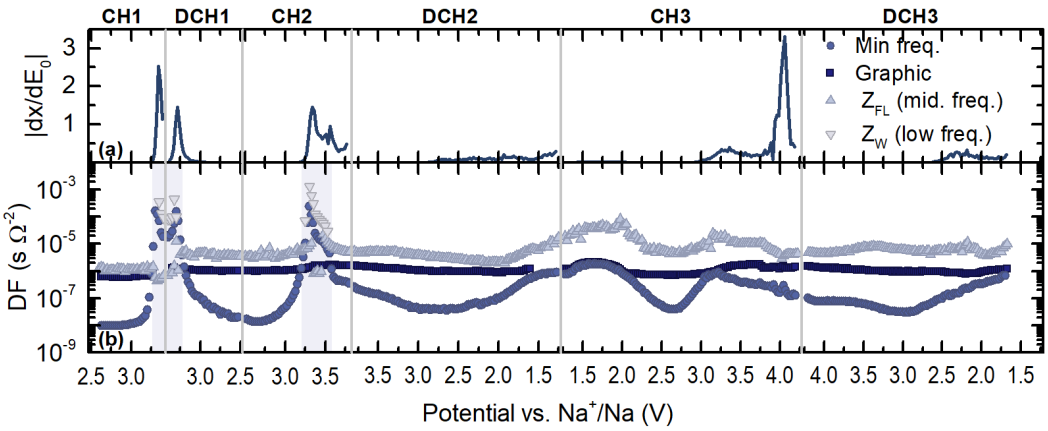

Figure 7.10: **(a)** Derivative curve $|\mathrm{d}x/\mathrm{d}E_0|$ and **(b)** dynamic factor of $NaFeO_2$ calculated from PEIS data as a function of potential. Dynamic factor has been calculated with three methods from PEIS data: with blue circles, values obtained from the minimum frequency impedance value (equation 7.6), with dark blue squares, values obtained from the graphical method shown in Fig. 7.9 (equation 7.7), and with up and down gray triangles, values obtained from Nyquist spectra fitting at mid and low frequencies respectively. On top the cycle state is shown, CH for charge and DCH for discharge, and the number representing the cycle number.

7.2.2.3.2 From PITT current relaxation

As shown in Section 2.5.5 in Chapter 2, during the current relaxation of the PITT steps, the diffusion of Na^+ occurs as a consequence of a concentration gradient induced by the potential change. In the short time limit, the path of the mobile species will be small compared with the radius of the particles, fulfilling the Cottrell or SILD regime conditions. In this region the current is expected to decay as the inverse of the square root of the time [33, 34]. Fig. 7.11a shows an example of experimental current decay with a solid line, together with the theoretical Cottrellian current ($I \propto 1/\sqrt{t}$) as a dashed line. The region at which the current decays as the Cottrellian current has been highlighted in gray, approximately at $t = 1$ s after the beginning of the potential step. It is worth noting that this 1 s time agrees well with the frequency of 1 Hz at which the diffusion related Warburg behavior is observed in the impedance spectra. In the Cottrellian region the value of $I\sqrt{t}$ is expected to remain constant [35], so that when plotting $I\sqrt{t}$ vs. t a local maximum is expected, which is actually seen near $t = 1$ s in the example of Fig. 7.11b. The Cottrellian region can thus be located with a graphical method, by finding the value $(\max |I\sqrt{t}|)$, and the Warburg element can be calculated with equation 7.8 [35].

$$A_w = \left| \frac{1}{\sqrt{2\pi}} \frac{\Delta E}{I_{Cot}\sqrt{t}} \right| = \frac{1}{\sqrt{(2\pi)}} \frac{|\Delta E|}{\max |I\sqrt{t}|} \tag{7.8}$$

where ΔE is the potential step and I_{Cot} is the Cottrellian current.

It is important to bear in mind that the current does not only depend on the diffusion, but also on all the contributions of the impedance of the cell, such as surface or charge transfer resistances, which as seen in a previous section, depend on the charge state. For this reason, the current has been corrected in the mass transport regime as [36]:

$$I_{corrected} = \frac{I_0 I_{Cot}}{I_0 - I_{Cot}} \tag{7.9}$$

where I_0 is the current at the beginning of the step.

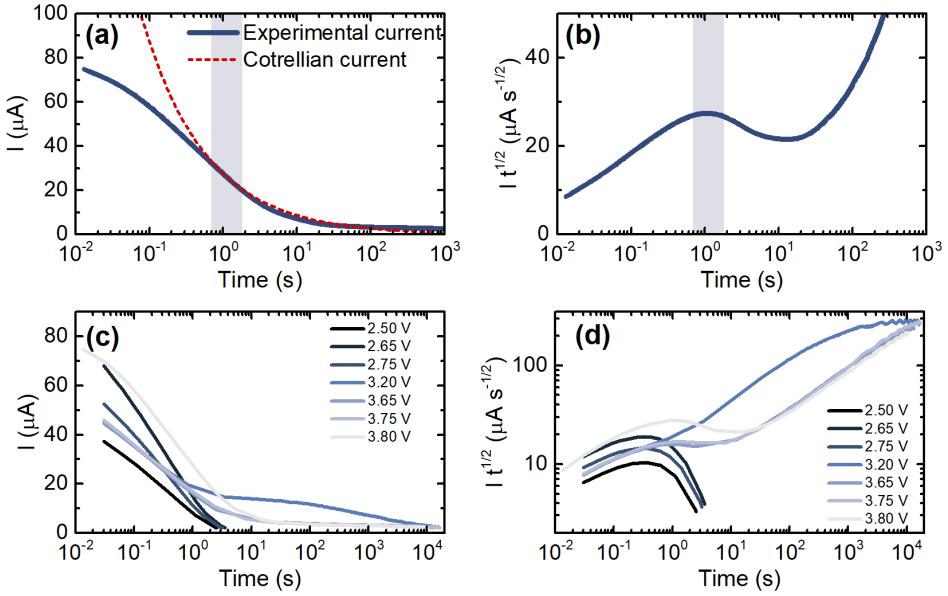

Figure 7.11: **(a)** Example of current evolution upon time ($V = 3.8$ V during second charge) and Cottrellian model current. **(b)** Graphical method for the Warburg coefficient calculation from PITT data according to equation 7.8. The region at which the Cottrellian conditions are fulfilled has been highlighted in gray. Several examples of the evolution of **(c)** the current and **(d)** the evolution of $I\sqrt{t}$ at several potential steps during the 2nd charge.

In Fig. 7.11c and d several examples are presented at different potentials, where two different cases are observed. At low potentials ($V \leqslant 2.75$ V) a single maximum can be seen in the $I\sqrt{t}$ curves. At high potentials on the other hand ($V \geqslant 3.20$ V) a local maximum can be seen at low response times and a second maximum at long response times near or above 10^3 s. The second maximum is generally attributed to a biphasic transformation mechanism [29, 37–41]. For this reason, whenever two local maxima have been observed, the maximum at short response time has been selected for the calculation of the Warburg element.

Once the Warburg coefficient has been determined, the dynamic factor (DF) can be calculated as shown previously with equation 7.5. In Fig. 7.12b the dynamic factor obtained from PEIS (graphic method) and PITT methods are presented, together with the $|\mathrm{d}x/\mathrm{d}E_0|$ derivative curve in

Fig. 7.12a. The DF values obtained from the two techniques are very close and follow the same evolution. This confirms the applicability of the graphical method for the PEIS data analysis. Since the dynamic factor DF obtained from the PEIS data are less noisy, these results will be used to calculate the diffusion.

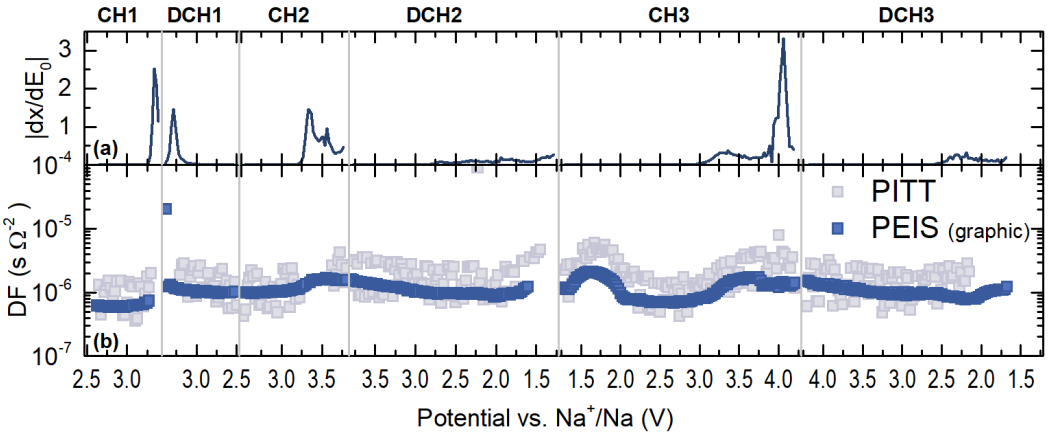

Figure 7.12: **(a)** Derivative curve $|\mathrm{d}x/\mathrm{d}E_0|$ and **(b)** dynamic factor of $NaFeO_2$ as a function of potential. The dynamic factor has been calculated with two methods: with the graphical method from PEIS (dark blue squares) and from PITT (light blue squares) data. On top the cycle state is shown, CH for charge and DCH for discharge, and the number representing the cycle number.

7.2.2.4 Ionic diffusion

The evolution of the diffusion coefficient has been determined from equation 7.1 based on the values of TF and DF presented in Figs. 7.8 and 7.12 respectively, and the results are presented in Fig. 7.13d as a function of composition. Together with the diffusion coefficient, the potential evolution is shown in Fig. 7.13a, the thermodynamic factor is shown in Fig. 7.13b and the dynamic factor in Fig. 7.13c. As can be seen from Fig. 7.13d, the diffusion coefficient changes more than six orders of magnitude in narrow composition ranges. Indeed, it can be seen that the data points are concentrated in the beginning of charge and discharge processes, and D varies from 10^{-10} cm^2 s^{-1} to 10^{-16} cm^2 s^{-1} in this regions, very close to the evolution of the thermodynamic factor: the low diffusion coefficient values are six orders of magnitude lower at the plateaus of the potential curves.

The same results have also been presented as a function of potential in Fig. 7.14. A sharp minimum can be seen during the first charge at 3.3 V, corresponding to the process A as described in Fig. 7.1e (indicated by a peak in $|\mathrm{d}x/\mathrm{d}E_0|$ in 7.14a). It is reversible on discharge and reproducible during the second charge. However, and probably related to the increase of the potential hysteresis, it is not reversed on the subsequent discharge. It is worth noting that the discontinuity of the diffusion coefficient value at the end of the charge and discharge processes once the cell has been

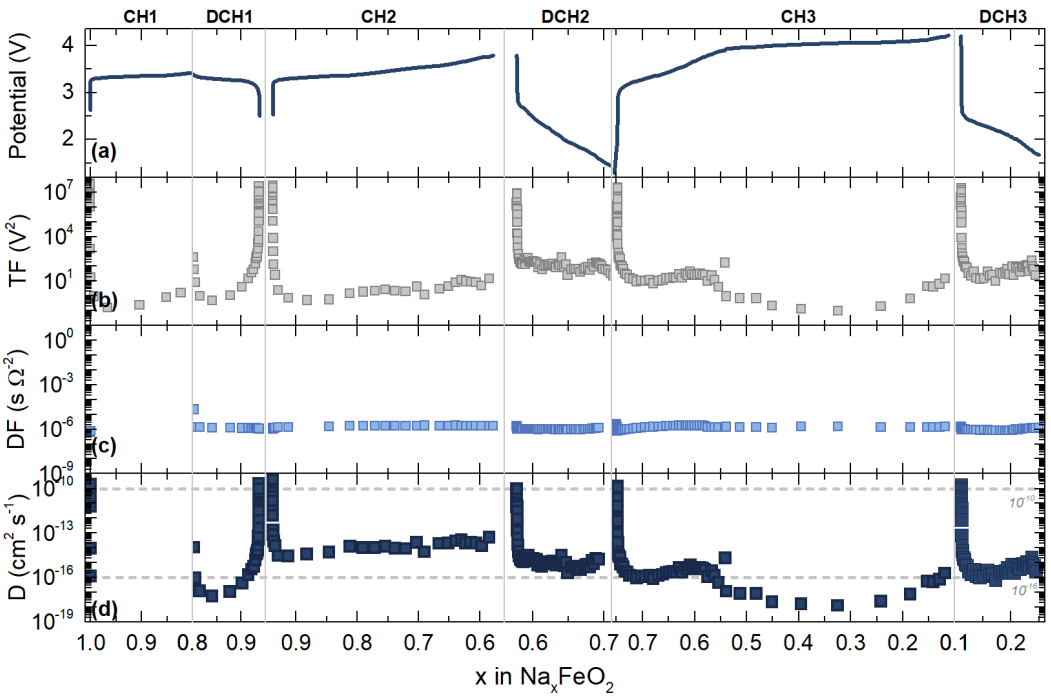

Figure 7.13: **(a)** Voltage evolution, **(b)** thermodynamic factor (from Fig. 7.8), **(c)** dynamic factor (from Fig. 7.12) and **(d)** diffusion coefficient of $NaFeO_2$ calculated with equation 7.1 as a function of composition. Horizontal dashed lines at $D = 10^{-10}$ cm^2s^{-1} and $D = 10^{-16}$ cm^2s^{-1} have been included as visual help. On top the cycle state is shown, CH for charge and DCH for discharge, and the number representing the cycle number.

charged beyond 3.6 V (the reversible voltage limit) comes from the potential hysteresis and the resulting discontinuity of TF (see Figs. 7.13b and 7.14b). After the second charge, the diffusion coefficient values are high at the beginning of every charge and discharge, and decreases at the end. It seems thus that the method used to calculate the diffusion coefficient is altered by the hysteresis of the potential so that one of the two values at least, before or after the discontinuity, does not represent the actual diffusion coefficient of the material.

In Fig. 7.15 the diffusion coefficient obtained in this work has been compared with that reported in the literature by Kataoka et al. [42] as a function of composition. Kataoka et al. calculated the diffusion coefficient by means of GITT, in which square current pulses of approximately C/80 were applied followed by a relaxation process of 2 hours.

Hwang et al. [43] also reported the diffusion coefficient of $NaFeO_2$. In this case, the value was obtained by means of EIS, by observing the Warburg diffusion related slope. It can be seen that the results are in good agreement with the different techniques: the diffusion is about $D \approx 10^{-14}$ cm^2s^{-1} at most sodium concentrations, although it is higher near the fully sodiated state.

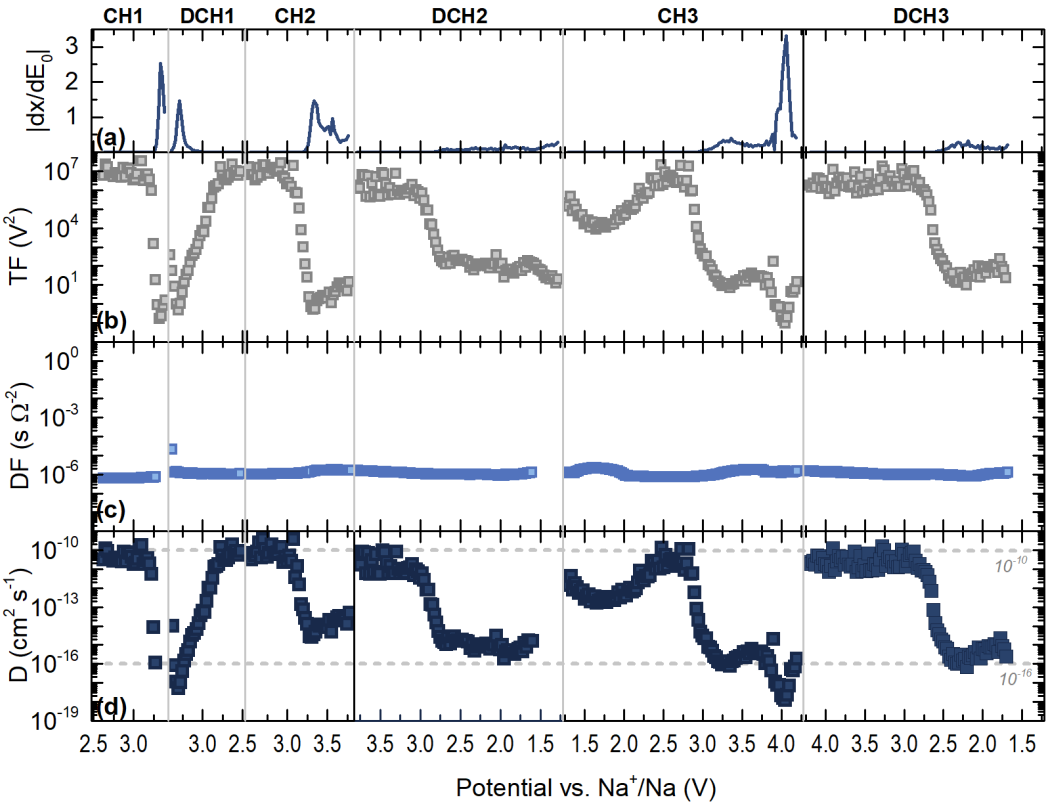

Figure 7.14: **(a)** Derivative curve $|\mathrm{d}x/\mathrm{d}E_0|$, **(b)** thermodynamic factor (from Fig. 7.8), **(c)** dynamic factor (from Fig. 7.12) and **(d)** diffusion coefficient of $NaFeO_2$ calculated with equation 7.1 as a function of potential. Horizontal dashed lines at $D = 10^{-10}$ cm^2s^{-1} and $D = 10^{-16}$ cm^2s^{-1} have been included as visual help. On top the cycle state is shown, CH for charge and DCH for discharge, and the number representing the cycle number.

When calculating the diffusion coefficient, as explained in the previous section, the dynamic factor has been corrected for the possible influence of the internal resistances in the current with the equation 7.9. However, the thermodynamic factor has not been corrected for the potential hysteresis caused by irreversible reactions. Moreover, the method presented above considers that the relaxation current throughout the potential step is only limited by the Na diffusion, without contribution of other processes except those limiting I_0, such as electronic conductivity or charge transfer resistance. However, and as shown in Fig. 7.11, the long time current response is altered at high potentials, where the current gets larger than the Cottrellian current, most likely by a crystalline structure change. Thus, the thermodynamic factor calculated from the derivative equilibrium potential curve is altered. During the GITT measurements to obtain the diffusion coefficient values from Kataoka et al. shown in Fig. 7.15 [42], the material was only allowed to rest

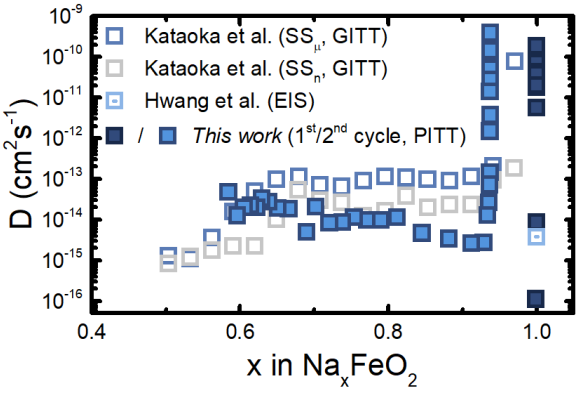

Figure 7.15: Comparison of the diffusion coefficient obtained in this work by means of PITT during 1st and 2nd charge (solid squares, corresponds to Fig. 7.13d) with those reported in the literature by Kataoka et al. (open squares) by means of GITT [42] and by Hwang et al. (open dotted square) [43] by means of EIS. The work by Kataoka et al. comprises the results of $NaFeO_2$ synthesized by solid state with micro-sized (blue, SS_μ) and nano-sized (SS_n) iron precursor.

for 2 hours at each step. Nevertheless we have seen in our measurements that two hours might be below the needed relaxation time to arrive to a steady state, and thus, the diffusion coefficient might be altered. In order to take these limitations into account, an alternative method will be used to calculate the diffusion coefficient in the next section.

7.2.3 Non-conventional method to calculate ionic diffusion

In this section the method developed by Li et al. will be applied [44]. With this alternative method the surface reaction resistances and diffusion coefficients are taken into account in the current response [45], but most importantly, it also allows the refinement of the transferred charge per step, avoiding two of the possible error sources present in the conventional methods. The refinement of the current contribution allows the discrimination of the sodium changes occurred due to diffusion or from other processes, such as crystalline structure transformation or surface reactions.

The diffusion coefficient is calculated by fitting the experimental current relaxation of the PITT steps to the following expression:

$$\begin{aligned} I(t) = -\frac{3DQ}{R^2}\Bigg\{ & -\frac{B}{B-1}\left(1-\operatorname{erfc}\frac{R}{\sqrt{Dt}}\right)+\frac{B^2}{B-1}\exp\left[\frac{Dt}{R^2}(B-1)^2\right] \\ & \operatorname{erfc}\left[(B-1)\sqrt{\frac{Dt}{R^2}}\right]+\frac{B^2-2B}{B-1}\exp\left[2(B-1)+\frac{Dt}{R^2}(B-1)^2\right] \\ & \operatorname{erfc}\left[\frac{R}{\sqrt{Dt}}+(B-1)\sqrt{\frac{Dt}{R^2}}\right]\Bigg\} \end{aligned} \tag{7.10}$$

where Q is the transferred charge in the potential step, D is the diffusion coefficient and B is the electrochemical Biot number. B is a refined dimensionless parameter that represent the ratio between the interface reaction rate and the diffusion rate, and is defined as:

$$B \equiv -R\, i_0 \frac{\partial U}{\partial C} \frac{1}{D R_g T} \tag{7.11}$$

where i_0 represents exchange current density (that is, the current transferred between the electrodes without an external overpotential), C represents the ionic concentration, U is the equilibrium potential, R_g is the gas constant and T is the temperature. Current and concentration values are taken at the end of the potentiostatic steps. Large B values mean a reaction governed by ionic diffusion, while low B values represent reactions governed by surface and charge transfer resistances. Similarly to the surface area in the prefactor of equation 7.2 for the previous method, the radius of the particles is used instead in this method. The value has been deduced from SAXS data of the pristine powder material (see Fig. 3.8), assuming spherical geometry of the particles. The expression in equation 7.10, has also been calculated based on Fick's laws of diffusion, as the conventional method presented in Section 7.2.2, considering spherical particles of radius R [44].

The Fig. 7.16 presents a few examples of the fitted currents during the second charge, in which a good agreement between the experimental and the fitted results can be observed for $t \leqslant 5$ s.

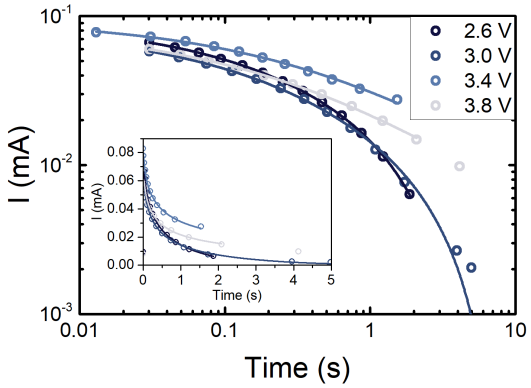

Figure 7.16: Examples of current fits using equation 7.10 during second charge at 2.6 V, 3.0 V, 3.4 V and 3.8 V at low times in log-log scale. The experimental points are presented with open circles and fittings with solid lines. In the inset the data are presented in linear scale.

The transferred charge, ΔQ, is presented in Fig. 7.17 as a function of potential. Note that in this case, since the diffusing species (Na^+ ions) are monovalent, $\Delta Q = \Delta x$. In light blue, the transferred charge from the whole voltage steps is presented, as deduced from the PITT curve at equilibrium and used for the calculation of TF within the previous method (Section 7.2.2.2). In dark blue, the transferred charge as calculated from the refinement of the current with equation 7.10, that corresponds to the ΔQ taking part in the ionic diffusion. Both methods are in good agreement when the value of ΔQ is low, but at the potential plateaus, where the majority of the charge is

transferred, it can be seen how the integral of the whole step overestimates the amount of current actually taking part in the diffusion. In these regions, phase transitions might be contributing to the current at long relaxation times, which as shown in Fig. 7.11 induces two peaks in the $I\sqrt{t}$ curves. Therefore, higher diffusion values are expected during the plateaus than those actually obtained with the conventional method (shown in Figs. 7.13 and 7.14).

During the beginning of the 3rd charge it can be seen that the ΔQ values obtained with the current fitting method (Biot) are slightly higher than those obtained from the integration of the current. This is probably related to the theory behind equation 7.10 used to fit the current. The model assumes a semi-infinite linear diffusion, where the current decays before the end of the diffusing phase is reached. However, if the diffusion path reaches the end (either due to a limited length of the diffusing phase or because its center is reached), the system would be in a finite-length or finite-space diffusion region, where the current decays prematurely due to physical limitations. The model used for the fitting of the current does not consider this situation, hence the higher Δx values calculated from the fits. In this region, the diffusion coefficient calculated with conventional methods should be slightly underestimated.

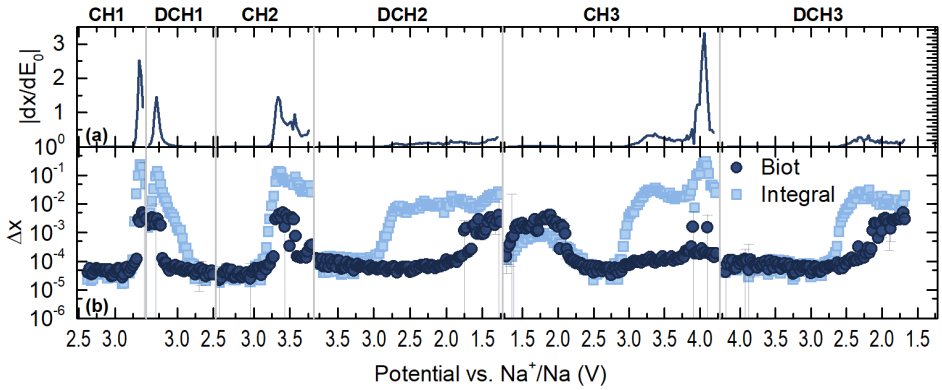

Figure 7.17: **(a)** Derivative curve $|\mathrm{d}x/\mathrm{d}E_0|$ and **(b)** transferred charge during PITT steps calculated as the integral of the current in the whole potential step (light blue squares) and from the refinement of current as shown in Fig. 7.16 (dark blue circles).

The refined values for the Biot number B are presented as a function of potential in Fig. 7.18b (dark blue circles, left axis), together with the charge transfer resistance R_2 (light blue squares, right axis) from Fig. 7.7b. The $|\mathrm{d}x/\mathrm{d}E_0|$ derivative curve is shown in 7.18a.

From this figure it can be clearly seen that the refinement of the Nyquist spectra in the PEIS measurements and the Biot number from current refinement are in good agreement: when the resistance R_2 is high, the Biot number is low, reflecting a reaction governed by internal resistances; on the other hand, when the resistance R_2 is low, the Biot number is high, reflecting a reaction governed by ionic diffusion. However, the Biot number is close to or above 1 at all states of charge, meaning that the surface or charge transfer resistances are non-negligible although

non-predominant. This result shows that the resistance R_2 is the limiting factor in the electrochemical activity of the material rather than the diffusion coefficient as it has been assumed in the literature [4, 46, 47], as it represents the kinetics of the major contribution to the current at the potential plateau, when most of the charge is transferred.

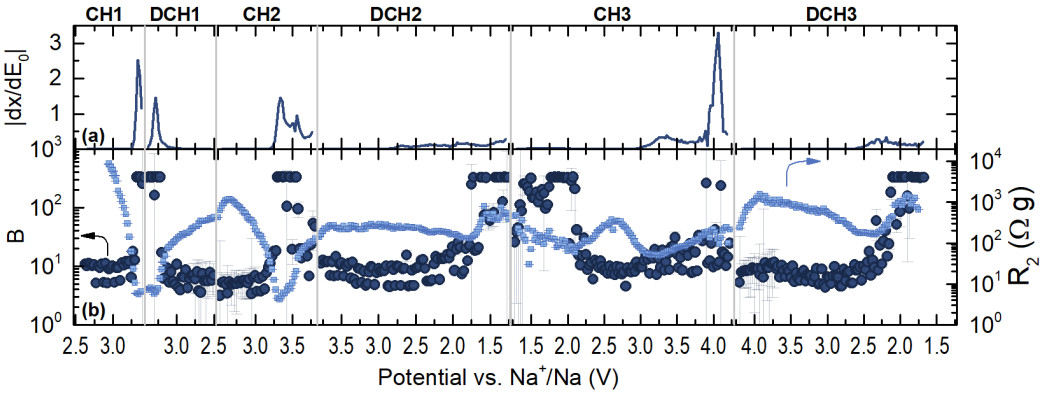

Figure 7.18: **(a)** Derivative curve $|\mathrm{d}x/\mathrm{d}E_0|$ as a function of potential. **(b)** Biot number of $NaFeO_2$ (circles, left axis) and R_2 as shown in Fig. 7.7b (squares, right axis) as a function of potential. On top the cycle state is shown, CH for charge and DCH for discharge, and the number representing the cycle number.

The diffusion coefficient results are presented in Fig. 7.19 as a function of composition. Conventional and non-conventional methods are compared: in light blue the results obtained from the Warburg coefficient extraction from PEIS data (conventional method) and in dark blue the results obtained from the present method based on the refinement of the current with equation 7.10.

It seems that the diffusion coefficient calculated from the current fit (D_{Biot}) is various orders of magnitude higher than that calculated from the conventional method (D_{PEIS}) throughout the cycling, $D_{Biot} \approx 10^{-10}$ cm^{2}s^{-1} vs. $D_{PEIS} \approx 10^{-16}$ cm^{2}s^{-1} except in the biphasic regions highlighted in gray. However, and as seen in Figs. 7.13 and 7.14, the low D values are gathered within small potential ranges although broad sodium content changes. Note that this are the regions where the transferred charge has been underestimated in the conventional method (see Fig. 7.17).

For a clearer visualization of all the data, D has been presented as a function potential in Fig. 7.20. As in the previous case, conventional and non-conventional methods are compared: in light blue the results obtained from the Warburg coefficient extraction from PEIS data (conventional method) and in dark blue the results obtained from the present method based on the refinement of the current with equation 7.10.

As shown earlier, the conventional method gives diffusion values in a range of more than seven orders of magnitude, $D_{PEIS} = 10^{-17} - 10^{-10}$ cm^{2}s^{-1}. The results obtained from current fitting

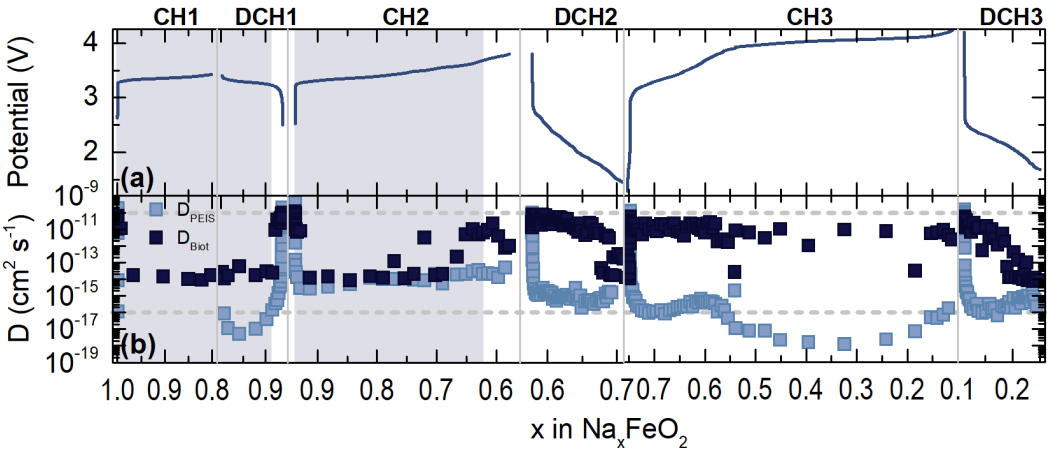

Figure 7.19: **(a)** Potential curve and **(b)** diffusion coefficient of $NaFeO_2$ obtained by different methods as a function of composition. The diffusion has been calculated with the conventional, from PEIS (light blue) and with the non-conventional method, by fitting the current (dark blue). The regions at which *operando* XRD has shown a biphasic behavior have been highlighted in gray. Dashed lines at $D = 10^{-16}$ cm^2s^{-1} and 10^{-10} cm^2s^{-1} have been added for visual help. On top the cycle state is shown, CH for charge and DCH for discharge, and the number representing the cycle number.

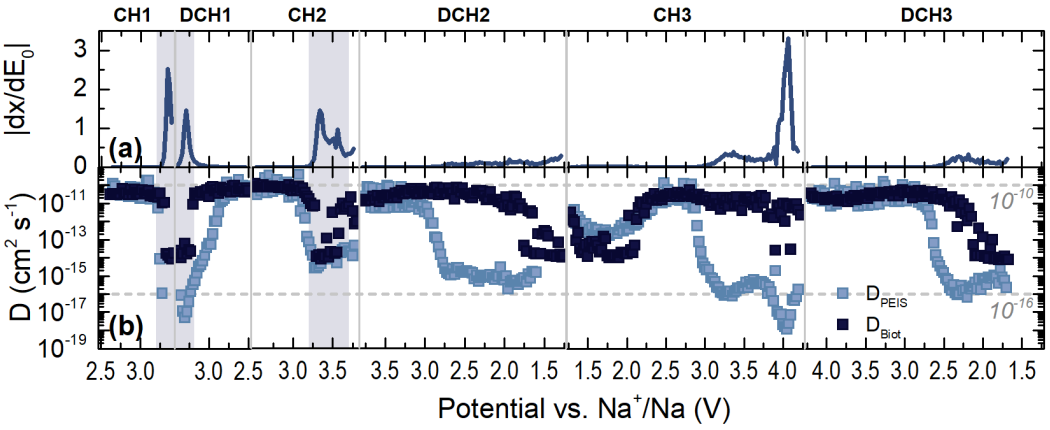

Figure 7.20: **(a)** Derivative $|\mathrm{d}x/\mathrm{d}E_0|$ curve and **(b)** diffusion coefficient of $NaFeO_2$ obtained by different methods as a function of potential. The diffusion has been calculated with the conventional, from PEIS (light blue) and with the non-conventional method, by fitting the current (dark blue). The regions at which *operando* XRD has shown a biphasic behavior have been highlighted in gray. Dashed lines at $D = 10^{-16}$ cm^2s^{-1} and 10^{-10} cm^2s^{-1} have been added for visual help. On top the cycle state is shown, CH for charge and DCH for discharge, and the number representing the cycle number.

also change several orders of magnitude, but the voltage range at which the values are low is significantly narrower, with variations of about four orders of magnitude: $D_{Biot} = 10^{-14} - 10^{-10}$

cm^2s^{-1}. The difference between the results obtained with the two methods lies in the voltage plateaus, where the transferred charge has been probably overestimated in the conventional method, since in the regions where ΔQ is similar from the integral and the current fitting (see Fig. 7.17), the diffusion coefficient values are the same for the two methods. Moreover, the current fitting method gives a stable value upon a broader voltage range than that obtained from conventional methods. The value stays around 10^{-10} cm^2s^{-1} at most states of charge, except for the expected biphasic regions based on the *operando* XRD data of this material and presented in Chapter 5 (shadowed in gray in Fig. 7.20) and the end of discharge. Unlike the values obtained from the conventional method, the current fitting method gives continuous values at the change from charge to discharge or from discharge to charge, at which discontinuities were observed with the traditional method. Since the cell shows a big potential hysteresis after being charged to 3.8 V or 4.20 V at the end of the PITT steps where the potential is expected to be at thermodynamic equilibrium, the beginning of every charge or discharge shows an abrupt change of potential, and the potential vs. composition plateaus appear at lower potentials during discharge. For this reason, the diffusion coefficient calculated with the conventional method presents discontinuities at the charge/discharge changes. In the non-conventional method on the other hand, the value does not depend on the derivative curve, and thus, does not depend on the cell voltage hysteresis after relaxation and no discontinuity is observed.

The process *B* at 3.55 V, based on the reaction potential, seems to be related to iron migration. After charging the material to 3.8 V the process is only partially reversible. The drop in D is not observed on discharge, and it stays at $D \approx 10^{-10}$ cm^2s^{-1}. It might be related to the irreversibility and the high R_2 values after the 2nd charge observed in these measurements.

It is worth noting that despite the large polarization and low reversibility of the material, the diffusion coefficient seems not to be affected and is very reversible. Moreover, iron migration at the end of the third charge, at 4.2 V, should be high, equal or above the 30% estimated in Chapter 5 (see Fig. 5.12), due to the slower cycling rate of this measurement that permits the slow processes to occur. The diffusion coefficient is however very close to the initial value, suggesting that the diffusion coefficient is not the limiting factor in the performance of $NaFeO_2$.

7.3 Conclusions

An advanced electrochemical characterization of $NaFeO_2$ diffusion kinetics has been carried out, based on coupled PITT and PEIS measurement technique. Na diffusion coefficient has been calculated with conventional and non-conventional methods, with some differences in the results. All the methods show sharp drops in the diffusion coefficient values in the biphasic regions. Since the expression of D is based on Fick's laws of diffusion, where a single phase is considered, the values at these biphasic regions have to be carefully considered. However, and based on *operando* XRD in Chapter 5, the main O3 phase follows a continuous solid solution transition while the secondary P3 phase does not evolve significantly. Thus, it seems that the majority of the sodium is extracted

from the main O3 phase. The ionic diffusion should therefore occur mainly in the majority O3 phase. Hence, the values obtained for the diffusion in this case should not be very different to the single phase values. Moreover, the refinement of transferred charge Q in the non-conventional method, should at least partially correct the effect of other processes contributing to the current relaxation.

Although differences can be seen between conventional and non-conventional methods, the obtained results are very close one from another except at the reaction potentials. A maximum value of $D \approx 10^{-10}$ cm^{2}s^{-1} can be seen quite steady during the whole cycling process except at the reaction potentials. Conventional method shows a discontinuity at the charge-discharge change associated with a drop in diffusion to $D \approx 10^{-16}$ cm^{2}s^{-1} when non-negligible amounts of sodium are being inserted, corresponding to a plateau in the potential vs. composition curve due an overestimation of the transferred charge. This drop appears thus to depend on the polarization of the cell. Indeed, it has been demonstrated that the diffusion coefficient values calculated with the conventional method are lower due to an overestimation of the transferred charge occurring at the potential steps.

When calculated with the non-conventional method, the diffusion coefficient also drops to $D \approx 10^{-14}$ cm^{2}s^{-1}, which is smaller than the drop observed in the conventional methods. The lower diffusion coefficient is observed at potentials below 2 V, at discharged state. Unluckily, the determination of the structures present at such low potentials is not easy. As shown for the sample discharged from 3.8 V to 1.0 V (Fig. 5.7 in Chapter 5), at discharged state most of the reflections in the XRD patterns have a low intensity and are close to parasitic reflections from the *operando* cell's window. Hence the large error bars in the obtained cell parameters (see Fig. 5.8b). Therefore, it is not easy to determine whether new phases are formed at low potentials. Indeed, monoclinic distorted structures have been reported for other electrochemically sodiated O3 layered oxides [48].

It is clear that the diffusion coefficient, if affected by the structural changes, is very reversible. It seems that diffusion coefficient is not the source of the electrochemical degradation of the material.

On the other side, both PEIS and Biot number show that a component of the internal resistance R_2 increase in more than two orders of magnitude. R_2 resistance is low at the 3.3 V plateau, but it increases afterwards, and it remains high once the cell has been charged to 3.8 V. The equilibrium potential shows then a voltage hysteresis of more than 1 V, which is not related to the kinetics. The potential hysteresis appears to be intrinsic of the material due to irreversible chemical or structural changes, such as the possible irreversible oxygen redox.

Different processes have been observed during the PEIS measurements that could be explained in the following terms. At high to mid frequencies, the component $(R_1 + Z_{w\,FL})||CPE_1$ seems to be related to solid permeable interface in the surface of the particles. This finite length layer is stable and is an electronic and ionic conductor. The mid to low frequency block, component $(R_2 + Z_{w\,SILD})||CPE_2$, seems more related to the bulk response of the material. Moreover, the resistance R_2 could be related to a charge transfer resistance, whose value reduces or increases

as the electronic conductivity is improved or deteriorated. At the pristine state, the material is an electronic insulator, hence the high R_2 values, and it becomes a conductor with sodium extraction and emptying of $3d$ orbitals of the iron. Upon cycling new structures might be forming, whose potentially lower electronic conductivity are reflected as an irreversible increment in R_2 resistance. Note that its value during the second discharge, $R_2 \approx 200\ \Omega$ g, would correspond to an overpolarization of 1.6 V at C/30 rate (the same at which the *operando* XRD measurements have been done in Chapter 5). This alone can explain the increment of the overpolarization of the material observed during galvanostatic cycling, and as a consequence, of the low amounts of sodium reinserted on discharge from high potentials, but it would not explain the voltage hysteresis observed in these quasi-equilibrium measurements. This potential hysteresis seems thus to be more related to irreversible changes produced in the material, which did not happen in the galvanostatic measurements due to the slow kinetics.

It can be reasonably concluded from this chapter that, surprisingly, the diffusion coefficient is not altered by the migration of Fe ions into the Na layers. However, an increment of R_2 resistance has been observed when Fe migration is expected (see 2nd charge in Fig. 7.7b). Interestingly, R_2 is not decreased on discharge after having charged to 3.8 V or 4.2 V. It seems thus that the structural changes induced by iron migration affect the electronic conductivity of the material and subsequently increases the value of R_2 resistance by several orders of magnitude. When charging over a certain potential, the reversibility of iron from Na layers is reduced, and so is the electrochemical response of the material as a consequence of the irreversible increase R_2 resistance. The oxygen oxidation observed by Li et al. [6] at high potentials, if occurring here as well as process *C*, would be irreversible too, as reflected by the large potential hysteresis of the equilibrium potential curves.

Finally, it seems that the slow cycling of the material permits irreversible parasitic reactions to occur at lower potentials that when cycling in galvanostatic mode damaging the electrochemical response. Thus, although faster cycling is generally related to an increased kinetics related polarization and a reduced capacity, the reversibility of the material is higher and the thermodynamic potential hysteresis is lower, increasing the cycle life of the material.

Bibliography

[1] N. Yabuuchi, K. Kubota, M. Dahbi, and S. Komaba. *Chemical Reviews*, 114(23):11636–11682, 2014.

[2] D. Mohanty, J. Li, D. P. Abraham, A. Huq, E. A. Payzant, D. L. Wood, and C. Daniel. *Chemistry of Materials*, 26(21):6272–6280, 20141.

[3] K. Kubota, I. Ikeuchi, T. Nakayama, C. Takei, N. Yabuuchi, H. Shiiba, M. Nakayama, and S. Komaba. *The Journal of Physical Chemistry C*, 119(1):166–175, 2015.

[4] X. Li, Y. Wang, D. Wu, L. Liu, S.-H. Bo, and G. Ceder. *Chemistry of Materials*, 28(18):6575–6583, 2016.

[5] I. Takahashi, K. Fukuda, T. Kawaguchi, H. Komatsu, M. Oishi, H. Murayama, M. Hatano, T. Terai, H. Arai, Y. Uchimoto, and E. Matsubara. *The Journal of Physical Chemistry C*, 120(48):27109–27116, 2016.

[6] Y. Li, Y. Gao, X. Wang, X. Shen, Q. Kong, R. Yu, G. Lu, Z. Wang, and L. Chen. *Nano Energy*, 47:519–526, 2018.

[7] E. McCalla, A. M. Abakumov, M. Saubanère, D. Foix, E. J. Berg, G. Rousse, M.-L. Doublet, D. Gonbeau, P. Novák, G. V. Tendeloo, R. Dominko, and J.-M. Tarascon. *Science*, 350(6267):1516–1521, 2015.

[8] X. Rong, J. Liu, E. Hu, Y. Liu, Y. Wang, J. Wu, X. Yu, K. Page, Y.-S. Hu, W. Yang, H. Li, X.-Q. Yang, L. Chen, and X. Huang. *Joule*, 2(1):125–140, 2018.

[9] R. A. House, U. Maitra, L. Jin, J. G. Lozano, J. W. Somerville, N. H. Rees, A. J. Naylor, L. C. Duda, F. Massel, A. V. Chadwick, S. Ramos, D. M. Pickup, D. E. McNally, X. Lu, T. Schmitt, M. R. Roberts, and P. G. Bruce. *Chemistry of Materials*, 31(9):3293–3300, 2019.

[10] D. Qian, B. Xu, M. Chi, and Y. S. Meng. *Physical Chemistry Chemical Physics*, 16(28):14665–14668, 2014.

[11] W. E. Gent, K. Lim, Y. Liang, Q. Li, T. Barnes, S.-J. Ahn, K. H. Stone, M. McIntire, J. Hong, J. H. Song, Y. Li, A. Mehta, S. Ermon, T. Tyliszczak, D. Kilcoyne, D. Vine, J.-H. Park, S.-K. Doo, M. F. Toney, W. Yang, D. Prendergast, and W. C. Chueh. *Nature Communications*, 8(1):2091, 2017.

[12] J. Vinckevičiūtė, M. D. Radin, N. V. Faenza, G. G. Amatucci, and A. Van der Ven. *Journal of Materials Chemistry A*, 7(19):11996–12007, 2019.

[13] Zfit - Bio-Logic Science Instruments. `https://www.bio-logic.net/zfit/`, (Accessed: 2019-11-27).

[14] S. Kikkawa, S. Miyazaki, and M. Koizumi. *Materials Research Bulletin*, 20:373–377, 1985.

[15] M. C. Blesa, E. Moran, C. Leon, J. Santamaria, J. D. Tornero, and N. Menendez. *Solid State Ionics*, 126(1):81–87, 1999.

[16] T. McQueen, Q. Huang, J. W. Lynn, R. F. Berger, T. Klimczuk, B. G. Ueland, P. Schiffer, and R. J. Cava. *Physical Review B*, 76(2):024420, 2007.

[17] M. H. N. Assadi and Y. Shigeta. *RSC Advances*, 8(25):13842–13849, 2018.

[18] Z. Zhang, Y. Shao, B. Lotsch, Y.-S. Hu, H. Li, J. Janek, L. F. Nazar, C.-W. Nan, J. Maier, M. Armand, and L. Chen. *Energy & Environmental Science*, 11(8):1945–1976, 2018.

[19] A. Honders, J. Derkinderen, A. Vanheeren, J. Dewit, and G. Broers. *Solid State Ionics*, 14(3):205–216, 1984.

[20] M. Ménétrier, I. Saadoune, S. Levasseur, and C. Delmas. *Journal of Materials Chemistry*, 9(5):1135–1140, 1999.

[21] C. Kim, N. S. Norberg, C. T. Alexander, R. Kostecki, and J. Cabana. *Advanced Functional Materials*, 23(9):1214–1222, 2013.

[22] R. Amin, D. B. Ravnsbæk, and Y.-M. Chiang. *Journal of The Electrochemical Society*, 162(7):A1163–A1169, 2015.

[23] E. Barsoukov and J. R. Macdonald, editors. *Impedance spectroscopy: theory, experiment, and applications*. Wiley-Interscience, Hoboken, N.J, 2nd ed edition, 2005.

[24] A. M. Andersson, D. P. Abraham, R. Haasch, S. MacLaren, J. Liu, and K. Amine. *Journal of The Electrochemical Society*, 149(10):A1358, 2002.

[25] P. Balbuena and Y. Wang, editors. *Lithium-ion Batteries: Solid-electrolyte Interphase*. Imperial College Press, 2004.

[26] Y. Zhu and C. Wang. *The Journal of Physical Chemistry C*, 114(6):2830–2841, 2010.

[27] P. P. Prosini, M. Lisi, D. Zane, and M. Pasquali. *Solid State Ionics*, 148:45–51, 2002.

[28] D. D. Lecce, D. Campanella, and J. Hassoun. *Journal of Physical Chemistry C*, 122:23925–23933, 2018.

[29] H. Anne. *Understanding the kinetic limitations of NaFePO4 as cathode active material for Na-ion battery*. Ph.D. thesis, Universidad del País Vasco / Euskal Herriko Unibertsitatea, Facultad de Ciencia y Tecnología, Departamento de Física Aplicada II, 2019.

[30] A. Van der Ven, J. Bhattacharya, and A. A. Belak. *Accounts of Chemical Research*, 46(5):1216–1225, 2013.

[31] D. Li and H. Zhou. *Materials Today*, 17(9):451–463, 2014.

[32] C. Ho, I. D. Raistrick, and R. A. Huggins. *Journal of the Electrochemical Society*, 127(2):343–350, 1980.

[33] F. G. Cottrell. *Zeitschrift fur Physikalische Chemie*, 42(4):385–431, 1903.

[34] H. Le, C. Lin, E. Kätelhön, and R. G. Compton. *Electrochimica Acta*, 298:778–787, 2019.

[35] M. D. Levi and D. Aurbach. *The Journal of Physical Chemistry B*, 101(23):4641–4647, 1997.

[36] C. Montella. *Journal of Electroanalytical Chemistry*, 518(2):61–83, 2002.

[37] M. D. Levi, K. Gamolsky, D. Aurbach, U. Heider, and R. Oesten. *Journal of The Electrochemical Society*, 147(1):25–33, 2000.

[38] V. Pralong, M. A. Reddy, V. Caignaert, S. Malo, O. I. Lebedev, U. V. Varadaraju, and B. Raveau. *Chemistry of Materials*, 23(7):1915–1922, 2011.

[39] G. Oyama, Y. Yamada, R.-i. Natsui, S.-i. Nishimura, and A. Yamada. *The Journal of Physical Chemistry C*, 116(13):7306–7311, 2012.

[40] V. Pralong, G. Venkatesh, S. Malo, V. Caignaert, R. Baies, and B. Raveau. *Inorganic Chemistry*, 53(1):522–527, 2014.

[41] E. Anger, A. Maignan, T. Barbier, and V. Pralong. *RSC Advances*, 8:26691–26695, 2018.

[42] R. Kataoka, K. Kuratani, M. Kitta, N. Takeichi, T. Kiyobayashi, and M. Tabuchi. *Electrochimica Acta*, 182:871–877, 2015.

[43] J. Hwang and J. Kim. *Materials Letters*, 206:100–104, 2017.

[44] J. Li, F. Yang, X. Xiao, M. W. Verbrugge, and Y.-T. Cheng. *Electrochimica Acta*, 75:56–61, 2012.

[45] J. Li, X. Xiao, F. Yang, M. W. Verbrugge, and Y.-T. Cheng. *The Journal of Physical Chemistry C*, 116(1):1472–1478, 2012.

[46] E. Lee, D. E. Brown, E. E. Alp, Y. Ren, J. Lu, J.-J. Woo, and C. S. Johnson. *Chemistry of Materials*, 27(19):6755–6764, 2015.

[47] S.-H. Bo, X. Li, A. J. Toumar, and G. Ceder. *Chemistry of Materials*, 28(5):1419–1429, 2016.

[48] B. Mortemard de Boisse, J.-H. Cheng, D. Carlier, M. Guignard, C.-J. Pan, S. Bordère, D. Filimonov, C. Drathen, E. Suard, B.-J. Hwang, A. Wattiaux, and C. Delmas. *Journal of Materials Chemistry A*, 3(20):10976–10989, 2015.

8 | Advanced electrochemical characterization of O3-$Na_xFe_{2/3}Mn_{1/3}O_2$ upon cycling

Contents

8.1 Introduction

This chapter presents a kinetic study of the electrochemical response of O3-$Na_{2/3}Fe_{2/3}Mn_{1/3}O_2$ through coupled PITT and PEIS techniques following the same protocol than for the isostructural $NaFeO_2$ compound presented in Chapter 7. Here we will try to relate the higher structural reversibility of O3-$Na_{2/3}Fe_{2/3}Mn_{1/3}O_2$ compared to $NaFeO_2$ as seen in Chapters 5 and 6 with the electrochemical response kinetics.

8.2 Coupled PITT and PEIS

The voltage and current evolution as a function of time during charge-discharge coupled PITT-PEIS measurements is shown in Figs. 8.1a, b and c for the 1st, 2nd and 3rd cycles respectively. The voltage is shown in black during the PITT steps and in blue during PEIS steps. The current, in red, corresponds to the relaxation during PITT steps. As it has been previously explained, the current evolution during both PITT and PEIS measurements, depend on the kinetic response of the material upon Na extraction and insertion. As in the previous chapter, the measurements presented here have been performed in three electrode Swagelok cells to avoid the contribution from the metallic sodium counter electrode. More details on the theoretical aspects and on the experimental set-up can be found in the experimental chapter (Sections 2.5.4-2.5.6). Unless otherwise specified, the methods used for the measurements and the data analysis are the same as those used in Chapter 7.

The equilibrium potential E_0 is presented in Fig. 8.1d as a function of Na composition. During the first charge (Fig. 8.1a) to 3.40 V, a sloping potential plateau can be observed from 3.15 V for the $Fe^{3+/4+}$ oxidation reaction. which can be seen as an increment in the $\mathrm{d}x/\mathrm{d}E_0$ derivative curve (labeled as *A* in Fig. 8.1e). The peak is centered around 3.38 V, to higher potentials than in the case of $NaFeO_2$ (3.30 V, see Fig. 7.1 in Chapter 7). Moreover, the plateau is sloppier, and thus, the reaction extends in a broader potential range. Upon discharge to 2.5 V, value chosen to remain above the manganese redox reaction, a reversible capacity of about 7% of the theoretical capacity is obtained upon discharge with a Coulombic efficiency of 75%. As for $NaFeO_2$ in the previous chapter, the potential hysteresis between charge and discharge is low in this first cycle ($\Delta V = 58$ mV). When the same potential window was applied for $NaFeO_2$ in PITT regime, the discharge capacity obtained was the double, i.e. nearly 15% of the theoretical capacity (see Fig. 7.1d). The reason for the difference can be ascribed to two different contributions: (a) only two thirds of the theoretical capacity is available in this case during the first charge due to the partially desodiated pristine state of O3-$Na_{2/3}Fe_{2/3}Mn_{1/3}O_2$, and (b) the reaction potential of the $Fe^{3+/4+}$ oxidation reaction is sloppier for O3-$Na_{2/3}Fe_{2/3}Mn_{1/3}O_2$ than for $NaFeO_2$, and thus, the limited upper cutoff potential will limit the reaction before the reaction is finished. The onset of another reaction is also observed at $V \approx 2.5$ V, that will be later described, when the cell is discharged to lower potentials.

During the second cycle (Fig. 8.1b), the upper voltage limit has been increased to 3.80 V, reaching a composition of $Na_{0.30}Fe_{2/3}Mn_{1/3}O_2$ at the end of the charge. The process that was observed

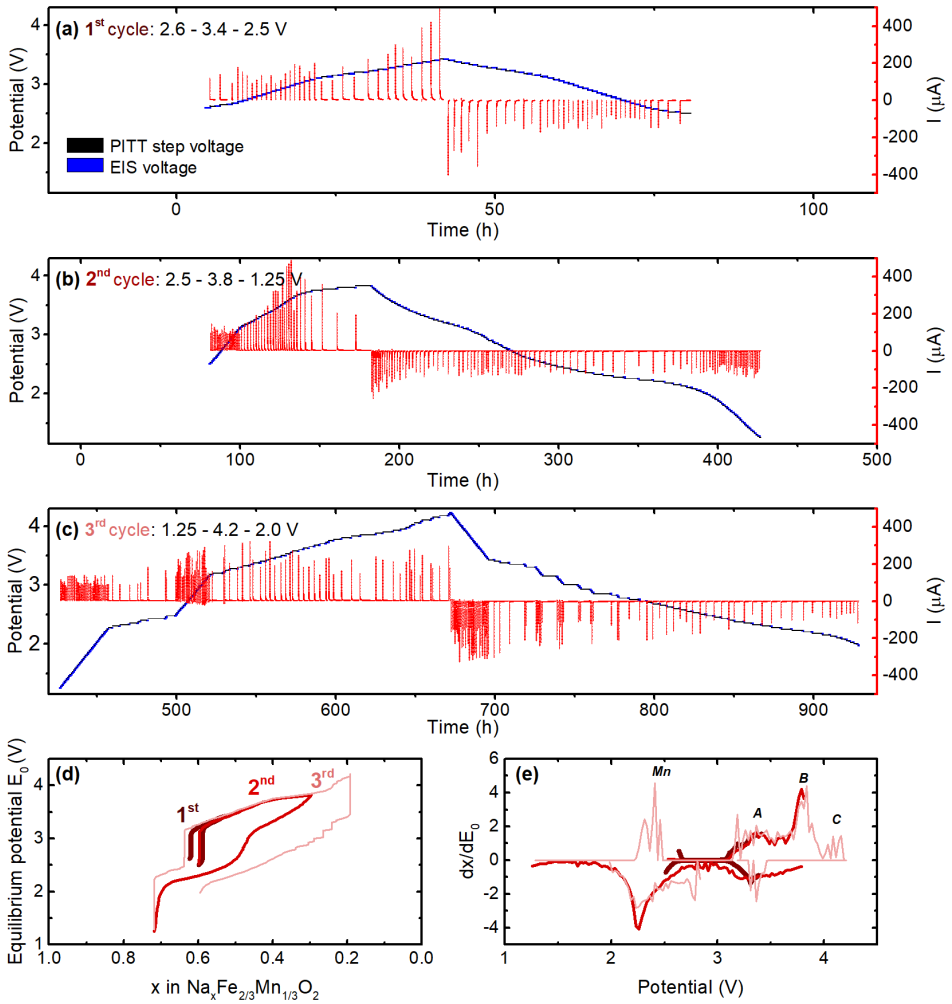

Figure 8.1: Voltage and current evolution of $Na_xFe_{2/3}Mn_{1/3}O_2$ during coupled PITT and PEIS measurements. Voltage (black during PITT and blue during PEIS) and current (red) evolution during **(a)** 1st cycle ($V = 2.6{-}3.6{-}2.5$ V), **(b)** 2nd cycle ($V = 2.5{-}3.8{-}1.25$ V) and **(c)** 3rd cycle ($V = 1.25{-}4.2{-}2.0$ V). Note that the time scale in panel (a) is scaled $\times 4$ compared to panels (b) and (c). **(d)** Equilibrium potential and **(e)** $\mathrm{d}x/\mathrm{d}E_0$ derivative curves. The different processes observed in the derivative curves as peaks have been labeled.

during the first charge, process *A*, appears centered at 3.40 V, which is 10 mV higher than for $NaFeO_2$. As for the first cycle, the potential plateau is also observed with a larger slope compared to $NaFeO_2$. The onset of a second process, labeled as *B*, can also be observed near 3.80 V. This process is most probably not finished, as reflected by the missing tail in the $\mathrm{d}x/\mathrm{d}E_0$ derivative curve, as it happened with process *A* during the 1st cycle. Based on the *operando* XRD structural characterization from Chapter 6, the process *B* could be related with the transformation of O3

to O'3 distorted structure or the onset of the iron migration. On discharge, similarly to $NaFeO_2$, processes *A* and *B* seem to overlap, and a single broad peak is observed in the derivative curve. The potential hysteresis is moreover increased to $\Delta V \approx 600$ mV during this second cycle. The lower voltage limit has been decreased to 1.25 V in order to account for this increment in the voltage hysteresis as it was done for $NaFeO_2$ sample in Chapter 7, which also allows to observe the $Mn^{4+/3+}$ reduction reaction near 2.25 V (process *Mn*). Upon charge 0.3 Na^+ ions have been extracted from the structure per formula unit (i.e. 30% of the theoretical capacity has been reached), and on discharge the reinserted amount is increased to 0.42 Na^+ ions per formula unit, that is, Coulombic efficiency is close to 140%.

The Coulombic efficiency value over 100% is allowed by the $Mn^{4+/3+}$ reduction reaction allowed by lowering the potential limit from 2.5 V to 1.25 V. Accordingly, at the end of discharge a higher sodium content than in the pristine material is obtained: $Na_{0.72}Fe_{2/3}Mn_{1/3}O_2$. However, as for $NaFeO_2$ this composition is still far from the fully sodiated state, despite the very slow reaction rate inherent to the PITT technique and the low discharge potential limit. In principle the capacity obtained from the manganese redox should be about one third of the total capacity. However, more capacity is obtained from the Mn redox than from Fe, as it can be seen from the potential profile during the second discharge (Fig. 8.1d).

During the 3rd charge (Fig. 8.1c) the cell has been charged to 4.2 V. Processes *A* and *B* related to the $Fe^{3+/4+}$ reaction are observed near 3.40 V and 3.80 V respectively. Process *Mn*, related to $Mn^{3+/4+}$ reaction appears centered at 2.40 V, and is observed for the first time upon charge, since the cell has been discharged to 1.25 V in the previous discharge, confirming its reversibility. A fourth process is observed at ≈ 4.10 V (process *C*), which has also been observed for $NaFeO_2$ and that has been ascribed to oxygen redox. It is worth noting that the equilibrium potential evolution in this third cycle is less smooth, and step-like potential changes can be seen in the curves. This is due to the current resolution of the potentiostat, which is close to the limiting current of C/500. It is worth noting that the current decays from a maximum of ≈ 400 µA at the beginning of the step down to 1.5 µA at C/500: the current detection range is quite broad, which requires the configuration of the potentiostat with a precision that is close to the limiting current value. Thus, the detected current value can oscillate close to the limiting current, which might result in the premature potential step change in the cycling program. This is reflected as a noisy $\mathrm{d}x/\mathrm{d}E_0$ curve, hindering the determination of the reaction potentials. However, it can still be seen how the reaction potentials match well with those observed during previous cycles, reflecting the reversibility of the material: the potential hysteresis stays close to that of the second cycle. During this 3rd cycle about 40% of the theoretical capacity is obtained on discharge to 2.0 V with a Coulombic efficiency of 77%. These measurements are very long to perform, over one month, and the measurement had to be stopped due to technical reasons (potentiostat maintenance) before the end of the discharge was reached: the measurement was stopped at 2.0 V instead of the programed 1.25 V. Thus, a higher discharge capacity and Coulombic efficiency would have been probably obtained if discharged to 1.25 V.

8.2.1 Analysis of the impedance spectra

In Fig. 8.2a few examples of the PEIS spectra can be seen in the form of Nyquist plots. The different rows correspond to the different charge-discharge cycles, while the different columns correspond to different scales: full scale is shown on the right column, and mid and high frequency regions are shown in the second and third columns respectively. The first thing to notice is the presence of inductive elements, that are reflected as loops in Nyquist plots (see for example the spectra at 3.32 V in Fig. 8.2c or the spectra at 2.50 V in Fig. 8.3f, where this effect is very apparent). The inductive effects generally come from the experimental set up rather than from the electrochemical phenomena. Experiment wiring, the spring inside the cell or electrode misalignment have been determined to cause inductive effects [1, 2].

The overall shape of the spectra, excluding the inductive effects, is very similar to the spectra presented for $NaFeO_2$ in Section 7.2.1 (Chapter 7): a semicircle is observed at high frequency, whose width changes by about a factor 3 with the state of charge of the material, and is followed by a $\approx 45^\circ$ slope near 1-0.1 Hz (see the third column in Fig. 8.2). At lower frequencies a second semicircle can be seen, whose radius changes by several orders of magnitude with the state of charge of the material (see first and second columns in Fig. 8.2). Finally, in some spectra, when the second semicircle is small enough, a second $\approx 45^\circ$ slope can be seen at the lowest frequency (see for example the spectrum at 2.5 V in Fig. 8.2h).

Given the similarities of these spectra with those of $NaFeO_2$, the same equivalent circuit has been used for the fitting (see Fig. 7.4), where the high frequency semicircle and the mid frequency slope have been refined with a resistor in series with a finite length impedance, all in parallel with a constant phase element: $(R_1 + Z_{W\,FL})||CPE_1$. The low frequency semicircle and the following 45° slope has been fitted with a resistor and a semi-infinite length diffusion impedance, all in parallel with a constant phase element: $(R_2 + Z_{W\,SILD})||CPE_2$. A few examples of the refinements are presented in Fig. 8.3 as a solid line. These spectra are the same as those shown in Fig. 8.2(g-i) during the second charge. When inductive effects are present, as highlighted in gray in Fig. 8.3b, the data has been separated in two parts, before and after the inductive behavior. In these spectra the inductive effects are generally present in two regions: after the first or after the second semicircle. In the former case, the spectra have been fitted with $R_1||CPE_1$ before the inductance and with $(R_2 + Z_{W\,SILD})||CPE_2$ after it. In the latter case, the spectra have been refined with the equivalent circuit $(R_1 + Z_{W\,FL})||CPE_1 + R_2||CPE_2$ before the inductance. Similarly to the methodology shown in the previous chapter, $Z_{W\,SILD}$ has been refined only when a clear $\approx 45^\circ$ slope could be identified at low frequencies.

The results of the refinements are graphically presented in Fig. 8.4. The numerical results are also presented in Tables B.12-B.17. The resistance R_0, as shown in Fig. 8.4b with dark red diamonds, is close to constant and in the range of 5 to 50 mΩ g throughout the whole cycling process. This resistance is related to the electrolyte and the cell resistances. The resistance R_1 (red squares) has also a stable value in the range of $0.2 - 5\ \Omega$ g, regardless of the state of charge or the cycle number. This can also be seen in the radius of the high frequency semicircle in the

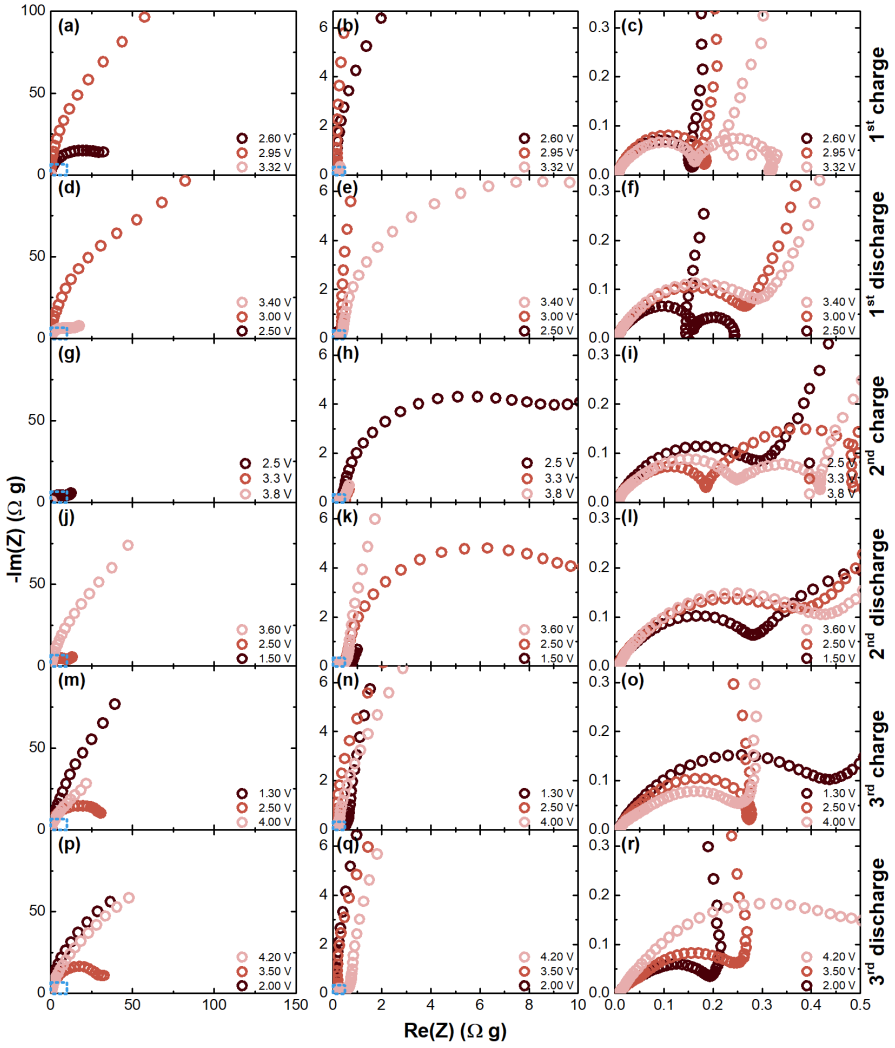

Figure 8.2: Examples of Nyquist spectra at different voltages during **(a-c)** 1st charge ($V = 2.6 - 3.4$ V), **(d-f)** 1st discharge ($V = 3.4 - 2.5$ V), **(g-i)** 2nd charge ($V = 2.5 - 3.8$ V), **(j-l)** 2nd discharge ($V = 3.8 - 1.25$ V), **(m-o)** 3rd charge ($V = 1.25 - 4.2$ V) and **(p-r)** 3rd discharge ($V = 4.2 - 2.0$ V). Each spectra is shown three times, with different zooms to show the details at high frequencies: the first column shows the whole spectra, the second is zoomed to show the mid-frequency region and the third column shows the high frequency region.

third column of Fig. 8.2. Based on the literature, the component $R_1||CPE_1$ seems to be related to the surface contributions [3, 4].

The value of R_2 on the other hand, presented in Fig. 8.4b as pink circles, changes more than three orders of magnitude depending on the charge state, similarly to what has been seen for

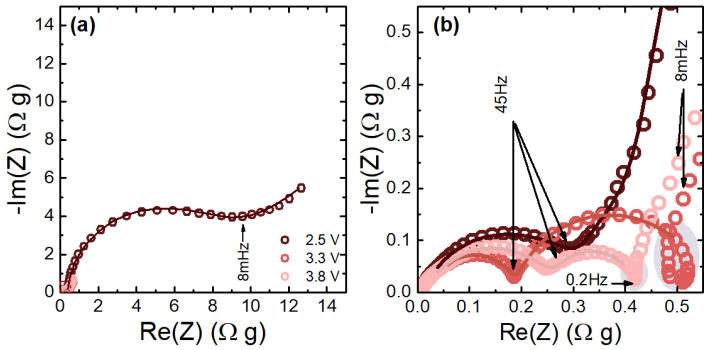

Figure 8.3: **(a)** Potentiostatic electrochemical impedance spectra at various potentials during the 2nd charge (2.5 V, 3.3 V and 3.8 V). Scatter data for the experimental data and solid lines for the simulated Nyquist spectra. Panel **(b)** shows a zoom of the high frequency region. The frequencies range has been selected so that it lies above the inductive processes, highlighted with gray in the inset.

$NaFeO_2$ in Chapter 7 (see Fig. 7.7). During the first charge, the value of R_2 starts at 30 Ω g and reaches a maximum of 300 Ω g at 2.90 V, which is right between the $Mn^{3+/4+}$ and $Fe^{3+/4+}$ reaction plateaus. This is more evident when the resistance evolution is presented as a function of composition, as in Fig. 8.5. Then, during the $Fe^{3+/4+}$ reaction plateau labeled as A in Fig. 8.1e (shown as a peak in the $|\mathrm{d}x/\mathrm{d}E_0|$ derivative curve, in Fig. 8.4a right axis), R_2 drops down to values of 0.1 Ω g. The evolution of R_2 is very reversible during the subsequent (1st) discharge, increasing back by three orders of magnitude and reaching values of 400 Ω g at $V = 2.90$ V, and further decreasing back by one order of magnitude, $\approx$ 10 Ω g at 2.50 V. These changes in R_2 could be related to changes in electronic conductivity [3, 5–7]. At 2.90 V, between the Fe and Mn redox processes, all the manganese should be Mn(IV) (electron configuration [Ar]$3d^3$), where an electron can be found in each t_{2g} orbital, and Fe should be Fe(III) (electron configuration [Ar]$3d^5$), where an electron lies in each t_{2g} and e_g orbital. A schematic representation of the orbital splitting and the electrons is presented in Fig. 8.6. At this composition, the electron conduction is not favored, inducing an increase of R_2. When electrons are removed from the iron the iron's e_g orbitals through Fe oxidation during reaction A on charge, or introduced in manganese's e_g orbitals through manganese reduction during process C on discharge, creating a half filled orbitals, the electron conduction is favored reducing the R_2 resistance.

The same behavior is observed during the second charge, with a maximum of $R_2 = 500$ Ω g at $V = 2.90$ V. On the following (2nd) discharge, R_2 is decreased back to 0.1 Ω g similarly to the first charge. On discharge a maximum of R_2 is observed between processes A and *Mn* at 2.90 V, as shown in the previous cycle. Upon further discharge, R_2 decreases down to a minimum of 10 Ω g at 2.40 V, that is, in the middle of the manganese reaction, and it increases at lower potentials, reaching values of $R_2 \approx 100$ Ω g at the end of discharge (1.25 V).

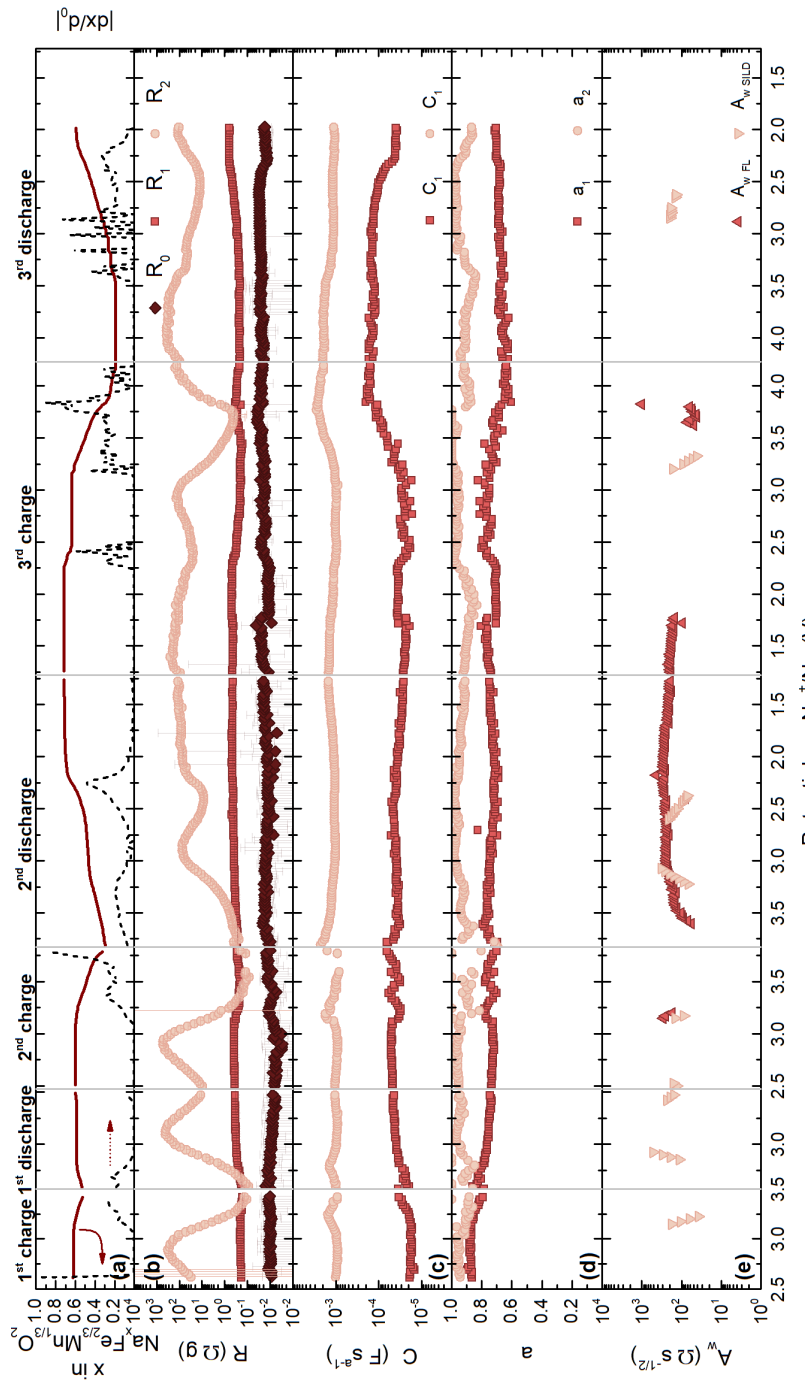

Figure 8.4: Results of the Nyquist spectra fitting with the equivalent circuit from Fig. 7.4 as a function of potential. **(a)** Sodium content (solid line, left) and derivative curve (dashed line, right), **(b)** resistance values, **(c)** admittance of the CPE component, **(d)** argument of the CPE component and **(e)** Warburg coefficient A_w. The components of the high frequency region $R_1||CPE_1$ are shown in dark colors and the low frequency region components $R_2||CPE_2$ are shown with dark colors.

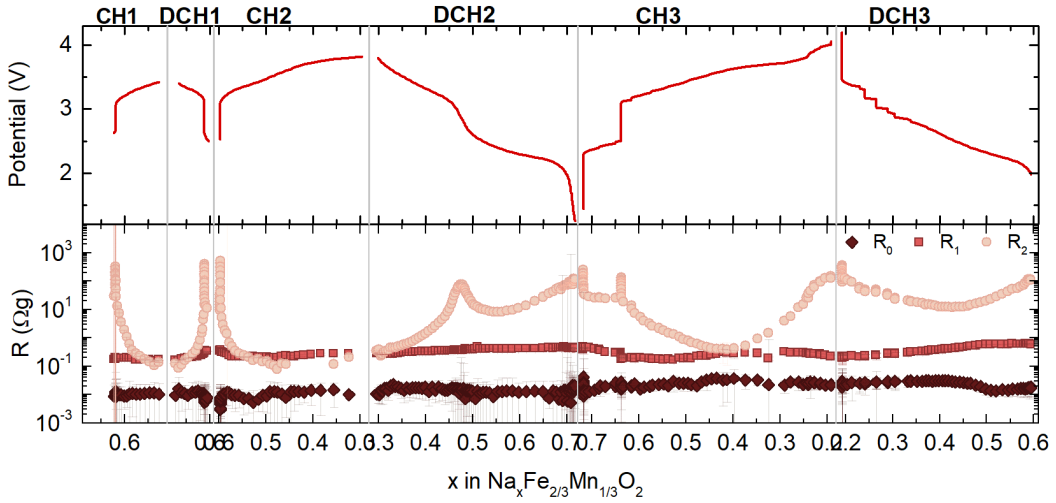

Figure 8.5: **(a)** Equilibrium potential and **(b)** resistance values obtained from PEIS data refinement with the equivalent circuit from Fig. 7.4 as a function of the sodium content.

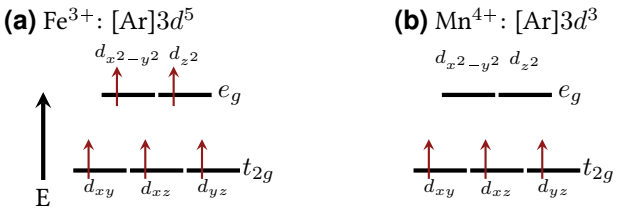

Figure 8.6: Crystal field diagram of the $3d$ orbital splitting of **(a)** HS Fe^{3+} and **(b)** HS Mn^{4+} in an octahedral environment. Electrons are represented as red arrows.

During the third charge, the same maximum of R_2 seen in previous cycles is observed at 2.90 V, together with a minimum at 3.75 V as shown during the 2nd charge. This allows to conclude that the electronic conductivity is limited when the iron is in Fe(III) oxidation state and manganese in Mn(IV), and that the partially filled e_g band due to iron oxidation during charge, increases the electronic conductivity. However, an increase of the resistance can be seen at the end of charge, during process *C*, as it occurred in $NaFeO_2$. These processes are not reversed on further discharge, and the maximum at 2.90 V or the minimum at 3.70 V are no longer observed during the third discharge, and the value of R_2 stays high. It can be thus concluded that the charge process *C*, most probably linked to the oxygen redox, induces and irreversible changes in the material. The electrochemical activity degradation and the irreversibility of R_2 seem to be closely related.

The admittance C_n and argument a_n of the refined CPE elements are presented in Fig. 8.4c and d respectively, n indicating the semicircle as for the resistances R_1 and R_2. As shown for

the $NaFeO_2$ sample in Fig. 7.7, the admittance values are in the order of $C_1 \approx 40$ µF s^{a-1} and $C_2 \approx 1$ mF s^{a-1} during the first two cycles. However, at the end of the third charge C_1 increases about one order of magnitude and is only partially reduced back at the end of the discharge. A similar behavior is also observed for C_2, with a threefold increase at the end of the third charge and a reduction on discharge. The value of the argument a_1 slowly decreases upon cycling, from the initial value of 0.85 down to ≈ 0.65 during the third discharge. This suggests the formation of inhomogeneities in the surface of the electrodes. Owing to the similarities in the behavior of O3-$Na_{2/3}Fe_{2/3}Mn_{1/3}O_2$ and $NaFeO_2$, the high frequency response is most likely related to a SPI layer at the surface of the particles. In Chapter 7 it has been shown that it was stable from the beginning in the case of $NaFeO_2$. However, it seems that the SPI layer in this sample needs longer times or the application of external perturbations to reach a stable state, which is reflected by the continuous albeit slow decrease of a_1 until its stabilization. The value of a_2 on the other hand stays close to 0.85 at all states of charge. However, and due to the inductive effects observed in the Nyquist plots, one should be careful when considering these values. For example, in the Nyquist spectra at 2.0 V and 3.5 V from Fig. 8.2q and r, it can be seen how the inductive effect do not form loops, but the low frequency semicircle starts with reducing $\mathrm{Re}(Z)$ values. The region selected for the fitting will affect the value of a_2, and hence the noise in the results. However, and considering the continuity of the obtained results, while the inductive behavior appears stochastically, the value of a_2 seems to be reliable at all states of charge. These results are different to those obtained for $NaFeO_2$, where a_1 remained constant at $a_1 \approx 0.65$, while a_2 varied between 0.50 and 0.95. It seems thus that in the case of O3-$Na_{2/3}Fe_{2/3}Mn_{1/3}O_2$, the SPI layer is slowly formed at the surface of the particles while the bulk does not suffer from the formation of irregularities.

As mentioned above, as for $NaFeO_2$, a $\approx 45°$ slope can be seen in two different zones: at mid and at low frequencies. The corresponding diffusion related Warburg coefficients are shown in Fig. 8.4e, with up triangles for the mid frequency finite length Warburg ($A_{w\,FL}$) and with down triangles the semi infinite linear diffusion Warburg coefficient ($A_{w\,SILD}$) at low frequencies. As said earlier, the low frequency semicircle tend to cover the 45° slope in most cases, so obtaining its value has only been possible for a few spectra. On the other hand, the refinement of $A_{w\,FL}$ can be seen, and thus its refinement has only been possible in the cases where the inductance was not present, for example, in the spectra during the second discharge (see a few Nyquist plot examples in Fig. 8.2(j-l)).

Although many values are missing due to the inductive effects, the regions at which A_w has been calculated show values that change by less than one order of magnitude. This is very similar to what has been observed in Chapter 7 for $NaFeO_2$, where the major changes in the impedance occur in R_2 rather than on the diffusion related Warburg impedance.

8.2.2 Conventional methods to determine ionic diffusion

Following the methodology described in Chapter 7, the diffusion coefficient will be calculated here also using conventional methods. The morphological, thermodynamic and dynamic factors will

be presented below.

8.2.2.1 Morphological factor

The morphological factor has been calculated using expression 7.2 described in Section 7.2.2.1 in Chapter 7. The amount of transferred electrons per formula unit is $z = 1$, the molar volume, calculated from the pristine structure's cell parameters (see Table 3.8 in Chapter 3), is $V_m = 41.86$ Å^3. The effective surface area S, calculated to be two thirds of the surface area calculated by SAXS (see Fig. 3.19 in Chapter 3) has a value of $S = 0.471$ m^{2}g^{-1}.

Due to the smaller surface area of this sample compared to that of $NaFeO_2$, the morphological factor of $Na_{2/3}Fe_{2/3}Mn_{1/3}O_2$ is two orders of magnitude higher: MF $= 2.079 \times 10^{-14}$ m^{2}C^{-2}.

As explained in Section 7.2.2.1, the changes in the unit cell described with *operando* XRD in Chapter 6 will affect the molar volume and the specific surface area. However, the $^{V_m}/_S$ ratio has been estimated to change by less than 3%, a negligible amount considering the changes of various orders of magnitude generally observed in the diffusion coefficient [8–11]. Thus, MF has been considered as a constant value upon cycling.

8.2.2.2 Thermodynamic factor

The thermodynamic factor TF has been calculated from the derivative of the equilibrium potential curve (see Fig. 8.1d) according to equation 7.4. The results are presented in Fig. 8.7b, together with the $|\mathrm{d}x/\mathrm{d}E_0|$ derivative curve in Fig. 8.7a.

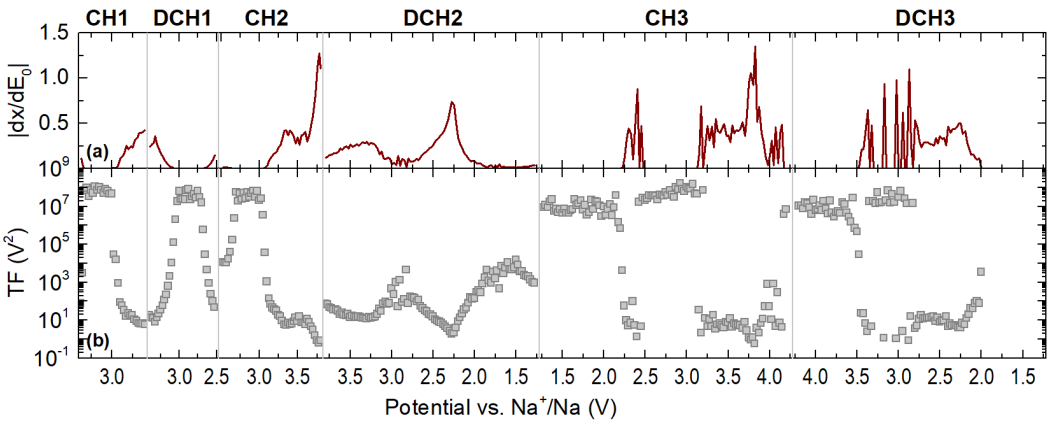

Figure 8.7: **(a)** Derivative curve $|\mathrm{d}x/\mathrm{d}E_0|$ and **(b)** thermodynamic factor of O3-$Na_{2/3}Fe_{2/3}Mn_{1/3}O_2$ as a function of potential. On top the cycle state is shown, CH for charge and DCH for discharge, and the number representing the cycle number.

At the beginning of the first charge, from 2.6V to 3.0 V, a constant value of TF $\approx 10^8$ V^2 can be seen. As TF is the square of the inverse of the derivative of the electrochemical curve, the

electrochemical process identified by local maxima of $|\mathrm{d}x/\mathrm{d}E|$ (see Fig. 8.1e), are reflected by local minima in TF. As shown for $NaFeO_2$ in the previous chapter, the potential hysteresis, as the one on the change from the third charge to the discharge, is reflected as a discontinuous TF evolution.

8.2.2.3 Dynamic factor

8.2.2.3.1 Dynamic factor calculated from PEIS

As described earlier, the diffusion coefficient depends on the Warburg coefficient. It has been calculated from impedance measurements in three different ways, as described in the previous chapter:

- with the Nyquist plots fitting with an equivalent circuit,
- at the minimum frequency using equation 7.6, or
- at the region where the imaginary part of the frequency evolves as the inverse square root of the frequency using equation 7.7.

The first method has been presented in section 7.2.1, and the Warburg coefficient is presented in Fig. 8.4e. Two different Warburg coefficients have been fitted: $A_{w\,FL}$ at mid frequencies and $A_{w\,SILD}$ at low frequencies.

The second and third methods will be presented below. The former, presented in Section 7.2.2.3.1, is useful to calculate the value of $A_{w\,SILD}$ at low frequencies, as it does not depend on the goodness of the fitting of the Nyquist plot. However, in many cases, such as in the spectrum taken at 2.95 V in Fig. 8.2a, when the $R_2||CPE_2$ semicircle is big enough to cover the diffusion related 45° slope, the obtained value will reflect the evolution of R_2 rather than being related to the diffusion.

Finally, the third method will be useful to graphically detect the diffusion behavior at intermediate frequencies as a local minimum in the $-\mathrm{Im}(Z)\sqrt{\omega}$ vs. frequency plot (see Section 7.2.2.3.1 in Chapter 7 for more information). In Fig. 8.8 a few examples of this behavior are presented, with the local minimum highlighted in light gray.

The results obtained with the three aforementioned methods are presented in Fig. 8.9. The graphical method (dark red squares) shows a stable value of DF $\approx 10^{-5}$ s Ω^{-2}, which suggests a constant diffusion coefficient process at mid frequencies. The values obtained at the minimum frequency on the other hand (red circles) follow a behavior opposite to that of R_2, with a minimum at ≈ 2.90 V and maxima at ≈ 3.60 V and 2.70 V, highlighting the fact that this method is not the best to calculate the Warburg coefficient in this sample. Indeed, what is mainly observed with this method is the evolution R_2 and not that of the Warburg impedance. Only when R_2 is low enough will this method give a value that can be relied as diffusion related Warburg impedance. With the values of DF determined from the Nyquist plot fitting (up and down pink triangles) it can be seen how, as shown for $NaFeO_2$ in a previous Chapter, the values of DF obtained from the graphical method corresponds well with those of the finite length diffusion values obtained at mid frequencies, while the values obtained from the minimum frequency method agrees with values

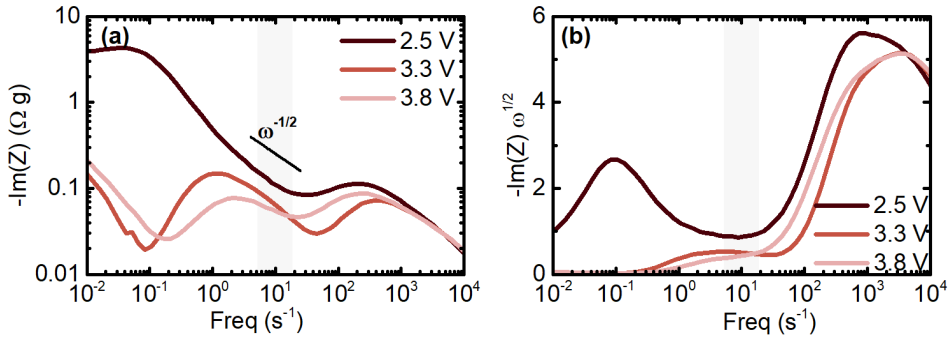

Figure 8.8: Graphical method for the Warburg coefficient calculation from PEIS data according to equation 7.7. **(a)** Imaginary part of impedance and **(b)** imaginary part of impedance times the square root of the frequency as a function of frequency. The frequency region where the diffusion-like conditions are fulfilled has been highlighted in gray.

determined from the semi-infinite linear diffusion method behavior at low frequencies. The minimum frequency method can only be trusted when $\mathrm{DF}_{min.\,freq} > \mathrm{DF}_{graphic}$, which corresponds to the regions where R_2 is low enough to be able to observe the 45° slope.

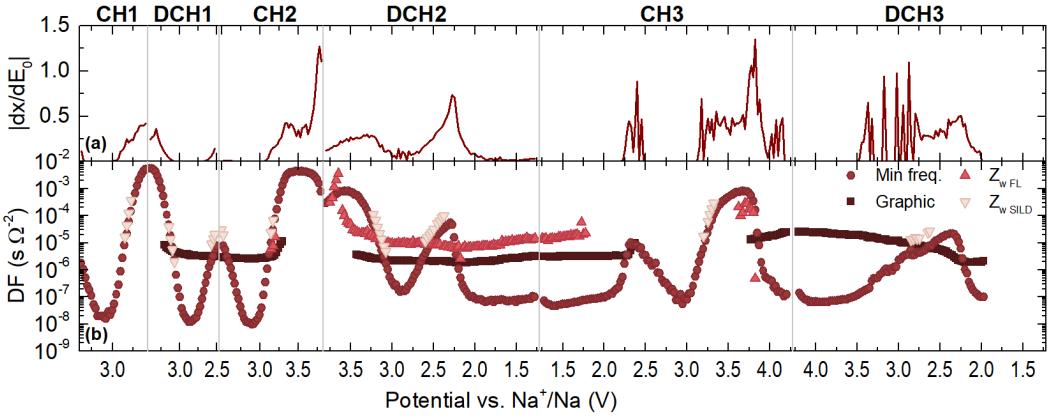

Figure 8.9: **(a)** Derivative curve $|\mathrm{d}x/\mathrm{d}E_0|$ and **(b)** dynamic factor of O3-$Na_{2/3}Fe_{2/3}Mn_{1/3}O_2$ as a function of potential. Dynamic factor has been calculated with three methods from PEIS data: with red circles, values obtained from the minimum frequency impedance value (equation 7.6), with dark red squares, values obtained from the graphical method shown in Fig. 8.8 (equation 7.7), and with up and down pink triangles, values obtained from Nyquist spectra fitting at mid and low frequencies respectively. On top the cycle state is shown, CH for charge and DCH for discharge, and the number representing the cycle number.

8.2.2.3.2 Dynamic factor calculated from PITT

As it has been explained earlier, the Warburg coefficient can also be calculated from the current relaxation during the PITT potential steps. As shown in Section 7.2.2.3.2 of Chapter 7, the diffusive behavior is reflected in the current relaxation when it evolves as the inverse square root of time ($I \propto 1/\sqrt{t}$), that is, when the current relaxation follows the Cottrellian behavior. An example of current relaxation is presented in Fig. 8.10a as a solid red line, together with the ideal Cottrellian current as a dashed blue line. Highlighted in gray is the region at which the behavior is Cottrellian. In Fig. 8.10b, the current has been multiplied by the square root of time, and a local maximum can be seen when the Cottrellian region is located, highlighted in gray. In order to calculate the Warburg coefficient, this local maximum has to be identified, according to equation 7.8.

The current may also depend on the contributions of the other sources of impedance of the cell, as shown in Section 8.2.1, which limits the current at the beginning of the relaxation (that is, at short time limit). Since this may influence the current in the Cottrellian region as well, as a first approximation the current has been corrected by the maximum current according to equation 7.9, as described in Chapter 7.

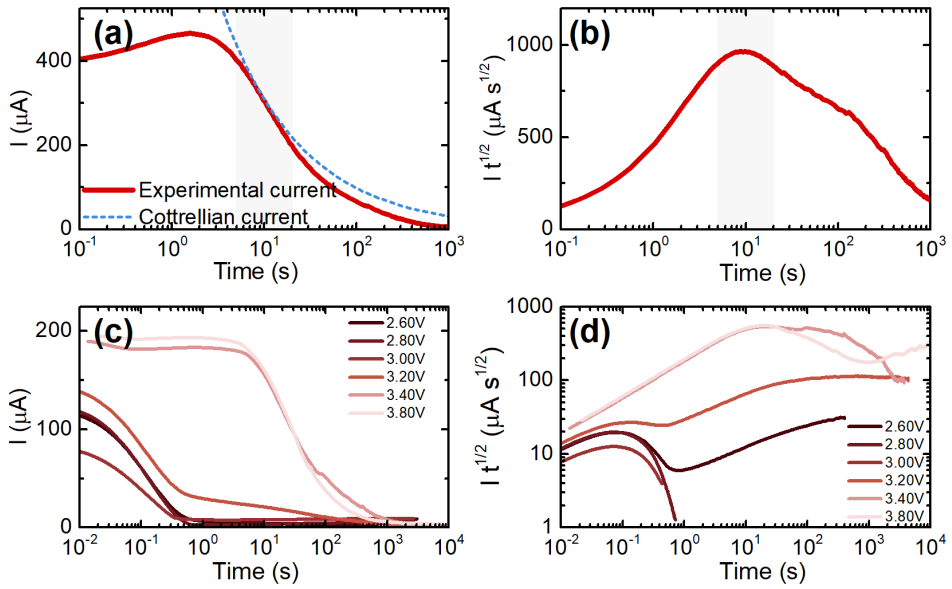

Figure 8.10: **(a)** Example of current evolution upon time ($V = 3.6$ V during second charge) and Cottrellian model current. **(b)** Graphical method for the Warburg coefficient calculation from PITT data according to equation 7.8. The region at which the SILD conditions are fulfilled has been highlighted in gray. Several examples of the evolution of **(c)** the current and **(d)** the evolution of $I\sqrt{t}$ at several potential steps during the 2nd charge.

Figs. 8.10c and d show several current relaxation examples during the second charge at various potentials. Different behaviors can be observed. In Fig. 8.10c it can be seen that at low potentials

($V \leqslant 3.20$ V) the current decreases fast at first reaching a plateau at longer times ($t \geqslant 1$ s). This is reflected in Fig. 8.10d as a local maximum at $t \approx 0.1$ s. However, at high potentials ($V \geqslant 3.40$ V), the current stays nearly constant until $t \approx 1$ s and decays afterwards, shifting the local maximum to longer times $t \approx 10$ s. In some of the steps ($V = 2.60$, 3.20 and 3.80 V), it can be seen how after the first local maximum in the $I\sqrt{t}$ curve, a second maximum appears at longer times. As explained in Section 7.2.2.3.2 of Chapter 7, this is generally related to a biphasic transformation mechanism [11–16]. Thus, when two local maxima are observed, the maximum at shorter relaxation times has been used to calculate the Warburg element.

The obtained results are presented in Fig. 8.11b in pink. For comparison, the values obtained with the graphical method from PEIS data are also presented in dark red color.

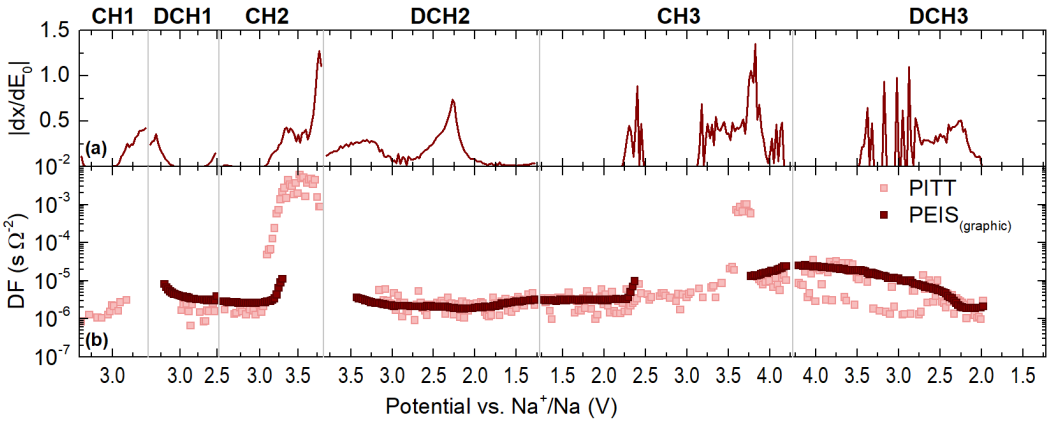

Figure 8.11: **(a)** Derivative curve $|\mathrm{d}x/\mathrm{d}E_0|$ and **(b)** dynamic factor of O3-$Na_{2/3}Fe_{2/3}Mn_{1/3}O_2$ calculated from PEIS and PITT data as a function of potential. The dynamic factor has been calculated with two methods: from PEIS data (dark red squares) with the graphical method shown in Fig. 8.8 and from PITT current relaxation (pink squares). On top the cycle state is shown, CH for charge and DCH for discharge, and the number representing the cycle number.

It can be seen how the results obtained with both methods are in good agreement. The results obtained from the PITT current relaxation are not affected by the inductive effects observed in the PEIS spectra, and it has been thus possible to obtain results for nearly all PITT steps. However, some of the steps relax too fast, and only a couple of current points are recorded, hampering the determination of DF. The value of the dynamic factor stays at DF $\approx 10^{-6}$ s Ω^{-2}. However, an increase in 3 orders of magnitude can be seen during process *A* in the second and third charge with the PITT method, and is reduced during process *B*. Only the onset of this increment can be seen when calculated with PEIS data, as the inductive effects did not allow the characterization of the DF value in these regions. It is not seen during first charge due to the impossibility of obtaining points in this region.

Since more points could be obtained from PITT data than from impedance data, these results will be used to calculate the diffusion, although the values are slightly noisier that those obtained from PEIS data.

8.2.2.4 Ionic diffusion

The diffusion coefficient has been calculated with equation 7.1 as explained in Chapter 7. The results are presented in Fig. 8.12d as a function of composition, together with the derivative curve (Fig. 8.12a), and the thermodynamic and dynamic factors (Figs. 8.12b and c respectively).

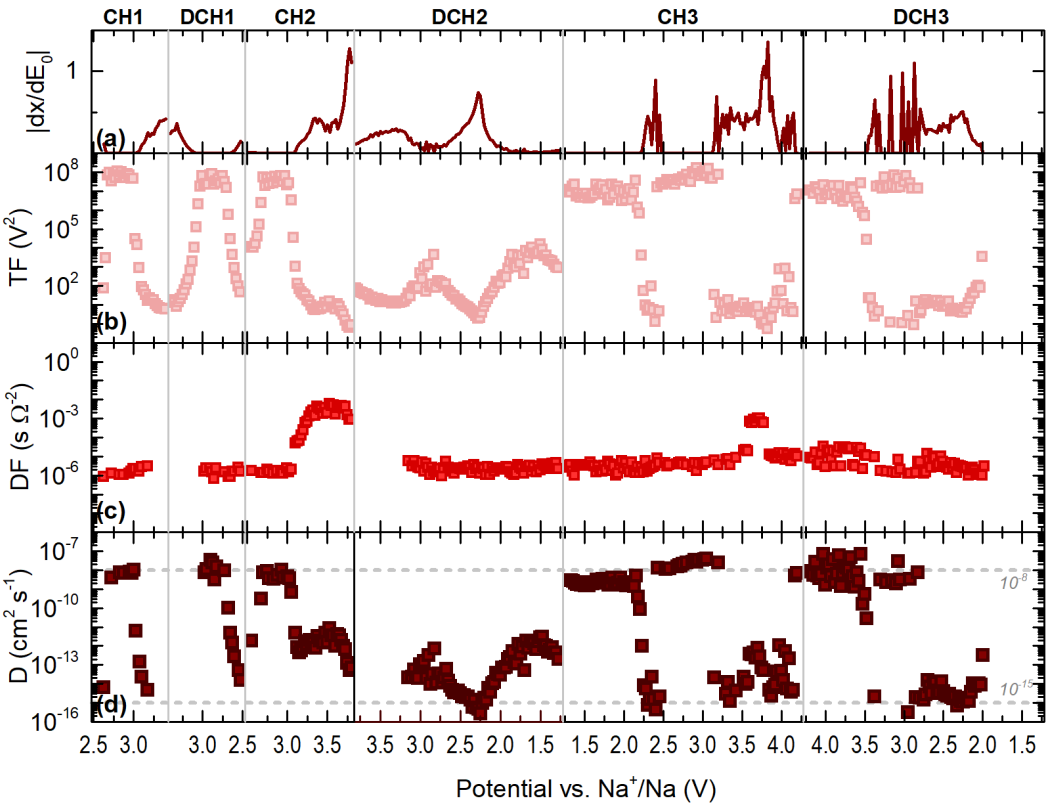

Figure 8.12: **(a)** Derivative curve $|\mathrm{d}x/\mathrm{d}E_0|$, **(b)** thermodynamic factor (from Fig. 8.7), **(c)** dynamic factor (from Fig. 8.11) and **(d)** diffusion coefficient of O3-$Na_{2/3}Fe_{2/3}Mn_{1/3}O_2$ calculated with equation 7.1 as a function of potential. Horizontal dashed lines at $D = 10^{-8}$ cm^2s^{-1} and $D = 10^{-15}$ cm^2s^{-1} have been included as visual help. On top the cycle state is shown, CH for charge and DCH for discharge, and the number representing the cycle number.

The diffusion coefficient has a rather high value of $D \approx 10^{-8}$ cm^2s^{-1}, which decreases during processes *A*, *B*, *C* and *Mn* to values below 10^{-11} cm^2s^{-1} reaching values as low as 10^{-15} cm^2s^{-1}.

The diffusion coefficient has been compared with values reported in the literature. Katcho et al. [17] measured the diffusion coefficient by means of electrochemical impedance and by means of PITT at the composisition $Na_{2/3}Fe_{2/3}Mn_{1/3}O_2$, obtaining results very close to those obtained in this work for the same composition.

Table 8.1: Comparison of the diffusion coefficient of O3-$Na_{2/3}Fe_{2/3}Mn_{1/3}O_2$ obtained in this work and those reported in the literature

Reference	**Technique**	**x in $Na_xFe_{2/3}Mn_{1/3}O_2$**	**D** (cm^2s^{-1})
Katcho et al. [17]	PITT	0.667	6.43×10^{-14}
	EIS	0.667	5.06×10^{-14}
This work	PITT	0.667	2.3×10^{-14}

However, it can be seen how, as in the case of $NaFeO_2$ presented in Chapter 7, the diffusion coefficient calculated follows mainly the evolution of the thermodynamic factor. Indeed, the discontinuities in TF are reflected also as discontinuities in the diffusion coefficient, meaning that at least one the values (high or low) is not representing the actual diffusion coefficient. In the next section the confirmation of this behavior will be checked with the non-conventional method presented in Section 7.2.3 in Chapter 7, which will also be used for the determination of the diffusion coefficient for this material.

8.2.3 Non-conventional method to calculate ionic diffusion from PITT current relaxation

In order to calculate the diffusion coefficient with the method developed by Li et al. [18], the PITT relaxation current has been fitted with equation 7.10, as shown in the previous chapter. A few examples of the fitting are presented in Fig. 8.13, for relaxation currents at various potentials during the second charge. It can be seen that there is a good agreement between the experimental data and the fitted results for $t \leqslant 1$ s. As for $NaFeO_2$, the R radius of the particles, a required parameter for this method, has been deduced from SAXS (Fig. 3.19 in Chapter 3), assuming spherical particles.

This method allows the differentiation of the current limitation due to the ionic diffusion in the material (Q in equation 7.10) or from other contributions such as surface layers and charge transfer. This is more rigorous that the correction for the maximum current and presented in the previous chapter with equation 7.9. It also allows to refine the part of the PITT capacity responding in SILD conditions. In Fig. 8.14 the results of the transferred charge $\Delta Q\ (= \Delta x)$ calculated from the current fitting method and from the relaxation current integration are compared.

From these results it can be seen that for many steps, see e.g. the second discharge, the refined transferred charge Δx is only part of the total charge of the PITT step. This means that with the traditional method $\mathrm{d}x/\mathrm{d}E$ is overestimated, and thus the thermodynamic factor is underestimated. Thus, diffusion coefficient will also be underestimated with the traditional method. When

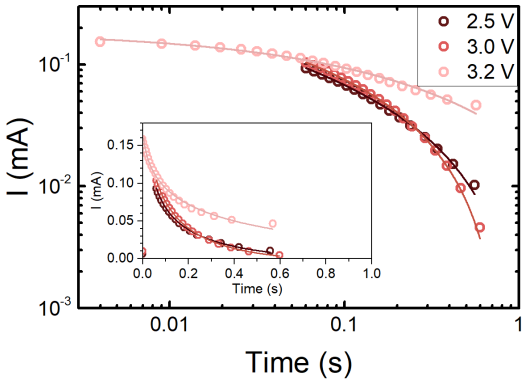

Figure 8.13: Examples of current fits using equation 7.10 during second charge at 2.5 V, 3.0 V and 3.2 V at low times in log-log scale. The experimental points are presented with open circles and fittings with solid lines. In the inset the data are presented in linear scale.

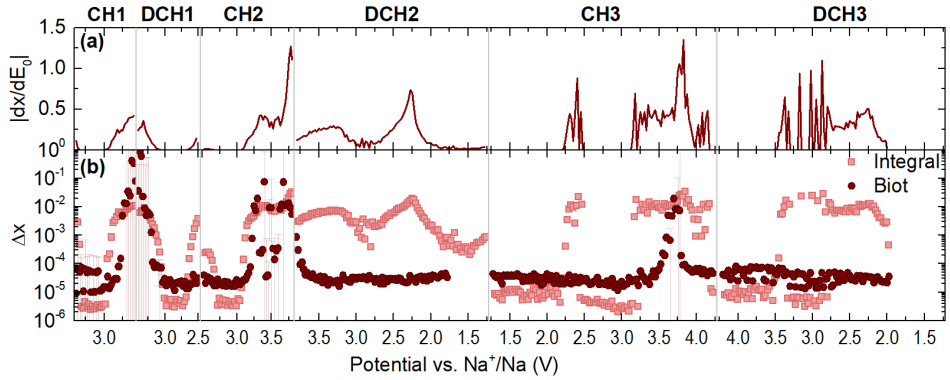

Figure 8.14: **(a)** Derivative curve $|\mathrm{d}x/\mathrm{d}E_0|$ and **(b)** transferred charge during PITT steps calculated as the integral of the current in the whole potential step (pink squares) and from the refinement of current as shown in Fig. 8.13 (dark red circles).

the transferred charge is calculated from the current fitting it remains at $\Delta Q \approx 10^{-5}$ at most potentials, and it increases up to 0.1 during the processes A and B in a narrow potential range. With the integration method on the other hand, Δx stays high for a broader potential range. As it has been explained in Section 7.2.3 in Chapter 7, the extra current can come from structure changes (as seen with the second peak appearing during the current relaxation in Fig. 8.10) or other unexpected reactions. Also, the slightly higher baseline value of ΔQ calculated with the current fitting, can be due to the finite linear diffusion, that produces a premature current decay, compared to the semi-infinite length diffusion region as expected from the theory.

The Biot number B, which represents the ratio between the interface reaction rate and the diffusion rate, is presented in Fig. 8.15b (left axis) together with the R_2 resistance (right axis), and

the $|\mathrm{d}x/\mathrm{d}E_0|$ derivative curve in Fig. 8.15a. As expected, Biot number and R_2 resistance follow opposite trends: when B is high, the R_2 resistance is low, reflecting a reaction kinetics governed by ionic diffusion; on the other hand, when B is low, R_2 is high reflecting a reaction kinetics governed by internal resistances. As shown for $NaFeO_2$ in the previous chapter, the value of B is close or above 1 at all states of charge, meaning that the surface or charge transfer resistances are non-negligible even when B is minimum.

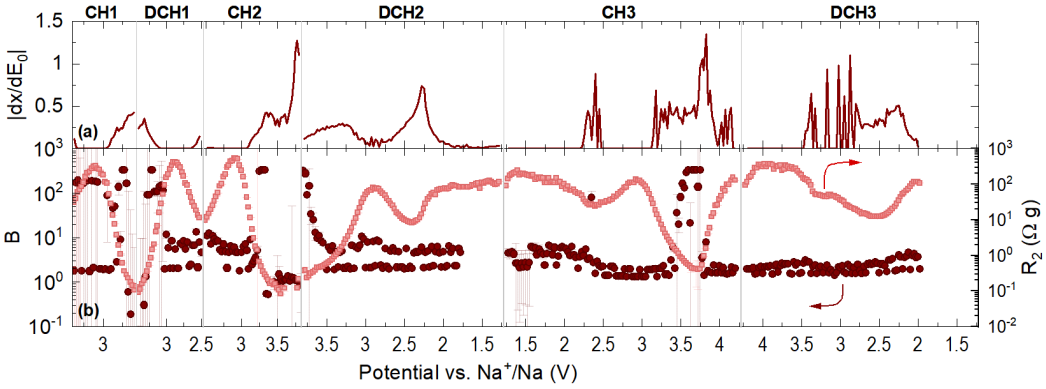

Figure 8.15: **(a)** Derivative curve $|\mathrm{d}x/\mathrm{d}E_0|$ as a function of potential. **(b)** Biot number of $NaFeO_2$ (circles, left axis) and R_2 as shown in Fig. 7.7b (squares, right axis) as a function of potential. On top the cycle state is shown, CH for charge and DCH for discharge, and the number representing the cycle number.

The diffusion coefficient results are presented in Fig. 8.16 as a function of potential. Conventional and non-conventional methods are compared: in pink the results obtained from PITT data (already presented in Fig. 8.12) and in dark red the results obtained from the current fitting method. As shown in Section 8.2.2.4, the values of diffusion coefficient calculated from conventional methods are within a range of about seven orders of magnitude, $D_{PITT} = 10^{-15} - 10^{-8}$ cm^2s^{-1}, being the low values concomitant with the processes *A*, *B*, *C* or *Mn*. On the other hand, the diffusion coefficient calculated from current fitting method remains constant at $D \approx 10^{-8}$ cm^2s^{-1}, except within processes *A* during the first cycle and process *B* during the second cycle and third charge, where D decreases four orders of magnitude down to 10^{-12} cm^2s^{-1}. It is worth noting that the non-conventional method gives a continuous value for the diffusion coefficient, as opposed to the conventional methods. When the transferred charge is low, Δx values as well as the diffusion coefficient values obtained with both methods are in good agreement. This suggests that the difference in the results between the two methods are mainly coming from the values Δx. When integrating the current throughout the whole potential step, Δx can come from the bulk diffusion (which is the sodium content that should be used for the calculation of the diffusion coefficient), as well as from parasitic reactions, such as structural transformation. Thus, one should be

careful when integrating the current, especially when the relaxation times are long which allows kinetically slow processes to take place.

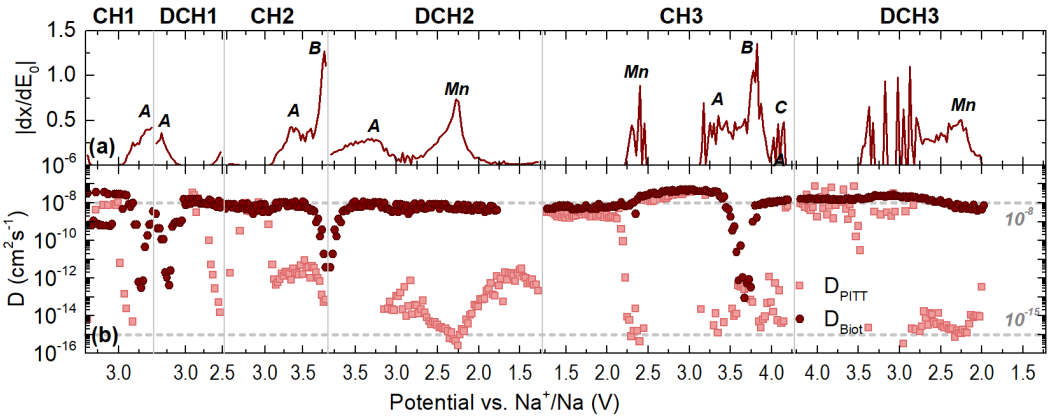

Figure 8.16: **(a)** Derivative $|\mathrm{d}x/\mathrm{d}E_0|$ curve and **(b)** diffusion coefficient of O3-$Na_{2/3}Fe_{2/3}Mn_{1/3}O_2$ obtained by different methods as a function of potential. The diffusion has been calculated with the conventional, from PITT (pink) and with the non-conventional method, by fitting the current (dark red). Dashed lines at D = 10^{-15} cm^2s^{-1} and 10^{-8} cm^2s^{-1} have been added for visual help. On top the cycle state is shown, CH for charge and DCH for discharge, and the number representing the cycle number.

The diffusion coefficient value of $D = 10^{-8}$ cm^2s^{-1} obtained with the non-conventional method is nearly constant, regardless of the charge state of the material, except for the negative sharp peaks at 3.3 V during the 1st cycle and at 3.8 during the 2nd cycle and 3rd charge. The negative peaks in D during process *B* might be related to the onset of O3 to O'3 structural transformation, or the onset of iron migration. The drop of D occurs in a very narrow potential range and is reversed on discharge (see the change from 2nd charge to discharge) and on further charging (see the evolution of D during the 3rd charge). As seen for the $NaFeO_2$ sample, the diffusion coefficient of O3-$Na_{2/3}Fe_{2/3}Mn_{1/3}O_2$ seems to be very stable upon cycling regardless of the structural changes observed in Chapter 6. Surprisingly, and as shown for $NaFeO_2$, the diffusion coefficient does not seem to be affected by the presence of the migrated ions. The electrochemical activity degradation seems to be related to the changes in R_2 and the thermodynamic potential hysteresis that appear when charged above 3.6 V rather than to the diffusion coefficient as stated in the literature [19]. The value of $R_2 \approx 120$ Ω g observed upon cycling is equivalent to an overpotential of about 0.6 V at C/50, the rate at which the *operando* XRD measurements were carried out in Chapter 6.

8.3 Conclusions

In this chapter an advanced characterization of O3-$Na_{2/3}Fe_{2/3}Mn_{1/3}O_2$ diffusion kinetics has been carried out based on coupled PITT and PEIS technique.

Two different processes have been identified with the electrochemical impedance spectroscopy measurements. At high frequencies a finite length surface SPI layer has been detected, with response at high to mid frequencies, which is continuously albeit slowly formed upon cycling. However, this layer is an electronic and ionic conductor, showing only slight changes in the internal R_1 resistance (that is, electronic conductivity seems not to be affected) as well as in the ionic diffusion related Warburg coefficient (that is, ionic conductivity is not affected either). At mid to low frequencies, the response of the bulk material has been observed. In this case, the ionic diffusion related Warburg coefficient is not affected, but R_2 resistance varies several orders of magnitude upon cycling. The evolution of R_2 resistance seems to be related to the electronic conductivity of the bulk. The conductivity is lower when an electron in placed in each orbital, that is, when transition metal ions are in Fe^{3+} and Mn^{4+} oxidation states. The conductivity is increased as the orbitals are partially emptied (through $Fe^{3+/4+}$ oxidation) or filled (through $Mn^{4+/3+}$ reduction). This process seems to be at least partially reversible when the material is charged to 3.8 V, but it is no longer reversible after charging up to 4.2 V (third charge). The process *C* that occurs at 4.10 V and is most likely related to oxygen redox, produces irreversible changes in the material that are reflected as a high R_2 value upon discharge.

The diffusion coefficient has been calculated with conventional and non-conventional methods. The assumption that is generally done in the conventional methods, that all the observed current is related to ionic diffusion, has been proven to be erroneous in this case. With this assumption the transferred charge per step is overestimated in the reaction potentials, and the obtained diffusion coefficient is then underestimated. The non-conventional method allows at least partially to correct this error source, and a very stable diffusion coefficient is obtained upon cycling, $D \approx 10^{-8}$ cm^2s^{-1}, except at the reaction potentials of process *A* during the first cycle and process *B* on further cycling where the diffusion coefficient drops about four orders of magnitude. It is worth noting that when the transferred charge per step is low and the values of Δx obtained from conventional and non-conventional methods are close, so is the diffusion coefficient.

These measurements have confirmed the higher reversibility of this material compared to $NaFeO_2$ when charged to the same potentials. Firstly, the diffusion coefficient is two to three orders of magnitude higher for $Na_{2/3}Fe_{2/3}Mn_{1/3}O_2$, which would be reflected in an improved electrochemical activity, especially at high cycling rates. However, this is not reflected in the rate capability measurements from Chapter 4 (Fig. 4.13). This could be related to the larger particle size in the Mn containing compound. Indeed, during fast cycles the reaction is usually limited to the surface, which will be proportionally larger in smaller particles. While the process *B*, related to iron migration, seems to produce irreversible changes in the electronic conductivity of $NaFeO_2$, it seems that it does not affect the electronic conductivity of O3-$Na_{2/3}Fe_{2/3}Mn_{1/3}O_2$. This could be related to a reorganization of the iron electronic configuration. In the case of the O3-$Na_{2/3}Fe_{2/3}Mn_{1/3}O_2$ sample, the manganese ions could help the stabilization of the material. However, the oxygen redox process at $V \geqslant 4.0$ V seems to irreversibly affect the electronic conductivity of both compounds.

Bibliography

[1] S. Klink, E. Madej, E. Ventosa, A. Lindner, W. Schuhmann, and F. La Mantia. *Electrochemistry Communications*, 22:120–123, 2012.

[2] H. Brandstätter, I. Hanzu, and M. Wilkening. *Electrochimica Acta*, 207:218–223, 2016.

[3] M. Zarrabeitia, F. Nobili, M. n. Muñoz-Márquez, T. Rojo, and M. Casas-Cabanas. *Journal of Power Sources*, 330:78–83, 2016.

[4] M. Frankenberger, M. Singh, A. Dinter, and K.-H. Pettinger. *Batteries*, 5(4):71, 2019.

[5] F. Croce, F. Nobili, A. Deptula, W. Lada, R. Tossici, A. D'Epifanio, B. Scrosati, and R. Marassi. *Electrochemistry Communications*, 1(12):605–608, 1999.

[6] F. Nobili, S. Dsoke, M. Minicucci, F. Croce, and R. Marassi. *The Journal of Physical Chemistry B*, 110(23):11310–11313, 2006.

[7] F. Nobili, F. Croce, R. Tossici, I. Meschini, P. Reale, and R. Marassi. *Journal of Power Sources*, 197:276–284, 2012.

[8] P. P. Prosini, M. Lisi, D. Zane, and M. Pasquali. *Solid State Ionics*, 148:45–51, 2002.

[9] Y. Zhu and C. Wang. *The Journal of Physical Chemistry C*, 114(6):2830–2841, 2010.

[10] D. D. Lecce, D. Campanella, and J. Hassoun. *Journal of Physical Chemistry C*, 122:23925–23933, 2018.

[11] H. Anne. *Understanding the kinetic limitations of NaFePO4 as cathode active material for Na-ion battery*. Ph.D. thesis, Universidad del País Vasco / Euskal Herriko Unibertsitatea, Facultad de Ciencia y Tecnología, Departamento de Física Aplicada II, 2019.

[12] M. D. Levi, K. Gamolsky, D. Aurbach, U. Heider, and R. Oesten. *Journal of The Electrochemical Society*, 147(1):25–33, 2000.

[13] V. Pralong, M. A. Reddy, V. Caignaert, S. Malo, O. I. Lebedev, U. V. Varadaraju, and B. Raveau. *Chemistry of Materials*, 23(7):1915–1922, 2011.

[14] G. Oyama, Y. Yamada, R.-i. Natsui, S.-i. Nishimura, and A. Yamada. *The Journal of Physical Chemistry C*, 116(13):7306–7311, 2012.

[15] V. Pralong, G. Venkatesh, S. Malo, V. Caignaert, R. Baies, and B. Raveau. *Inorganic Chemistry*, 53(1):522–527, 2014.

[16] E. Anger, A. Maignan, T. Barbier, and V. Pralong. *RSC Advances*, 8:26691–26695, 2018.

[17] N. A. Katcho, J. Carrasco, D. Saurel, E. Gonzalo, M. Han, F. Aguesse, and T. Rojo. *Advanced Energy Materials*, 7(1):1601477, 2017.

[18] J. Li, F. Yang, X. Xiao, M. W. Verbrugge, and Y.-T. Cheng. *Electrochimica Acta*, 75:56–61, 2012.

[19] N. Yabuuchi and S. Komaba. *Science and Technology of Advanced Materials*, 15(4):043501, 2014.

9 Advanced structural characterization of P2-$Na_xFe_{2/3}Mn_{1/3}O_2$ upon cycling

Contents

9.1 Introduction

It has been long proposed that the TM migration is not favored in the P-type structures due to the lack of tetrahedral vacancies to which TM can migrate, and the prismatic sites being too large to accommodate the migrated ions [1–4], inducing a better cycling stability of the P-type layered oxides compared to the O-type ones. Indeed, TM migration in O-type phases is usually associated with a transformation towards an electrochemically inactive spinel-like 3D structure, affecting therefore to the cyclability. However, it is also common to observe phase transition through layer gliding in P2-type structures when Na is extracted beyond $x = 0.5 - 0.4$, leading to an O2 or OP4 phase [5–7], or the so-called "Z" structure, a disordered OP structure consisting in randomly alternated stacking of O and P-type layers [8, 9]. In such scenario, tetrahedral vacancies would be present in the O-type layers of the newly formed phase, which could be prone to the TM migration phenomena similarly to what was observed in Chapters 5 and 6 for iron-rich O3-type layered oxides. A closer look to the phase transitions occurring in the P2-type compounds at low Na content is thus needed in order to apprehend their better cyclability compared to the O3-type compounds.

Within this scope the structural evolution of P2-$Na_{2/3}Fe_{2/3}Mn_{1/3}O_2$ upon cycling will be here revisited. This compound has been chosen because it has the same chemical composition as O3-$Na_{2/3}Fe_{2/3}Mn_{1/3}O_2$ studied in Chapter 6, which will allow to observe the influence of the initial P2 structure. The *operando* XRD measurements that have been used for this purpose, were measured at CICe in 2014 by Elena Gonzalo et al., which published only a preliminary qualitative analysis [10]. The analysis has been then pushed further in the scope of this thesis, comparing the results with those of O3-$Na_{2/3}Fe_{2/3}Mn_{1/3}O_2$ already presented in Chapter 6. The synthesis method and pristine powder characterization can be found in Appendix A, Sections A.1-A.3.

9.2 Operando structural evolution by XRD

The first part of the charge process of P2-$Na_{2/3}Fe_{2/3}Mn_{1/3}O_2$ ($t < 5$ h) consists in Na extraction through solid solution from the initial P2 phase, as indicated by the continuous shift of the peaks in Fig. 9.1. At about 5.5 h, a phase transition toward a higher symmetry phase can be observed, as indicated by the abrupt high angle shift of the $(0\,0\,2)$ peak, while $(0\,0\,4)$ and $(1\,0\,2)$ peaks vanish. Moreover, as can be seen in the pattern stack in Fig 9.2a, the $(0\,0\,2)$ reflection experiences a broadening and a decrease of its intensity, indicating a loss of crystallinity in the stacking direction. Its shift to higher angles also reflects a decrease of the interlayer distance. Concomitant with this trend change, the $(1\,0\,0)$ reflection shows a slight broadening as well, and a change in the shifting rate, showing that the metal-metal distance decreases slightly faster at the end of the charge (Fig. 9.2b). The process is reversed during discharge, with a constant rate of change. Moreover, the $(1\,0\,0)$ peak also shows a broadening in the second part of the charge, although less pronounced than for the $(0\,0\,2)$ peak. This reflects that the structure suffers a loss of crystallinity that is more pronounced in the stacking direction. This behaviour has been previously observed

in P2 compounds, such as P2-$Na_xFe_{1/2}Mn_{1/2}O_2$ [8, 11] and $Na_xNi_{1/3-y}Mn_{2/3}Cu_yO_2$ [12]. It has been ascribed to the transformation through layers gliding towards a so called "Z" phase, made of the stacking of randomly alternated P- and O-type layers [9].

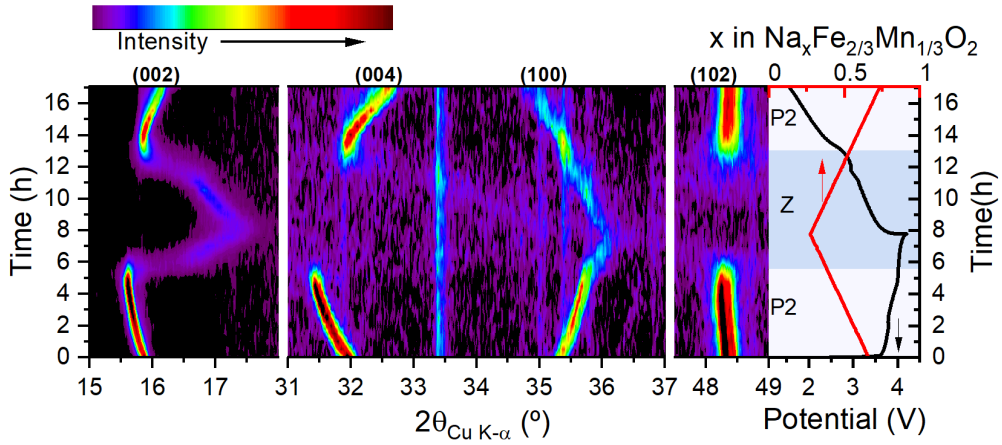

Figure 9.1: 2D operando XRD results of P2-$Na_xFe_{2/3}Mn_{1/3}O_2$, together with the potential and sodium content evolution in the right panel. The structures formed upon cycling have been highlighted in the right panel. Measurements carried out in 2014 by E. Gonzalo et al. [10]. The Le Bail characterizatoin of this cell is presented in Appendix A.3.3.

Besides the obvious differences in the structural evolution of O3- and P2-$Na_xFe_{2/3}Mn_{1/3}O_2$, both compounds present similarities in the cell parameter evolution (see Fig. 9.3b): an increment of *d* with sodium extraction for $2/3 \leqslant x \leqslant 0.35$, followed by a shrinking for $x < 0.35$. This general behavior for TMLOs is usually ascribed to changes in the balance between Coulombic and Van der Walls forces between the layers as a consequence of the decrease of Na content [13]. Surprisingly, the shrinking of the interlayer distance is more abrupt in the case of the "Z" phase of the P2-$Na_{2/3}Fe_{2/3}Mn_{1/3}O_2$ sample than for the O'3-$Na_xFe_{2/3}Mn_{1/3}O_2$. This could be related to inhomogeneous Na concentration in the stacking direction within the "Z" structure, as Somerville et al. [9] proposed it is constituted by the succession of Na-rich P- and Na-poor O-type interlayers, with large and short interlayers respectively. On the contrary, within the O3 phase the Na extraction is probably more homogeneous with all O-type interlayers presenting the same Na concentration. For the O3-$Na_{2/3}Fe_{2/3}Mn_{1/3}O_2$ compound it has been shown in Chapter 8 that the shrinking of *d* at the end of charge was concomitant with Fe migration to the Na layers, as shown by the reduction of intensity of the $(0\,0\,3)_{O3}$ peak, see Fig. 9.3c. In order to verify if Fe migration is also occurring within the "Z" phase of the P2 compound, the intensity evolution at the vicinity of the $(0\,0\,2)$ reflection has been extracted and compared to that of the $(0\,0\,3)$ reflection of the O3-$Na_{2/3}Fe_{2/3}Mn_{1/3}O_2$ compound from Chapter 8, see Fig. 9.3c. The intensity of the $(0\,0\,2)$ reflection of the P2 compound follows the same monotonous increase as that of the O3 compound until $x = 0.4$, beyond which it drops drastically, faster than $(0\,0\,1)_{O'3}$, suggesting that TM does

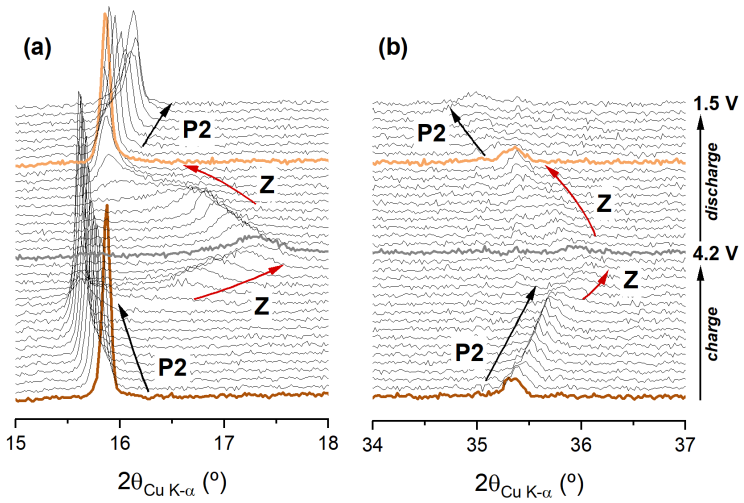

Figure 9.2: Stack plot of the **(a)** $(0\,0\,2)$ and **(b)** $(1\,0\,0)$ reflections of the P2-$Na_xFe_{2/3}Mn_{1/3}O_2$ compound. The patterns in the initial (brown), charged (gray) and *after discharge* (light orange) state patterns have been highlighted. The *after discharge* pattern is the most similar one to the initial one, as it will be described below.

migrate. This pronounced decay of intensity can hardly be ascribed to the transformation from P2 to "Z" alone, as in e.g. P2-$Na_xNi_{1/6}Mn_{1/2}Fe_{1/3}O_2$ Somerville et al. did not observe it [9]. These authors show by TEM and Mössbauer spectroscopy techniques that migration of TM did not occur in the studied compound. Therefore, the intensity decay observed for P2-$Na_{2/3}Fe_{2/3}Mn_{1/3}O_2$ suggests that in this compound TM does migrate to the tetrahedral vacancies within the O interlayers of the "Z" phase, and does so much more abruptly than in the O3 compound. This migration does not occur in P2-$Na_xNi_{1/6}Mn_{1/2}Fe_{1/3}O_2$ from Ref. [9] probably as a consequence of the different TM composition, especially the lower Fe content.

The discharge of P2-$Na_xFe_{2/3}Mn_{1/3}O_2$ (Na re-intercalation) starts as a solid solution within the "Z"-type structure, as indicated by the continuous increase of the interlayer distance *d*, see Figs. 9.1 and 9.2a. Contrary to O3-$Na_{2/3}Fe_{2/3}Mn_{1/3}O_2$ whose structure remains O'3 all along the discharge (the P3 phase observed upon charge does not reappear upon discharge), the "Z" phase of P2-$Na_{2/3}Fe_{2/3}Mn_{1/3}O_2$ transforms back into the P2 structure within the range $0.45 < x < 0.6$ through a "Z"-P2 biphasic transformation (Fig. 9.3b), a slightly larger composition range that during charge. The degree of reversibility is significantly higher compared to O3-$Na_{2/3}Fe_{2/3}Mn_{1/3}O_2$. Indeed, at $x \approx 0.60$ (highlighted with orange arrows), both the initial interlayer distance and intensity of P2-$Na_{2/3}Fe_{2/3}Mn_{1/3}O_2$ are recovered, reflecting the high structural reversibility of this material upon cycling. In particular, the fact that the initial intensity is restored suggests that the migrated TM moves back to its original site in the TMO_2 layers when the P2 structure comes back to its initial value, while this reversibility was only partial for O3-$Na_{2/3}Fe_{2/3}Mn_{1/3}O_2$. Indeed, as can be appreciated in Fig. 9.3 at $x = 0.43$ upon discharge of O3-$Na_xFe_{2/3}Mn_{1/3}O_2$ (red arrows),

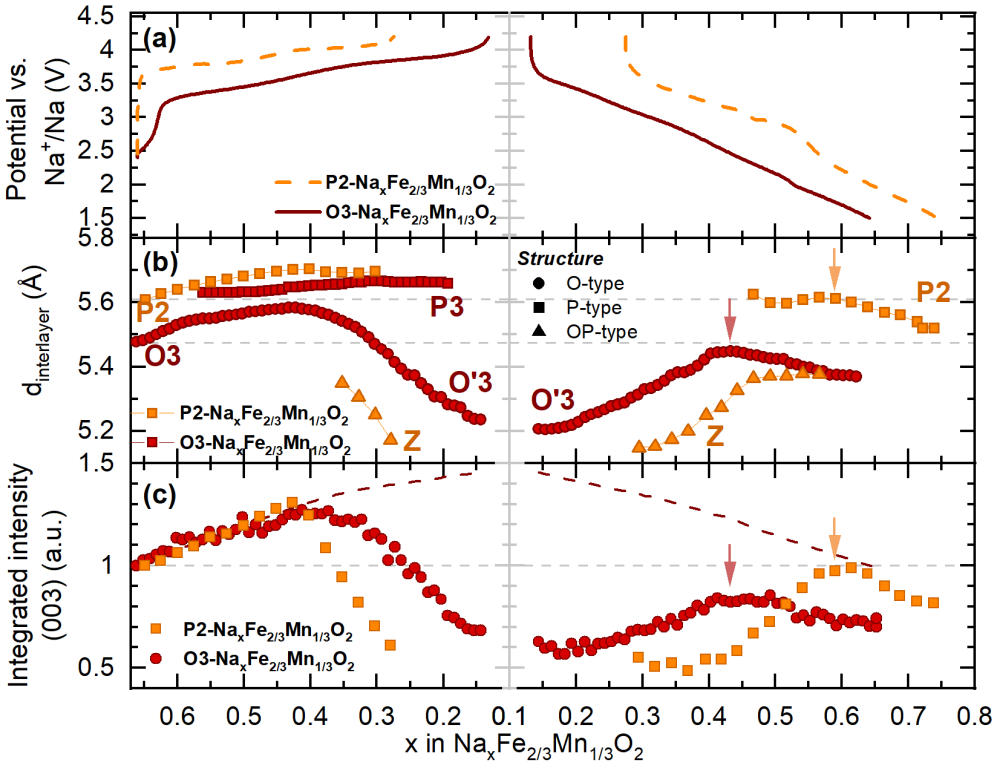

Figure 9.3: Comparison of the operando XRD analysis of O3-$Na_xFe_{2/3}Mn_{1/3}O_2$ (red) and P2-$Na_xFe_{2/3}Mn_{1/3}O_2$ (orange) compounds. **(a)** Voltage-composition curve, **(b)** evolution of the interlayer distance, and **(c)** intensity of the $(0\,0\,\ell)$ reflection (points), together with the simulated intensity of O3-$Na_xFe_{2/3}Mn_{1/3}O_2$ without considering the Fe migration (dashed line). The arrows in panels (b) and (c) highlight the patterns on discharge that are more similar to the initial pattern, called *after discharge* throughout the text. Numerical results can be found in Tables B.3 and B.18 for the O3 and P2 polymorphs respectively.

although d and I values are the closest to the initial values they are clearly different, especially their intensity.

This difference in the extent of the reversibility in the two polymortphs is particularly evident in Fig. 9.4, where the initial XRD patterns of O3- and P2-$Na_{2/3}Fe_{2/3}Mn_{1/3}O_2$ are compared with the most similar pattern during the discharge, that has been called *after discharge* (corresponding to composition highlighted with arrows in Fig. 9.3 for each compound). For O3-$Na_{2/3}Fe_{2/3}Mn_{1/3}O_2$, in Fig. 9.4a, it can be seen that various peaks are split in two after discharge, such as $(0\,1\,2)$ and $(1\,0\,4)$, as a result of the monoclinic distortion suffered by the material during the desodiation process, see Chapter 6 for more details. Moreover, the rest of the reflections, although close to the initial ones, are slightly shifted, meaning that the initial cell parameters are not fully recovered. Finally, the peaks intensity is also not fully recovered upon discharge, which is particularly visi-

ble for the $(0\,0\,3)$ peak. As discussed in Chapter 6, this is an indication that a significant amount of the iron ions that have migrated to the Na layers during charge have stayed there upon discharge. On the other hand, the similarities between the initial and *after discharge* patterns of P2-$Na_{2/3}Fe_{2/3}Mn_{1/3}O_2$ (Fig. 9.4b) are patent. Only a very slight intensity difference can be seen in reflections $(0\,0\,2)$ and $(1\,0\,2)$, but the position of the peaks perfectly overlaps, reflecting the high structural reversibility of this material upon cycling.

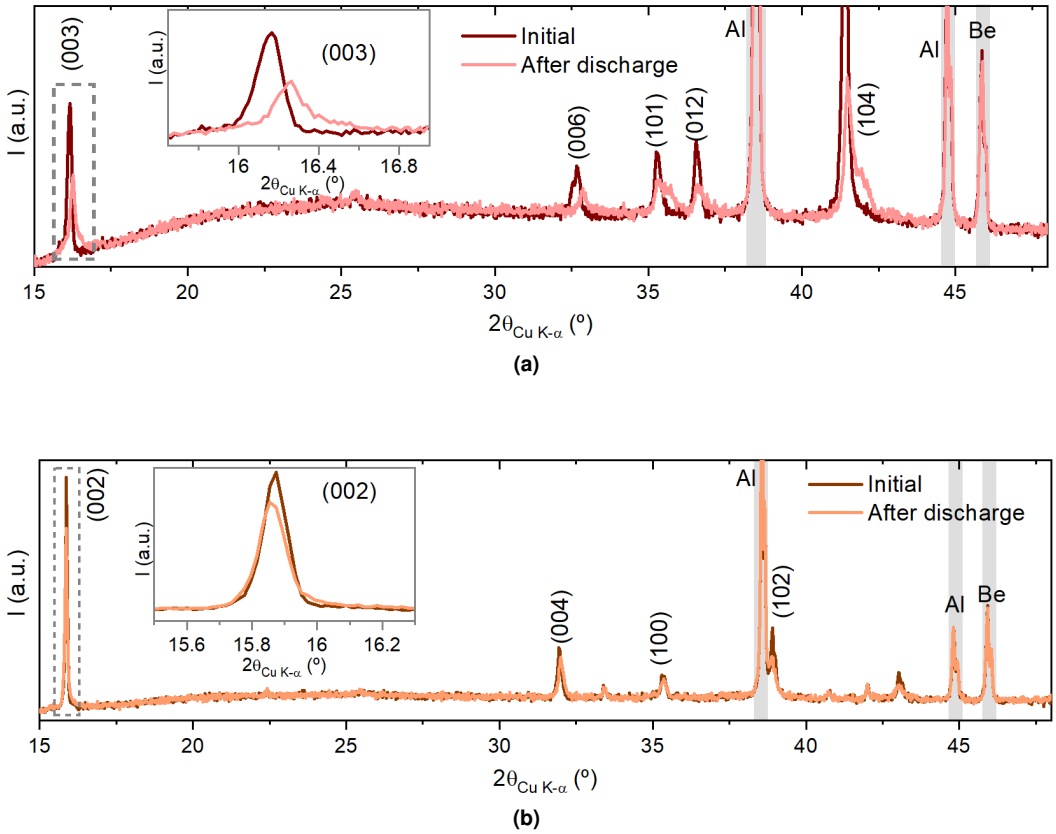

Figure 9.4: Comparison of the initial (dark) and *after discharge* (light) XRD patterns of **(a)** O3-$Na_{2/3}Fe_{2/3}Mn_{1/3}O_2$ and **(b)** P2-$Na_{2/3}Fe_{2/3}Mn_{1/3}O_2$. In the insets, the region of the $(0\,0\,\ell)$ reflection has been highlighted.

The reason for this superior reversibility of structural change at the end of charge of P2-$Na_{2/3}Fe_{2/3}Mn_{1/3}O_2$ compared to the O3-$Na_{2/3}Fe_{2/3}Mn_{1/3}O_2$ can be related to the different structural properties at low Na content: monoclinic distorted O'3 for O3-$Na_{2/3}Fe_{2/3}Mn_{1/3}O_2$ and a "Z" phase for P2-$Na_{2/3}Fe_{2/3}Mn_{1/3}O_2$, made of a random alternance of O- and P-type layers. In full O-type structures it has been shown that the migration of TM ions upon Na extraction can locally result in local transition toward spinel-like 3D structures with strong interplane O-TM-O bonds

that are hardly reversed [1, 14, 15], possibly assisted by irreversible O redox [16, 17]. Although the “Z” phase of P2-$Na_{2/3}Fe_{2/3}Mn_{1/3}O_2$ also contain O-type layers suffering TM migration, they are next to P-type layers which are known to be stronger against TM migration. This peculiarity of the OP (ordered) or "Z" (disordered) structure, i.e. to the intimately intermix of O- and P-type layers, might be what increases the reversibility of the TM migration process by hindering the irreversible transition to a more 3D structure.

9.3 Conclusions

In this Chapter we have studied the structural evolution of P2-$Na_{2/3}Fe_{2/3}Mn_{1/3}O_2$ by means of *operando* XRD. The results have been compared with those of O3-$Na_{2/3}Fe_{2/3}Mn_{1/3}O_2$ polymorph presented in Chapter 6 in order to study the effect on the initial structure on the electrochemical behavior, especially the high voltage stability.

Even though O3- and P2-$Na_{2/3}Fe_{2/3}Mn_{1/3}O_2$ compounds present a different phase transition sequence upon cycling, both follow the general Na-TMLO behavior on charge: an increment of the interlayer distance in the range $0.66 \geqslant x_{Na} \gtrsim 0.35$ followed by a shrinking upon further desodiation. This later in the P2-$Na_{2/3}Fe_{2/3}Mn_{1/3}O_2$ compound is associated with a transformation of the P2 structure into a more disordered phase. The similitudes of this behavior with earlier reports of other P2 compounds indicates that the structure of this Na-poor phase is a sequence of randomly stacked P- and O-type layers, the so called “Z” phase. Interestingly, the evolution of the $(0\,0\,\ell)$ peak intensity of the "Z" phase indicates that TM migrates to the Na layers.

Upon discharge, the intercalation first occurs as a solid solution within the "Z" phase before transforming back into the original P2-phase. The fact that the intensity increases upon discharge to reach its initial value shows that the TM migrated to the Na layers has moved back to the original octahedral site in the TM layers with a level of reversibility higher than for O3-$Na_xFe_{2/3}Mn_{1/3}O_2$.

Instead of being related to the nature of the P2 structure as commonly argued in the literature, the better reversibility of the P2-$Na_{2/3}Fe_{2/3}Mn_{1/3}O_2$ compound is actually related to the nature of its highly desodiated "Z" structure, which allows a higher degree of reversibility of the TM migration compared to O3-$Na_{2/3}Fe_{2/3}Mn_{1/3}O_2$. We believe this is due to the fact that the "Z" structure, contrary to the desodiated O3 structure, includes a large amount of randomly distributed P interlayers which might make the "Z" phase stronger against irreversible structural changes related to the TM migration.

We have thus seen in this chapter that, unlike commonly believed, the initial structure is not as important as it is the structure formed at charged state. In order to understand the electrochemical properties and their reversibility of a certain compound, one needs to understand the structures formed at $x_{Na} < 0.5$. *Operando* XRD has been proven to be a very important technique, although complementary techniques or a solid background knowledge is required to fully understand the occurring processes.

Bibliography

[1] S. Kim, X. Ma, S. P. Ong, and G. Ceder. *Physical Chemistry Chemical Physics*, 14(44):15571, 2012.

[2] N. Yabuuchi, M. Yano, H. Yoshida, S. Kuze, and S. Komaba. *Journal of the Electrochemical Society*, 160(5):A3131–A3137, 2013.

[3] P. Vassilaras, D.-H. Kwon, S. T. Dacek, T. Shi, D.-H. Seo, G. Ceder, and J. C. Kim. *Journal of Materials Chemistry A*, 5(9):4596–4606, 2017.

[4] Y. You, S. Xin, H. Y. Asl, W. Li, P.-F. Wang, Y.-G. Guo, and A. Manthiram. *Chem*, 4(9):2124–2139, 2018.

[5] N. Sharma, M. H. Han, J. C. Pramudita, E. Gonzalo, H. E. A. Brand, and T. Rojo. *J. Mater. Chem. A*, 3(42):21023–21038, 2015.

[6] R. J. Clément, J. Billaud, A. Robert Armstrong, G. Singh, T. Rojo, P. G. Bruce, and C. P. Grey. *Energy Environ. Sci.*, 9(10):3240–3251, 2016.

[7] U. Garg, W. Rexhausen, N. Smith, J. Harris, D. Qu, and P. Guptasarma. *Journal of Power Sources*, 431:105 – 113, 2019.

[8] E. Talaie, V. Duffort, H. L. Smith, B. Fultz, and L. F. Nazar. *Energy & Environmental Science*, 8(8):2512–2523, 2015.

[9] J. W. Somerville, A. Sobkowiak, N. Tapia-Ruiz, J. Billaud, J. G. Lozano, R. A. House, L. C. Gallington, T. Ericsson, L. Häggström, M. R. Roberts, U. Maitra, and P. G. Bruce. *Energy & Environmental Science*, 12(7):2223–2232, 2019.

[10] E. Gonzalo, M. H. Han, J. M. López del Amo, B. Acebedo, M. Casas-Cabanas, and T. Rojo. *Journal of Materials Chemistry A*, 2(43):18523–18530, 2014.

[11] B. Mortemard de Boisse, D. Carlier, M. Guignard, L. Bourgeois, and C. Delmas. *Inorganic Chemistry*, 53(20):11197–11205, 2014.

[12] K. Kubota, Y. Yoda, and S. Komaba. *Journal of The Electrochemical Society*, 164(12):A2368–A2373, 2017.

[13] B. Mortemard de Boisse, M. Reynaud, J. Ma, J. Kikkawa, S.-i. Nishimura, M. Casas-Cabanas, C. Delmas, M. Okubo, and A. Yamada. *Nature Communications*, 10(1):2185, 2019.

[14] D. Mohanty, J. Li, D. P. Abraham, A. Huq, E. A. Payzant, D. L. Wood, and C. Daniel. *Chemistry of Materials*, 26(21):6272–6280, 2014.

[15] X. Li, Y. Wang, D. Wu, L. Liu, S.-H. Bo, and G. Ceder. *Chemistry of Materials*, 28(18):6575–6583, 2016.

[16] W. E. Gent, K. Lim, Y. Liang, Q. Li, T. Barnes, S.-J. Ahn, K. H. Stone, M. McIntire, J. Hong, J. H. Song, Y. Li, A. Mehta, S. Ermon, T. Tyliszczak, D. Kilcoyne, D. Vine, J.-H. Park, S.-K. Doo, M. F. Toney, W. Yang, D. Prendergast, and W. C. Chueh. *Nature Communications*, 8(1):2091, 2017.

[17] Q. Chen, Y. Pei, H. Chen, Y. Song, L. Zhen, C.-Y. Xu, P. Xiao, and G. Henkelman. *Nature Communications*, 11(1):3411, 2020.

10 | Discussion on the performance of iron containing layered oxides

Contents

10.1 Introduction

In this chapter we will try to understand the effect of the iron dilution in the electrochemical and structural evolution upon cycling of iron rich of TMLOs. To this end, results obtained in previous chapters of the two isostructural O3-$NaFeO_2$ and $Na_{2/3}Fe_{2/3}Mn_{1/3}O_2$ will be compared: by a direct comparison of the PITT voltage curves and the structural evolution described by means of *operando* XRD we will try to determine the reasons behind the better electrochemical performance of the manganese containing compound, especially when charged to high potentials. This comparison will also allow us to gain a better insight in the mechanism of the TM migration towards the Na layers. In order to extrapolate these results to other layered oxides and shed light in the degradation mechanism in iron-rich layered oxides, recent literature for these and other similar compounds will be reviewed. Moreover, the results of the P2-$Na_{2/3}Fe_{2/3}Mn_{1/3}O_2$ compound, presented in Chapter 9, will also be reviewed in the light of the obtained conclusions.

10.2 Equilibrium potential from PITT measurements

In Fig. 10.1 the PITT equilibrium potential curves, as studied in Chapters 7 and 8, are shown for O3-$NaFeO_2$ (Fig. 10.1a) and O3-$Na_{2/3}Fe_{2/3}Mn_{1/3}O_2$ (Fig. 10.1c). The curves are presented as a function of sodium content. The corresponding derivative curves are presented in Fig. 10.1b and Fig. 10.1d for $NaFeO_2$ and O3-$Na_{2/3}Fe_{2/3}Mn_{1/3}O_2$ respectively.

By comparing the behavior of these two materials, strong similarities can be found. First, in the limited potential range, $V = 2.5-3.4$ V, the potential curves are fairly reversible: both compounds show a low voltage hysteresis, below 60 mV, and a reasonable CE (85% and 75% for $NaFeO_2$ and $Na_{2/3}Fe_{2/3}Mn_{1/3}O_2$ respectively, see Table 10.1). The hysteresis has been determined according to the position of the *A* and *B* reaction peaks in the derivative curves as labeled in Figs. 10.1b and d. During the subsequent cycles, the potential hysteresis increases with the charge potential for both materials (see ΔV in Table 10.1). Interestingly, this hysteresis is essentially due to a decrease of the discharge potential; the charge potential is not changing.

Nonetheless, differences can also be observed from both measurements. First, the voltage plateaus are sloppier in the case of O3-$Na_{2/3}Fe_{2/3}Mn_{1/3}O_2$, and therefore, the derivative peaks are also broader. Then, the potential of iron oxidation reaction is found slightly higher when manganese is present in the structure (3.33 V for $NaFeO_2$ vs. 3.40 V for O3-$Na_{2/3}Fe_{2/3}Mn_{1/3}O_2$). The latter is probably related to the shift of the charge reactions to higher potentials in this compound due to the Fe and Mn cationic mixture. Indeed, a similar tendency towards a sloppy profile and increase of average potential reaction has been observed with mixed cations in Li-based olivine compounds [1–3]. Combined with the sloping profile, this higher voltage will induce a more pronounced capacity limitation when the upper potential limit is too low. In Table 10.1 it can be seen how the capacity is lower for O3-$Na_{2/3}Fe_{2/3}Mn_{1/3}O_2$ compared to O3-$NaFeO_2$ during the 1st cycle (see also the change in x_{Na} in Figs. 10.1a and c), when the upper potential limit is set to 3.4 V. However, the reversibility of the reaction in O3-$Na_{2/3}Fe_{2/3}Mn_{1/3}O_2$ compound is higher when charged

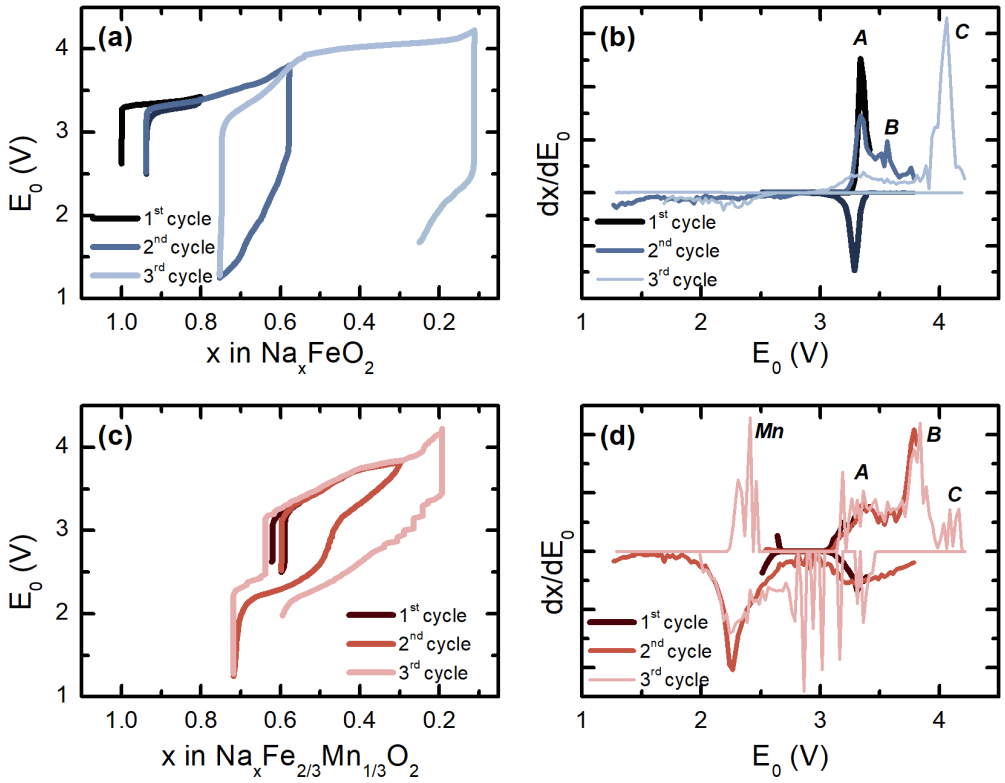

Figure 10.1: Comparison of equilibrium potential cycling (PITT cycling) and corresponding derivative curves for **(a-b)** $NaFeO_2$ and **(c-d)** O3-$Na_{2/3}Fe_{2/3}Mn_{1/3}O_2$.

to higher potentials. This can also be seen in Table 10.1, where higher discharge capacity and Coulombic efficiency values are displayed by the Mn containing compound. The higher reversibility after charging to high potentials of the Mn containing compound can be related to the reaction *C*, occurring at potentials above 4.0 V (see 3rd charge in Fig. 10.1) and which seems to make the reinsertion of Na irreversible as described in Chapters 7 and 8, by an irreversible increment of the charge transfer resistance. Indeed, $NaFeO_2$ delivers much more capacity than $Na_{2/3}Fe_{2/3}Mn_{1/3}O_2$ during this reaction *C*, reducing the reversible capacity of $NaFeO_2$. It is though worth reminding that not all the discharge capacity during the second cycle of $Na_{2/3}Fe_{2/3}Mn_{1/3}O_2$ corresponds to the reversible $Fe^{4+/3+}$ reduction, but to the reduction of Mn ions, since the cell has been discharged below 2.5 V, allowing the Mn redox reaction. Still, the CE related to Fe redox reaction is higher than that in the $NaFeO_2$ compound (48% vs. 61% for $NaFeO_2$ and $Na_{2/3}Fe_{2/3}Mn_{1/3}O_2$ respectively, see Table 10.1). During the 3rd cycle both Fe and Mn redox reaction occur during charge and discharge in $Na_{2/3}Fe_{2/3}Mn_{1/3}O_2$. This can be seen in Figs. 10.1c and d during charge, with the Mn low potential and Fe high potential sloppy plateaus (*Mn*, and *A*, *B* and *C* peaks in the derivative curve). However, it is hard to distinguish between both reactions during the discharge.

It is thus hard to distinguish between the Fe and Mn redox related reversibility. It is nonetheless clear, as seen in Table 10.1, that the overall reaction is more reversible within this potential window for $Na_{2/3}Fe_{2/3}Mn_{1/3}O_2$ (CE = 77%) than for $NaFeO_2$ (CE = 26%).

Regarding the potential hysteresis of the $Fe^{3+/4+}$ redox reaction (also shown in Table 10.1), it increases to $\Delta V > 1$ V when $NaFeO_2$ is charged to 3.8 V or beyond, while it stays below 0.5 V for O3-$Na_{2/3}Fe_{2/3}Mn_{1/3}O_2$ under the same cycling conditions. This, together with the higher discharge capacity after charging to high potentials, highlights the better performance of the Mn-Fe material when cycled to high potentials, as it was previously observed in Chapter 4.

Summarizing, this comparison of the PITT curves of O3-$NaFeO_2$ and O3-$Na_{2/3}Fe_{2/3}Mn_{1/3}O_2$ has allowed to gather some interesting insight in the reason for the better electrochemical performance of O3-$Na_{2/3}Fe_{2/3}Mn_{1/3}O_2$:

(i) The irreversible reaction C occurs to a lesser extent, possibly because its voltage is higher pushing it beyond the maximum voltage limit of 4.2 V. This limits the Fe redox reaction and its related capacity, but it occurs with a higher reversibility.

(ii) It has an extended capacity at low potentials from the manganese redox reaction, which compensates for the reduced Fe capacity.

(iii) A lower thermodynamic voltage hysteresis is observed, possibly as a consequence of (i).

Table 10.1: Comparison of the discharge capacity (Q_{DCH}), the Coulombic efficiency (CE) and potential hysteresis of the $Fe^{3+/4+}$ redox reaction (ΔV) of $NaFeO_2$ and O3-$Na_{2/3}Fe_{2/3}Mn_{1/3}O_2$ during cycling at equilibrium potential. The column V_{CH} refers to the potential limit upon charge.

Sample	Cycle	V_{CH}	Q_{DCH} (mA h g^{-1})	CE (%)	$\Delta V_{Fe^{3+/4+}}$
$NaFeO_2$	1st	3.4 V	36	85	40 mV
	2nd	3.8 V	87	48	$\approx$ 1.15 V †
	3rd	4.2 V	36*	23*	1.18 V
$Na_{2/3}Fe_{2/3}Mn_{1/3}O_2$	1st	3.4 V	17	75	$\approx$ 58 mV ‡
	2nd	3.8 V	102	140 ($\approx$61§)	0.17V
	3rd	4.2 V	97*	77 *	$\approx$ 0.40 V †

* Measurement stopped before the end of the discharge was reached.
† Low signal to noise ratio.
‡ Upper potential limit close to reaction potential.
§ Coulombic Efficiency related to the Fe redox reaction.

10.3 Structural evolution upon cycling

Fig. 10.2(a-c) shows the evolution of cell potentials, normalized interlayer distance d/d_0 and in-plane distance b/b_0 as a function of Na content. From these figures it can be clearly seen that

although the two isostructural materials exhibit similarities in their structural parameters' evolution, the main features of occur at different Na concentrations. Suspecting that these differences might be related to the dilution of Fe by Mn, the parameters presented in Fig. 10.2(a-c) versus Na concentration have also been represented in Fig. 10.2(d-f) as a function of the ratio of oxidized iron, Fe^{4+}/Fe, calculated as such:

$$Fe^{4+}/Fe = 1 - \frac{x}{1-y} \tag{10.1}$$

where x and y represent the sodium and iron content, respectively, as in $Na_xFe_yMn_{1-y}O_2$.

Interestingly, when the cell parameters are presented as a function of Fe^{4+}/Fe (Figs. 10.2(d-f)), their evolution is nearly identical for the two materials. Indeed, in both samples the interlayer distance shows a maximum at $Fe^{4+}/Fe \approx 0.4$, while the in-plane distance reaches its minimum at $Fe^{4+}/Fe \approx 0.55$. These are quite surprising results as the common belief in the community, as shown in Fig. 10.3, is that the main driver for the changes in the cell parameters, and more importantly, in the interlayer distance, is the Na concentration [4]. Indeed, in such scenario the evolution of d is driven by the screening effect of Na on the balance between O-O repulsion at high x_{Na} concentration, which tends to increase d, and Van der Waals attraction between TM-O layers at low x_{Na} concentration, which tends to decrease d. The present results demonstrate that, rather than the Na concentration, it is the oxidation state of Fe that is the main driver of the observed structural changes upon charge.

As can be clearly seen in Fig. 10.4b, when the amount of migrated Fe is plotted as a function of sodium content, beyond the point at which Fe starts to migrate ($x = 0.6$ in Na_xFeO_2 and $x = 0.4$ in $Na_xFe_{2/3}Mn_{1/3}O_2$), the amount of migrated Fe increases at the same rate for the two samples, which corresponds to one migrated Fe per extracted Na (slope indicated by the dashed triangle) and reaches for both compounds very large concentration by the end of the charge (up to more than 30%). Moreover, when the amount of migrated Fe is plotted as a function of oxidized iron content (Fig. 10.4d), Fe migration starts at the same Fe^{4+}/Fe content for both samples (≈ 0.40). These observations are important findings contributing to the deciphering of the mechanism of Fe migration. First, it demonstrates that the Fe migration, as for the cell parameters evolution discussed above, is driven by the oxidation state of Fe rather than by the concentration of Na. Second, the fact that the values are large at the end of charge means that Fe migration is not simply a thermally activated diffusion process, as proposed by previous studies and shown in Fig. 10.5 [5, 6], in which case the concentration of migrated Fe would be small (more details on this later on), but Fe rather migrates spontaneously toward a site of lower energy. Finally, once the onset of Fe migration is reached, the $1:1$ slope means that the rate of Fe migration is controlled by the rate with which Fe^{3+} is oxidized to $4+$. If above $Fe^{4+}/Fe \approx 0.40$ all Fe would be more stable in Na layers, the material would experience a cascade-like transition with all Fe migrating at once to the Na layers, which is not the case. This means that for each Fe^{4+} above $Fe^{4+}/Fe \approx 0.40$, only one Fe migrates spontaneously to the Na layer.

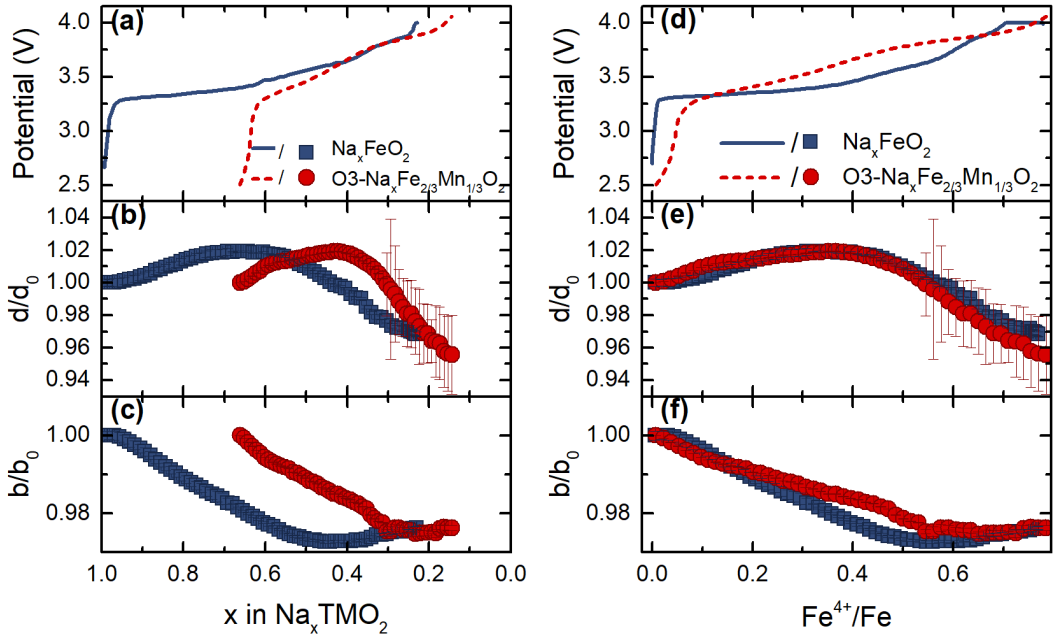

Figure 10.2: Comparison of cell parameter evolution upon the first charge of $NaFeO_2$ and O3-$Na_{2/3}Fe_{2/3}Mn_{1/3}O_2$ samples as a function of **(a-c)** sodium content and **(d-f)** oxidized iron. **(a,d)** Voltage profiles, and **(b,e)** d interlayer distance and **(c,f)** b in-plane distance, normalized to pristine parameters. Values obtained from Le Bail refinements, previously shown in Figs. 5.6 and 6.6 for $NaFeO_2$ and O3-$Na_{2/3}Fe_{2/3}Mn_{1/3}O_2$ respectively.

To understand the implication of these findings it is important to review the state of the art concerning TM migration. Li et al. [5] demonstrated in 2016 from computational calculations that the Fe migration to the Na layers is Fe concentration dependent in Fe containing NaTMLOs; as shown in Fig. 10.5a, a higher Fe concentration reduces the energy penalty (E_P) for Fe migration. They ascribed it to the shortening of the Fe-O bonds in the tetrahedron accommodated by the distortion of the neighboring JT active Fe^{4+} ions. However, even for the largest considered Fe cluster and without Na (Fig. 10.5a), the energy penalty remains positive. This means that Fe migration would be simply a thermally activated diffusion process, which would become progressively more facile as Fe concentration increases, but Fe would still be more stable in the TM-O layers. This would induce only a marginal amount of migrated Fe. In e.g. $Na_{1/3}FeO_2$ (Fig. 10.5b), Li et al. still estimate E_P to be positive, ≈ 0.8 eV, with a total energy barrier of 1.2 eV [6]. Such high energy barrier cannot explain the 20% of migrated Fe observed here at this composition (Fig. 10.4b). The computational results of Refs. [5] and [6] can neither explain the existence of a threshold at $Fe^{4+}/Fe \approx 0.40$ as well as the high amount of migrated Fe above this later with its $1:1$ dependency on

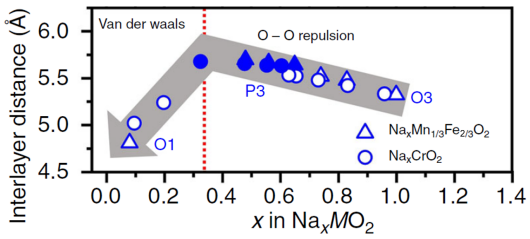

Figure 10.3: Interlayer distance evolution of Na_xTMO_2 layered oxides and the dominant forces as a function of composition [4].

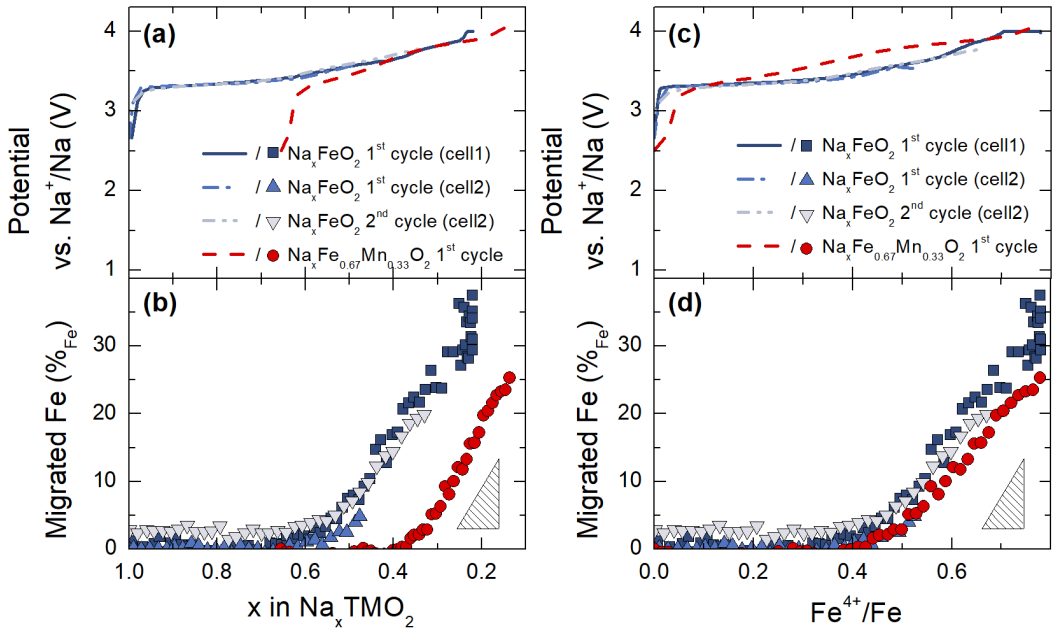

Figure 10.4: Analysis of *operando* XRD patterns for $NaFeO_2$ and O3-$Na_{2/3}Fe_{2/3}Mn_{1/3}O_2$ samples as a function of **(a,b)** sodium content and **(c,d)** oxidized iron. **(a,c)** Voltage profile curves, **(b,d)** estimation of migrated Fe. O3-$Na_{2/3}Fe_{2/3}Mn_{1/3}O_2$ cell has been charged to 4.2 V and discharged to 1.5 V (correspond to the results shown in Fig. 6.8). For $NaFeO_2$ two cells are shown: *cell 1* has been charged to 4.0 V (correspond to Fig. 5.12) and *cell 2* has been charged to 3.6 V during the first cycle and to 3.8 V during the second (corresponds to Fig. 5.13). The dashed triangle shows a $1:1$ slope for migrated Fe and $Fe^{3+/4+}$ oxidation reaction.

extracted Na.[1] An additional factor needs thus to be considered.

Interestingly, transitions towards negative energy penalty values for TM migration have actually been reported in Li-ion batteries when oxygen redox activity is involved. For instance, as seen in Fig. 10.6, Qian et al. described by means of DFT the drastic effect of oxygen vacancies in

[1]Further description on the implication of the Boltzmann statistics on Fe migration assumed above can be found in Appendix A, Section A.4

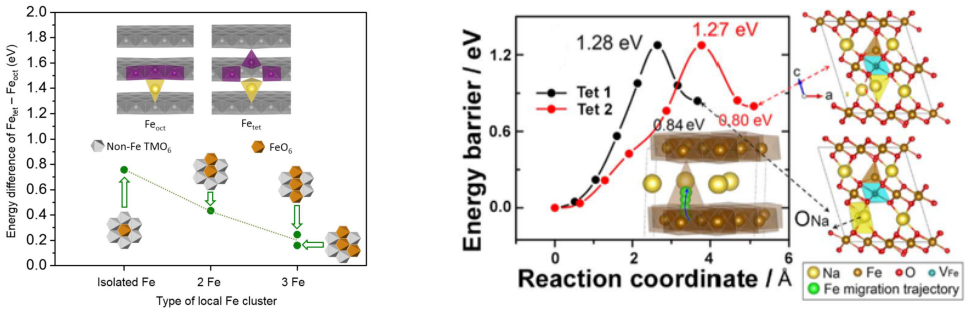

Figure 10.5: **(a)** Energy penalty E_P (here called *Energy difference*) for Fe migration from the original octahedral site to a tetrahedral site in Na layers creating a dumbbell defect in a layered Na(Fe,TM)O_2 oxide. E_P has been calculated in the presence of different local Fe clusters as shown in the insets, the largest one corresponding to the most probable cluster in a $Na_xFe_{1/3}TM_{2/3}O_2$ [5]. **(b)** Two migration energy pathways for Fe to the tetrahedral site in $Na_{1/3}FeO_2$ [6].

the migration energy path of Ni ions in $Li(Li_{1/6}Ni_{1/6}Co_{1/6}Mn_{1/2})O_2$ [7]. More specifically, when oxygen vacancies are in the not shared O plane, the energy penalty is negative with a low energy barrier. In this scenario, the TM migration would occur spontaneously, which is what we observe in $NaFeO_2$ and $Na_{2/3}Fe_{2/3}Mn_{1/3}O_2$.

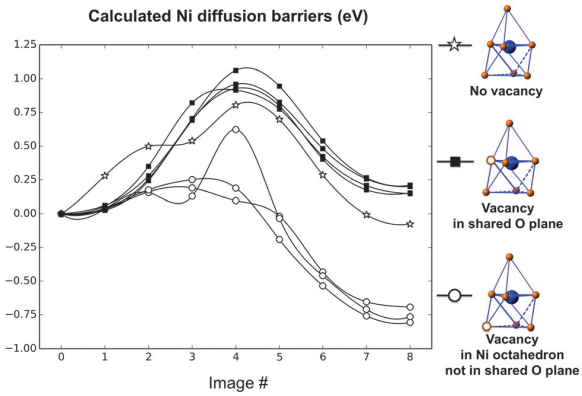

Figure 10.6: Energy migration path of Ni ions from the initial octahedral site to a tetrahedral vacancy in Li layers in the Li-rich layered oxide $Li(Li_{1/6}Ni_{1/6}Co_{1/6}Mn_{1/2})O_2$ in the absence of oxygen vacancies (stars), and in the presence of oxygen vacancies in shared O plane (solid squares) or in the not shared O plane (open circles) [7].

This correlation between TM migration and oxygen redox reaction has been actually reported in several examples of Li-rich layered oxides [6–18], that is, in Li layered oxides where TM has been partially substituted by Li. Oxygen redox is a very peculiar process that not only contributes to the capacity, but it may also be correlated to changes in the energy band structure [19–23]. Indeed,

in A_xTMO_2 type materials, where A is an alkali ion, the redox potential is generally related to the iono-covalence of TM-O bonds [24]. The band structure of these compounds typically consists of a low-lying band coming from bonding TM-O electronic levels and a high-lying band coming from antibonding TM-O states. Due to the high ionicity of the insertion layered oxides these two bands are generally well separated, and the electron density close to the Fermi level is attributed to the TM *d*-bands, that is, to transition metal redox activity (see Fig. 10.7a).

In some cases, a TM(*d*)-O(*p*) hybridization can occur when too many A^+ ions are extracted [25, 26]. When this occurs, the O^{2-} ligand can become less electronegative than the TM^{n+} cation, and the electrons from the O p-band are poured into the TM d-band, that is, oxygen will be oxidized as shown in Fig. 10.7b [19, 21]. Consequently, oxygen redox assisted TM transition only occurs beyond a certain concentration of oxidized TM, and can in certain cases trigger spontaneous TM migration at the vicinity of the O vacancies. Beyond this threshold the amount of migrated TM would thus be controlled by the concentration of vacancies. Such scenario would perfectly match with what is observed here for O3-$NaFeO_2$ and O3-$Na_{2/3}Fe_{2/3}Mn_{1/3}O_2$, i.e. the $1:1$ slope of migrated TM vs Na. The Na extraction controls the concentration of O vacancies, which in turns control the concentration of migrated TM. Note that in Li-rich TMLOs, if the anionic oxidation is pushed further, oxygen gas can be formed and be irreversibly released from the structure (Fig. 10.7c) [13].

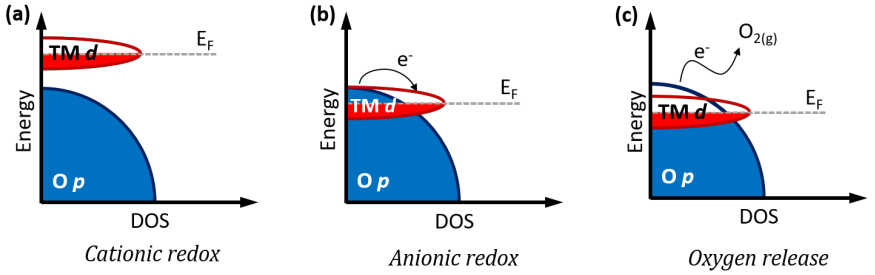

Figure 10.7: Schematic energy band evolution of a layered oxide based on Refs. [13, 21]. Energy as a function of density of states (DOS), where Fermi energy level is shown as E_F. Schema of **(a)** cationic redox, with separated TM d and Op bands; **(b)** reversible anionic redox, with hybridized TM-O band; and **(c)** irreversible anionic redox with oxygen gas release.

A reversible anionic redox has actually been recently reported for $NaFeO_2$ by means of X-ray photoelectron spectroscopy (XPS), with the presence of O^{n-} detected upon charge for $x_{Na} \lesssim 0.8$, and predicted by DFT for $x_{Na} < 0.4$ [6]. Later on, Susanto et al. [27] showed the release of CO_2 gas upon charge at $Fe^{4+}/Fe \approx 0.57$ ($x = 0.43$, ≈ 3.8 V), as a consequence of the immediate reaction of the evolved oxygen with the electrolyte. By analogy with the mechanism discussed above in Li-rich TMLOs, we can conclude that O redox is most probably what triggers TM migration at $Fe^{4+}/Fe \approx 40\%$ and controls the rate of this process as well as its reversibility beyond that point.

Within this scenario, the process *A* identified in the electrochemical curves of $NaFeO_2$ and $Na_{2/3}Fe_{2/3}Mn_{1/3}O_2$ (see Fig. 10.1(b,d)) would be pure Na extraction coupled with $Fe^{3+/4+}$ redox and a reversible structural transition from O3 to P3 through layer gliding. Process *B* would then correspond to TM migration, assisted by the O redox observed by Li et al. [6], inducing monoclinic structural distortion and shrinking of d. Finally, process *C* which when activated degrades strongly the reversibility, might be related to the O_2 evolution observed by Susanto et al. [27]. The degree of reversibility of the process of TM migration would then be intimately related with the reversibility of O redox.

It is worth noting that since the Fe migration onset is determined by the amount of oxidized iron, this onset will be pushed to deeper desodiation levels as Fe is substituted by other TM reacting at lower potentials. Indeed, based on equation 10.1, to obtain $Fe^{4+}/Fe = 0.40$ (as it has been seen that the migration onset occurs at this composition), and assuming the other TM is oxidized, the threshold in terms of sodium content should be equal to:

$$x = (1 - Fe^{4+}/Fe) \cdot (1 - y) = 0.6 \cdot (1 - y) \tag{10.2}$$

The higher the content y of the substituting TM, the lower the Na concentration x that can be reached before the Fe migration onset limit is achieved. This can be clearly seen in Fig. 10.4b, where the onset of Fe migration occurs at a deeper desodiation state in $Na_{2/3}Fe_{2/3}Mn_{1/3}O_2$. In this particular case, it corresponds to $x = 0.6$ for $NaFeO_2$ and $x = 0.4$ for $Na_{2/3}Fe_{2/3}Mn_{1/3}O_2$. This explains why larger reversible capacities can be obtained reducing the Fe content, as observed for instance by Wang et al. [28], Mu et al. [29] and in the present work.

As presented in Chapter 9, the *operando* XRD results have suggested that migration of TM towards Na layers also occur in P2-$Na_{2/3}Fe_{2/3}Mn_{1/3}O_2$. Therefore, one can reasonably assume that anionic redox also occurs in this P2-$Na_{2/3}Fe_{2/3}Mn_{1/3}O_2$ compound. However, the electrochemical and structural reversibility of this compound is higher than for the O3-structured ones, suggesting that the anionic redox reversibility is also higher in this case. This can be explained in terms of a more stable presence of the reduced oxygen species in the structure. Indeed recent publications have presented direct proof of O-O peroxo-like dimer formation as a result of the oxygen oxidation, for both Na- and Li-TMLOs, and these peroxo-like species are thought to be more stable in P-type structures than in the O-type ones [13, 30, 31]. As a consequence, the irreversible oxygen release will be probably less pronounced in P-type structures than in O-type ones [32, 33]. It should be noted that, as presented in Chapter 9, when the intensity drop suggesting TM migration is observed in P2-$Na_{2/3}Fe_{2/3}Mn_{1/3}O_2$ the structure is not P2 anymore but a “Z” phase consisting of a random stacking of P- and O-type layers. The better reversibility of the TM migration process in this compound suggest that the presence of the P-layers within the "Z" structure is enough to protect the compound from oxygen release by stabilizing the peroxo-like O-O dimers. That is, the nature of the “Z”-phase, formed during the desodiation of the P2-$Na_{2/3}Fe_{2/3}Mn_{1/3}O_2$ compound, is the reason for its better stability compared to the O3-type compounds.

10.4 Conclusions

In this chapter we have compared some of the results of O3-$NaFeO_2$ and O3-$Na_{2/3}Fe_{2/3}Mn_{1/3}O_2$ presented in previous chapters to understand the effect of Fe dilution in the electrochemical properties of the iron-rich layered oxides. We observed that this process depends on the average oxidation state of iron, instead of the sodium concentration as commonly believed. It starts at $Fe^{4+}/Fe \approx 0.4$ and is followed by constant rate of one migrated ion per oxidized iron afterwards. Therefore, the migration process starts at higher desodiation states in those compounds with a lower Fe content. Based on a review of the literature on the mechanism of anionic redox and TMLOs, as well as recent publications reporting O redox in $NaFeO_2$, we have been able to relate the TM migration process to the O redox process. The later would control both the rate and the reversibility of the former. In particular, we believe that the O_2 evolution observed in a recent published work in $NaFeO_2$ correspond to the process labelled as *C* throughout chapters 4, 7 and 8, which was the redox process occurring at the highest potential upon charge and responsible for the degradation of the reversibility when triggered. Moreover, it has previously been reported that the oxygen release is harder in P-type structures. Therefore, those compounds in which the charged state is a P-type or P-containing structure, the anionic redox activity will be more reversible. This explains why higher voltages and higher capacities can be reached in those TMLOs with a lower Fe content before the irreversible reaction occurs, or when the structure still contains P-type layers at the end of charge.

We can thus conclude that the loss of reversibility of the Na extraction observed in TM layered oxide compounds are not related to the occurrence of TM migration as commonly believed, but to the degree of reversibility of the associated oxygen release.

On the light of these conclusions it seems reasonable to propose that, instead of trying to avoid TM migration, one could rather focus the design of new TMLO cathodes on improving the reversibility of the O redox process.

Bibliography

[1] R. Malik, F. Zhou, and G. Ceder. *Physical Review B*, 79:214201, 2009.

[2] T. Muraliganth and A. Manthiram. *The Journal of Physical Chemistry C*, 114(36):15530–15540, 2010. Publisher: American Chemical Society.

[3] S. K. Martha, O. Haik, E. Zinigrad, I. Exnar, T. Drezen, J. H. Miners, and D. Aurbach. *Journal of The Electrochemical Society*, 158(10):A1115, 2011.

[4] B. Mortemard de Boisse, M. Reynaud, J. Ma, J. Kikkawa, S.-i. Nishimura, M. Casas-Cabanas, C. Delmas, M. Okubo, and A. Yamada. *Nature Communications*, 10(1):2185, 2019.

[5] X. Li, Y. Wang, D. Wu, L. Liu, S.-H. Bo, and G. Ceder. *Chemistry of Materials*, 28(18):6575–6583, 2016.

[6] Y. Li, Y. Gao, X. Wang, X. Shen, Q. Kong, R. Yu, G. Lu, Z. Wang, and L. Chen. *Nano Energy*, 47:519–526, 2018.

[7] D. Qian, B. Xu, M. Chi, and Y. S. Meng. *Physical Chemistry Chemical Physics*, 16(28):14665–14668, 2014.

[8] Z. Lu, L. Y. Beaulieu, R. A. Donaberger, C. L. Thomas, and J. R. Dahn. *Journal of The Electrochemical Society*, 149(6):A778–A791, 2002.

[9] H. Koga, L. Croguennec, M. Ménétrier, P. Mannessiez, F. Weill, C. Delmas, and S. Belin. *The Journal of Physical Chemistry C*, 118(11):5700–5709, 2014.

[10] E. Lee and K. A. Persson. *Advanced Energy Materials*, 4(15):1400498, 2014.

[11] J. Zheng, P. Xu, M. Gu, J. Xiao, N. D. Browning, P. Yan, C. Wang, and J.-G. Zhang. *Chemistry of Materials*, 27(4):1381–1390, 2015.

[12] E. Talaie, V. Duffort, H. L. Smith, B. Fultz, and L. F. Nazar. *Energy & Environmental Science*, 8(8):2512–2523, 2015.

[13] E. McCalla, A. M. Abakumov, M. Saubanère, D. Foix, E. J. Berg, G. Rousse, M.-L. Doublet, D. Gonbeau, P. Novák, G. V. Tendeloo, R. Dominko, and J.-M. Tarascon. *Science*, 350(6267):1516–1521, 2015.

[14] P. Rozier, M. Sathiya, A.-R. Paulraj, D. Foix, T. Desaunay, P.-L. Taberna, P. Simon, and J.-M. Tarascon. *Electrochemistry Communications*, 53:29–32, 2015.

[15] G. Assat, C. Delacourt, D. A. D. Corte, and J.-M. Tarascon. *Journal of The Electrochemical Society*, 163(14):A2965–A2976, 2016.

[16] E. Talaie, S. Y. Kim, N. Chen, and L. F. Nazar. *Chemistry of Materials*, 29(16):6684–6697, 2017.

[17] G. Assat, A. Iadecola, C. Delacourt, R. Dedryvère, and J.-M. Tarascon. *Chemistry of Materials*, 29(22):9714–9724, 2017.

[18] X. Rong, J. Liu, E. Hu, Y. Liu, Y. Wang, J. Wu, X. Yu, K. Page, Y.-S. Hu, W. Yang, H. Li, X.-Q. Yang, L. Chen, and X. Huang. *Joule*, 2(1):125–140, 2018.

[19] E. McCalla, A. S. Prakash, E. Berg, M. Saubanere, A. M. Abakumov, D. Foix, B. Klobes, M.-T. Sougrati, G. Rousse, F. Lepoivre, S. Mariyappan, M.-L. Doublet, D. Gonbeau, P. Novak, G. Van Tendeloo, R. P. Hermann, and J.-M. Tarascon. *Journal of the Electrochemical Society*, 162(7):A1341–A1351, 2015.

[20] W. E. Gent, K. Lim, Y. Liang, Q. Li, T. Barnes, S.-J. Ahn, K. H. Stone, M. McIntire, J. Hong, J. H. Song, Y. Li, A. Mehta, S. Ermon, T. Tyliszczak, D. Kilcoyne, D. Vine, J.-H. Park, S.-K. Doo, M. F. Toney, W. Yang, D. Prendergast, and W. C. Chueh. *Nature Communications*, 8(1):2091, 2017.

[21] A. Grimaud, W. T. Hong, Y. Shao-Horn, and J.-M. Tarascon. *Nature Materials*, 15(2):121–126, 2016.

[22] M. Saubanère, E. McCalla, J.-M. Tarascon, and M.-L. Doublet. *Energy and Environmental Science*, 9:984–991, 2016.

[23] J. Vinckevičiūtė, M. D. Radin, N. V. Faenza, G. G. Amatucci, and A. Van der Ven. *Journal of Materials Chemistry A*, 7(19):11996–12007, 2019.

[24] J. B. Goodenough and Y. Kim. *Chemistry of Materials*, 22(3):587–603, 2010.

[25] G. Ceder, M. Aydinol, and A. Kohan. *Computational Materials Science*, 8(1-2):161–169, 1997.

[26] J. Tarascon, G. Vaughan, Y. Chabre, L. Seguin, M. Anne, P. Strobel, and G. Amatucci. *Journal of Solid State Chemistry*, 147(1):410–420, 1999.

[27] D. Susanto, M. K. Cho, G. Ali, J.-Y. Kim, H. J. Chang, H.-S. Kim, K.-W. Nam, and K. Y. Chung. *Chemistry of Materials*, 31(10):3644–3651, 2019.

[28] H. Wang, X.-Z. Liao, Y. Yang, X. Yan, Y.-S. He, and Z.-F. Ma. *Journal of The Electrochemical Society*, 163(3):A565–A570, 2016.

[29] L. Mu, S. Xu, Y. Li, Y.-S. Hu, H. Li, L. Chen, and X. Huang. *Advanced Materials*, 27(43):6928–6933, 2015.

[30] H. Chen and M. S. Islam. *Chemistry of Materials*, 28(18):6656–6663, 2016.

[31] A. S. Tygesen, J. H. Chang, T. Vegge1and, and J. M. García-Lastra. *npj Computational Materials*, 6(65), 2020.

[32] X. Rong, F. Gao, Y. Lu, K. Yang, and Y. Hu. *Chinese Chemical Letters*, 29(12):1791–1794, 2018.

[33] X. Rong, E. Hu, Y. Lu, F. Meng, C. Zhao, X. Wang, Q. Zhang, X. Yu, L. Gu, Y. S. Hu, H. Li, X. Huang, X. Q. Yang, C. Delmas, and L. Chen. *Joule*, 3(2):503–517, 2019.

11 Conclusions

11.1 Conclusions

This thesis aimed at understanding the mechanism of transition metal migration toward the Na layers, as one of the main sources of performance degradation in Fe-rich sodium transition metal layered oxides (TMLOs) as the cathode of Na-ion batteries (SIBs).

Among the cathode candidates for SIBs TMLOs are highly considered for allowing one of the largest energy densities vs. Na at full cell level, they suffer from a trade-off between capacity and cycling stability. This is related to irreversible structural changes occurring when too much Na is extracted, inducing the stacked 2D layered structure to transform into more 3D-bound structures such as the spinel.

Although TM migration has been identified soon as the main cause of performance degradation in Fe-rich Na-TMLOs based on *ex-situ* studies at deintercalated state, at the beginning of this thesis very little was known on this phenomenon. In particular, not only the concentration of migrated TM was unknown, but also the Na composition at which is starts to occur, its dynamics, kinetics as well as the mechanism. Moreover, a recent publication reported a totally different structural evolution for O3-$NaFeO_2$ compared to O3-$Na_xFe_{1-y}Mn_yO_2$ ($1/2 \leqslant y \leqslant 2/3$), with very little structural change observed for the former compared to the later, while O3-$NaFeO_2$ is known to present the more pronounced performance degradation.

The present thesis work has thus been focused on the study of structural evolution in Fe-rich Na-Fe-Mn TMLOs, with special focus on the mechanism of TM migration toward the Na layers, and its correlation with the electrochemical response and its degradation.

The first part of this work consisted in the preparation of O3-$Na_xFe_{1_y}Mn_yO_2$ ($y = 0, 0.1, 0.33$; $x \approx y$) powder materials, their characterization in the as prepared ("pristine") state and evaluation of electrochemical performance. These compounds have been synthesized to high purity through ceramic method, all sharing the aimed O3 layered structure as shown by powder X-ray diffraction (PXRD), in which TMO_2 layers formed by FeO_6 octahedra, are alternatively stacked with Na ion layers where Na^+ is in an octahedral environment. All these samples shared a similar morphology of sub-micron sized spherical particles agglomerated into bigger secondary particles of a few microns. Magnetic measurements showed the same antiferromagnetic response for the three compounds, confirming the similarity of their crystalline structure. Mössbauer measurement confirmed that, according to the stoichiometry, as prepared all iron is in the $3+$ state, while all manganese is in the $4+$ state. Consequently, during the first electrochemical Na extraction (charge) Mn will not be active until $x_{Na} > y$, so that only the $Fe^{3+/4+}$ redox couple is supposed to contribute to the capacity during the first charge.

The study of their electrochemical response has revealed strong similarities between these compounds when the $Fe^{3+/4+}$ redox couple is involved, according to previous reports. Three redox processes have been identified upon the first charge (*A*, *B* and *C* here after). The first reaction occurring upon 1st charge (process *A*), is observed around $3.3 - 3.5$ V at C/10 as a clear plateau in the voltage-composition profile. When the charge capacity is limited to this process (about 80

mA h g^{-1}, $1 < x_{Na} < 0.6$ for Na_xFeO_2), the charge-discharge reaction is very reversible, with a low voltage hysteresis.

The second reaction observed upon 1st charge, process *B*, is identified as a broad peak near $3.6 - 3.8$ V in the derivative voltage-composition curves. Once this process *B* is activated, the voltage hysteresis increases and the discharge capacity decreases, but this process seems to be at least partially reversible as even $NaFeO_2$ is able to sustain various charge-discharge cycles when charged to 3.8 V.

When these compounds are charged over 4.0 V, process *C* is activated, also identified as a peak centered around $4.0 - 4.2$ V in the derivative voltage-composition curves. When this occurs, the voltage hysteresis further increases, leading to a fast capacity fading. For instance, in $NaFeO_2$, if charged to 4.5 V the discharge capacity is nearly zero at 2.5 V, in agreement with previous reports. Surprisingly, if the discharge voltage is reduced down to 1.5 V to compensate for the large voltage hysteresis when discharged from 4.5 V, about 30 mA h g^{-1} discharge capacity is reached, which can be sustained for at least 20 cycles in the $1.5 - 4.5$ V voltage window. This was not reported before in the literature, probably because the discharge voltage was not low enough, and it was on the contrary commonly considered that the structural change occurring at high voltage in $NaFeO_2$ led to electrochemical inactivity. Interestingly, in the case of $Na_{2/3}Fe_{2/3}Mn_{1/3}O_2$ process *C* is found less detrimental than for $NaFeO_2$ when activated upon 1st charge, as reflected by the lower voltage hysteresis (1.18 V for $NaFeO_2$ vs. 0.40 V for $Na_{2/3}Fe_{2/3}Mn_{1/3}O_2$) and slower capacity fading.

The second part of this work consisted in a mechanistic study of Na extraction/insertion in O3-$Na_xFe_{1_y}Mn_yO_2$ ($0 \leqslant y \leqslant 1/3$), with special focus on $NaFeO_2$. For that purpose, *ex-situ*, *in-situ* and *operando* XRD and Mössbauer spectroscopy techniques have been used.

The *operando* XRD studies of O3-Na_xFeO_2 and O3-$Na_xFe_{2/3}Mn_{1/3}O_2$ using CIC Energigune-designed in-situ cell with rigid Beryllium windows have revealed that the structure of both compounds evolved in a very similar manner upon cycling. For $NaFeO_2$, this is in total contradiction with previous reports; we believe this was due to the cell design (coin cell with flexible Kapton windows for those previous reports), which prevented the authors to properly observe the structural evolution in the measured area. Indeed, reproducing their experimental conditions, in collaboration with New South Wales University (Australia), we could neither observe any significant structural change, highlighting the importance on the cell design for such experiment. Using CIC Energigune-designed in-situ cell, the observed structural changes for $NaFeO_2$ and $Na_{2/3}Fe_{2/3}Mn_{1/3}O_2$ start as a solid solution upon charge, where the interlayer distance increases upon desodiation from the initial O3 structure, due to the increasing electrostatic repulsion of the oxygen ions in adjacent layers. This corresponds to process *A* identified in the electrochemical charge-discharge profiles. At a certain point, near $x_{Na} = 0.57$ for $Na_xFe_{2/3}Mn_{1/3}O_2$ and $x_{Na} = 0.65$ for Na_xFeO_2, a O3-P3 biphasic reaction starts to take place, but the initially growing P3 phase fades back near $x = 0.3$ and $x = 0.2$ for Na_xFeO_2 and $Na_xFe_{2/3}Mn_{1/3}O_2$, respectively. However, when the material is allowed to relax inside the cell for large time periods (over 24 hours), or after heating the desodiated compound to relatively high temperatures (190°C), the

P3 phase re-appears. This lets us conclude that the O3-P3 transformation is the thermodynamic path of lower energy, and the apparent disappearance of the P3 phase during the constant current *operando* measurement is then probably kinetically induced. Instead of being constant during the O3-P3 transition, as would be expected for an ideal two-phase reaction, the cell parameters of the O3 phase continue evolving indicating Na is still extracted from this phase. More precisely, the interlayer distance of the O3 phase, which was increasing during the first part of the charge, reaches a maximum near $x = 0.6$ in Na_xFeO_2 ($x = 0.4$ in $Na_xFe_{2/3}Mn_{1/3}O_2$), before it starts reducing again. This quite generic behavior of O phases upon deintercalation is commonly considered to be a result of the change in the balance between repulsive Coulombic forces and attractive Van der Walls forces between TM-O layers driven by the decrease of Na concentration. However, despite the very similar structural evolution observed in $NaFeO_2$ and $Na_{2/3}Fe_{2/3}Mn_{1/3}O_2$, the inflexion point in the interlayer distance evolution upon Na extraction occurs at different sodium contents. Surprisingly, assuming all redox activity is due to Fe, the inflexion point actually corresponds to the same average oxidation state of Fe in both compounds: $Fe^{4+}/Fe \approx 0.4$. The process at origin of this inflection in the interlayer distance evolution seems thus to be rather driven by the iron oxidation state, i.e. the position of the chemical potential with respect to the $Fe^{3+/4+}$ band, rather than the sodium content. According to the voltage-composition profile during the *operando* XRD experiments, this inflection point seems to correspond to process *B*.

Unfortunately, it has not been possible to observe any specific feature in the structural evolution that could give an insight into process *C*. This is because when charged beyond 3.8 V in $NaFeO_2$ the diffraction peaks become very weak, indicating a loss of crystallinity. This later could be due to various causes, possibly inter-correlated, such as inhomogenous Na concentration as a consequence of sluggish reaction kinetics, presence of stacking faults or TM migration and associated local degradation of the layered structure. In particular, it is commonly considered that TM migration degrades the electrochemical reactivity by blocking Na diffusion.

During the discharge, independently from the charge voltage, the structures of $NaFeO_2$ and $Na_{2/3}Fe_{2/3}Mn_{1/3}O_2$ evolve as a solid solution, with no reappearance of P3 phase, revealing the asymmetry of the charge-discharge process. As for the disappearance of the P3 phase at the second part of the charge, this might not reflect the thermodynamic path of minimum energy but rather be kinetically induced by the constant reaction rate during the experiment. As observed during the electrochemical characterization, although the structural reversibility is reduced when the upper voltage limit is increased, partial structural reversibility is observed, e.g. when discharged from 3.8 V in $NaFeO_2$ and 4.2 V in $Na_{2/3}Fe_{2/3}Mn_{1/3}O_2$ indicating Na resinsertion into the structure.

Due to experimental limitations inherent to *operando* experiment using lab-scale XRD instrument, the collected *operando* XRD data did not allow to refine occupancies through Rietveld refinement, so that only cell parameters could be refined through the Le Bail method. However, a strong decrease of intensity of the $(0\,0\,3)$ reflection of the O3 phase has been observed upon charge in both $NaFeO_2$ and $Na_{2/3}Fe_{2/3}Mn_{1/3}O_2$ during the second part of the charge when the

interlayer distance is reduced, indicating a change in occupancies in the stacking direction. Simulating the patterns using the FullProf software based on experimental cell parameters, we verified that Na extraction is expected to increase the $(0\,0\,\ell)$ reflection intensity while TM migration to the Na layers leads to a decrease. The intensity decrease would then be due to the occurrence of TM migration in these compounds upon charge, which has been confirmed using Mössbauer spectroscopy. In particular, it has demonstrated the presence of Fe^{3+} ions in the tetrahedral vacancies of the Na layers. The intensity lost during charge for the $(0\,0\,\ell)$ reflection is also partially recovered during discharge, suggesting that at least part of the migrated TM go back to the TMO_2 layers. This is a very surprising result, as TM migration is commonly considered an essentially irreversible process.

In order to quantify the amount of migrated TM, the simulated intensity of the $(0\,0\,3)$ reflection has been parameterized as a function of the content of Na and migrated TM, allowing to estimate the amount of migrated TM from the experimental $(0\,0\,3)$ peak intensity all along the *operando* XRD experiments of $NaFeO_2$ and $Na_{2/3}Fe_{2/3}Mn_{1/3}O_2$. Based on this method, the migration of TM has been found to initiate upon charge when the inflection in the interlayer distance is observed, that is when $Fe^{4+}/Fe \approx 0.4$ in both Na_xFeO_2 and $Na_xFe_{2/3}Mn_{1/3}O_2$. This indicates that the two phenomena have a causal relation, both being part of process *B*. Beyond $Fe^{4+}/Fe \approx 0.4$, the concentration of migrated TM seems to be controlled by the amount of Na that is extracted, with a slope of one Fe migrated per Na extracted, reaching concentrations as high as 35% in Na_xFeO_2 at 4.0 V or 26% in $Na_xFe_{2/3}Mn_{1/3}O_2$ at 4.2 V. The reversibility of the TM migration upon discharge has also been confirmed, with, at the end of discharge, 28% and 65% of migrated TM back into the TM layers for Na_xFeO_2 and $Na_xFe_{2/3}Mn_{1/3}O_2$, respectively. Rather than limiting TM migration, substituting Mn for Fe seems to improve the electrochemical reversibility by increasing the reversibility of the TM migration process as well as decreasing the Na concentration at which it initiates.

Although the *operando* XRD study has not been able to shade light on the cause for the onset of TM migration when Fe^{4+}/Fe approaches 0.4 upon charge, a closer look at the literature offered some elements of answer. First, based on the literature on Li-rich TMLOs, TM migration to the alkali metal layers appears intimately correlated with the oxidation of oxygen, since this can change the energy profile of the local migration path of the TM ions, making the migration energetically favorable, i.e. spontaneous. The presence of O redox in Na_xFeO_2 has been actually recently reported, including O_2 evolution above 4.0 V. This led us to conclude that O redox is most probably the process that is driving and controlling the onset and rate of TM migration in Na_xFeO_2 and $Na_xFe_{2/3}Mn_{1/3}O_2$. Within this scenario, TM would start to migrate upon charge when O redox initiates, and the rate of this migration would then be controlled by the O redox process, each additional Na extracted induced the oxidation of an O, which in turn induced spontaneous migration of a neighbor TM. When this O is reduced back upon Na reinsertion (discharge), the neighbor migrated TM returns to its initial position. When oxidation of O is too deep, O-O peroxo-like dimers can be formed and result in irreversible O vacancies as a consequence of O_2 evolution, in

which case the neighbor migrated TM cannot return to its position, causing electrochemical and structural irreversibility. This is possibly what process *C* consists of.

In order to get a deeper insight into the influence of the structural evolution, and especially of TM migration, on the kinetics of electrochemical reaction, coupled PEIS-PITT tests have been performed on Na_xFeO_2 and $Na_xFe_{2/3}Mn_{1/3}O_2$ in order to track the evolution of Na diffusion coefficient and surface processes such as charge transfer.

Surprisingly, contrary to the common belief that TM migration blocks Na diffusion, but consistent with our finding that this process is at least partially reversible, the Na diffusion coefficient has shown very little variation with the state of charge, regardless of the cycling history. Even after charging $NaFeO_2$ to 4.0 V, where 35% of TM is expected to have migrated to the Na layers, the diffusion coefficient is not significantly reduced. The charge transfer resistance on the other hand, has been found to change strongly with the state of charge. First of all, it shows a local maximum when all the Fe and Mn ions are in III and IV oxidation states, respectively, that is when $x_{Na} \approx y_{Mn}$. This could be simply due to a minimum of electronic conductivity as a consequence, for instance, of a charge localization occurring at that composition. Second, when reaction *C* is triggered upon charge the charge transfer resistance increases by more than two orders of magnitude, and it stays high upon the next discharge. This can account for the increase in polarization that these materials suffer when reaction *C* occurs, which in turn affects the electrochemical reversibility.

In order to investigate the influence of the initial crystalline structure on the high voltage evolution, P2-$Na_{2/3}Fe_{2/3}Mn_{1/3}O_2$ has been studied and compared to O3-$Na_{2/3}Fe_{2/3}Mn_{1/3}O_2$. Indeed, it is believed that O structures are more prone to TM migration than P-type structure, since the size of available sites in the Na layers being too large in P-type structure. In P2-$Na_{2/3}Fe_{2/3}Mn_{1/3}O_2$ the desodiation has been found to occur through an extended solid solution region upon charge ($^2/_3 \leqslant x_{Na} \leqslant 0.35$), in agreement with previous studies. No noticeable reduction of $(0\,0\,\ell)$ peaks intensity is observed during this range, indicating that TM migration has not occurred. However, near $x_{Na} \approx 0.35$, the P2 structure quickly transforms into a disordered "Z" phase, formed by randomly stacked P- and O-type layers. The interlayer distance of the "Z" phase shrinks similarly to what was observed in O3-$Na_xFe_{2/3}Mn_{1/3}O_2$ in the same x_{Na} range, down to values below those of the pristine P2 material, accompanied by a strong decrease of the intensity of the $(0\,0\,\ell)$ reflection. Although due to the complexity of the structure an approximate quantification of migrated TM has not been possible for this compound, these observations are a strong indication of TM migration. Interestingly, the reversibility of these structural changes upon discharge in P2-$Na_xFe_{2/3}Mn_{1/3}O_2$ is significantly higher than those of O3-$Na_xFe_{2/3}Mn_{1/3}O_2$, which is also reflected in the better electrochemical reversibility. This could be related to the fact that, as recently reported, the formation of the O-O dimer resulting from the oxygen oxidation is more stable in P-type structures rather than in O-type ones, which results in a more difficult oxygen release thus avoids the O redox to become irreversible. Since the "Z"-phase consists of an intimate intermixture of P and O interlayers, the presence of P-type layers next to the O-type layers where TM migration is supposed

to occur might help to hinder O_2 release, resulting in a more reversible anionic redox activity, which it is finally reflected in a more reversible electrochemical activity. However, irreversibility would eventually occur if too many Na ions are extracted, as the concentration of O layers into the "Z" phase would increase to the point that irreversible TM migration and O_2 evolution are not prevented.

In conclusion, we believe this work reveals that the reason for the degradation of O3-Na-TMLOs structural and electrochemical reversibility when too many Na are extracted does not so much rely on the TM migration to the Na layers, but instead on the reversibility of the anionic redox activity. Instead of simply avoiding TM migration, efforts could be focused on improving the reversibility of the TM migration through that of the anionic redox activity. We found that substituting Mn for Fe improves the reversibility by allowing more Na extraction before these irreversible processes occur, at the cost, however, of a reduced voltage for an overall limited gain in terms of energy density. The fact that the P phase seems robust against TM migration, and the "Z" phase it transforms into allows a better reversibility of the TM migration process compared to an O3 phase, offers an interesting angle of approach for materials optimization. Indeed, while TM and O redox are processes that are quite challenging to detect and quantify, the presence of P or "Z" phases is quite easily detected by *operando* XRD analysis. A possible strategy to design improved materials could thus be to look for P compounds with an extended range of stability of their P structure, or O compounds that fully transform into a P phase upon charge.

Appendices

A Supplementary material characterization

Contents

A.1 Synthesis and structural characterization of P2-$Na_{2/3}Fe_{2/3}Mn_{1/3}O_2$

P2-$Na_{2/3}Fe_{2/3}Mn_{1/3}O_2$ compound was synthesized by E. Gonzalo via ceramic method mixing anhydrous sodium carbonate (Na_2CO_3, $\geqslant 99\%$, Sigma Aldrich), iron (III) oxide (Fe_2O_3, $\geqslant 99\%$, Alfa Aesar) and manganese (III) oxide (Mn_2O_3, $\geqslant 99\%$, Sigma Aldrich) stoichiometrically using an agate mortar and a pestle [1]. The pelletized material has been heated at 5°C/min rate and held at 1000°C during 15h under oxygen flow, and the sample has been removed from the furnace above 100°C and transferred into an argon glove-box to avoid moisture contamination. The reaction formula can be described as follows:

$$\frac{1}{3}Na_2CO_3 + \frac{1}{3}Fe_2O_3 + \frac{1}{6}Mn_2O_3 + \frac{1}{12}O_2 \xrightarrow{1000°C,\ 15h,\ O_2} Na_{2/3}Fe_{2/3}Mn_{1/3}O_2 + \frac{1}{3}CO_2$$

A.2 Magnetic properties characterization of Na_xTMO_2 layered oxides

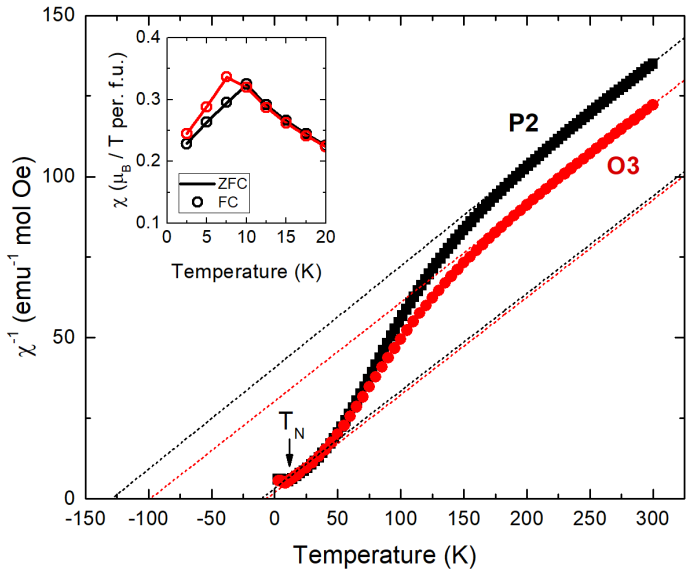

Figure A.1: Inverse susceptibility of O3-$Na_{2/3}Fe_{2/3}Mn_{1/3}O_2$ (red) and P2-$Na_{2/3}Fe_{2/3}Mn_{1/3}O_2$ (black) synthesized by E. Gonzalo and measured by D. Saurel. In the inset, susceptibility curves in ZFC and FC curves.

Table A.1: Effective moment μ_{eff} and Weiss temperature θ deduced from the linear fit of the inverse susceptibility of O3- and P2-$Na_{2/3}Fe_{2/3}Mn_{1/3}O_2$ of Fig. A.1 near room temperature (high temperature) and near Néel temperature (low temperature).

Structure	$\mathbf{T_N}$ (K)	**High Temperature**		**Low Temperature**	
		μ_{eff}	θ (K)	μ_{eff}	θ (K)
P2	11(3)	5.107(7)	-141(2)	5.40(7)	-8.7(7)
O3	8(3)	5.109(6)	-100(1)	5.364(6)	-8.9(5)

A.3 Structural characterization of P2-$Na_{2/3}Fe_{2/3}Mn_{1/3}O_2$

A.3.1 Rietveld refinement of powder sample

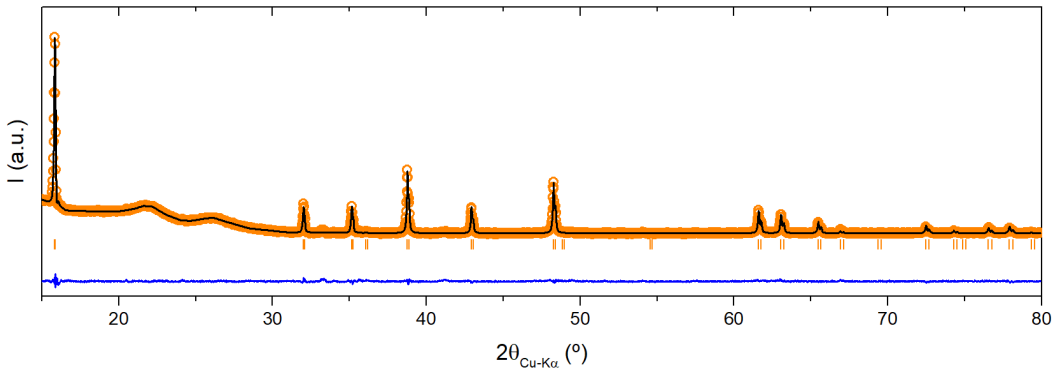

Figure A.2: Rietveld refinement of P2-$Na_{2/3}Fe_{2/3}Mn_{1/3}O_2$ synthesized by E. Gonzalo and measured at CIC Energigune by E. Gonzalo and E. Martin. Experimental data is presented with open circles and the refined pattern with a black line. The vertical lines correspond to the reflection angle positions and the blue line to the difference between the experimental and the calculated values.

Table A.2: Rietveld refinement of pristine P2-$Na_{2/3}Fe_{2/3}Mn_{1/3}O_2$ synthesized by E. Gonzalo. Measurement carried out at ALBA synchrotron by E. Gonzalo, M. Han, D. Saurel, M. Casas-Cabanas and E. Martin.

Space group			**Cell parameters**		
$P6_3/mmc$			***a*** = ***b*** = 2.9455(2)Å		***c*** = 11.1738(4)Å
Atom	**Atomic position**			**B_{iso} (Å^2)**	**Occ.**
	x	**y**	**z**		
Na1	0	0	0.25	6.0(10)	0.31(5)
Na2	0.0667	0.333	0.25	6.0(10)	0.61(8)
Fe	0	0	0	0.83(6)	0.667
Mn	0	0	0	0.83(6)	0.333
O	0.333	0.667	0.881(3)	2.4(1)	1
Agreement factors			$\chi^2 = 3.25$	$R_b = 5.18$	$R_p = 24.2$

A.3.2 *In-situ* Le Bail refinement of pristine P2-$Na_{2/3}Fe_{2/3}Mn_{1/3}O_2$

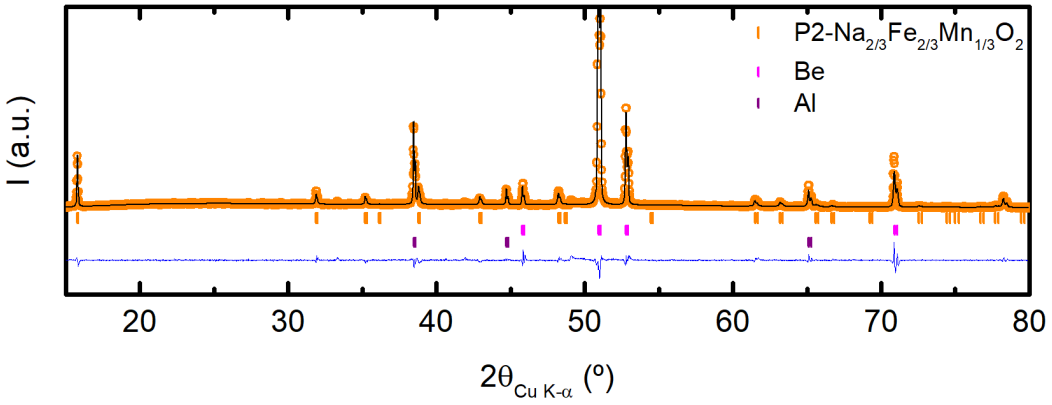

Figure A.3: Le Bail refinement of the initial pattern of P2-$Na_{2/3}Fe_{2/3}Mn_{1/3}O_2$ synthesized by E. Gonzalo and measured *in-situ* at CIC EnergiGUNE by E. Gonzalo, M. Han, M. Casas-Cabanas and E. Martin. Experimental data is presented with open circles and the refined pattern with a black line. The vertical lines correspond to the reflection angle positions of the active material (orange), Be window (pink) and Al foil (purple), and the blue line to the difference between the experimental and the calculated values.

Table A.3: Le Bail refinement parameters of the initial pattern of P2-$Na_{2/3}Fe_{2/3}Mn_{1/3}O_2$ inside the cell: space group, cell parameters, SYCOS (related to sample height) and agreement factors. Sample synthesized by E. Gonzalo. Measurement carried by E. Gonzalo, M. Han, M. Casas-Cabanas and E. Martin.

Space group	**Cell parameters**		**SYCOS**
$P6_3/mmc$	$\boldsymbol{a}$ = $\boldsymbol{b}$ = 2.9408(3) Å	$\boldsymbol{c}$ = 11.215(2) Å	-0.017(10)
Agreement factors	$\chi^2 = 5.78$	$R_b = 4.75$	$R_p = 19.2$

A.3.3 *Operando* Le Bail refinements of P2-$Na_{2/3}Fe_{2/3}Mn_{1/3}O_2$

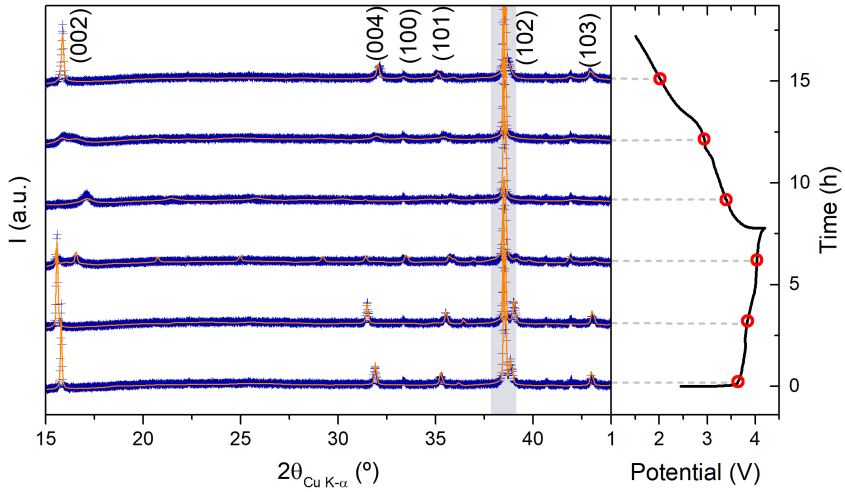

Figure A.4: Le Bail refinement examples of P2-$Na_{2/3}Fe_{2/3}Mn_{1/3}O_2$. Experimental data are presented with blue crosses and Le Bail refinements with an orange line. On top, the $(h\,k\,\ell)$ index according to the pristine structure. Reflection from the aluminum foil has been highlighted in gray.

A.4 Boltzmann statistics and Fe migration

According to previous studies [2, 3], the migration of the TM is expected to be thermally activated according to Boltzmann statistics. Within this scope, for the iron to migrate in significant amount to the Na interslab, the energy barrier E_B to overcome in the migration path should be small, smaller than the thermal energy ($E_B < k_BT$). The probability (P) for the iron ion to overcome an energy barrier E_B is given by the Boltzmann distribution:

$$P = \exp\left(-\frac{E_B}{k_BT}\right) \tag{A.1}$$

At best, having near zero activation energy E_B, (situation illustrated in Fig. A.5a), the concentration of the migrated iron would be 50%, which cannot explain by itself the migration of one Fe per each Na extracted beyond $x = 0.4$, as observed in Fig. 10.4. For such spontaneous migration to occur, in addition to a small activation energy for Fe diffusion, the migration should induce a reduction of energy in the system. The energy penalty E_P needs to be introduced, defined as the difference in the energy between having a Fe migrated in Na layers (Fe$_{tet}$) and that of its initial octahedral site in Fe layers (Fe_{oct}):

$$E_P = E_{tet} - E_{oct} \tag{A.2}$$

Assuming that the energy barrier E_B is small compared to thermal agitation, the percentage of the migrated Fe ($P_{Fe\ mig}$) is given by Boltzmann statistics:

$$P_{Fe\ mig} = \exp\left(-\frac{E_P}{k_BT}\right) \tag{A.3}$$

Two different cases can arise, besides the already described zero energy penalty case (see Fig. A.5):

Positive energy penalty ($\mathbf{E_P > 0}$): The initial octahedral site is energetically more stable than the tetrahedral one resulted from the migration (see Fig. A.5b), the amount of Fe migrated is small, thermally activated and proportional to:

$$P_{Fe\ mig} = \exp\left(-\frac{E_P + E_B^{'}}{k_BT}\right) \tag{A.4}$$

This situation cannot account for the migration observed here beyond $x = 0.4$ upon charge.

Negative energy penalty ($\mathbf{E_P < 0}$): The tetrahedral site resulted from the migration is energetically more stable than the initial octahedral site (see Fig. A.5c). In this case, when the energy barrier is smaller than the thermal energy ($E_B^{''} < k_BT$), the migration to the tetrahedral sites would actually be spontaneous. The back-migration on the other hand would be hindered, as the energy needed to overcome is $E_P + E_B^{''}$. Thus, unless $E_P \ll E_B^{''}$ (which would be the case similar to $E_P = 0$), the population of Fe$_{tet}$ will tend to be near 100%, that is, spontaneous migration of Fe towards Na interlayers.

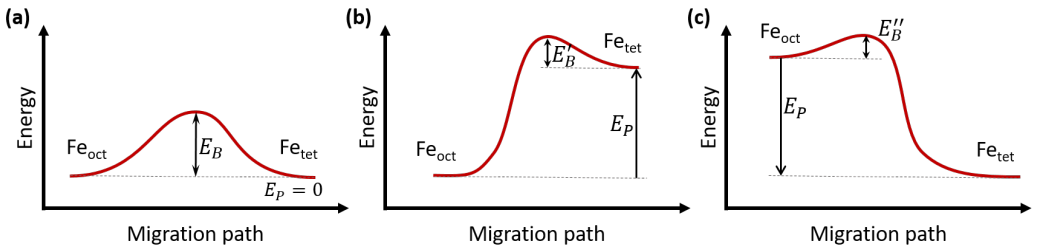

Figure A.5: Energy barrier (E_B) for Fe migration from the octahedral site in Fe layers (Fe$_{oct}$) to the tetrahedral site in Na layers (Fe$_{tet}$) in three different cases. **(a)** With a zero energy penalty ($E_P = 0$), **(b)** with a positive energy penalty ($E_P > 0$) and **(c)** with a negative energy penalty ($E_P < 0$).

In the case of described in this work, with $1:1$ Fe migration : Fe oxidation ratio, neither of the static situations described above is valid. Otherwise, we would find a cascade-like migration when $E_P < 0$ with a low-enough energy barrier to be thermally surpassed.

Bibliography

[1] E. Gonzalo, M. H. Han, J. M. López del Amo, B. Acebedo, M. Casas-Cabanas, and T. Rojo. *Journal of Materials Chemistry A*, 2(43):18523–18530, 2014.

[2] X. Li, Y. Wang, D. Wu, L. Liu, S.-H. Bo, and G. Ceder. *Chemistry of Materials*, 28(18):6575–6583, 2016.

[3] Y. Li, Y. Gao, X. Wang, X. Shen, Q. Kong, R. Yu, G. Lu, Z. Wang, and L. Chen. *Nano Energy*, 47:519–526, 2018.

B Numerical results

Contents

B.1 *Operando* XRD refinement results of $NaFeO_2$

Table B.1: Refinement results of *operando* XRD results of $NaFeO_2$. The 2D patterns are presented in Fig. 5.3 and these results are graphically presented in Fig. 5.6, charged to 4.0 V. The subindices LB and PV refer to Le Bail and pseudo-Voigt refinements respectively. The sodium content x refers to the composition Na_xFeO_2. Results of one every five patterns are presented.

x	$d_{O3\,PV}$ (Å)	$d_{O3\,LB}$ (Å)	$b_{O3\,LB}$ (Å)	$d_{P3\,PV}$ (Å)	I_{O3} (a.u.)	I_{P3} (a.u.)	Fe mig. (%)
0.993	5.369	5.370	3.024	-	1	0	0.0
0.930	5.379	5.380	3.019	-	1.10	0	-0.4
0.868	5.405	5.409	3.005	-	1.22	0	0.6
0.805	5.435	5.440	2.992	-	1.44	0	-0.6
0.742	5.460	5.465	2.981	-	1.48	0	0.4
0.679	5.474	5.472	2.971	5.488	1.52	0.01	0.7
0.616	5.471	5.469	2.959	5.488	1.23	0.20	1.9
0.553	5.447	5.458	2.949	5.488	1.04	0.36	4.5
0.491	5.398	5.415	2.943	5.488	0.89	0.26	7.3
0.428	5.333	5.361	2.942	5.488	0.56	0.28	12.7
0.365	5.275	5.317	2.942	5.488	0.36	0.18	22.4
0.302	5.228	5.243	2.948	-	0.45	0	23.7
0.246	5.200	5.219	2.950	-	0.41	0	29.4
0.231	5.176	5.199	2.952	-	0.36	0	28.1

Table B.2: Refinement results of *operando* XRD results of $NaFeO_2$. The 2D patterns are presented in Fig. 5.7 and these results are graphically presented in Fig. 5.8, cycled with the upper potential limits of 3.6 V and 3.8 V. Results from pseudo-Voigt refinements are presented. The sodium content x refers to the composition Na_xFeO_2. Results of one every five patterns are presented.

Time (h)	**x**	$\mathbf{d_{O3}}$ (Å)	$\mathbf{d_{P3}}$ (Å)	$\mathbf{I_{O3}}$ (a.u.)	$\mathbf{I_{P3}}$ (a.u.)	**Fe mig.** (%)
0	1	5.390	-	1	0	0
2.8	0.914	5.406	-	1.15	0	0.0
5.6	0.822	5.441	-	1.29	0	-0.1
8.4	0.728	5.475	-	1.51	0	0.0
11.2	0.636	5.508	-	1.80	0	0.5
14.0	0.542	5.490	5.597	1.33	0.31	1.7
16.8	0.495	5.417	5.588	1.20	0.59	3.7
19.6	0.589	5.435	5.536	1.26	0.37	2.9
22.4	0.681	5.436	-	1.24	0	3.2
25.2	0.775	5.405	-	1.03	0	2.7
28.0	0.868	5.384	-	0.90	0	2.7
30.8	0.962	5.383	-	0.85	0	1.2
33.6	0.995	5.383	-	0.91	0	1.5
36.4	1.016	5.383	-	0.91	0	1.6
39.2	1.037	5.382	-	0.84	0	1.7
42.0	1.059	5.382	-	0.91	0	1.0
44.8	1.017	5.382	-	0.90	0	1.6
47.6	0.923	5.391	-	1.06	0	2.7
50.4	0.829	5.415	-	0.96	0	2.5
53.2	0.737	5.447	-	1.19	0	2.4
56.0	0.643	5.443	5.487	0.85	0.59	2.5
58.8	0.551	5.431	5.571	1.13	0.17	4.2
61.6	0.457	5.349	5.576	1.31	0.32	9.8
64.4	0.362	5.173	5.559	2.57	0.19	18.6
67.2	0.386	5.210	-	0.25	0	18.4

B.2 *Operando* XRD refinement results of O3-$Na_{2/3}Fe_{2/3}Mn_{1/3}O_2$

Table B.3: Refinement results of *operando* XRD results of O3-$Na_{2/3}Fe_{2/3}Mn_{1/3}O_2$. The 2D patterns are presented in Fig. 6.2 and these results are graphically presented in Figs. 6.6 and 6.8. Results from Le Bail refinements of one every five patterns are presented.

Time (h)	$\mathbf{d_{O3}}$ (Å)	$\mathbf{b_{O3}}$ (Å)	**MD** (%)	$\mathbf{d_{P3}}$ (Å)	$\mathbf{b_{P3}}$ (Å)	$\mathbf{I_{O3}}$ (a.u.)	$\mathbf{I_{P3}}$ (a.u.)	**Fe mig.** (%)
0	5.477	2.969	0	-	-	1	0	0
2.7	5.518	2.955	0	-	-	1.12	0	-0.7
5.2	5.549	2.945	0	5.631	2.945	1.09	0.11	-1.1
7.7	5.562	2.938	0	5.630	2.936	0.99	0.27	-1.1
10.2	5.577	2.929	0	5.637	2.927	0.84	0.45	-0.3
12.7	5.580	2.922	0	5.650	2.921	0.89	0.46	-0.9
15.1	5.551	2.914	0	5.656	2.912	0.78	0.55	1.6
17.6	5.492	2.902	0	5.666	2.908	0.74	0.51	5.1
20.1	5.394	2.897	-0.362	5.662	2.913	0.61	0.50	10.0
22.6	5.307	2.894	1.410	5.662	2.911	0.65	0.29	15.7
25.1	5.247	2.899	7.822	-	-	0.64	0	22.7
27.6	5.206	2.921	8.315	-	-	0.57	0	25.4
30.1	5.243	2.940	11.522	-	-	0.59	0	23.2
32.6	5.282	2.949	12.740	-	-	0.61	0	21.0
35.1	5.333	2.960	13.833	-	-	0.65	0	18.1
37.6	5.382	2.971	14.830	-	-	0.63	0	14.7
40.1	5.445	2.979	16.230	-	-	0.63	0	10.9
42.6	5.437	2.977	15.604	-	-	0.87	0	9.7
45.0	5.424	2.979	14.936	-	-	0.77	0	9.0
47.5	5.388	2.995	13.362	-	-	0.57	0	9.2
50.0	5.372	3.006	12.748	-	-	0.56	0	9.4

B.3 Refinement results of operando Mössbauer experiment of $NaFeO_2$

Table B.4: Results of the *operando* Mössbauer spectra fits shown in 5.14 for $NaFeO_2$. The units for central shift (CS), quadrupole splitting (QS) and FWHM are millimeters per second ($mm\,s^{-1}$). The name refers to the label shown in the panels of Fig. 5.14, and Int. to the intensity percentage of each of the signals.

Name	Signal 1 (Fe^{3+} oct. A)				Signal 2 (Fe^{3+} oct. B)			
	CS	QS	FWHM	Int.	CS	QS	FWHM	Int.
b	0.369(2)	0.476(3)	0.256(5)	98(2)	-	-	-	-
c	0.328(18)	0.69(8)	0.26(8)	24(16)	0.355(13)	0.92(8)	0.27(7)	31(15)
d	-	-	-	-	0.330(10)	0.91(2)	0.32(3)	46(4)
e	-	-	-	-	0.368(11)	0.85(2)	0.32(4)	44(11)
f	0.352(11)	0.64(4)	0.21(6)	10(7)	0.338(5)	0.96(3)	0.33(2)	42(6)
g	0.366(14)	0.48(4)	0.19(12)	17(16)	0.37(4)	0.8(2)	0.40(7)	46(22)
h	0.383(8)	0.51(5)	0.31(3)	59(19)	0.316(14)	1.1(1)	0.38(8)	21(11)
i	0.358(3)	0.495(12)	0.27(3)	52(6)	0.337(8)	.90(5)	0.41(4)	41(6)

Name	Signal 3 (Fe^{4+} oct.)				Signal 4 (Fe^{3+} tet.)			
	CS	QS	FWHM	Int.	CS	QS	FWHM	Int.
b	0.03(6)	0.34(11)	0.2(2)	2(2)	-	-	-	-
c	-0.01(2)	0.59(3)	0.39(5)	45(13)	-	-	-	-
d	-0.04(2)	0.65(1)	0.28(3)	37(4)	0.22(3)	0.48(4)	0.30(7)	17(4)
e	-0.03(3)	0.65(3)	0.34(5)	39(11)	0.16(4)	0.71(4)	0.3(2)	17(15)
f	-0.027(7)	0.658(6)	0.32(2)	38(5)	0.22(2)	0.58(4)	0.23(7)	10(5)
g	0.09(6)	0.4(3)	0.4(4)	17(19)	0.12(5)	0.87(13)	0.32(2)	20(14)
h	-0.2(3)	0.4(6)	0.4(2)	10(5)	0.25(7)	0.62(7)	0.25(16)	10(23)
i	-0.06(3)	0.57(4)	0.24(6)	7(2)	-	-	-	-

B.4 Refinement results of operando Mössbauer experiment of O3-$Na_{2/3}Fe_{2/3}Mn_{1/3}O_2$

Table B.5: Results of the *operando* Mössbauer spectra fits shown in 6.9 for O3-$Na_{2/3}Fe_{2/3}Mn_{1/3}O_2$. The units for central shift (CS), quadrupole splitting (QS) and FWHM are millimeters per second (mm s^{-1}). The name refers to the label shown in the panels of Fig. 6.9, and Int. to the intensity percentage of each of the signals. The spectrum labeled as *4.2 V* corresponds to the second cell, shown with a light blue line in Fig. 6.9a.

Name	Signal 1 (Fe^{3+})				Signal 2 (Fe^{4+})			
	CS	QS	FWHM	Int.	CS	QS	FWHM	Int.
b	0.371(7)	0.648(11)	0.30(3)	88(7)	0.16(5)	0.47(8)	0.28(15)	12(7)
c	0.357(6)	0.674(12)	0.32(2)	90(5)	0.08(7)	0.28(15)	0.3(2)	10(5)
d	0.355(15)	0.74(3)	0.32(5)	57(9)	0.14(4)	0.49(6)	0.45(12)	43(9)
e	0.34(3)	0.72(4)	0.36(7)	76(18)	0.17(7)	0.28(15)	0.4(4)	24(18)
f	0.359(10)	0.70(2)	0.42(4)	94(4)	0.04(6)	0.26(11)	0.19(15)	6(4)
g	0.369(6)	0.74(2)	0.40(2)	92(3)	0.03(4)	0.34(8)	0.26(11)	8(3)
4.2 V	0.44(3)	0.79(4)	0.36(8)	33(8)	0.14(3)	0.61(3)	0.53(8)	67(8)

B.5 Impedance spectra refinements of $NaFeO_2$

Table B.6: Numerical results of the Nyquist spectra refinement of $NaFeO_2$ during the 1st charge. For the sake of simplicity, $Z_{W\,SILD}$ has only been refined when a 45° slope was clear in the spectra and it has been set to zero otherwise. The # symbol represents the spectrum number. The results of only one every five patterns are shown, plus the first and the last.

#	$\mathbf{R}_d$ (Ω)	τ (s)	$\mathbf{C}_1$ (F s^{a-1})	$\mathbf{a}_1$	$\mathbf{C}_2$ (F s^{a-1})	$\mathbf{a}_2$	$\mathbf{R}_1$ (Ωg)	$\mathbf{R}_2$(Ωg)	$\mathbf{A}_{W\,SILD}$
1	329.9	0.5578	4.40E-5	0.6256	0.00148	0.9573	1.7	-	-
5	341.7	0.5388	3.81E-5	0.6447	0.00147	0.9537	1.7	-	-
10	333.4	0.5624	4.92E-5	0.6103	0.00147	0.9526	1.8	-	-
15	343.4	0.5599	4.61E-5	0.6186	0.00149	0.9501	1.8	8595.5	-
20	338.7	0.5534	4.55E-5	0.6208	0.00154	0.9399	1.8	1880.5	-
25	292.1	0.4855	4.47E-5	0.6238	0.00157	0.8941	1.7	296.2	-
30	71.0	0.0089	1.54E-5	0.7604	0.00087	0.6502	1.1	5.9	-
33	55.4	0.0083	1.90E-5	0.753	0.00121	0.6169	1.0	6.5	73.5

Table B.7: Numerical results of the Nyquist spectra refinement of $NaFeO_2$ during the 1st discharge. For the sake of simplicity, $Z_{W\,SILD}$ has only been refined when a 45° slope was clear in the spectra and it has been set to zero otherwise. The # symbol represents the spectrum number. The results of only one every five patterns are shown, plus the first and the last.

#	$\mathbf{R}_d$ (Ω)	τ (s)	$\mathbf{C}_1$ (F s^{a-1})	$\mathbf{a}_1$	$\mathbf{C}_2$ (F s^{a-1})	$\mathbf{a}_2$	$\mathbf{R}_1$ (Ωg)	$\mathbf{R}_2$(Ωg)	$\mathbf{A}_{W\,SILD}$
1	52.9	0.0074	1.91E-5	0.7551	0.00131	0.5945	1.0	7.5	78.3
5	40.7	0.0806	3.06E-5	0.6985	0.00129	0.7240	1.3	5.7	72.2
10	101.6	0.2280	3.74E-5	0.6741	0.00156	0.8091	1.4	34.1	-
15	121.1	0.2586	3.79E-5	0.6724	0.00152	0.8532	1.5	101.2	-
20	116.9	0.2501	3.92E-5	0.6689	0.00147	0.8714	1.4	160.7	-
25	148.5	0.2583	3.19E-5	0.6959	0.00144	0.8956	1.4	222.0	-
30	146.9	0.3104	4.10E-5	0.6636	0.00145	0.9116	1.5	346.2	-
35	162.9	0.3610	4.17E-5	0.6621	0.00150	0.9273	1.5	392.8	-
37	162.2	0.3645	4.15E-5	0.6630	0.00152	0.9165	1.5	425.7	-

Table B.8: Numerical results of the Nyquist spectra refinement of $NaFeO_2$ during the 2nd charge. For the sake of simplicity, $Z_{W\,SILD}$ has only been refined when a 45° slope was clear in the spectra and it has been set to zero otherwise. The # symbol represents the spectrum number. The results of only one every five patterns are shown, plus the first and the last.

#	$\mathbf{R}_d$ (Ω)	τ (s)	$\mathbf{C}_1$ (F s^{a-1})	$\mathbf{a}_1$	$\mathbf{C}_2$ (F s^{a-1})	$\mathbf{a}_2$	$\mathbf{R}_1$ (Ωg)	$\mathbf{R}_2$(Ωg)	$\mathbf{A}_{W\,SILD}$
1	163.4	0.3781	4.36E-5	0.6563	0.00153	0.9270	1.5	424.0	-
5	174.6	0.3628	3.77E-5	0.6753	0.00150	0.9393	1.5	1080.0	-
10	162.3	0.3698	4.32E-5	0.6572	0.00148	0.9355	1.5	982.0	-
15	152.6	0.3154	3.70E-5	0.6776	0.00148	0.9214	1.4	531.5	-
20	128.3	0.2426	3.51E-5	0.6842	0.00146	0.8807	1.5	307.3	-

#	$\mathbf{R}_d$ (Ω)	τ (s)	$\mathbf{C}_1$ (F s^{a-1})	$\mathbf{a}_1$	$\mathbf{C}_2$ (F s^{a-1})	$\mathbf{a}_2$	$\mathbf{R}_1$ (Ωg)	$\mathbf{R}_2$(Ωg)	$\mathbf{A}_{W\,SILD}$
25	129.6	0.2708	3.58E-5	0.6817	0.00155	0.8612	1.5	109.2	-
30	86.32	0.1867	3.40E-5	0.6885	0.00154	0.7814	1.5	22.1	-
35	55.05	0.0095	2.42E-5	0.7294	0.00124	0.6908	1.1	5.0	41.1
40	43.03	0.1670	3.83E-5	0.6773	0.00166	0.7220	1.4	7.7	94.7
45	100.2	0.2998	3.89E-5	0.6745	0.00207	0.7795	1.3	56.4	-
50	123.6	0.3255	3.48E-5	0.6886	0.00217	0.7571	1.3	97.6	-
53	139.9	0.3954	3.85E-5	0.6743	0.00229	0.7526	1.3	126.3	-

Table B.9: Numerical results of the Nyquist spectra refinement of $NaFeO_2$ during the 2nd discharge. For the sake of simplicity, $Z_{W\,SILD}$ has been set to zero since a 45° slope is not visible in these spectra. The # symbol represents the spectrum number. The results of only one every five patterns are shown, plus the first and the last.

#	$\mathbf{R}_d$ (Ω)	τ (s)	$\mathbf{C}_1$ (F s^{a-1})	$\mathbf{a}_1$	$\mathbf{C}_2$ (F s^{a-1})	$\mathbf{a}_2$	$\mathbf{R}_1$ (Ωg)	$\mathbf{R}_2$(Ωg)	$\mathbf{A}_{W\,SILD}$
1	139.5	0.4207	4.19E-5	0.6628	0.00235	0.7512	1.4	137.0	-
5	149.0	0.4062	3.88E-5	0.6710	0.00225	0.7754	1.4	225.0	-
10	136.7	0.3764	4.00E-5	0.6657	0.00210	0.7844	1.3	228.0	-
15	128.6	0.3391	3.98E-5	0.6654	0.00196	0.7993	1.3	216.7	-
20	121.2	0.3061	4.08E-5	0.6611	0.00179	0.8136	1.3	253.6	-
25	128.0	0.3024	4.02E-5	0.6624	0.00170	0.8435	1.3	253.7	-
30	141.4	0.3223	4.31E-5	0.6524	0.00161	0.8683	1.3	259.7	-
35	148.6	0.3209	4.23E-5	0.6544	0.00155	0.8864	1.3	249.0	-
40	154.4	0.3223	4.38E-5	0.6497	0.00151	0.8961	1.3	246.2	-
45	166.7	0.3373	4.34E-5	0.6506	0.00150	0.9054	1.4	230.0	-
50	173.1	0.3296	3.99E-5	0.6606	0.00152	0.9113	1.3	238.6	-
55	179.8	0.3412	4.15E-5	0.6553	0.00154	0.9089	1. 3	234.8	-
60	184.9	0.3294	3.90E-5	0.6621	0.00157	0.8977	1.3	185.7	-
65	183.8	0.3241	3.97E-5	0.6591	0.00162	0.8816	1.3	194.4	-
70	194.9	0.3311	3.69E-5	0.6681	0.00166	0.8648	1.4	179.6	-
75	206.6	0.3654	3.70E-5	0.6668	0.00168	0.8382	1.5	154.7	-
80	170.8	0.3451	3.64E-5	0.6682	0.00171	0.7867	1.5	133.4	-
85	142.6	0.3794	3.81E-5	0.6615	0.00173	0.6988	1.6	153.4	-
90	129.7	0.4492	3.65E-5	0.6675	0.00192	0.6153	1.6	781.8	-
95	135.1	0.5464	4.00E-5	0.6538	0.00202	0.6011	1.7	506.0	-
100	111.9	0.6218	4.42E-5	0.6388	0.00193	0.5810	1.7	499.9	-
103	101.5	0.6787	4.57E-5	0.6341	0.00184	0.5714	1.7	383.8	-

Table B.10: Numerical results of the Nyquist spectra refinement of $NaFeO_2$ during the 3rd charge. For the sake of simplicity, $Z_{W\,SILD}$ has been set to zero since a 45° slope is not visible in these spectra. The # symbol represents the spectrum number. The results of only one every five patterns are shown, plus the first and the last.

#	$\mathbf{R}_d$ (Ω)	τ (s)	$\mathbf{C}_1$ (F s^{a-1})	$\mathbf{a}_1$	$\mathbf{C}_2$ (F s^{a-1})	$\mathbf{a}_2$	$\mathbf{R}_1$ (Ωg)	$\mathbf{R}_2$(Ωg)	$\mathbf{A}_{W\,SILD}$
1	95.8	0.6826	4.51E-5	0.6355	0.00177	0.5647	2.0	461.0	-
5	79.1	0.7543	4.50E-5	0.6374	0.00162	0.5352	1.9	353.0	-
10	74.3	0.6500	3.88E-5	0.6586	0.00174	0.5187	1.6	69.1	-
15	87.3	1.1930	4.59E-5	0.6379	0.00180	0.4956	1.7	150.4	-
20	75.0	1.1100	4.26E-5	0.6487	0.00174	0.4860	1.7	197.1	-
25	86.5	1.0080	4.88E-5	0.6275	0.00175	0.5285	1.8	87.1	-
30	56.7	0.5558	4.26E-5	0.6440	0.00155	0.5625	1.8	63.3	-
35	78.6	0.4115	4.58E-5	0.6304	0.00142	0.6466	2.1	79.2	-
40	85.0	0.3914	5.20E-5	0.6127	0.00143	0.7162	2.0	112.9	-
45	133.6	0.4209	5.01E-5	0.6160	0.00144	0.7889	2.0	147.2	-
50	138.5	0.4239	5.50E-5	0.6078	0.00141	0.8151	2.1	268.3	-
55	155.2	0.4847	5.56E-5	0.6014	0.00142	0.8458	2.1	206.4	-
60	162.5	0.4594	5.12E-5	0.6118	0.00141	0.8564	2.1	281.4	-
65	123.1	0.4191	5.63E-5	0.5990	0.00138	0.8332	2.2	156.4	-
70	109.5	0.3962	5.13E-5	0.6111	0.00140	0.8049	2.1	73.8	-
75	94.7	0.2388	3.73E-5	0.6528	0.00142	0.7585	1.9	52.9	-
80	73.3	0.4224	5.03E-5	0.6141	0.00158	0.7661	1.8	49.1	-
85	86.6	0.3327	3.57E-5	0.6588	0.00171	0.7689	1.3	62.1	-
90	92.8	0.3369	3.36E-5	0.6681	0.00187	0.7707	1.1	75.2	-
95	98.0	0.4064	4.11E-5	0.6455	0.00201	0.7705	1.0	86.0	-
100	95.2	0.4063	3.91E-5	0.6573	0.00212	0.7511	1.0	115.9	-
105	144.7	0.5623	5.04E-7	0.6362	0.00216	0.7391	1.7	178.7	-
110	204.6	0.6942	5.72E-5	0.6092	0.00244	0.8077	1.7	220.6	-
115	243.5	1.0040	6.81E-5	0.5467	0.00254	0.8430	1.9	200.4	-
119	258.1	1.1670	7.01E-5	0.5416	0.00280	0.8667	1.9	211.7	-

Table B.11: Numerical results of the Nyquist spectra refinement of $NaFeO_2$ during the 3rd discharge. For the sake of simplicity, $Z_{W\,SILD}$ has been set to zero since a 45° slope is not visible in these spectra. The # symbol represents the spectrum number. The results of only one every five patterns are shown, plus the first and the last.

#	$\mathbf{R}_d$ (Ω)	τ (s)	$\mathbf{C}_1$ (F s^{a-1})	$\mathbf{a}_1$	$\mathbf{C}_2$ (F s^{a-1})	$\mathbf{a}_2$	$\mathbf{R}_1$ (Ωg)	$\mathbf{R}_2$(Ωg)	$\mathbf{A}_{W\,SILD}$
1	231.4	1.0490	6.66E-5	0.5483	0.00281	0.8600	1.8	235.0	-
10	258.6	1.1700	6.65E-5	0.5438	0.00256	0.8610	1.9	1210.0	-
20	223.9	1.1000	6.35E-5	0.5467	0.00224	0.8318	1.9	969.1	-
30	167.3	0.8540	6.06E-5	0.5502	0.00184	0.8193	1.9	787.1	-
40	155.9	0.6832	5.99E-5	0.5501	0.00164	0.8478	2.0	681.6	-
50	165.8	0.6767	6.04E-5	0.5494	0.00161	0.8769	2.0	504.5	-
60	175.3	0.5897	4.84E-5	0.5752	0.00165	0.8708	1.8	285.8	-
70	163.2	0.6540	5.62E-5	0.5541	0.00167	0.8336	2.1	170.2	-
80	131.5	0.5966	4.96E-5	0.5573	0.00159	0.7294	2.2	239.4	-
90	253.2	0.9834	3.47E-5	0.5805	0.00196	0.6616	2.2	834.7	-

#	$\mathbf{R}_d$ (Ω)	τ (s)	$\mathbf{C}_1$ (F s^{a-1})	$\mathbf{a}_1$	$\mathbf{C}_2$ (F s^{a-1})	$\mathbf{a}_2$	$\mathbf{R}_1$ (Ωg)	$\mathbf{R}_2$(Ωg)	$\mathbf{A}_{W\,SILD}$
100	203.8	1.2010	3.10E-5	0.5901	0.00196	0.6020	2.3	-	-
102	169.8	1.1240	2.98E-5	0.5945	0.00187	0.5851	2.2	-	-

B.6 Impedance spectra refinements of O3-$Na_{2/3}Fe_{2/3}Mn_{1/3}O_2$

Table B.12: Numerical results of the Nyquist spectra refinement of O3-$Na_{2/3}Fe_{2/3}Mn_{1/3}O_2$ during the 1st charge. The # symbol represents the spectrum number. The results of only one every five patterns are shown, plus the first and the last.

#	$\mathbf{R}_d$ (Ω)	τ (s)	$\mathbf{C}_1$ (F s^{a-1})	$\mathbf{a}_1$	$\mathbf{C}_2$ (F s^{a-1})	$\mathbf{a}_2$	$\mathbf{R}_0$ (Ωg)	$\mathbf{R}_1$ (Ωg)	$\mathbf{R}_2$(Ωg)	$\mathbf{A}_{W\,SILD}$
1	-	-	1.88E-5	0.8615	9.91E-4	0.9432	0.008	0.17	30.8	-
5	-	-	1.56E-5	0.8865	0.00094	0.9662	0.011	0.17	83.2	-
10	-	-	1.75E-5	0.8690	0.00091	0.9602	0.009	0.19	265.8	-
15	-	-	1.62E-5	0.8790	0.00093	0.9583	0.010	0.19	196.5	-
20	-	-	1.62E-5	0.8784	0.00106	0.9108	0.010	0.19	28.1	-
25	-	-	1.89E-5	0.8495	0.00146	0.8864	0.008	0.19	1.0	37.4
30	-	-	2.67E-5	0.8207	0.00111	0.8902	0.010	0.17	0.1	-
33	-	-	3.31E-5	0.7908	0.00092	0.8823	0.010	0.16	0.1	-

Table B.13: Numerical results of the Nyquist spectra refinement of O3-$Na_{2/3}Fe_{2/3}Mn_{1/3}O_2$ during the 1st discharge. The # symbol represents the spectrum number. The results of only one every five patterns are shown, plus the first and the last.

#	$\mathbf{R}_d$ (Ω)	τ (s)	$\mathbf{C}_1$ (F s^{a-1})	$\mathbf{a}_1$	$\mathbf{C}_2$ (F s^{a-1})	$\mathbf{a}_2$	$\mathbf{R}_0$ (Ωg)	$\mathbf{R}_1$ (Ωg)	$\mathbf{R}_2$(Ωg)	$\mathbf{A}_{W\,SILD}$
1	-	-	3.51E-5	0.7820	0.00097	0.8597	0.009	0.16	0.1	-
5	-	-	2.63E-5	0.8028	0.00107	0.9319	0.009	0.20	0.1	-
10	-	-	2.92E-2	0.7943	0.00138	0.8475	0.010	0.24	1.4	-
15	-	-	3.51E-5	0.7730	0.00107	0.9381	0.010	0.28	28.2	512.6
20	-	-	3.81E-5	0.7618	0.00094	0.9666	0.009	0.30	260.3	-
25	-	-	4.18E-5	0.7494	0.00091	0.9591	0.007	0.31	333.7	-
30	-	-	4.19E-5	0.7487	0.00090	0.9144	0.007	0.32	90.8	-
35	-	-	4.66E-5	0.7331	0.00101	0.9310	0.006	0.34	18.1	235.2
37	-	-	4.38E-5	0.7419	0.00104	0.9449	0.007	0.33	11.2	157.8

Table B.14: Numerical results of the Nyquist spectra refinement of O3-$Na_{2/3}Fe_{2/3}Mn_{1/3}O_2$ during the 2nd charge. The # symbol represents the spectrum number. The results of only one every five patterns are shown, plus the first and the last.

#	$\mathbf{R}_d$ (Ω)	τ (s)	$\mathbf{C}_1$ (F s^{a-1})	$\mathbf{a}_1$	$\mathbf{C}_2$ (F s^{a-1})	$\mathbf{a}_2$	$\mathbf{R}_0$ (Ωg)	$\mathbf{R}_1$ (Ωg)	$\mathbf{R}_2$(Ωg)	$\mathbf{A}_{W\,SILD}$
1	-	-	4.61E-5	0.7340	0.00105	0.9508	0.006	0.34	9.2	131.8
5	-	-	4.76E-5	0.7275	0.00099	0.9646	0.005	0.36	24.1	-
10	-	-	4.84E-5	0.7253	0.00094	0.9779	0.005	0.36	99.8	-
15	-	-	5.07E-5	0.7163	0.00090	0.9624	0.003	0.37	432.6	-
20	-	-	5.00E-5	0.7205	0.00093	0.9603	0.006	0.37	327.3	-
25	-	-	4.58E-5	0.7320	0.00107	0.9466	0.007	0.36	22.1	-

#	$\mathbf{R}_d$ (Ω)	τ (s)	$\mathbf{C}_1$ (F s^{a-1})	$\mathbf{a}_1$	$\mathbf{C}_2$ (F s^{a-1})	$\mathbf{a}_2$	$\mathbf{R}_0$ (Ωg)	$\mathbf{R}_1$ (Ωg)	$\mathbf{R}_2$(Ωg)	$\mathbf{A}_{W\,SILD}$
30	-	-	3.02E-5	0.7813	0.00135	0.8159	0.012	0.27	1.4	-
35	-	-	4.87E-5	0.7212	0.00109	0.9033	0.007	0.22	0.2	-
40	-	-	4.33E-5	0.7356	0.00095	0.8670	0.008	0.21	0.1	-
45	-	-	5.10E-5	0.7165	0.00082	0.8683	0.007	0.23	0.1	-
50	-	-	4.92E-5	0.7340	-	-	0.013	0.25	-	-
53	-	-	6.44E-5	0.6993	0.00158	0.8043	0.009	0.28	0.2	-

Table B.15: Numerical results of the Nyquist spectra refinement of O3-$Na_{2/3}Fe_{2/3}Mn_{1/3}O_2$ during the 2nd discharge. The # symbol represents the spectrum number. The results of only one every five patterns are shown, plus the first and the last.

#	$\mathbf{R}_d$ (Ω)	τ (s)	$\mathbf{C}_1$ (F s^{a-1})	$\mathbf{a}_1$	$\mathbf{C}_2$ (F s^{a-1})	$\mathbf{a}_2$	$\mathbf{R}_0$ (Ωg)	$\mathbf{R}_1$ (Ωg)	$\mathbf{R}_2$(Ωg)	$\mathbf{A}_{W\,SILD}$
1	-	-	6.39E-5	0.7000	0.00226	0.6905	0.010	0.28	0.3	-
5	-	-	4.33E-5	0.7435	0.00175	0.9205	0.013	0.26	0.2	-
10	10.81	0.07023	3.12E-5	0.7898	0.00147	0.9000	0.021	0.27	0.4	-
15	26.76	0.08235	3.47E-5	0.7634	0.00129	0.9432	0.017	0.31	0.6	-
20	29.87	0.08229	3.48E-5	0.7588	0.00124	0.9208	0.016	0.32	1.2	-
25	34.65	0.07986	3.34E-5	0.7637	0.00118	0.9195	0.018	0.33	3.3	67.7
30	45.28	0.08717	3.55E-5	0.7524	0.00109	0.9575	0.017	0.35	15.4	262.5
35	51.05	0.09135	3.87E-5	0.7367	0.00102	0.9786	0.014	0.37	59.1	-
40	46.66	0.08277	4.10E-5	0.7282	0.00101	0.9736	0.013	0.37	75.3	-
45	48.16	0.08308	4.18E-5	0.7253	0.00103	0.9681	0.013	0.38	39.1	-
50	51.88	0.09199	4.36E-5	0.7178	0.00106	0.9714	0.012	0.39	15.6	210.6
55	55.66	0.09945	4.48E-5	0.7110	0.00107	0.9725	0.012	0.41	9.2	-
60	56.78	0.09309	3.91E-5	0.7200	0.00106	0.9744	0.013	0.40	9.0	-
65	58.19	0.08385	3.69E-5	0.7142	0.00104	0.9610	0.012	0.42	27.6	-
70	63.95	0.09881	3.70E-5	0.7083	0.00106	0.9710	0.012	0.44	49.2	-
75	55.05	0.08248	3.44E-5	0.7135	0.00110	0.9469	0.011	0.44	75.4	-
80	52.29	0.08039	3.22E-5	0.7218	0.00114	0.9377	0.015	0.45	87.9	-
85	51.95	0.08732	3.01E-5	0.7296	0.00120	0.9396	0.016	0.44	81.6	-
90	41.74	0.07730	2.88E-5	0.7328	0.00129	0.9227	0.013	0.43	92.6	-
95	41.95	0.08454	2.74E-5	0.7406	0.00138	0.9141	0.017	0.43	105.4	-
100	41.89	0.08982	2.72E-5	0.7393	0.00145	0.9161	0.016	0.43	103.7	-
103	38.65	0.08212	2.55E-5	0.7489	0.00147	0.9085	0.020	0.42	115.6	-

Table B.16: Numerical results of the Nyquist spectra refinement of O3-$Na_{2/3}Fe_{2/3}Mn_{1/3}O_2$ during the 3rd charge. The # symbol represents the spectrum number. The results of only one every five patterns are shown, plus the first and the last.

#	$\mathbf{R}_d$ (Ω)	τ (s)	$\mathbf{C}_1$ (F s^{a-1})	$\mathbf{a}_1$	$\mathbf{C}_2$ (F s^{a-1})	$\mathbf{a}_2$	$\mathbf{R}_0$ (Ωg)	$\mathbf{R}_1$ (Ωg)	$\mathbf{R}_2$(Ωg)	$\mathbf{A}_{W\,SILD}$
1	41.7	0.09797	2.72E-5	0.7337	0.00148	0.9215	0.011	0.44	88.4	-
5	37.61	0.07779	2.43E-5	0.7548	0.00141	0.9097	0.021	0.42	203.3	-
10	34.32	0.07409	2.38E-5	0.7582	0.00140	0.9040	0.023	0.41	191.4	-
15	29.03	0.06219	2.35E-5	0.7589	0.00137	0.8885	0.023	0.41	181.8	-

#	$\mathbf{R}_d$ (Ω)	τ (s)	$\mathbf{C}_1$ (F s^{a-1})	$\mathbf{a}_1$	$\mathbf{C}_2$ (F s^{a-1})	$\mathbf{a}_2$	$\mathbf{R}_0$ (Ωg)	$\mathbf{R}_1$ (Ωg)	$\mathbf{R}_2$(Ωg)	$\mathbf{A}_{W\,SILD}$
20	16.92	0.06355	3.41E-5	0.7020	0.00134	0.8783	0.008	0.44	145.4	-
25	-	-	3.50E-5	0.7040	0.00124	0.8633	0.011	0.46	112.6	-
30	-	-	3.46E-5	0.7047	0.00118	0.8820	0.012	0.46	84.1	-
35	-	-	3.44E-5	0.7060	0.00114	0.9014	0.012	0.45	64.8	-
40	-	-	3.61E-5	0.6990	0.00111	0.9151	0.010	0.45	48.2	-
45	-	-	2.59E-5	0.7390	0.00098	0.9804	0.016	0.39	26.6	-
50	-	-	2.02E-5	0.7835	9.38E-4	0.9637	0.023	0.29	30.6	-
55	-	-	2.52E-5	0.7541	0.00101	0.9595	0.018	0.25	36.1	-
60	-	-	3.10E-5	0.7314	0.00101	0.9642	0.015	0.24	59.2	-
65	-	-	2.11E-5	0.7862	0.00097	0.9523	0.022	0.20	110.5	-
70	-	-	2.86E-5	0.7457	0.00096	0.9530	0.017	0.20	124.3	-
75	-	-	1.68E-5	0.8223	0.00102	0.9598	0.026	0.18	52.7	-
80	-	-	3.17E-5	0.7501	0.00109	0.9873	0.020	0.19	10.3	-
85	-	-	4.13E-5	0.7329	0.00126	1.0000	0.021	0.17	2.6	-
90	-	-	6.16E-5	0.7131	0.00166	1.0000	0.025	0.19	1.1	-
95	-	-	8.87E-5	0.6945	0.00203	0.9590	0.027	0.23	0.5	-
100	9.984	0.1071	1.12E-4	0.6850	0.00240	1.0000	0.032	0.29	0.3	-
105	-	-	1.99E-4	0.6050	0.00256	0.8730	0.021	0.32	3.9	-
110	-	-	1.81E-4	0.6220	0.00237	0.9103	0.023	0.29	25.3	-
115	-	-	1.71E-4	0.6290	0.00207	0.9199	0.023	0.26	98.4	-
119	-	-	1.55E-4	0.6360	0.00193	0.9146	0.021	0.22	126.2	-

Table B.17: Numerical results of the Nyquist spectra refinement of O3-$Na_{2/3}Fe_{2/3}Mn_{1/3}O_2$ during the 3rd discharge. The # symbol represents the spectrum number. The results of only one every five patterns are shown, plus the first and the last.

#	$\mathbf{R}_d$ (Ω)	τ (s)	$\mathbf{C}_1$ (F s^{a-1})	$\mathbf{a}_1$	$\mathbf{C}_2$ (F s^{a-1})	$\mathbf{a}_2$	$\mathbf{R}_0$ (Ωg)	$\mathbf{R}_1$ (Ωg)	$\mathbf{R}_2$(Ωg)	$\mathbf{A}_{W\,SILD}$
1	-	-	1.64E-4	0.6258	0.00202	0.9349	0.019	0.21	93.9	-
5	-	-	1.30E-4	0.6666	0.00196	0.9313	0.025	0.20	206.5	-
10	-	-	1.46E-4	0.6461	0.00190	0.9184	0.022	0.21	302.1	-
15	-	-	1.40E-4	0.6507	0.00190	0.9088	0.023	0.21	343.8	-
20	-	-	1.23E-4	0.6746	0.00194	0.9122	0.026	0.21	240.7	-
25	-	-	1.27E-4	0.6708	0.00179	0.8752	0.026	0.21	301.2	-
30	-	-	1.21E-4	0.6803	0.00171	0.8492	0.026	0.20	179.5	-
35	-	-	1.34E-4	0.6694	0.00145	0.8499	0.026	0.23	93.3	-
40	-	-	1.53E-4	0.6551	0.00127	0.9097	0.023	0.23	48.2	-
45	-	-	1.39E-4	0.6759	0.00115	0.9599	0.027	0.24	49.1	-
50	-	-	1.41E-4	0.6741	0.00111	0.9677	0.028	0.27	36.0	-
55	-	-	1.33E-4	0.6830	0.00113	0.9734	0.028	0.27	22.4	-
60	-	-	1.24E-4	0.6832	0.00112	0.9603	0.029	0.32	16.5	185.6
65	-	-	1.09E-4	0.6862	0.00117	0.9766	0.030	0.37	12.6	137.8
70	-	-	9.95E-5	0.6750	0.00117	0.9815	0.027	0.43	12.1	-
75	-	-	7.13E-5	0.6790	0.00115	0.9698	0.021	0.53	15.8	-
80	-	-	3.97E-5	0.7025	0.00107	0.9215	0.014	0.59	34.4	-
85	-	-	3.91E-5	0.7014	0.00107	0.8999	0.016	0.60	73.1	-
90	-	-	3.63E-5	0.7109	0.00107	0.8613	0.018	0.58	112.5	-

B.7 *Operando* XRD refinement results of P2-$Na_{2/3}Fe_{2/3}Mn_{1/3}O_2$

Table B.18: Refinement results of *operando* XRD results of O3-$Na_{2/3}Fe_{2/3}Mn_{1/3}O_2$. The 2D patterns are presented in Fig. 9.1 and these results are graphically presented in Fig. 9.3. Results from Le Bail refinements are presented.

Time (h)	$\mathbf{d_{P2}}$ (Å)	$\mathbf{b_{P2}}$ (Å)	$\mathbf{d_Z}$ (Å)	$\mathbf{b_Z}$ (Å)	**I** (a.u.)
0.248	5.607	2.938	-	-	1
0.744	5.628	2.933	-	-	1.02
1.240	5.641	2.928	-	-	1.06
1.736	5.653	2.925	-	-	1.09
2.232	5.664	2.921	-	-	1.13
2.728	5.673	2.919	-	-	1.15
3.224	5.681	2.916	-	-	1.19
3.721	5.690	2.913	-	-	1.23
4.216	5.697	2.911	-	-	1.27
4.713	5.703	2.909	-	-	1.30
5.209	5.704	2.907	-	-	1.24
5.705	5.696	2.906	-	-	1.08
6.201	5.693	2.887	5.349	2.887	0.94
6.697	5.691	2.888	5.306	2.888	0.81
7.193	5.696	2.892	5.250	2.892	0.70
7.689	-	-	5.171	2.901	0.60
8.185	-	-	5.148	2.896	0.54
8.681	-	-	5.153	2.891	0.50
9.178	-	-	5.173	2.899	0.52
9.674	-	-	5.199	2.899	0.48
10.170	-	-	5.249	2.899	0.54
10.666	-	-	5.274	2.896	0.54
11.162	-	-	5.327	2.889	0.58
11.658	5.624	2.918	5.365	2.918	0.66
12.154	5.598	2.925	5.370	2.925	0.72
12.650	5.597	2.930	5.372	2.930	0.81
13.145	5.608	2.934	5.378	2.934	0.89
13.643	5.615	2.935	5.378	2.935	0.95
14.139	5.611	2.939	-	-	0.97
14.635	5.601	2.942	-	-	0.98
15.131	5.586	2.948	-	-	0.95
15.627	5.568	2.954	-	-	0.89
16.123	5.560	2.959	-	-	0.85
16.619	5.539	2.964	-	-	0.82
17.115	5.519	2.975	-	-	0.81
17.612	5.519	2.972	-	-	0.80

C Contributions

Publications

- **Resolving the rate-dependant structure-electrochemistry relationships in P2-type and O3-type $Na_{2/3}Fe_{2/3}Mn_{1/3}O_2$ layered oxides.** Damian Goonetilleke, Begoña Silván, Elena Gonzalo, Damien Saurel, Montserrat Galceran, Montse Casas-Cabanas, François Fauth, Teófilo Rojo, Neeraj Sharmaa. *Under preparation.*

- **Importance of composite electrolyte processing to improve the kinetics and energy density of Li metal solid-state batteries.** Jakub Zagórski, Begoña Silván, Damien Saurel, Frédéric Aguesse, Anna Llordés. *ACS Applied Energy Materials, **3**(9), 8344-8355. 2020.* DOI: 10.1021/acsaem.0c00935

- **On the dynamics of transition metal migration and its impact on the performance of layered oxides for sodium-ion batteries: $NaFeO_2$ as a case study.** Begoña Silván, Elena Gonzalo, Lisa Djuandhi, Neeraj Sharma, François Fauth and Damien Saurel. *Journal of Materials Chemistry A, **6**, 15132-15146. 2018.* DOI: 10.1039/C8TA02473A

Conferences

- **Mechanistic Insight into the High Voltage Stability of Fe-Rich Transition Metal Layered Oxides As the Positive Electrode of Na-Ion Batteries.** Damien Saurel, Begoña Silván, Elena Gonzalo, Jian Xiang Lian, Javier Carrasco. *Pacific Rim Meeting, PRiME 2020.* Online event. 2020. Poster presentation.

- **On the reversibility of transition metal migration and its impact on the performance of layered oxides as cathode for sodium ion batteries.** Begoña Silván, Elena Gonzalo, Mario Valvo, Tore Ericsson, Lennart Häggström and Damien Saurel. *European Materials Research Society, Spring Meeting (E-MRS).* Nice, France. 2019. Oral presentation.

- **On the dynamics of transition metal migration and its impact on the performance of layered oxides for sodium-ion batteries: $NaFeO_2$ as a case study.** Begoña Silván, Elena Gonzalo, Lisa Djuandhi, Neeraj Sharma, François Fauth and Damien Saurel. *5th International Conference on Sodium Ion Batteries (ICNaB 2018).* Saint Malo, France. 2018. Poster presentation.

- **Study of transition metal migration in Fe rich layered oxides for Sodium Ion Batteries.** Begoña Silván, Elena Gonzalo, Lisa Djuandhi, Neeraj Sharma, François Fauth and Damien Saurel. *V Congreso Hispano-Luso de Cerámica y Vidrio / LVI Congreso Nacional de la SECV (VCHLCV).* Barcelona, Spain. 2018. Invited talk.

- **Study of transition metal migration in Fe rich layered oxides for Sodium Ion Batteries.** Begoña Silván, Elena Gonzalo, Lisa Djuandhi, Neeraj Sharma, François Fauth and Damien Saurel. *I Jornada de Jóvenes Investigadores de Cerámica y Vidrio en el ICMA (IJJICV-ICMA).* Zaragoza, Spain. 2018. Oral presentation, best SECV communication award.

- **Improving the stability of Fe rich layered oxides for Sodium Ion batteries.** Begoña Silván, Elena Gonzalo, Brahim Orayech and Damien Saurel. *XXXVIII Reunión del Grupo de Electroquímica de la Real Sociedad Española de Química y XIX Encontro Ibérico de Electroquímica (XXXVIII RGRSEQ).* Vitoria-Gasteiz, Spain. 2017. Oral presentation.

- **Improving the stability of Fe rich layered oxides for Sodium Ion batteries.** Begoña Silván, Elena Gonzalo, Brahim Orayech and Damien Saurel. *Power Our Future (POF).* Vitoria-Gasteiz, Spain. 2017. Poster presentation.

- **Improving the stability of Fe rich layered oxides for Sodium Ion Batteries.** Begoña Silván, Elena Gonzalo, Brahim Orayech and Damien Saurel. *Lithium Batery Discussions (LiBD 2017).* Arcachon, France. 2017. Oral and poster presentation.